

# World Renewable Energy Congress – Sweden

8–13 May, 2011  
Linköping, Sweden

Editor

Professor Bahram Moshfegh

## Copyright

The publishers will keep this document online on the Internet – or its possible replacement – from the date of publication barring exceptional circumstances.

The online availability of the document implies permanent permission for anyone to read, to download, or to print out single copies for his/her own use and to use it unchanged for non-commercial research and educational purposes. Subsequent transfers of copyright cannot revoke this permission. All other uses of the document are conditional upon the consent of the copyright owner. The publisher has taken technical and administrative measures to assure authenticity, security and accessibility.

According to intellectual property law, the author has the right to be mentioned when his/her work is accessed as described above and to be protected against infringement.

For additional information about Linköping University Electronic Press and its procedures for publication and for assurance of document integrity, please refer to its www home page: <http://www.ep.liu.se/>.

Linköping Electronic Conference Proceedings, 57  
Linköping University Electronic Press  
Linköping, Sweden, 2011

[http://www.ep.liu.se/ecp\\_home/index.en.aspx?issue=057](http://www.ep.liu.se/ecp_home/index.en.aspx?issue=057)  
ISBN: 978-91-7393-070-3  
ISSN 1650-3740 (online)  
ISSN 1650-3686 (print)

© The Authors

Volume 11

Photovoltaic Technology

## Table of Contents

<b>Impacts of CO<sub>2</sub> Emission Constraints on Penetration of Solar PV in the Bangladesh Power Sector</b> <i>Alam Hossain Mondal</i> .....	2698
<b>Comparing Push and Pull Measures for PV and Wind in Europe</b> <i>Ruben Laleman and Johan Albrecht</i> .....	2706
<b>Combined Solar Power and TPV</b> <i>Erik Dahlquist, Björn Karlsson and Eva Lindberg</i> .....	2714
<b>Comparative Performance of Various PV Technologies in Different Italian Locations</b> <i>A. Colli, M. Marzoli, W. Zaaiman, S. Guastella and W. Sparber</i> .....	2722
<b>An Investigation of the Impact of Time of Generation on Carbon Savings from PV Systems in Great Britain</b> <i>P. A. Burgess, M. M. Vahdati and D. Davies</i> .....	2730
<b>Concentrator Photovoltaic Technologies and Market: A Critical Review</b> <i>Alaeddine Mokri and Mahieddine Emziane</i> .....	2738
<b>Environmental Impacts of Large-Scale Grid-Connected Ground-Mounted PV Installations</b> <i>Antoine Beylot, Jérôme Payet, Clément Puech, Nadine Adra, Philippe Jacquin, Isabelle Blanc and Didier Beloin-Saint-Pierre</i> .....	2743
<b>Progress in Luminescent Solar Concentrator Research: Solar Energy for the Built Environment</b> <i>Paul P. C. Verbunt and Michael G. Debije</i> .....	2751
<b>Design and Simulation of a PV and a PV-Wind Standalone Energy System: A Case Study for a Household Application in Nicosia, Cyprus</b> <i>Gregoris Panayiotou, Soteris Kalogirou and Savvas Tassou</i> .....	2759
<b>High Efficiency Multijunction Tandem Solar Cells with Embedded Short-Period Superlattices</b> <i>Argyrios C. Varonides</i> .....	2767
<b>Simulations of Implantation Temperature Impact on Three-dimensional Texturing in Silicon Solar Cells</b> <i>F.Jahanshah, K. Sopian, S. H. Zaidi and E.Gholipour</i> .....	2774
<b>Development and New Application of Single-Crystal Silicon Solar Cells</b> <i>G. S. Khrypunov, V. R. Kopach, M. V. Kirichenko and R. V. Zaitsev</i> .....	2780
<b>Improvement of Solar Cells Efficiency and Radiation Stability by Deposition of Diamond-Like Carbon Films</b> <i>Nickolai I. Klyui, Anatoliy N. Lukyanov, Anatoliy V. Makarov, Volodymyr B. Lozinskii, Gennadiy S. Khrypunov and Andriy N. Klyui</i> .....	2787
<b>Formation of Transparent and Ohmic Nanostructure Thin Films of Fluorine-Doped Indium Oxide Prepared by Spray</b> <i>S. M. Rozati and Z. Bargbidi</i> .....	2795

<b>Research and Development of Dye-Sensitized Solar Cells in the Center for Molecular Devices: From Molecules to Modules</b> <i>Gerrit Boschloo, Anders Hagfeldt, Håkan Rensmo, Lars Kloo, Licheng Sun and Henrik Pettersson</i> .....	2800
<b>Studies of the Anionic Micelles Effect on Photogalvanic Cells for Solar Energy Conversion and Storage in Sodium Lauryl Sulphate-Safranine-D-Xylose System</b> <i>Prem Prakash Solanki and K M Gangotri</i> .....	2807
<b>New Cadmium Sulfide Nanomaterial for Heterogeneous Organic Photovoltaic Cells</b> <i>Jan Rohovec, Jana Tousekova, Jiri Tousek, Frantisek Schauer and Ivo Kuritka</i> .....	2815
<b>CdS Nanoparticles Surfactant Removal Transport Study by Transient Charge Measurements</b> <i>F. Schauer, V. Nadáždý, Š. Lányi, J. Rohovec, I. Kuřitka, J. Toušková and J. Toušek</i> .....	2823
<b>Charge Transient and Electrochemical Measurements as a Tool for Characterization and Degradation Study of Organic Semiconductors - PMPSis and MEH-PPV</b> <i>V. Nadáždý, K. Gmucová, Š. Lányi, F. Schauer and I. Kuřitka</i> .....	2830
<b>Fabrication of Annealing-Free High Efficiency and Large Area Polymer Solar Cells by Roller Painting Process</b> <i>Jae Woong Jung and Won Ho Jo</i> .....	2838
<b>Bi-Layer GaOHPc:PCBM/P3HT:PCBM Organic Solar Cell</b> <i>I. Kaulachs, I. Muzikante, L. Gerca, G. Shlihta, P. Shipkovs, G. Kashkarova, M. Roze, J. Kalnachs, A. Murashov and G. Rozite</i> .....	2846
<b>Pulse and Direct Current Electrodeposition of Zinc Oxide Layers for Solar Cells with Extra Thin Absorbers</b> <i>G. Khrypunov, N. Klochko, N. Volkova, V. Kopach, V. Lyubov and K. Klepikova</i> .....	2853
<b>Rope-Pump System Modelling using Renewable Power Combinations</b> <i>Cai Williams, Andrew Beattie, Tim Parker, Jo Read and Julian D. Booker</i> .....	2861
<b>Machine Learning Approach for Next Day Energy Production Forecasting in Grid Connected Photovoltaic Plants</b> <i>L. Mora-López, I. Martínez-Marchena, M. Piliougine and M. Sidrach-deCardona</i> .....	2869
<b>PSpice Model for Optimization of battery Charging using Maximum power point Tracker</b> <i>Fahim Ansari, Anis Afzal, S. Chatterji, Atif Iqbal, N. K Nautiyal and Padmanabh Thakur</i> .....	2875
<b>Photovoltaic for Rural Development: A Study of Policy Impact and Scope of Market Development in South Asian Region</b> <i>Siddha Mahajan and Shirish Garud</i> .....	2883
<b>Case Study: Modelling and Sizing Stand-Alone PV Systems for Powering Mobile Phone Stations in Libya</b> <i>Salem Ghozzi and Khamid Mahkamov</i> .....	2891

<b>Designing a Photovoltaic Solar Energy System for a Commercial Building. Case Study: Rosa Park Hotel in Khartoum-Sudan</b> <i>Asim M. Widatalla and Heimo Zinko</i> .....	2899
<b>Analytical Model and Experimental Validation of the Heat Transfer and the Induced Flow in a PV Cooling Duct in Environmental Conditions</b> <i>R. Mazón, A. S. Káiser, B. Zamora, J. R. García and F. Vera</i> .....	2907
<b>Design, Fabrication and Testing of Micro-Channel Solar Cell Thermal (MCSCT) Tiles in Indoor Condition</b> <i>Sanjay Agrawal, S. C. Solanki and G. N. Tiwari</i> .....	2916
<b>Using Structured Aluminum Reflectors in Flux Scattering on Module Performance</b> <i>Joseph Simfukwe, Sylvester Hatwaambo and Kabumbwe Hansingo</i> .....	2924
<b>Semi-Virtual Laboratory Design for Photovoltaic Generator Characterization Performance</b> <i>Hocine Belmili, Mourad Haddadi, Salah Med Aitcheikh and Ahmed Chikouche</i> .....	2930
<b>Two Phase Change Material with Different Closed Shape Fins in Building Integrated Photovoltaic System Temperature Regulation</b> <i>M. J. Huang</i> .....	2938
<b>Performance-Based Analysis of a Double-Receiver Photovoltaic System</b> <i>Alaeddine Mokri and Mahieddine Emziane</i> .....	2946
<b>Improving the Performance of Solar Panels by the Use of Phase-Change Materials</b> <i>Pascal Biwole, Pierre Eclache and Frederic Kuznik</i> .....	2953
<b>Assessing the Impact of Micro Generation in Radial Low Voltage Distribution Networks Taking into Consideration the Uncertainty</b> <i>Alvaro Gomes and Luís Pires</i> .....	2961
<b>Optimal Sizing of an Islanded Micro-Grid for an Area in North-West Iran Using Particle Swarm Optimization Based on Reliability Concept</b> <i>H. Hassanzadehfard, S.M.Moghaddas-Tafreshi and S.M.Hakimi</i> .....	2969
<b>Evaluation of the Solar Hybrid System for Rural Schools in Sabah, Malaysia</b> <i>Abdul Muhaimin Mahmud</i> .....	2977
<b>Analysis of Dust Losses in Photovoltaic Modules</b> <i>J. Zorrilla-Casanova, M. Piliougine, J. Carretero, P. Bernaola, P. Carpena, L. Mora-López and M. Sidrach-de-Cardona</i> .....	2985
<b>An Experimental Study of Combining a Photovoltaic System with a Heating System</b> <i>R. Hosseini, N. Hosseini and H. Khorasanizadeh</i> .....	2993

## Impacts of CO<sub>2</sub> emission constraints on penetration of solar PV in the Bangladesh power sector

Md. Alam Hossain Mondal<sup>1,\*</sup>

<sup>1</sup> Energy Institute, Atomic Energy Research Establishment (AERE), Ganakbari, Dhaka-1349, Bangladesh

\* Corresponding author. Tel: +88027790009, Fax: +88027789337, E-mail: alam\_90119@yahoo.com

---

**Abstract:** This paper examines the impacts of CO<sub>2</sub> emission reduction targets and carbon tax on future technologies selection especially solar PV and energy use in Bangladesh power sector during 2005-2035. It also examines the co-benefits of energy security of the country. The analyses are based on a long-term energy system optimization model of Bangladesh using the MARKAL framework. The results of the study show that on a base **scenario**, power generated from solar PV is not yet competitive with that of fossil fuel-based power plants. Alternative **policy scenarios** on CO<sub>2</sub> emission constraints reduce the burden of imported fuel, improve energy security and reduce environmental impacts. The results show that the introduction of the CO<sub>2</sub> emission reduction targets and carbon tax directly affect the shift of technologies from high carbon content fossil-based to low carbon content fossil-based and clean solar PV technologies compared to the base scenario. The cumulative net energy imports during 2005-2035 would be reduced in the range of 33-61% compared to the base scenario. The total primary energy requirement would be reduced in the range of 4.5-22.37% and the primary energy supply system would be diversified. Solar PV plays an important role in achieving reasonable energy security.

**Keywords:** Solar PV, CO<sub>2</sub> emission, MARKAL Model, Bangladesh Power Sector

---

### 1. Introduction

The future economic development of Bangladesh is likely to result in a rapid growth in the demand for energy with accompanying shortages and problems. The country has been facing a severe power crisis for about a decade. Known reserves (e.g., natural gas and coal) of commercial primary energy sources in Bangladesh are limited in comparison to the development needs of the country [1]. Power generation in the country is almost entirely dependent on fossil fuels, mainly natural gas that accounted for 81% of the total installed electricity generation capacity (5,719 MW) in 2009 [2]. Only about 42% of total population has been connected to electricity [3], with vast majority being deprived of a power supply. The government of Bangladesh has declared that it aims to provide electricity for all by the year 2020, although at present there is high unsatisfied demand for energy, which is growing by more than 8% annually [4, 5]. Coal is expected to be the main fuel for electricity generation. The government of Bangladesh has planned to generate 2,900 MW power from coal in the next 5 years [1], although coal power has adverse environmental effects and coal reserves are limited. The government has also focused on furnace-oil-based peaking power plants. As a result, the share of CO<sub>2</sub> emissions coming from fossil-fuel-based power plants in the national CO<sub>2</sub> inventory is expected to grow, and there is a growing dependency on imported fossil fuels for power generation. On the other hand, technical potential of grid-connected renewable energy technologies specifically solar PV to generate electricity is relatively very high in Bangladesh that is 10 times higher than present generation capacity [3]. Increasing the use of fossil fuels to meet the growing worldwide electricity demand, especially in developing countries, not only counteracts the need to prevent climate change globally but also has negative environmental effects locally. In Bangladesh, the power sector alone contributes 40% of the total CO<sub>2</sub> emissions [6, 7]. CO<sub>2</sub> is the principal greenhouse gas (GHG), produced mainly from the combustion of fossil fuels. Improved efficiency in the use of fossil fuels and increased use of renewable energy sources are among the most promising options for reducing CO<sub>2</sub> emission [8]. In this case, it is necessary to develop and promote alternative energy sources that ensure energy security of Bangladesh without increasing

environmental impacts. Since developing countries are not obliged to reduce GHG emissions, studies in evaluating the impacts or co-benefits of GHG mitigation policies in developing countries are lacking [9]. For a developing country like Bangladesh, the evaluation of the impacts of GHG mitigation policies in the power sector would provide a basis for more comprehensive technological choice, and economic and environmental analysis. Such an evaluation would also support climate change mitigation policies aimed on sustainable power-sector development as part of the efforts to address the climate change issues identified in the United Nations Framework Convention on Climate Change (UNFCCC) which Bangladesh has already ratified.

This study examines the future technologies selection applying CO<sub>2</sub> emission reduction targets and carbon tax in the Bangladesh power sector during 2005-2035. This study also analyzes the co-benefits on energy security of the country from the CO<sub>2</sub> emission constraints. A bottom-up least cost energy system optimization model of Bangladesh was developed on the market allocation (MARKAL) modeling framework and the following scenarios were considered:

- 1) Base scenario: It presumes a continuation of current energy and economic dynamics and provides a reference for comparing impacts of future policies.
- 2) 10% CO<sub>2</sub> emission reduction scenario (hereafter referred as “CO210”): It evaluates the effects of CO<sub>2</sub> emission reduction in the entire energy-supply system. The CO210 is the ‘what if’ scenario, in which a cumulative reduction of not less than 10% of the cumulative CO<sub>2</sub> emission during the planning horizon in the base scenario is desired, all other things remaining the same as in the base scenario.
- 3) 20% CO<sub>2</sub> emission reduction scenario (hereafter referred as “CO220”): The CO220 scenario is defined similarly for cumulative reduction in CO<sub>2</sub> emission of not less than 20% from the base scenario.
- 4) 2500 Taka/ton (1 USD = 70 Bangladeshi Taka) carbon tax scenario (hereafter referred as “CT2500”): The CT2500 is the ‘what if’ scenario, in which a carbon tax of 2500 Taka/ton is applied during the planning horizon in the base scenario.

## 2. MARKAL methodology

The MARKAL model mainly consists of the description of a large set of energy technologies, linked together by energy flows, jointly forming a reference energy system. The reference energy system is the structural backbone of MARKAL for any particular energy system and its great advantage is that it gives a graphic idea of the nature of the system. Another important characteristic of MARKAL is that it is driven by a set of demands for energy services. The feasible solutions are obtained only if all specified end-use demands for energy for all the periods are satisfied. The user exogenously supplies these demands in the model. Once the reference energy system has been specified, the model generates a set of equations that hold the system together. In addition, the MARKAL model possesses a clearly defined objective, which is usually chosen to be the long-term discounted cost of the energy system. The objective is optimized by running the model, which means that configuration of the reference energy system, is dynamically adjusted by MARKAL in such a way that all MARKAL equations are satisfied and the long-term discounted system cost is minimized. In this process the model computes a partial equilibrium of the energy system at all intermediate stages in all aspects e.g. flow conservation, demand satisfaction, capacity transfer, capacity utilization, source capacity, growth constraints, emission and other constraints.

### 3. The MARKAL Bangladesh model

#### 3.1. Reference energy system of Bangladesh power sector

For the purpose of this study, MARKAL-Bangladesh was developed. A major part of the work was to develop input parameter values. In MARKAL, the reference energy system is the first step towards building a model of the Bangladesh power sector (Fig. 1). The reference energy system represents the activities and technologies of an energy system, depicting energy demands, energy conversion technologies, fuel mixes, and the resources required to satisfy energy service demands [10]. The reference energy system is able to allocate energy sources for a given sectoral demand depending upon the efficiencies and other losses from the energy conversion device. The system does not provide any information about economics of a solution neither about the cost to the national economy for providing the energy supply. An optimized energy system can be obtained from the MARKAL model.

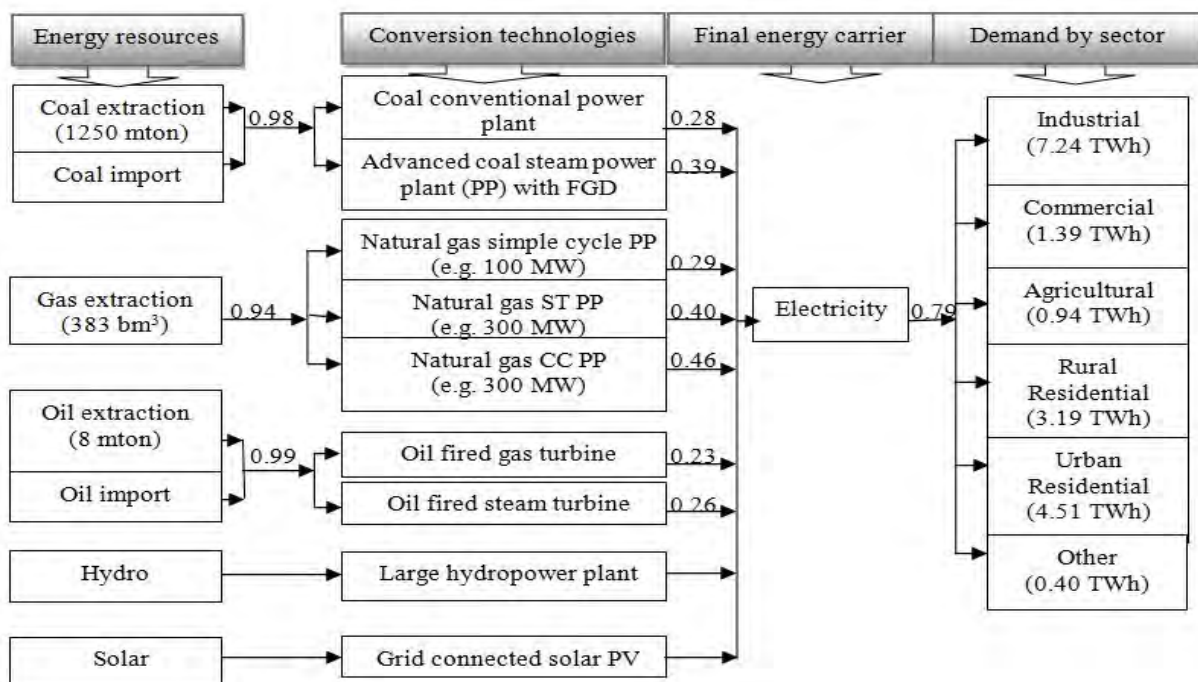


Fig 1. Simplified reference energy system of Bangladesh power sector

(Values shown indicate proven reserves, conversion & transmission efficiency, and demand in 2005)

(CC refers combined cycle, FGD refers flue gas desulphurization, mton refers million ton and bm<sup>3</sup> refers billion m<sup>3</sup>)

#### 3.2. Energy resources and emissions

The model requires that the cost of all primary energy sources be defined along with constraints on their availability. It is provided supply cost estimates and upper bounds on resource availability for fossil fuels and the maximum rates of introduction of solar PV and hydro are given in [1]. A limit on imported coal is not considered here. In mined coal, the average sulfur content is 0.57% and carbon 46.2% [11]. These values form the basis of the calculated emission coefficients used in this study. The IPCC (1996a) database is used for the CO<sub>2</sub> emission of imported coal. Due to different carbon content percentages in different gas fields in Bangladesh, the IPCC (1996a) emission factor is used in the model. CO<sub>2</sub> and SO<sub>2</sub> emission factors are calculated separately for diesel, kerosene and fuel oil products based on the IPCC workbook [12] and IPCC reference manual [13].

### 3.3. Energy demand

In 1994, the total electrical energy demand was 9.63 TWh and had increased to 17.64 TWh in 2005 [14]. The Long-range Energy Alternatives Planning (LEAP) tool was examined to form demand scenarios according to the trend of gross domestic product (GDP) growth rates (5.5%, 6.8% and 8%) and the nature of the energy sector itself, and taking into consideration broader factors, e.g., population, households, urbanization and other influencing factors for the time span 2005 to 2035. It is worth mentioning here that the actual GDP growth rate in Bangladesh is neither low nor high and therefore, in this study, the demand projection is based on a GDP growth rate of 6.8% is given in [15].

### 3.4. Conversion technologies<sup>1</sup>

The characteristics of all technologies must be provided to the model. Conversion technologies convert primary energy into final energy carriers. The model requires users to create detailed profiles for two sets of energy conversion technologies: one for converting primary into final energy carriers, and one for converting final energy carriers into energy services. A reasonably representative set of conversion technologies is developed, which includes a total of 9 distinct conversion technology types (coal steam conventional, advanced coal flue gas desulphurization (FGD) 300 M W, fuel oil-based steam, fuel oil-based gas turbine, gas-based simple cycle (SC) and steam turbine (ST), gas-based combined cycle (CC, hydro and solar PV). Other renewable energy technologies are not considered due to their limited technical potential to generate electricity [3]. For each of the technology types, values are specified for energy input per unit energy output (efficiency), capital cost, fixed and variable operation and maintenance costs, NO<sub>2</sub> and SO<sub>2</sub> emissions per unit of energy output, and the first year in which the technology was introduced. All costs are in Bangladesh Taka (1 USD = 70 Taka). The characteristics are performance and cost level inputs to the model for 2005-2035. For most of the technologies, the performance and cost levels are assumed to be constant over the whole analysis period except for solar PV, where the investment cost is expected to decrease by 3% annually [16] due to technological learning effects on solar PV cost after introduction in 2010. The model determines the capacity level for any technology. In this modeling, the most reliable studies are selected and evaluated to yield as consistent a set of cost data as possible.

### 3.5. Generic details

Besides the technical and financial parameters related to different stages of reference energy system of the Bangladesh power sector, the other parameters, assumptions and boundaries are also required by MARKAL which are discussed in [1].

## 4. Results

Under the base scenario, the total generation capacity is expected to increase from 5.56 GW in 2005 to 50.85 GW in 2035, i.e., at an average growth rate of 7.6%. At the same time, the generation structure changes significantly. The share of gas-fired power plants reduces from 86% (4.83 GW) in 2005 to 37.4% (19.04 GW) in 2035 in total capacity, whereas the increase in the capacity of coal-based power plants 0.25 GW in 2010 to 30.75 GW in 2035 (60.4% of total capacity) is extremely high. It is observed that coal is the dominant electricity generation technology in base scenario. In the base scenario, the advanced coal flue gas desulphurization (FGD) produces 32% of electricity in 2015 and 91% in 2035, due to unused capacity of oil-

---

<sup>1</sup> Cost data, technology selection and technology specification data mainly based on Bangladesh Power Sector Master Plan, Bangladesh Power Development Board and Ministry of Power, Energy and Mineral Resources.

based power plants and limited gas is mainly used in the early period (2005-2025). Hydro capacity reaches its allowed upper limit in the base scenario. Solar photovoltaic (PV) is not selected in the base scenario due to its high investment cost and low efficiency.

The switch from gas- to coal-based power plants leads to a strong increase in coal consumption (178 PJ in 2015 to 1913 PJ in 2035), i.e., at an average growth rate of 26%. This rate is higher than the domestic availability. Thus, the country would need to import energy resources such as coal from 2025 onwards to meet the required demand. The proportion of imported coal in the total fossil fuel consumption would increase substantially from 16% (187 PJ) in 2025 to 57% (1178 PJ) in 2035. This deficiency would have adverse impacts on the country's balance of payments and the availability of foreign currency resources.

The introduction of the CO<sub>2</sub> emission reduction targets and carbon tax scenarios (the CO<sub>2</sub> emission reduction of 10%, 20% and carbon tax 2500 Taka/ton are referred to hereafter as CO210, CO220 and CT2500, respectively) directly affects the shift of technologies from high carbon content fossil-based to low carbon content fossil-based and clean renewable energy-based solar PV technologies. As a result of emission constraints, power generation based on solar PV is introduced and its generation capacity gradually increases during 2010–2035. Compared to the base scenario, 15.12 G W, 34.92 G W and 40.62 G W solar PV-based generation capacities are additionally selected in 2035 in the CO210, CO220 and CT2500 scenarios, respectively. Solar PV generation starts with a capacity of 0.02 GW, 0.05 GW and 0.06 GW in 2010 in the CO210, CO220 and CT2500 scenarios, respectively and grows at a rate of 29.5% per year. The total generation capacity is expected to increase from 5.56 GW in 2005 to 65.72 GW, 86.15 GW and 91.23 GW in 2035 in the CO210, CO220 and CT2500 scenarios, respectively (Fig. 2). The generation capacity is relatively higher in the CO<sub>2</sub> emission constraint scenarios than in the base scenario due to implementation of a higher solar PV capacity, which generates electricity only during the day.

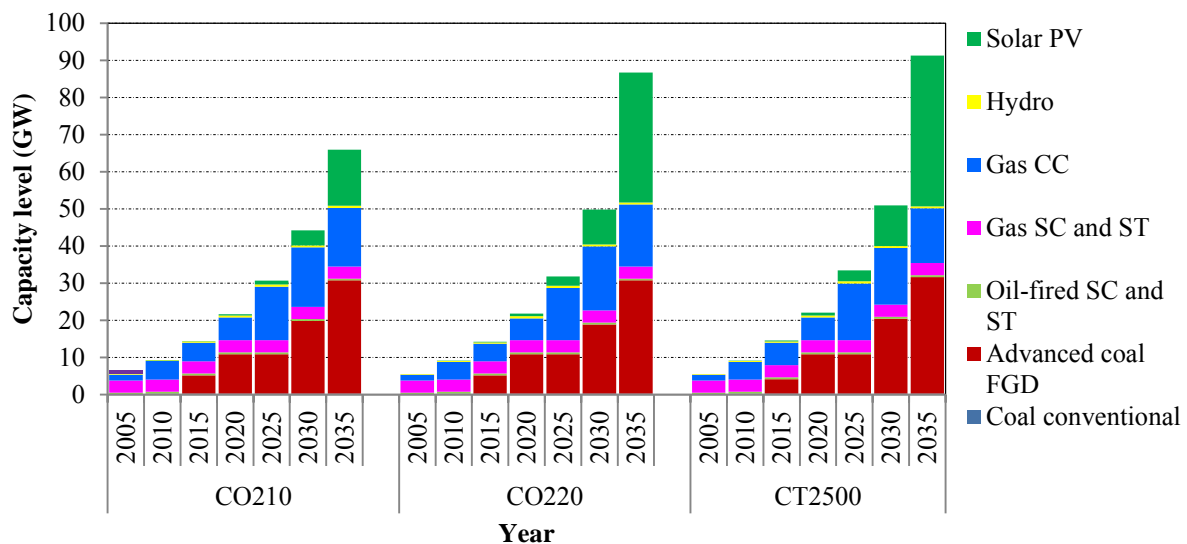


Fig 2. Technology capacity level in all CO<sub>2</sub> constraint scenarios

Gas-based combined cycle (CC) power plant capacity increases significantly in the later period (2020-2030) in all alternate scenarios compared to the base scenario. The model reveals that the least-cost solution is to use the limited gas reserves in the mid-term period, although the gas-based CC plants are mostly unused in the end period (2035). That is why the

power generation capacity based on coal FGD decreases significantly in the later period (2025-2030) in the CO<sub>2</sub> emission constraint scenarios compared to the base scenario. Due to high oil prices, oil-based power plants do not receive higher allocation in the CO<sub>2</sub> emission reduction targets and carbon tax scenarios. Gas-based simple cycle (SC) and steam turbine (ST) plants, coal conventional also do not get more allocation in the alternate scenarios. The capacity levels of hydro are the same in all scenarios. Coal FGD maintains the almost same capacity level in 2035 in all scenarios as gas resource is limited. Fossil fuel-based technologies would be required, as solar PV technology cannot cater for the entire future energy demand. The learning cost for solar PV enhances competitiveness of the technologies and leads to a higher rate of implementation of this technology in the analysis period.

To summarize the extensive results generated for each of the CO<sub>2</sub> emission reduction target and carbon tax scenarios by the MARKAL-Bangladesh model, the primary energy mix in 2035 is selected as the principal metric (Fig. 3). This provides a good indication of the types of choices made by the model to meet the various CO<sub>2</sub> emission constraints applied. The colored bars (except yellow in the middle) provide the breakdown of primary energy use for the base scenario in 2005 and all scenarios in 2035. The numbers above each bar indicate the total and percentage of the cumulative imported coal and the total cumulative and percentage of CO<sub>2</sub> emission reduction compared to the base scenario during the study period. Oil is not indicated, as it is not selected for power generation during the study period. The center yellow bar in the three scenarios on the right in this figure shows the change in cumulative total system cost relative to the base scenario. Due to the large uncertainties in this kind of analysis, the percentage change in system cost between the various scenarios as the measure of the cost impact of the changes imposed by each scenario is applied. The system cost for the base scenario is the reference cost in all cost comparisons.

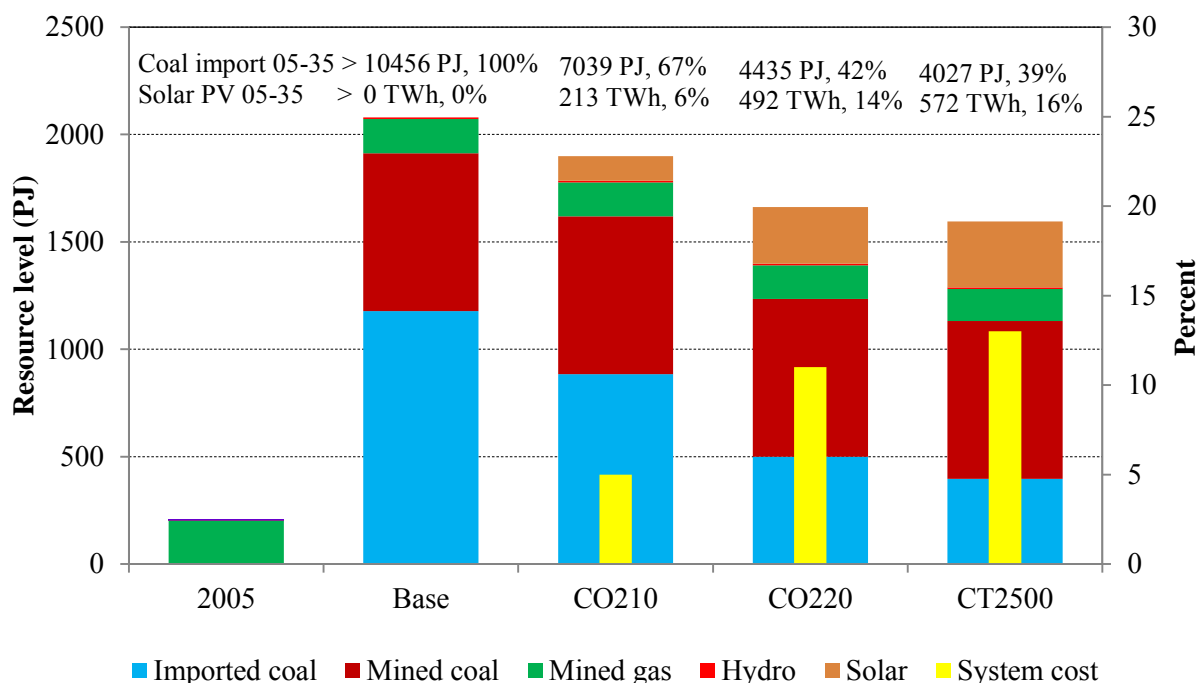


Fig 3. Primary energy mix in 2035 in all scenarios and percentage change in cumulative (2005-2035) system cost. Also indicated are the energy mix in 2005, the cumulative total and percentage of total imported coal, and the total electricity generation from solar PV.

CO<sub>2</sub> emission constraints have positive impacts on the energy security of the country. The energy security issue is analyzed in terms of changes in net energy import dependency and diversification of energy resources resulting from the selected CO<sub>2</sub> emission reduction targets and carbon tax. The CO210 scenario allowed a reduction in imported coal use of about 33% contributing an only 5% increase in system cost during 2005-2035. Import dependency reduces by 58%, and 61% in CO220 and CT2500 scenarios, respectively, compared to the base scenario during the study period, but led to an increase in the total system cost of 11% and 13%. Alternatively, import dependency based on the base scenario value 100%, drops to 67%, 42%, and 39% in the CO210, CO220 and CT2500 scenarios, respectively.

A reduction in the total primary energy requirement is another co-benefit of the CO<sub>2</sub> emission constraints. It is revealed that the total primary energy supply reduces by about 4.6%, 9.4% and 10.8% in the CO210, CO220 and CT2500 scenarios, respectively, during 2005-2035 as compared to the total primary energy supply in the base scenario due to efficient technology selection by the model. In the base scenario, primary energy use in 2035 is expected to be 2079 PJ, and reduces to 1595 PJ in the CT2500 scenario. Gas is the dominant energy source in 2005, and coal is dominant in all scenarios in 2035. Coal imports decrease from 1178 PJ in the base scenario to 884, 499 and 396 PJ (25%, 58% and 65%) in the CO210, CO220 and CT2500 scenarios in 2035, respectively. Solar energy use increases by 114 PJ, 263 PJ and 306 PJ in 2035 in the CO210, CO220 and CT2500 scenarios, respectively. In the base scenario, the expected electricity generation from solar PV is 0 TWh between 2005 and 2035; it is expected to increase by 213 TWh, 492 TWh and 572 TWh in the CO210, CO220 and CT2500 scenarios, respectively, during the study period.

## **5. Conclusions**

This paper has analyzed the effects of selected CO<sub>2</sub> emission reduction targets and carbon tax on environmental emissions as well as energy technology and resource mix using the MARKAL model for Bangladesh power sector. It is observed that coal is the dominant electricity generation technology in all scenarios in the later period (2020-2035). In the later period, advanced coal FGD trends to be the first choice for Bangladesh. The introduction of the CO<sub>2</sub> emission constraints directly affects the shift of technologies from high carbon content fossil-based to low carbon content efficient fossil-based and clean solar PV-based technologies. Solar PV is an attractive technology in almost all alternate scenarios. It becomes more and more attractive with introduction of higher carbon tax and higher CO<sub>2</sub> emission reduction target.

The analysis results show that the degree of diversification in the total energy requirement would increase with the applied CO<sub>2</sub> emission constraints. The primary energy supply system would diversify from the one dominated by coal in the later period (2020-2035) to that involving a greater use of solar energy and gas under the selected emission reduction targets and carbon tax scenarios. The analysis results show that the primary energy requirement would decrease in the alternate scenarios. This would enhance the country's energy security.

Furthermore, the results show that the increase in total system cost for reduction of cumulative CO<sub>2</sub> emissions over the study period is around 543 Taka/ton, 603 Taka/ton and 615 Taka/ton in the CO210, CO220 and CT2500 scenarios, respectively. These costs are much lower than those in developed countries, as the solar-PV-based power generation is relatively much cheaper in Bangladesh. It could thus be attractive for developed countries to invest in solar PV to generate electricity in Bangladesh to reduce their committed CO<sub>2</sub> emissions defined in the Kyoto Protocol through the "clean development mechanism (CDM)".

## References

- [1] M. A. H. Mondal, M. Denich, and P. L. G. Vlek, "The future choice of technologies and co-benefits of CO<sub>2</sub> emission reduction in Bangladesh power sector," *Energy*, vol. 35, pp. 4902-4909, 2010.
- [2] BPDB, "BPDB Annual Report 2008-09, Bangladesh Power Development Board, Dhaka - 1000, Bangladesh," 2009.
- [3] M. A. H. Mondal and M. Denich, "Assessment of renewable energy resources potential for electricity generation in Bangladesh," *Renewable & Sustainable Energy Reviews*, vol. 14, pp. 2401-2413, 2010.
- [4] A. H. Mondal and M. Denich, "Hybrid systems for decentralized power generation in Bangladesh," *Energy for Sustainable Development*, vol. 14, pp. 48-55, 2010.
- [5] M. A. H. Mondal, L. M. Kamp, and N. I. Pachova, "Drivers, barriers, and strategies for implementation of renewable energy technologies in rural areas in Bangladesh-An innovation system analysis," *Energy Policy*, vol. 38, pp. 4626-4634, Aug 2010.
- [6] ADB, "Asia Least-cost Greenhouse Gas Abatement Strategy (ALGAS) Bangladesh, Asian Development Bank," Manila, Philippines, p 1871998.
- [7] R. M. Shrestha, G. Anandarajah, and M. H. Liyanage, "Factors affecting CO<sub>2</sub> emission from the power sector of selected countries in Asia and the Pacific," *Energy Policy*, vol. 37, pp. 2375-2384, Jun 2009.
- [8] G. Dutt and F. Glioli, "Coping with Climate Change," in *Economic and Political Weekly*, October 20, 2007 2007, pp. 4239-4250.
- [9] R. M. Shrestha and S. Pradhan, "Co-benefits of CO<sub>2</sub> emission reduction in a developing country," *Energy Policy*, vol. 38, pp. 2586-2597, 2010.
- [10] J. Mathur, N. K. Bansal, and H. J. Wagner, "Investigation of greenhouse gas reduction potential and change in technological selection in Indian power sector," *Energy Policy*, vol. 31, pp. 1235-1244, Sep 2003.
- [11] B. Imam, *Energy Resources of Bangladesh*. Dhaka: University Grants Commission of Bangladesh, 2005.
- [12] IPCC, "Revised 1996 IPCC Guidelines for National Greenhouse Gas Inventories: Workbook (Volume 2), Intergovernmental Panel on Climate Change," 1996a.
- [13] IPCC, "Revised 1996 IPCC Guidelines for National Greenhouse Gas Inventories: Reference Manual, Intergovernmental Panel on Climate Change," 1996b.
- [14] PSMP, "Power Sector Master Plan Update, Power Cell, Power Division, Ministry of Power, Energy and Mineral Resources, Dhaka, Bangladesh, p 180," 2005.
- [15] M. A. H. Mondal, W. Boie, and M. Denich, "Future demand scenarios of Bangladesh power sector," *Energy Policy*, vol. 38, pp. 7416-7426, 2010.
- [16] S. Messner, "Endogenized technological learning in an energy systems model," *Journal of Evolutionary Economics*, vol. 7, pp. 291-313, Sep 1997.

## Comparing push and pull measures for PV and wind in Europe

Ruben Laleman<sup>1\*</sup>, Johan Albrecht<sup>1</sup>

*1 Ghent University, Faculty of Economics and Business administration, Ghent, Belgium*

*\*corresponding author. Tel: +32 92644209, E-mail: [ruben.laleman@ugent.be](mailto:ruben.laleman@ugent.be)*

---

**Abstract:** Successful technological innovation frameworks are based on synergistic packages of technology-push and demand-pull measures. As the massive deployment of premature renewable energy technologies risks becoming very expensive, the debate on the optimal trajectory of renewable technologies should explicitly consider the balance between deployment incentives and R&D efforts.

This paper explores this balance regarding wind and PV technology support in Europe. Based on rather conservative estimates, we calculate future deployment costs and compare these figures to the current public investments in PV and wind R&D. We find that, today, for each Euro spent on R&D to develop future technologies, 35 to 41 Euros are spent on the deployment of existing technologies. Furthermore, private PV and wind technology companies tend to underinvest in R&D for various reasons. In an alternative scenario, we assess the optimal R&D efforts for the PV and wind sectors based on a 7% R&D-to-sales benchmark that is typical for engineering sectors. If public R&D efforts would increase according to this benchmark, and hence compensate for the private underinvestments in R&D, pull/push ratios between 6 and 8 could be achieved. This leads us to conclude that the current balance between deployment and R&D is far from optimal.

**Keywords:** *Wind energy, PV-systems, Energy policy, Research and Development, Deployment subsidies*

---

### 1. Introduction

Climate and energy policies need to address at least two well-known market failures (1). Without a direct price on negative externalities such as CO<sub>2</sub> emissions, welfare losses will persist because economic agents lack incentives to invest in CO<sub>2</sub> abatement. In addition, private companies tend to underinvest in low carbon energy R&D. For both market failures, economists often advocate appropriate government interventions such as carbon pricing and comprehensive public R&D programs. This is essential in successful technological innovation frameworks, based on synergistic packages of technology-push and demand-pull measures (2) (3) (4) (5) (6). The high deployment cost of renewable technologies - especially of PV - attracts more and more attention in the largest European economies (7), also, R&D efforts are generally considered to be insufficient (8) (9). We argue that the debate on the optimal deployment trajectory for renewables should explicitly consider the balance between deployment incentives and R&D support. This paper aims to provide insight in the balance between wind and PV deployment and R&D efforts in Europe.

### 2. Methodology

#### 2.1. *Expected growth in wind and PV electricity production*

In order to estimate future costs we used two conservative scenarios (a moderate scenario and a policy driven scenario) on wind and PV electricity production up until 2020. These scenarios are based on reports by the European Photovoltaic Industry Association (EPIA) (10) and Tradewind (11) (Appendix, table 1-A). In the latter report we found projections of wind capacity growth (MW) which we then multiplied with full load hour data (FLH; [MWh/MW/y]) to estimate yearly wind electricity production. FLH data were calculated based on real production data for 2007 and 2008 by Eurobserv'er (12). We would like to point out that our FLH assumptions based on Eurobserv'er data are slightly lower than those based on EWEA (European Wind Energy Association) data (13). With respect to PV, the data on installed capacity (10) was multiplied with data on the yearly energy output [kWh/kWp/y]

obtained from PV-GIS Europe (Photovoltaic Geographical Information System) (14) to obtain estimates of total annual PV electricity production.

## 2.2. Current and future deployment costs

Current deployment costs in Euro/MWh are based on data by the European Renewable Energies Federation (EREF) (15). To estimate the further evolution of deployment costs, we follow the IEA (16) and assume that support schemes will be gradually phased out by 2020. Thus, we assume that PV-systems or wind turbines installed after December 31<sup>st</sup> 2019 no longer receive subsidies. For PV this assumption is a challenge, on-shore wind however is already competitive under optimal conditions. We are fully aware that the fading out of support schemes should not necessarily become a reality. This assumption however keeps the total deployment costs within a reasonable range. As a result, our calculations of the total deployment costs should be interpreted as very conservative. Based on existing schemes of Green Certificates or Feed-in Tariffs, the average production subsidies in the EU for PV and wind are estimated at respectively 326 €/MWh and 56 €/MWh in 2010. In practice, deployment subsidies vary significantly across Member States (15). We assumed that these support levels will decline steadily to be phased out by 2020 (Figure 1).

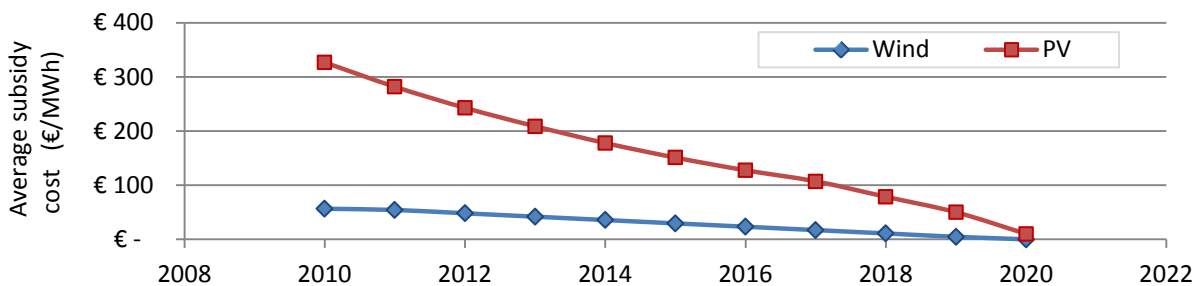


Fig. 1: Decline of average subsidies (€/MWh) for PV and wind electricity in the EU (based on(15))

In order to obtain total PV and wind deployment costs for each EU Member State, the estimated electricity production in a given year was multiplied with the corresponding production subsidy. In most countries the subsidies for PV electricity are guaranteed for 20-25 years, starting when the first MWh of electricity is produced. In this paper, a support period of 20 years was assumed for PV. Wind subsidies were assumed to be guaranteed for only 15 years. Note that these conservative assumptions on the duration of the guaranteed support have a huge impact on the total cumulative cost.

## 2.3. Research, development and demonstration

Public RD&D investment data from EU Member States were retrieved from the IEA RD&D database (17). Missing data from 2009 or 2008 were replaced by the most recent data available for a given Member State. For the alternative R&D scenario, R&D/sales ratios for PV and wind technology companies are compared to relevant benchmark values in competitive engineering sectors. As PV and wind technology companies have low R&D/sales ratios, an R&D-investment gap based on projected total sales for both technologies and the 7% R&D/sales benchmark of engineering sectors was calculated. As a matter of reference, we compare our investment gap estimates to investment needs obtained from recent IEA reports (8) (9). The methodology of the IEA is however fundamentally different since it uses a partial equilibrium model to find the cost-effective technology portfolios to halve global emissions by 2050. Nevertheless we believe it to be a good reference point in this framework.

### 3. Results and Discussion

#### 3.1. Expected growth in wind and PV electricity production

From our conservative scenarios we find that, by 2020, 102-159 TWh is estimated to be produced by PV-systems and 311-399 TWh by wind turbines, in the EU-27. Table 1 shows that our estimates of future electricity production are quite conservative when compared to the standard scenarios from EREC (18), EPIA (19), EWEA (13) and the EU (20). We opted for this approach to ensure that the cost estimates resulting from our scenarios (see below) are within reasonable range. Furthermore, the wide range of projections given in Table 1 illustrate that estimating future electricity production comes with great uncertainty.

Table 1: Estimated wind and PV electricity production and share in total demand in the EU by 2020

Technology		This Paper	EPIA (19)	EWEA (13)	EREC (18)	EU (20)
PV	Prod (TWh)	102-159	140-420		180	
	Share (%)	2.7-4.2	3.7-11.1		4.7	
Wind	Prod (TWh)	311-399		580-681	477	399-525
	Share (%)	8.2-10.5		15.3-17.9	12.6	10.5-13.8

Sources: (13) (20) (18) and (19); total electricity demand in 2020 is estimated to be 3795 TWh (20)

#### 3.2. Current and future deployment costs

Figure 2 shows the evolution of annual and cumulative PV and wind electricity subsidy costs in the EU-27 from 2007 until 2040 in a moderate (Mod) and a policy driven (PD) scenario. It is clear that PV subsidy costs will be much higher than wind subsidy costs, and (given the above mentioned assumptions) also last for a longer period. We find that annual subsidy costs for PV in the period 2020-2026 will be €18-26 Bio. Annual wind subsidy costs will rise up to € 6-9 Bio by 2020 and fade out by 2034. Total annual subsidy costs (PV + wind) will probably peak in 2020 and, depending on the scenario, could amount to €25-35 Bio in that year. The total nominal cumulative cost of wind and PV subsidies are estimated to reach around €471-661 Bio by 2040 for the whole of the EU-27.

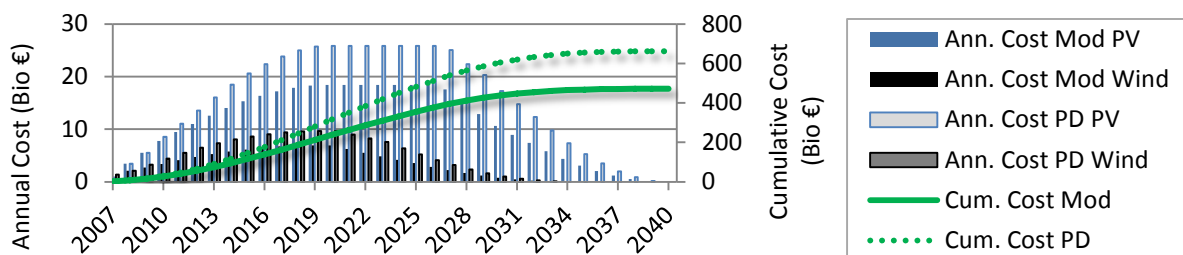


Fig. 2: Annual and cumulative deployment costs for PV and wind (based on (10), (11) and (15))

Table 2 illustrates that in 2020 the total average annual deployment cost per person (ADCPP) in Germany could reach € 156 in the policy driven scenario. These high costs are caused mainly by the high PV FIT's granted in Germany in the period 2007-2010, resulting in annual costs of €4-5 Bio by 2010 already. By 2020, annual PV deployment costs in Germany are estimated at €9-11 Bio, which is almost 50% of the total of EU-27 PV subsidy costs, and more than total annual wind subsidy costs for the whole of the EU. The data in Table 2 also indicates that countries that rely more on wind energy and invest little in PV will have fewer problems facing the subsidy costs. To illustrate this we compare the U.K. and the Czech Republic. Both are estimated to have a similar combined share of wind and PV in total electricity supply by 2020 (Wind and PV together account for 6-9% of total supply). The U.K.

will reach this primarily through the deployment of wind energy (wind shares of 5.2-8.5%), the Czech Republic, on the other hand will invest heavily in PV. Table 2 shows that this has major consequences for electricity consumers, with ADCPP by 2020 for the Czech electricity consumer of 72-115 € compared to only 13-22 € for the U.K. consumer.

Table 2: Average annual deployment cost per person (ADCPP) across member states in the year 2020

ADCPP (€)		DE	EL	CZ	BE	ES	IT	PT	BU	FR	UK
PV	Mod	105	36	71	48	76	43	22	18	16	4
(€)	PD	132	91	121	56	92	62	47	44	28	7
Wind	Mod	18	11	2	12	22	18	45	3	15	10
(€)	PD	24	18	7	19	27	25	48	4	20	15
Total	Mod	123	46	72	60	98	61	67	21	31	13
(€)	PD	156	109	128	75	119	88	94	48	48	22
PV/wind	Mod	5,95	3,30	42,61	3,91	3,54	2,44	0,49	6,91	1,05	0,41
	PD	5,56	5,18	16,46	2,92	3,39	2,44	0,97	10,9	1,38	0,48

(Based on data from (10), (11) and (15))

These figures do not reflect the net-cost for society since the production of renewable electricity avoids the production of fossil or nuclear electricity. More intermittent renewable electricity production will however imply significant additional grid investments. It is at this stage very speculative to derive the net-cost from the deployment cost between now and 2040. We can nevertheless assume that the cost increase to the average electricity consumer will be significant. Keep in mind that our calculations are restricted to PV and wind while most countries have regimes to support other renewable energy technologies as well. Adding for instance biomass or geothermal FIT's will further increase these costs.

### 3.3. Investments in Research, Development and Demonstration

#### 3.3.1. RD&D needs according to the IEA

The IEA (8) (9) (17) claims that global annual public RD&D budgets for wind and solar (PV + concentrated solar power + solar boilers) should be around USD 1800-3600 Mio, which is about a fivefold increase compared to current PV public RD&D investments and a tenfold increase in wind public RD&D. In line with these recommendations, we assume that current public RD&D budgets in the EU-27 should be 5 times higher in the case of PV and 10 times higher in the case wind. Given current EU-27 RD&D budgets for wind and PV of respectively € 136 Mio and € 184 Mio, the above mentioned assumption resulted in estimated annual RD&D needs for wind and PV in the EU-27 of €1360 Mio and €920 Mio respectively.

#### 3.3.2. Estimating optimal R&D expenditures

It is difficult to define the optimal R&D efforts for PV and wind technologies since these sectors are still in transformation and operate in an artificially protected and fully subsidized environment with production targets up to 2020. If the sectors would collectively agree not to innovate, they can continue to sell current technologies. Nemet (3), for example, has pointed out that demand-pull measures might negatively impact non-incremental technological change. In general, manufacturing firms in Korea and Canada spend about 5-6% of their turnover on R&D (21). Major consumer electronics firms that operate in competitive markets like Siemens, Samsung, Nokia, Sony and Robert Bosch spend about 6-10% of their sales on R&D (22). Based on the annual reports of the major international PV and wind companies however, we find that these companies invest on average only 2% of their sales in R&D. As

renewable energy companies are less R&D-intensive compared to comparable mature industries, we have strong indications of private underinvestment in renewable energy R&D.

To quantify this investment gap, we assume that the PV and wind industry should invest at least 7% of sales in R&D to replicate the average innovation dynamics of the engineering sectors. For this purpose we estimated total sales in the wind and PV sector between now and 2020. This was achieved by multiplying annual installed capacities with the cost per Watt. We assumed that wind energy investment costs would decline from 1.3 €/W in 2005 to 1 €/W in 2020. For PV we assumed a decline from 4 €/Wp in 2007 to 3.5 €/Wp in 2010 and 2 €/Wp in 2020 (cost estimates based on (11), (23), (24) and (25)). This resulted in fairly constant annual sales in the wind and PV industry between 2010 and 2020 (Fig. 3). Sales in wind are about 9 Bio/y in a moderate scenario and 14 Bio/y in a policy driven scenario. PV sales are higher, reaching around 30 Bio/y in a policy driven scenario and 18 Bio/y in a moderate scenario. If the public sector were to support the industry by funding R&D to obtain the 7% ratio, they would have to spend a complementary amount equal to 5% of sales (7% in total minus 2% private). Using this method we obtained “5% of sales” R&D estimates, which are much higher than current public RD&D investments in PV and wind (Table 3).

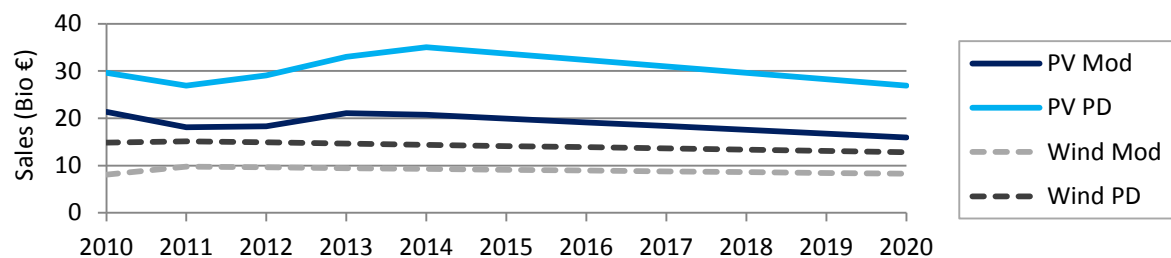


Fig. 3: Estimated annual sales for PV and wind in the EU-27 (based on (10) (11) (23) (24) & (25))

Table 3: Annual R&D gap as 5% of sales in the EU in the period 2010-2020

	Current EU public RD&D (€Mio)	Annual sales (€Mio)		R&D gap as 5% of sales (€Mio)	
		Mod	PD	Mod	PD
PV	184	18000	30000	900	1500
Wind	136	9000	14000	450	700

(Based on data from (17) and annual reports from the solar and wind industry)

### 3.4. Balancing push and pull measures

#### 3.4.1. Results

EU Member States have invested - and are likely to continue to invest - huge sums in demand-pull measures to stimulate the deployment of renewable technologies like PV and wind. When comparing these high costs to the low investments in RD&D supply-push measures, it appears that the budgets are not in balance. To obtain better insight in the imbalance between demand-pull and supply-push measures, we calculated a pull/push ratio under difference scenarios. Table 4 shows that the pull/push ratio would increase from 35-41 today to about 79-111 by 2020 if current RD&D budgets were to remain unchanged (baseline scenario). Such that by 2020, in a policy driven scenario, for every euro going to wind or PV RD&D, there are 111 euro's going to deployment subsidies. Wind and PV industries currently invest on average 2% of sales in R&D. Therefore, we believe that governments could support the industry by investing an amount equal to 5% of annual sales, such that a 7% sales/R&D ratio - common in engineering and electronics industry - would be achieved. This would result

in a significant decrease of the pull/push ratio from 35-41 (Baseline scenario) to 6-8 (“5% of sales” scenario) in 2010. Since in the “5% of sales” scenario R&D budgets evolve in line with annual sales, pull/push ratios are more flexible to changing market circumstances. Notice for example that the “5% of sales” pull/push ratio does not differ that much when comparing wind and PV, this in contrast to the other scenarios. The estimates of needed RD&D investments based on IEA suggestions result in pull/push ratios that are quite similar to the “5% of sales” ratio. However, the differences between the pull/push ratio for wind and PV are much bigger. Despite this fact, we are convinced that following the IEA’s advice would certainly be a step in the right direction.

Table 4: Comparison of Push and Pull measures for wind and PV in the EU in 2010 and 2020

		PV (€Bio/year)		Wind (€Bio/year)		Total (€Bio/year)	
		Mod	PD	Mod	PD	Mod	PD
Push	Baseline	0.184	0.184	0.136	0.136	0.32	0.32
	R&D 5% of annual sales	0.90	1.50	0.45	0.70	1.35	2.20
	IEA Annual RD&D needs	0.92	0.92	1.36	1.36	2.28	2.28
Pull	2010	7.77	8.57	3.37	4.43	11.1	13.0
	2020	18.4	25.6	6.95	9.67	25.4	35.5
Pull		pull/push		pull/push		pull/push	
2010	Baseline	42	47	25	33	35	41
	R&D 5% of annual sales	9	6	7	6	8	6
	IEA Annual RD&D needs	8	9	2	3	5	6
2020	Baseline	100	141	51	71	79	111
	R&D 5% of annual sales	20	17	15	14	19	16
	IEA Annual RD&D needs	20	28	5	7	11	16

(Based on (8), (9), (10), (11), (15), (17) and annual reports of solar and wind companies)

### 3.4.2. Sensitivity analysis and remarks

Many authors agree that governments should invest more in renewable R&D; however the “optimal” amount of R&D efforts is difficult to estimate. Fischer and Newell (26) search for optimal R&D subsidy levels using a theoretical model that optimizes renewable policies. They find that the optimal R&D subsidy should be equal to 6%, which is remarkably close to our empirically estimated value of 5%. Furthermore, the optimal public R&D estimates by the IEA are also quite comparable to our estimates. From this we can conclude that our estimated “5% of sales” public RD&D budget is in line with recent findings. Nevertheless, it is interesting to evaluate the effect of the “5% of sales” assumption on the overall results. Table 5 shows that adapting this assumption does have significant effects on the pull/push ratio. However, even the very conservative estimate of 2.5% results in pull push ratios that are smaller than currently found in the EU (namely 25-33 for wind and 42-47 for PV). The ratios rise by 2020 due to rising deployment costs, however not as dramatic as compared to the status quo scenario (see Table 4).

When interpreting these results one should keep in mind that, throughout this paper, we have always opted for the more conservative approach. For example, the growth of wind and PV electricity production is assumed to be moderate compared to other scenario’s (see Table 1). Also, the assumption that subsidies will gradually fade out by 2020 is a tentative one. To our knowledge, only a few governments have presented such decreasing policy schemes (for example Greece (15) and the region of Flanders). It remains to be seen whether or not this practice becomes widespread in Europe. Governments that do not reduce renewables support

over time will experience higher costs than the estimates mentioned above. If PV and wind electricity production were to grow at rates mentioned by the EWEA's 'high' scenario (13) or the EPIA's 'paradigm shift' scenario (19) costs will be much higher, resulting in even higher burdens on electricity consumers.

Table 5: Pull Push ratio under different assumptions on optimal public R&D budgets

Pull/Push year	R&D/Sales ratio	PV		Wind		Total	
		Mod	PD	Mod	PD	Mod	PD
2010	2.5% of annual sales	17	11	15	13	17	12
	7.5% of annual sales	6	4	5	4	6	4
2020	2.5% of annual sales	41	34	31	28	38	32
	7.5% of annual sales	14	11	10	9	13	11

#### 4. Conclusion

Despite the uncertainties surrounding the mechanisms behind technology support measures, it seems that a pull/push ratio of 40, estimated here, does not seem optimal. This ratio could increase up to 79-111 by 2020 if current policies were to remain in place. Overall, we can safely say that European governments should critically evaluate current renewables subsidy schemes, especially for PV systems, and raise public RD&D investments. These higher RD&D budgets could drive down production costs, which will result in a decreasing need for demand-pull measures in the longer run. Further efforts should be made to obtain more reliable and complete data on public and private RD&D expenditure and to improve our understanding on the interactions between demand-pull and supply-push policy measures, such that policy makers have the knowledge and the tools to bring new, promising technologies to the market in an effective and efficient manner.

#### References

- [1] R. G. Newell, The role of markets and policies in delivering innovation for climate change mitigation, Oxford Review of Economic Policy 26, 2010, pp. 253-269.
- [2] V. Norberg-Bohm, The role of government in energy technology innovation: insights for government policy in the energy sector, Harvard University, Belfer Center for Science and International Affairs, 2002.
- [3] G. F. Nemet, Demand-pull, technology-push, and government-led incentives for non-incremental technical change, Research Policy 38, 2009, pp. 700-709.
- [4] T. Jamasb, W. J. Nuttal, and M. Pollit, The case for a new energy research, development and promotion policy for the UK, Energy Policy 36, 2008, pp. 4610-4614.
- [5] P. H. Kobos, J. D. Erickson and T. E. Drennen, Technological learning and renewable energy costs: implications for US renewable energy policy, Energy Policy 34, 2006, pp. 1645-1658.
- [6] G. F. Nemet and E. Baker, Demand subsidies versus R&D: Comparing the uncertain impacts of policy on a pre-commercial low-carbon energy technology, The Energy Journal 30, 2009, pp. 49-80.
- [7] M. Frondel, N. Ritter and C. M. Schmidt, Germany's solar cell promotion: Dark clouds on the horizon, Energy Policy 36, 2008, pp. 4198-4204.
- [8] IEA, Global gaps in clean energy R&D, International Energy Agency, 2010.

- [9] IEA, Global gaps in clean energy research, development and demonstration, International Energy Agency, 2009.
- [10] EPIA, Global Market outlook for photovoltaics until 2014, European Photovoltaic Industry Association, 2010.
- [11] Tradewind, Integrating Wind, 2009.
- [12] Euroserv'er, State of renewable energy in Europe, 2009.
- [13] EWEA, Pure power, wind energy targets up to 2020 and 2030, 2009.
- [14] M. Šúri, T. A. Huld, E. D. Dunlop and H. A. Ossenbrink, Potential of solar electricity generation in the European Union member states and candidate countries, *Solar Energy* 81, 2007, pp. 1295-1305.
- [15] EREF, Prices of renewable energies in Europe, European Renewable Energies Federation, 2009.
- [16] IEA, Energy Technology Perspectives 2010, International Energy Agency, 2010.
- [17] IEA, RD&D statistics [accessed 28 October 2010] <<http://www.iea.org/stats/rd.asp>>
- [18] European Commission, EU energy trends to 2030, 2010.
- [19] EREC, RE-thinking 2050, European Renewable Energy Council, 2010.
- [20] EPIA, Set for 2020, European Photovoltaic Industry Association, 2010.
- [21] OECD, Measuring Innovation: a new perspective, 2010.
- [22] National Science Board, Science and engineering indicators 2010, 2010. [accessed 25 November 2010] <<http://www.nsf.gov/statistics/seind10/c/cs1.htm>>
- [23] EWEA, Wind energy the facts, 2010. [accessed 5 December 2010] <<http://www.wind-energy-the-facts.org/documents/download/Chapter3.pdf>>
- [24] EPIA, Solar Generation 6, 2010. [accessed 25 November 2010] <<http://www.epia.org/publications/epia-publications.html>>
- [25] IEA, Technology Roadmap: Solar Photovoltaic Technology, 2010. [accessed 5 December 2010] <[http://www.iea.org/papers/2010/pv\\_roadmap.pdf](http://www.iea.org/papers/2010/pv_roadmap.pdf)>
- [26] R.G. Newell and C. Fischer, Environmental and technology policies for climate mitigation, *Journal of Environmental Economics and Management* 55, 2008, pp. 142-162

## Combined solar power and TPV

Erik Dahlquist<sup>1,\*</sup>, Björn Karlsson<sup>1</sup>, Eva Lindberg<sup>2</sup>,

<sup>1</sup> Malardalen University, Box 883, 721 23 Vasteras, Sweden, <sup>2</sup> Dalarna University College, Borlänge, Sweden.

Corresponding author: tel + 46-21-151768, fax +46-21-101370, erik.dahlquist@mdh.se,

---

**Abstract:** In this paper design for a combined TPV and solar power system for local heat and power production is discussed. PV cells are producing electricity when there is light, while TPV cells are used when it is dark. Biomass is combusted and the heat is generating photons for the TPV system. Higher combustion temperature will give higher electric output, but also faster deterioration of the materials in the combustor, where the temperature of the emitter is 1050-1250 °C. By combining PV-cells generating electric power summer time with TPV-cells generating electric power winter time, we can achieve a flexible local heat and power system all year round. As both systems generate DC-power, we also can see a potential to use the same DC components for e.g for charging batteries for electrical vehicles, DC-pumps, LED-lamps etc. Design criteria for the systems are discussed in this paper for a house that is principally self sufficient on energy. Both theoretical and practical obstacles are discussed, as there are a number of issues to solve before the technique can be used in "real life". The TPV system is not yet commercially available, but is tested in pilot scale.

**Keywords:** Solar power, TPV, combination, heat, electricity

---

### 1. Introduction

There will be a shortage of fossil fuels in the future and thus renewable energy like solar power and biomass will be interesting alternatives. One type of solar power is PV-cells, although there are other alternatives like Stirling engines, organic ranking cycles and even steam turbines when the sunshine is concentrated to heat an organic solvent or water/steam to high temperatures.

In this paper we are concentrating on the combination of PV-cells and TPV-cells, where the principles are to convert photons into electric power directly. In the PV-cells the photons are in the range 0.4- 0.8  $\mu\text{m}$  mostly, while in TPV cells we extend the wave lengths up to approximately 1.9  $\mu\text{m}$ . The advantage with a combination of PV and TPV cells is that we will consume no fuel during spring to autumn periods, but still can produce both heat and power when there is no or little light. At the same time we can use the same infrastructure with respect to DC-current and lower voltage than the normal 220 V in Europe. In this way we can be both self-producing all electric power needed without having to store electricity in batteries. The cost to store biomass is radically lower than the cost for storage in the batteries, and thus makes sense.

### 2. Conversion of biomass to heat and electric power using TPV

The combustion unit can be a conventional boiler extended with a TPV-unit where heat and electricity are produced simultaneously. The principles for a TPV unit developed by Malardalen University together with Dalarna university college in Borlange is principally making use of photons produced by combustion flames heating a steel plate, the emitter [1],[2],[3] and [4]. The photons produced are then filtered in an energy glass, and thereby only the energy rich ones hit a PV-cell, but with a slightly lower band gap than normal PV-cells. The cut off wave length and correspondingly band gap are seen in table 1 for different materials. Silica (Si) with a cut off at 1.1  $\mu\text{m}$  is good for visible light but not for longer wave length. GaSb and InGaAs are better giving cut offs suitable for TPV cells.

Table 1. Cut off and threshold energy for different materials

	Cut off wave length	Band gap
Si:	1.1 $\mu$ m	1.12eV
GaSb:	1.7 $\mu$ m	0.72eV
InGaAs	2.3 $\mu$ m	0.55eV
InGaAsSb	2.4 $\mu$ m	0.53eV

The cut-off here means that photons with a wave length higher than the cut-off are filtered off, while those with short wave lengths are passing through the glass to the PV-cell. The data are from [5]. By this the same amount of electricity can be produced with a surface area 100 times smaller than for conventional PV-cells. This means that the power output could be around 10 kW per m<sup>2</sup>, compared to some 0,1 kW/m<sup>2</sup> for typical solar PV cells. As the TPV system can operate whenever you have a need, it can be used even when it is dark and in that way be acting as a back-up system for "normal" PV cells.

Biomass can have many different origins. It can be biogas produced from household waste or crop waste like straw. The gas then will be mainly methane, which is the same fuel as if we use fossil "natural gas". The biomass could also be produced from different algae specie, where the production will depend on the actual sun intensity, nutrients and temperature. Of course the technology can also be used for fossil fuels like oil, but that is from our perspective not interesting long term. Typical values of solar intensity at different places in Europe are seen in figure 1 below.

As can be seen the irradiation is approximately 8 kWh/m<sup>2</sup>,day summertime at all sites, while only less than 1 kWh/m<sup>2</sup>,day during December- January. We can assume that the growth rate for biomass is in the range 0.5 % to at best 5 % of the incoming sun light, which means 0.04-0.4 kWh/m<sup>2</sup>,day summer time and 0.005 – 0.05 kWh/m<sup>2</sup>,day winter time. The heat demand winter time would be some 0.5 – 240 kWh<sub>th</sub>/d in single houses depending on the house type, and to this we can add an electricity demand for the house hold use of approximately 5 kWh<sub>el</sub>/d for low consumers up to 40-50 kWh<sub>el</sub>/d for high consumers. [6]. The lower heat demand is for modern "passive" houses while the higher values are for houses older than some 40 years and not retrofitted to modern standard.

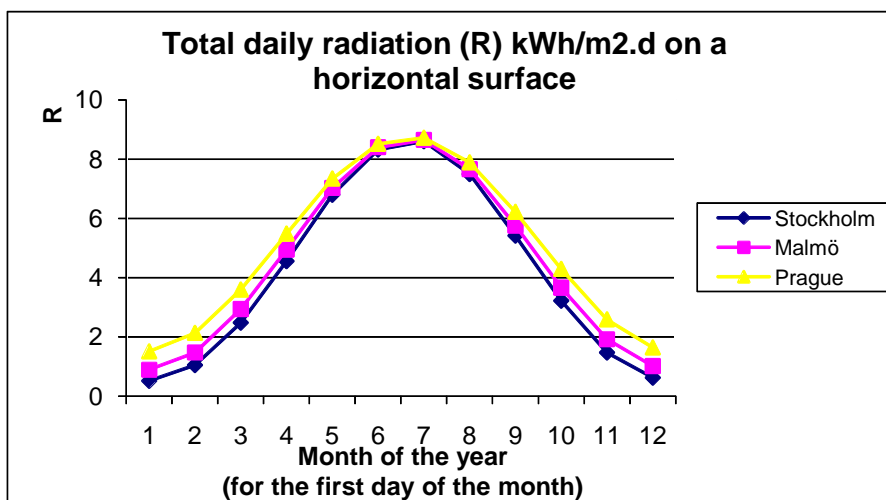


Figure 1 The total daily radiation by the sun on a horizontal surface in Stockholm, Malmo and Prague

The cells in the small pilot plant we have developed consist of 21 cells in three lines with 7 cells in each. The total surface area is 40 cm<sup>2</sup>. The cells are from JX Crystals. The cells are mounted on a surface with water cooling, to keep the cell temperature below 50 °C. Different emitter materials were tested, but normal black iron actually turned out to be as efficient as more advanced materials. The reflectors were made of vacuum formed aluminium that was electro polished to get good reflectance properties. We had different type of edge filters. There was one specially designed glass surface, but it turned out that a normal energy glass was good enough. This simple pilot module thus was used in the tests performed and described below.

The heat source was an electrical furnace from Kanthal. This was a stable heat source which was easy to control. The experiments were made as seen in figure 2 below.

At the bottom we have the electric furnace, above the emitter and the reflecting cones. The glass edge filter was mounted between the two Aluminium cones as seen in figure 2. At the top are the cooled TPV-cells. The actual experimental set up is seen at the photo to the right, where also two of the authors (Eva Lindberg and Erik Dahlquist) are seen aside of Svante Nordlander.

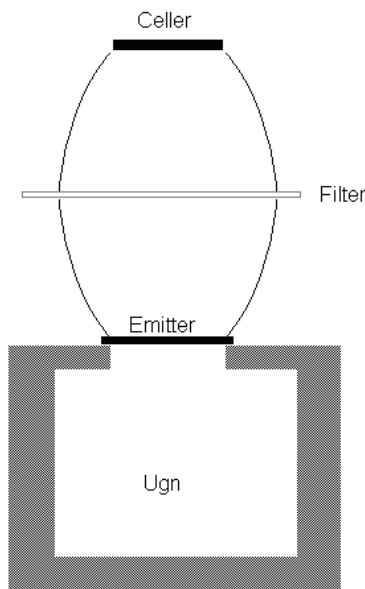


Figure 2. The experiment set up with the pilot TPV unit.

The efficiency calculations were made using the following formulas:

For the first experiment the efficiency was calculated according to equation (1)

$$\eta_1 = (P_c / A_c) / G \quad (1)$$

$P_c$  = Electric power of the TPV cells [W]

$A_c$  = Cell area [m<sup>2</sup>]

$G$  = Irradiation intensity at the plane of the cells [W/m<sup>2</sup>]

For the second experiment equation (2) was used for the efficiency calculation:

$$\eta_2 = (P_c / A_c) / E_u \quad (2)$$

$E_u$  [ $W/m^2$ ] is the irradiation power per area unit from the emitter and is calculated from equation (3).

$$E_u = \varepsilon \sigma T_e^4 \quad (3)$$

$\varepsilon$  =emissivity [-]

$\sigma$  =Stefan-Boltzmanns constant =  $5,66697 \cdot 10^{-8}$  [ $W/(m^2K^4)$ ]

$T_e$  =Emitter temperature [K]

Equation (3) also was used for the efficiency calculation in experiment 3. In figure 3 we see the results from experiment 1, where the effect of water cooling of the TPV cells was studied. As seen the water cooling of the cells gives a very strong impact on the cell performance. The efficiency calculations according to equation (1) was 4,8 % at  $1950 W/m^2$  and 8,7 % at  $3000 W/m^2$ .

$$\eta_3 = (P_c / A_c) / (\gamma E_u)$$

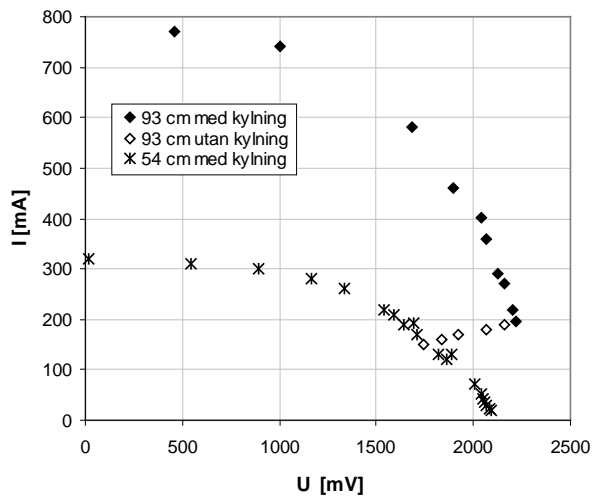


Figure 3. Results from experiment 1. Current – voltage curve for water cooled GaSb-cells irradiated with a halogen lamp at  $1950 W/m^2$  (93 cm) and ca  $3000 W/m^2$  (54 cm). The black prisms are with water cooling at 93 cm distance, the uncoloured prisms the same without cooling and the crosses at 54 cm distance with cooling.

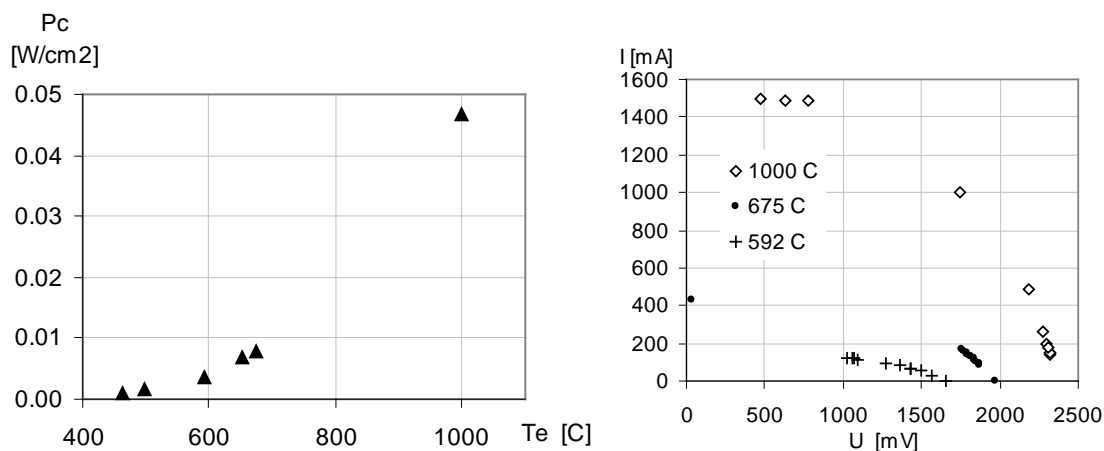


Figure 4. Power output as a function of the emitter temperature and current – voltage plot for different emitter temperatures.

In figure 4 we see the power output as a function of the emitter temperature. The average fill factor for the experiments was 0.6 calculated by the formula  $\text{Fill factor} = \text{MPP}/(I_{\text{SC}} \times U_{\text{OC}})$ . Still, the spreading was relatively high as it was a bit difficult to measure the short cut current  $I_{\text{SC}}$  and the voltage at open circuit  $U_{\text{OC}}$  as well as the maximum power point MPP.

In figure 5 we see the current- voltage plots for emitter temperatures up to 1200 °C.

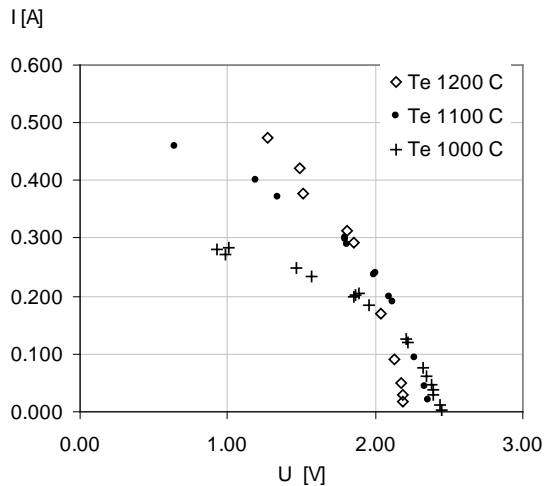


Figure 5. Current – emitter plot for higher emitter temperatures.

These higher emitter temperatures were tested in a special high temperature electric furnace from Kanthal which could be kept at constant temperatures up to 1700 °C. Still, it was not that easy to perform the actual measurements at the very high temperatures, so in practice we stopped at 1200 °C. These were the experiment 3 tests. In this last experiment we also tested the impact of the cones and the energy glass. The outcome can be seen in figure 6 below.

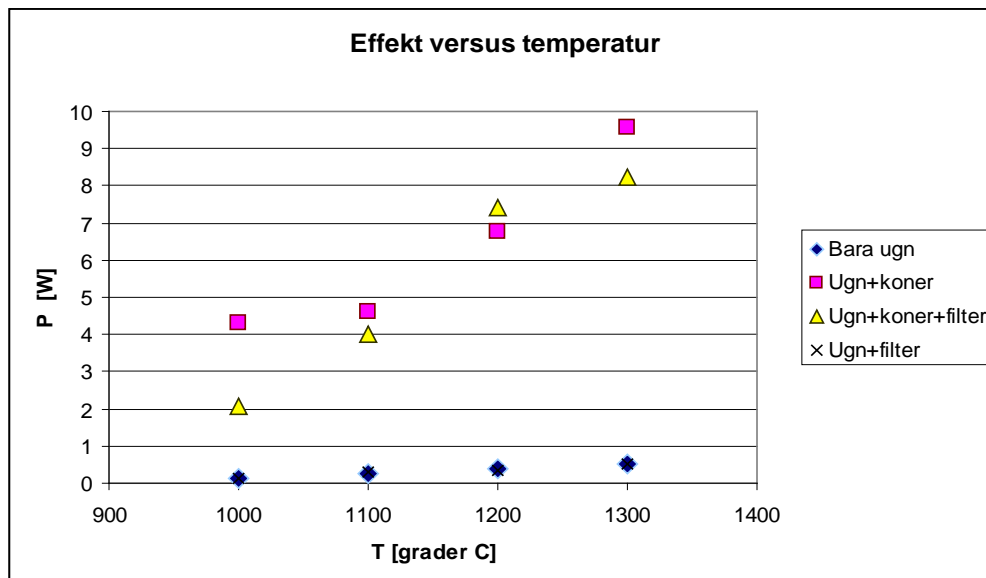


Figure 6. The power output from the TPV cells. At bottom (dark prisma) with radiation from furnace directly towards the TPV cell, (pink squares) furnace + reflecting cones and (yellow triangles) furnace, reflecting cones and edge filter using a standard energy glass.

At the bottom in figure 6 we see the power output when we only had the irradiation directly towards the cells placed at a distance corresponding to one cone. The squares are for furnace plus one reflector cone, but with no edge filter. Finally the triangles are for the two reflector cones with an energy glass in-between as seen in figure 2. The electric efficiency from fuel heating value to electricity production is going from around 0.5 % to 4- 5 % in the <1 kW<sub>thermal</sub> pilot plant tested. As we can see the reflector cones give a strong impact, and the two cones + an edge filter glass does not give significantly lower power output than with only one cone. Still, with two cones plus the glass we can have a long term good performance, which would not be possible without the energy glass, as the TPV cell would become too hot and deteriorate. The temperature drop in the combustion gases due to the TPV was negligible. By having a larger emitter and TPV area the electric output in relation to the heating value of the fuel can be increased. By this the efficiency as electricity divided by fuel heating value could be up towards 20%. Still, this also mean an increased cost for the TPV module. It should also be noticed that the remaining heat can be used to both heating water or drive an absorption cooling machine.

### **3. System aspects considering the demand and production capability of energy in detached houses.**

The lowest heating demand is in so called passive houses that only utilize the heat from appliances and human bodies (approximately 100 W per person). If we should produce all electricity by TPV cells (5% efficiency) this means a fuel demand around  $(5 \text{ kWh/d}) / (0,05) = 100 \text{ kWh fuel/day}$ . For a four times larger TPV area the demand would be 25 kWh fuel per day. We assume that the electricity demand is only during 3 of 12 months, while the production is during 12 month, with an average of 5 kWh/m<sup>2</sup>,day.

This means a demand of  $100 \text{ kW h/d} * 90 \text{ days} = 9\,000 \text{ kWh/year}$  and assuming a net efficiency from the sun of 1% the biomass production will be  $5 \text{ kWh/m}^2, \text{day} * 0.01 * 360 \text{ days} = 18 \text{ kWh/m}^2, \text{year}$  with respect to biomass. This means a need for  $9\,000/18 = 500 \text{ m}^2$ , if all the fuel should be produced in this way and all electricity come from the TPV-cells. For the four time larger TPV area the demand would be 25 kWh/d and the area for growing biomass would be 125 m<sup>2</sup> instead. With an efficiency from incoming sun to biomass of 5% would mean 100 m<sup>2</sup> instead of 500 m<sup>2</sup>, which might be economically feasible, but still on the high side. If we reduce the electricity consumption significantly by using low energy lamps, low energy refrigeration, using hot water instead of electricity in the washing machine and stay with low consuming TV and computers, it might be possible to reach perhaps even 50 m<sup>2</sup> solar heating surface area, and then also we could have PV-cells covering the rest of the need for the summer, autumn and spring time. With 5 kWh/ m<sup>2</sup>, d, sunshine and 10-15 % net solar power efficiency, an average electric power output of 0.5 – 0.75 kWh/m<sup>2</sup>,day could be achieved. We then would need some 5 m<sup>2</sup> for the house hold electricity for a single house. During summer there can be a net production that could be passed on to the power grid, while there might be a deficiency in October-November and February – March. A small battery would be good to have to give power also in the evening when it is dark, if there is enough PV-area to charge it during the day. Typical hot water and electricity demand for households have been presented in [6] and [7].

Summer time hot water production can be produced by solar heating panels. With a design with a tank above the solar heaters a self circulation can be achieved, but the technical installation and the need to insulate the tank may make it less cost effective than using a circulation pump and a tank in the building..

#### 4. Combination of PV cells and TPV cells

In figure 1 we can see that the sun can give a significant energy contribution from March to October. We already said earlier that TPV-cells can be used during the dark period November - February to produce both heat and electric power. Still, during the more sunny part of the year, we can utilize a combination of PV-cells and solar collectors described above. The good thing with a combination of PV and TPV cells is that all the electrical equipments for DC/AC conversion could be the same for TPV and PV-cells. The TPV system also is an alternative to investing in a large battery.

#### 5. Energy utilization in a household in relation to local production

From a design perspective a single household would need some 0.4 kW base load electricity as an average over the year. The need for hot water production will be significant. If we assume that every person take a 4 minute shower three times a week, and the water used has an average temperature of 15 °C and is heated to 40°C, the heat consumption per shower will be at 10 l/min:  $0.17 \text{ kg/s} * 4.2 * (40-15) = 17.5 \text{ kW}$ . During 4 minutes this means 1.17 kWh. For five persons taking three showers per week this will mean  $1.17 * 5 * 3 * 52 = 910 \text{ kWh/year}$ . Teen agers often take 10 minute showers and seven times a week, which would mean  $2.9 \text{ kWh/shower} * 3 * 7 \text{ times/w} * 52 = 3\ 200 \text{ kWh/y}$  + two grown-ups  $1.17 * 2 * 3 * 52 = 365 \text{ kWh/y}$  with a total amount 3 565 kWh/y.

To this we should add hot water for washing cloths and porcelain, which will add up another 500 kWh/y at least. A total of some 4 000 kWh hot water then is needed. If we distribute this per day, it means some 11 kWh/day.

With the assumption that the incoming sun light is 3-4 kWh/m<sup>2</sup>,day in April a solar panel will produce some 35 liter per m<sup>2</sup>, day in April at the longitude of Vasteras/Stockholm with a temperature lift of 35 °C. This corresponds to  $35 * 4.2 * 35 / 3600 = 1.43 \text{ kWh/m}^2, \text{day}$ . 11 kWh/day then mean 7.7 m<sup>2</sup> solar panel. In March we only will get 15 liter/m<sup>2</sup>,day, which would mean a need for 18 m<sup>2</sup> to cover all.

#### 6. Use of DC in households

As both PV and TPV systems generate DC-power, we also can see a potential to use DC components generally, e.g for charging batteries for electrical vehicles, DC-pumps, LED-lamps etc. The advantage with this would be that normally lower voltages could be used for many applications. This is important as the voltage normally is quite low in PV-systems, typically 12, 24 or 48 Volt. The draw-back is that it is causing more losses to transport energy as low voltage, and thus the distance has to be optimized between the production units and the appliances. It is not clear where the economic limits are for using DC on a larger scale in the buildings, but worth to investigate more in the future. Normal distances within a single house of average size will be no problem.

#### 7. Discussion

To sum up: We assume a house-hold electricity demand of 3600- 5400 kWh/year = 10-15 kWh/day. To this a hot water demand of the same amount 10 kWh/d is assumed. The heat demand will vary over the year with a demand around 70-120 kWh/day in November-February, some 30- 50 during March-April and in September- October. The rest of the year there will be no demand for heating. With a TPV system giving 10 kWh/d electricity we would produce also 50- 200 kWh/ heat and hot water, which would be enough to cover the

demand during November – February. During the rest of the year a 18 m<sup>2</sup> solar panel + 20 m<sup>2</sup> PV cells would be enough to cover all energy demands.

Adding some 5-10 m<sup>2</sup> PV-cells will give a house producing more energy than it consumes (emitting < 20 W/ m<sup>2</sup> building area when the outdoor temperature is – 15 °C - the definition used in Sweden for so called “low energy houses”). If the roof area is some 170 m<sup>2</sup> the solar panel units will cover less than 50% of the roof area, which is quite feasible.

For the case with the TPV system and production of biomass as such it would be primarily the TPV that is an issue, as the unit only exists as a pilot plant today, and not a full commercial product. Still, the prize tag is estimated to be relatively low (1000 – 3000 €/kW<sub>el</sub>).

## 8. Conclusions

The conclusions are that the alternatives discussed can be motivated economically if we can achieve high efficiencies for all technologies and steps. It is difficult to judge which technology is the economically best comparing different systems that are not yet commercial. Still, the alternative with biomass production followed by TPV for heat and power production locally has a relatively short distance to being realized commercially, and the potential to be economically competitive is reasonably high.

## Acknowledgements

We would like to thank Swedish energy agency for supporting the work with especially the development of the TPV technology.

## References

- [1] Lindberg, E. och Broman, L. (2003a) An animation tool for demonstrating the importance of edge filters in thermo photovoltaic applications. *Renewable Energy* 28(2003)1305-1315.
- [2] Lindberg, E. och Broman, L. (2003b) Fabergé optics and edge filter for a wood powder fuelled thermo photo voltaic system. *Renewable Energy* 28(2003)373-384.
- [3] Lindberg, E. och Broman, L. (2003c) Non-imaging optics in a thermo photovoltaic generator. *Fifth NREL Conf. on Thermo photovoltaic Generation of Electricity*, AIP Conference Proceedings 653, pp 222 -231. *Sixth NREL Conf. on Thermo photovoltaic Generation of Electricity*, AIP Conference Proceedings 738, pp 114-1223
- [4] Dahlquist E. , Karim A., Bard G., Lindberg E., Broman L. and Nordlander S.: Modeling of a Thermo-photovoltaic System (TPV). Proceedings IIIrd International green energy conference in Vasteras, June 16-20, 2007.
- [5] Qiu Kuanrong: Low Band gap TPV Cells and TPV Power Generation Systems, Proceedings IV<sup>th</sup> International green energy conference in Beijing, October 20-22, 2008
- [6] Vassileva I., Lundh M., Dahlquist E. : Efficiency of interactive information on energy consumption in households in Sweden. Proceedings of the first International Conference on Applied Energy in Hong-Kong Jan 5-8, 2009.
- [7] Widen J., : System studies and Simulations of Distributed Photovoltaic. PhD thesis 10 December, 2010, Uppsala University Press.

## Comparative Performance of Various PV Technologies in Different Italian Locations

A. Colli<sup>1,\*</sup>, M. Marzoli<sup>2</sup>, W. Zaaïman<sup>3</sup>, S. Guastella<sup>2</sup>, W. Sparber<sup>1</sup>

<sup>1</sup> EURAC Research, Institute for Renewable Energy, Bolzano, Italy.

<sup>2</sup> Ricerca sul Sistema Energetico - RSE S.p.A., Milano, Italy.

<sup>3</sup> EC Joint Research Centre, Institute for Energy, Renewable Energy Unit, Ispra (VA), Italy.

\* Corresponding author. Tel: +39 0471 055630, Fax: +39 0471 055699, E-mail: [alessandra.colli@eurac.edu](mailto:alessandra.colli@eurac.edu)

---

**Abstract:** With the increasing number of photovoltaic (PV) installations on a worldwide scale, an outdoor performance analysis of various types of modules is needed. The purpose to assess and compare the performance of different types of modules in specific geographical locations, under various climatic conditions and to identify benefits/losses given by a specific surrounding context, is very important to evaluate the energetic behavior of future installations and direct them toward the most suitable technology to apply. The installations taken into consideration are located in Bolzano, Milan, and Catania, allowing comparison among three different Italian climate conditions and irradiance levels: the Alpine region, the upper Padana valley, and the sea-side area in Sicily. In Bolzano, a multi-technology ground-mounted PV field is taken into analysis. For Milan and Catania, two multi-section PV power plants are monitored. The monitoring activities are done taking the international norm IEC 61724 as reference document, together with the best practice already existing in the field. The PV modules are evaluated in relation to ambient conditions, installation characteristics, module-specific behavior and state. Results are provided in a comparative way among the three considered geographical locations. Results are validated and an uncertainty estimation is shown. As instrumentation and environmental conditions are not the same, uncertainties for the locations might be different. Possible issues related to monitoring activities, as well as the performance of different PV technologies, will be highlighted.

**Keywords:** Monitoring, PV System Performance, Energy Rating, Site-Dependent Performance Ratio.

---

### 1. Introduction

The number of photovoltaic (PV) installations in Italy is quickly increasing, thanks to the national “Conto Energia” programme. An increasing trend has been also registered at European level, as well as worldwide. In this context, a detailed monitoring of selected PV plants and the analysis of operational data of these plants is needed to support a realistic outdoor performance analysis of various types of modules in specific geographical environments. This action supports both the scientific community and the different actors in the PV environment, such as developers, producers, installers, financing institutions, as well as decision-makers and customers.

### 2. The PV installations

The installations taken into consideration in this work are located in Bolzano, Milan, and Catania, allowing comparison among three different Italian climate conditions and irradiance levels: the Alpine region, the upper Padana valley, and the sea-side area in Sicily. The evaluation has been limited to two months (September and October 2010) due to the recent operation activity of the installation located in Bolzano. From the different locations, four PV technologies are analyzed and evaluated: back-contact monocrystalline silicon cells (BC m-Si), heterojunction cells with intrinsic thin layer (HIT), copper indium gallium selenide (CIGS) and cadmium telluride (CdTe). All groups are mounted on 30°-tilted supports.

It must be stressed that the monitoring systems are, at the moment, different for Bolzano (supervised by EURAC Research and reading electrical data through the inverter system, with an SMA amorphous silicon reference device) in comparison with the installations of Milan and Catania (supervised by RSE and adopting a dedicated electrical monitoring system, using

a crystalline silicon reference device from the type EstiSensor [1]). This leads to differences in the acquired data, which are visible in their representation, but are also discussed and justified along the paper to make the comparison possible and valuable. A validation of the results of the performance ratio (PR) among the different groups, locations and monitoring systems is done in Section 4.

### 2.1. Airport of Bolzano Dolomiti (ABD) PV field

The multitechnology ground-mounted grid-connected PV field at the Airport of Bolzano Dolomiti (ABD), in the North-East of Italy, is in operation since August 10, 2010 and has a total peak power of 724 kW<sub>p</sub>. It is divided into two main parts: a 662 kW<sub>p</sub> commercial installation, mounting 8538 CdTe modules, and a 62 kW<sub>p</sub> experimental installation, mounting 24 different types of modules, divided into groups ranging between 1 and 2 kW each. The groups selected for the analysis are listed in Table 1. Results for two CIGS and two BC m-Si groups are shown, to highlight possible differences among the same product. For the commercial field using CdTe modules the monitoring results for a single inverter has been considered, connecting a total of 120 modules divided into 20 strings of 6 modules each. Figure 1 and 2 show the instantaneous PR for the four PV technologies calculated on a 15-minute base for each day of the month, respectively for September and October 2010.

Table 1. Groups and characteristics from ABD PV field in Bolzano.

Group	Type	kWp	Inverter	Overview
E2	HIT	3.87	SB4000TL-20	
E10	CIGS	1.12	SB1100	
E11	CIGS	1.12	SB1100	
E14-A	BC m-Si	1.2	SB1100	
E14-B	BC m-Si	1.2	SB1100	
Commercial	CdTe	9.3	SMC9000TL-10	

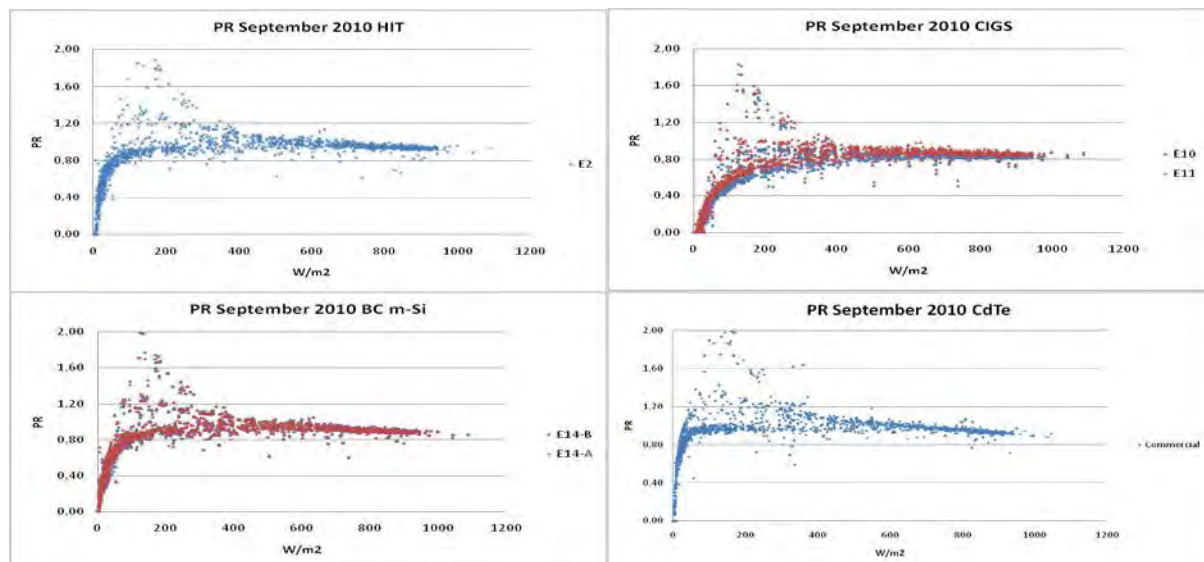


Fig. 1. PR ( $P_{AC}/(P_p \cdot Irrad.)$ ) evaluated every 15 minutes for each day of September 2010 in Bolzano.

The graphs highlight clouds of data at low irradiance levels (mainly between 100 and 200 W/m<sup>2</sup>), due to the fact that the efficiency of the inverter is not stable for values of irradiance lower than 200 W/m<sup>2</sup>. A general high performance and differences in behavior for the same

technology (as for CIGS, where differences in the trends are visible, especially clear in the month of October) can also be noticed.

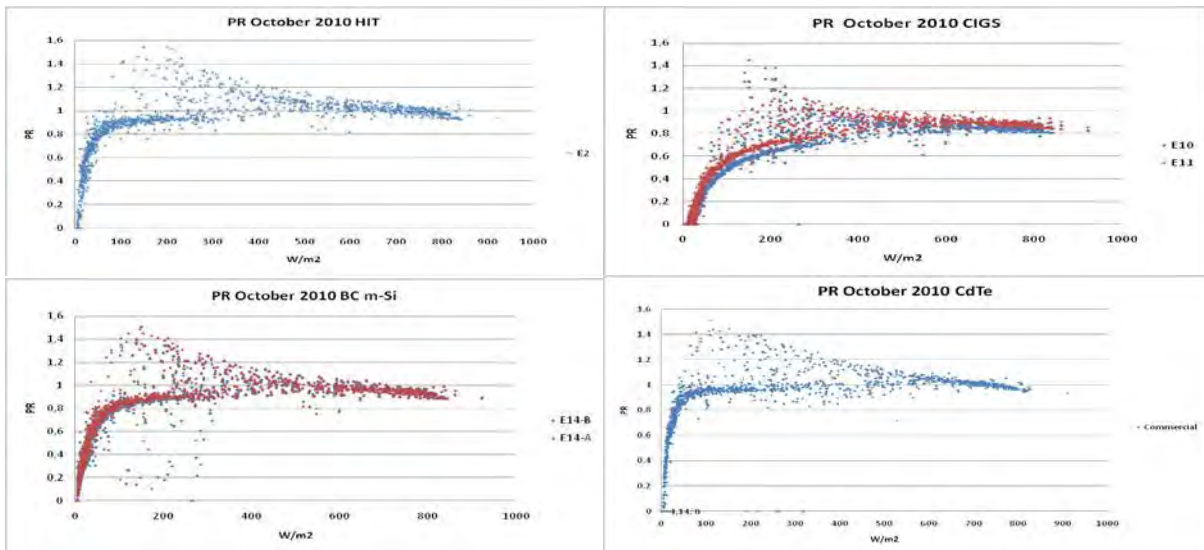


Fig. 2. PR ( $P_{AC}/(P_p * Irrad.)$ ) evaluated every 15 minutes for each day of October 2010 in Bolzano.

## 2.2. PV test installation in Milan

The RSE test installation in Milan has a peak power around 8 kWp and consists of 6 groups of different technologies (polycrystalline silicon, two high-performance monocrystalline silicon, CIS, CdTe and amorphous silicon). The power production is monitored with a custom-made system to evaluate the current and voltage on both DC and AC sides of the inverter.

Table 2. Groups and characteristics in Milan.

Group	Type	kWp	Inverter	Overview
GFV11	HIT	1.05	SB1100	
GFV14	CIGS	1.2	SB1100	
GFV15	CdTe	1.16	SB1100	
GFV16	BC m-Si	1.2	SB1100	

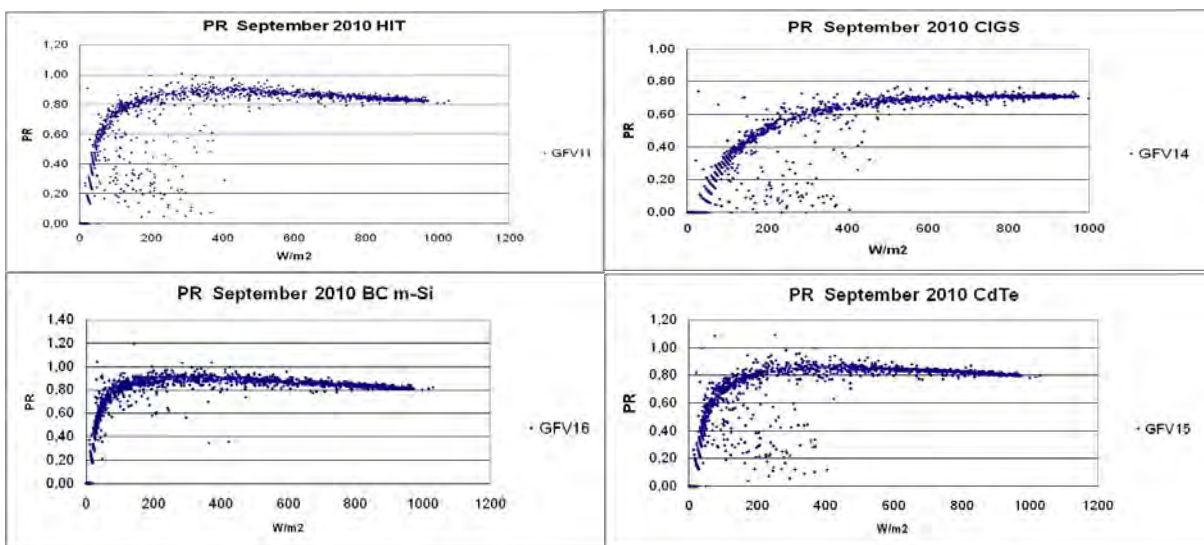


Fig. 3. PR ( $P_{AC}/(P_p * Irrad.)$ ) evaluated every 15 minutes for each day of September 2010 in Milan.

The groups taken into consideration are listed in Table 2. Figure 3 and 4 show the instantaneous PR for the four PV technologies calculated on a 15-minute base for each day of the month, respectively for September and October 2010.

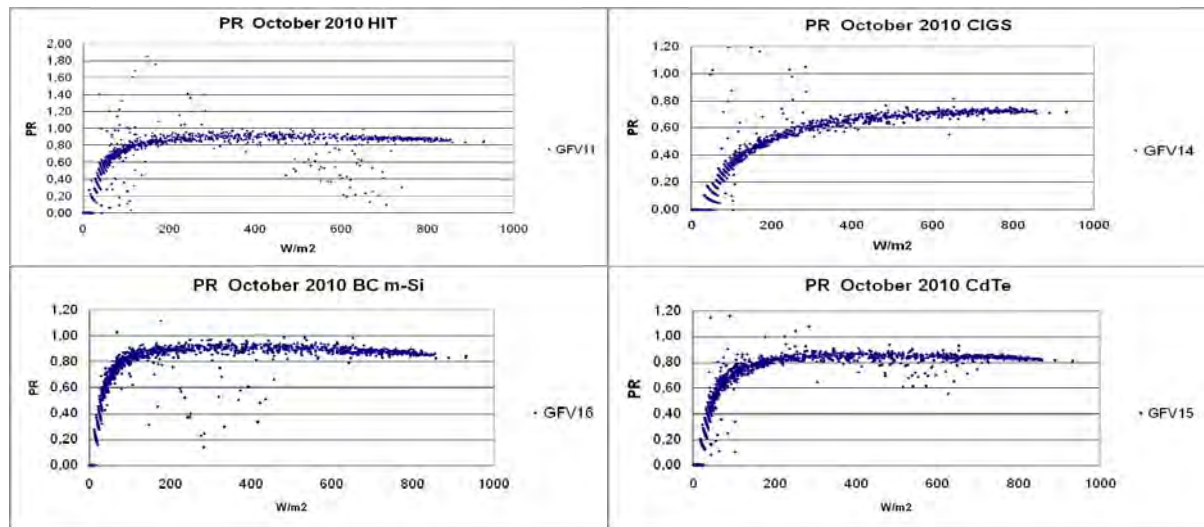


Fig. 4. PR ( $P_{AC}/(P_p \cdot Irrad.)$ ) evaluated every 15 minutes for each day of October 2010 in Milan.

### 2.3. PV test installation in Catania

The RSE test installation in Catania replicates the installation previously described for Milan in all its characteristics. The groups taken into consideration are listed in Table 3. Figure 5 and 6 show the instantaneous PR for the four PV technologies calculated on a 15-minute base for each day of the month, respectively for September and October 2010.

Table 3. Groups and characteristics in Catania.

Group	Type	kWp	Inverter	Overview
GFV1	HIT	1.05	SB1100	
GFV4	CIGS	1.2	SB1100	
GFV5	CdTe	1.16	SB1100	
GFV6	BC m-Si	1.2	SB1100	

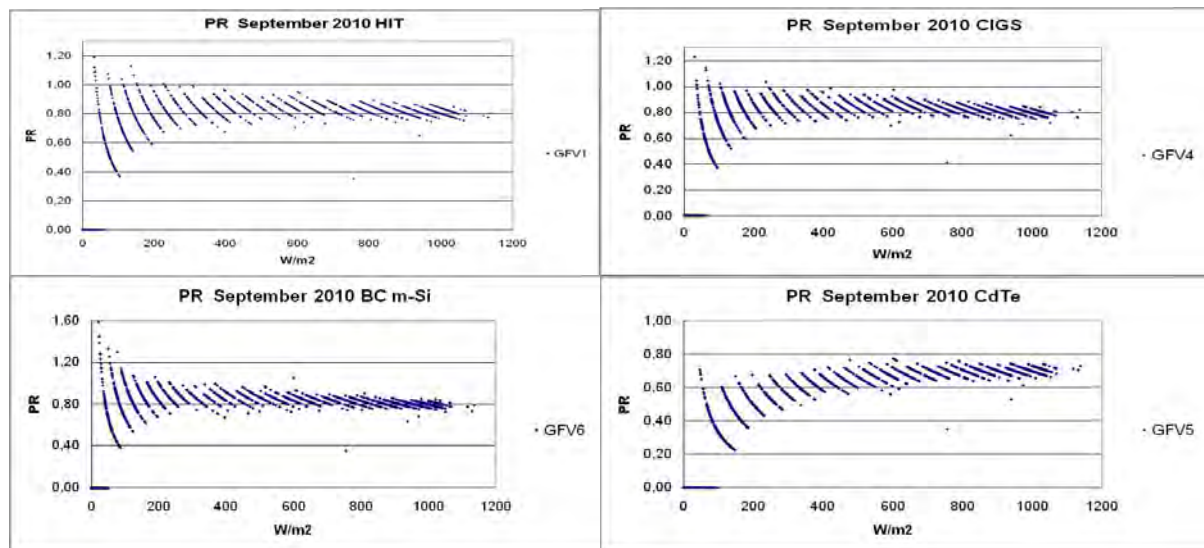


Fig. 5. PR ( $P_{AC}/(P_p \cdot Irrad.)$ ) evaluated every 15 minutes for each day of September 2010 in Catania.

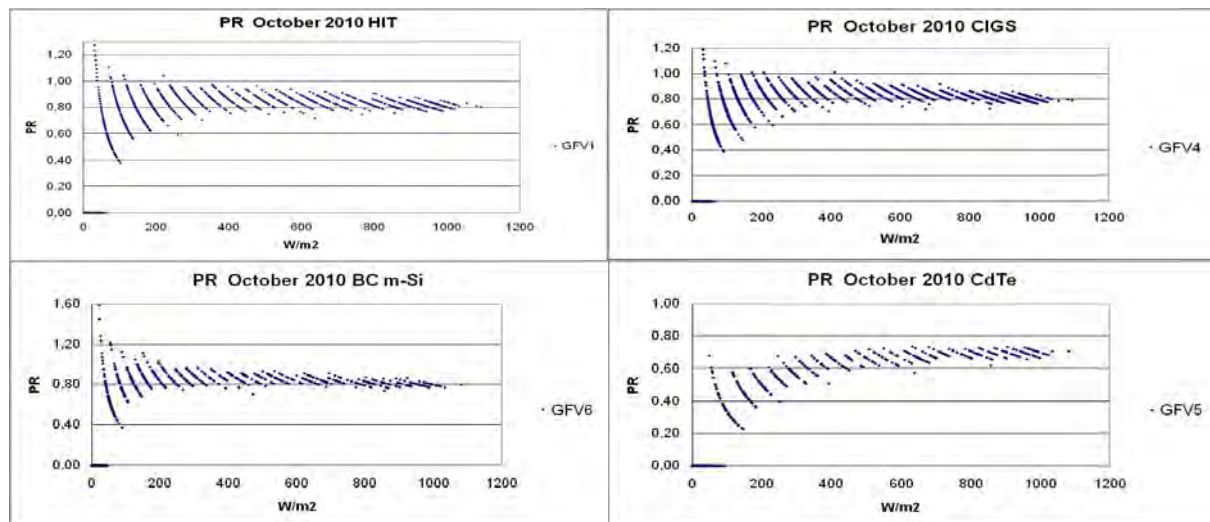


Fig. 6. PR ( $P_{AC}/(P_p \cdot Irrad.)$ ) evaluated every 15 minutes for each day of October 2010 in Catania.

The shape of the plots PR vs Irradiance in Catania is different from the previous considered cases. This is due to different settings of the resolution of the data acquired by the monitoring system, which takes into consideration only two decimal digits in the recorded AC power. The trend of the PR is, for higher irradiances, in line with the previous graphs.

### 3. Comparison

The comparison is conducted according to two indicators: the energy production per kWp of installed power and the PR, both processed for each month taken into consideration. Moreover, geographical environments and technology-specific behaviors are taken into account while evaluating the results.

#### 3.1. Methodology

The calculation of the energy production in kWh/kWp is the main element of comparison among the various PV technologies; in fact, using this indicator the irradiance value is omitted as element in the calculation, avoiding the problem rising from mismatch and the difference in the reference devices among the sites. All inverters are from SMA, and each PV technology refers to the same module producer in all cases; anyhow, the issue of accuracy of the data acquisition system, as well as the accuracy in the kWp value by label, has to be considered. Following the indications of the international standard IEC 61724 [2], the performance of a PV system can be expressed by the PR, that shows the overall effect of losses (due to module temperature, irradiance usage, low components efficiency, faults) on the power output of the plant. The PR is calculated on a monthly base, according to the following ratio:

$$PR = \frac{Y_f}{Y_r} \quad (1)$$

Where  $Y_f = E/P_0$  and  $Y_r = H/G$ , and respectively E is the energy produced by the PV system,  $P_0$  the installed peak power, H is the in-plane insolation (in kWh/m<sup>2</sup>), and G is the irradiance at STC (1 kW/m<sup>2</sup>).

#### 3.2. Results

The energy production in kWh reported to the kWp of installed power (specific yield) allows a comparison among groups in the same location, but for different locations the energy

production has to be always seen in perspective of the irradiance value for the considered period. The values of the monthly global irradiance on 30° angle, respectively for September and October 2010, in the three considered locations are: Bolzano: 139.60 kWh/m<sup>2</sup> and 92.96 kWh/m<sup>2</sup>; Milan: 144.01 kWh/m<sup>2</sup> and 88.32 kWh/m<sup>2</sup>; Catania: 169.94 kWh/m<sup>2</sup> and 126.54 kWh/m<sup>2</sup>. Among c-Si technologies, HIT are performing better in Bolzano, while BC m-Si are dominant in Milan and Catania (see Table 4). CdTe modules compete with c-Si mainly in Bolzano and Catania, where the diffuse component of the irradiance is higher for the location characteristics. The production level (in terms of specific yield) of CIGS generally remains lower, with the exception of Milan, where production from CIGS is comparable to HIT. The PR can be compared only by taking into account the correction coefficient from Table 6.

Table 4. kWh of energy production per kWp of installed power per month, location and technology.

Date	Type	Bolzano	Bolzano	Milan	Catania
Sep-10	BC-	127.7 (E14-A)	127.5 (E14-B)	121.8	139.4
Oct-10	mSi	88.7 (E14-A)	87.3 (E14-B)	76.5	105.5
Sep-10	HIT	134.0		118.6	138.5
Oct-10		93.2		73.9	103.7
Sep-10	CIGS	112.5 (E10)	118.9 (E11)	115.5	112.6
Oct-10		74.3 (E10)	79.4 (E11)	72.1	80.3
Sep-10	CdTe	135.6		93.3	138.6
Oct-10		90.9		56.4	103.6

Table 5. PR per month, location and technology.

Date	Type	Bolzano	Bolzano	Milan	Catania
Sep-10	BC-	0.91 (E14-A)	0.91 (E14-B)	0.85	0.82
Oct-10	mSi	0.95 (E14-A)	0.95 (E14-B)	0.87	0.83
Sep-10	HIT	0.96		0.82	0.81
Oct-10		1.00		0.84	0.82
Sep-10	CIGS	0.81 (E10)	0.85 (E11)	0.65	0.66
Oct-10		0.80 (E10)	0.85 (E11)	0.64	0.63
Sep-10	CdTe	0.98		0.80	0.82
Oct-10		1.00		0.82	0.81

#### 4. Validation of the measurement systems

In order to validate the results of the performance ratio, an attempt is made to compare the DC output power of the various groups with reference to the calculated installed power (kWp). Data sets with an average irradiance level (on 15 minutes) of 900 W/m<sup>2</sup> or higher, and available module temperatures are used to extrapolate the output power to standard reporting conditions of 25°C and 1000 W/m<sup>2</sup> irradiance level (excluding correction to airmass 1.5 global spectral irradiance). The values of the temperature coefficients for P<sub>max</sub> used for the different PV technologies are as from [3] and are listed in Table 6. Concerning Bolzano, remarkable is the difference between two identical CIGS groups. The difference of 4% is also noted in Fig. 1 and 2. This is caused partially by the inverter data acquisition. Both BC m-Si groups show an overestimation in power of nearly 10%, but the difference between the two systems is negligible (< 0.5%). Also HIT technology shows an overestimation in power, which can be attributed to the mismatch in the spectral responsivity between the reference detector and the modules. This is valid for both silicon-based technologies.

Table 6. Correction coefficient for PR values.

Technology	BC m-Si	BC m-Si	HIT	CIGS	CIGS	CdTe
TC_Pm [%/°C]	-0.45	-0.45	-0.50	-0.36	-0.36	-0.21
Location	Bolzano					
Average DC_STC [kWp]	1.30	1.30	4.16	1.10	1.15	9.28
Standard deviation DC_STC [kWp]	0.03	0.03	0.12	0.03	0.02	0.13
Difference [%]	<b>7.9</b> (E14-A)	<b>8.3</b> (E14-B)	<b>7.6</b>	<b>-1.5</b> (E10)	<b>2.5</b> (E11)	<b>-0.2</b>
Location	Milan					
Average DC_STC [kWp]	1.16		1.03	1.01		1.17
Standard deviation DC_STC [kWp]	0.01		0.01	0.01		0.01
Difference [%]	<b>-3.2</b>		<b>-1.9</b>	<b>-16.0</b>		<b>0.5</b>
Location	Catania					
Average DC_STC [kWp]	1.14		1.00	1.10		1.05
Standard deviation DC_STC [kWp]	0.02		0.02	0.03		0.02
Difference [%]	<b>-5.0</b>		<b>-4.7</b>	<b>-8.7</b>		<b>-9.3</b>

For Milan, the difference between calculated power at 1000W/m<sup>2</sup> and 25°C and the measured DC power for the CIGS is very large, and cannot be justified by the spectral mismatch between c-Si reference detector and the spectral responsivity of the CIGS material. The differences of the BC m-Si and HIT materials can be attributed to spectral mismatch. The very small difference of the CdTe is also remarkable, as the spectral mismatch between c-Si and CdTe is normally around 8-10%. In Catania, it must be considered that the module temperatures are higher than for the two northern locations. The -8.7% difference for CIGS can be attributed to spectral mismatch, as well as the -9.3 for CdTe. The values for BC m-Si and HIT can originate from the temperature (as correction for T is more dominant than for the locations of Milan and Bolzano), as well as being influenced by the spectral mismatch.

As general remarks for the reference detector, guidelines are given in IEC 61724 [2] and require an irradiance reference detector with an accuracy better than 5%. As for the technologies CIGS, HIT, BC m-Si, a c-Si reference detector (as used by RSE in Milan and Catania) would reduce the effect of spectral mismatch. A rough estimation of ± 7% spectral mismatch for the above mentioned technologies should be taken in consideration for the Bolzano data (as an a-Si reference detector is used). For CdTe the spectral mismatch is estimated around ± 3%. These data will be used in the uncertainty calculation table. Some assumptions are made to estimate the overall uncertainty of the final PR value. For all uncertainty components, a “B” type standard uncertainty and a “R” (rectangular) distribution is assumed. Therefore the reduction factor is  $\sqrt{3}$ . The total index of uncertainty that is reported is calculated as the square root of the sum of the squares of the individual contributions. The uncertainties given in Table 7 are with a coverage factor (k) of 2. With a Gaussian probability distribution, this gives a confidence level of 95 %.

Table 7. Uncertainty values for the different PV technologies in the three considered locations.

	Location				Estimated Uncertainty	
	Bolzano		Milan&Catania		TF	Si
					[%]	[%]
Standard uncertainty component	TF	Si	TF	Si		
Stability of Reference Device	1.73	1.73	0.58	0.58	3	1
Calibration of reference device	4.62	4.62	1.44	1.44	8	2.5
Spectral Mismatch	1.73	4.04	4.04	1.73	3	7
Irradiance DAS	0.00	0.00	0.58	0.58	0	1
Inverter / DAS	0.58	0.58	0.58	0.58	1	1
Installed power	2.31	1.15	2.31	1.15	4	2
Combined standard uncertainty	<b>5.7</b>	<b>6.5</b>	<b>5.0</b>	<b>2.7</b>		
Expanded standard uncertainty k=2	<b>11.5</b>	<b>13.0</b>	<b>9.9</b>	<b>5.4</b>		

## 5. Conclusions

The analysis shows a relevant impact of the geographical location (temperature, irradiance components) on the performance of selected PV technologies. In fact it clearly appears that certain technologies have a better energy production compared to others in the same location. Nevertheless, the importance of the monitoring devices and system components results clear while evaluating the performance. Commercial-type monitoring systems need improvements in quality and reference devices need regular maintenance activity. It is also important to match the module technology with an appropriate reference device. This issue becomes relevant when evaluating the PR. The monitoring system in Bolzano is under way to be improved to reduce data uncertainty and a collaboration with RSE is set to install additional monitoring devices on the DC and AC sides of the inverters for selected groups.

## Acknowledgements

The Authors from EURAC Research would like to thank the European Regional Development Fund (ERDF) for co-financing the PV ABD project.

The Authors from RSE would like to acknowledge that their work has been financed by the Research Fund for the Italian Electrical System under the Contract Agreement between RSE (formerly known as ERSE) and the Ministry of Economic Development - General Directorate for Nuclear Energy, Renewable Energy and Energy Efficiency stipulated on July 29, 2009 in compliance with the Decree of March 19, 2009.

## References

- [1] H. Ossenbrink, K.A. Münzer, "The ESTIsensor – A New Reference Cell for Monitoring of PV Plant Performance", 11th European Photovoltaic Solar Energy Conference and Exhibition, Montreux, Switzerland, 1992.
- [2] International standard IEC 61724:1998 "Photovoltaic System Performance Monitoring - Guidelines for Measurement, Data Exchange and Analysis".
- [3] A. Virtuani, D. Pavanello, G. Friesen, "Overview of Temperature Coefficients of Different Thin Film Photovoltaic Technologies", 25<sup>th</sup> EU PV SEC, 6-10 September 2010, Valencia, Spain.

## An investigation of the impact of time of generation on carbon savings from PV systems in Great Britain.

P. A. Burgess<sup>1,\*</sup>, M.M. Vahdati<sup>2</sup>, D. Davies<sup>3</sup>

<sup>1</sup> Technologies for Sustainable Built Environments, University of Reading, United Kingdom

<sup>2</sup> School of Construction Management and Engineering, University of Reading, United Kingdom

<sup>3</sup> Solarcentury, London, United Kingdom

\* Corresponding author. Tel: +44 (0)7977 255 964, E-mail: p.a.burgess@pgr.reading.ac.uk

---

**Abstract:** PV only generates electricity during daylight hours and primarily generates over summer. In the UK, the carbon intensity of grid electricity is higher during the daytime and over winter. This work investigates whether the grid electricity displaced by PV is high or low carbon compared to the annual mean carbon intensity using carbon factors at higher temporal resolutions (half-hourly and daily).

UK policy for carbon reporting requires savings to be calculated using the annual mean carbon intensity of grid electricity. This work offers an insight into whether this technique is appropriate.

Using half hourly data on the generating plant supplying the grid from November 2008 to May 2010, carbon factors for grid electricity at half-hourly and daily resolution have been derived using technology specific generation emission factors.

Applying these factors to generation data from PV systems installed on schools, it is possible to assess the variation in the carbon savings from displacing grid electricity with PV generation using carbon factors with different time resolutions.

The data has been analyzed for a period of 363 to 370 days and so cannot account for inter-year variations in the relationship between PV generation and carbon intensity of the electricity grid. This analysis suggests that PV displaces more carbon intensive electricity using half-hourly carbon factors than using daily factors but less compared with annual ones.

A similar methodology could provide useful insights on other variable renewable and demand-side technologies and in other countries where PV performance and grid behavior are different.

**Keywords:** Renewable Energy, Photovoltaics, Carbon accounting

---

### 1. Introduction

The carbon intensity of grid electricity varies with the seasons and also with the time of day. Similarly the production of electricity from PV is strongly dependent on the time of year and time of day. In the case of the variation in carbon intensity of the electricity grid, this is a function of the way that overall energy demand varies and the economics of the different electricity production methods. As the UK has a diverse mix of generation technologies, the variation in carbon intensity of the grid can be quite large. At times of low demand when nuclear makes up a relatively large proportion of the active generating plant, the carbon intensity tends to be relatively low; at times of the highest demand, the grid has all available nuclear and renewable power and a roughly equal mix of coal and gas supplying the remaining demand, leading to an intermediate carbon intensity figure. The times of highest carbon intensity occur when there is moderate to high demand and the cost of producing electricity from coal is lower than the cost of producing electricity using gas.

In the UK, company carbon reporting of the energy exported from microgeneration must be reported using the annual grid average carbon emissions factor [1] which may not be truly reflective of the grid mix at the time of generation.

This paper seeks to determine the relationship between the variation of the carbon intensity of the mixture of sources feeding the grid and the variation in the time of PV.

## 2. Methodology

There are three sources of data that are central to this work. Firstly, the half-hourly generation by fuel type data for the UK national grid [2]. This provides gross electricity production from eleven sources (including interconnectors and pumped storage hydro) for Great Britain. Data has been collated from November 2008 to June 2010. These figures do not make any allowance for parasitic loads within power stations which are considered in the second set of data, the average emissions factor for each fuel type in the half hourly generation by fuel type data. These generation emission factors (GEFs) are taken from AMEE [3] based on data in DUKES [4]. The GEFs provided by AMEE are for gross generation with a generated to supplied gross factor to allow for conversion from carbon intensity of gross electricity generation to the carbon intensity of the electricity fed into the grid. To convert these from grid supplied factors to the carbon intensity of electricity at the point of use, the losses in transmission and distribution (T&D) must be considered. We have used a flat figure for T&D losses of 9% [5].

Table 1 End use CO<sub>2</sub> emissions factors for each generation technology.

Fuel Type	Generated To Supplied Gross Factor	Mass CO <sub>2</sub> Produced per Energy Unit (kg/kWh)	Derived Supplied Net Factor (kg/kWh)	Derived End-use Factor allowing for T&D losses
CCGT	0.984	0.385	0.391	0.430
Coal	0.949	0.861	0.907	0.997
INTFR	1	0.082	0.082	0.090
INTIRL	1	0.549	0.549	0.603
NPSHYD	0.997	0	0	0
Nuclear	0.908	0	0	0
OCGT	0.944	0.525	0.556	0.611
Oil	0.828	0.737	0.889	0.977
Other	1	0	0	0
PS	0.997	0	0	0
Wind	1	0	0	0

Applying the resulting end-use GEFs (Table 1) to the generation by fuel type data gives the total CO<sub>2</sub> emissions from each fuel type for every half hour. Once this is completed, the task of deriving grid mix carbon intensity for any given time frame is achieved by dividing the total carbon emissions over the time by the electricity generated over that time. For this work, the time intervals considered are half hourly, daily and total period which varies slightly from system to system but all start between the 13<sup>th</sup> and 26<sup>th</sup> May 2009 and all run for between 363 and 370 days and can be thought of as an annual grid average carbon factor.

No account has been made for non-CO<sub>2</sub> GHG emissions from generation, for upstream emissions, for the embodied emissions associated with the generation infrastructure or end-of life disposal. The official methodology published by the UK Government [1] has only recently started including non-CO<sub>2</sub> GHGs in their electricity factors and these were not included for simplicity. The remaining omissions from this study are categories that are not consistent with the GHG reporting guidelines prevalent in the UK at the time of writing.

The final dataset used for this work was the generation from seven PV systems in the North of England provided by Solarcentury. All systems are 4 kW<sub>p</sub> crystalline silicon systems oriented due south with a tilt of 30°. All data was for a period from a point in May 2009 to a point in May 2010 in 15-minute time steps. These were converted to half-hourly generation data. In 32 half hourly periods across the generation by fuel type dataset only interconnector data had been recorded. In this study these half hours have been excluded from the analysis. The carbon savings from PV generation were calculated using half hourly, daily and overall period emissions factors and the results compared. All calculations were done using MS Excel 2007.

### 3. Results

The analysis of the variation in time of generation and carbon intensity of the grid presented in this section gives a clear indication of the main findings of the study. For systems with a similar generation profile, the differences between carbon savings from the annual average and from half-hourly carbon emissions factors are very similar.

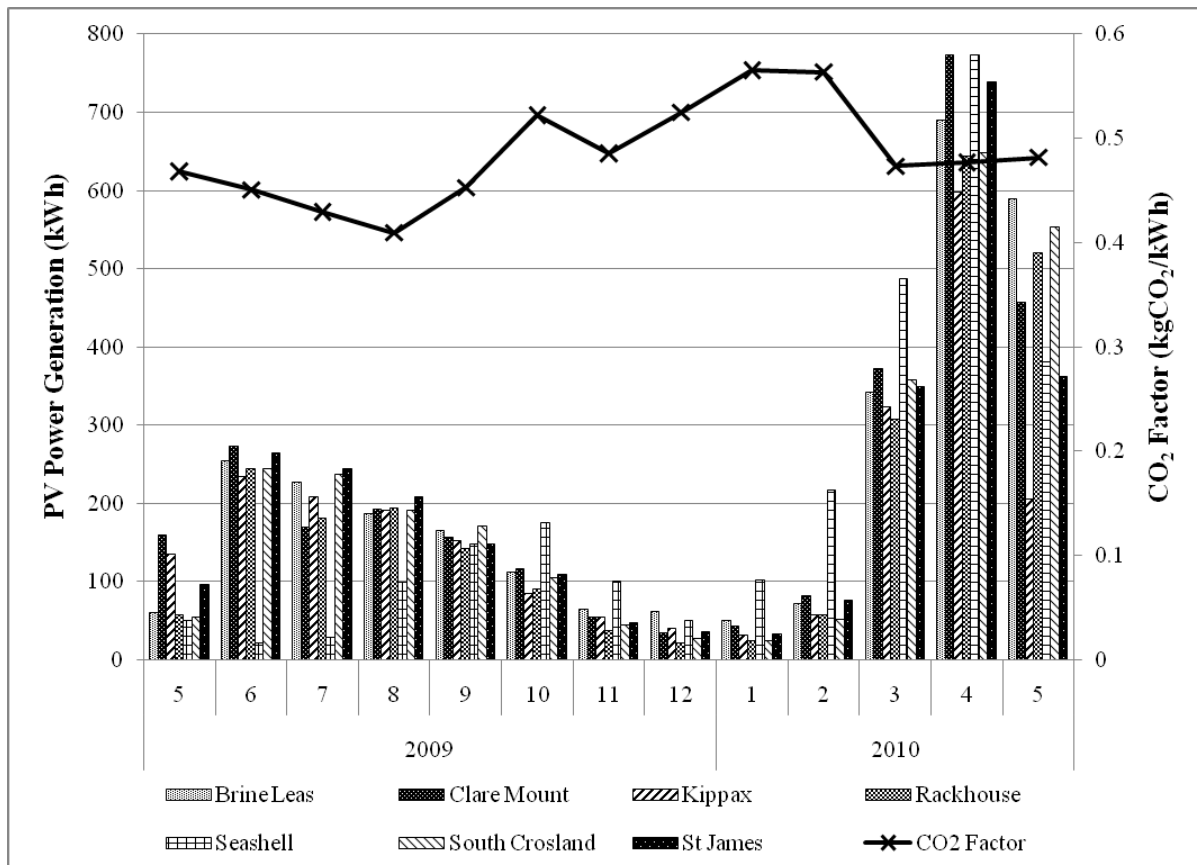


Figure 1 Monthly generation by each system (kWh) and Monthly average grid mix CO<sub>2</sub> emissions factor

Figure 1 shows a similar generation profile for all seven systems over the monitoring period with the exception of Seashell which has significantly lower generation in 2009 relative to the other systems. In all cases the generation in March to May 2010 is significantly higher than summer 2009 indicating that conditions for solar generation were more favorable in 2010 than 2009.

Figure 1 also gives a clear indication of the seasonal variation in CO<sub>2</sub> intensity with the highest monthly emissions factors being over the winter months (note the graph shows a year from May to May so winter is in the middle).

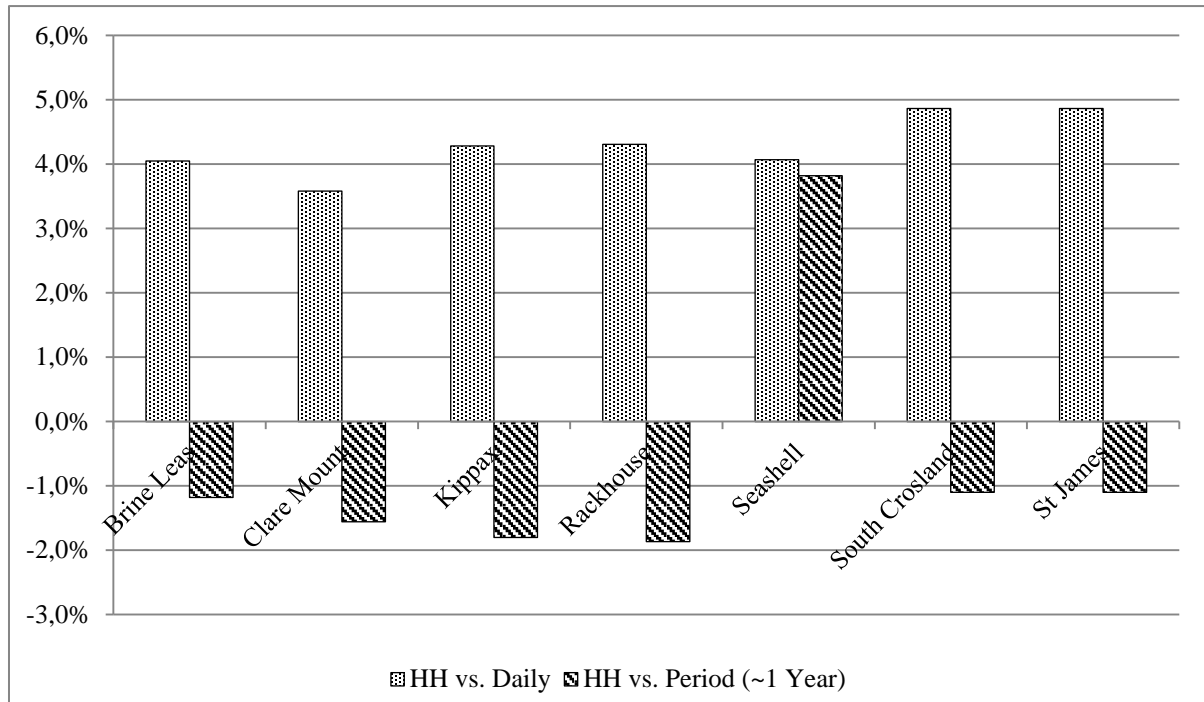


Figure 2 The difference between carbon savings using carbon factors with different time resolutions.

Figure 2 shows a clear trend across six of the seven systems analyzed with CO<sub>2</sub> savings assessed using half hourly emissions factors for the time of generation outperforming the average daily factor for the day of generation by between 3.5 and 5 percent. Comparing the half hourly performance against the period average grid mix emissions factor, carbon savings were 1 to 2 percent lower using the half hourly emissions factors. The clear exception to this is the comparison between the period average and half hourly figure for Seashell. This is likely to be a consequence of the different pattern of generation for Seashell seen in Figure 1 with a much smaller proportion of the system's generation in 2009 than in the other six cases.

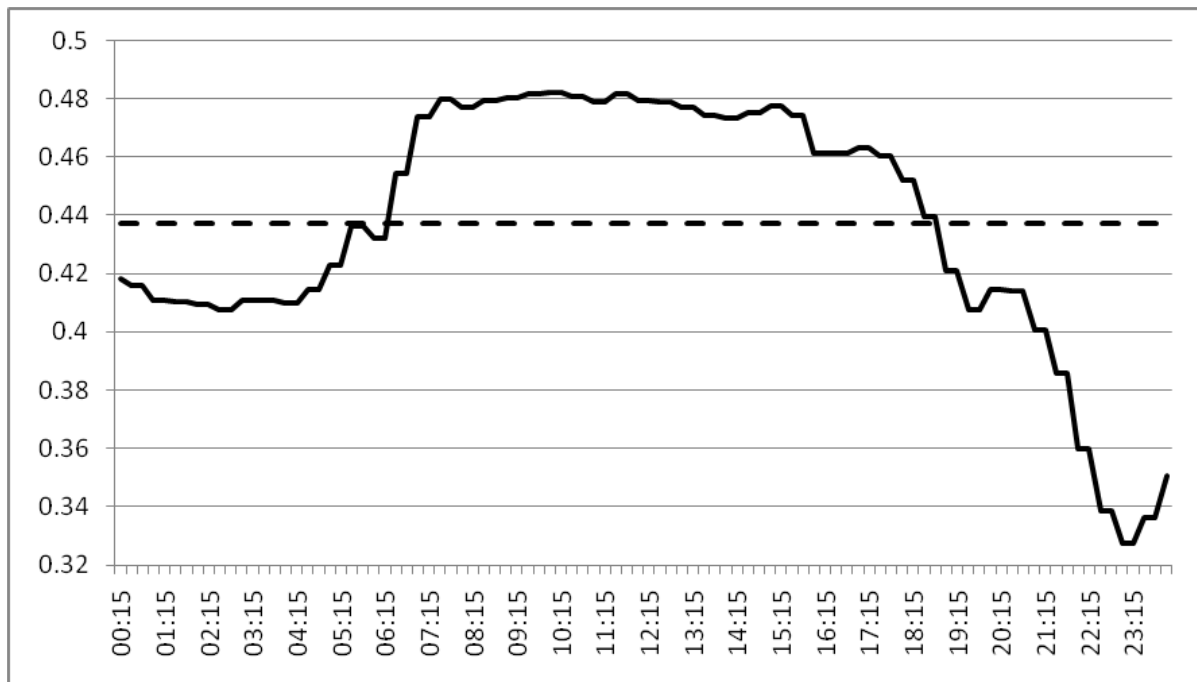


Figure 3 CO<sub>2</sub> factor variation for 17 July 2009 (typical summer day). Solid line is half hourly variation, dashed line is daily average.

The difference in carbon savings between half hourly and daily emissions factors can be easily understood by observing figure 3 which shows the variation in grid CO<sub>2</sub> for a typical summer's day. The profile is essentially a step function with lower carbon generation overnight and higher carbon generation over the daytime when PV will be generating. The typical winter profile is similar but with a still higher level in the evening corresponding to high demand for electricity for lighting, electric heating etc.

## 4. Discussion and Conclusions

### 4.1. Previous work

Previous studies have considered the carbon intensity of grid energy as it relates to PV generation for the purpose of life cycle analysis [6],[7] however these typically model emissions the typical conditions for an 'average' year rather than real data used for a historical analysis as in this work. Studies have also modeled the impact of PV at times of peak demand [8] but not the type of full year, short time-step analysis presented in this paper; the average relationship between time of generation and marginal emissions of CO<sub>2</sub> [9] and evaluated marginal emissions factors over a number of years [10].

Molin et al. [11] presented a study on the financial impacts of net metering for PV based on variable time intervals; hourly, monthly and yearly. This study suggested that net metering is most beneficial for PV using a full year for the time interval. This held true when assessed against data for Sweden, Germany and Spain using a 13-year long dataset. There are interesting parallels between this work which deals with financial performance at different time steps and our work which deals with carbon accounting at different time-steps. The key result of this study which applies to our own work is the suggestion that year-to-year variation is relatively modest. It also highlights that an international version of our study would be of great value, particularly as the grid carbon intensity profile can be very different from country to country. As a caveat to this point, electricity markets where a single fuel dominates such as

France (nuclear) and hence only have limited variation in carbon intensity, a repeat of our study would not be worthwhile.

This work has as its basis the variation in average grid mix emissions factor on a half hourly basis without any consideration of inter-year variability. The aim of this work was to assess the validity of using annual average grid mix electricity emissions factors for calculating the carbon savings resulting from exported renewable microgeneration. Current company carbon reporting guidelines use overall grid mix carbon factors rather than marginal factors (which on the existing UK grid will almost always be higher than the average grid mix) on the basis that all consumers have a shared responsibility for electricity emissions rather than different consumers taking electricity from different sources, this work maintains this philosophy of shared responsibility at any given time but with variability introduced depending on the time of PV generation. The authors consider that there is merit to the use of a time-varying emissions factor as an incentive to businesses to engage in more active demand-side management, Gyamfi et al [12] found that the reduction of CO<sub>2</sub> emissions would be as significant motivation for consumers to initiate demand side management as price signals and second only to avoiding blackouts.

#### **4.2. Sources of error**

The results of this work are based on PV generation for a single year. As can be seen from the clear difference between the results for Seashell and for the other six systems, PV generation data gathered over a longer timescale would allow for more authoritative findings. It is clear that for systems with similar generation profiles, the resulting carbon savings are closely related.

The gaps in the half hourly generation by fuel type tables were explicitly omitted from the remainder of the study on the basis that they accounted for an extremely small proportion of the dataset. A more thorough treatment would entail the generation of synthetic data to fill these gaps based on a logical process which may include some combination of activity either side of the data gaps, prevailing conditions and additional datasets such as those for overall electricity demand.

The emissions factors for the grid used in this study are exclusively for direct carbon emissions from electricity generation and do not take account of any emissions upstream of the power station. Including these indirect emissions would result in a truer picture of the emissions associated with electricity generation at the cost of increased uncertainty about the exact level of GEFs depending on which indirect emissions are included and the assumptions made when calculating indirect emissions.

#### **4.3. Simplifications and assumptions**

In this study, PV generation is treated as a negative load on the grid. In Great Britain where there is only a small amount of PV on the grid, this approach is adequate however with a significant amount of PV generation on the grid the low carbon electricity produced by PV will be rolled into the overall grid mix emissions factor. In this scenario, a negative demand approach would lead to double counting of the carbon emissions reductions from PV.

#### **4.4. Future & applications**

The results of this work clearly show that for PV, the carbon emissions saved by the renewable electricity generated are different from that which is estimated using the annual average grid mix emissions factor. If similar work for other technologies including other

renewables and energy efficiency technologies which have a time-varying behavior can also be shown to differ from the annual average grid mix emissions factor, there may be a case for altering the reliance on the annual average for company reporting of carbon emissions. With the arrival of improved metering technology allowing for measurement of electricity use at high time resolution, this kind of temporally sensitive reporting would become genuinely feasible.

This study has shown that carbon savings from PV appear to be lower based on emissions factors for the time of generation than with annual average emissions factors in Great Britain where the grid is higher in carbon over the winter where demand peaks. The situation may well be reversed in a region where peak electricity demand and carbon intensity are over summer as a result of cooling loads.

The authors intend to develop a system for including real time carbon savings in PV system monitoring. The study presented here will be widened to cover a larger number of PV systems and a longer timeframe, given the similarity of the results across PV systems it may be possible to reliably estimate the percentage difference between half hourly and annual emissions factors for systems where this kind of analysis is not undertaken. An investigation of how real time carbon savings against marginal grid carbon emissions can be reliably calculated may also prove to be a valuable exercise.

### **Acknowledgements**

The authors would like to thank the EPSRC for funding this work.

### **References**

- [1] DEFRA, Guidance on how to measure and report your greenhouse gas emissions, 2009, pp. 49 - 53
- [2] Elexon Portal, Historic Generation By Fuel Type Data Files, [https://elexonexchange.bsccentralservices.com/page\\_object\\_view.php?uid=76](https://elexonexchange.bsccentralservices.com/page_object_view.php?uid=76), Accessed online August 2010 (login required)
- [3] AMEE, Fuel Emission Factors, [http://explorer.amee.com/categories/Electricity\\_Generation\\_Emission\\_Factors/data](http://explorer.amee.com/categories/Electricity_Generation_Emission_Factors/data), accessed online August 2010 (login required)
- [4] DECC, Digest of United Kingdom Energy Statistics, 2009
- [5] DTI, Future Network Technologies, 2006, pp. 4-5
- [6] S. Krauter, Greenhouse Gas Reduction by PV, Proceedings of 3<sup>rd</sup> World Conference on Photovoltaic Energy Conversion, 2003, pp. 2610 - 2613
- [7] R. Laleman et al, Life Cycle Analysis to estimate the environmental impact of residential photovoltaic systems in regions with a low solar irradiation, Renewable and Sustainable Energy Reviews Vol 15, 2011, pp. 267-281
- [8] R. Spiegel et al, Demonstration of the Environmental and Demand-Side Management Benefits of Grid-Connected Photovoltaic Power Systems, Solar Energy Vol. 62, No. 5, 1998, pp. 345–358
- [9] G. Keolian and G. Lewis, Modeling the life cycle energy and environmental performance of amorphous silicon BIPV roofing in the US, Renewable Energy 28, 2003, pp. 271–293

- [10] A.D. Hawkes, Estimating marginal CO<sub>2</sub> emissions rates for national electricity systems, *Energy Policy* 38, 2010, pp. 5977–5987
- [11] A. Molin et al, Positive power market value for grid-connected roof-top solar power in Sweden, in *Proceedings of the 11<sup>th</sup> World Renewable Energy Congress (WREC XI)*, Abu Dhabi, UAE, 25-30 September 2010
- [12] S. Gyamfi et al. Demand Response in the Residential Sector: A Critical Feature of Sustainable Electricity Supply in New Zealand, 3<sup>rd</sup> International Conference on Sustainability Engineering and Science, Auckland, NZ, 2008

## Concentrator photovoltaic technologies and market: a critical review

Alaeddine Mokri, Mahieddine Emziane

*Solar Energy Materials and Devices Lab,  
Masdar Institute of Science and Technology,  
Masdar City, PO Box 54224, Abu Dhabi, UAE  
E-mailS: amokri@masdar.ac.ae, memziane@masdar.ac.ae*

---

**Abstract:** This paper offers an overview about the current status of the concentrator photovoltaic technologies and market. It highlights the potential of this technology to bring the cost of electricity to competitive levels with fossil-fuel based resources. It starts with an overview about the photovoltaic market and then it narrows its scope to describe the concentrator photovoltaic technology (CPV). Then, it goes on quantifying the world CPV capacity based on the latest industry reports released in 2010. In this paper, we estimate the current world operational CPV capacity to be 21 MW. This paper also reports a minimum installation cost as low as 3.05 \$/W and a levelised cost of electricity as low as 0.14 \$/kWh. Those are the minimum costs announced in 2010. One interesting conclusion of this study is that CPV systems with high concentration have a higher economic potential comparatively with low concentration CPV systems.

**Keywords:** solar energy, photovoltaic, concentrator photovoltaics, LCOE, grid parity.

---

### 1. Introduction

Past and current trends in energy generation, supply and consumption have shown their unsustainability at the economic, social, and more importantly, environment levels. These trends led to the following [1]:

- The current GHG emission levels have not been seen for at least 800 000 years.
- By the year 2050, CO<sub>2</sub> concentration in the atmosphere will reach 380 part per million which is higher than the upper safe limit (i.e. 350 part per million) for avoiding severe climate change effects [2].
- In the past century, temperature of the planet increased by 0.7° C and the sea levels by 20 cm.
- Ice caps are disappearing.
- The International Energy Agency (IEA) expects an increase of 50% in energy demand by 2030.
- Half of the CO<sub>2</sub> emissions from burning fossil fuels over the last 200 years were emitted in the last 30 years.

Without a decisive action, on the top of the facts listed above, increasing energy demand will raise concerns over energy security because of the continuous growth of the world population and economy [3].

The solution to this issue is to use clean renewable energy sources like solar, wind, geothermal, etc. Although these energy sources are abundant and free, their conversion to useful power comes at a higher cost than power from non-renewable sources and makes them less advantageous. Therefore, the main condition for the transition to a renewable energy era is to generate power from renewable sources at competitive costs with power from fossil-fuel based resources.

Since 2000, global photovoltaic (PV) capacity has been growing at an average rate of 40% per year to reach 14 Giga Watt in 2008 [3]. Expectedly, the annual photovoltaic capacity will represent 11% of the global electricity capacity by the year 2050 [3]. This will cancel 2.3 Giga tons of CO<sub>2</sub> emissions from the atmosphere [3].

PV energy encompasses a wide range of technologies: silicon, thin films and concentrator photovoltaics (CPV). While silicon modules represent 85-90% of the global annual market and thin film modules represent 10-15%, CPV modules represent less than 1% of the global annual market [3]. However, CPV is still emerging and has the highest potential of bringing the LCOE (Levelized Cost of Electricity) down to values that make solar power cost-competitive with conventional sources of electricity [4].

This article offers an overview of the current status of the CPV market and discusses the potential to achieve low LCOE.

## **2. Concentrator photovoltaic technology**

A CPV system consists simply of a small solar cell and an optical component to concentrate light on it. Using low-cost optical components with small solar cells instead of large expensive solar cells is a key feature to achieve a low LCOE [5].

By doing some simple math, one can conclude that to generate a 1W of electricity, a 25% efficient solar cell under a 1000 concentration ratio requires 1775 less cell surface than a 14% efficient cell under no concentration. In the real world, CPV modules using 27%-36% efficient multi-junction solar cells are 25% efficient [4]. This is higher than the efficiency of converting power by using any of the other PV technologies. Comparatively with the other PV technologies, high CPV systems efficiency means that less land is needed to generate a given amount of power; or alternatively, more power can be generated if the same land area is used.

The claims above all depend to a large extent on the solar resource available. For instance, high-concentration CPV modules are economically viable in areas with more than 2200 kW/m<sup>2</sup> year of direct normal irradiance (DNI). Humid regions, areas with cloudy weather, windy areas and spots with an inappropriate topography all may not be suitable places for installing CPV power plants [4].

Based on their concentration ratio and the type of solar cells used, CPV technologies can be classified into three categories:

### **2.1. Low-Concentration Photovoltaic (LCPV):**

Systems with a concentration lower than 40 suns fit in this category. These systems use Si solar cells and require passive cooling only to maintain their performance. Due to their large acceptance angle, high-precision tracking might not be required. Today, more than 20 companies are known for supplying LCPV modules.

### **2.2. Mid-Concentration Photovoltaic (MCPV):**

This applies to systems with concentration ratios in the range 40-300 suns. These systems use multi-junction cells and may require active cooling. Active cooling is a requirement because typically when the temperature of the solar cells increases, their conversion efficiency goes down. High-precision tracking is also required to convert the maximum of the incident

sunlight. Based on the CPV Today Industry Report, 3 companies only supply MCPV modules [4].

### **2.3. High-Concentration Photovoltaic (HCPV):**

These are systems with concentration ratios in the range 300-2000 suns. These systems require a high capacity heat sink, high-precision tracking and high-performance multi-junction solar cells; hence, their high cost. The potential of this technology relies on the very high-efficient multi-junction cells used. The 41.6 % efficiency recorded on a multi-junction cell under concentration in August 2009 by Spectrolab and the 35.6 % efficiency recorded on a solar cell under no concentration by Sharp, both highlight the potential of these CPV systems to achieve high efficiencies [4, 6]. Theoretically, the efficiency of multi-junction solar cells can reach 87 %. By using these high-performance cells, module efficiencies above 30% have been recorded [7]. About 33 companies do supply HCPV modules.

## **3. CPV installations worldwide**

The total CPV capacity grew up from few kilowatts installed in 2006, to 1 MW in 2007, to 13 MW in 2008, and unexpectedly to 4 MW only in 2009 because of the world financial crisis. 50 MW capacity was expected to be installed worldwide in 2009 [8]. Nevertheless, 2009 witnessed the announcement of a 60 MW CPV power plant in Taiwan by Ya-Fei Green Energy and Guascor Foton.

Those numbers are much below the potential CPV capacity that can be provided. Today, the world manufacturing capacity of CPV is 1.23 GW and it is expected to reach 2.65 GW by 2012-2013.

Currently, the total operational HCPV capacity is estimated at 20.15 MW distributed among 48 installations worldwide. As for the pre-operational HCPV capacity, it is predicted that 23 installations will be operational to produce 247 MW.

For LCPV, the total operational capacity is 0.81 MW and it is distributed among 19 installations worldwide. Fig. 1 lists the CPV companies worldwide and the operational and the preoperational capacity of each one.

## **4. Current costs of electricity from CPV systems**

The installed cost is a common criterion for ranking and comparing solar installations. It is the cost of the entire installation divided by the peak-power rating. The installed cost of CPV systems varies from one installation to the other; therefore, many values have been reported in the literature. Based on the CPV today Industry Report 2010, the overall installed cost of HCPV systems in 2010 ranges from 3.05 \$/W to 7.25 \$/W; however, for LCPV systems, the installed cost is 5.05 \$/W [4].

The LCOE is also another useful measure for comparing and ranking solar installations. It is the cost of 1 kWh of energy from the system during its life time. For HCPV systems, the LCOE has been reported to vary between 0.14 \$/kWh and 0.50 \$/kWh. For LCPV systems, the LCOE has been reported to be 0.24 \$/kWh.

These costs can be brought down by improving the efficiency of the cells, improving their reliability and also lowering the cost of the solar cells [4].

## 5. Conclusions

In this paper, we discussed the potential of CPV as a choice for generating clean energy at a low LCOE. The most up-to-date data indicate that the total installed CPV capacity in the world does not exceed 300 MW. We have also shown that this is much below the 1.23 GW manufacturing capacity available today.

For HCPV, installation costs as low as 3.05 \$/W and LCOE as low as 0.14 \$/kWh have been reported in 2010 based on real data. For LCPV, an installed cost of 5.05 \$/W and LCOE of 0.24 \$ have been reported. These numbers show that CPV systems with high concentration have a high economic potential comparatively with low concentration CPV systems.

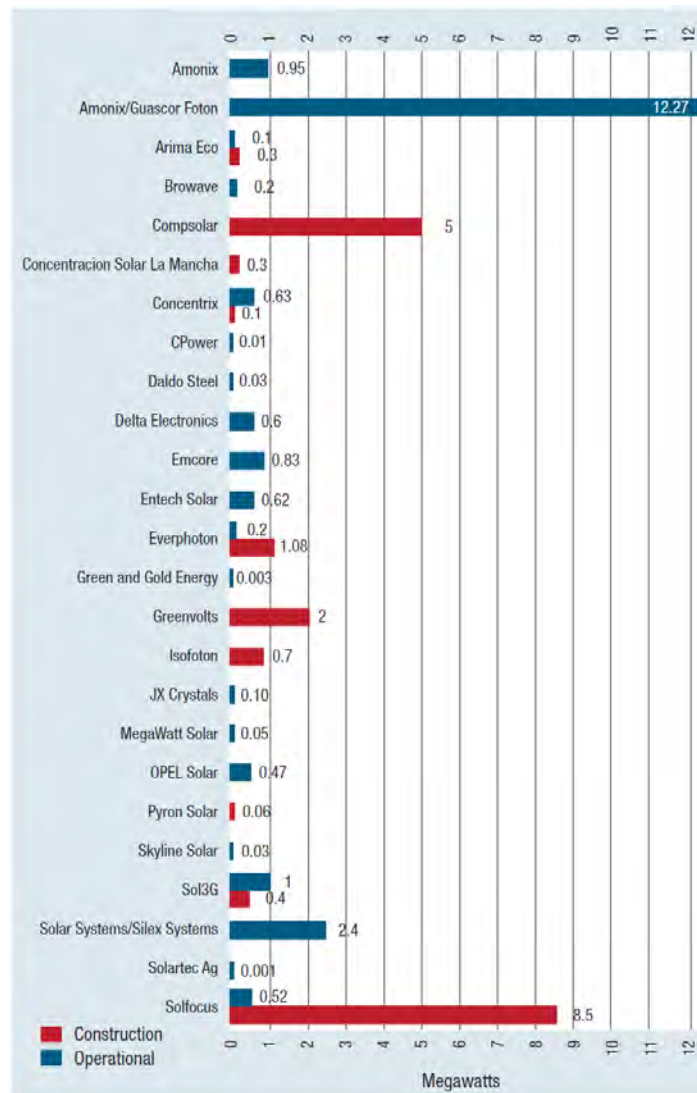


Fig. 1. Pre-operational and operational CPV power generation capacity by company (from reference [4]).

## **References**

- [1] Trevor M. Letcher, "Future Energy: Improved, sustainable and clean options for our planet." Elsevier, 2008.
- [2] K. Rajeshwar, R. McConnell, S. Licht "Solar hydrogen generation toward a renewable energy future", Springer, 2008.
- [3] "Technology roadmap: solar photovoltaic energy," International Energy Agency, 2010.
- [4] A. Extance, C. Marquez, "The Concentrated Photovoltaics Industry Report 2010," CPV Today, 2010.
- [5] R. A. Sherif, N. H. Karam, R. R. King, D. R. Lillington, "The Path to 1 GW of Concentrator Photovoltaics Using multi-junction Solar Cells," 31 IEEE PVSC pp17-22, 2005; "multi-junction Solar Cells," Nature Photonics 2008.
- [6] M. A. Green, K. Emery, Y. Hishikawa and W. Warta, Progress in Photovoltaics: Research and Applications, 2010; 18:346–352.
- [7] R. Gordon, G. Kinsey, A. Nayaak, V. Garboushian, "30% CPV module milestone," in proceedings of the 6<sup>th</sup> International Conference on Photovoltaic Systems (CPV-6), pp171, 2010.
- [8] S. Kurtz, "Opportunities and Challenges for Development of a Mature Concentrating Photovoltaic Power Industry", Technical Report NREL/TP-520-43208, Revised November 2009.
- [9] D. Friedman, "National solar technology roadmap: concentrator PV", Management Report NREL/MP-520-41735, June 2007.

## Environmental impacts of large-scale grid-connected ground-mounted PV installations

Antoine Beylot<sup>1,\*</sup>, Jérôme Payet<sup>1</sup>, Clément Puech<sup>2</sup>, Nadine Adra<sup>2</sup>, Philippe Jacquin<sup>3</sup>,  
Isabelle Blanc<sup>4</sup>, Didier Beloin-Saint-Pierre<sup>4</sup>

<sup>1</sup> CYCLECO, Ambérieu-en-Bugey, France

<sup>2</sup> Transénergie, Ecully, France

<sup>3</sup> PHK consultants, Ecully, France

<sup>4</sup> MINES ParisTech Sophia Antipolis, France

\* Corresponding author. Tel: +33 437860712, E-mail: antoine.beylot@cycleco.eu

**Abstract:** This study characterizes the environmental performances of large-scale ground-mounted PV installations by considering a life-cycle approach. The methodology is based on the application of the existing international standards of Life Cycle Assessment (LCA). Four scenarios are compared, considering fixed-mounting structures with (1) primary aluminum supports or (2) wood supports, and mobile structures with (3) single-axis trackers or (4) dual-axis trackers. Life cycle inventories are based on manufacturers' data combined with additional calculations and assumptions. Fixed-mounting installations with primary aluminum supports show the largest environmental impact potential with respect to human health, climate change and energy consumption. The climate change impact potential ranges between 37.5 and 53.5 gCO<sub>2</sub>eq/kWh depending on the scenario, assuming 1700 kWh/m<sup>2</sup>.yr of irradiation on an inclined plane (30°), and multi-crystalline silicon modules with 14% of energy production performance. Mobile PV installations with dual-axis trackers show the largest impact potential on ecosystem quality, with more than a factor 2 of difference with other considered installations. Supports mass and composition, power density (in MW<sub>p</sub>/acre of land) and energy production performances appear as key design parameters with respect to large-scale ground mounted PV installations environmental performances, in addition to modules manufacturing process energy inputs.

**Keywords:** Environmental impacts, LCA, PV installations

### 1. Introduction

PV systems deployment and solar energy use are developing rapidly in Europe. In particular, Austria, Switzerland, Germany, France, Italy and the Netherlands experienced a two to four-fold increase in their annual installed photovoltaic power in 2009 [1]. Large scale PV systems (> 500 kWp) represent a lower share of the photovoltaic power production compared to small scale systems (< 3 kWp). However, their market is showing a dramatic increase in number of installations. In France a 90% increase was observed between the 2<sup>nd</sup> and 1<sup>st</sup> trimesters 2010 for installations of power superior to 500 kWp, compared to a 38% increase for small scale installations [2].

In this context of rapid development, the issue of PV systems environmental impacts characterization has been intensively addressed and discussed. While several initial publications underlined the higher external environmental costs of PV compared to those of nuclear energy and natural-gas-fuel power plants [3,4], new LCA databases have been built to comply with the improvements in PV systems [5,6]. They highlighted the photovoltaic potential for a low carbon energy supply and the environmental benefits of PV as opposed to fossil-fuel based energy [7, 8]. LCA data currently consider solar cells, panels and installation equipments production in the supply chain of different technologies. Up to now, most studies have focused on module technologies and small-scale installations. They exposed the key parameters for environmental performances of PV installations, when focusing on greenhouse gas emissions and primary energy use as environmental indicators: irradiation intensity received by PV installations, modules manufacturing electricity use and its corresponding fuel

mix and PV technology [9, 12]. However, only few evaluations of large-scale PV installations can be found in the literature [13, 14].

This study aims at characterizing the environmental impacts of large-scale grid-connected ground-mounted PV installations (5MWp), considering one module technology (mc-Si) with different structures and types of supports (fixed-mounting or mobile). The results highlight key parameters related to large scale PV systems environmental performances on a life cycle perspective. Impacts on climate change and energy consumption are considered as indicators for the environmental assessment together with human health and ecosystem quality indicators. Recommendations are finally given to enable stakeholders in the field of large scale PV systems to minimize the environmental impacts of future installations.

## 2. Methodology

This Life Cycle Assessment (LCA) study was performed in compliance with the ISO standards 14040 and 14044 [15, 16] and followed the provisions of the ILCD handbook [17].

### 2.1. Scope of the study

The Functional Unit is defined as the kWh of electricity produced by a large-scale grid-connected ground-mounted PV installation (5MWp), considering 1700 kWh/m<sup>2</sup>.yr of irradiation on an inclined plane (30°) and 30 years of life expectancy.

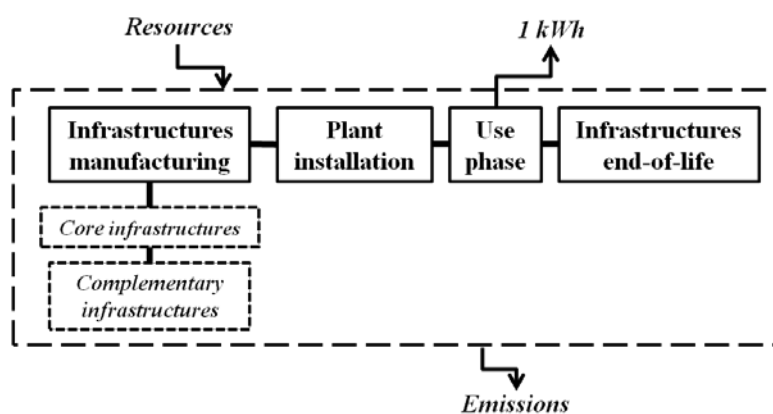


Fig. 1. Scheme of system boundaries

(excavation, modules and structures end-of-life). Recycled waste material is assumed to substitute for primary produced material, without considering any correction factor.

Four grid-connected ground-mounted PV installations are compared in the study. Their differentiating key features are detailed in Tables 1 and 2. The multi-crystalline silicon (mc-Si) PV technology is chosen for every scenario. Consequently, only the type of structure and its related system energy production differentiate the scenarios.

Life cycle impact assessment is performed with the use of the IMPACT 2002+ method (v2.04) [18]. The results focus on four damage impact categories: climate change, resources, human health and ecosystem quality. The temporary carbon storage in bio-based goods (wood supports in one scenario) is taken into account in compliance with ILCD provisions, i.e. by considering “-0.01 kg CO<sub>2</sub>-equivalents” per 1 kg carbon dioxide and 1 year of storage/delayed emissions.

Table 1. Scenarios key features

Scenarios	1	2	3	4
Module Technology	mc-Si	mc-Si	mc-Si	mc-Si
Structure key features	Fixed mounting Primary aluminum supports	Fixed mounting Wood-based supports	Mobile Single-axis trackers	Mobile Dual-axis trackers

## 2.2. Inventory

The inventory distinguishes between:

- foreground processes, corresponding to PV systems parameters, land occupation and electricity use and generation, for which specific data have been used.
- upstream and downstream processes, corresponding to materials extraction and transformation, PV modules fabrication, materials and products transport, electricity production mix, infrastructures end-of-life, for which semi-specific or generic data have been used. Ecoinvent v2.0 [19] was used as the reference database for semi-specific data.

### 2.2.1. PV installations electricity production

Energy efficiency of the PV modules is set at 14%, with an average performance ratio of 0.855 for the system. The increase in production thanks to mobility is respectively set to 5% for Scenario 3 considering single-axis trackers and to 32.5% for Scenario 4 considering dual-axis trackers, based on average manufacturers' data. The corresponding electricity generated over the 30 years installation life-time is given in Table 2 for the 4 scenarios.

Table 2. Energy production in scenarios

Scenarios	1	2	3	4
Increase in production due to mobility	-	-	5% (Average data from a Spanish supports manufacturer)	32.5% (Average data from an Italian supports manufacturer)
Electricity production over 30 years (in GWh)	218.0	218.0	228.9	288.9

### 2.2.2. Infrastructures

Data on infrastructures of large-scale PV installations have been either directly collected or calculated from manufacturers data, as detailed in Table 3. Ten 500 kW inverters are necessary for each PV installation, assuming 10 years of life expectancy (i.e. 30 inverters over each installation life-time), and five 1MW transformers, considering 30 years of life expectancy.

### 2.2.3. Key additional assumptions

In the absence of specific or semi-specific data for plant building operations (excavation, track construction), for engines composition (used in mobile installations) and for waste structures management (waste modules and supports), the model is based on hypothesis gathered in a Supporting information sheet. In particular, the necessary road to access the installation is assumed to be 3 km long. Moreover, multi-crystalline modules are assumed to be entirely recycled at the end of the installation life, by use of a thermal/chemical treatment. The life cycle inventory corresponding to modules recycling is partly based on literature data [20] completed with additional assumptions.

Table 3. Data collection for infrastructures in scenarios

	Scenario 1	Scenario 2	Scenario 3	Scenario 4
<i>Modules</i>	35714 m <sup>2</sup> - value based on calculations from energy production performances			
<i>Area</i>	92 888 m <sup>2</sup> (*)	92 888 m <sup>2</sup> (*)	96 922 m <sup>2</sup> (*)	418 770 m <sup>2</sup> (*)
<i>Supports</i>	Primary aluminum – Mass values from technical sheets from a German manufacturer	Wood, primary aluminum and iron – Mass values from data from a multi-MWp installation in France	Galvanized steel – Mass values from technical sheets from a Spanish manufacturer	Galvanized steel – Mass values from technical sheets from an Italian manufacturer
<i>Foundations</i>	Cast iron stakes - approximation based on technical sheets from an Austrian manufacturer	Concrete – Mass values from data from a multi-MWp installation in France	Concrete - Mass values from implementation schemes (*)	Concrete - Mass values from implementation schemes (*)
<i>Cabling</i>	Copper, aluminum and PVC – Mass values from implementation schemes (*)			
<i>Transformers</i>	Reference flows data compiled from a French manufacturer			
<i>Complementary infrastructures</i>	Control center building made of steel reinforced concrete + steel wire fences - Reference flows data compiled from a German manufacturer for one installation			

(\*) computed from the experience of the consulting and engineering partner (Transénergie)

### 3. Results

#### 3.1. Scenarios comparison

The Life Cycle Impact Assessment results are shown in Figure 2 and Table 4. Negative values represent the environmental benefits of recycling. Those environmental benefits are not taken into account in the global results since they could be applied in another production chain where recycled aluminum is used. Scenario 1, considering fixed-mounting virgin aluminum supports, shows the largest environmental impacts in terms of human health, global warming and resources, while Scenario 4 (dual-axis tracker systems) generates the largest impacts on ecosystem quality. Scenarios 2 and 3 (fixed-mounting wood-based and single-axis trackers) globally show the best environmental performances, with gaps between their potential damage impacts ranging from 1 to 3% depending on the considered category.

#### 3.2. Detailed environmental performances

##### 3.2.1. Climate change

Modules manufacturing represents the largest share of climate change impact for all scenarios (38 - 56% of the total impact). Moreover, virgin aluminum supports manufacturing stands for a large proportion of the total impact of scenario 1 (36%, if including environmental benefits due to aluminum recycling), contrarily to wood-based fixed-mounting supports (Scenario 2, 21% of the total impact) and galvanized steel mobile supports (Scenarios 3 and 4, respectively 5 and 12%). The climate change impact due to supports is 2 to 10 times larger in scenario 1 than in scenarios 2, 3 and 4. As a consequence, the total climate change impact is 28% larger in scenario 1 than in scenario 2, whereas the climate change impact due to modules is equal for both scenarios (21.4 g. CO<sub>2</sub> eq/kWh, a relatively low value to be related with the assumed use of the French electricity mix for modules manufacturing in scenarios).

Depending on the considered scenario, electric equipments (inverters, transformers and engines in case of mobile structures), complementary infrastructures (road, control centers) and foundations may represent a significant share of the total impact. For example, for

scenario 4, these elements represent up to 50% of the total climate change burden. This large share is partly due to the increase in electricity production, generating the decrease in environmental impacts of modules (16.1 g. CO<sub>2</sub>eq/kWh), combined with an increase of the impacts of these balance of system (BOS) components.

Table 4. Damage impact assessment results for the four scenarios (Impact 2002+method v2.04)

Study case	Human health (DALY/kWh)	Ecosystem quality (PDF.m <sup>2</sup> .yr/kWh)	Climate change (g. CO <sub>2</sub> eq./kWh)	Resources (MJ primary/kWh)
Scenario 1	4.65E-08	2.46E-02	53.5	1.10
Scenario 2	3.24E-08	2.35E-02	38.0	0.88
Scenario 3	3.34E-08	2.32E-02	37.5	0.90
Scenario 4	4.12E-08	5.15E-02	42.8	0.88

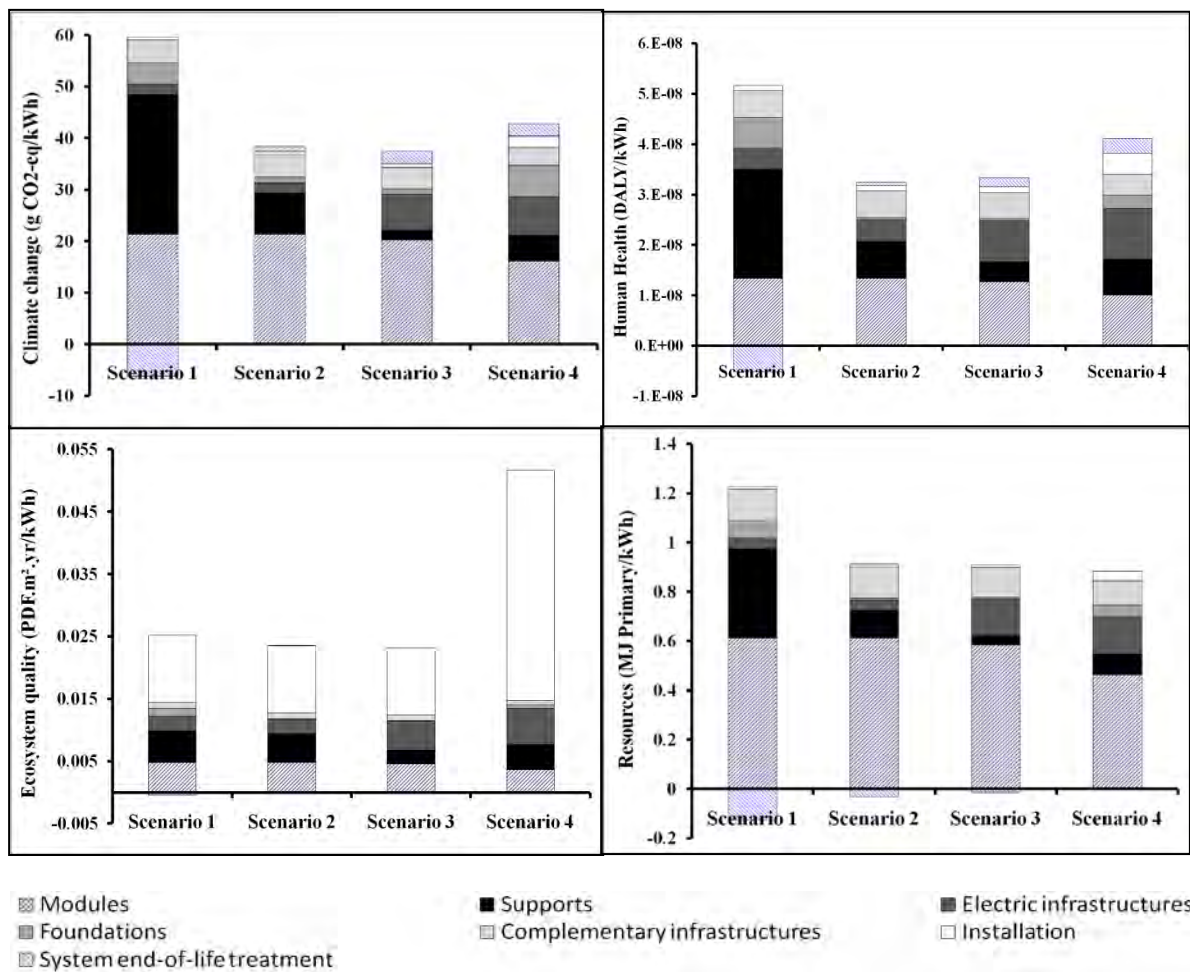


Fig. 2. Detailed environmental impacts of the 4 scenarios (considering 1700 kWh/m<sup>2</sup>.yr of irradiation on an inclined plane, mc-Si modules with 14% of energy production performance and IMPACT2002+v2.04 damage indicators)

### 3.2.2. Human health

Impacts on human health show a similar trend with the impacts on climate change, both in terms of overall impact comparison and predominant Life Cycle phases. Modules manufacturing generates the largest environmental burden for scenarios 2, 3 and 4 (from 29 to 41% of the total impact depending on the scenario), while virgin aluminum supports manufacturing represents the largest share for scenario 1 (33% if including benefits due to

recycling). Small particulates, NO<sub>x</sub> and SO<sub>2</sub> air emissions related to aluminum production (due in particular to electricity requirements and mostly emitted in the aluminum country of origin) represent 22% of the total impact on human health for scenario 1. On the other hand, the human health impact of wood (scenario 2) and galvanized steel supports (scenarios 3 and 4) is lower in absolute value and also stands for a lower share of the total impact.

### 3.2.3. Resources

Modules manufacturing contribution to the total burden on resources amounts to 53 to 70% depending on the scenario. The environmental benefit gained from the increase in electricity production in case of mobile installations, which is directly reflected in terms of modules impacts, is counterbalanced by different requirements in infrastructures (e.g. electric equipments). As a consequence, whereas scenarios 3 and 4 consider larger electricity production from 5 to 32.5% compared to scenario 2, the gap in impacts on resources between these 3 scenarios is lower than 2%.

Impact on resources of virgin aluminum supports accounts for 24% of scenario 1 total impact (if including benefits from aluminum recycling). This impact is 2 to 6 times larger than impacts of wood-based and galvanized steel supports of scenarios 2, 3 and 4.

### 3.2.4. Ecosystem quality

The impact on ecosystem quality is mainly influenced by land occupation, which represents 44 to 47% of the impact in case of scenarios 1 to 3 and up to 72% of the impact in case of scenario 4. The difference in impacts on ecosystem quality amounts to a factor 2.1-2.2 between mobile scenario 4 (dual-axis trackers) and scenarios 1 to 3, to compare with a 4.5 ratio between scenario 4 and scenarios 1-3 occupied surfaces. Indeed, power plants with dual-axes trackers require expanding the distances between each element of the PV field, because the shades induced by the moving PV planes are more important: the “power density” in terms of MWp/acre of land used is therefore much lower than for fixed-mounting systems.

## 4. Discussion

### 4.1. Key environmental parameters

Irradiation intensity received by PV installations, modules manufacturing electricity use and its corresponding fuel mix and solar radiation conversion efficiency were shown to be key environmental parameters of PV installations in several studies [9, 12]. Similarly, this study highlights the large influence of modules production, and to a lower extent of electricity production increase in mobile conditions, on the environmental performances of large-scale grid-connected ground-mounted PV installations. In addition, two other critical parameters arise: structure supports and occupied surfaces.

#### 4.1.1. Metal/Wood supports

The environmental impact of supports production is predominant considering climate change, resources consumption and impacts on human health, and is responsible for the environmental gap between scenarios in several cases (e.g. between Scenarios 1 and 2). The impact of supports is firstly related with their weight: as observed by Mason *et al.* [15], decreasing the quantity of metal supports in large-scale installations results in significant environmental improvements. However, materials nature appears as an even more critical environmental parameter. For example, the galvanized steel supports mass is 8% larger in scenario 4 than the primary aluminum supports mass in scenario 1 (considering mass per produced kWh), whereas the corresponding impact on e.g. climate change is 81% larger for supports of

scenario 1. Moreover, a sensitivity analysis has been conducted on aluminum supports, by considering secondary material (from old scrap) instead of virgin material. The use of secondary material generates significant decreases in environmental impacts of scenario 1: 42% for climate change, 39% for human health and 25% for resources, in compliance with the predominance of supports composition on the impacts of a large-scale PV installation.

#### *4.1.2. Occupied surface*

The occupied surface mainly determines the impact of large-scale PV installations on ecosystem quality. Consequently, land consuming alternatives such as mobile installations with dual-axis trackers will show relatively large impacts on ecosystem quality compared to fixed-mounting solutions, if considering the same modules technology.

#### **4.2. Comparing large-scale grid-connected ground-mounted PV installations**

The ranking of alternatives and their associated key parameters may differ from one environmental indicator to another, as observed when putting in perspective large-scale PV installations impacts on climate change and ecosystem quality. This study therefore enhances the need for a multi-criteria impact assessment method when comparing large-scale grid-connected ground-mounted PV installations. In addition, the results underline the multiplicity of parameters which may affect large-scale PV installations environmental performances. The environmental impacts of large-scale PV installations are the result of the interplay between a number of distinct parameters (e.g. energy production, supports mass and nature, electric equipments, etc.), whose related influence may counterbalance each other.

### **5. Conclusions, recommendations and perspectives**

The impact assessment of large-scale ground mounted PV installations therefore gives a detailed picture of their related environmental performances. Key installations design parameters arise in an environmental perspective: supports mass and composition, power density (in MWp/acre of land) and energy production performances, in addition to key parameters related to modules manufacturing (in particular electricity consumption and electricity production mix).

The environmental performances of large-scale PV installations are not in linear correlation with a unique quantified plant parameter. In that sense, for example, increasing the electricity production thanks to mobile technologies does not necessarily bring environmental benefits if combined with an increase in requirements in materials. A multi-criteria perspective - with respect to environmental indicators and installations key design parameters - should be undertaken with a view to optimizing PV large-scale installations environmental performances in a near future.

#### **Acknowledgements**

ADEME is co-financing this project which brings together different French specialists from the PV industry and LCA fields.

#### **References**

- [1] IEA. Trends in photovoltaic applications: Survey report of selected IEA countries between 1992 and 2006, Report IEA-PVPS T1-16:2007
- [2] Syndicat des énergies renouvelables (SER), SOLER. Etat des lieux du parc photovoltaïque français au 30 juin 2010. 2010.

- [3] European Commission, Directorate-General for Research. External Costs. Research results on socio-environmental damages due to electricity and transport. Office for Official Publications of the European Communities, Luxembourg. 2003.
- [4] Australian Coal Industry Association, ACARP. Coal in a sustainable society. 2004.
- [5] V.M. Fthenakis, E.A. Alsema, M.J. de Wild-Scholten. Life Cycle Assessment of Photovoltaics: perceptions, needs and challenges. 31<sup>st</sup> IEEE Photovoltaic Specialists Conference. 2005.
- [6] N. Jungbluth, M. Tuchschnid, R. Dones. Photovoltaics:ecoinvent report N° 6-XII. Swiss Center for Life Cycle Inventories, Dübendorf, CH. 2007.
- [7] E.A. Alsema, M.J. de Wild-Scholten, V.M. Fthenakis. Environmental impacts of PV electricity generation - A critical comparison of energy supply options. 2006.
- [8] IEA. Analysis of PV system's values beyond energy – by country and stakeholder. Report IEA-PVPS 10-02:2008
- [9] S. Pacca, D. Sivaraman, G. A. Keolian. Parameters affecting the life cycle performance of PV technologies and systems, Energy Policy, 2007, vol. 35, n°6, pp. 3316-3326
- [10] R. Kannan, K.C. Leong, R. Osman, H.K. Ho, C.P. Tso. Life cycle assessment study of solar PV systems: An example of a 2.7 kW(p) distributed solar PV system in Singapore, Solar Energy, 2006, vol. 80, n°5, pp. 555-563
- [11] I. Blanc, D. Beloin-Saint-Pierre, J. Payet, P. Jacquin, N. Adra, D. Mayer. Espace-PV: key sensitive parameters for environmental impacts of grid-connected PV systems with LCA. 23rd European Photovoltaic Energy Conference. 2008.
- [12] D. Beloin-Saint-Pierre, I. Blanc, J. Payet, P. Jacquin, N. Adra, D. Mayer. Environmental impact of PV systems: effects of energy sources used in production of solar panels. 24th European Photovoltaic Energy Conference. 2009.
- [13] K. Komoto, H. Uchida, M. Ito, K. Kurokawa, A. Inaba. Estimation of Energy Payback Time and CO<sub>2</sub> Emission of Various Kinds of PV Systems, 23rd European Photovoltaic Energy Conference. 2008.
- [14] J.M. Mason, V.M. Fthenakis, T. Hansen and H.C. Kim. Energy Pay-Back and Life Cycle CO<sub>2</sub> Emissions of the BOS in an Optimized 3.5 MW PV Installation. 2006.
- [15] International Standard Organization. ISO 14040. Environmental management – Life Cycle Assessment – principles and framework. 2006.
- [16] International Standard Organization. ISO 14044. Environmental management – Life Cycle Assessment – requirements and guidelines. 2006.
- [17] Institute for Environment and Sustainability. Joint Research Centre. European Commission. International Reference Life Cycle Data System handbook. 2010
- [18] O. Jolliet, M. Margni, R. Charles, S. Humbert, J. Payet, G. Rebitzer, R. Rosenbaum. Impact 2002+: A new life cycle impact assessment methodology, International Journal of Life Cycle Assessment. 2003. Volume: 8, Issue: 6, Pages: 324-330.
- [19] Swiss Center for Life Cycle Inventories. The life cycle inventory data version 2.0. <http://www.ecoinvent.ch>. 2008.
- [20] A. Müller, K. Wambach, E. Alsema. Life Cycle Analysis of solar module recycling process. 20th European Photovoltaic Solar Energy Conference. 2005.

## Progress in Luminescent Solar Concentrator Research: Solar Energy for the Built Environment

Paul P. C. Verbunt<sup>1</sup>, Michael G. Debije<sup>1\*</sup>,

<sup>1</sup> Eindhoven University of Technology, Eindhoven, The Netherlands

\* Corresponding author: Tel: +31 40 2475881, Fax: +31 40 2436999, E-mail: mgdebije@tue.nl

---

**Abstract:** This paper presents a concise review of recent research on the luminescent solar concentrator (LSC). The topics covered will include studies of novel luminophores and attempts to limit the losses in the devices, both surface and internal. These efforts include application of organic and inorganic-based selective mirrors which allow sunlight in but reflect emitted light, luminophores alignment to manipulate the emitted light path, and patterning of the dye layer. Finally, the paper will offer some possible ‘glimpses to the future’, and offer some additional research paths that could result in a device that could make solar energy a ubiquitous part of the built environment as sound barriers, bus stop roofs, awnings or siding tiles. Considering the reported efficiencies of the LSC are comparable to those reported for organic PVs, which are also being considered for use in the built environment, the results of the research on the LSC to date warrants more widespread attention.

**Keywords:** Solar energy, Luminescent solar concentrator, Building integrated photovoltaics, Review

---

### 1. Introduction

The European Committee wants all newly built buildings to be near-zero energy by 2020<sup>[1]</sup>. This demands architects integrate energy saving and energy generation into their designs. To give architects more freedom, the devices saving and/or generating energy must be easily adaptable. A readily available energy source in a built environment is the sun, which is clean, safe, inexhaustible and reliable but generation of electricity with conventional photovoltaic (PV) cells has several disadvantages in this environment: the cells remain costly, modules are heavy, and limited in coloration (black and dark blue). Furthermore, PV cells respond optimally to direct sunlight, while in the built environment much of the sunlight is diffuse due to scattering and reflections by other objects, such as trees, buildings, and even clouds.

An alternative solar energy harvester was proposed in the 1970's, the luminescent solar concentrator (LSC)<sup>[2]</sup>. In the LSC, sunlight penetrates the top surface of an inexpensive plastic or glass waveguide. This light is absorbed by luminescent molecules which are either embedded in the waveguide or applied in a separate layer on top or bottom of the waveguide. The luminescent molecules can be organic fluorescent dyes, or inorganic phosphors or quantum dots. The absorbed light is re-emitted at longer wavelengths, and a fraction of the re-emitted light is trapped in the waveguide by total internal reflection and becomes concentrated along the edges of the plate. Small PV cells attached to edges of the waveguide collect the emission light and convert it to electricity.

The LSC has potential advantages over silicon-based PV panels, especially in the built environment. For one, they can reduce the size of the PV cells more than 90% and the materials for making LSCs are inexpensive, reducing module prices. The plastic waveguide is lighter than the silicon PV panels, leading to a reduction in weight, which makes LSCs more viable for mounting to the sides of buildings. Sunlight can better penetrate the surface of the LSC waveguide from all angles, making them more appropriate for collecting non-direct sunlight. Lastly, LSCs have a great flexibility in design, which make them attractive for architects: they may be made thin and can be cut in any desired shape, cast in almost any color and may be transparent. Since LSCs can be thin, it becomes possible to make curved device. If the photon in/ photon out efficiency is high enough, the cost of electricity generated by the LSC could be competitive<sup>[3]</sup>. These combined features make

LSCs interesting devices for increasing public acceptance of solar energy: while the efficiency of an LSC will be lower than an equivalent area of a silicon PV, the reduced cost and flexibility in design could make LSCs viable for the urban area. The LSC hasn't yet been commercialized owing to several drawbacks which limit their efficiency<sup>[4]</sup>. Loss mechanisms for LSCs are shown in **Figure 1**.

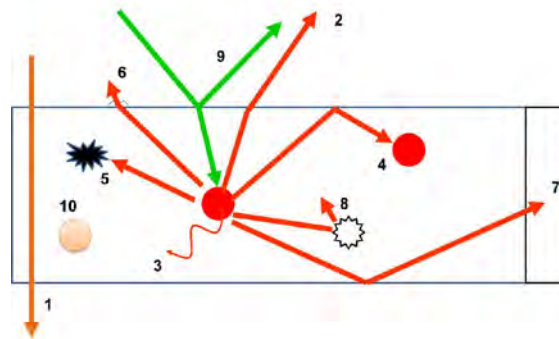


**Figure 1.** Loss mechanisms in LSCs: 1) Input light not absorbed by the dye molecules, 2) Light emitted outside capture cone, 3) Quantum efficiency of the dye molecules  $< 1$ , 4) Re-absorption of emitted light by another dye molecule, 5) Absorption of emitted light by the waveguide, 6) Surface scattering, 7) Solar cell losses, 8) Internal waveguide scattering, 9) Reflection from the  $e$  surface, 10) Limited dye stability.

The first loss is sunlight not absorbed by the dye molecules: this light is lost through the bottom surface. The second is light emitted by dye molecules under an angle which is refracted out of the waveguide instead of reflected internally- ( $> 40\%$  of all absorbed energy may be lost through the top and bottom surfaces of the LSC<sup>[5]</sup>). The third loss is absorbed photons not re-emitted by the dye molecules, but instead lost as heat and vibrations. Re-absorption of emitted photons by subsequent dye molecules via overlap of emission and absorption bands is a fourth loss. Waveguides can exhibit parasitic absorption, especially in the near infrared, and is the fifth loss cited. Sixth, imperfections of the waveguide surface can cause photons in the waveguide mode to leave the surface. Seventh, the PV cell at the waveguide edge has a non-uniform spectral response, with a fraction of incident photons being lost due to the finite conversion efficiency. Imperfections in the waveguide bulk lead to the eighth loss, scattered waveguided photons. In addition, a small part of the input light is reflected from the surface of the waveguide, shown as the ninth loss. Finally, there is loss caused by degradation of the dye molecules, primarily due to UV absorption.

## 2. Losses and Proposed Solutions

### 2.1. Surface Loss

Dye-emitted photons emitted inside the escape cone will be lost through the surfaces, and measurements suggest that 40-55% of all absorbed energy is lost in this way (this translates into a 50-70% loss of photons)<sup>[5]</sup>: these results were confirmed by simulation<sup>[6]</sup>. This surface loss is a key one for LSCs, and in the last couple of years multiple groups have done research on minimizing them by two processes: aligning the luminophores and applying selective mirrors.

*Aligned luminophores:* Organic luminophores are often dichroic in absorption and transmission<sup>[7]</sup>, opening new possibilities in controlling the spatial distribution of emitted light, provided that the physical ordering of the dyes is macroscopically controlled. The alignment of dichroic dyes in liquid crystalline (nematic) materials has been previously investigated<sup>[8]</sup> and it was shown that the macroscopic alignment of the dyes in the liquid crystalline host resulted in anisotropy and dichroism in both absorption and emission. Aligning the dye luminophores perpendicular to the waveguide surface leads to an emission primarily in the direction of the waveguide, resulting in a sharp decrease of surface loss to less than 10%<sup>[9]</sup>, confirmed by simulations using collimated light<sup>[6]</sup>.

However, in this configuration the luminophores have low absorption, and concurrent low edge emission: trapping efficiency of emitted photons increases from ~65% to over 80% when vertically aligned luminophores in LSCs are excited by an isotropic light source<sup>[10]</sup>.

Luminophores can also be aligned planarly, or parallel to the waveguide surface. This configuration can direct light so that 60% more energy is emitted from two edges of the LSC compared to the other two edges<sup>[11]</sup>: in this way the LSC can be used as a energy harvesting polarizer<sup>[12]</sup> which could be used in displays, for example. Additionally, if light is emitted primarily towards just two edges, the number of PV cells on the LSC can be reduced to two or even one, further reducing LSC cost.

*Selective mirrors:* A second way to reduce surface loss is by applying wavelength-selective mirrors<sup>[7, 21-31]</sup>. These mirrors are placed on top the LSC-waveguide with the goal that the reflectors not interfere with incoming sunlight that can be absorbed by the luminophores, but reflect only the luminophore-emitted light, which has a longer wavelength. Wavelength selective mirrors, made from chiral nematic (cholesteric) liquid crystals<sup>[13]</sup> or inorganics<sup>[13b,15]</sup>, have both been applied to the LSC. Up to 30% of the light that had previously escaped the surface was turned into edge emission, translating into a 12% LSC output improvement using the organic reflectors<sup>[14f]</sup>. Similar enhancements were determined using the inorganic reflectors<sup>[4b]</sup>. Organic reflectors are cast from solution and spontaneously form the reflective layer: this is generally a much simpler and less expensive process than application of multilayer inorganic Bragg reflectors.

## 2.2. Re-absorption of emitted photons by other dye molecules

Most organic luminophores used in LSCs have small Stokes-shifts, leading to relatively large overlaps between the absorption and the emission spectrum<sup>[15]</sup>. As a consequence, luminophores-emitted photons can be re-absorbed by another luminophore molecule during transportation through the waveguide. Re-absorptions are not losses by themselves, but the limited quantum efficiency of the luminophores and re-emission into the escape cone do result in losses<sup>[16]</sup>.

To reduce re-absorption events, researchers have experimented with luminophores with large Stokes-shift, like lanthanides<sup>[17]</sup> and quantum dots<sup>[18]</sup>, but these classes of luminophore bring other challenges to the production of LSCs. Inorganics tend to suffer from low solubility in organic matrices, and often also suffer from a low absorption. To reduce the amount of reabsorptions Taleb et al.<sup>[19]</sup> doped a dye with a polar and highly mobile material, like thionin. The dopant increased the separation of the absorption and fluorescence bands of the dye molecules, increasing the Stokes-shift and reducing (but not eliminating) the overlap in absorption and emission spectrum.

An option to reduce encounters of emitted light with the dyes is to only attach the dyes in a thin layer at the surface of the waveguide rather than filling the luminophore within the bulk of the waveguide. In this way, emission light may be transported predominantly in the clear host material, and only encounter the dye layer again every second internal reflection. These layers have been made of acrylates, via sol-gel techniques<sup>[20]</sup>, and polymerized liquid crystals<sup>[11]</sup>.

Using spatially-separated patterns of luminophores on top of a waveguide, the number of re-encounters emitted light could have with other dye molecules was reduced<sup>[21]</sup>. The transport efficiency of the photons through the LSC increased with decreasing dye coverage. However, due to reduction in absorption, the total system output decreased. A lens system on top of the LSC is being developed that would increase absorption and thus the system output<sup>[22]</sup>.

### 2.3. *Dyes: Limited absorption, stability and fluorescence efficiency*

The spectral breadth of the dye absorption is an important factors determining the potential efficiency of the LSC waveguide. There are a number of luminescent materials being studied for possible inclusion in the LSC. The workhorse of the organic dyes are based on perylenes or perylene derivatives<sup>[23]</sup>. The limitation of the organic dyes are often their lifetimes of operation in sunlight. Numerous studies are somewhat inconclusive as to the photostability of these materials: much depends on the processing conditions and polymeric environment of the fluorophore<sup>[24]</sup>. Organo-metallic molecules with good photostability (such as porphyrins) have also been proposed<sup>[25]</sup>. Inorganics such as lanthanides<sup>[17]</sup> hold promise as long-lasting replacements for organics, possibly with extended Stokes shifts. However, they tend to suffer from decreased absorption, and solubility becomes a definite issue. There is a large research effort directed at using quantum dots in the LSC<sup>[18]</sup>, but they have not yet reached their promise as they continue to generally display small Stokes-shifts with limited photostability. A possible future research direction is into the use of surface plasmonics to enhance the emission of the dye materials, allowing the use of potentially lower quantum efficiency luminophores<sup>[26]</sup>.

To aid in luminophore absorption, it is standard practice to apply a rear layer to an LSC to act as a reflector. The reflecting back layer effectively doubles the path length of incident light through the dye layer for enhanced absorption. Some of the initial experiments used a silver mirror<sup>[2b]</sup>, but such a mirror is absorbing in the visible range. To avoid absorptive losses, most recent work has employed a white scatterer<sup>[4, 27]</sup>. When separated from the waveguide by a small air gap, the rear scatterer can provide additional light for waveguides least 35 cm long<sup>[28]</sup>. The scatterer also may direct that fraction of incident light that cannot be absorbed by the dye directly at the PV cell, allowing it to generate electricity. The separation of the scatterer from the waveguide by a low refractive index layer is important to maintain waveguided light in the trapping modes of the waveguide: every encounter with the attached scattering layer re-distributes the light, and a significant fraction of this re-directed light will be outside the waveguide modes of the system.

Another option is to allow the LSCs to be transparent. In this form, the device could be used as a window while generating electrical current. An alternative design uses, rather than a waveguide with embedded, inflexible dyes, two glass plates coated with a conductor, the space between being filled by a liquid crystal containing a dye molecule<sup>[29]</sup>. The liquid crystal can be continually switched between orientations, from planar to homeotropic through application of a voltage across the plates. In the former state, the dye molecules follow the alignment of the LC host, and into a position of maximal absorption. The dye may then emit light which is partially trapped in the glass panes making up the 'window', and generate electrical current. By switching from planar to a tilt configuration, the output of the window necessarily drops due to reduced light absorption, but still produces a current, and the efficiency of edge output is actually increased. This design, while still needing considerable work to get transmissive properties correct with acceptable coloration, has advantages over other 'smart' windows. Photo- and thermochromics<sup>[30]</sup> or standard blinds<sup>[31]</sup> can, for example, be automatically switched between light and dark states, but generate no electricity. Thin-film PV modules can generate electricity<sup>[32]</sup>, but cannot have their transparency switched.

### 2.4. *Photovoltaic losses*

The standard silicon-based PV has a band gap corresponding to a photon of around 1100 nm (~1.1eV). Photons with energies above this threshold may still be processed by the solar cell, of course, but the excess energy of the photon is wasted, and converted most often into heat, and there is a reduction in the response of the cell for these shorter wavelengths. However, the LSC does not emit a spectrum remotely similar to the solar spectrum. Rather, it emits a narrow range of wavelengths, most-often centered at red and near-infrared wavelengths (630-720 nm at the

maximum). To better exploit the spectrum of the LSC, researchers have used type III-V PV cells based on GaAs and InGaP cells<sup>[4a]</sup> and obtained record-setting efficiencies. If these cells could be produced economically, it could hold great promise for widespread adoption of the LSC in future. Another option could be the use of organic-based PV cells, which often have a ‘sweet spot’ in the spectral range where the LSC emits<sup>[33]</sup>.

### 2.5. Waveguide losses

Around 4% of incoming light is reflected from the waveguide surface (the refractive indexes of polymethylmethacrylate (PMMA) and polycarbonate (PC) being between about 1.49 and 1.59) and never enter the waveguide, and could thus be considered a loss. While anti-reflection coatings are very common in PV cells, they have not yet been applied to LSCs. As the LSC relies on total internal reflection from two smooth surfaces, textured systems as used in many antireflective coatings<sup>[34]</sup> are not a viable option. Rather, coatings utilizing differences refractive indices can reduce these reflective losses and can be applied to polymeric materials<sup>[35]</sup>.

One challenge to produce luminophores with emissions approaching 800 nm for use in LSCs is that the waveguides, which are predominantly made of PMMA or PC, become parasitic, and absorb strongly at these wavelengths<sup>[36]</sup>. Additionally, additives made for improvement of various characteristics of the host matrix (such as altering UV stability or hardness) can have large impact on the device’s capability of transporting light. For example, an additive that only shows a small absorption when measured through the width of the waveguide can have a severe impact on the edge output of the same object, for the pathlength is magnified many tenfold<sup>[37]</sup>. As waveguides age, UV-generated damage creates light ‘traps’ within the polymer. Research into co-polymer systems has demonstrated enhanced photostability over the single component<sup>[38]</sup>. Non-uniform edge emission from waveguides also causes additional losses, as illumination of the attached PV at anything less than uniformity results in decreased performance. Thus, the shape of the waveguide also influences the emitted light distribution<sup>[39]</sup>.

### 3. Future directions

There are a great number of improvements that can and need to be made on the LSC to make it a more viable option for use in the urban environment. One aspect we find particularly intriguing is to provide an opportunity for the use of organic-based photovoltaics (OPV). One of the greatest challenges for OPV has been the inability of utilizing the ultraviolet portion of the UV spectrum, as well as survive the high energies of the UV light which causes premature degradation of the OPVs through destruction of the dye materials. However, the LSC does not illuminate the attached solar cell with a solar spectrum, but a much more narrow-band of light, generally in the near infrared, the range of wavelengths where OPVs perform their best. Coupled with the lack of exposure to UV light, this could provide the OPV with the first real niche application where they could excel.

A second largely unexploited research area is in the field of plasmonics. Many research publications show when a fluorescent molecule is brought close to a small metallic nanoparticle there is an enhancement of the fluorescence<sup>[40]</sup>. There has been application of surface plasmonics in PVs<sup>[41]</sup>, but to our knowledge, no extensive work in the field of LSCs.

It is the opinion of the authors that the rôle of the LSC in future urban renewable energy plan should be re-defined. Given the decrease in the costs associated with traditional silicon-based PV, it would seem folly to attempt to compete directly with the well-established, traditional PV panel on a rooftop. Rather, the LSC could best be used as a complement to silicon PV rather than a competitor, positioning itself in areas not normally accessible, such as areas with increased fractions of diffuse

light. The LSC is to be brought directly into public view, not ‘hidden away’ as most silicon PV panels. Applications could include sound barriers, telephone poles, and bus stop roofing.

## References

- [1] Directive 2010/31/EU of the European parliament and of the council of 19 May 2010 on the energy performance of buildings, Vol. 2010.
- [2] a) W. H. Weber and J. Lambe, Luminescent greenhouse collector for solar radiation *Applied Optics* 15, 1976, 2299, b) A. Goetzberger and W. Greube, Solar energy conversion with fluorescent collectors, *Applied Physics A: Materials Science & Processing* 14, 1977, 123.
- [3] E. Bende et al., Proc. of the 23<sup>rd</sup> European PV and Solar Energy Conference 2008, 461.
- [4] a) L. H. Slooff, et al., A luminescent solar concentrator with 7.1% power conversion efficiency *Physica Status Solidi (RRL) - Rapid Research Letters* 2, 2008, 257.
- [5] M. G. Debije et al., Measured surface loss from luminescent solar concentrator waveguides, *Applied Optics* 47, 2008, 6763.
- [6] S. McDowall, et al., Simulations of luminescent solar concentrators: Effects of polarization and fluorophore alignment, *Journal of Applied Physics* 108, 2010, 053508.
- [7] a) M. van Gorp and Y. K. Levine, Determination of transition moment directions in molecules of low symmetry using polarized fluorescence. I. Theory, *The Journal of Chemical Physics* 90, 1989, 4095, b) C. Sanchez et al., Polarized photoluminescence and order parameters of *in situ* photopolymerized liquid crystal films, *Journal of Applied Physics* 87, 2000, 274.
- [8] a) G. H. Heilmeyer and L. A. Zanoni, Guest-host interactions in nematic liquid crystals. A new electro-optic effect *Applied Physics Letters* 13, 1968, 91, b) R. L. van Ewyk et al., Anisotropic fluorophores for liquid crystal displays *Displays* 7, 1986, 155, c) H.-W. Schindt, Dichroic dyes, and liquid crystalline side chain polymers *Advanced Materials* 1, 1989, 218.
- [9] P. P. C. Verbunt, D. J. Broer, C. W. M. Bastiaansen and M. G. Debije, The effect of dyes aligned by liquid crystals on luminescent solar concentrator performance, Proc. of the 24<sup>th</sup> European PV Solar Energy Conference 2009, 381.
- [10] C. L. Mulder et al., Dye alignment in luminescent solar concentrators: I. Vertical alignment for improved waveguide coupling, *Optics Express* 18, 2010, A79.
- [11] P. P. C. Verbunt et al., Controlling Light Emission in luminescent solar concentrators through use of dye molecules aligned in a planar manner by liquid crystals, *Advanced Functional Materials* 19, 2009, 2714.
- [12] C. L. Mulder et al., Dye alignment in luminescent solar concentrators: II. Horizontal alignment for energy harvesting in linear polarizers, *Optics Express* 18, 2010, A91.
- [13] a) M. G. Debije, et al., Using selectively-reflecting organic mirrors to improve light output from a luminescent solar concentrator, Proc. of the WREC IX 2006, b) J. C. Goldschmidt et al., Theoretical and experimental analysis of photonic structures for fluorescent concentrators with increased efficiencies, *Physica Status Solidi (a)* 205, 2008, 2811, c) M. G. Debije et al., Effect on the output of a luminescent solar concentrator on application of organic wavelength-selective mirrors, *Applied Optics* 49, 2010, 745.
- [14] B. S. Richards, A. Shalay and R. P. Corkish., A low escape-cone-loss luminescent solar concentrator, Proc. of the 19<sup>th</sup> European PV Solar Energy Conference, 2004.

- [15] S. A. El-Daly and S. Hirayama, Re-absorption and excitation energy transfer of N,N'-bis(2,5-di-tert-butylphenyl)-3,4,9,10-perylenebis(dicarboximide) (DBPI) laser dye, *Journal of Photochemistry and Photobiology A: Chemistry* 110, 1997, 59.
- [16] a) R. W. Olson, et al., Luminescent solar concentrators and the reabsorption problem, *Applied Optics* 20, 1981, 2934, b) R. Soti et al., Photon transport in luminescent solar concentrators, *Journal of Luminescence* 68, 1996, 105, c) L. R. Wilson et al., Characterization and reduction of reabsorption losses in luminescent solar concentrators, *Applied Optics* 49, 2010, 1651.
- [17] B. C. Rowan, et al., Visible and near-infrared emitting lanthanide complexes for luminescent solar concentrators, *Proc. of the 24th European PV Conference 2009*, 346.
- [18] a) A. J. Chatten et al., A new approach to modelling quantum dot concentrators, *Solar Energy Materials and Solar Cells* 75, 2003, 363, b) S. J. Gallagher, et al., Quantum dot solar concentrators: Electrical conversion efficiencies and comparative concentrating factors of fabricated devices, *Solar Energy* 81, 2007, 813, c) V. Sholin, et al., Semiconducting polymers and quantum dots in luminescent solar concentrators for solar energy harvesting, *Journal of Applied Physics* 101, 2007, 123114, d) G. V. Shcherbatyuk et al., Viability of using near infrared PbS quantum dots as active materials in luminescent solar concentrators, *Applied Physics Letters* 96, 2010, 191901.
- [19] A. M. Taleb, Self absorption treatment for the luminescent solar concentrators, *Renewable Energy* 26, 2002, 137.
- [20] R. Reisfeld, Fluorescent Dyes in Sol-Gel Glasses, *Journal of Fluorescence* 12, 2002, 317.
- [21] S. Tsoi, et al., Patterned dye structures limit reabsorption in luminescent solar concentrators, *Optics Express* 18, 2010, A536.
- [22] S. Tsoi, C. W. M. Bastiaansen and M. G. Debije, Enhancing light output of fluorescent waveguides with a microlens system, *Proc. of the 24<sup>th</sup> European PV and Solar Energy Conference 2009*, 377.
- [23] a) R. Reisfeld, et al., Photostable solar concentrators based on fluorescent glass films, *Solar Energy Materials and Solar Cells* 33, 1994, 417, b) G. Seybold and G. Wagenblast, New perylene and violanthrone dyestuffs for fluorescent collectors, *Dyes and Pigments* 11, 1989, 303, c) M. G. Debije et al., A promising fluorescent dye for solar energy conversion based on a perylene perinone, *Applied Optics* 50, 2011, 163.
- [24] a) I. Baumberg, et al., Effect of polymer matrix on photo-stability of photo-luminescent dyes in multi-layer polymeric structures, *Polymer Degradation and Stability* 73, 2001, 403, b) R. Kinderman et al., Performance and stability study of dyes for luminescent plate concentrators, *Journal of Solar Energy Engineering* 129, 2007, 277.
- [25] M. J. Currie et al., High-efficiency organic solar concentrators for photovoltaics, *Science* 321, 2008, 226.
- [26] a) W. R. Holland and D. G. Hall, Waveguide mode enhancement of molecular fluorescence, *Optics Letters* 10, 1985, 414, b) H. R. Wilson, Fluorescent dyes interacting with small silver particles; a system extending the spectral range of fluorescent solar concentrators, *Solar Energy Materials* 16, 1987, 223, c) K. Aslan, et al., Metal-enhanced fluorescence from plastic substrates, *Journal of Fluorescence* 15, 2005, 99.
- [27] a) K. Heidler, Efficiency and concentration ratio measurements of fluorescent solar concentrators using a xenon measurement system, *Applied Optics* 20, 1981, 773, b) J. Roncali and F. Garnier, New luminescent back reflectors for the improvement of the spectral response and efficiency of luminescent solar concentrators, *Solar Cells* 13, 1984, 133.

- [28] M. G. Debije et al., The effect of a scattering layer on the edge output of a luminescent solar concentrator, *Solar Energy Materials and Solar Cells* 93, 2009, 1345.
- [29] M. G. Debije, Solar energy collectors with tunable transmission, *Advanced Functional Materials* 20, 2010, 1498.
- [30] a) C. G. Granqvist, Oxide electrochromics: Why, how, and whither *Solar Energy Materials and Solar Cells: Selected Papers from the Seventh International Meeting on Electrochromism (IME-7)*, 92, 2008, pp. 203, b) C. Bechinger and B. A. Gregg, Development of a new self-powered electrochromic device for light modulation without external power supply, *Solar Energy Materials and Solar Cells* 54, 1998, 405.
- [31] M.-C. Dubois, *Solar Shading and Building Energy Use*, Ph.D. Thesis, Lund Institute of Technology, Lund, Sweden, 1997, pp. 1-100.
- [32] a) J. Yoon et al., Ultrathin silicon solar microcells for semitransparent, mechanically flexible and microconcentrator module designs, *Nature Materials* 7, 2008, 907, b) P. Fath, H. Nussbaumer and R. Burkhardt, Industrial manufacturing of semitransparent crystalline silicon POWER solar cells, *Solar Energy Materials and Solar Cells* 74, 2002, 127.
- [33] A. W. Hains, et al., Molecular semiconductors in organic photovoltaic cells, *Chemical Reviews* 110, 2010, 6689.
- [34] S. Chattopadhyay et al., Anti-reflecting and photonic nanostructures, *Materials Science and Engineering: R: Reports* 69, 2010, 1.
- [35] U. Schulz, Review of modern techniques to generate antireflective properties on thermoplastic polymers, *Applied Optics* 45, 2006, 1608.
- [36] a) G. W. Chantry et al., Far infrared and millimetre-wave absorption spectra of some low-loss polymers, *Chemical Physics Letters* 10, 1971, 473, b) H. Ma, et al., Polymer-based optical waveguides: materials, processing, and devices, *Advanced Materials* 14, 2002, 1339.
- [37] M. J. Kastelijjn, et al., Influence of waveguide material on light emission in luminescent solar concentrators, *Optical Materials* 31, 2009, 1720.
- [38] A. F. Mansour, Photostability and optical parameters of copolymer styrene/MMA as a matrix for the dyes used in fluorescent solar collectors, *Polymer Testing* 23, 2004, 247.
- [39] a) M. Sidrach de Cardona et al., Edge effect on luminescent solar concentrators, *Solar Cells* 15, 1985, 225.
- [40] T. K. Sau et al., Properties and applications of colloidal nonspherical noble metal nanoparticles, *Advanced Materials* 22, 2010, 1805.
- [41] V. E. Ferry, et al., Design considerations for plasmonic photovoltaics *Advanced Materials* 22, 2010, 4794.

## Design and simulation of a PV and a PV-Wind standalone energy system: A case study for a household application in Nicosia, Cyprus

Gregoris Panayiotou<sup>1,2</sup>, Soteris Kalogirou<sup>1,\*</sup> and Savvas Tassou<sup>2</sup>

<sup>1</sup> Department of Mechanical Engineering and Materials Science and Engineering,  
Cyprus University of Technology, P. O. Box 50329, 3603 Limassol, Cyprus

<sup>2</sup> School of Engineering and Design, Brunel University, Uxbridge, Middlesex UB8 3PH, UK

\* Tel: +357 25 002621, Fax: +357 25 002637, E-mail: soteris.kalogirou@cut.ac.cy

---

**Abstract:** In this work the design and simulation of two stand-alone renewable energy sources (RES) based systems for application in a household in Cyprus is presented. More specifically, the household is located in Nicosia and is used as the residence of a typical Cypriot family for which a baseline scenario of energy consumption is specified in order to define the annual load profile of the house. The first system is based on photovoltaic (PV) modules for the generation of electricity by harvesting the very high solar potential of Cyprus while the second one is a hybrid system combining PVs with a domestic wind turbine in order to take advantage of the wind potential especially during winter. Since both systems are stand alone the energy produced is stored in a battery bank. The software used for the modeling and simulation processes is TRNSYS. A comparison of the two systems in terms of both technical and economical aspects is presented in this study where it is concluded that the wind potential of the specific location of the house, which generally applies on the entire island, cannot substitute and compete in any way with the very high solar potential.

**Keywords:** Stand-alone system, baseline scenario, Cyprus, hybrid, wind potential, solar potential

---

### 1. Baseline Scenario Characteristics

In order to design the domestic standalone energy systems a typical house is considered for which a baseline scenario concerning several parameters is defined. It is very important to note that the baseline scenario concerns a future situation where all energy for the household is supplied by a RES system and the system is isolated from the grid. The characteristics of the baseline scenario concern the structure, location, occupancy and energy systems installed in the house examined. The data used to define these characteristics were based on the statistical analysis conducted by Panayiotou et al. [1] which concerned the characteristics and the energy behavior of the residential building stock of Cyprus in view of Directive 2002/91/EC.

The house examined in the baseline scenario is a single ground floor house with an area of 160 m<sup>2</sup> which was built in year 2000 and is located in Nicosia, Cyprus where the climatic conditions are those for lowland inland Mediterranean areas. The house has 3 bedrooms and it does not have pilotis, sofitta or a basement while it has a flat concrete roof with 140 m<sup>2</sup> of free space for any systems such as solar thermal or PVs to be installed. The house has a 5 cm polyurethane wall insulation and double glazing. The heating and cooling is covered with split type air conditioning units and the number of units installed are two 9,000 BTU (2.6 kW) in two of three bedrooms and one 12,000 BTU (3.5 kW) unit in the living room. For the production of domestic hot water (DHW) a solar water heating system is used while an immersed electric element is installed for backup.

### 2. Typical annual load profile definition

The typical annual load profile definition was also based on the statistical analysis conducted by Panayiotou et al. [1]. In this statistical analysis a sample of 500 houses along with analytical data given by the Electricity Authority of Cyprus were used and it was concluded that there are two peaks observed on the consumption of electricity in the domestic sector

annually; one in summer, which is the highest, and one in winter. On the other hand, autumn and spring periods have more or less the same consumption of electricity which is lower compared to that of summer and winter. Also, another very important thing to notice is that the daily average electricity consumption of a house is around 24 kWh during summer, 21 kWh during winter and 15 kWh during autumn and spring.

To be more precise on the definition of the typical annual load profile this was split into weekdays and weekends for each of the four seasons. The months contained in each season are as follows; Winter: December, January and February; Spring: March, April and May; Summer: June, July and August; and Autumn: September, October and November. Additionally, it should be noted that holiday periods are not considered in the examined typical annual load profile. The typical load profiles for weekdays of spring, autumn and winter are shown in Figs. 1-3 respectively.

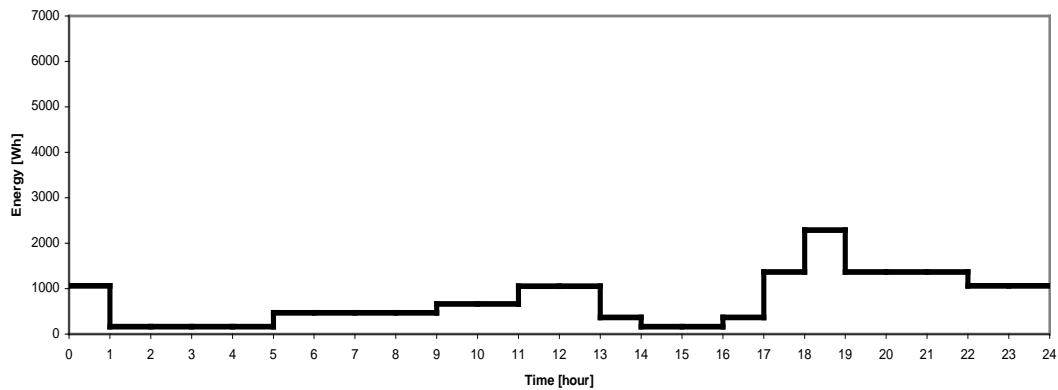


Fig. 1 Load profile for a typical spring/autumn weekday

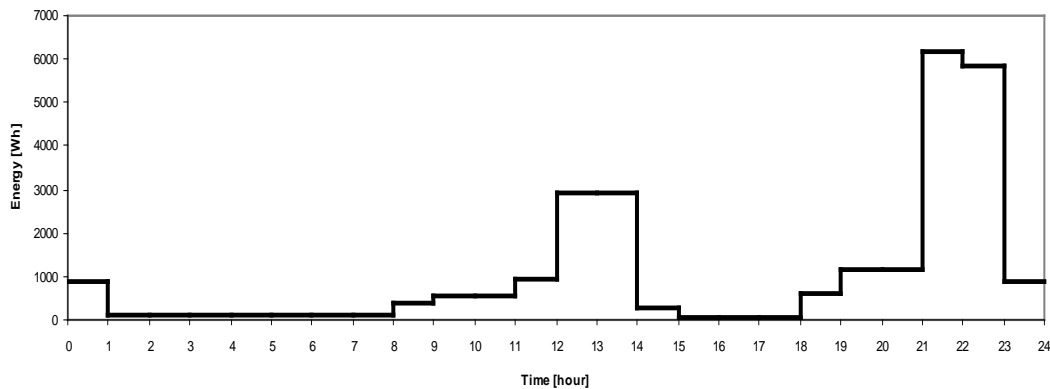


Fig. 2 Load profile for a typical winter weekday

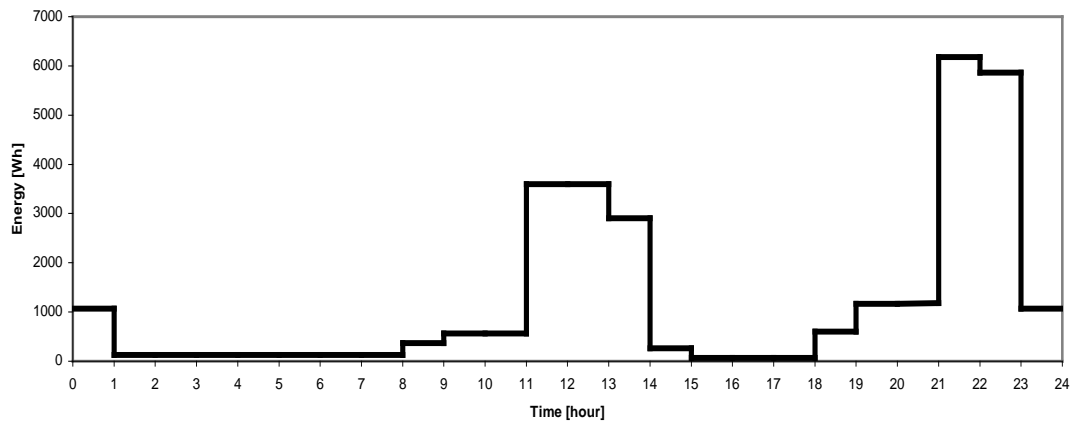


Fig. 3 Load profile for a typical summer weekday

### 3. Model design for standalone PV system

The model design process was carried out in the TRNSYS environment [2] which is considered to be a complete and extensible simulation environment for the transient simulation of solar and other energy systems.

The model of the standalone PV system includes the following components:

- Weather data processor model (Type 109)
- PV model (Type 180e)
- Inverter/Regulator model (Type 48b)
- Battery model (Type 47a)
- Load Profile model (Type 9a)

A very important parameter to consider when designing a standalone PV system is the nominal voltage of the battery bank which can be 12, 24 or 48 VDC. The parameters affecting the determination of the suitable nominal voltage for a system are the nominal voltage of the PVs, the size of the system and the input requirements of the inverter. For example, inverters which have a power of 6 to 12 kW require nominal voltage to be 48 V while inverters with a power of 2 to 5 kW require the nominal voltage to be 24 V. Since the system examined is neither a large system nor a small one, it was decided that the nominal system voltage is considered initially to be 24 V. The main reason for this decision is that since with a rough estimation the system will not exceed 10-13 kW of PV power it is much better to use three inverters of 4 kW instead of one inverter of 10-13 kW in order to secure basic load coverage in the case of a failure of one inverter.

It is also essential to know the slope of the PVs. A rule of thumb followed by the PV technicians in Cyprus is that the slope of the PVs should be somewhere between 27-31°. In order to define the optimum slope to be used in the modelling process a small model consisting of a typical meteorological year (TMY) and a single PV was developed and a series of simulations were carried out for slopes between 27-33°. The energy production for each slope is recorded and presented in Table 1.

Table 1 PV characteristics on standard testing conditions

Slope of the PV	Energy Produced [Wh/yr]
27°	89,516
28°	89,650
29°	89,748
30°	89,810
31°	<b>89,835</b>
32°	89,823
33°	89,775

According to the results of Table 1 the maximum energy production occurs for a slope of 31° (shown with bold on Table 1) and thus this is the optimum angle for the location examined and consequently for the island of Cyprus.

#### 3.1. Simulation and economic analysis of standalone PV system

After the proper setting up of the complete model for the standalone PV system a series of simulations were carried out in order to specify the required storage capacity and PV array

power needed to cover the load over the time period of a typical year. Before running the simulations it is essential to decide the acceptable loss of load probability (LOLP) of the specific system which defines the required battery autonomy in days. For example, if a 1% acceptable LOLP is chosen it means that during the time period of a year there is probability to have 3.65 days where the load will not be covered. Thus, if we want to design a system where we will have a 100% annual load coverage, in order not to compromise the occupants' quality of living, then a first estimate for the required battery autonomy should be that of 4 days. It should be noted that the batteries capacity must be larger than that calculated for the 4 days of autonomy due to the fact that it is impossible to start the 4 days of autonomy with the batteries fully charged as these always supply electricity to the system during nighttime. Thus, in the system examined, it is predefined that one of the most important parameters to consider for the selection of the PV array size and the required storage capacity is to have 100% annual load coverage.

Since the nominal voltage of the battery bank is decided to be at 24 V and the nominal voltage of each battery cell is 2 V then the configurations of the battery bank used during the simulation consisted of 1, 2, 3 or 4 strings of 12 batteries connected in series.

The results of the simulation process were recorded in a data file and subsequently processed to evaluate the load coverage achieved by each configuration. The most important results estimated during the simulation are presented in Table 2.

Table 2 Results of the simulation process for the standalone PV system

Configuration No	No of PVs	PV array power	No of batteries	Battery capacity	Annual energy deficiency	Annual period of energy deficiency
	[-]	[kW]	[-]	[kWh]	[kWh]	[hrs]
1	40	7.2	36	108	566	607
2	45	8.1	36	108	381	451
3	50	9.0	36	108	228	220
4	60	10.8	36	108	25	33
5	63	11.34	36	108	12	2
6	65	11.7	36	108	2	10
7	40	7.2	48	144	496	503
8	45	8.1	48	144	320	365
9	50	9.0	48	144	193	186
10	55	9.9	48	144	80	97
11	58	10.44	48	144	13	29
12	59	10.62	48	144	0	0

From the results of Table 2 it can be seen that the systems that achieve 100% annual load coverage over a typical year are those of Configurations 6 and 12. Additionally, it is observed that the system of Configuration 5 is rather acceptable since it has a very low energy deficiency of 12 kWh or 2 hrs per year. Configuration 11 gives also a low energy deficiency of 13 kWh but it is not considered due to its high annual period of energy deficiency which is 29 hrs per year. It should be noted that two different approaches are considered for these systems with the difference between them being that Configuration 12 has larger energy storage capacity and lower PV array power (smaller size) while Configurations 5 and 6 have larger PV array power (larger size) and lower energy storage capacity. This is a very

important fact to consider when deciding which is the optimum configuration for the system to be designed. To do so, Configurations 5, 6 and 12 are evaluated in terms of economic viability for a total system life of 25 years. During this process the lifetime of each component is taken into consideration along with its current cost and is recorded in Table 3. The results of this analysis are presented in Table 4.

Table 3 Equipment prices used in the economic analysis

	Equipment Description	Price
1	Photovoltaic panels	€3.2 per W
2	Batteries	€640 per pc
3	Inverter (2.5 kW, 12 V)	€2069
4	Mounting system (for flat roof)	€200/kW
5	Electrical equipment (cables etc.)	€10/kW

Table 4 Economic analysis results for the systems of Configurations 5, 6 and 12

<b>Configuration 5</b>						
	Equipment	Number	Power	Lifetime	Price	Price overall
1	PV	63	180	25	€36,288	€36,288
2	Inverter/Controller	3	4500	15	€7,977	€15,954
3	Elec. Equip.	-	-	25	€2,381	€2,381
4	Mounting	-	-	25	€2,268	€2,268
5	Batteries	36	1500 Ah	18	€23,040	€46,080
					TOTAL	€102,971
<b>Configuration 6</b>						
	Equipment	Number	Power	Lifetime	Price	Price overall
1	PV	65	180	25	€37,440	€37,440
2	Inverter/Controller	3	4500	15	€7,977	€15,954
3	Elec. Equip.	-	-	25	€2,457	€2,457
4	Mounting	-	-	25	€2,340	€2,340
5	Batteries	36	1500 Ah	18	€23,040	€46,080
					TOTAL	€104,271
<b>Configuration 12</b>						
	Equipment	Number	Power	Lifetime	Price	Price overall
1	PV	59	180	25	€33,984	€33,984
2	Inverter/Controller	3	4500	15	€7,977	€15,954
3	Elec. Equip.	-	-	25	€2,230	€2,230
4	Mounting	-	-	25	€2,124	€2,124
5	Batteries	48	1500 Ah	18	€30,720	€61,440
					TOTAL	€115,732

By evaluating the results of the economic analysis it is concluded that the optimum system is Configuration 5 which consists of 63 PVs (11.34 kW) and 36 batteries. The cost of such a system is €102,971. It is very important to notice that in all cases examined the main part of the cost, around 50%, concerns the batteries. Since the optimum configuration estimated has 36 batteries it is concluded that the decision for the nominal voltage of the battery bank to be at 24 V was correct due to the fact that if 48 V was chosen then the battery bank configuration

should have been either 1 or 2 strings of 24 batteries and it is obvious that the option of 24 batteries (1 string) would be undersized and thus insufficient while the option of 48 batteries (2 strings) would be oversized with a consequent increase of the overall cost of the system.

#### 4. Model design for hybrid standalone PV-Wind system

The model for the hybrid standalone PV-Wind is based on the previously developed model for the standalone PV system. The difference between the two models relies on the addition of a small domestic wind turbine (Type 90). In this system, as in all hybrid power systems, more than one source of energy is used in order to diversify the sources and achieve load coverage under various climatic conditions during the entire 24 hours period. Furthermore, it is very important to note that the operation of this system differs from that of the PV system due to the fact that the power produced by the wind turbine is directly supplied to the load through a power conditioner and the rest of the load is covered by the PV subsystem. For the design of this model two wind turbines were chosen to be considered a 1.5 kW and a 2 kW. The reason for choosing these two low power domestic wind turbines is due to the fact that the wind potential in the area examined is rather low as it is illustrated in Fig. 4 where it can be seen that more than 86% of the time the wind velocity is between 0-6 m/s and the average wind velocity is 4 m/s. The curves of power against wind velocity for the wind turbines considered are presented in Fig. 5.

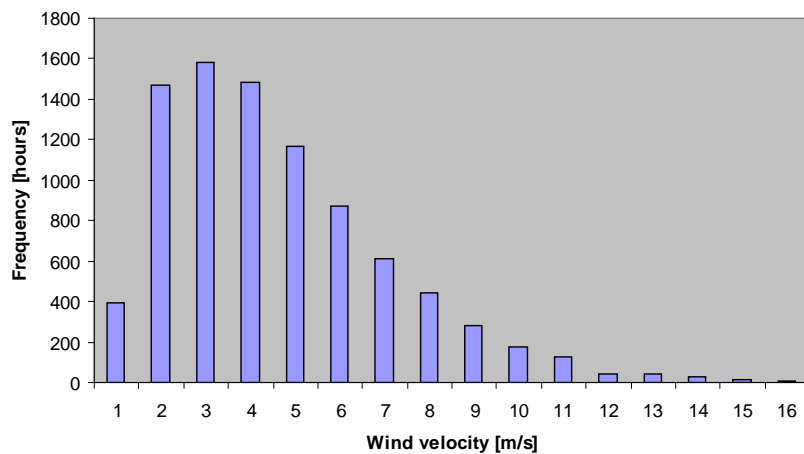


Fig.4 The wind profile of the examined location

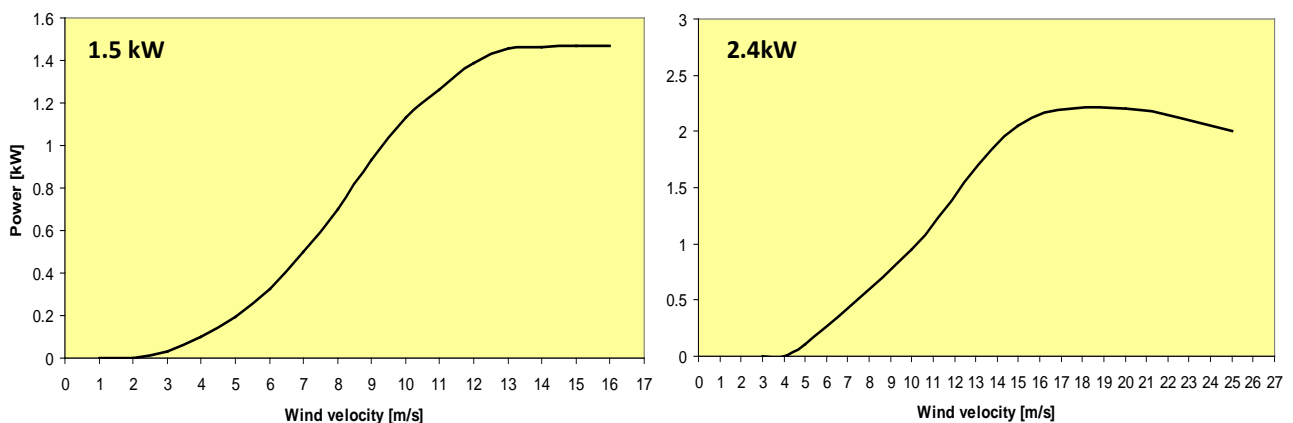


Fig. 5 Characteristic power curves for both wind turbines considered

By carefully analyzing the power curves of each wind turbine in conjunction with the wind profile of the examined location it is hypothesized that the most suitable wind turbine to be used in the system designed is the 1.5 kW one. This of course is only a hypothesis and in order to be validated a series of simulations using a simple model consisting of a TMY and a wind turbine were carried out. The results obtained are presented in Table 5. From these results it is concluded that the hypothesis was correct since the 1.5 kW wind turbine generates more energy than the 2.4 kW one. This is caused by the fact that the 1.5 kW wind turbine operates with higher efficiency at low wind velocity which prevail at the location examined.

Table 5 Simulation results for both wind turbines examined

Energy Produced [Wh]	1.5 kW-Wind turbine	2.4 kW-Wind turbine
Maximum	1,500	2,274
Average	146	145
Annual	1,279,346	1,271,074

#### 4.1. Simulation and economic analysis of standalone PV-Wind system

The simulation process followed for this system was similar to the one carried out for the PV system. From the results concerning the two wind turbines it is clear that the wind turbine that should be used in the system designed is that of 1.5 kW.

Since the optimum capacity of the batteries to cover the load over a typical year was calculated during the simulation process for the PV system and found to be 108 kWh it is decided that this capacity should also be the same for the case of the PV-Wind system as the energy provided by the wind turbine is very small.

The results of the simulation process were recorded and processed to evaluate the load coverage achieved by each configuration. The most important of the results calculated during the simulation process are presented in Table 6. From these results it can be seen that the system that achieve 100% annual load coverage over a typical year is that of Configuration F. On the other hand the systems of Configurations B, C, D and E also gave rather acceptable results since the annual energy deficiency varied between 1-15 kWh while the annual period of energy deficiency varied between 7-22 hrs per year. Since all systems have the same battery capacity it is decided that the configuration to be compared with the PV system in the following section is that of Configuration C in order to have the same energy deficiency so as to be comparable.

Table 6 Results of the simulation process for the standalone PV-Wind system

Configura- tion Number	No of PVs [-]	PV array power [kW]	No of batteries [-]	Battery capacity [kWh]	Energy deficiency [kWh/yr]	Period of energy deficiency [hrs/yr]
A	55	9.90	36	108	24	33
B	57	10.26	36	108	15	22
C	58	10.44	36	108	11	7
D	59	10.62	36	108	7	10
E	60	10.80	36	108	1	10
F	61	10.98	36	108	0	0

## 5. Comparison and Conclusions

The comparison is carried out for a lifetime of 25 years for both systems and the results are recorded in Table 7. From the results of the economic analysis it can be seen that the two systems have the same lifecycle cost with a slight decrease in favor of the PV-Wind system. Nevertheless, the difference in cost is very small (€1000) and it is judged to be insignificant for the cost range of the systems examined.

Table 7 Economic analysis results for PV and PV-Wind systems

		PV system				
Equipment	Number	Power	Lifetime	Price	Price overall	
1 PV	63	180	25	€36,288	€36,288	
2 Inverter/Controller	3	4500	15	€7,977	€15,954	
3 Elec. Equip.	-	-	25	€2,381	€2,381	
4 Mounting system	-	-	25	€2,268	€2,268	
5 Batteries	36	1500 Ah	18	€23,040	€46,080	
TOTAL					€102,971	
		PV-Wind system				
Equipment	Number	Power	Lifetime	Price	Price overall	
1 PV	58	180	25	€33,408	€33,408	
2 Windturbine	1	1500	20	€2,250	€2,250	
3 Inverter/Controller	3	4500	15	€7,977	€15,954	
4 Elec. Equip.	-	-	25	€2,192	€2,192	
5 Mounting system	-	-	25	€2,088	€2,088	
6 Batteries	36	1500 Ah	18	€23,040	€46,080	
TOTAL					€101,972	

From the results presented in this paper it is concluded that in spite of the fact that due to their ability to diversify the energy sources, hybrid systems are generally considered to be a better option for standalone applications, in the case of the location examined, the PV-only system is a better option. This lies on the fact that the PV system is based fully on the very high solar potential of Cyprus in contradiction to the PV-Wind system which is based on the very low wind potential observed in the area examined, which is also typical for the whole island.

It should also be noted that by not using the wind turbine in a domestic area several other possible negative aspects are avoided such as noise caused from the operation of the wind turbine, optical pollution and maintenance requirements which are not considered in the above analysis. By observing the cost analysis of both systems it can be seen that batteries represent over 50% of the overall systems' cost.

## References

- [1] G.P. Panayiotou, S.A. Kalogirou, G.A. Florides, C.N. Maxoulis, A.M. Papadopoulos, M. Neophytou, P. Fokaidis, G. Georgiou, A. Symeou, G. Georgakis, The characteristics and the energy behaviour of the residential building stock of Cyprus in view of Directive 2002/91/EC, Energy and Buildings, 42, 2010, pp. 2083-2089.
- [2] TRNSYS program manual.

## High Efficiency Multijunction Tandem Solar Cells with Embedded Short-Period Superlattices

Argyrios C. Varonides<sup>1,\*</sup>

<sup>1</sup>University of Scranton, 800 Linden Street, Scranton Pennsylvania 18510, USA

\* Corresponding author. Tel: +1(570)941-6290, Fax: +1(570) 941-4015, E-mail: varonides@scranton.edu

**Abstract:** We propose a  $1\text{cm}^2$  tandem solar cell with different lattice-matched materials based on a  $2\text{eV}/1.42\text{eV}/0.66\text{eV}$  energy gap sequence. The top unit is a p-n-n AlAs/GaAs cell, connected in series with a bottom cell which is a bulk GaAs/Ge p-n-n cell; a narrow GaAs/Ge superlattice region embedded in the middle region. Transition of carriers between the two units is possible via a tunnel junction connecting the two units. More specifically, the upper cell is a  $20\ \mu\text{m}$  bulk p-n-n cell tuned to the visible range of the solar spectrum, producing short circuit currents near  $30\text{mA}/\text{cm}^2$ , and open-circuit voltage (OC) of  $1.04\text{V}$ ; the bottom cell is an  $80\ \mu\text{m}$  bulk p-n-n GaAs/Ge with an embedded GaAs/Ge superlattice tuned at  $1\text{eV}$ . The bottom cell produces short circuit current density at  $18.5\ \text{mA}/\text{cm}^2$  in the bulk; however a 20-period GaAs/Ge embedded short superlattice provides an additional  $10\ \text{mA}/\text{cm}^2$  thermionic current density, so that total bottom current reach  $28.5\text{mA}/\text{cm}^2$ , in close matching (5%) with the top currents, and an OC voltage of  $0.968\text{V}$ . The tandem cell's basic parameters are (a) average fill factor of (FF) 85% (b) short circuit current  $28.5\ \text{mA}/\text{cm}^2$  and (c) OC voltage  $2.008\text{V}$  (due to the series connection); for  $100\text{mW}/\text{cm}^2$  standard solar radiation, collection efficiency of such a device is depicted in excess of 47% under one sun. Such small area cells are useful for CPV for their minimized size and material requirements.

**Keywords:** Solar cells, Superlattices, Tuned quantum wells, High efficiency photovoltaics

### Nomenclature

$J_{TH}$ thermionic current density ..... $\text{mA}/\text{cm}^2$	$n_{ph}$ photo-excited carriers ..... $\text{cm}^{-3}$
$J_{sc}$ short-circuit current..... $\text{mA}/\text{cm}^2$	$g_o, g(E)$ density of states..... $\text{eV}^{-1}\text{cm}^{-2}$
$V_{oc}$ open-circuit voltage.....Volts	$g_o, g(E)$ density of states..... $\text{eV}^{-1}\text{cm}^{-2}$
$L_w$ quantum well width..... $\text{nm}$	

### 1. Introduction

The field of high efficiency photovoltaics (HEPV) is maturing steadily; already the threshold of 40% efficiency has been reached and exceeded to 42.2 % [1, 2, 3, 4, 5, 6]. It is common place in the PV community that the 50% limit for crystalline solar cells will be within reach in the next five years. The common denominator of high efficiency cells is the idea of two to three different band gaps that absorb in different wavelengths, preferably in a successive fashion along with the visible and the infrared parts of the solar spectrum. A typical cell of such geometry contains three major layers of lattice-matched or suitably metamorphic semiconductor layers joined (in series) by means of tunnel junctions. The latter are needed to ensure current matching. The obvious advantage of such structures is the series connection of two p-n junctions essentially, with increased overall open circuit voltage (due to the series connection). In this communication we are proposing an ostensibly high efficiency structure based on the series connection idea, as mentioned above, but with a different design, especially in the area of long wavelength absorption. The latter is a process that can be realized by means of two dimensional geometry selections (or one dimensional option as well). The device is described in brief as follows: a top p-n or p-i-n bulk GaAs/AlAs/Alloy cell is proposed for short wavelength absorption (mainly visible). The unit is then grown on top of a tunnel junction (guaranteeing the series connection) and the bottom cell follows with a similar topography, namely, a p-i-n cell matched with the layers above it. The intrinsic region of this cell is replaced by a GaAs/Ge superlattice with reduced tunneling. The latter

selection is adopted for two reasons (a) Ge is lattice-matched with GaAs and (b) we want to ensure thermal current generation from the mid- (intrinsic/low-doped) to the n-region of the device, as shown in Figure 1 below:

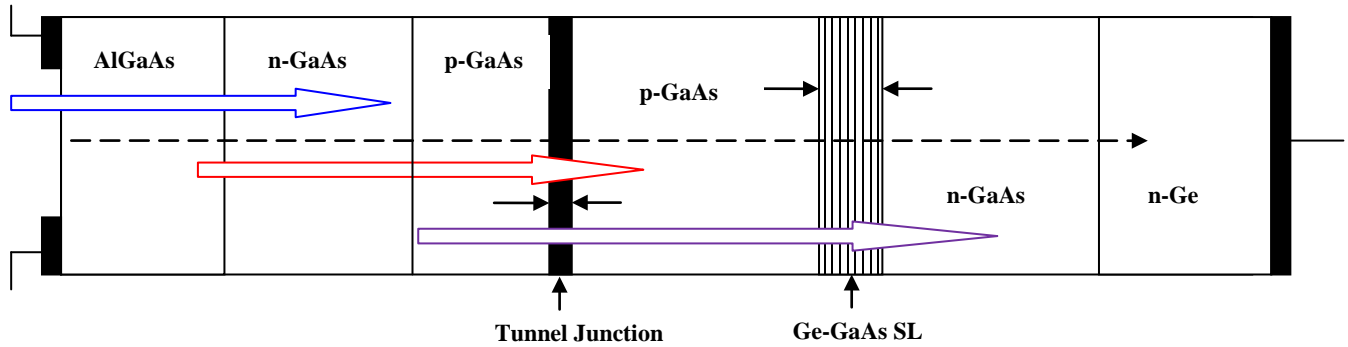


Fig. 1 Proposed tandem ( $1\text{cm}^2$ )  $p\text{-}n\text{-}n^+/p\text{-}n$  (Superlattice (SL))- $n^+$  multijunction solar cell, for high efficiency. Two cells in series through a tunnel junction. Maximum current density depicted at  $28.5\text{mA}/\text{cm}^2$ ; Open-circuit voltage values 1.04 and 0.968V respectively. Total  $V_{oc} = 2.008\text{V}$ ,  $J_{sc} = 30\text{mA}/\text{cm}^2$ .

The structure promotes the series connection of two cells, with current matching. As seen from the figure above, the goal is to produce a composite cell where both short and long wavelengths are absorbed simultaneously; in this context, this can be succeeded via the two layers shown. Visible and near infrared absorption is guaranteed by the two cells respectively, while the MQW geometry is tuned to longer wavelengths via pre-selected eigen-state resonance. Therefore, analysis and simulation of the device will have to include both regions as depicted through (a) the top and (b) bottom cells and (c) through the tunnel junction (TJ). The latter is basically selected to be a double barrier heterostructure of  $p^{++}$  and  $n^{++}$  highly doped GaAs layers (TJ modeling for this purpose will be reported elsewhere). Fundamentally, photoelectrons induced from the top, tunnel through the mid-junction to join carriers from the lower cell. Ultimately, due to the series connection, matching will dictate the final current, in other words, the lowest current will keep the connection at the ON state. On the other hand, the series connection is expected to provide enhanced voltage (ideally the sum of the two OC voltages as they come from the two sub-cells). It is imperative therefore to model all regions for optimum current and voltage generation. In the following sections, modeling and simulations for two of the three mentioned regions is provided as a tool for optimization in design.

## 2. Top Cell for the visible solar spectrum

It is desirable to obtain a top layer suitable for visible spectrum absorption. Graded AlGaAs layers of variable aluminum fractional content is proposed according to the following table:

Table 1: Bandgap and wavelength at different Aluminum percentage content for AlGaAs

Al content (%)	Band-gap (eV)	Wavelength $\lambda$ ( $\mu\text{m}$ )
0.98 (AlAs)	2.16	0.574
0.90	2.11	0.582
0.80	2.07	0.592
0.70	2.05	0.602
0.60	2.02	0.612
0.50	1.998	0.620

As seen from the table above, a feasible succession of lattice-matched AlAs-AlGaAs graded layer ensures visible spectrum absorption. Modeling of a 0.5 to 1.0 $\mu\text{m}$  p-AlAs/AlGaAs layer on top of an n-n<sup>+</sup> GaAs arrangement (upper part of Figure 1) leads to short circuit current at 30.50 mA/cm<sup>2</sup>, and open-circuit (OC) voltage at 1.04V, with max power 28.30 mW [temperature 300 °K; one-sun exposure and power input of 100mW/cm<sup>2</sup>; 10% internal reflection]. Figure 2 shows the J-V characteristics of the top cell, where both current-voltage and power-current curves are depicted. This is a high current solar cell and can stand alone. Note also that with an 88 to 90% fill factor (FF), this is a 27.9 % cell. Note also that a second junction could be used as the bottom cell, with exactly the same characteristics; in such a case, one (provided the tunnel junction can sustain 30mA/area) may end up with a double junction cell with 2V and 30mA/unit area, which would lead to a double-junction cell (area 1square centimeter) with collection efficiency with collection efficiency n(%) = (2x30mA/cm<sup>2</sup>) x (FF)/(100mW/cm<sup>2</sup>). For a collective fill factor near 80%, this leads to 48% collection efficiencies. Figure-2 below depicts a simulated J-V characteristic (extrapolation to the horizontal axis leads to 1.04V):

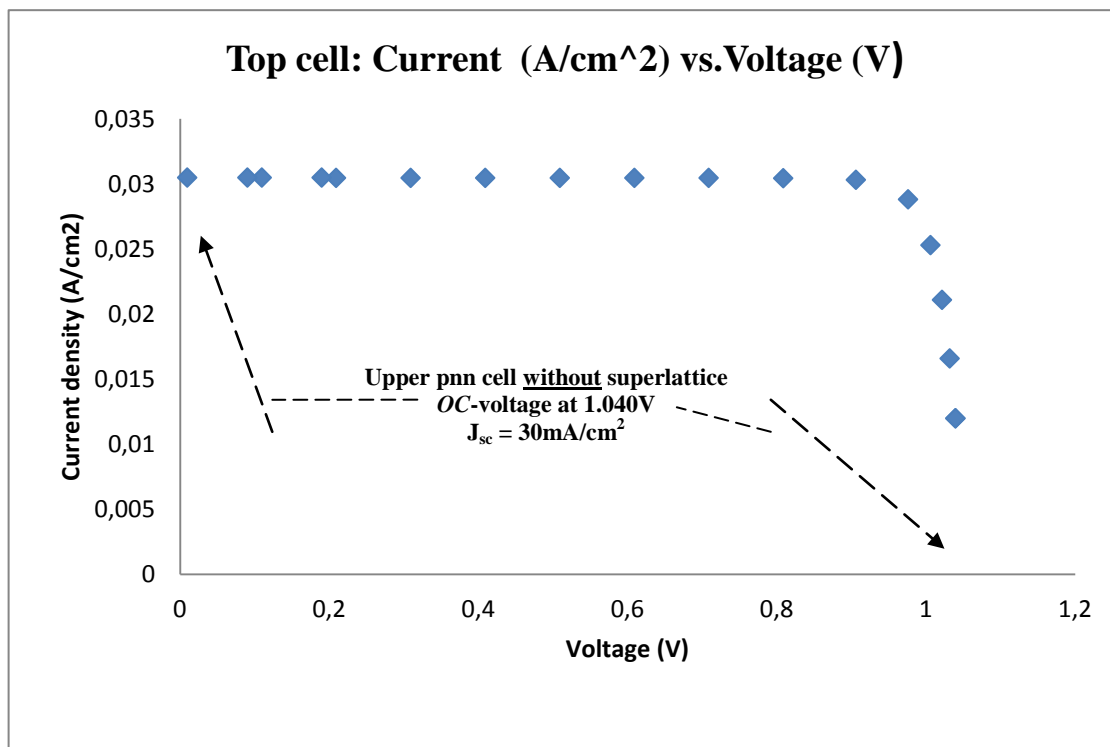


Fig.2. p (Al<sub>x</sub>Ga<sub>1-x</sub>As)-n(GaAs)-n<sup>+</sup>(GaAs) top cell. The AlGaAs layer (wide band gap) absorbs in the visible (see Table 1). Max current and OC-voltage extrapolated at 30.5mA/cm<sup>2</sup> and 1.04V respectively.

### 3. Bottom Cell

Out of several options for a double junction cell, we select a p-n-n 1.82eV/1.42eV/0.66eV cell in order to demonstrate two points (a) to include long wavelength absorption and (b) to introduce the idea of tuning layers in the mid-regions to desired wavelengths. In this paper we are proposing a quantum well structure embedded in the mid-region of the bottom cell and tuned to 1eV solar photons. Regarding the 0.66 eV material (for long wavelengths: 1.24/0.66 = 1.878  $\mu\text{m}$ ) include in the bottom cell design, simulations lead to short circuit current density at J<sub>sc</sub> = 18.50 mA/cm<sup>2</sup> and OC-voltage V<sub>oc</sub> = 0.968V. Simulation and modeling of the bottom unit is basically in a structure depicted by lower portion of Figure-1, *without* the mqw region. The mqw region is a 20-period GaAs/Ge superlattice (no tunneling) with thin Ge-quantum

wells tuned at 1eV or with a 19.6 nm width. Potential barriers are selected at 100nm (in order to minimize tunneling). The total thickness of the reduced dimensionality superlattice is  $20 \times (200+19.6) = 4,392 \text{ nm} = 4.392 \text{ }\mu\text{m}$ ; the latter is just 5.3% of the total lower cell, which is essentially a pnn GaAs/Ge solar cell with its J-V graph shown by figure-3:

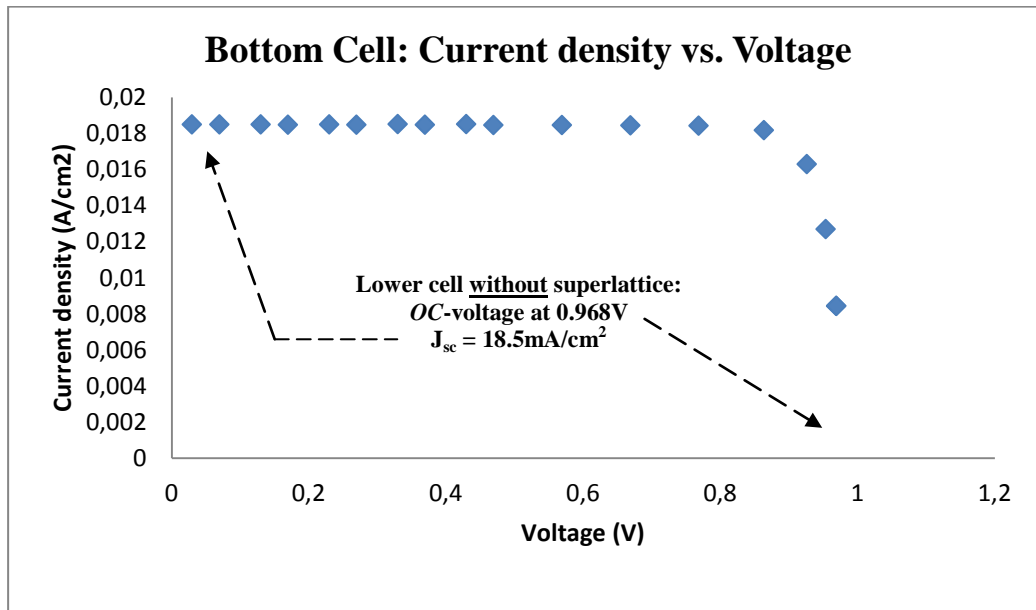


Fig. 3: Bottom cell J-V characteristics: a bulk pnn GaAs/Ge cell with 0.968V and  $18.5 \text{ mA/cm}^2$  (OC and SC) parameters respectively.

By proposing a superlattice in the mid region of the lower cell (in future designs this could be proposed for both cells as well!) we actually introduce a second channel of carrier current per unit area, such that the current in the lower part of the device might go increase as well. In the next section, we develop a formalism of thermionic current escape that contributes to the main bulk current of the bulk device as depicted in Figure-4 below:

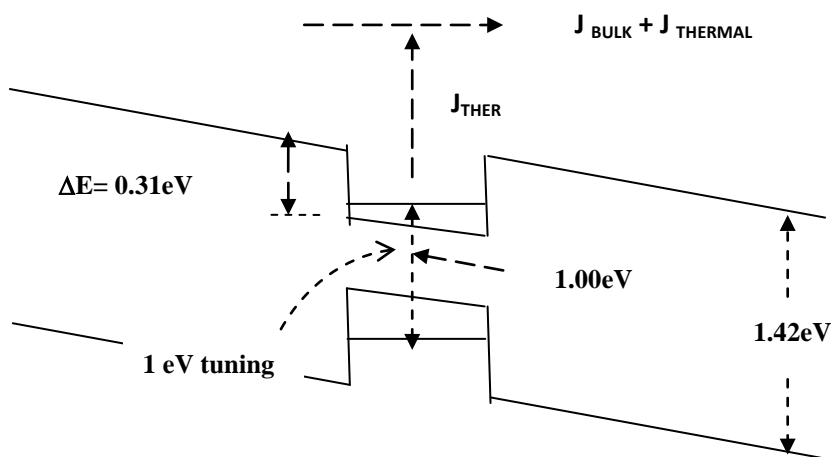


Fig. 4: Fine tuning at specific wavelengths can be achieved through quantum size effects in the traps of the intrinsic region. Electrons' thermionic conduction, from 20nm quantum wells, is schematically shown at the conduction band. Note the Fermi and intrinsic Fermi levels, and the addition of the two current components: bulk and thermal current components respectively.

Final current from the quantum traps adds constructively to the bulk current generated by the GaAs/Ge cell (18 mA/unit area, see Figure-3 above). Due to current matching, overall SC-current output is going to be based on the lowest current off the two cells. Thus, thermal escape generation becomes essential: simultaneous high current and voltage generation may lead to higher “ground” collection efficiency (one sun conditions). In the next section, modeling is geared towards thermionic current generation and current matching near 30mA/cm<sup>2</sup>.

#### 4. Modeling of Thermionic current

As mentioned above and discussed elsewhere, photo-excitation forces excess carriers in quantum wells and an increase of total carrier population near 10<sup>12</sup> cm<sup>-2</sup>, per well [6]. Trapped photocarriers recombine and thermionically escape from the quantum traps. With recombination losses includes [8,9] and given that there is a non-zero probability for thermal escape, we model escaping carriers as thermionic currents over ΔE<sub>C</sub> barriers. Once this is established, we consider the two current components as two current sources (in the bottom cell always), and we are adding these two components to find the total lower-cell current. In all probability, this result is not necessarily expected to match the top component, however, by imposing required conditions, selective doping and superlattice geometry; we expect total lower current to reach (as close as possible) the top one.

In the following, we briefly discuss this process. Thermionic emission from wells of depth ΔE<sub>C</sub> leads to current density values of the type [8]:

$$j = q \int dx dE g(E) f(E) v(E) \delta n(x) \quad (1)$$

Where q is the electronic charge, g(E) is the density of states (DOS) of the quantum trap (here quantum wells or quantum dots etc), f(E) is the Fermi level position in the gap of the semiconductor layer, v(E) is the “velocity” of the carriers at energy E and where δn(x) is the net carrier population in the traps of length/width L<sub>w</sub> and after recombination. For an average excess carrier density <δ(x)> = δN = 10<sup>12</sup> cm<sup>-2</sup> per well, the above integral simplifies as follows:

$$j = q(\delta N)(L_w) g_o \int dE f(E) v(E) \quad (2)$$

Thermionic currents can be calculated from the latter expression, where DOS represents the quantum system involved. In the present case we adopt quantum wells (faster and less cumbersome compared to quantum dots fabrication), where DOS is a constant function: (2-d DOS of quantum wells, eV<sup>-1</sup>cm<sup>-2</sup>). Based on the above and on the fact that the Fermi level is near (and above) 3(kT)’s below the conduction band of the low gap layer (E<sub>C</sub> - E<sub>F</sub>) (Fermi-Dirac approaches the Maxwell-Boltzmann distribution), the current relation yields the following explicit expression (by replacing for g(E) with g<sub>o</sub> and relating the speed of the carriers with energy barrier ΔE<sub>C</sub> of the heterojunction discontinuity):

$$j = q \times n_{ph} \times g_o \times L_w \times \sqrt{\frac{2}{m^*}} \times \int_E^\infty dE \sqrt{E - E_1} \times \exp\left(-\frac{E_1 - E_F}{kT}\right) \quad (3)$$

Where the difference E-E<sub>F</sub> is the activation energy relative to the Fermi level, E<sub>1</sub> is the lowest eigen-energy in the germanium quantum wells (near 10meV from the bottom of the wells, for

~20 nm width (L)). Note also that the excess carrier per unit area available per well is  $n_{ph}$ , and  $m^*$  is the effective mass in germanium layers. Taking the lowest limit to be the ground eigenstate, the last expression leads to the following result:

$$j = q \times n_{ph} \times L_w \left( \frac{\sqrt{2\pi m^* k^3}}{\pi \hbar^2} \right) \times T^{3/2} \times \exp\left(-\frac{E_1 - E_F}{kT}\right) \quad (4)$$

Note from the above the dependence of the current on the activation energy through the exponential. For undoped germanium layers, activation energy values are the sum of eigenenergy value plus the  $E_C - E_F$ . The latter (for germanium) can be quickly computed [ ]:

$$\Delta E_{CF} = E_C - E_F = kT \ln\left(\frac{N_c^{Ge}}{n_i}\right) = 0.338eV \quad (5)$$

Where the factors in the fraction above are (a) the conduction band density and (b) the intrinsic concentration for Ge, and the 0.33 eV is essentially the intrinsic Fermi level. For such a result, our derived formula provides negligible thermal current (fraction of  $\mu A$ ). For moderate doping levels near  $10^{16} \text{ cm}^{-3}$ , we compute thermal currents  $0.0429 \text{ mA/cm}^2$ , which, for desired  $10 \text{ mA/cm}^2$ , would require a long superlattice (large number of periods, about 240). On the other hand, selecting doping levels near  $10^{18} \text{ cm}^{-3}$ , however, leads to current density near  $0.4 \text{ mA/cm}^2/\text{well}$ , which translates into 25 superlattice periods in all. Based on this, we propose an n-Ge/GaAs multi-junction layer in the middle region of the pnn GaAs/GaAs/Ge bulk lower cell, where total current will essentially reach the top-cell current and hence current matching will be succeeded within ~5% (note: top cell current  $30 \text{ mA/cm}^2$ , bottom cell currents:  $18.5 \text{ mA/cm}^2$  plus  $10 \text{ mA/cm}^2 = 28.5 \text{ mA/cm}^2$ ). Based on this current matching and on the computed data (see short circuit currents, Figures 2 and 3), we estimate the following for the composite cell of Fig.-1: short circuit current of  $28.5 \text{ mA/cm}^2$ , and open circuit voltage  $V_{oc1} + V_{oc2} = 1.04 \text{ V} + 0.968 \text{ V} = 2.008 \text{ V}$ . This means that the composite cell (as long as the tunnel junction sustains normal operation) is expected to provide two volts at OC conditions and at least  $28 \text{ mA/cm}^2$  at SC conditions. Both units of the tandem structure have fill factor values of 85 and 85.5 % respectively, as it can be found from the open-circuit voltages of each [12]. Under one sun (AM 1.5), such a one-square centimeter tandem PV-device exhibits collection efficiency of  $[0.85 \times 28.5 \times 2] / 100 = 48.45\%$ . Obvious advantages in such a design are (a) minimal material usage (small area, and narrow superlattice layers; the latter suitable for growth technique selection (chemical vapor deposition or molecular epitaxy) (b) simultaneous short and long wavelength absorption (c) short-period tuned superlattice (d) high carrier mobility due to GaAs/Alloy major components (in contrast to mismatched cells with low mobility) (e) extension of design to include more than one superlattice tuned at desired wavelengths.

## 5. Conclusion

High efficiency solar cells are becoming a reality while collection efficiency levels near 40% have been achieved. It has been realized in recent years that more than one layer may lead to higher photon absorption due to varying energy band gaps involved. Indeed, this is the case for hetero-junction cells that include two or more materials in one unit; however, recently proposed tandems do not utilize superlattice components [5, 8]. In this paper we explore efficiency enhancement via (matched) current and voltage increase, with a 1eV-tuned superlattice embedded in one of the cells. Thus, a multijunction cell is proposed, with visible

and IR wavelength absorption capabilities. The proposed structure is a  $1\text{cm}^2$  cell and is composed of two sub-cells: the bottom unit is a 20-period GaAs-Ge superlattice embedded in a pnn GaAs-Ge bulk solar cell. On top of this cell an AlAs-AlGaAs-GaAs cell is proposed, suitable for short wavelengths. The two units are connected in series via a standard tunnel junction, modeling of which is not discussed in this paper. Assuming ideality factors near one, modeling and simulation of the two devices shows a total voltage near 2 Volts and minimum current density  $28.5\text{ mA/cm}^2$ . Collection efficiency is expected to exceed the 42% current threshold (one sun conditions). The cell structures involved, could individually perform well on their own at different wavelengths and with appreciable efficiencies respectively. Our proposed structure involves tuning of the lower device at desired photon energy input (1 eV). Under the same token, optimum tuning can be pre-arranged via specific superlattice geometry selections, while more than one superlattice in tandems seems to open the way for higher efficiencies. To probe further, two part-tandem cells, with a tuned superlattice in each region, should lead to collection efficiency in excess of 45% in the immediate future.

## References

- [1] M Yamaguchi et al, Super high-efficiency multijunction and concentrator solar cells, *Solar Energy Materials & Solar Cells* 90 (2006) 3068–3077
- [2] AC Varonides, High Efficiency Lattice-Matched Multijunction Solar Cells via Tuned GaAs/Ge Quantum Wells 25<sup>th</sup> European PVSEC, 2010
- [3] M Yamaguchi et al, Novel materials for high-efficiency III–V multi-junction solar cells, *Solar Energy* 82, 173 (2008).
- [4] R. King, et al, High Concentration PV Using III-V Solar Cells, 20th European PVSEC, 2005.
- [5] Richard R. King, Daniel C. Law, Kenneth M. Edmondson, Christopher M. Fetzer, Geoffrey S. Kinsey, Hojun Yoon, Dimitri D. Krut, James H. Ermer, Raed A. Sherif, and Nasser H. Karam, *Advances in High-Efficiency III-V Multijunction Solar Cells*, Hindawi Publishing Corporation, *Advances in OptoElectronics*, Volume 2007, Article ID 29523
- [6] R Jones, J Ermer, P Pien, O Al Taher, R King, Spectrolab Progress in Multi-Junction Cell Performance and Cost, April 28-29, Toledo, Spain
- [7] R.S. Miller, T.I. Kamins, *Device Electronics for Integrated Circuits*, J Wiley & Sons, 2nd Ed, 1986, pp 16-25
- [8] C Algora, 2<sup>nd</sup> CPV Summit, April 28-29, Toledo, Spain.
- [9] JF Geisz, S Kurz, MW Wanlass, JS Ward, A Duda, DJ Friedman, JM Olson, WE McMahon, TE Moriarty, and JT Kiehl, 40.8% efficient inverted triple-junction solar cell with two independently metamorphic junctions, *Applied Phys. Letters* 91, 023502 (2007).
- [10] AC Varonides and RA Spalletta, Hopping currents in the intrinsic region of III-N-V quantum well structures in the tight binding approximation, *Physica Stat. Sol.* 5, No. 2 441 (2008)
- [11] AC Varonides, Tunneling vs. Thermionic Currents in Multi-Quantum Well Photovoltaic Structures, *Physics E* 14, 142 (2002)
- [12] E. Lorenzo, *Solar Electricity, Engineering of Photovoltaic Systems*, Protomora General de Estudios, SA, 1994, Sevilla, Spain, p. 77

## Simulations of Implantation Temperature Impact on Three-dimensional Texturing in Silicon Solar Cells

F.Jahanshah<sup>1,\*</sup>, K. Sopian<sup>2</sup>, S. H. Zaidi<sup>3</sup>, E.Gholipour<sup>1</sup>

<sup>1</sup> Isfahan High Educations and Research Institute, I.R. Iran

<sup>2</sup> Solar Energy Research Institute, Universiti Kebangsaan Malaysia, Malaysia

<sup>3</sup> Gratings, Incorporated, USA

\* Corresponding author. Tel: +98 3114436396, Fax: +98 3113802061, E-mail: f.jahanshah@ieht.ac.ir

**Abstract:** Recently new advance texturing is one of the candidates for enchaining optical absorption in mono crystalline thin film solar cells and making low cost solar cell. Silicon has relatively large reflection in UV-visible spectral region, also absorbs strongly in this region; however, its near IR absorption is weak. The absorption enhancement can occur through diffractive scattering from surface with feature dimension larger than  $\lambda/n$ , where  $n$  is silicon refractive index. For surface feature with size smaller than  $\lambda/n$ , surface is behaving like a gradient index film. By creating three-dimensional surface with sub wavelength textures on front and sidewalls, it may be possible to enhance absorption beyond the  $4n^2$  statistical limit. There is an idea that says implantation process during fabrication process affect solar cell efficiency because of p-n junction dependence to temperature. This maybe complicated the efficiency prediction. Since Because of difficulty of laboratory test and fabrication the simulation of implantation temperature method is considered for a well know three dimensional texturing at first. Simulations in first step are done for an ideal three dimensional surface texturing with  $21\mu\text{m}$  depth and an ideal p-n junction below  $1\mu\text{m}$  under frontal surface. In this simulation the p-n junction has a constant depth all over the solar cell. Then by using implantation modeling tries to predict the p-n junction place by varying the temperature all over the surface. It is shown that the p-n junction position and its shape completely depend on the temperature that causes a variety of efficiency for a well known advanced texture. In this case the p-n junction shows a discontinuity at  $700\text{ }^\circ\text{C}$  that case an efficiency drop for 21% to 10%. These simulations confirm the impact of implantation temperature on optical simulation. Results are shown to find out the best design for advance three-dimensional texturing need to predict discontinuity temperature in fabrication process. Simulations also show the dependence of efficiency with geometrical surface features and how discontinuity temperature change by shape and size of the periodic texture pattern. Results show there is a limitation in final performance of mono-crystalline solar cell with periodic texture pattern.

**Keywords:** Renewable energy, solar cells, thin film, surface texturing.

### Nomenclature

$d$ grating period .....	$\mu\text{m}$	$\theta_{m,i}$ diffraction order angle .....	
$n$ refractive index .....	..	$\Phi$ ion dose per square centimeter .....	$\text{cm}^{-2}$
$\lambda$ wavelength .....	$\text{nm}$	$\eta_{i,j}$ coupling efficiency .....	
$\theta_c$ critical angle .....		$R_p$ projected range .....	$\text{cm}$

### 1. Introduction

Silicon has relatively high reflectance in UV-Visible spectral region, however it also absorbs strongly in this region [1]. In near IR (800-1100 nm) spectral region, particularly near the band edge, absorption is weak, i.e., absorption depth is  $\sim 100\text{ }\mu\text{m}$  at  $\lambda \sim 1\text{ }\mu\text{m}$ . This weak absorption fundamentally limits the efficiency of Si solar cells: in thin films due to incomplete optical absorption, and in thick films due to bulk recombination losses. Light trapping schemes based on geometrical optics considerations have been extensively investigated in conventional [2]. Maskless, random, pyramidal texturing with feature sizes  $\gg \lambda$  on the front surface not only helps randomize scattering within the substrate, but also takes advantage of

the high refractive index of Si leading to total internal reflection of light rays outside the narrow cone defined by the critical angle ( $\theta_c = \sin^{-1}(1/n)$ ).

In reducing reflection using sub-wavelength structures, defined either by lithography or random masking methods, light incident on the Si substrates generates no diffraction orders, and preferably only obliquely propagating orders inside the Si substrate [3-5]. For lithographically-defined surface, the period is chosen such that there are no diffraction orders in air, i.e.,  $\lambda/d > 1$ . Inside the semiconductor, first and second diffraction orders are propagating due to its higher refractive index  $n$ , i.e.,  $2 * \lambda/(n*d) < 1$ . For the case of a randomly textured surface, incident light will support a large number of diffraction orders since it is a composite of several periodic structures[6]. The total optical path length neglecting back surface reflection for sake of simplicity is give by

$$\text{optical - path - length} = \sum_{i,j} \eta_{i,j} T_{i,j},$$

where the summation index  $i$  corresponds to grating period  $d_i$  of the random surface, and the summation index  $j$  corresponds to diffraction orders of the period  $d_i$ , and  $\eta_{i,j}$  represents the coupling efficiency of the transmitted intensity  $T_{i,j}$ . The optical paths of each of the diffraction order is enhanced by  $1/\cos(\theta_{m,i})$ , where  $\theta_{m,i}$  is the diffraction order angle with surface normal defined earlier. In this manner, frequency space inside the Si substrate can be effectively populated. Finally, for the third case, where features are smaller than the wavelength inside Si, no diffraction orders are propagate inside the Si substrate, which is similar to a gradient-index anti-reflection film, and is not conducive to enhanced solar cell performance.

In case of three-dimensional texturing, the trench sidewalls are also randomly textured with sub-wavelength features as described in Fig. 1.d. In such a case, each transmitted diffraction order on incidence at sidewalls, generates multiple beams, therefore, creating several more light paths than would have existed within textured/planar sheet [7]. Such an approach can potentially exceed  $4n^2$  optical enhancement limit predicted by Yablonovitch [8].

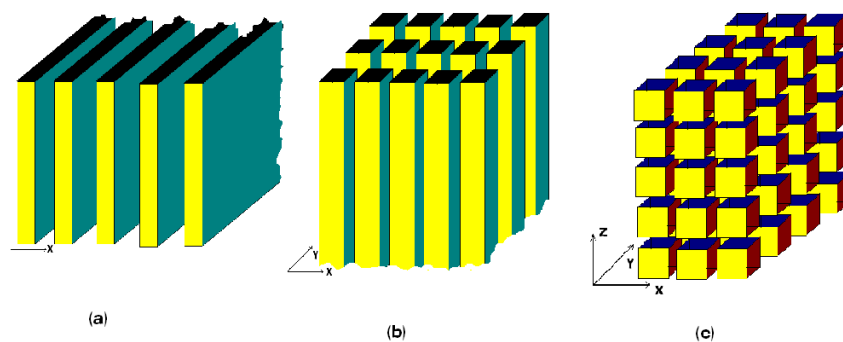


Fig. 1. Grating texture with (a) one dimension repetition (b) two dimension repetition (c) three dimension repetition. One dimension and two dimension use for solar cell application.

## 2. Mathematical implantation models

### 2.1. Gaussian Implant Model

There are several ways to construct 1D profile. The simplest way is using the Gaussian

distribution, which is specified by:

$$C(x) = \frac{\phi}{\sqrt{2\pi}\Delta R_p} \exp \frac{-(x - R_p)^2}{2\Delta R_p^2} \quad (1)$$

where  $\Phi$  is the ion dose per square centimeter specified by the dose parameter.  $R_p$  is the projected range.  $R_p$  is the projected range straggling or standard deviation .

## 2.2. Pearson Implant Model

Generally, the Gaussian distribution is inadequate because real profiles are asymmetrical in most cases. The simplest and most widely approved method for calculation of asymmetrical ion-implantation profiles is the Pearson distribution. The Pearson function refers to a family of distribution curves that result as a consequence of solving the following differential equation:

$$\frac{df(x)}{dx} = \frac{(x - a)f(x)}{b_0 + b_1x + b_2x^2} \quad (2)$$

in which  $f(x)$  is the frequency function. The constants  $a$ ,  $b_0$ ,  $b_1$  and  $b_2$  are related to the moments of  $f(x)$  by:

$$a = -\frac{\Delta R_p \gamma(\beta + 3)}{A} \quad (3)$$

$$b_0 = -\frac{\Delta R_p^2(4\beta - 3\gamma^2)}{A} \quad (4)$$

$$b_1 = a \quad (5)$$

$$b_2 = -\frac{2\beta - \gamma^2 - 6}{A} \quad (6)$$

where  $A = 10\beta - 12\gamma^2 - 18$  ;  $\gamma$  and  $\beta$  are the skew-ness and kurtosis respectively.

## 2.3. Dual Pearson Model

To extend the applicability of the analytical approach toward profiles heavily affected by channeling, the dual (or Double) Pearson was suggested Method. With this method, the implant concentration is calculated as a linear combination of two Pearson functions:

$$C(x) = \Phi_1 f_1(x) + \Phi_2 f_2(x) \quad (7)$$

where the dose is represented by each Pearson function  $f_{1,2}(x)$ .  $f_1(x)$  and  $f_2(x)$  are both normalized, each with its own set of moments. The first Pearson function represents the random scattering part (around the peak of the profile) and the second function represents the channeling tail region. Equation (7) can be restated as:

$$C(x) = \Phi[\mathfrak{R}f_1(x) + (1 - \mathfrak{R})f_2(x)] \quad (8)$$

where  $\Phi = \Phi_1 + \Phi_2$  is the total implantation dose and  $\mathfrak{R} = \frac{\Phi_1}{\Phi}$ .

### 3. Simulation

Changing the period and depth of groove would affect efficiency. The goal is to find the best design with maximum efficiency. In modeling, physically-based process simulation predicts the structures that result from specified process sequences. In a complete simulation usually we need doing three stages; 1- process simulation 2- device simulation and 3- circuit simulation. SILVACO International provides an opto-electronic software product that models the behavior of semiconductor materials, devices, and circuits using finite element techniques. In fact it is “Virtual Wafer Fab” which can determine electrical characteristics of that device based conditions are inputted. There are different models that must take into account based on; drift and diffusion current, position dependent doping, optical carrier generation, and so on. The most important tools for solar cell simulation are ATLAS, ATHENA and Luminous which have been recently used [7]. Fig.2. shows typical solar cell simulations to find implantation impact on texturing effect.

By using etching process in different time it is possible to make rectangular texture in various depths and periods. In this investigation we consider phosphorous atom to implantation on a p-type Si substrate which heat up to 900K. By using Dual Pearson model we find there are some discontinuities in p-n junction which it appears in deep groove. Fig. 3 shows simulation results in some period and depths.

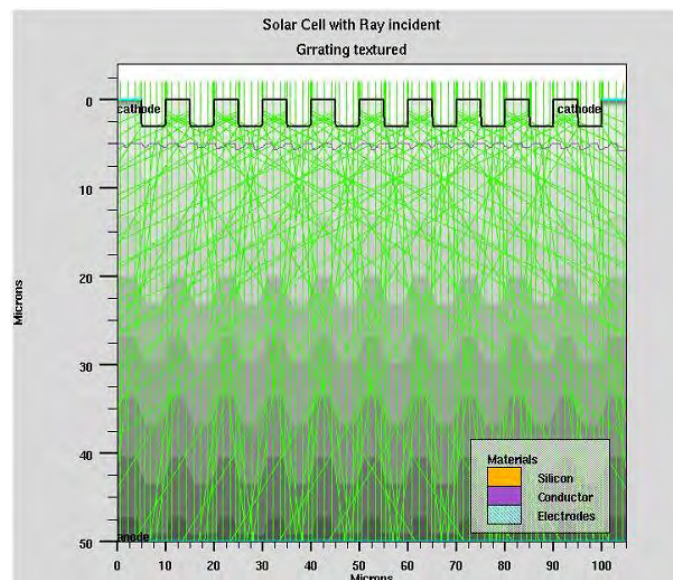


Fig. 2 Simulation of solar cell by using SILVACO software's, 1D grating structure with 10- $\mu\text{m}$  period and 3- $\mu\text{m}$  depth

### 4. Results

Table (1) and its related graphs (Fig. 4) shows output efficiency for different rectangular 2-D texturing. In all of those cases the temperature and time of doping consider constant with

700K and 30 minute respectively. The data shown in actual fabrication there is another limitation for efficiency boosting by implantation process. It is found out beside optimization of groove depth and period according to optical absorption by using wave optics, p-n junction discontinuity due to fabrication process might be considered as another parameter.

Table 1. Modeling results for solar cell efficiency due to variation in period and depth groove in 3D texturing

Depth ( $\mu\text{m}$ )	n(%) period 5 ( $\mu\text{m}$ )	n(%) period 10 ( $\mu\text{m}$ )	n(%) period 20 ( $\mu\text{m}$ )
50	0.76	6.17	9.4
40	1.24	8.21	9.44
30	2.45	9.5	9.47
20	9.5	9.54	9.2
10	9.6	9.56	9.52
5	9.6	9.5	9.53

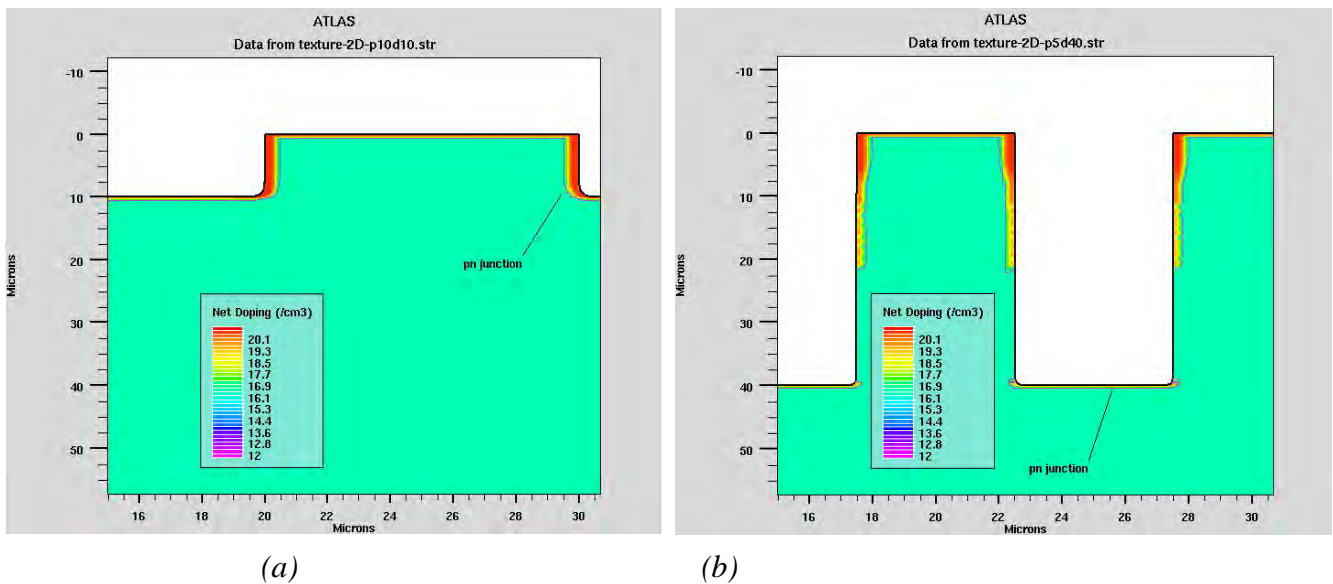


Fig. 3 Simulation of solar cell by using SILVACO software's, (a) 2D grating structure with 20- $\mu\text{m}$  period and 10- $\mu\text{m}$  depth, and (b) 2D grating structure with 20- $\mu\text{m}$  period and 40- $\mu\text{m}$  depth. The discontinuity happened for the last at 20- $\mu\text{m}$ .

## 5. Conclusion

Although rectangular grating on solar cell increase the efficiency but implantation impact during fabrication could affect on efficiency boosting. P-N junction discontinuing make a lost in thin monocrystalline solar cell. Simulation shows maximum relative efficiency is in the period range of 10-15 micrometer and 10-20 groove depth for phosphorus doping with 900K in 30 minutes. This result helps to design optimum configuration for solar cell texturing. It is shown that the p-n junction position and its shape completely depend on the temperatures that cause a variety of efficiency for a well known advanced texture. In this case the p-n junction shows a discontinuity at 700 °C that case an efficiency drop for 21% to 10% (figure 4).

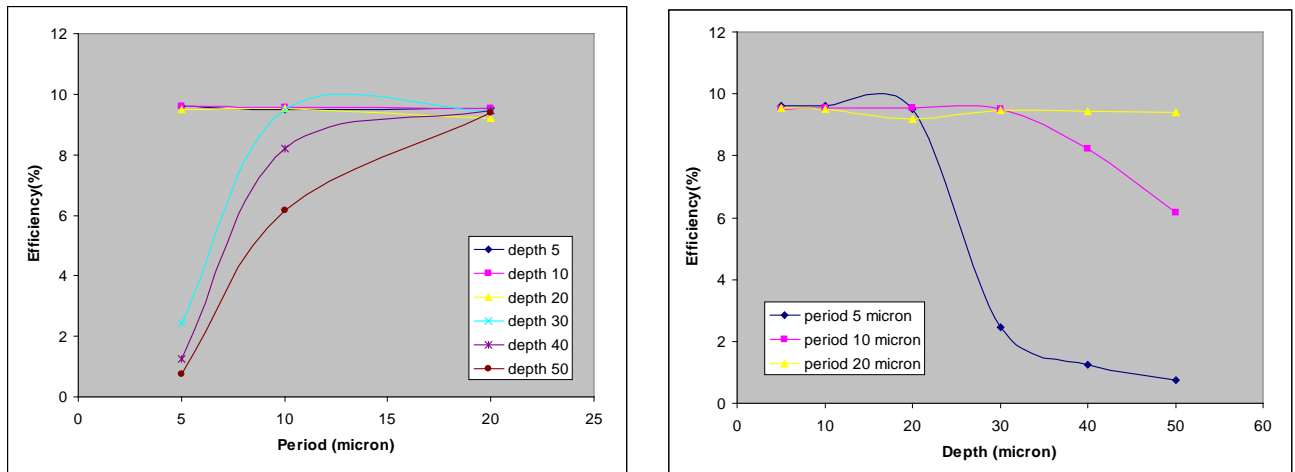


Fig. 4. Implantation period impact on solar cell efficiency. (a) Maximum relative efficiency was happened in 10-15 micrometer period.(b) Maximum relative efficiency was happened in 10-20 micrometer groove depth

### Acknowledgment

The authors would like to express their thanks to Prof. I. Ahmad, VLSI Micro-fabrication and packaging of UKM.

### References

- [1] A. A. Munzer, K T. Holdermann, R. E. Schlosser, and S. Sterk, "Thin Monocrystalline Silicon Solar Cells", *IEEE*, 1999, vol. 46, p. 2055-2061.
- [2] T. Tiedje, E. Yablonovitch, G. D. Cody, B. G. Brooks, "Limiting Efficiency of Silicon Solar Cells," *IEEE*, 1984, p. 711-716.
- [3] K. Yamamoto, M. Yoshini, T. Suzuki, T. Nakata, T. Swada and K. Hagashi, "Large-Area and High Efficiency a-Si/poly-Si Stacked Solar Cell Submodule," 2000, *28th IEEE PVSC*, p. 1428-1432.
- [4] K. Yamamoto, "Very Thin Film Crystalline Silicon Solar Cells on Glass Substrate Fabricated at Low Temperature," 1999, *IEEE*, vol. 46, p. 2041.
- [5] M. A. Green, and M. J. Keevers, *Photovoltaics: Research and Applications*, vol. 3, 1995, p. 189-230.
- [6] S. H. Zadi, R. Marquadt, B. Minhas, J. W. Tringe, "Deeply Etched Grating Structure For Enhanced Absorption in Thin C-Si Solar Cells", *IEEE* 2002, p. 1290-1293
- [7] F. Jahanshah, K. Sopian, Y. Othman, H. R. Fallah, "pn Junction depth impact on short circuit current of solar cell", *Solar Energy*, 2009, p. 1629-1633.
- [8] E. Yablonovitch, G. D. Cody, "Intensity Enhancement in Textured Optical Sheets for Solar Cells," *IEEE* vol. ED-29, 1982, p. 300-305.

## Development and new application of single-crystal silicon solar cells

G.S. Khrypunov\*, V.R. Kopach, M.V. Kirichenko, R.V. Zaitsev

National Technical University «Kharkiv Polytechnical Institute», 21, Frunze Str., 61002, Kharkiv, Ukraine  
Tel: +38-057-731-5691, E-mail: khrip@ukr.net

**Abstract:** The aim of research was development of the improved designs of high-efficiency single-crystal Si solar cells (Si-SC), intended for work in the conditions of ordinary and high-concentrated sun radiation, and also finding out of possibility to use of such devices as energy independent and enough sensitive sensors in the optical location systems. It was shown that for increase of the efficiency at cost reduction and production manufacturability of single-crystal Si-SC with base crystals (BC) thickness  $180 \leq t_{BC} \leq 200 \mu\text{m}$  having a polished light receiving surface (LRS) and back surface reflector (BSR) consisting of a transparent oxide and Al layers, a conductive transparent indium-tin oxide (ITO) layer of  $t_{ITO} = 0.25 \mu\text{m}$  interference thickness without of perforation is to be used. In case of Si-SC with inverted pyramid type texture of LRS at which the specificity of light distribution in the BC causes essentially total internal reflection of radiation from Si/ITO interface, the  $t_{ITO}$  value should be optimized in the  $1 \div 2 \mu\text{m}$  range independently of  $t_{BC}$ . For efficiency increase of vertical multi-junction (VMJ) Si-SC by a factor of 1.2 approximately the modernization of in series connected unit diode structures (UDS) by the introduction along their vertical Si-boundaries single-layer ITO reflectors by thickness more than  $1 \mu\text{m}$  is promising too. Accordingly to results of numerical simulation the character of open circuit voltage  $U_{OC}$  dependence on  $\alpha$  angle value of light incidence onto LRS of VMJ Si-SC considerable depends on the minority charge carriers lifetime  $\tau$  value in the BC of VMJ Si-SC, while light reflection coefficient  $R$  value for UDS Si/ITO boundaries effects on absolute  $U_{OC}$  value. It has been shown that purposeful decrease of  $\tau$  value and providing of  $95 < R < 100 \%$  should allowed to create the VMJ Si-SC with practically linear and easily registered  $U_{OC}(\alpha)$  dependence for use the VMJ Si-SC as energy independent and enough sensitive sensors in the optical location systems.

**Keywords:** High-Efficiency, Silicon Solar Cells, ITO Reflectors, New Application

### 1. Introduction

Efficiency increasing at cost reduction as well as expansion of single-crystal silicon solar cells (Si-SC) application fields continue to remain the actual research and development tasks. Therefore the research purposes were development of the improved designs of high-efficiency single-crystal Si-SC, intended for work in the conditions of ordinary and high-concentrated sun radiation, and also finding out of possibility to use of such devices as energy independent and enough sensitive sensors in the optical location systems.

### 2. Results and discussion

#### 2.1. Single-junction solar cells

One of the known methods to increase the efficiency of single junction (SJ) Si-SC is creation of back surface reflector (BSR) consisting of perforated  $\text{SiO}_2$  and continuous Al films deposited layer-by-layer onto surface of Si base crystal (BC) from the side opposite to SJ Si-SC light receiving surface [1]. Such construction of BSR is used, for example, in most high-efficiency SJ Si-SC with PERL (Passivated Emitter, Rear Locally-diffused) and PERT (Passivated Emitter, Rear Totally-diffused) structures. At the same time the electrical contact of Al layer with Si-BC is realized via numerous through holes in  $\text{SiO}_2$  the total area thereof making less than 1 % of the total Si-BC back surface area. Such multipoint contact character results in somewhat increased SJ Si-SC series resistance that compensates in part the efficiency gain attained due to reduction of solar radiation power losses resulting from using the double-layer BSR with dielectric oxide. Therefore, and also from the necessity to decrease the cost of such devices, when manufacturing SJ Si-SC with PERT-structure, it seems to be

reasonable to replace the BSR perforated dielectric oxide layer by a continuous layer of transparent conductive material. Accordingly to the results of this problem analysis, it can be solved by using the transparent indium-tin oxide (ITO) in double-layer BSR structure instead of SiO<sub>2</sub>. In this connection, one of the research targets was to determine the most optimum thicknesses  $l_{OX}^{opt,max}$  of conducting oxide providing a highest integral reflection coefficient  $R$  of solar radiation within the required wavelength  $\lambda$  range and to decrease the series resistance for SJ Si-SC of PERT-types both with smooth and with textured light receiving surfaces. As shown in [2], the required  $\lambda$  range depends on thickness  $t$  of Si-BC and at  $180 \leq t_{BC} \leq 200 \mu\text{m}$  (typical values of serial SJ Si-SC) is  $0.88 \leq \lambda \leq 1.11 \mu\text{m}$ .

In case of SJ Si-SC with smooth light receiving surfaces the  $l_{OX}^{opt,max}$  determination method for ITO layer was similar to that used in [2] to find interference thicknesses  $l_{OX}^{opt,max}$  for SiO<sub>2</sub>/Al BSR and TiO<sub>2</sub>/Al BSR oxide layers. Conceptually this method consisted of the following. Accordingly to [3], the optimum thicknesses  $l_{OX}^{opt}(\lambda)$  of oxide providing the maximum  $R$  values for  $\lambda$  values from the above-mentioned  $\lambda$  range were determined first of all. Further, from the obtained  $l_{OX}^{opt}(\lambda)$  dependence, the  $l_{OX}^{opt}$  values were selected corresponding to  $\lambda_1 = 0.8 \mu\text{m}$ ,  $\lambda_2 = 0.9 \mu\text{m}$ ,  $\lambda_3 = 1.0 \mu\text{m}$  and  $\lambda_4 = 1.1 \mu\text{m}$ , being  $l_{OX1}^{opt} = 0.18 \mu\text{m}$ ,  $l_{OX2}^{opt} = 0.21 \mu\text{m}$ ,  $l_{OX3}^{opt} = 0.25 \mu\text{m}$  and  $l_{OX4}^{opt} = 0.28 \mu\text{m}$ , respectively. For these  $l_{OX}^{opt}$  values, the dependences  $R[\lambda, l_{OX}^{opt}(\lambda), n_0]$  in the  $0.88 \leq \lambda \leq 1.11 \mu\text{m}$  range according to [3] were calculated using appropriate relations in cases when light receiving surface of SJ Si-SC is protected by glass ( $n_0 = 1.5$ ) and when it is not protected ( $n_0 = 1.0$ ). The analysis of all the  $R[\lambda, l_{OX}^{opt}(\lambda), n_0]$  dependences set shows that optimal oxide thickness  $l_{OX}^{opt,max}$  providing the maximum integral reflectivity of ITO/Al BSR in the specified  $\lambda$  range is  $0.25 \mu\text{m}$  at both  $n_0$  values. Dependences  $R(\lambda, n_0)$  for  $l_{OX}^{opt,max} = 0.25 \mu\text{m}$  are presented in Fig. 1.

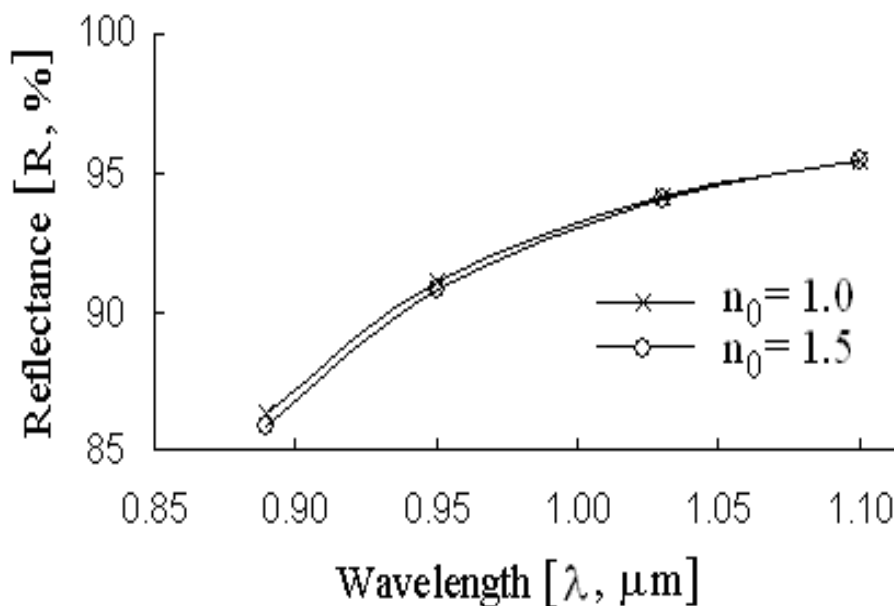


Figure 1: Dependences of  $R$  on  $\lambda$  and on  $n_0$  for ITO/Al back surface reflector with  $l_{OX}^{opt,max} = 0.25 \mu\text{m}$

In case of textured light receiving surface with the pyramids faceted by (111) type planes, the optimal oxide thickness for ITO/Al BSR is not so critical. This is due to the specificity of light ray trajectory inside Si-BC shown in Fig. 2 according to [4].

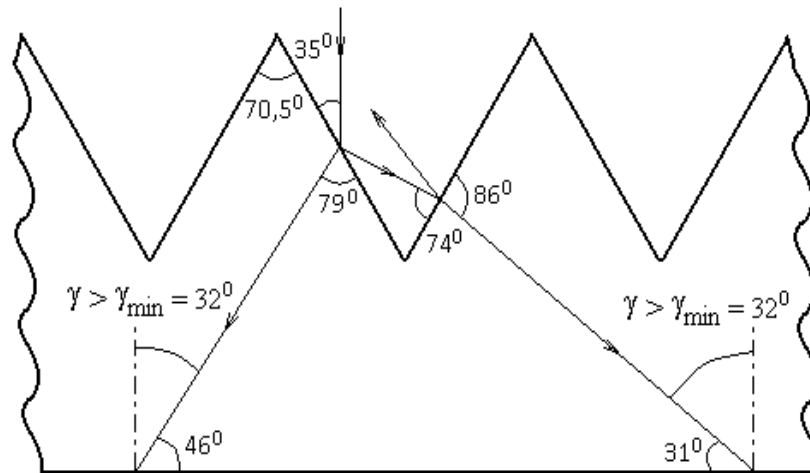


Figure 2: Light rays trajectory inside the Si-BC of the SJ Si-SC with textured frontal surface and smooth back surface

The angles  $\gamma$  of light incidence on a smooth back surface of such SJ Si-SC exceed  $40^\circ$ . It is a more than limit angle  $\gamma_{min}$  of light complete internal reflection from the Si/ITO interface because  $\gamma_{min} = \arcsin(n_{ITO}/n_{Si}) \approx 32^\circ$  [5], where  $n_{ITO} \approx 1.9$  [6] and  $n_{Si} \approx 3.6$  [7] are refractive indexes of ITO and of Si correspondingly at  $0.88 \leq \lambda \leq 1.11 \mu\text{m}$ . Thus, the above mentioned texture on the light receiving surface makes it possible to use a quite other approach to  $I_{OX}^{opt.max}$  determination based on the account for light total reflection from the Si/ITO interface. In this case, to suppress the possible partial radiation power losses in the metal [8] being in contact with ITO and also to minimize the series resistance for SJ Si-SC the ITO layer thickness should be experimentally optimized in the  $1 < I_{OX}^{opt.max} < 2 \mu\text{m}$  range.

## 2.2. Vertical multi-junction solar cells

Use Si-SC of the special construction in the conditions of high concentrated radiation is perspective direction for the increase of efficiency and cost decreasing of solar energy photovoltaic conversion [9]. Such Si-SC include, in particular [10], vertical multi-junction (VMJ) Si-SC consisting of a monolithic set (more than 10) of single-crystal silicon plane-parallel vertical unit diode structures (UDS) with p-n junctions oriented perpendicular to the light receiving surface and connected in series by the metal interlayers between the appropriate planes of adjacent UDS. Let's notice, that at the unitary light reflection coefficient  $R = 0,89$  in case of double light reflection the effective reflection coefficient  $R_{EFF} \approx R^2 \approx 0.79$  and it corresponds to losses more than 20 % of solar radiation energy on absorption. From this follows, that elimination of such losses would allow increasing the efficiency of considered type VMJ Si-SC approximately at 1.2 times.

The analysis, carried out by us, indicate a capability of such efficiency increase for VMJ Si-SC with UDS at the expense of maximum approximation to 1 the reflection coefficient of solar radiation with  $0.95 < \lambda < 1.11 \mu\text{m}$  by vertical boundaries of these cells inside VMJ Si-SC. However, on reasons, to analogical indicated before, highly reflecting  $\text{SiO}_2/\text{Al}$  and  $\text{TiO}_2/\text{Al}$  double-layer reflectors with calculated in [2] optimum thickness of  $\text{SiO}_2$  and  $\text{TiO}_2$  dielectric layers, contacting with a silicon crystal, concerning to considered type VMJ Si-SC

are unacceptable. The above mentioned multipoint character of SC back electrode with a Si-BC contact leads to certain increase of SJ Si-SC series resistance, what partially compensates a benefits in efficiency achieved at the expense of solar radiation energy losses decrease at use of dielectric oxide/metal two-layer reflector. It is natural, that in case of VMJ Si-SC the multidot contact influence effect on the device series resistance should grow in direct proportion to amount of UDS in-series, and therefore reflectors from side of UDS vertical borders should provide a good electrical contact between the next UDS on all area of the mentioned borders.

For efficiency increase of the VMJ Si-SC the modernization of in series connected UDS by the introduction along their vertical Si-boundaries single-layer ITO reflectors by thickness more than  $1 \mu\text{m}$  is promising too. The VMJ Si-SC of new design is shown schematically in Fig. 3. The new VMJ Si-SC design gives possibility to exclude the photoactive radiation losses depended on partial light absorption by metal interlayers between UDS in case of VMJ Si-SC using for photovoltaic conversion of high concentrated solar radiation the main part of which always incidence onto VMJ Si-SC light receiving surface at the angles  $0 < \alpha < 90^\circ$ . Thus taking into account that the highest angle of refraction  $\beta_{max} = \arcsin(1/n_{Si})$  [5] it is easy obtain  $0 \leq \beta \leq 16.1^\circ$ , that for  $0.88 \leq \lambda \leq 1.11 \mu\text{m}$  gives  $73.9 \leq \gamma \leq 90^\circ$ , and consequently  $\gamma > \gamma_{min} \approx 32^\circ$  at  $0 < \alpha < 90^\circ$ .

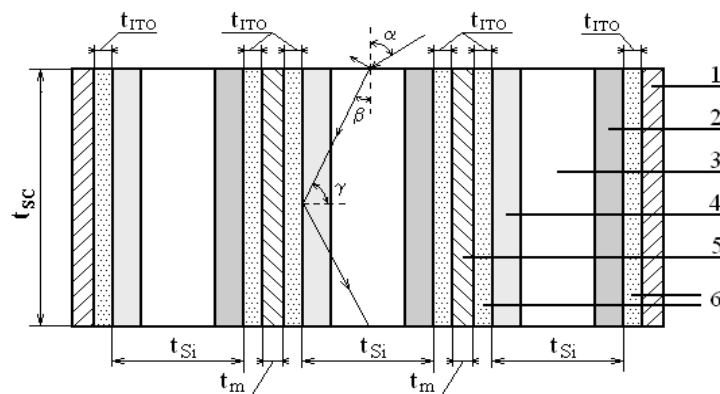


Figure 3: Cross-section of new VMJ Si-SC of  $t_{sc} \approx 850 \mu\text{m}$  thickness with ITO reflectors belonging to UDS of  $n^+p-p^+$  type (schematic image): 1 – metal electrode; 2 –  $p^+$ -Si layer of less than  $1 \mu\text{m}$  thickness; 3 – p-Si layer of  $t_{Si} \approx 160 \mu\text{m}$  thickness; 4 –  $n^+$ -Si layer of less than  $1 \mu\text{m}$  thickness; 5 – metal interlayer of  $t_m \approx 10 \mu\text{m}$  thickness; 6 – ITO reflectors of  $1 < t_{ITO} < 2 \mu\text{m}$  thickness

Therefore, at all actual values of light incidence angle  $\alpha$  on the VMJ Si-SC external surface, hitting inside the UDS of such Si-SC, light with  $0.9 \leq \lambda \leq 1.1 \mu\text{m}$  should experience practically full internal reflection from considered reflectors that should essential approach the optical reflection coefficient from ITO/Si boundaries to unity. Obviously, that this effect will be result in to previously stated increase of VMJ Si-SC efficiency approximately in 1.2 times. Since according to [8] effect of full internal reflection is caused by wave processes in ITO layer by thickness no more wavelength of light, it, on the one hand, for suppression of radiation energy losses, which can be connected to penetration of radiation energy part into metal, contacting with ITO, and on the other hand, with the purpose of ITO layer resistance minimization to the current carrying through it, the thickness  $t_{ITO}$  of this layer should be experimentally optimized in the range of values  $1 \mu\text{m} < t_{ITO} < 2 \mu\text{m}$ .

Besides as is known [6], the modern methods of ITO films with submicron and micron thicknesses deposition, inclusive of pulverization with following pyrolyze, allow to realize the

appropriate process at temperatures below 450 °C. It is well agree with the concept of single-crystal silicon SC manufacturing technology, according to which the most of high-temperature technological process operation should be the operation of submicron and highly-doped n<sup>+</sup>-Si and p<sup>+</sup>-Si layers manufacturing realized, as a rule, at 900÷1000 °C.

Accordingly to results of numerical simulation the character of open circuit voltage  $U_{OC}$  dependence upon  $\alpha$  value considerable depends on the minority charge carriers lifetime  $\tau$  value in the VMJ Si-SC base crystals, while  $R$  value for vertical UDS Si/ITO boundaries effects on absolute  $U_{OC}$  value. It has been shown that purposeful decrease of  $\tau$  value and providing of  $95 < R < 100$  % should allowed to create the VMJ Si-SC with practically linear and easily registered  $U_{OC}(\alpha)$  dependence for use the VMJ Si-SC as energy independent and enough sensitive sensors in the optical location systems. The numerical dependence

$U_{OC}^{norm}(\alpha, R, \Delta\xi)$ , got as the result of indicated simulation using early resulted in [11] relation

$$U_{OC}^{norm}(\alpha, R, \Delta\xi) = \frac{U_{OC}(\alpha, R, \Delta\xi)}{U_{OC}(\alpha = 0, R, \Delta\xi)} = 1 + \frac{\ln[f(\alpha, R) \cos \alpha]}{2.3(\xi_2 - \xi_1)} \quad (1)$$

where

$$f(\alpha, R) = R \frac{t_{Si}}{t_{SC}} \sqrt{\frac{n_{Si}^2 - 1 + \cos^2 \alpha}{1 - \cos^2 \alpha}} + R^2 \left( 1 - \frac{t_{Si}}{t_{SC}} \sqrt{\frac{n_{Si}^2 - 1 + \cos^2 \alpha}{1 - \cos^2 \alpha}} \right) \quad (2)$$

and  $\xi_1 < \xi_2$  are absolute values of indexes in degrees of short circuit current  $J_{SC}$  and diode saturation current  $J_0$  densities accordingly, is presented in Fig. 4.

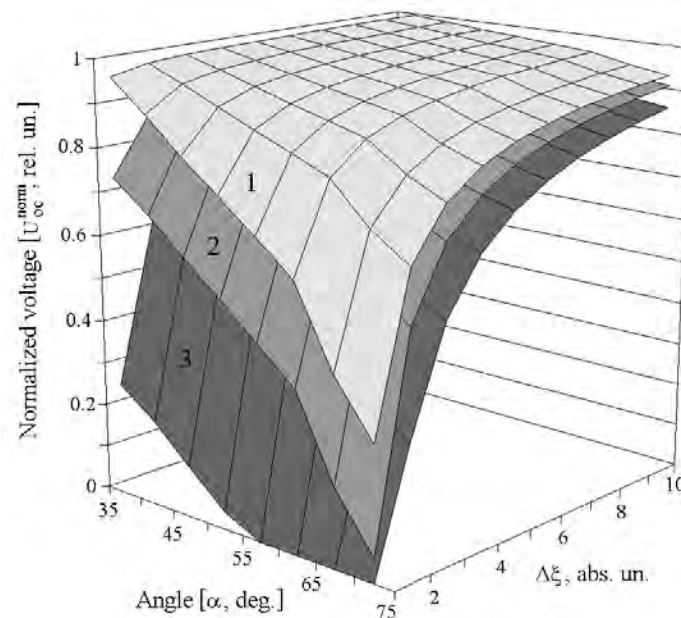


Figure 4: Dependence  $U_{OC}^{norm}$  values versus  $\alpha$  and  $\Delta\xi$  for considered VMJ Si-SC at the light reflection coefficients from vertical UDS boundaries: 1 -  $R = 100$  %, 2 -  $R = 60$  %, 3 -  $R = 20$  %

It is well known [4] that values of  $J_{SC}$  and  $J_0$ , and consequently  $\Delta\xi$ , substantially depends from  $\tau$  value in SC base crystals. Therefore at the use VMJ Si-SC as sensors the required

value of  $\Delta\xi$  possibly to attain by a purposeful decrease of  $\tau$  value in Si-BC. In accordance to numerical simulation results for using VMJ Si-SC as sensors in the optical location systems the optimal combination of parameters influencing on  $U_{OC}(\alpha)$  dependence are  $1 \leq \Delta\xi \leq 2$  and  $95 < R < 100\%$ .

### 3. Conclusions

It was shown that for increase of the efficiency at cost reduction and production manufacturability of single-crystal Si-SC with base crystals thickness  $180 \leq t_{BC} \leq 200 \mu\text{m}$  having a polished light receiving surface and back surface reflector consisting of a transparent oxide and Al layers, a conductive transparent ITO layer of  $t_{ITO} = 0.25 \mu\text{m}$  interference thickness without of perforation is to be used. In case of Si-SC with inverted pyramid type texture of light receiving surface at which the specificity of light distribution in the base crystals causes essentially total internal reflection of radiation from Si/ITO interface, the  $t_{ITO}$  value should be optimized in the  $1 \div 2 \mu\text{m}$  range independently of  $t_{BC}$ . For efficiency increase of vertical multi-junction Si-SC by a factor of 1.2 approximately the modernization of in series connected unit diode structures by the introduction along their vertical Si-boundaries single-layer ITO reflectors by thickness more than  $1 \mu\text{m}$  is promising too. Accordingly to results of numerical simulation the character of open circuit voltage  $U_{OC}$  dependence on  $\alpha$  angle value of light incidence onto light receiving surface of vertical multi-junction Si-SC considerable depends on the minority charge carriers lifetime  $\tau$  value in the base crystals of vertical multi-junction Si-SC, while light reflection coefficient  $R$  value for unit diode structures Si/ITO boundaries effects on absolute  $U_{OC}$  value. It has been shown that purposeful decrease of  $\tau$  value and providing of  $95 < R < 100\%$  should allowed to create the vertical multi-junction Si-SC with practically linear and easily registered  $U_{OC}(\alpha)$  dependence for use the vertical multi-junction Si-SC as energy independent and enough sensitive sensors in the optical location systems.

### Acknowledgment

The work was supported by STCU under Project 4301.

### References

- [1] M.A. Green, J. Zhao, A. Wang and S.R. Wenham, "Progress and outlook for high-efficiency crystalline silicon solar cells", *Solar Energy Materials and Solar Cells*, 65, 2001, pp. 9-16.
- [2] V.R. Kopach, M.V. Kirichenko, S.V. Shramko, R.V. Zaitsev, I.T. Tymchuk, V.A. Antonova, A.M. Listratenko, "Back surface reflector optimization for thin single crystalline silicon solar cells", *Functional Materials*, 14, 2007, pp. 555-561.
- [3] M.M. Koltun, "Selective optical surfaces of solar energy converters", Nauka, Moscow, 1979 (in Russian).
- [4] A.L. Fahrenbruch, R.H. Bube, "Fundamentals of solar cells. Photovoltaic solar energy conversion", Academic Press, New York, 1983.
- [5] G. S. Landsberg, "Optics", Nauka, Moscow, 1976 (in Russian).
- [6] D.E. Morton, A. Dinca, "Ion-assisted deposition of E-gun evaporated ITO films at low substrate temperatures", <http://www.dentonvacuum.com/n-paper>.

- [7] H.R. Philipp, E.A. Taft, “Optical constants of silicon in the region 1 to 10 eV”, *Phys. Rev.*, 120, 1960, pp. 37-38.
- [8] V.A. Kizel, “Light refraction” (Series “Physics and technology of spectral analysis”), Nauka, Moscow, 1973 (in Russian).
- [9] P.J. Verlinden, “High–efficiency concentrator silicon solar cells”, in: “Practical Handbook of Photovoltaics: Fundamentals and Applications”, edited by T. Markvart and L. Castaner, Elsevier Science Ltd., Kidlington, Oxford, 2003 pp. 436–455.
- [10] B.L. Sater, N.D. Sater, “High voltage silicon VMJ solar cells for up to 1000 suns intensities”, *Proceedings of the 29<sup>th</sup> IEEE Photovoltaic Specialists Conference*, New Orleans, USA, 2002 pp. 1019–1022.
- [11] V.R. Kopach, M.V. Kirichenko, S.V. Shramko, R.V. Zaitsev, S.A. Bondarenko, “New approach to the efficiency increase problem for multi-junction silicon photovoltaic converters with vertical diode cells”, *Functional Materials*, 15, 2008 pp. 253-258.

## Improvement of solar cells efficiency and radiation stability by deposition of diamond-like carbon films

Nickolai I. Klyui<sup>1\*</sup>, Anatoliy N. Lukyanov<sup>1</sup>, Anatoliy V. Makarov<sup>1</sup>, Volodymyr B. Lozinskii<sup>1</sup>, Gennadiy S. Khrypunov<sup>2</sup>, Andriy N. Klyui<sup>3</sup>

<sup>1</sup> V. Lashkarev Institute of Semiconductor Physics National Academy of Sciences of Ukraine, Kiev, Ukraine

<sup>2</sup> National Technical University "Kharkiv Polytechnic Institute", Kharkiv, Ukraine

<sup>3</sup> Taras Shevchenko Kyiv National University, Kiev, Kiev, Ukraine

\* Corresponding author. Tel: +38044 5256202, Fax: +38044 5256202, E-mail: klyui@isp.kiev.ua

**Abstract:** Diamond-like carbon films (DLC) deposited by PE-CVD technique were used as antireflection and protective coatings for Si and A<sup>II</sup>B<sup>VI</sup> based solar cells (SC). Application of the DLC films as single- or double-layer antireflection coatings allows us to improve the Si-based solar cells efficiency up to 1.4-1.5 times (from ~10% to ~15%). It has been shown that optical bandgaps of DLC films were increased after UV irradiation. The films with greater amount of nitrogen show better irradiation resistance. It was also established that Si (both mono- and multicrystalline) and A<sup>II</sup>B<sup>VI</sup> based SCs with even thin antireflection DLC film demonstrate higher stability against action of gamma-irradiation up to dose of 10<sup>8</sup> rad. The effect is connected with hydrogen atoms those are released from the film as a result of broken of carbon-hydrogen bonds by  $\gamma$ - or UV-quanta, diffuse to the SC, and passivate dangling bonds in the SC volume. It has been also shown that due to application of the DLC antireflection films with low refractive index the transparency of front ITO or ZnO (Al) contacts in A<sup>II</sup>B<sup>VI</sup> based SCs may be substantially improved integrally to 10% in spectral range of 430-850 nm. As a result, short circuit current and efficiency of thin film SCs may be also improved.

**Keywords:** Solar Cells, Antireflection Coatings, Radiation Stability

### 1. Introduction

At present diamond-like carbon (DLC) films are rather widely used as very promising antireflection (AR) and protective coatings for silicon solar cells (SCs) [1-3]. The main advantages of DLC films are high hardness, chemical and radiation stability, and the possibility to change their optical properties under the variation of deposition conditions. The last one allows formation of multi-layer antireflection and protective coatings for SCs just during the same technological process. Thus, it enables to avoid deposition of different antireflection layers, such as, for example, SiO<sub>2</sub>, Si<sub>3</sub>N<sub>4</sub>, SiN:H, ZnO, ZnS, MgF<sub>2</sub> etc. As a result the technological procedure of antireflection layers formation becomes simpler and cheaper. Moreover, it was also shown that hydrogen containing DLC films may be successfully used as protective coatings for SCs against action of radiation. The improvement of radiation resistance of the SCs is still of great importance. One of the factors for space SC efficiency degradation is the action of proton and electron irradiation of "solar wind". It leads to reduction in carrier concentration of the base region and decreasing the minority carrier lifetime. One more part of "solar wind" is  $\gamma$ -irradiation. It is less dangerous but more penetrating than proton and electron particles. So, space SCs should have resistivity to penetrating irradiation like  $\gamma$ -quanta. So, the protective coatings must protect from radiation, improve the SC's optical properties and be radiation stable themselves. To achieve simultaneously the aim of protection, passivation and antireflection the diamond-like carbon thin films may be used both for space and terrestrial SCs.

In this paper antireflection and protective properties of the DLC films and their applications for improvement of SC efficiency and radiation stability were investigated.

## 2. Methodology

The a-C:H:N films were deposited by the plasma-enhanced chemical vapor deposition method from the plasma of the RF discharge (13.56 MHz) at various RF discharge powers (100-250 Wt) and nitrogen contents in the gas mixture (10-45%). The gas mixture CH<sub>4</sub>:N<sub>2</sub>:H<sub>2</sub> was used, and the nitrogen content in it was varied by the gradual replacement of hydrogen by nitrogen. The gas pressure in a chamber was varied within the limits of 25–105 Pa. The film deposition was carried out onto substrates maintained at room temperature. The deposition time was 15 min.

The thicknesses of DLC films were measured with a Dektak profilometer (the instrumental error was ±5 nm) and an LEF-3G laser ellipsometer ( $\lambda=632.8$  nm). The film topography was studied making use of a Digital Instruments scanning atomic force microscope (AFM) Nanoscope IV. Optical constants of the films were measured by using spectral ellipsometer. Measurements of the DLC film's transmission were conducted on the Fourier spectrometer firm "Perkin Elmer" Spectrum BX-II in the range (400 ÷ 2000) cm<sup>-1</sup>. The transmission spectra of the films deposited onto glass substrates were measured by an S2000 spectrometer (Ocean Optics, USA) in the range 300— 800 nm.

Solar cell samples were fabricated on single- or multi-crystallite p-silicon, according to the technological routine which included diffusion of the doping impurity (phosphorus) from a POCl<sub>3</sub> source, formation of the front contacts by the screen printing method (multi-Si) or the photolithography method (mono-Si), formation of the Al back contacts. Some of the fabricated specimens of solar cells were irradiated by  $\gamma$ -quanta from a Co<sup>60</sup> source to the exposure doses of 10<sup>5</sup>, 10<sup>6</sup>, 5×10<sup>6</sup>, 10<sup>7</sup>, 5×10<sup>7</sup>, and 10<sup>8</sup> rad. The SCs with and without thick DLC films were subjected to proton implantation (E=50-150 keV, D=1.10<sup>14</sup> – 1.10<sup>16</sup> cm<sup>-2</sup>). The proton depth distribution was calculated by Monte-Carlo simulation using TRIM-98 program. Some of DLC films and DLC – Si SCs structures were subjected to ultraviolet (UV) and focused UV (by 350 times) irradiation using light of Hg-lamp during 2 hours.

The solar cell samples were used to study the spectral dependences of the short circuit photocurrent and the light current-voltage load characteristics (LCVLCs). For this purpose, a special original certified setup was used [4]. The LCVLCs were used to determine the density of the short circuit current J<sub>sc</sub>, the open-circuit voltage V<sub>oc</sub>, the fill factor FF of the current-voltage characteristic, and the SC efficiency  $\eta$ . The spectral dependences were measured in the wavelength range 400-1200 nm. The spectral characteristics that had been obtained were used to determine the effective diffusion length *L* of minority charge carriers in the base region of SCs.

## 3. Results and Discussion

### 3.1. Application of DLC films as antireflection coatings for silicon solar cells

It is well-known that for optimal antireflection effect when single-layer antireflection coating is used refractive index of an antireflection coating must meet completely the equation

$$n_{film} = (n_{substrate})^{1/2} \quad (1)$$

where  $n_{film}$  and  $n_{substrate}$  are refractive indexes for substrate and antireflection film, respectively.

Refractive index of Si in spectral range where Si-SCs are photosensitive changes from 3.7 to

5.5. It means that for Si-based SCs the  $n$  value must be  $\sim 1.92$ - $2.3$ , and on the average must be close to  $2.0$ . As we can see from Fig. 1 so-called “hard” film satisfied this conditions very good in rather wide spectral range.

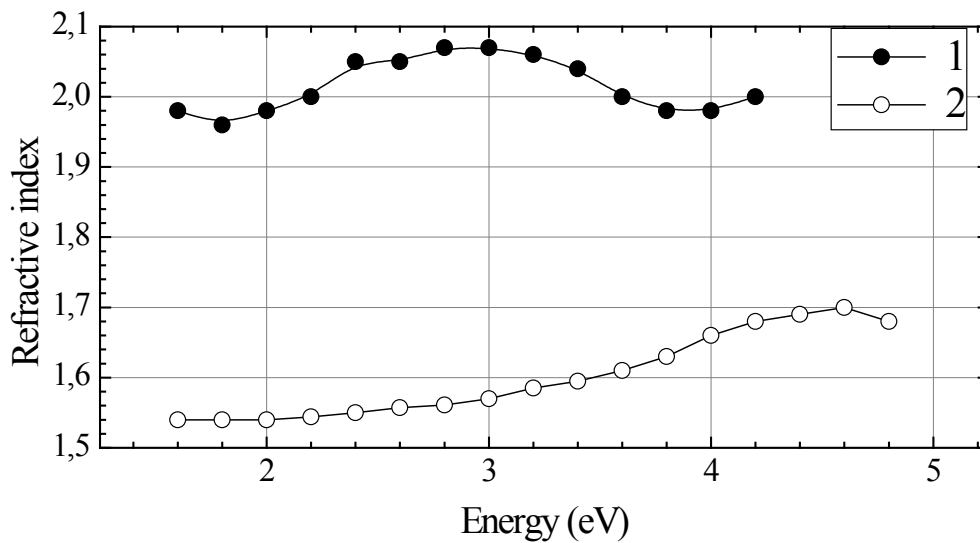


Fig. 1. Spectra of refractive index  $n(E)$  of “hard”(1) and “soft” (2) DLC films. Nitrogen content in gas mixture is 1 – 0 %, 2 – 45%.

Indeed, as its seen from Table 1, after deposition of single layer (SL) or double layer (DL) DLC films significant increasing of the SC efficiency (up to 1.5 times) is observed due to not only simple antireflection effect (short circuit current density  $J_{sc}$  increasing) but due to passivation of recombination active centers by hydrogen (fill factor FF and open circuit voltage  $V_{oc}$  increasing) as well [2]. It was also established that the FF and  $V_{oc}$  improvement effect is more pronounced for low quality SCs with high concentration of recombination active centers. On the whole, hydrogenation is very effective method for modification of defect recombination activity in Si, especially in multicrystalline-Si where high concentration of defects at grain boundaries exist. It should be noted that hard and stable DLC films also acts as a barrier against hydrogen diffusion from the SCs.

The SCs parameters were measured under AM 1.5 spectral conditions.

Table 1. Parameters of SCs with and without DLC antireflection coatings.

Sample number	$I_{sc}$ (mA)	$J_{sc}$ (mA/cm <sup>2</sup> )	$V_{oc}$ (V)	Fill factor	Efficiency (%)
Initial 1	59.5±0.93	25.54±0.40	0.598±0.001	0.722±0.001	11.03±0.51
Initial 1 covered by SL-DLC* coating	80.3±0.93	34.4±0.40	0.607±0.001	0.754±0.001	15.74±0.62
Initial 2	66.4±0.25	24.3±0.11	0.600±0.001	0.677±0.001	9.88±0.43
Initial 2 covered by DL-DLC* coating	91.4±0.93	34.3±0.40	0.613±0.001	0.707±0.001	14.87±0.53

\*The refractive index and thickness for the coatings 1 and 2 are: 2.03, 71 nm ; 2.03/1.6, 71/108 nm, respectively. The films parameters were measured by laser ellipsometer at  $\lambda=632.8$  nm.

On the other hand, in case that the DLC films are used as antireflection coatings for materials with rather low refractive index value the films with as low as possible  $n_{film}$  value must be

deposited. We can satisfied this requirement by changing the DLC film deposition conditions. For example, we can decrease the rf discharge power, increase the gas pressure in plasma reactor during film deposition and add nitrogen and oxygen to gas mixture [5]. As a result, the film with rather low  $n_{\text{film}}$  value in wide spectral range may be obtained (so-called “soft” film) (Fig. 1).

It should be also noted that deposition rate of the DLC film may be rather high. For example, the SL-DLC film with refractive index  $\sim 2.0$  and thickness of 71 nm may be deposited at 200 Wt discharge power during 3.5 minutes (Fig. 2). The deposition rate depends on rf discharge power and nitrogen content in gas mixture (Fig. 2).

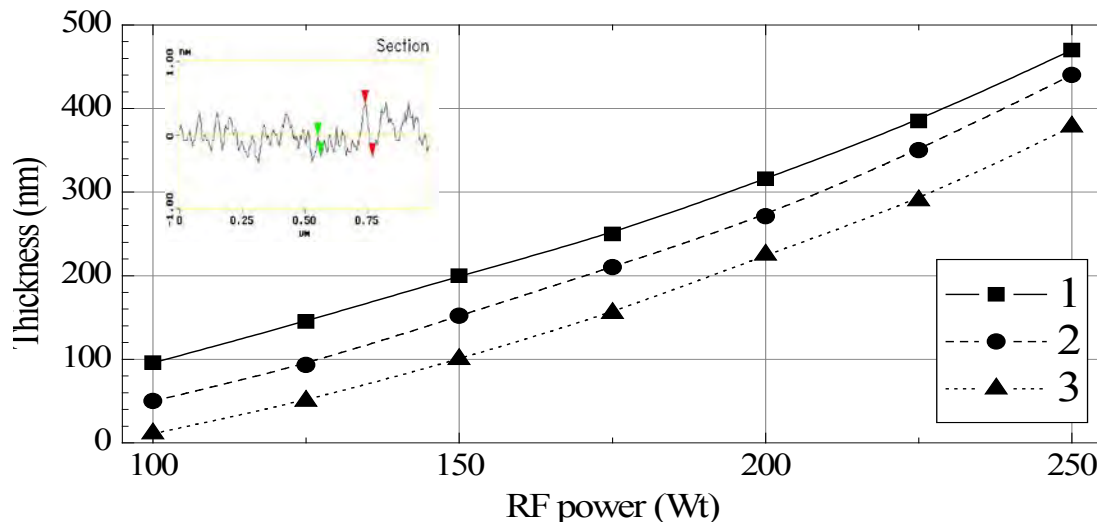


Fig. 2. Dependencies of the DLC (a-C:H:N) film thickness on RF power discharge. Deposition time is 15 minutes and nitrogen content in gas mixture is equal: 1 –20%; 2 – 30%; 3 –45%. Inset shows roughness of the DLC films measured by AFM.

Investigations of the DLC film surface by atomic force microscope show that the films have high surface homogeneity with the average roughness less than 0.65 nm (see insert to Fig. 2).

### 3.2. Application of thick DLC films as protective coatings

For application of DLC films as protective coatings for SCs of space application as thick as possible films should be deposited to prevent degradation of SCs under action of so-called “solar wind”. The films must possess proper optical properties, namely high transparency to decrease absorption losses in the film. It was earlier shown that nitrogen containing DLC films have low level of internal mechanical strains [6]. It allows us to deposit rather thick films. We studied SC-DLC film structures with the film thickness of 1300 nm. Test SC without any protective film was also studied.

The SCs were subjected to implantation of protons of different energies (50-150 keV) and doses ( $10^{14} - 10^{16} \text{ cm}^{-2}$ ). Fig. 3 shows dose dependencies of efficiency ( $\eta$ ) for the test SC and the SCs covered by DLC (a-C:H:N) protective film. In order to calculate depth distribution we used Monte-Carlo simulation (TRIM-98 program). It was established that for ion energies 50 and 100 keV protons do not penetrate into Si SC and stopped in DLC films (Fig. 3). As we can see from Fig. 4 in this case decreasing of efficiency for the irradiated SCs is not observed up to high implantation dose ( $10^{16} \text{ cm}^{-2}$ ). And only in case that proton energy is 150 keV marked decreasing of the SC efficiency takes place at doses higher than  $10^{15} \text{ cm}^{-2}$ . The degradation of the SC efficiency is caused by penetration of proton into the SC volume,

generation of defects and reduction minority carrier lifetime in the SC [3]. The conclusion is confirmed by calculations and in this case proton mean projective range is close to DLC film – Si SC interface (Fig. 3). At the same time, unprotected SC become dramatically degraded at this dose and proton energy of 100 keV (Fig. 3).

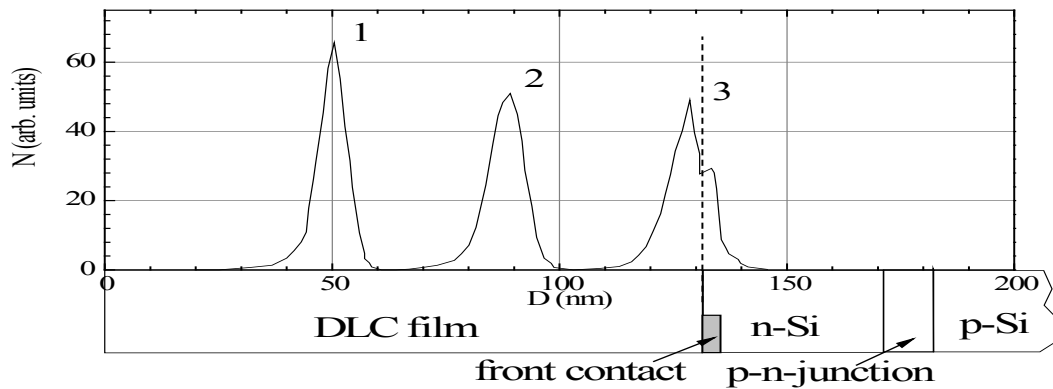


Fig. 3. Proton depth distribution of different energy in DLC film/Si-solar cell structure: 1 – 50 keV; 2 – 100 – keV; 3 – 150 keV.

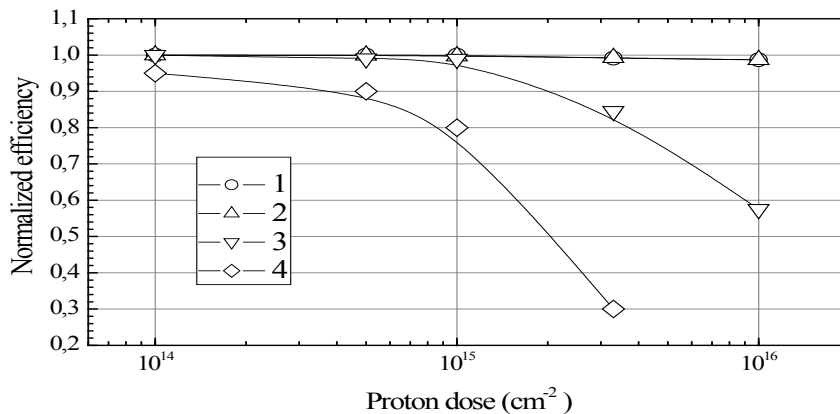


Fig. 4. Dependencies of normalized efficiency of solar cells from proton doses of different energy: 1 – 50 keV; 2 – 100 – keV; 3 – 150 keV; 4 – 100 keV, solar cell without DLC coating.

### 3.3. Application of thin DLC films as protective coatings

Figs 5 and 6 present results of investigations of Si SCs subjected to  $\gamma$ -irradiation. It is seen from Fig. 4, that radiation resistance of the SCs covered by DLC films (curves 2, 4 in Fig. 5) is higher compared to unprotected SCs (curves 1, 2 in Fig. 5).

It should be pointed out that in this case we used thin (71 nm) DLC antireflection coatings. The statistical significance of the variation in Fig. 5 did not exceed  $\pm 0.01$ . Thus, for majority of points it is substantially lower than observed changes in normalized efficiency values. It should be noted that no marked changes of results presented in figs 5, 6 were observed in one year after  $\gamma$ -irradiation of the samples. So, the degradation stability of the SCs covered by DLC films is higher than that without any coatings. The effect is observed both for SCs produced from mono-crystalline silicon and from multi-crystallite one. We proposed the following mechanism of  $\gamma$ -radiation effect on Si SCs properties. The effect is connected with hydrogen atoms those are released from the film as a result of broken of carbon-hydrogen bonds by gamma-quanta, diffuse to the SC, and passivate silicon dangling bonds at grain boundaries and in the SC volume. As a result, lifetime and, consequently, diffusion length of minor charge carriers in the SCs degrade slower in the SCs covered by the DLC films (Fig. 6)

[7]. Effect of silicon dangling bonds passivation in the SCs volume is confirmed by appearance of absorption band near  $580\text{ cm}^{-1}$  in infrared spectrum of irradiated DLC-SC structures (Fig. 7) those correspond to Si-H bonds.

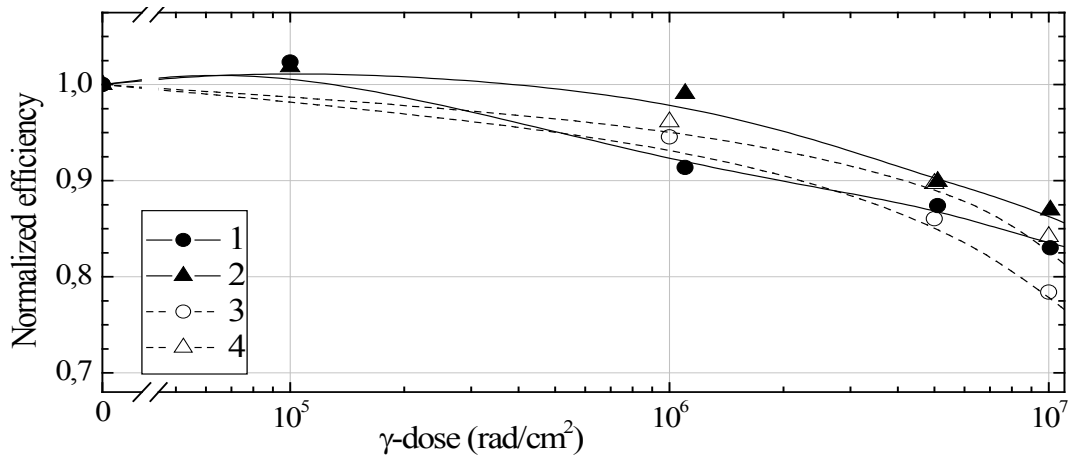


Fig. 5 Dependencies of normalized by initial value efficiency of solar cells from dose of  $\gamma$ -irradiation: 1 – mono-Si SC; 2 - mono-Si SC with DLC cover; 3 – multi-Si SC; 4 – multi-Si SC with DLC cover.

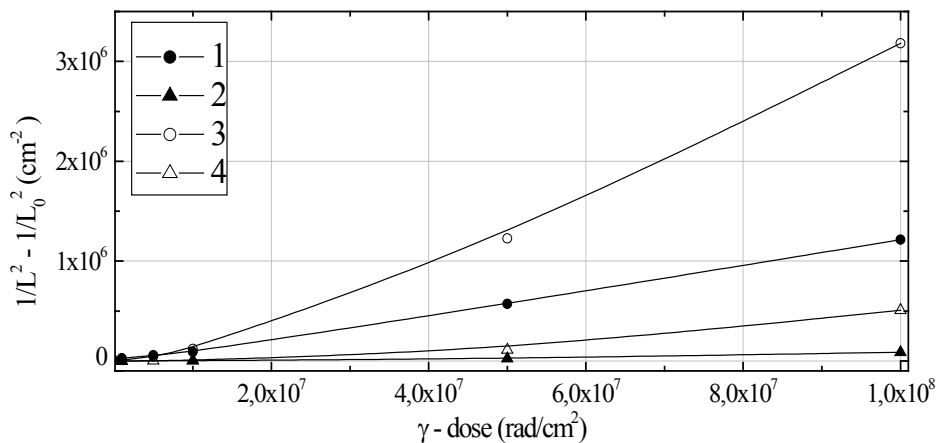


Fig. 6. Dependencies of  $(1/L^2 - 1/L_0^2)$  of solar cells on dose of  $\gamma$ -radiation: 1 – mono-Si SC; 2 – mono-Si SC with DLC cover; 3 – multi-Si SC; 2 – multi -Si SC with DLC cover; Here  $L_0$  and  $L$  are diffusion length of minor charge carrier of initial and irradiated SC, respectively.

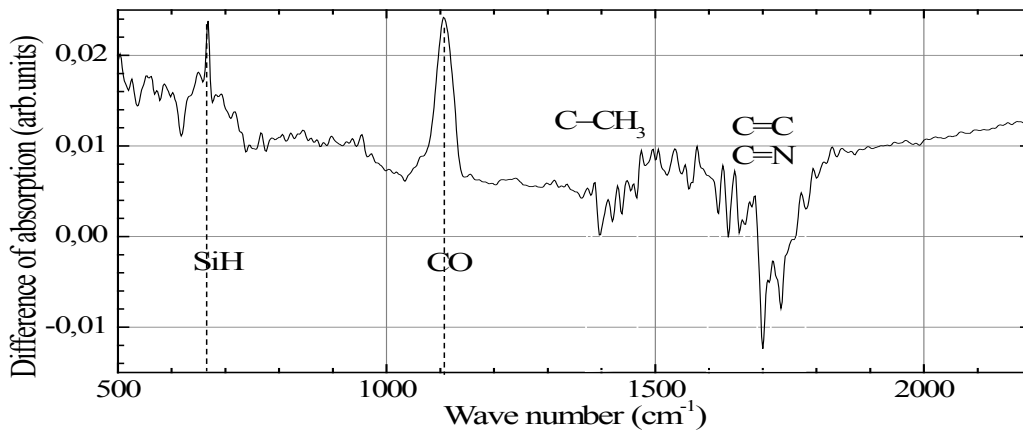


Fig. 7. Absorption difference between spectra of irradiated ( $\gamma$ -irradiation dose  $10^6\text{ rad/cm}^2$ ) and initial DLC film deposited from precursor gas with 45% of  $\text{N}_2$ .

### 3.4. Application of DLC films as antireflection coatings for materials with low refractive index

CdS, CdTe, CIS, and CIGS films are widely used for production of thin film or even flexible solar cells (SC). Because of low diffusion length of non-equilibrium carriers for the films it is especially important for such SCs to obtain highly conductive and transparent continuous front contact. As usual, for such contact indium-tin oxide (ITO) or ZnO doped with Al films are used. Refractive index of such films is higher than 2.0 [8] in the spectral region where the SCs are sensitive, therefore, rather significant reflection losses take place. In order to decrease the losses we propose to use diamond-like carbon (DLC) films with low refractive index to meet requirement for optimal antireflection effect. The DLC films were deposited by PE-CVD technique from gas mixture of nitrogen, methane and hydrogen. In some cases oxygen was also added to the gas mixture. As it was mentioned above we can deposit the DLC film with low refractive index (see Fig. 1). Theoretical modelling of optical properties for such multi-layered structures was also carried out to determine the required parameters of the antireflection DLC films. It has been shown that due to application of the DLC films transparency of front ITO or ZnO (Al) contacts may be substantially improved (Fig. 8). Further optimization of the DLC film deposition process allowed us to increase integral transmission of ZnO(Al) in spectral region 400-830 nm up to 1.1. times.. As a result short circuit current and efficiency of thin film SCs may be also improved.

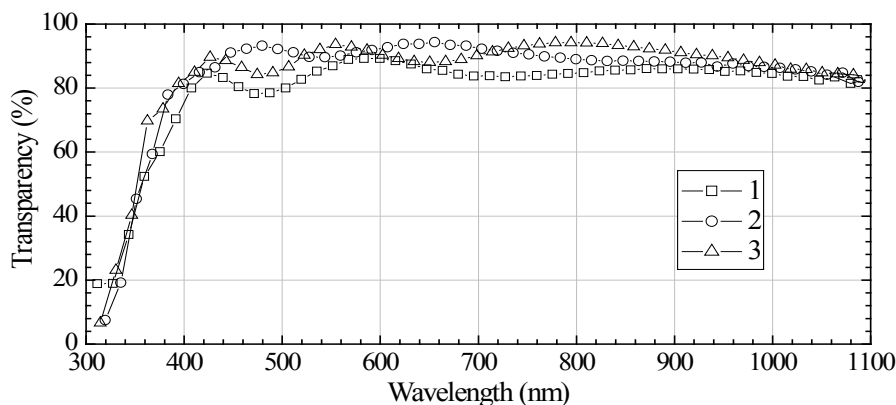


Fig. 8. Transparency of ZnO films ( $30 \text{ Ohm/cm}^2$ ): 1 – initial; 2 – covered by DLC film of 67 nm thickness; 3 – covered by DLC film of 100 nm thickness.

### 3.5. Effect of ultraviolet irradiation on DLC films properties

Diamond-like carbon films (a-C:H:N) were deposited by PE-CVD technique from gas mixture of nitrogen, methane and hydrogen. The films were irradiated by UV and focused UV (by 350 times) light of Hg-lamp during 2 hours.

Transparency in visible and IR range and Raman spectra were measured. It has been shown that optical bandgap of the DLC films was increased after UV irradiation (Fig. 9). It was connected with oxygen incorporation into the DLC films, changing of carbon-nitrogen bonds concentration and graphite-like clusters size. The films with greater amount of nitrogen show better irradiation resistance. Because of increasing of the films optical bandgap after UV irradiation no changes of parameters for Si SCs covered by the DLC coatings after UV irradiation was observed.

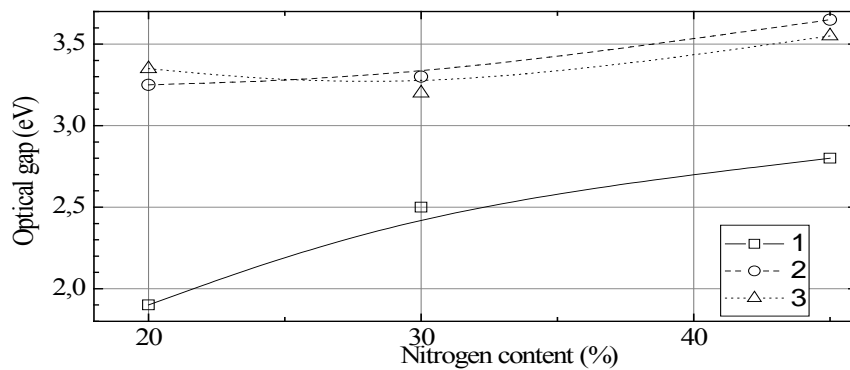


Fig. 9. Dependencies of DLC film optical energy gap on nitrogen content in gas mixture: 1 – initial DLC films; 2 – UV-irradiated DLC films; 3 – DLC films irradiated by concentrated UV light.

#### 4. Conclusions

Finally, we may conclude that diamond-like carbon films are very prospective antireflection coatings not only for solar cells based on materials with high refractive index (like silicon) but for SCs produced on the base of materials with low refractive index (like  $A^{II}B^{VI}$  materials). In particular, efficiency of Si-based SCs may be improved up to 1.5 times due to deposition of the antireflection and passivative DLC films. It has been shown for the first time that even thin antireflection films ( $d=70$  nm) allows us to substantially improve radiation resistance of silicon based solar cells against action of  $\gamma$ -radiation with the dose up to  $10^8$  rad. In its turn, thick DLC film ( $d=1300$  nm) enable to protect SCs against action of intermediate energy protons (50-100 keV).

#### Acknowledgements

The work was supported by Science and Technology Center in Ukraine (project #4301) and by the Ukrainian governmental scientific-technical program “Creation of chemical-metallurgical branch for production of pure silicon in 2009-2012” (project #4.2).

#### References

- [1] M.Allon-Alaluf, The influence of diamond-like carbon films on the properties of silicon solar cells, *Thin Sol. Films* 303, No. 8, 1997, pp. 273-276.
- [2] N.I. Klyui, Silicon solar cells with antireflection diamond-like carbon and silicon carbide films, *Solar Energy Materials & Solar Cells* 72, 2002, pp. 597-603.
- [3] V.G.Litovchenko, Solar Cells Based on DLC Film – Si Structures for Space Application, *Solar Energy Materials & Solar Cells* 68, No.1, 2001, pp. 55-70.
- [4] Certificate of accreditation for center of photoelectric converters and batteries testing. Given to V.Lashkaryov ISP NASU by Ukrainian governmental centers of standardization, metrology, and certification. Date of issue – 29.04.2003.
- [5] G. Adamopoulou, Electron cyclotron resonance deposition, structure, and properties of oxygen incorporated hydrogenated diamondlike amorphous carbon films *Journal of Applied Physics* 96, No. 10, 2004, pp. 5456-5461.
- [6] D. F. Franceschini, Structural modifications in a-C:H films doped and implanted with nitrogen, *Diamond and Related Materials* 3, 1993, pp. 88-93.
- [7] N.I. Klyui, Influence of  $\gamma$ -irradiation on the parameters of silicon-based solar cells, *Ukrainian Physical Journal* 52, No. 3, 2007, pp. 245-250.
- [8] D.R. Sahu, Development of ZnO-based transparent conductive coatings, *Solar Energy Materials & Solar Cells* 93, 2009, pp.1923–1927.

## Formation of transparent and ohmic nanostructure thin films of fluorine-doped indium oxide prepared by spray

S.M. Rozati\*, Z. Bargbidi

Department of Physics, University of Guilan, Rasht 42335, Iran

\* Corresponding author. Tel: +981313220912, Fax: +981313220066, E-mail: smrozati@guilan.ac.ir

**Abstract:** In this research, indium oxide nanostructure undoped and doped with F were prepared on glass substrates using spray pyrolysis technique. Various parameters such as dopant concentration, deposition temperatures, amount of indium oxide powder were discussed. Structural properties of these films were investigated by XRD & SEM. Electrical and optical properties have been studied by Hall Effect and UV-Visible spectrophotometer respectively. The thickness of the films is determined by PUMA software. The variation in refractive index, extension coefficient and band gap of these films also were investigated.

**Keywords:** Indium oxide, Indium doped oxide, Spray pyrolysis

### 1. Introduction

Transparent conducting oxide (TCO) such as  $\text{In}_2\text{O}_3$ ,  $\text{ZnO}$ ,  $\text{SnO}_2$  and  $\text{In}_2\text{O}_3:\text{Sn}$  (ITO) and  $\text{In}_2\text{O}_3:\text{F}$  (IFO) because of their high optical transparency in the visible region, good electrical conductivity are important. These characteristics are required in various applications research fields dealing with transparent heating elements for air craft and car windows [1], photovoltaic devices [2], solar cell [3], gas sensors [4]. A variety of deposition techniques such as vacuum evaporation [5], sputtering [6], spray pyrolysis [7], sol-gel [8], etc. have been used. All of these methods have advantages and disadvantage, but spray pyrolysis has a noticeable advantage, it is a low-cost and non-vacuum technique for large area applications.  $\text{In}_2\text{O}_3$  transparent conducting thin films are n-type semiconductors with wide energy band gap equal to 3.6 eV. The structure of  $\text{In}_2\text{O}_3$  in its crystalline form is body centred cubic with lattice constant  $a=10.118 \text{ \AA}$ . Doping indium oxide with fluorine, zinc, tin etc. as donor impurities yields films with low sheet resistance [1]. This paper describes the results of our study in an attempt to correlate the electrical conduction with the optical and structural properties of prepared  $\text{In}_2\text{O}_3:\text{F}$  thin films.

### 2. Experimental Details

The chemical spray pyrolysis technique is one of the most commonly used techniques for preparation of transparent and conducting oxides owing to its simplicity, non-vacuum system of deposition and hence inexpensive method. The spray pyrolysis apparatus used in this work consists of a home made spraying unit, substrate holder with heater, and enclosure. The glass substrate is kept on a stainless steel (ss) plate. The heater is capable of heating the substrate up to a temperature of  $700^\circ\text{C}$ . The carrier gas used in all the experiments was air, which is supplied from an air compressor. The air produced by the compressor was first filtered and then connected to the glass spray-gun (atomizer) through a flow meter for controlling its flow. The custom glass spray gun having a nozzle diameter of 0.2 mm was positioned at a distance of 30cm above the substrate. The whole assembly is kept in an enclosure connected to an exhaust.

In this research,  $\text{In}_2\text{O}_3:\text{F}$  thin films were prepared by spraying a water solution containing indium chloride (0.2gr  $\text{InCl}_3$ ) and  $\text{NH}_4\text{F}$  used as dopant onto glass substrates heated at

different substrate temperatures. The structural, electrical, and optical properties of TCOs are strongly affected by the temperature of substrate.

Deposition of parameters conclude: distance between the spray nozzle and substrates 25cm, the carrier gas using filtered compressed air, the spray rate 19 lit/min, volume of solution is 40 ml. All the above mentioned parameters were kept constant and only the concentration of  $\text{NH}_4\text{F}$  (0-15wt%) and substrate temperature (400-600 °C) were changed.

In this work we first optimize the concentration of F wt% using electrical resistivity and optical transparency and secondly focused on the effect of substrate temperature on structural, electrical, optical properties of the samples with a constant fluorine concentration of 2wt%. X-ray diffraction (XRD) (Philips-pw-1830) was used to characterize the crystal structure of the films. Morphology of the films was examined by Cambridge scanning electron microscopy (SEM). The optical measurements of the  $\text{In}_2\text{O}_3:\text{F}$  thin films were carried out at room temperature using UV-Visible spectrophotometer (Cary 100 Scan Version). The electrical properties of thin films measured by Hall effect and Vander-Pauw set-up (RH 2010 PhysTech system).

### 3. Results and Discussion

Concentration of F in these films have been varied from 0-15wt%. As a result, the resistivity decreased quickly with increasing F concentration reaching a minimum of  $\rho=1.35 \times 10^{-3} \Omega\text{cm}$  for an F concentration of 1wt% which demonstrate a good ohmic contact for electrode applications. For higher dopant content, the resistivity increased (Table 1). The higher transmittance observed in the films for 2wt% of F doped. Since we were looking for a layer with both high transparent and good resistivity, we used figure of merit (FOM). Thus the optimized layer with 2wt% of F concentration was selected according to the most FOM [9].

The X-ray diffraction result of IFO films in various concentrations are shown that, films are polycrystalline and crystallize in a cubic structure with preferential orientation along (222) and (400). Note also that no characteristic peaks of impurity and dopant phases have been observed.

Substrate temperature is an important parameter for spray pyrolysis deposition. It is observed that at lower substrate temperature (less than 250 °C), the growth rate is controlled by activated processes. At higher substrate temperature (greater than 550 °C), the size of the droplet decreases appreciably due to the evaporation of water molecule, resulting in a homogeneous reaction, the reaction may be completed above the substrate, leading to powder formation. Hence very low and very high temperatures are not suitable for preparation of these TCOs. For investigation of temperature effect on the growth mode, we fixed the doping concentration at 2wt% F and studied the effect of the substrate temperature on the transparency. Figure shows the variation of substrate temperature of IFO films with change in transmission. Films deposited at substrate temperatures of 400 to 450 °C exhibited less transmission in visible region, while by increasing the substrate temperature we get better transparency (Fig. 1).

Table 1. The variation of electrical properties of IFO films as a function of dopant concentration deposited at 575 °C.

F wt%	R <sub>sh</sub> (Ω/□)	ρ(×10 <sup>-3</sup> Ω cm)	n(×10 <sup>20</sup> cm <sup>-3</sup> )	μ (cm <sup>2</sup> /V.s)	T% λ=550 nm	FOM (×10 <sup>-5</sup> )
0	5850	147	0.06	6.71	77	1.25
0.5	335	6.36	0.26	37.4	77	21.9
1	96.5	1.35	2.53	18.2	68.2	22.6
2	140	1.92	1.13	28.6	87.6	190
10	333	8.73	0.99	7.23	77	7.79
15	527	15.30	0.72	5.63	81	23.07

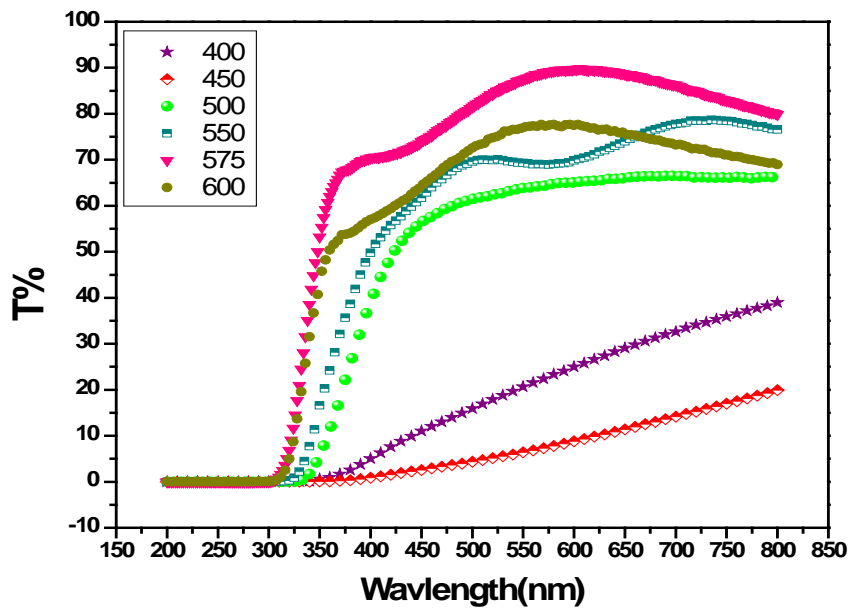


Fig. 1:Optical transmission of IFO films prepared at 2wt% F various substrate temperature

The XRD results (Fig.2) show that, films deposited at substrate temperature of 400 and 450 °C, in addition to (222), (400) peaks have (211), (411), (341), (440), (622) peaks with high intensity. The presence and intensity of peaks decreased with increasing substrate temperature; as a result crystallinity improves leading to well-transmission and resistivity.

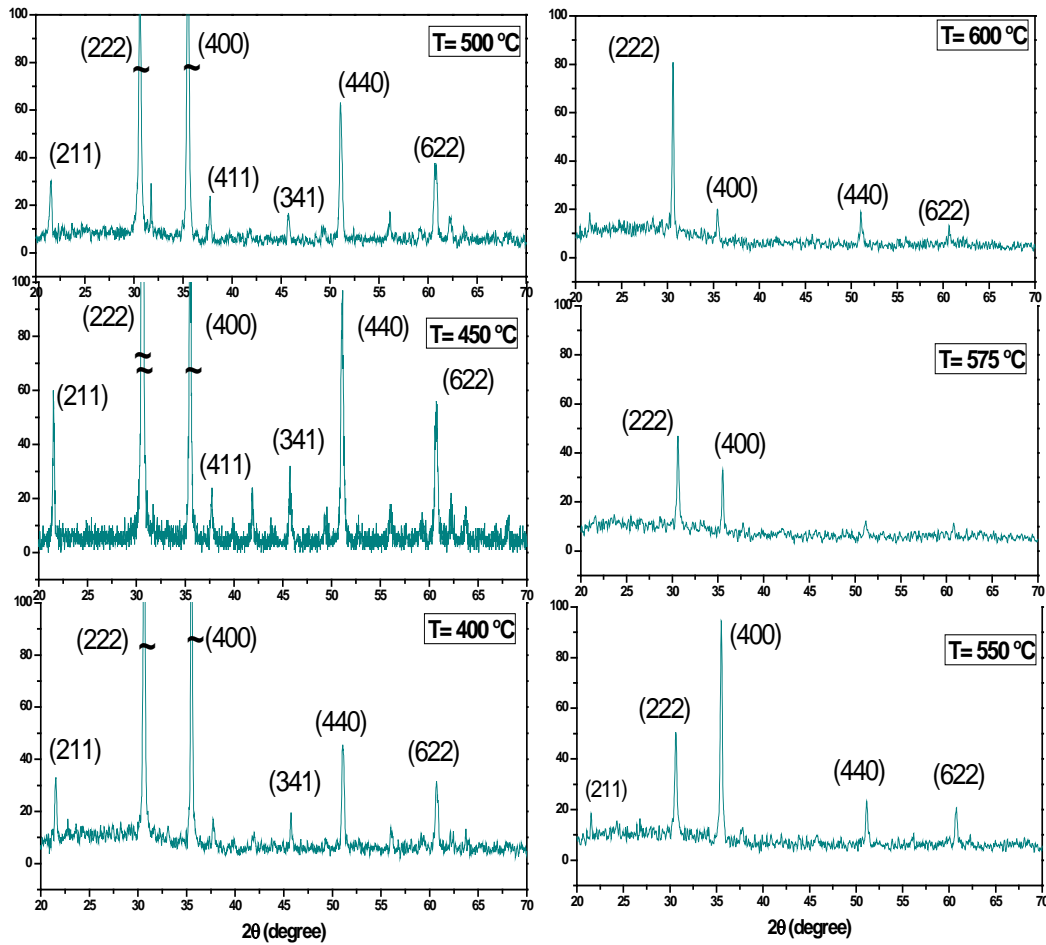


Fig. 2: XRD patterns of IFO films prepared at various substrate temperatures

The SEM results show that the size of crystals is in the range on nanometer. The size of particles changing with respect to deposition parameters. Fig. 3 shows that, the crystalline improved with increasing substrate temperature. Furthermore, the density of grain boundaries and dislocation therefore decreases, leading to the improvement of conductivity and transparency of IFO films.

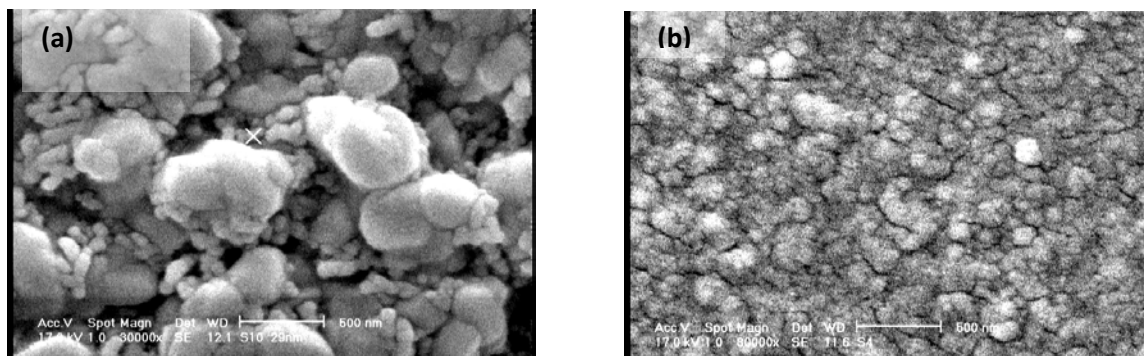


Fig.3 SEM images of IFO films prepared at different substrate temperature: a) 450°C and b) 575°C.

Subsequently the amount of indium powder also was investigated for the prepared films. Result show that the resistivity is decreased by increasing of indium powder but transparency is decreased. Besides, the thickness of the films is determined by PUMA software [10].

#### 4. Conclusions

In this research, fluorine doped indium oxide (IFO) nanostructure were prepared at different F concentration, substrate temperature and  $\text{InCl}_3$  concentration using spray pyrolysis technique. Then effects of above parameters on structural, electrical and optical properties of nanostructure thin films of IFO were investigated. The SEM results show that the size of crystals is in the range on nanometer. The size of particles changing with respect to deposition parameters. The presence and intensity of XRD peaks decreased with increasing substrate temperature; as a result crystallinity improves leading to well-transmission and resistivity. In conclusion, the optimum IFO films were prepared using 0.2 gr  $\text{InCl}_3$  with F concentration of 2wt% at substrate temperature of 575 ° C. With this condition sheet resistance was 140  $\Omega/\square$  and the optical transmission in visible region was 87.6%.

#### Acknowledgment

This work was supported by the department of research of the University of Guilan.

#### References

- [1] K.I. Chopra, S. Major, D.K. Pandya, *Thin Solid Films*, **102**, (1983), 1.
- [2] C.V.R. Vasant Kumar, A.A. Mansingh, *J. Appl. Phys.*, **65**, (1989), 1270.
- [3] J.A. Anna Selvan, A.E. Delahoy, S. Guo, Y. Li, A new light trapping TCO for nc-Si:H solar cells, *Solar Energy Mater. Solar Cells*, **90**, (2006), 3371–3376.
- [4] G. Korotcenkov, V. Brinzari, A. Cerneavschi, *Sensors and Actuators B*, **98**, (2004), 122–129.
- [5] S.M. Rozati, S. Mirzapour, M.G. Takwale, B.R. M arathe, V.G. Bhide, *Materials Chemistry and Physics*, **34**, (1993), 119.
- [6] S. Boycheva, A.K. Sytchkova, M.L. Grilli, A. Piegari, *Thin Solid Films*, **515**, (2007), 8469.
- [7] S. Golshahi, S.M. Rozati, R. Martins, E. Fortunato, *Thin Solid Films*, **518**, (2009), 1149-1152.
- [8] R.B.H. Tahar, T. Ban, Y. Ohya, Y. Takahashi, *J. Appl. Phys.*, **82**, (1997), 865.
- [9] G. Haacke, *J. Appl. Phys.*, **47** (1976) 4086.
- [10] E.J. Biring, I. Chambouleyron, J.M. Martinez, Estimation of the optical constants and the thickness of thin films using unconstrained optimization, *Journal of Computational Physics*, **155** (1999) 862-880.

## Research and development of dye-sensitized solar cells in the Center for Molecular Devices: from molecules to modules

Gerrit Boschloo<sup>1,\*</sup>, Anders Hagfeldt<sup>1</sup>, Håkan Rensmo<sup>1</sup>, Lars Kloo<sup>2</sup>, Licheng Sun<sup>2</sup>, Henrik Pettersson<sup>3</sup>

<sup>1</sup> Uppsala University, Uppsala, Sweden

<sup>2</sup> Royal Institute of Technology, Stockholm, Sweden

<sup>3</sup> Swerea IVF, Mölndal, Sweden

\* Corresponding author. Tel: +46 18 4713303, E-mail: gerrit.boschloo@fki.uu.se

**Abstract:** Dye-sensitized solar cells (DSCs) represent a relatively new photovoltaic technology with great potential: investment costs for initiating production are low and manufacturing costs below 0.5 US\$/W<sub>peak</sub> are predicted. Furthermore, DSC offers the possibility of various colors and attractive designs, such as semitransparent modules. Record solar cell efficiencies are 11% for DSCs containing liquid redox electrolyte and 6% for DSCs with solid hole conductors. Promising stability data suggesting more than 20 years lifetime has been achieved. This paper presents the Center for Molecular Devices (CMD) in Sweden, which has as its objective to investigate and develop DSCs. Using a multi-disciplinary approach, significant advances in the scientific understanding of DSCs have been made, such as the demonstration of the presence of an internal electric field at the semiconductor / dye / electrolyte interface. Furthermore, novel components, such as triphenylamine-based dyes and cobalt-based mediator have been successfully tested. Finally, a monolithic DSC module technology with good performance is presented.

**Keywords:** Dye-sensitized solar cell, PV modules.

### 1. Introduction

Dye-sensitized solar cells (DSCs) represent a relatively new photovoltaic technology with great potential.[1] Certified record solar cell efficiencies are 11% for DSCs containing liquid redox electrolyte and 6% for DSCs with solid hole conductors. It is believed that this technology has the potential to reach production costs as low as 0.5 US\$/W<sub>peak</sub>,[2] which would make solar electricity generation competitive with conventional (fossil fuel based) electricity generation. Module efficiencies of 10% and lifetimes of 15 year were assumed for this calculation. More recent calculations, based on actual DSC devices and current material costs, give a manufacturing cost of 2.5 Euro/W<sub>peak</sub>, which may decrease to less than 1 Euro/W<sub>peak</sub> taking the expected decrease in material cost into account.[3]

Dye-sensitized solar cells differ much from conventional solid state semiconductor based solar cells.[1] Dye molecules, rather than an inorganic semiconductor material, are responsible for light absorption. Furthermore, the functions of light absorption, electron transport and hole transport are separated into different materials. Electron transport takes place in a porous TiO<sub>2</sub> structure, while hole transport occurs in a liquid redox electrolyte.

In its standard form the DSC consists of the following components (see Figure 1a):

- The working electrode: a mesoporous film of TiO<sub>2</sub> nanoparticles (size ~20 nm) with a thickness of about 10 μm, on a fluorine-doped tin oxide (FTO) coated glass substrate. Dye-molecules are adsorbed at the surface of TiO<sub>2</sub>. The TiO<sub>2</sub> framework acts as electron acceptor and transport medium.

- A redox electrolyte: solution containing a suitable redox couple in a high concentration, as well as some additives that improve solar cell performance. The most common redox couple used in DSC is iodide / triiodide.
- A counter electrode: an electrode with good catalytic activity for electron transfer to the redox electrolyte. The most common counter electrode in DSCs is platinum-coated FTO-glass. This electrode has the advantage that it can be transparent, as a very low loading of Pt is needed.
- Sealing. Hermetic sealing is very important in order to obtain stable solar cells with good long term stability. The most common DSC sealing material is thermoplastic. A thermoplastic frame is used to connect the WE and CE together, which ensures a fixed separation between the two electrodes.

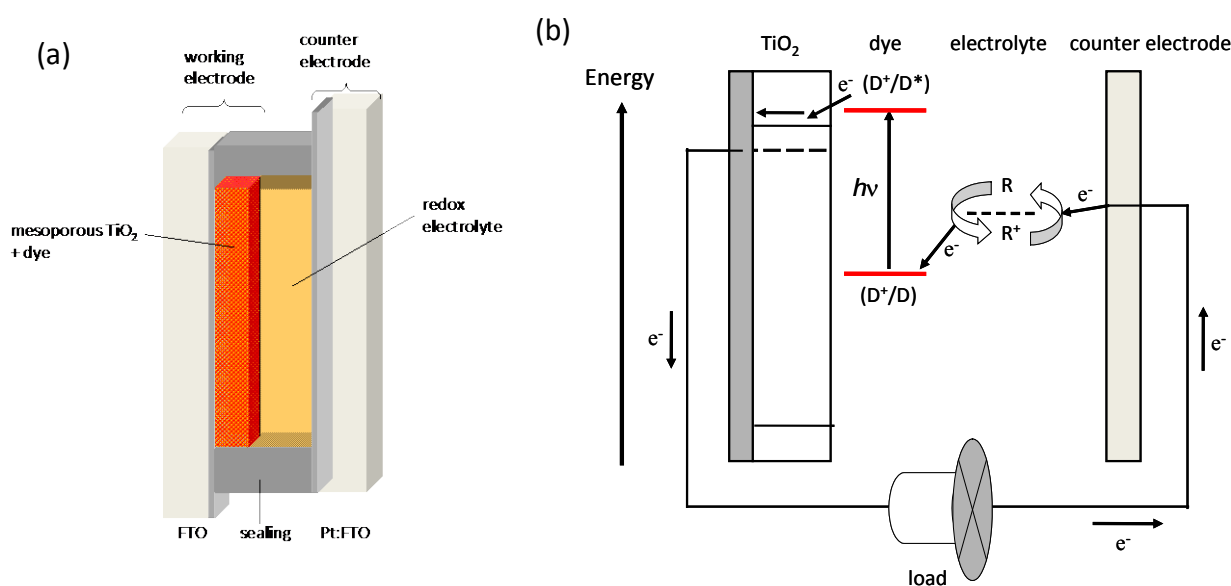


Figure 1. (a) Schematic structure of a dye-sensitized solar cell (sandwich design). FTO stands for fluorine-doped tin oxide-coated glass. (b) Energy scheme of a dye-sensitized solar cell. The arrows indicate electron transfer reactions.

The working mechanism of the dye-sensitized solar cell is displayed in Figure 1b. Light is absorbed by the dye molecules D resulting in excited dye molecules (D<sup>\*</sup>). Ultrafast electron injection takes place from the excited dye into the conduction band of TiO<sub>2</sub>. Regeneration of the oxidized dye by the redox mediator R. Electrons are collected at the conducting substrates and can perform electrical work in an external circuit. At the counter electrode, electrons reduce R<sup>+</sup>, the oxidized form of mediator.

Despite intense research in the field of dye-sensitized solar cells, many fundamental aspects are still unclear. The Center for Molecular Devices (CMD) in Sweden has as its objective to investigate and develop DSCs. Using a multi-disciplinary approach, significant advances in the scientific understanding of DSCs, development of low-cost DSC components, and DSC module manufacturing have been made, as will be discussed here in this paper.

## 2. Methodology

We refer to our research papers (ref. 4-17) for details on mesoporous  $\text{TiO}_2$  electrode preparation, dye synthesis, electrolyte preparation, solar cell assembly and solar cell characterization.

## 3. Results and Discussion

### 3.1. Design, synthesis and characterization of dye molecules for DSC

Research on dyes within CMD has been mainly focused on organic dyes with the general structure: donor - conjugated bridge - acceptor (D- $\pi$ -A). Upon excitation, electron density will be displaced from the electron rich donor moiety towards the electron withdrawing acceptor moiety. The acceptor moiety is also equipped with suitable binding groups for attachment of the molecules onto the  $\text{TiO}_2$  surface. The general structure of D- $\pi$ -A dyes favors electron injection into  $\text{TiO}_2$  upon excitation, while the remaining positive charge will be located on the donor part, positioned relatively far away from the  $\text{TiO}_2$  surface. This will decrease the rate for direct geminate recombination. A very suitable donor group for D- $\pi$ -A dyes is the triphenylamine (TPA) unit, while a suitable acceptor / binding unit is cyanoacrylic acid.

In 2005 the D5 dye was developed within CMD as the first in a series of D- $\pi$ -A dyes (see Figure 2a).[4] Although the absorption spectrum has a maximum at about 480 nm and does not extend significantly beyond 600 nm, promising solar cell efficiencies of 6% were obtained in combination with the iodide / triiodide electrolyte. Other interesting results obtained with D5 are its suitability in solid-state DSCs, and its capacity for hole conduction when it is adsorbed on  $\text{TiO}_2$  as a monolayer.[5]

Several modifications of the D5 base structure have been synthesized and tested. One of the most promising dyes developed within CMD to date is the D35 dye (see Figure 2). The most prominent alteration is the addition of two *o,p*-dibutoxyphenyl groups on the TPA unit. This provides the dye with suitable steric properties, making the dye very suited to be used in combination with cobalt-based redox electrolytes [6] or in solid-state DSC.

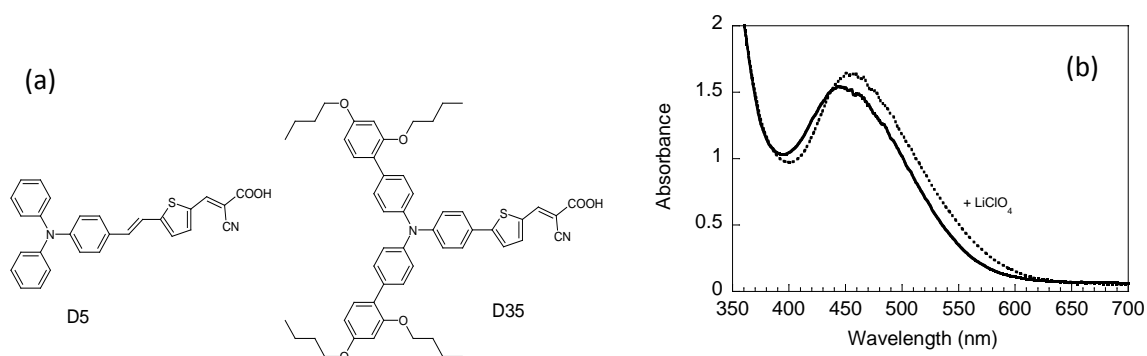


Figure 2. (a) Chemical structure of two efficient organic sensitizing dyes developed at CMD: D5 and D35. (b) UV-visible spectra of a D35-sensitized  $\text{TiO}_2$  film in air (drawn line) and in contact with  $\text{LiClO}_4$  in ethanol (dotted line).

### 3.2. Redox electrolytes and hole conductors

The standard redox electrolyte for DSC comprises of the iodide / triiodide ( $I^-/I_3^-$ ) redox couple in an organic solvent. It is used in best performing DSCs to date, both in terms of efficiency and stability. It has good solubility, absorbs not too much visible light, it has a suitable redox potential, and provides rapid dye regeneration. But what  $I^-/I_3^-$  makes particularly successful is the very slow recombination kinetics between electrons in  $TiO_2$  and the oxidized part of the redox couple, triiodide. A serious disadvantage of this redox mediator is that a significant part of the potential is lost due to intermediate reactions.[7] After electron injection, the oxidized dye ( $D^+$ ) is reduced by iodide in the following way:



The diiodide radical ( $I_2^{\cdot-}$ ) is produced as an intermediate in this process (reaction 2). We estimate that the disproportionation reaction 3 corresponds to an internal loss of potential of as much as 400 mV. We believe that it is this internal loss that is largely responsible for the observed ‘stagnation’ in record efficiencies obtained for DSCs.

In order to obtain efficiencies larger than 12 %, it may be necessary to use one-electron redox couples or hole conductors instead of  $I^-/I_3^-$ , so that the losses due to internal conversion are avoided. Unfortunately, the use of one-electron mediators in DSC nearly always leads to strongly increased recombination between electrons in  $TiO_2$  and the oxidized part of the redox couple, which seriously limits the solar cell efficiency. Recently, however, we obtained a breakthrough with cobalt polypyridine-based mediators in combination with D35 dye.[6] Careful matching of the steric bulk of the mediator and the dye molecules minimizes the recombination between electrons in  $TiO_2$  and Co(III) species in the electrolyte and avoids mass transport limitations of the redox mediator. The organic sensitizer D35, equipped with bulky alkoxy groups, efficiently suppresses recombination, allowing the use of cobalt redox mediators with relatively small steric bulk. Its high extinction coefficient allows for making DSCs with thin  $TiO_2$  films, which is favorable with respect to charge recombination and mass transport of redox mediator in the porous structure. The best efficiency obtained for a DSC sensitized with D35 and employing a  $[Co(bpy)_3]^{3+/2+}$ -based electrolyte was 6.7 % at full sunlight ( $1000 \text{ W m}^{-2}$  AM1.5G illumination), which is more than a doubling of previously published record efficiencies using similar Co-based mediators. Notably, similar efficiencies with the D35 dye are obtained with  $I^-/I_3^-$  as a redox couple.

The use of a solid-state hole conductor in DSCs is very attractive, but also very challenging. Besides the above mentioned problem of enhanced recombination, an additional problem is to fill the pores of the dye-modified mesoporous  $TiO_2$  electrodes completely with the solid hole conductor. A possible solution investigated within CMD is melting infiltration of the hole conductor into the pores of the dye-sensitized  $TiO_2$  electrode.[8] The rather high temperatures required for melting is damaging for the organic dye molecules and so far is limiting the efficiencies of the resulting solar cells.

The most well-tested hole conductor in solid-state DSCs is 2,2',7,7'-tetrakis(*N,N*-di-*p*-methoxyphenylamine)-9,9'-spirobifluorene (spiro-MeOTAD). With the help of photoinduced absorption spectroscopy it was shown that in principle all dye molecules appeared to be in contact with the hole conductor for a 6  $\mu\text{m}$  thick  $TiO_2$  film, even though pores are not filled to

100%.[9] A compelling result obtained within CMD research is that some perylene-based dyes performed much better in solid-state DSCs using spiro-MeOTAD than in standard iodide / triiodide electrolyte-based DSCs.[10] This can be attributed to the much faster regeneration kinetics observed in solid-state DSCs.

### **3.3. Advanced characterization of DSC components and complete devices**

The dye-sensitized solar cell is a complex system with many interactions between its individual components. We have performed detailed characterization of dye-sensitized TiO<sub>2</sub> films using advanced techniques such as X-ray photoelectron spectroscopy [11] and scanning tunneling microscopy,[12] giving valuable information of the binding morphology of the dyes and energy levels.

Investigations on complete DSC devices have been particularly fruitful, as the interactions between different components can be studied. For instance, we have studied the effect of the DSC electrolyte additive 4-*tert* butylpyridine in detail and found that it was responsible for a band edge shift of the TiO<sub>2</sub> as well as for a reduction in the electron recombination rate constant.[13] More recently, we found that the additives guanidinium thiocyanate and *N*-methylbenzimidazole have a synergistic effect on the solar cell performance of DSCs with ionic liquid ( $\Gamma/I_3^-$ ) electrolytes.[14]

Recently, we discovered that the Stark effect plays an important role in the transient absorption spectroscopy of DSCs.[15] The occurrence of the Stark effects implies that the electric field across the adsorbed dye molecules changes. The effect of electric fields can be even observed under steady-state conditions. Figure 2b shows the absorption spectrum of D35 adsorbed on mesoporous TiO<sub>2</sub>. In the presence of lithium ions, a significant red shift of the spectrum is observed. This shift can be attributed to the Li<sup>+</sup> ions that adsorb onto the TiO<sub>2</sub> surface, thus changing its surface charge. This in turn affects the electric field across the dye monolayer, giving rise to a Stark shift. The occurrence of this shift implies that the dyes are, at least partially, located within the Helmholtz double layer at the metal oxides / electrolyte interface. The effect of the electric field is that the donor-acceptor character of the dye is enhanced, resulting in a red-shift of the absorption spectrum.

### **3.4. Monolithic DSC Modules**

Screen printing as is low cost, scalable method to prepare thin films. Within CMD, a monolithic design is used in the development of DSC modules, see Figure 3a.[16, 17] The monolithic design has several advantages: it can give significant cost reduction as only one FTO-coated glass plate is needed, compared to two in other (sandwich) designs. FTO substrates are responsible for up to 25% of the total manufacturing costs in a sandwich design DSC. Furthermore, problems with alignment and glass bending encountered for large sandwich-design modules are avoided.

In Figure 3b some typical photocurrent density - voltage (*J-V*) curves of a 13.5 cm<sup>2</sup> sized DSC module are shown. The module consists of 4 cells connected in parallel. The solar to electrical power conversion efficiency depends on incident light intensity and ranges from 4.0% (1000 W m<sup>-2</sup>) to 6.6% (56 W m<sup>-2</sup>). This dependency is caused by internal resistance losses, of which the origin is currently under investigation. Stability tests as well as outdoor tests are ongoing. When the components in the DSC modules are well chosen (dye, electrolyte), the modules are completely stable after 2000 h in an accelerated aging test (1000 W m<sup>-2</sup> simulated sunlight, 50°C), with an efficiency of 5.0% at 200 W m<sup>-2</sup> illumination.[17] Significant degradation is, however, observed under storage in the dark at 80°C. These tests

were performed with the ruthenium-based complex K77 as the sensitizer and an iodide/triiodide electrolyte with 3-methoxypropionitrile as solvent.

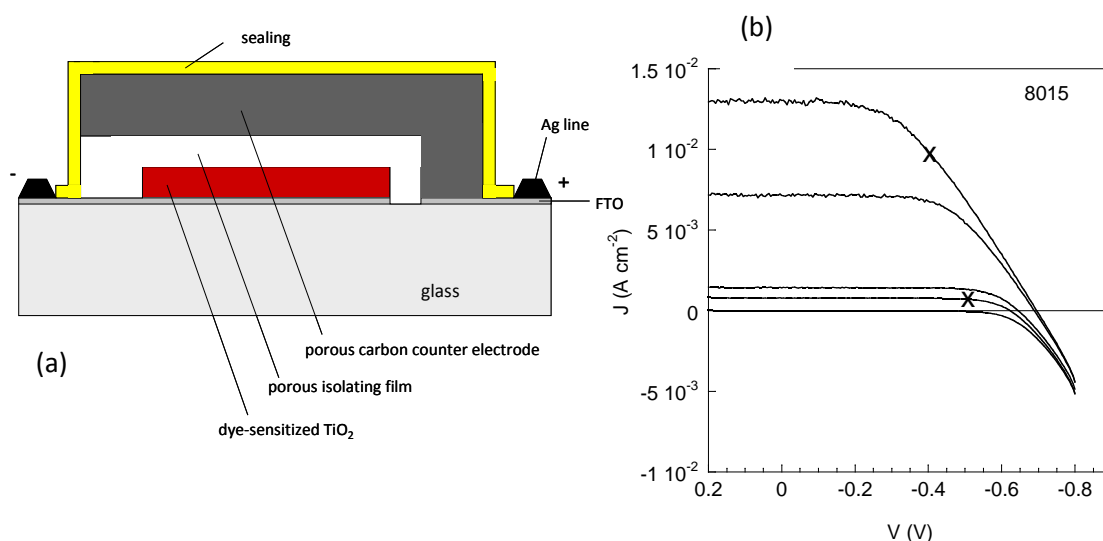


Figure 3. (a) Schematic structure of the monolithic design of the dye-sensitized solar cell. (b) J-V characteristics of a monolithic DSC module (active area: 13.5 cm<sup>2</sup>). Light intensities: 1000; 534; 105; 56 and 0 W m<sup>-2</sup>.

#### 4. Conclusions

The work performed at the Center for Molecular Devices in Sweden has significantly contributed to the research field of dye-sensitized solar cells. CMD was among the first to develop organic sensitizer dyes equipped with triphenylamine donor groups, which are currently among the most efficient sensitizers in DSC. Cobalt-based redox couples were shown to be viable alternatives to the standard iodide / triiodide system, provided that a dye with suitable steric properties is used. Detailed in-situ studies of DSCs have revealed the occurrence of a Stark-effect, where an internal electric field changes the absorption of the dye. This effect can be used to provide fundamental understanding of the DSC. In development work, CMD has shown that monolithic DSC is a viable PV technology, although further development and testing is required.

#### Acknowledgement

We thank the Swedish Energy Agency, the Swedish Research Council, Vinnova, BASF SE and the Knut and Alice Wallenberg foundation for financial support.

#### References

- [1] A. Hagfeldt, G. Boschloo, L. Sun, L. Kloo, H. Pettersson, Chem. Rev. 110 (2010) 6595.
- [2] G. Smestad, C. Bignozzi, R. Argazzi, Sol. Energy Mater. Sol. Cells 33 (1994) 253.
- [3] J. M. Kroon, N. J. Bakker, H. J. P. Smit, P. Liska, K. R. Thampi, P. Wang, S. M. Zakeeruddin, M. Grätzel, A. Hinsch, S. Hore, U. Würfel, R. Sastrawan, J. R. Durrant, E. Palomares, H. Pettersson, T. Gruszecki, J. Walter, K. Skupien, G. E. Tulloch, Prog. Photovolt.: Res. Appl. 15 (2007) 1.
- [4] D. P. Hagberg, T. Edvinsson, T. Marinado, G. Boschloo, A. Hagfeldt, L. Sun, Chem. Commun. (2006) 2245.

- 
- [5] G. Boschloo, T. Marinado, K. Nonomura, T. Edvinsson, A. G. Agrios, D. P. Hagberg, L. Sun, M. Quintana, C. S. Karthikeyan, M. Thelakkat, A. Hagfeldt, *Thin Solid Films* 516 (2008) 7214–7217.
- [6] S. M. Feldt, E. A. Gibson, E. Gabrielsson, L. Sun, G. Boschloo, A. Hagfeldt, *J. Am. Chem. Soc.* 132 (2010) 16714.
- [7] G. Boschloo, A. Hagfeldt, *Acc. Chem. Res.* 42 (2009) 1819.
- [8] K. Fredin, E. M. J. Johansson, T. Blom, M. Hedlund, S. Plogmaker, H. Siegbahn, K. Leifer, H. Rensmo, *Synth. Metals* 159 (2009) 166.
- [9] U. B. Cappel, E. A. Gibson, A. Hagfeldt, G. Boschloo, *J. Phys. Chem. C* 113 (2009) 6275.
- [10] U. B. Cappel, M. H. Karlsson, N. G. Pschirer, F. Eickemeyer, J. Schöneboom, P. Erk, G. Boschloo, A. Hagfeldt, *J. Phys. Chem. C* 113 (2009) 14595.
- [11] M. Hahlin, E. M. J. Johansson, S. Plogmaker, M. Odellius, D. P. Hagberg, L. Sun, H. Siegbahn, H. Rensmo, *Phys. Chem. Chem. Phys.* 12 1507.
- [12] M. Zuleta, S. Yu, S. Ahmadi, G. Boschloo, M. Göthelid, A. Hagfeldt, *Langmuir* 26 (2010) 13236.
- [13] G. Boschloo, L. Häggman, A. Hagfeldt, *J. Phys. Chem. B* 110 (2006) 13144.
- [14] Z. Yu, M. Gorlov, G. Boschloo, L. Kloo, *J. Phys. Chem. C* ASAP.
- [15] U. B. Cappel, S. M. Feldt, J. Schoneboom, A. Hagfeldt, G. Boschloo, *J. Am. Chem. Soc.* 132 (2010) 9096.
- [16] H. Pettersson, T. Gruszecki, R. Bernhard, L. Häggman, M. Gorlov, G. Boschloo, T. Edvinsson, L. Kloo, A. Hagfeldt, *Prog. Photovolt: Res. Appl.* 15 (2007) 113–121.
- [17] H. Pettersson, T. Gruszecki, C. Schnetz, M. Streit, Y. Xu, L. Sun, M. Gorlov, L. Kloo, G. Boschloo, L. Häggman, A. Hagfeldt, *Prog. Photovolt.: Res. Appl.* 18 (2010) 340.

## Studies of the anionic micelles effect on photogalvanic cells for solar energy conversion and storage in Sodium lauryl sulphate-Safranin-D-Xylose system

Prem Prakash Solanki<sup>1\*</sup>, K M Gangotri<sup>2</sup>

<sup>1</sup> Department of Chemistry, Faculty of Science, Banaras Hindu University, Varanasi-221005, INDIA

<sup>2</sup> Solar Energy Laboratory, Department of Chemistry, Jai Narain Vyas University, Jodhpur-342005, INDIA

\* Corresponding author. Tel: +542 6702469, Fax: +291 2614162, E-mail: ppsolankibhu@gmail.com

**Abstract:** The Sodium lauryl sulphate (NaLS) has been used as anionic micelle species, Safranin as photosensitizer and D-Xylose as electron donor for the enhancement of the electrical output and performance (storage capacity) of the photogalvanic cell with reduce the cost of construction for commercial viability. The photopotential and photocurrent generated were 893.0 mV and 207.0  $\mu$ A, respectively. The observed conversion efficiency and the fill factor were 0.6800% and 0.3233, respectively at the power point of the cell. The photogalvanic cell can be used for 98.0 minutes in the dark. The effect of different parameters like concentration of micelles; photosensitizer and electron donor, variation of pH, light intensity and diffusion path length were observed. A current – voltage (i-V) characteristics of the photogalvanic cell was studied experimentally and a mechanism has also been proposed for the generation of the photocurrent. All observed results of the system were lower in absence of the micelles species.

**Keywords:** Photogalvanic cell, Micelles effect, Safranin, D-Xylose, Conversion efficiency

### Nomenclature

$i_{eq}$ photocurrent at equilibrium..... $\mu$ A	$M$ Concentration in molarity.....mol/L
$i_{max}$ maximum photocurrent..... $\mu$ A	$t_{1/2}$ performance (storage capacity) .....min
$i_{pp}$ photocurrent at power point..... $\mu$ A	$V_{oc}$ open circuit voltage..... mV
$i_{sc}$ short circuit current..... $\mu$ A	$V_{pp}$ photopotential at power point ..... mV
$pp$ power point..... $\mu$ W	$\eta$ Fill fact

### 1. Introduction

The flow of current between two unsymmetrical illuminated metal electrodes in sunlight was first observed by Becquerel<sup>1</sup> in 1839 and photogalvanic effect was first reported by Rideal and Williams<sup>2</sup> in 1925 but, it was systematically investigated by Rabinowitch<sup>3</sup> for iron–thionine system.

The photogalvanic and photovoltaic effects with anodized zirconium and niobium electrodes were observed by Graven et al.<sup>4</sup> while the photogalvanic effect with semiconductor anode was reported by Hall et al.<sup>5</sup>.

Electron transfer via organic dye molecule and photo-induced electron transfer between micelle and thionine dye through a charge transfer interaction have observed by Alfredo et al.<sup>6</sup> and Mukhopadhyay and Bhowmik<sup>7</sup>.

Bisquert et al.<sup>8</sup> have reported the physical–chemical principle of dye–sensitized solar cells, and Mayer<sup>9</sup> has presented the molecular approaches to solar energy conversion with coordination compounds.

Ameta et al.<sup>10</sup> Khamesara et al.<sup>11</sup> Pramila and Gangotri<sup>12</sup>, Gangotri and Gangotri<sup>13</sup>, and Genwa and genwa<sup>14</sup> have used micellar species with different photosensitizer and reductant in photogalvanic system for solar energy conversion and storage.

Jana and Bhowmik<sup>15</sup>, Gangotri and Lal<sup>16</sup> and Lal<sup>17</sup> have used mixed dyes while Dube<sup>18</sup> and Gangotri and Indora<sup>19</sup> have used mixed reductant with different photosensitizer in the photogalvanic systems.

Recently Genwa et al.<sup>20</sup> Gangotri and Gangotri<sup>21</sup>, Yadav and Lal<sup>22</sup>, Gangotri and Bhimwal<sup>23</sup>, Gangotri et al.<sup>24</sup> and Gangotri and Solanki<sup>25</sup> have developed some intrested photogalvanic cells with reasonable electrical output for solar energy conversion and storage.

They have used different photosensitizes, reductant and surfactants in photogalvanic cells but no attention has been paid to use Sodium lauryl sulphate-Safranin-D-Xylose system to enhance the electrical output and storage capacity of the cell. Our study reveals that a system of Sodium lauryl sulphate-Safranin-D-Xylose gives higher electrical output with better storage capacity, in addition, the cell is cost effective which makes it suitable for commercialization in near future, therefore, the present work was undertaken.

## 2. Methodology

All the solutions were prepared in doubly distilled water and the stock solutions of all the chemicals were prepared by direct weighing and were kept in coloured container to protect them from light. A mixture of known amounts of solution of Safranin, D-Xylose, Sodium lauryl sulphate and Sodium hydroxide were taken in an H-shaped glass tube. The total volume of the mixture was always kept at 25.0 mL with make up by doubly distilled water. A platinum electrode (1.0 X 1.0 cm<sup>2</sup>) was immersed in one limb of the H-tube having a window and a saturated calomel electrode was immersed in the other limb. The terminals of the electrodes were connected to a digital pH meter (Systronics -335) and a microammeter as shown in Fig. 1.

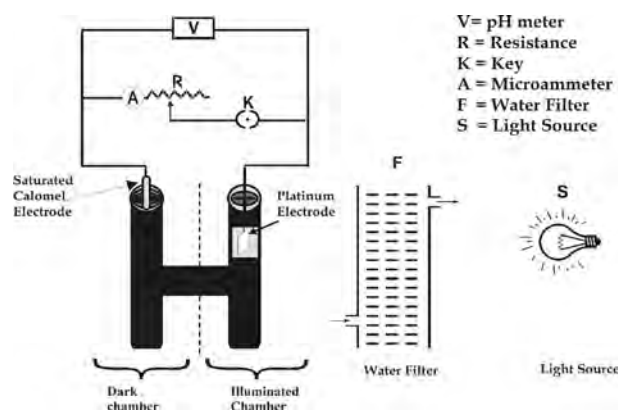


Fig.1. Experimental set up of photogalvanic cell

The whole system was first placed in the dark till a stable potential was obtained. Then, the limb having platinum electrode (whole platinum electrode area) was exposed to a 200 W tungsten bulb (Sylvania) while other limb having the saturated calomel electrode was kept in dark. A water filter was used to avoid thermal radiations. On illumination, the photochemical bleaching of photosensitizer was studied potentiometrically. The current-voltage (i-V) characteristics of the cell were studied by using an external load with the help of a carbon pot (log 470 K) connected in the circuit.

### 3. Results and discussions

#### 3.1. Effect of variation of photosensitizer and reductant concentration

The electrical output of the cell was affected by variation of photosensitizer (Safranin) and reductant (D-Xylose) concentration. The results are summarized in Table 1. It was observed that on increasing the concentration of safranin, electrical parameters photopotential ( $\Delta V$ ) and photocurrent ( $i_{sc}$ ) increases, which reaches a maximum value at a concentration  $4.60 \times 10^{-5}$  M, above which both parameters decrease. A lower concentration of safranin ( $[Safranin] < 4.60 \times 10^{-5}$  M) resulted into a decrease in electrical parameters because limited number of photosensitizer molecule were available for the excitation and consecutive donation of the electrons to the platinum electrode whereas a higher concentration of safranin ( $[Safranin] > 4.60 \times 10^{-5}$  M) again resulted into a decrease into electrical output as the intensity of light reaching the photosensitizer molecule near the electrode decreased due to absorption of the major portion of the light by photosensitizer molecules present in the path.

Table 1: Effect of variation of various parameters concentrations on the electrical output

Parameters	Photopotential(mV)	Photocurrent ( $\mu A$ )	Power ( $\mu W$ )
[NaLS] X $10^3$			
5.56	791.0	170.0	134.47
5.60	827.0	189.0	156.30
5.64	893.0	207.0	184.85
5.68	837.0	186.0	155.68
6.72	796.0	164.0	130.54
[Safranin]X $10^5$ M			
4.48	803.0	177.0	142.13
4.54	843.0	192.0	161.86
4.60	893.0	207.0	184.85
4.66	837.0	189.0	158.19
4.72	800.0	169.0	135.20
[D-Xylose]X $10^3$ M			
1.34	767.0	161.0	123.48
1.38	817.0	185.0	151.15
1.42	893.0	207.0	184.85
1.46	820.0	180.0	147.60
1.50	777.0	157.0	121.98
pH			
12.66	817.0	179.0	146.24
12.68	849.0	195.0	165.55
12.70	893.0	207.0	184.85
12.72	840.0	192.0	161.28
12.74	812.0	176.0	142.91

A similar result was observed for variation of the concentration of reductant. A lower concentration of reducing agent ( $[D-Xylose] < 1.42 \times 10^{-3}$  M) resulted into a fall in electrical output because fewer reducing agent molecule were available for electron donation to the photosensitizer molecules whereas a higher concentration of reducing agent ( $[D-Xylose] > 1.42 \times 10^{-3}$  M) again resulted in a fall in a electrical output because the larger number of reducing agent molecule hinder the photosensitizer molecule from reaching the electrode in the desired time limit.

### 3.2. Effect of variation of micelles concentration

The electrical output of the cell was found to increase on increasing the concentration of NaLS, reaching a maximum value at the concentration  $5.64 \times 10^{-3}$  M, and then, further increase in their concentration a decrease in electrical output of the cell was observed. The observed results are summarized in Table 1

It was observed that maximum electrical output obtain from the cell around their critical micelle concentration (CMC) of the surfactant. It indicates the presence of the some charge transfer interaction between the dye-surfactant and the photoejection of electron from dye-surfactant depends on the charge on micelle. The surfactant has not only solublized the dye molecules to a maximum extent and their cmc value but have stabilizes also the system. In present work, the photogalvanic cell containing micelles system was compared with the cell containing photosensitizer and reductant sysem only (without micelles). The results are summerized in the Table 2.

Table 2: A comparative study of electrical parameters of the photogalvanic systems (With & without micelles)

S. No.	Electrical parameters	Observed Values	
		With Micelles <sup>1</sup>	Without micelles <sup>2</sup>
1.	Open circuit potential ( $V_{OC}$ )	1057.0 mV	917.0 mV
2.	Short circuit current ( $i_{sc}$ )	207.0 $\mu$ A	167.0 $\mu$ A
3.	Photopotential ( $\Delta V$ )	893.0 mV	743.0 mV
4.	Maximum photocurrent ( $i_{max}$ )	337.0 $\mu$ A	247.0 $\mu$ A
5.	Charging time	110.0 min.	150.0 min.
6.	Rate of fall in photopotential	15.26mV min. <sup>-1</sup>	15.20mV min. <sup>-1</sup>
7.	Rate of initial generation of photocurrent	19.92 $\mu$ A min. <sup>-1</sup>	16.26 $\mu$ A min. <sup>-1</sup>
8.	Power at power point (pp)	70.74 $\mu$ A	54.54 $\mu$ A
9.	Fill factor	0.3233	0.2478
10.	Conversion efficiency	0.6800 %	0.4426 %
11.	Performance of the cell, $t_{1/2}$	98.0 min.	87.0 min.

### 3.3. Effect of variation of pH

It was observed that there is an increase in the electrical output of the cell with increase in pH values and maximum value reaches at a particular pH value (pH=12.70). On further increasing in the pH value, a decrease in the electrical output of the cell was observed. The results are summarized in the Table 1

It is quite interesting to observe that the pH at the optimum condition for the reductant has a relation with its pKa value, i.e. the desired pH value should be slightly higher then their pKa value (pH > pKa), this may be due to the availability of the reductant in an anionic form, which is a better electron donor then its unionized form.

<sup>1</sup> [NaLS] =  $5.64 \times 10^{-3}$  M, [Safranin] =  $4.60 \times 10^{-5}$  M; [D-Xylose] =  $1.42 \times 10^{-3}$  M; pH = 12.70; Light intensity =  $10.4 \text{ mW cm}^{-2}$ ; Temperature = 303 K

<sup>2</sup>; [Safranin] =  $4.32 \times 10^{-5}$  M; [D-Xylose] =  $1.40 \times 10^{-3}$  M; pH = 12.92; Light intensity =  $10.4 \text{ mW cm}^{-2}$ ; Temperature = 303 K

### 3.4. Effect of diffusion path length

The effect of variation of diffusion path length on the electrical output and initial rate of generation of different photocurrent of the cell was studied by using H-shaped cell of different dimensions. The results are summarized in Table 3.

Table 3: Effect of diffusion path length

Diffusion path length $D_L$ (mm)	Maximum photocurrent $i_{max}$ ( $\mu A$ )	Equilibrium photocurrent $i_{eq}$ ( $\mu A$ )	Rate of initial generation of current ( $\mu A \text{ min.}^{-1}$ )
35.0	329.0	213.0	17.25
40.0	333.0	210.0	18.82
45.0	337.0	207.0	19.12
50.0	340.0	205.0	19.92
55.0	342.0	202.0	20.24

It was observed that in first few minutes of illumination there was a sharp increase in photocurrent and there was a gradual decrease to a stable value of photocurrent. This photocurrent at equilibrium state is known as equilibrium photocurrent ( $i_{eq}$ ). This kind of photocurrent behaviour is due to an initial rapid reaction followed by a slow rate-determining step at later stage. On the basis of effect of diffusion path length on the current parameters, it may be concluded that the leuco or semi reduced form of dyes and dyes itself are the main electroactive species at the illuminated and the dark electrodes, respectively. However, the reducing agent and their oxidized products behave as the electron carriers in the cell diffusing through the path.

### 3.5. Current-voltage (*i-V*) characteristics of the cell

The open circuit voltage ( $V_{oc}$ ) and short circuit current ( $i_{sc}$ ) of the cell were measured with the help of a digital pH meter (keeping the circuit open) and with a micrometer (keeping the circuit closed), respectively. The potential and current values in between these two extreme values ( $V_{oc}$  and  $i_{sc}$ ) were recorded with the help of a carbon pot (log 470K) that was in the circuit of the microammeter and through which an external load was applied. The current voltage (*i-V*) characteristic of the cell is shown in Fig. 2.

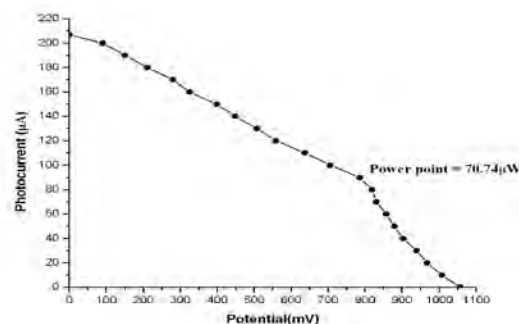


Fig. 2. Current-voltage (*i-V*) curve of the photogalvanic cell

It was observed that *i-V* curve for the cell deviated from their regular rectangular shape. A point in the *i-V* curve, known as power point (pp), was determined where the product of potential and current was maximum. With the help of the curve; fill factor ( $\eta$ ) value 0.3233 was calculated using the following formula:

$$\text{Fill factor } (\eta) = \frac{V_{pp} \times i_{pp}}{V_{oc} \times i_{sc}} \quad (1)$$

Where  $V_{pp}$  and  $i_{pp}$  represent the value of potential and the current at the power point, respectively, and  $V_{oc}$  and  $i_{sc}$  represents open circuit voltage and short circuit current, respectively.

The conversion efficiency of cell was determined with help of photocurrent and photopotential values at power point (pp) and the power of incident radiation (light intensity  $10.4 \text{ mW cm}^{-2}$  which is measured by Solarimeter, CEL model SM 203 ), and it was 0.6800 % obtained by using the following formula:

$$\text{Conversion efficiency} = \frac{V_{pp} \times i_{pp}}{10.4 \text{ mW cm}^{-2} \times \text{Electrode area (cm}^2)} \times 100\% \quad (2)$$

### 3.6. Performance of the cell

The performance of the cell was studied by applying the desired external load ie resistance (carbon pot log 470 K) used as rheostate to vary the resistance, necessary to have the potential and current corresponding to the power point, after removing the light source of illumination till the output (power) was reduced to half its value (power =  $70.74 \mu\text{W}$ ) at the power point in the dark. The performance was determined in terms of  $t_{1/2}$  and it was observed that the cell can be used in the dark for 98.0 minutes, which directly indicates the storage capacity of the photogalvanic cell. The observed results are graphically shown in Fig.3.

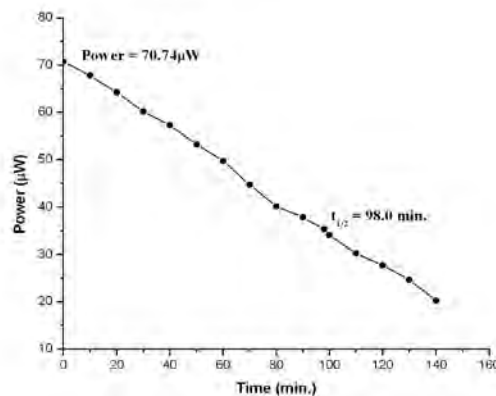


Fig. 3 Performance of the cell

## 4. Mechanism

On the basis of above observations, a tentative mechanism has been proposed for the generation of photocurrent in the cell as follows:

### In illuminated chamber



At platinum electrode



### ***In dark chamber***

At counter (SCE) electrode



Where safranin\* and D-xylose<sup>+</sup> are excited form of dye and oxidized form of reductant, respectively.

## **5. Conclusions**

On the basis of the observed results of the photogalvanic cell containing NaLS, safranin and D-xylose system, we have observed that the micelles have not only enhanced the conversion efficiency but the performance of the cell also. Exhaustive efforts still have the scope to enhance the electrical output as well as performance of the photogalvanic cells along with reduction in their cost to make commercial viability.

## **References**

- [1] K. Becquerel, on electric effects under the influence of solar radiation, C. R. Acad. Sci., 9, 1839, 561
- [2] E. K. Rideal, and E. G. Williams, The action of light on the ferrous iodine iodide equilibrium, J. Chem. Soc., 127, 1925, 258-269
- [3] E. Rabinowitch, The photogalvanic effect I: The photochemical properties of the thionine-iron system. J. Chem. Phys., 8, 1940, 551-559
- [4] Wendell M. Graven, Robert E. Salomon, and George B. Adams, Photogalvanic and photovoltaic effects with anodized zirconium and niobium electrodes, At. Energy Comm. TID-6514, 1960, 45-45
- [5] D. E. Hall, William D. K. Clark, J. A. Eckert, N. N. Lichtin and P. D. Wildes, A photogalvanic cell with semiconductor anode, Ame. Ceramic. Soc. Bull., 56(4), 1977, 408
- [6] O. Alfredo, P. Georgina and P. J. Sebasteian, Electron transfer via organic dye for solar energy conversion, Solar Energy Materials & Solar Cells, 59, 1990, 137-143
- [7] M. Mukhopadhyay and B. B. Bhowmik, Kinetics of photoinduced electron transfer in a photoelectrochemical cell consisting of thiazine dyes and Triton X-100 surfactant, J. Photochem. Photobiol. A: Chem., 69, 1992, 223-227
- [8] J. Bisquert, D. Cahen, G. Hodes, S. Riihle and A. Zaban, Physical chemical principles of photovoltaic conversion with nanoparticles, mesoporous dye-sensitized solar cells, J. physical chemistry B, 108, 2004, 8106-8118
- [9] G. J. Meyer, Molecular approaches to solar energy conversion with coordination compounds anchored to semiconductor surfaces, Inorganic Chemistry, 44, 2005, 6852-6864

- [10] S. C. Ameta, S. Khamesra, M. Bala and K. M. Gangotri, Use of micelles in photogalvanic cell for solar energy conversion and storage, *Phill. J Sc.*, 119(4) 1990, 371-373
- [11] S. Khamesra, S. Lodha, N. K. Jain and S. C. Ameta, Use of micelles in photogalvanic cell for solar energy conversion and storage: azur C-glucose system, *Polish Journal of Chemistry*, 65(2-3), 1991, 473-448
- [12] S. Pramila and K. M. Gangotri, Use of anionic micelles in photogalvanic cells for solar energy conversion and storage: Dioctylsulfosuccinate–Mannitol–Safranin system, *Energy Sources, Part A.*, 29, 2007, 1253-1257
- [13] K. M. Gangotri and P. Gangotri, Studies of the micellar effect on photogalvanics: Solar energy conversion and storage–EDTA–Safranin O–Tween-80 system, *Energy & Fuels*, 23, 2009, 2767-2772
- [14] K. R. Genwa and Mahaveer, Photogalvanic cell: A new approach for green and sustainable chemistry, *Solar Energy Mat. & Solar Cells*, 92(5) 2008, 522-529
- [15] A. K. Jana and B. B. Bhowmik, Enhancement in power output of solar cell consisting of mixed dye, *J. Photochem. and Photobio. A*, 110, 1997, 41-46
- [16] K. M. Gangotri and C. Lal, Studies in photogalvanic effect and mixed dye system: EDTA–Methylene blue–Toluidine blue system, *Int. J. Energy Res.*, 24, 2000, 365-371
- [17] C. Lal, Use of mixed dyes in a photogalvanic cell for solar energy conversion and storage: EDTA – thionine – Azur B system, *J. Power Sources*, 164(2), 2007, 926–930
- [18] S. Dube, Simultaneous use of two reductants in a photogalvanic cell for solar-energy conversion and storage, *Int. J. Energy Res.*, 17(4), 1993, 311-314
- [19] K. M. Gangotri and V. Indora, Studies in the photogalvanic effect in mixed reductants system for solar energy conversion and storage: Dextrose and EDTA–Azur A System, *Solar Energy*, 84, 2010, 271-276
- [20] K. R. Genwa, Arun Kumar and Abhilasha Sonel, Photogalvanic solar energy conversion: study with photosensitizers Toluidine Blue and Malachite Green in presence of NaLS, *Applied Energy*, 86, 2009, 1431-1436
- [21] K. M. Gangotri and P. Gangotri, Studies of the micellar effect on photogalvanics: Solar energy conversion and storage–EDTA–Safranin O–CTAB system, *The Arabian Journal for Science and Engineering*, 35(1A), 2010, 19-28
- [22] S. Yadav and C. Lal, Photogalvanic cells as a device for solar energy conversion and storage: An EDTA–New Methylene blue and Safranin O system, *Energy Sources, Part A*, 32, 2010, 1028-1039
- [23] K. M. Gangotri and M. K. Bhimwal, Study the performance of photogalvanic cells for solar energy conversion and storage: Rose Bengal–D Xylose–NaLS system, *Solar Energy*, 84(7), 2010, 1294-1300
- [24] K. M. Gangotri P. P. Solanki and M. K. Bhimwal, Use of anionic micelles in photogalvanic cells for solar energy conversion and storage storage: Sodium lauryl sulphate–Mannose–Brilliant cresyl blue system, *Energy Sources: Party A*, 2010, **accepted**.
- [25] K. M. Gangotri and P. P. Solanki, Use of Sodium lauryl sulphate as a surfactant in photogalvanic cell for solar energy conversion and storage: Sodium lauryl sulphate–Methylene blue–Mannose system, *Energy Sources: Party A*, 2010, **accepted**.

## New cadmium sulfide nanomaterial for heterogeneous organic photovoltaic cells

Jan Rohovec<sup>1,\*</sup>, Jana Touskova<sup>2</sup>, Jiri Tousek<sup>2</sup>, Frantisek Schauer<sup>3</sup>, Ivo Kuritka<sup>3</sup>

<sup>1</sup> Institute of Geology AS CR v.v.i, Prague, Czech Republic

<sup>2</sup> Department of Macromolecular Physics, Charles University in Prague, Prague, Czech Republic

<sup>3</sup> Polymer Centre, Tomas Bata University, Zlin, Czech Republic

\* Corresponding author. Tel: +420 233 087 258, Fax: +420 220 922 670, E-mail: rohovec@gli.cas.cz

---

**Abstract:** Nanocrystalline cadmium sulfide particles were prepared by a new bench-top mild temperature procedure starting from cadmium ethylxanthate and using alkanolamines DEA, TEA as reaction media. The role of DEA, TEA in the whole reaction-nanocrystallization process is discussed. Basic spectroscopical properties of the new nano-CdS material formed were studied in order to characterize it as a material for the construction of photovoltaic solar cells.

**Keywords:** Nanocrystalline Cadmium Sulfide, Preparation, Photovoltaic Solar Cells, Triethanolamine, Diethanolamine

---

### 1. Introduction

Nanocrystalline cadmium sulfide is one of the most widely discussed and used material in the construction of photovoltaic solar cells. Several procedures for its preparation have been suggested. First synthetic approach to the nano-CdS is based on reactions in oleic acid or hexadecylamine at comparatively high temperatures (e.g., 160 °C), which results in the formation of nanoparticles covered by a surface shell of long, hydrophobic alkyl chains.<sup>1</sup> The prepared material is easy-to-handle, easily soluble in organic solvents, stable over a long shelf life, but the protective hydrophobic shell covering the nanoparticles hampered good performance of the material in solar cells. Some disadvantage of this approach is represented by the need of two different sources of cadmium and sulfur, e.g., Cd(oleate)<sub>2</sub> and S<sub>8</sub>.

Another similar CdS synthesis based on the use of a trioctylphosphine oxide TOPO /trioctylphosphine TOP protective shell has been used for relatively long time, despite of the high toxicity and air sensitivity of the precursors.<sup>2</sup> It supplied cadmium sulfide nanomaterial of improved quality, but the photovoltaic properties were still not optimum.

A similar approach leading to CdS nanoparticles covered by long-chain alkylamine protective shell was designed, overcoming the need of two different educts bearing Cd and S for the product formation. As a starting compound bearing cadmium and sulfur in one molecule, various cadmium–sulfur containing precursors, like Cd-xanthates, thiocarbonates, thiophosphates etc. in alkylamine media (e.g., hexadecylamine HDA) were used in thermal decomposition techniques. In the reaction, the alkylamine molecule acts as a solvent and as a protective shell-forming agent at the same time.<sup>3-6</sup>

Experimental effort was then concentrated on the synthesis of protective shell-free nanoparticles. This was accomplished by the synthesis of CdS covered by HDA. The HDA protective shell was finally removed from the nanoparticle surface by extensive washing with pyridine.<sup>7,8</sup>

A more elegant method, directly leading to shell-free nano-CdS, is based on a template-free/shell-free formation of the target material by precipitation of Cd<sup>2+</sup> salt in the medium of

*in situ* formed sulfide anion in aqueous media.<sup>9</sup> Sulfide is formed by hydrolytic reaction of thiosulfate anion  $S_2O_3^{2-}$ , thiourea, thioacetamide etc., possibly catalyzed by thioglycerol. The shell-free particles formed are less stable and much more difficult to handle, easily forming a coagulate, which is hardly re-dispersed. This type of nano-CdS is insoluble in organic solvents. On the other hand, improved material properties were demonstrated, such as electron exchange favorable for the construction of photovoltaic cells.

The optimized synthetic method of the nanocrystalline CdS formation should be a bench-top technique starting from well-defined, low-cost, stable and accessible educts, employing mild conditions, and not necessitating special precautions like inert atmosphere. Of course, a steady attention is given to the size, shape, homogeneity and size distribution of the nanoparticles formed.

In this paper, we report a synthesis of nano-CdS particles using a single-precursor, mild-temperature decomposition procedure. Cadmium ethylxanthate was used as a precursor. The key role in the procedure is played by the reaction medium used, namely diethanolamine DEA or triethanolamine TEA. The influence of alkanolamine on the material properties of the nano-CdS formed is discussed.

## 2. Methods

All chemicals used were supplied by the Sigma-Aldrich company. The alkanolamines diethanolamine DEA, triethanolamine TEA, and cadmium chloride hydrate were used as supplied without any further purification step, while potassium ethylxanthate was purified by dissolving in water and filtering through the 0.45  $\mu$ m RC filtration disc (Merck) in order to remove insoluble impurities. The potassium xanthate solution was reacted immediately after filtration.

UV VIS spectra were measured on the Cintra 303 spectrometer (GBC) in  $H_2O$ , DEA or TEA as a medium, in the range of 300–600 nm with a resolution of 2 nm. The course of nanocrystalline CdS formation was followed either by taking a sample of the reaction mixture and diluting it by  $H_2O$  or by a direct use of the reaction mixture.

Elemental analysis of the CdS product was performed on liquid samples formed by dissolution of sample in mixture of conc. nitric acid hydrogen peroxide in a closed vessel to ensure complete oxidation of the hydrogen sulfide released into the sulfate ion state. The samples were analyzed with the Intrepid DUO II ICP EOS instrument (Thermo Electron Corp.), using standard plasma conditions recommended by the manufacturer. In the same analytical run, trace impurities were checked as well.

Organic carbon content of the separated CdS nanoparticles was quantified in aqueous suspensions of the products by the Shimadzu analyzer, operated at 600 °C (catalytic oven temperature) with a run cycle of 10 min.

Samples for physical measurements were prepared by spin coating technique on either ITO glass substrates or p-silicon substrates. Approximately 100  $\mu$ l of the DEA/TEA solutions of CdS were spread on the substrate at a rotation speed of 30–70 rps. The covered substrates were freeze-dried in the Alpha 1-2 (Christ) freeze-drying unit at 1E-4 kPa/-50 °C on a cooling system. The dried samples were handled in air at room temperature, being submitted for physical measurements as soon as possible.

### **Cadmium ethylxanthogenate (cadmium ethylxanthate) preparation and purification:**

Cadmium ethylxanthate [ $\text{Cd}(\text{S}_2\text{C-OC}_2\text{H}_5)_2$ ] was prepared basically according to the literature procedure, combining well stirred aqueous solutions of potassium ethylxanthate  $\text{KS}_2\text{C-OC}_2\text{H}_5$  and cadmium chloride in a stoichiometric ratio.<sup>3</sup> The immediately formed white precipitate of cadmium ethylxanthate was filtered off and carefully washed with water to ensure removal of potassium and chlorides. After purification by re-crystallization, the product was dried overnight *in vacuo* and stored in a freezer at  $-20\text{ }^\circ\text{C}$ . Elem. anal.: 31.9 % Cd, 36.26 % S, (ICP EOS).

### **Nanocrystalline cadmium sulfide was prepared using the following bench-top procedure:**

Cadmium ethylxanthate (5–50 mg) was dissolved at a room temperature in alkanolamine (3 ml) without air exclusion. The dissolution was quite slow and was facilitated by intensive stirring by a glass rod. The yellowish solution obtained after a complete dissolution of the solid was heated in an air bath to  $75\text{--}80\text{ }^\circ\text{C}$ . The course of the reaction was followed by UV-VIS spectroscopy. After the formation of the target product, the reaction was interrupted by cooling of the reaction solution to a room temperature. The nanocrystals of the cadmium sulfide formed were either isolated by precipitation with copious amount of acetone and centrifugation, and purified by re-precipitation with acetone, or the reaction solution was used directly for the preparation of samples for physical measurements.

### **3. Results and Discussion**

The procedure described above offers a preparative bench-top technique for the synthesis of CdS nanoparticles without the need of any special precautions like protection against air or moisture. It is based generically on literature reports, where the use of hexadecylamine HDA, oleylamine OA etc. as Lewis bases/reaction media, as well as shell-forming protective molecules is widely employed.<sup>3-6</sup> Similarly to the previous procedures, also the procedure described in this paper starts from easily accessible cadmium ethylxanthate, commonly used as a single-compound precursor for CdS formation. The mechanism of the cadmium ethylxanthate decomposition reaction used for CdS formation was proposed quite early and is generally accepted.<sup>4</sup>

We observed that the purity of the starting cadmium ethylxanthate is an important factor influencing the reproducibility of the crystallization of CdS. Older samples of cadmium ethylxanthate generally turn yellow due to decomposition, leading in our experience to a more rapid formation of CdS in the course of preparation.

The principal difference from the art known is based on the application of alkanolamines as reaction media for cadmium ethylxanthate decomposition. Alkanolamines, namely diethanolamine DEA  $\text{NH}(\text{CH}_2\text{CH}_2\text{OH})_2$  and triethanolamine TEA  $\text{N}(\text{CH}_2\text{CH}_2\text{OH})_3$ , are commercially accessible, low-cost compounds with a good dissolution ability. We found that the above mentioned compounds can be successfully applied as solvents for cadmium ethylxanthate.

In the reaction course, they clearly play several roles. They act as:

i) high-boiling solvents with favorable viscosity characteristics,

- ii) a weak base, catalysing the thermal decomposition of the Cd ethylxanthate precursor,
- iii) a weakly coordinating medium for Cd ions,
- iv) a shell-forming molecule.

The influence of the base on the thermal decomposition reactions of xanthates leading to the formation of metal sulfides was described in the literature. Similarly to the previous observation, the choice of solvent with appropriate basicity is essential also in the procedure discussed. In highly basic solvents, the decomposition of a xanthate precursor proceeds too fast upon the crystallization of sulfide of insufficient quality for photovoltaics, while in media of low basicity the thermal decomposition does not proceed at all. We had tried about 25 solvents before we concentrated on DEA/TEA. Aniline and its derivatives, pyridines or heterocycles, typically act as low basicity solvents. In contrast, short-chain primary amines were found to be too basic for the discussed application. The choice of over-basic medium leads to the decomposition of cadmium ethylxanthate already during the dissolution, thus the formation of CdS proceeds in a heterogeneous medium with serious consequences on the quality of the product formed.

There has been no discussion conducted yet as for the effect of coordination properties of the solvent used for nano-crystallization of cadmium sulfide. On the other hand, the coordination ability of the solvent during the thermal decomposition reaction governs the concentration of cadmium in the solution and can therefore strongly influence the crystallization process of CdS. The ability of DEA, TEA to coordinate cadmium ions in aqueous solutions is well documented, as well as the use of TEA as a masking agent in various analytical applications. In our case we expect that the nano-crystallization can be influenced by the formation of a complex between cadmium ions present in the reaction medium and DEA/TEA solvent. This complex consequently drives the crystallization process in the direction of the formation of CdS nanocrystals.

The reaction was followed by means of UV-VIS spectroscopy. In order to get a better insight into the time course of the reaction, lower temperatures and lower precursor concentrations were used than in the preparative procedure.

The evolution of UV-VIS spectra of the reaction system cadmium ethylxanthate/TEA vs. the reaction time is shown in Fig. 1. Absorption spectra obtained in the course of the nano-CdS formation show a gradual increase in the intensity of the excitonic transition as well as a shift of the signal toward higher wavelengths. The intensity of the transition reaches a plateau approximately after 60 min. as a result of the completion of the decomposition reaction. The shift of the signal reflects a gradual particle size increase. At the same time, the transition becomes broader, pointing to an increasing polydispersity of the product formed. This interpretation of UV-VIS spectral characteristics is in line with the previous works.<sup>3,5</sup> The particle size depends on the reaction time applied, thus the choice of the reaction time is a parameter useful for controlling the CdS particle size.

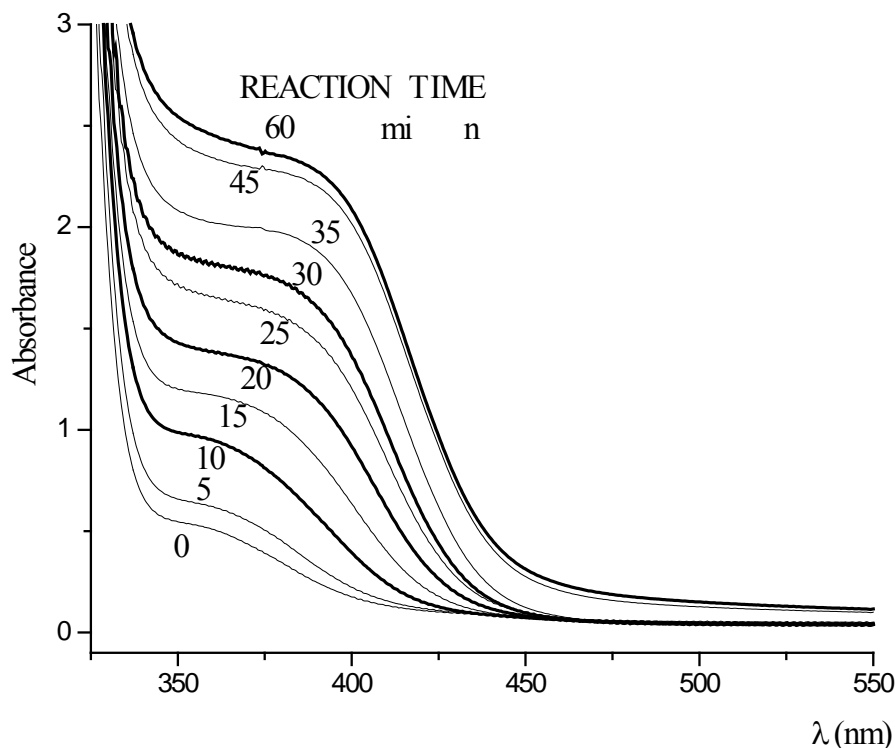


Fig. 1. UV-VIS spectral study of the reaction course. Concentration of cadmium ethylxanthate 0.5 mg in 5 ml of TEA, reaction temperature 75 °C.

Another established parameter governing the growth and particle size is the concentration of the precursor in the reaction medium. In our case, we fixed the concentration of cadmium ethylxanthate at an appropriate value of 10 mg/ml given by the solubility of the precursor in all alkanolamines, without attempting to study this parameter in detail.

Reaction temperature critically influences the reaction course, reaction rate, size and the quality of the product formed. Alkanolamines are high-boiling compounds, so the reaction temperature can be chosen over a relatively wide range. Typical UV-VIS spectra in a preparation run at several temperatures are demonstrated in Fig. 2.

In our experience, the decomposition reactions proceeds too fast at high temperatures, leading to smaller particles of insufficient quality. Therefore, the temperature area of 80 °C applied in the procedure described in the experimental section seems to be the optimum one, as the course of the reaction can be easily followed and the quality of the material produced is acceptable.

The nano-CdS particles can be easily isolated from the reaction medium by precipitation with an organic solvent, like ethanol or acetone. As the alkanolamines used as reaction media are freely miscible with common precipitation solvents, the choice of precipitants is not restricted to EtOH or acetone. After the synthesis, the alkanolamine molecule remains in touch with the nano-CdS particle, permitting the following manipulations, stabilizing the particle against coagulation, but can be easily removed as well.

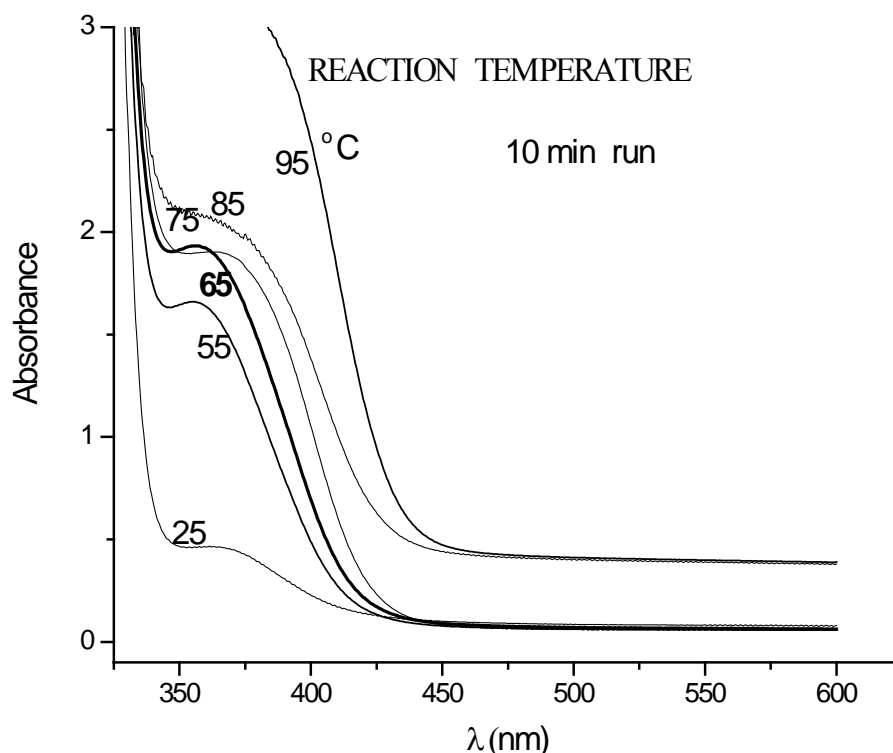


Fig. 2. UV-VIS spectral study of the reaction course. Concentration of cadmium ethylxanthate 0.5 mg in 5 ml of TEA, reaction time 10 min.

The presence of the alkanolamine protective shell on the surface of the CdS nanocrystals formed is another important point to be discussed. We tried to prove the presence of a DEA/TEA shell on the nano-CdS isolating the nanocrystals from the reaction medium by the precipitation procedure, washing the isolated material ten times with water and repeating the precipitation. The absence of free DEA in the final washings was proved by ninhydrine reaction, which is a sensitive color test for primary and secondary amine groups. After drying the preparation in a freeze drier, an elemental analysis was performed. Carbon content found in the preparation was 18 % C, which we explain by the presence of bonded/coordinated DEA/TEA on the surface of nano-CdS.

Indirect evidence also exists of the presence of the protective alkanolamine shell on the surface of the CdS nanocrystals. The nanocrystals formed are hydrophilic and can be easily re-dispersed in water. It should be emphasized that the short alkyl-OH chains present in the alkanolamine molecules should not interfere in the electron transfer between CdS nanocrystals as strongly as the previously used long alkyl chains (HDA).

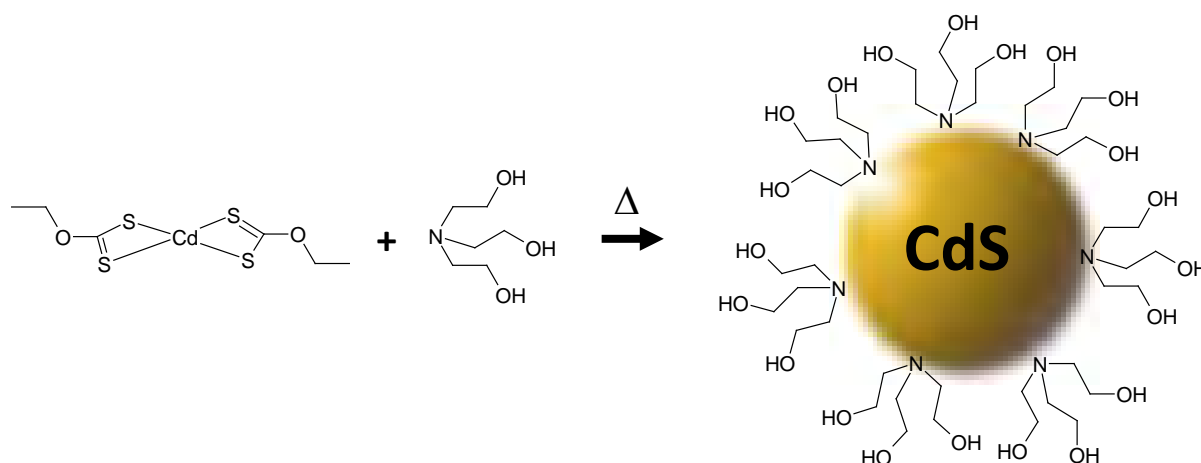
The elemental analysis of nano-CdS samples formed by the procedure under discussion proved the expected stoichiometric ratio Cd:S 1:1. The content of other metallic contaminants (Al, Ca, Fe, K, Mg, Mn, Na) in the sample was found to be negligible.

Spectral properties of the nano-CdS prepared were further studied by photoluminescence and Raman spectroscopy. In the PL spectrum, the peaks near 410 and 435 nm (excitation) are visible. In the Raman spectra of CdS nanoparticles isolated from the solutions in DEA and TEA, signals of DEA, resp. TEA are visible. This is in accordance with the results of

elemental analysis proving the presence of DEA/TEA in the final product. It is highly probable that the organic molecules form a protective shell on the nanoparticle surface. Besides the DEA/TEA signals, also spectral signals with Raman shifts of 300, 600 and 872  $\text{cm}^{-1}$  (nano-CdS-DEA spectrum) and of 301, 602, 687 and 909  $\text{cm}^{-1}$  (nano-CdS-TEA spectrum) were observed. The product was further studied by the TEM technique. The samples of nano-CdS taken from the reaction solution in DEA after a 20min. reaction at 85 °C (sample A), as well as in TEA after 20 min. and 120 min., respectively (samples B and C) were spin-coated. A successful observation of the nanocrystals was performed on silicon substrates. The TEM study was complicated by a very difficult removal of DEA, TEA from the samples.

#### 4. Conclusions

We herein described the preparation of a new nanocrystalline CdS material, covered with a protective shell composed of triethanolamine or diethanolamine molecules. Due to the presence of the protective shell, the particles are highly hydrophilic. The new material is prepared from an accessible single precursor using a bench-top procedure and applying very mild reaction conditions. The factors controlling the reaction and nanocrystal formation are discussed. The preparation of the nano-CdS can be illustrated on the scheme below:



#### Acknowledgements

The project was funded by the Czech Science Foundation (GACR 202/09/1206) and Institutional Research Plan AV0Z30130516.

## References

- [1] Jin Joo, Hyon Bin Na, Taekung Yu, Jung Ho Yu, Young Woon Kim, Fanxin Wu, Jin Z. Zhang, Taeghwan Hyeon, Generalized and facile synthesis of semiconducting metal sulfide nanocrystals, *J. Am. Chem. Soc.* 125, 2003, pp. 11100 – 11105.
- [2] Yongan Yang, Ou Chen, A. Angerhofer, C. Y. Cao, Radial-position-controlled doping in CdS/ZnS core/shell nanocrystals, *J. Am. Chem. Soc.* 128, 2006, pp.12428 – 12429.
- [3] P. Sreekumari Nair, Thottaqckad Radhakrishnan, Neerish Revaprasadu, Gabriel Kolawole, Paul O'Brien, Cadmium ethylxanthate: A novel single-source precursor for the preparation of CdS nanoparticles, *J. Mater. Chem.* 12, 2002, pp. 2722 – 2725.
- [4] Narayan Pradhan, Beni Katz, Shlomo Efrima, Synthesis of high-quality metal sulfide nanoparticles from alkyl xanthate single precursors in alkylamine solvents, *J. Phys. Chem.*, 107, 2003, pp. 13843 – 13854.
- [5] Narayen Pradhan, Shlomo Efrima, Single-precursor, one-pot versatile synthesis under near ambient conditions of tunable, single and dual band florescing metal sulfide nanoparticles, *J. Am. Chem. Soc.* 125, 2003, pp. 2050 – 2051.
- [6] Yunchao Li, Xiaohong Li, Chunhe Yang, Yongfang Li, Controlled synthesis of CdS nanorods and hexagonal nanocrystals, *J. Mater. Chem.* 13, pp. 2003, 2641 – 2648.
- [7] Li Wang, YanShan Liu, Xi Jiang, DongHuan Qin, Yong Cao, Enhancement of Photovoltaic Characteristics Using a Suitable Solvent in Hybrid Polymer/Multiarmed CdS nanorod Solar Cells, *J. Phys. Chem. C* 111, 2007, pp. 9538 – 9542.
- [8] Yan-Shan Liu, Wang Li, Dong-Huan Qin, Yong Cao, Photovoltaic devices from Multi-armed CdS nanorods and conjugated polymer composites, *Chin. Phys. Lett.* 23(12), 2006, pp. 3345 – 3348.
- [9] C. Unni, Daizy Philip, S. L. Smitha, K. M. Nissamudeen, K. G. Gopchandran, Aqueous synthesis and characterization of CdS, CdS:Zn<sup>2+</sup> and CdS:Cu<sup>2+</sup> quantum dots, *Spectrochimica Acta Part A* 72, 2009, pp. 827 – 832.

## CdS nanoparticles surfactant removal transport study by transient charge measurements

F. Schauer<sup>1,3\*</sup>, V. Nadáždy<sup>2</sup>, Š. Lányi<sup>2</sup>, J. Rohovec<sup>4</sup>, I. Kuřitka<sup>5</sup>, J. Toušková<sup>6</sup> and J. Toušek<sup>6</sup>

<sup>1</sup> Department of Electronics and measurement, Tomas Bata University, Zlin, Czech Republic

<sup>2</sup> Institute of Physics, Slovak Academy of Sciences, Bratislava, Slovak Republic

<sup>3</sup> Department of Physics, Trnava University in Trnava, Trnava, Slovak Republic

<sup>4</sup> Institute of Geology, Academy of Sciences of the Czech Republic, Prague, Czech Republic

<sup>5</sup> Polymer centre, Tomas Bata University, Zlin, Czech Republic

<sup>6</sup> Department of Macromolecular Physics, Charles University in Prague, Prague, Czech Republic

\* Corresponding author. Tel: +420 605876867, E-mail: fschauer@fai.utb.cz

**Abstract:** The electronic transport of CdS nanoparticles (nano-CdS) covered by hydrophilic alkanolamine molecules as surfactants was studied. The nanomaterial was prepared by low-temperature decomposition of cadmium ethylxanthate in hydrophilic solvents like mono-, di- or triethanolamine. The nanoparticles were isolated by precipitation procedures in solid state and they are easy to re-disperse in water systems. Films with nanoparticles were exposed to UV radiation, with the exposure varying in time interval 10 – 60 min.

The goal of the work was to study the electronic transport in the array of nanoparticles. The experimental techniques used was the Isothermal charge transient spectroscopy (IQTS) working with the a unique charge transient processor in the sampling range 2  $\mu$ s – 900 ms with resolving power of about several hundreds of electrons. The second method was the surface photovoltaic method (SPV). Two basic novel phenomena were observed on the film formed by nano-CdS provided with tu surfactant, in *I-V* characteristics the increase of current was observed with a strong nonlinearity, marking the increased transport via nanoparticles, and the occurrence of charging–discharging phenomena with strong maximum described by the distribution of relaxation times and/or trapping states occurrence. The photoconductivity action spectra agree with the absorption edge of size distributed nanoparticles.

**Keywords:** CdS nanoparticles, Alkanolamine surfactants, Isothermal charge transient spectrum, Hybrid solar cells.

### 1. Introduction

The organic/inorganic hybrid solar cells work on the concept of bulk heterojunction, where excitons created upon photoexcitation are separated into free charge carriers at interfaces between two semiconductors-inorganic nanoparticle and bulk organic polymer forming a composite thin film[1][2][3]. Electrons will be then accepted by the inorganic nanomaterial with the higher electron affinity (electron acceptor, here the inorganic nanoparticle) and the hole by the polymer with the lower ionization potential (electron donor, here the polymer matrix). Both types of carriers are then transported by independent mechanisms to corresponding electrodes. The contemporary problems with the hybrid solar cells are the choice of suitable components for hybrid solar cells to match the solar spectrum, the solubility of both components and the transport of holes on the array of nanoparticles[4][5].

The aim of the paper is to elucidate the influence of the surfactant in the core – shell model on the transport of carriers (holes) by the process of diffusion on the array of nanoparticles. The main idea is to change the medium distance of nanoparticles by the surfactant length and thus changing the hopping probability of charge carriers resulting in the change of the average mobility and diffusion coefficient. For this purpose a new, extremely sensitive method for the study of transport and traps distribution, isothermal charge transient spectroscopy (IQTS) and surface photovoltaic method (SPV) for the diffusion study was used. For this purpose we examine one component of the hybrid organic/inorganic system MEH – PPV/nano-CdS nanoparticles covered by alkanolamine molecules as surfactant produced by a new technique.

## 2. Methodology

### 2.1. Sample preparation

The preparation of nano-CdS was described in detail elsewhere [6] so we will mention only few facts here. A new nano-CdS covered by hydrophilic alkanolamine molecules was prepared by low-temperature decomposition of cadmium ethylxanthate in hydrophilic solvents of mono-, di- or triethanolamine. By appropriate choice of reaction time, temperature and xanthate concentration, it was possible to tune the size and physical properties of resulting nanoparticles. The samples were deposited from ethanolamine solution by spincoating or drop casting on Au film evaporated on p-Si substrate or on borosilicate glass provided with ITO film and dried under the vacuum (rotary pump 10 Pa annealed at 80 °C and turbomolecular 10<sup>-4</sup> Pa annealed at 100°C) to remove the solvent. For the characterization of nanoparticles the UV-VIS absorption, photoluminescence and Raman spectroscopy was used [6].

### 2.2. Isothermal charge transient spectroscopy (IQTS) and Surface photovoltaic method (SPV)

Electronic transport measurements were performed with charge transient processor (CTP) in local mode [7], when the usual evaporated top electrode is replaced by the tip of the scanning probe in form of a sharpened 80- $\mu\text{m}$ -tungsten wire oriented perpendicularly to the surface. The charge to voltage converter has the resolution of hundreds of electrons and time resolved transients from 2  $\mu\text{s}$  to hundreds of ms can be recorded. The input converter integrates the current transients following the voltage pulses periodically applied to the sample. The duration of excitation pulses was set from 1 to 100 ms, their amplitude from 0.5 to 5 V, and the period from 147 to 547 ms. The isothermal charge transient spectrum (IQTS) is created by combining samples from charge transients at particular times using the formula  $\Delta Q(t_1) = Q(t_1) - 1.5Q(2t_1) - 0.5Q(4t_1)$  [8] with  $t_1$  swept with 2  $\mu\text{s}$  step starting at the trailing edge of the pulse up to the maximal point for which  $4t_1$  fits before start of the next pulse. This way of transient processing acts as a filter of measured relaxation times, i.e., IQTS signal is detected when the time constant of the relaxation process is comparable to  $t_1$ . In addition, this formula eliminates the linear component of the response, which is caused by the integration of dc current. The peak maximum corresponds to 0.174 of the total charge  $Q_0$  responsible for the peak. To reduce the noise usually 50 transients were summed. The charge transient processor allows to evaluate in one special mode also the dc current by measurements of charge without application of excitation pulses using the formula:  $I_{\text{DC}} = \Delta Q(t_2) - Q(t_1) / (t_2 - t_1)$ , and to obtain the current voltage characteristic by sweeping the bias voltage.

#### 2.2.1. Surface photovoltaic method (SPV) [9] [10]

Electrical field of space charge region (SCR) of the thickness  $d$  (Fig.1). drives the photogenerated charge carriers leading to the photovoltage. The photovoltage was measured in a sandwich structure between the substrate silicon and the top glass / ITO with a Mylar sheet serving as a separating dielectric layer. The scanning microscope view of the film is in Fig.1. A capacitive couple is formed in this way. Illumination was performed through the top electrode into the bulk. The samples were irradiated by low-intensity monochromatic light chopped with a low frequency of 11 Hz generating an alternating voltage which was measured by lock-in amplifier Stanford SR 830. In our experiment the chopper frequency was sufficiently low to obtain saturated pulses not influenced by relaxations. The spectra were taken at room temperature and in air.

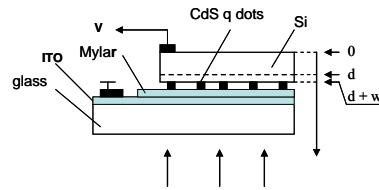


Fig.1. Arrangement of the SPV experiment. The polymer is illuminated with a chopped monochromatic light through transparent conductive electrode. As the second electrode serves the Si substrate.

### 3. Results

The SEM picture of the nano-CdS is in Fig.2 with the nanoparticles in the range of 20-30 nm. The representative  $I-V$  characteristics of Au / nano-CdS nanoparticles film / W probe (prepared in the standard way, i.e. annealed at 80 °C in the rotary pump 10 Pa vacuum) taken by IQTS for as deposited and UV irradiated sample ( for 20, 40 and 60min are in Fig.3). We adjusted the filling and waiting time to ensure near to the steady-state characteristics. Corresponding IQTS signals are in Fig.4. The enormous increase of the  $I-V$  characteristics for positive applied voltage on ITO is recorded for degradation time 20 min, which gradually disappears with progressive degradation ( 40, 60 min). IQTS signals show for both polarities of the applied excitation pulses and do not depend on injection as the ability of both contacts (ITO and W ) contacts are quite different as obvious from  $I-V$  transient characteristics. If we take into consideration the fact that the IQTS is stripped of the dc current, we then may conclude the observation is a bulk (contrary to contact) effect and most probably enhanced due to the decreased average distance among particles in the nano-CdS array.

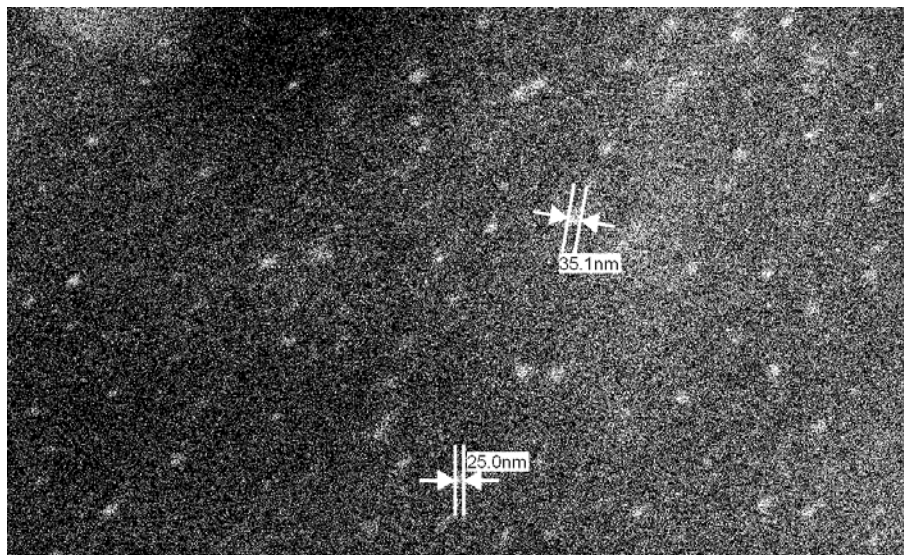


Fig.2. SEM photograph of nano-CdS on silicon substrate.

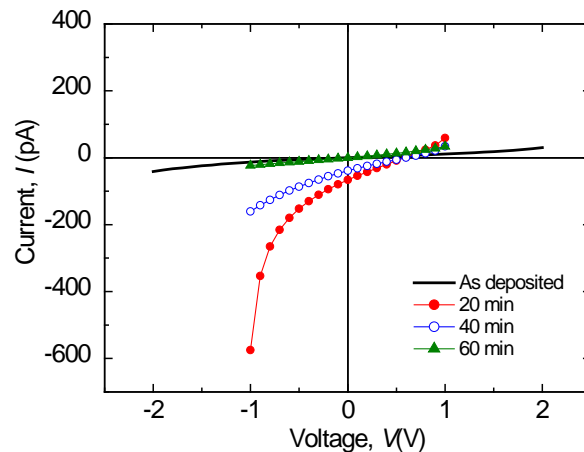


Fig. 3. Evolution of I-V characteristics (voltage is taken with respect to W probe) of the structure Au / nano-CdS nanoparticles film / W probe with exposure time to UV irradiation.

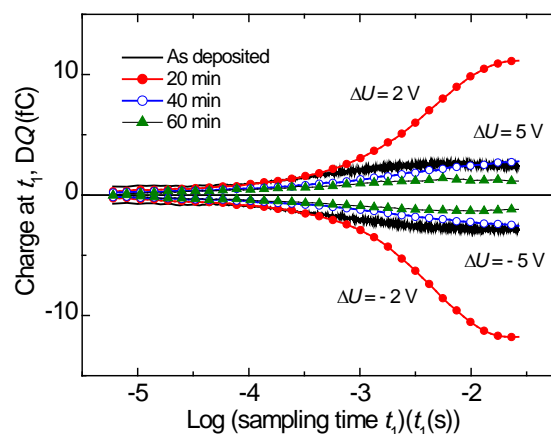


Fig. 4. Evolution of IQTS spectra of Au/nano-CdS /W. The parameter was the UV irradiation time and the polarity with respect to W tip. Bias voltage,  $U_b = 0$ ,  $U_{ex} = 5$  V for as deposited and 60 min exposed states, 2 V for 20 and 40 min exposed states. The period and duration of excitation pulses were set to 147 ms and 10 ms, respectively.

As the next step we measured we took the measurements on the identical sample degraded by 60 min UV (see Fig. 3 and Fig. 4) and carried out the anneal in vacuum  $10^{-4}$  Pa at  $100^\circ\text{C}$  for 10 min. The I–V characteristics taken by CTP for annealed at  $100^\circ\text{C}$  and corresponding IQTS signals nearly returned to their original shapes (in Fig.3 and Fig.4). UV irradiation (for 20, 40 min) caused the same changes in I – V characteristics (Fig. 5) and corresponding IQTS signals in Fig. 6. The surprising recovery tendency and susceptibility to UV degradation changes are evident both in I - V and IQTS signals. The degradation for 20 min creates the bulk relaxation, similar to that in Fig.3 and Fig. 4. This observation may be due to the metastable degradation – recovery steps.

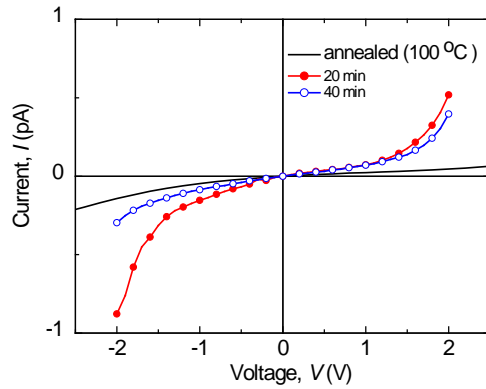


Fig. 5. Influence of annealing (100 °C for 10 min) on I-V characteristics (voltage is taken with respect to W probe ) of the structure Au / nano-CdS nanoparticle film / W probe.

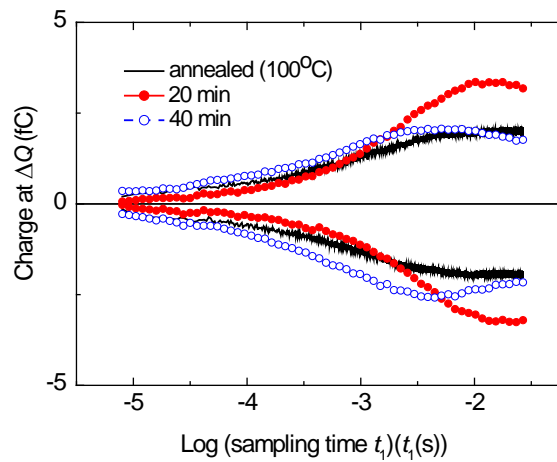


Fig.6. Influence of annealing (100 °C for 10 min) on IQTS, all parameters identical to those in Fig.4.

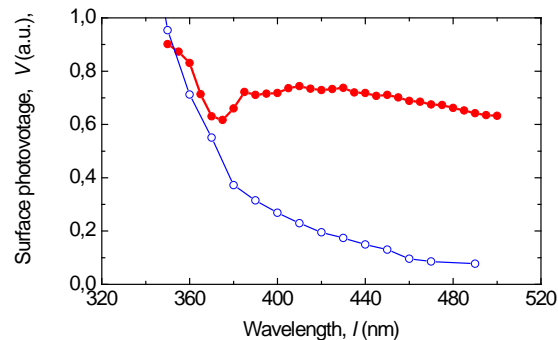


Fig.7. SPV spectrum of p-type silicon with nano-CdS (solid circles). The quantum size effect in the nanoparticles influences the spectrum from the 375 nm to 500 nm. SPV spectrum of the wafer is shown for comparison (open circles).

The SPV signals of nano-CdS on p-Si substrate is visible in Fig. 7. The composed signal results both from photoconductivity of nano-CdS and from the Si substrate, as it is obvious from the signal on the bare Si substrate. The measurements of the diffusion coefficient in CdS due to the hopping transport diffusion is under way.

#### 4. Discussion and Conclusions

The idea behind this experimental activity presented here was the obvious knowledge about the limiting influence of the hole transport in hybrid solar cells by hopping transport, where the average distance and coupling among particles was given by the shell (surfactant in this case) [4][5]. With this on mind and realizing our recent results on UV degradation of  $\sigma$  conjugated polymers resulting in weak bonds concept and metastability of PMPSi that may be recovered by alloying [11] we attempted to modify the interaction of nano-CdS provided with alkanolamine molecules as surfactant by UV radiation.

The results are encouraging. On the UV degradation considerable changes in relaxation processes of the fresh prepared sample (dried under vacuum 10 Pa and annealed at 80 °C) to irradiated (for 20 min), where relaxation process is emerging – subsequently disappearing (for 40 and 60 min) (Fig. 3 and Fig. 4). The same ordering of observations is visible when the same sample of nano-CdS is subjected to anneal at the turbomolecular vacuum  $10^{-4}$  Pa and annealed at 100 °C (Fig. 5 and Fig. 6). No traps connected with the nano-CdS were visible on these experiments.

The detailed explanation is not obvious at the moment, there are following possibilities for explaining the observed phenomena. One is the decrease of the average distance among nanoparticles due to the decreased lengths of alkanolamine molecules due to their scissoring, or the stripping of the part of the alkanolamine molecules from CdS surface. Both these phenomena should possess the metastability in reconstruction of the original state by anneal.

The conclusions drawn from the presented results may be formulated:

- both applied highly sensitive methods of isothermal charge transient spectroscopy and surface photovoltaic method turned out to be very suitable methods for characterizing the transport processes in nanomaterials due to their sensitivity and spectroscopical character,

- the changes in surfactant on U V radiation cause the changes in collective relaxation processes and may positively influence the transport of hole charge carriers after their injection or charge-transfer processes. This may positively influence the efficiency of conversion of hybrid solar cells.

### Acknowledgements

The work in Czech Republic was supported by the Grant agency of the Czech Republic under the project 202/09/1206. The work in Slovak Republic was supported by the ASFEU project Applied research of advanced photovoltaic cells, Activity 4.2, ITMS code 26240220047, supported by the Research & Development Operational Programme funded by the ERDF and by Slovak grant agency VEGA 2/0041/11.

### References

- [1] S. Gúnes, N. S. Sariciftci, Hybrid solar cells, *Inorganica Chimica Acta* 361, 2008, pp.581–588, D. J. Milliron, I. Gur, A. P. Alivisatos, Hybrid organic - Nanocrystal solar cells. *Mrs Bulletin*, 30, 2005, pp. 41-44.
- [2] W. U. Huynh, J. J. Dittmer, A. P. Alivisatos, Hybrid nanorod-polymer solar cells, *Science* 295, 2002, pp. 2425-2427.
- [3] W. U. Huynh, J. J. Dittmer, N. Tecler, D. J. Milliron, A. P. Alivisatos, K. W. J. Barnham, Charge transport in hybrid nanorod-polymer composite photovoltaic cells, *Physical Review B* 67, 2003, (11) 115326.
- [4] I. Gur, N. A. Fromer, C. P. Chen, A. G. Kanaras, A. P. Alivisatos, Hybrid solar cells with prescribed nanoscale morphologies based on hyperbranched semiconductor nanocrystals. *Nano Letters* 2007, 7, pp. 409 -414, J. Rohovec, J. Tousek, J. Tousek, F. Schauer, I. Kuritka New cadmium sulfide nanomaterial for heterogenic organic photovoltaic cells, this conference.
- [5] Š. Lányi, V. Nádaždy, *Ultramicroscopy* 110, 2010, p. 685.
- [6] I. Thurzo, K. Gmucová, *Rev. Sci. Instrum.* 65, 1994, p.2244.
- [7] J. Toušek, J. Toušková, *Sol. Energy Mater. Solar. Cells*, 92, 2008, p. 1020.
- [8] J. Toušek, J. Toušková., I. Křivka, P. Pavlačková, D. Výprachtický, V. Cimrová, *Org. Electronics* 11, 2010, 50.
- [9] F. Schauer, P. Schauer, I. Kuřitka, H. Bao., *Conjugated Silicon-Based Polymer Resists for Nanotechnologies: EB and UV Mediated Degradation Processes in Polysilanes. Materials Transactions, Special Issue on Development and Fabrication of Advanced Materials Assisted by Nanotechnology and Microanalysis*, 51, 2010, pp.197-201.

## Charge transient and electrochemical measurements as a tool for characterization and degradation study of organic semiconductors - PMPSis and MEH-PPV

V. Nadáždy<sup>\*1</sup>, K. Gmucová<sup>1</sup>, Š. Lányi<sup>1</sup>, F. Schauer<sup>2,\*</sup>, and I. Kuřitka<sup>2</sup>

<sup>1</sup>*Institute of Physics, Slovak Academy of Sciences, Bratislava, Slovak Republic*

<sup>2</sup>*Department of Electronics and measurement, Tomas Bata University, Zlin, Czech Republic*

*\* Corresponding author. Tel: +421 220910761, E-mail:vojtech.nadazdy@savba.sk*

---

**Abstract:** This contribution deals with application of several techniques based on charge transient contactless measurements (isothermal charge transient spectroscopy - IQTS), and by electrochemical methods of double step voltacoulometry and cyclic voltammetry, two complementary methods, which are potentially suitable for obtaining information about bulk relaxation and transport processes and the structure of electronic localized states and their basic parameters. Both methods were tested by two well known polymers, the first, Poly[methylphenylsilylene] and the second Poly(p-phenylene vinylene). The results were explained both in terms of bulk relaxation and transport processes, trap parameters and the influence of UV degradation. The metastability in reconstruction of dangling bonds ensuing after the UV degradation due to the Si-Si  $\sigma$  conjugated bond scission and its ability to reconstruct after the thermal anneal was again found in accord with the previous results.

**Keywords:** *Organic semiconductors characterization, Electron structure, Transient charge method, Electrochemical method.*

---

### 1. Introduction

The material research in organic semiconductors is moving towards the applications. When optimizing the properties of devices one has to start from the correct microphysical parameters of materials in question. The complicating factors in this direction is weak (molecular) coupling and the disordered structure, which both make the spectroscopic methods known from disordered inorganic semiconductors difficult and sometimes impossible to apply. So the need for new methods is acute and the new methods have been developed for organic material characterization.

It was shown that suitable techniques to electrical characterization of organic materials are space charge limited currents [1] and thermally stimulated currents [2]. As a favorable approach turns out capacitance or charge transient measurements which are processed by properly combined values of measured transients taken at specified time instants originally applied in deep-level transient spectroscopy of defect states in inorganic semiconductors. This transient processing allows to determine salient features of the transport states distribution [3] and charge traps induced by structural or chemical defects [4-6]. Electron transport based on hopping is important in polymers and localized molecular traps serve as redox sites. These facts authorize the application of solid-state electrochemical measurements. Some issues related to the principles and analytical aspects of electrochemical techniques were discussed in review by P.J. Kulesza and J.A. Cox [7].

Here we present two new methods with expressed advantages for the application in the field of molecular materials, isothermal charge transient spectroscopy and double state voltacoulometry. Both methods are based on the injection (extraction) contacts and the resulting signals in the time domain, which is analyzed for the capacitance and diffusion currents, respectively. Thus, we obtain information about capacitive (displacement) and

diffusive (reduction-oxidation) phenomena that are quite complementary for the defects elucidation.

In the presented paper, we starting from the well known prototypical polymer - Poly[methylphenylsilylene] (PMPSi), intend to test both the methods by comparison with previous results and then to apply it on quite important in the field of organic photovoltaics - Poly(p-phenylene vinylene) (PPV).

## 2. Methodology

### 2.1. Sample preparation

Poly[methylphenylsilylene] (PMPSi) was purchased from Flurochem. PMPSi thin films were spin-coated from solution in toluene on the UV-ozone treated ITO substrates with a spin rate of 1500 rpm for 30 s and dried in vacuum of  $3 \times 10^3$  Pa at 60 °C for 4 hrs. Poly[2-methoxy-5-(2'-ethyl-hexyloxy)-1,4-phenylene vinylene] (MEH-PPV) was supplied by Aldrich and solved in tetrahydrofuran. The MEH-PPV films were also spin-coated on the UV-ozone treated ITO substrates with a spin rate of 4800 rpm for 30 s and dried in vacuum of  $10^4$  Pa at 100 °C for 12 hrs. Exposition to UV irradiation + ozone of thin films under investigation were done with low-pressure mercury lamp with the total UV intensity at the sample surface of 2 mW/cm<sup>2</sup> and the ozone concentration was 150 mg/m<sup>3</sup>.

### 2.2. Isothermal charge transient spectroscopy - IQTS

The principle of the method IQTS is based on the time representation of the charge, induced in the external circuit by the driving pulse applied to the sample. This charge may be either due to the bulk relaxation processes, charge redistribution or release of charges from localized centres (traps). In this respect it is very similar to the method of post-transit extraction spectroscopy, where charges released from traps are time resolved collected and evaluated spectroscopically [1]. The IQTS spectrum is created by combining samples from charge transients at particular times using the formula  $\Delta Q(t_1) = Q(t_1) - 1.5Q(t_2 = 2t_1) - 0.5Q(t_3 = 4t_1)$  [8] (see Fig. 1). The rate window  $\tau$  defined by this filter is  $1/t_1$  and it removes the linear component of the response, which is caused by the integration of direct current. The peak maximum corresponds to 0.174 of the total collected charge  $Q_0$  responsible for the peak. Omitting the excitation pulse and the charge processing using the filter formula  $I_{DC} = (Q(t_2) - Q(t_1)) / (t_2 - t_1)$  (see Fig.1) allows to evaluate direct current which flows through the sample. The measurement of current-voltage (I-V) characteristic is obtained by sweeping the bias voltage applied to the sample.

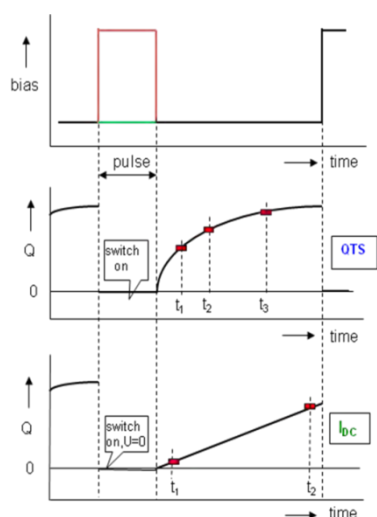
Electronic transport measurements were performed with charge transient processor (CTP) in local mode [9] when the usual evaporated top electrode is replaced by the tip of the scanning probe in form of a sharpened 80- $\mu$ m-tungsten wire oriented perpendicularly to the surface. The charge to voltage converter has the resolution of hundreds of electrons and time resolved transients from 2  $\mu$ s to hundreds of ms can be recorded. The duration of excitation pulses was set from 1 to 100 ms, their amplitude from 2 to 5 V, and the period from 147 to 547 ms. To reduce the noise usually 50 transients were collected and averaged. The I-V characteristics were measured with the sweeping rate of 100 mV/s. All IQTS and I-V measurements were done at room temperature.

### 2.3. Double step volt coulometry - DSVCM

The double step volt coulometry (DSVCM) is a complementary method for studying the electrochemical processes in investigated material. While with the help of the electrical

methods the concentration of the active species and their energies either for the capture or for the emission from a defect/deep trap is measured, electrochemical methods yield the potential at which either reduction or oxidation of species under consideration take place. Realizing that oxidation describes the loss of electrons, while the reduction describes the gain of electrons, the emission from electron traps can be regarded as an oxidation process, the capture of electrons in electron traps as a reduction process. On the contrary, for hole traps the emission of holes from hole traps can be regarded as a reduction process, the capture of holes in hole traps as an oxidation process. Thereby the electrochemical methods can serve as a complementary and powerful tool for the study of the defect states formation or removing in organic semiconductors. Recently, we have reported the electrochemical observation of the formation of hydrogen- and hydroxyl-related defects in pentacene thin films [10].

The electrochemical analyser used in this work, developed in our laboratory, is similar in function to CTP [11]. During the single potential scan both the ramp voltage (voltammetric wave) and the incremental charge (voltcoulometric signal) are obtained. The excitation pulse is switched on and the transient current flowing in external circuit is integrated and processed by the time-domain filter  $\Delta Q(t_1) = Q(t_1) - 2Q(t_2 = 5t_1) - Q(t_3 = 9t_1)$ . This filtering scheme analogous to filter for IQTS eliminates both the constant and linear components of the signal, i.e. suppression of both the steady-state and capacitive contributions of the transient current with respect to the diffusion current contribution. The amplitude of measured signal reflects not only the concentration of measured species, but also the kinetics of the measured charge transfer. A peak present only at the recorded voltcoulometric signal, which is not accompanied with a voltammetric wave, originates in the charging of an electrical double layer only.



$$\Delta Q = Q(t_1) + aQ(t_2) + bQ(t_3),$$

$$I_{DC} = \left[ \frac{Q(t_2) - Q(t_1)}{t_2 - t_1} \right].$$

Fig. 1. Timing chart of the applied voltage and measured charge transients used for isothermal charge transient spectroscopy (IQTS), direct current,  $I_{DC}$ , measurement, and double step voltcoulometry (DSVCM). The coefficients  $a$ ,  $b$ ,  $t_2$ , and  $t_3$  are set as follows  $a = -1.5$ ,  $b = 0.5$ ,  $t_2 = 2t_1$ ,  $t_3 = 4t_1$  for IQTS and  $a = -2$ ,  $b = 1$ ,  $t_2 = 5t_1$ ,  $t_3 = 9t_1$  for DSVCM.

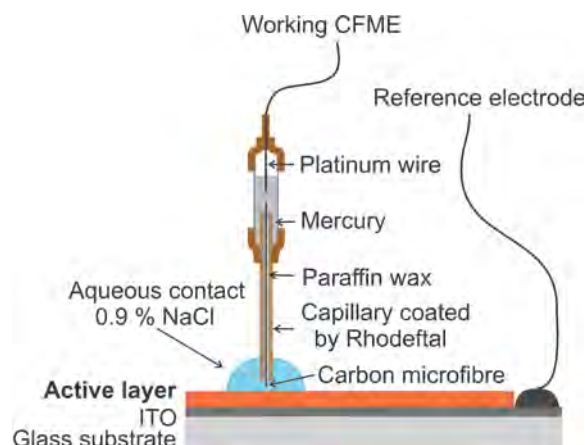


Fig. 2. Setup of electrochemical experiments.

The electrochemical experiments were carried out by the apparatus depicted in Fig. 2. The working carbon fiber microelectrode (CFME) was formed of a glass micropipette with up to eight carbon fibers (diameter of each fiber being approximately 7 - 8  $\mu\text{m}$ ). The pipette tip (diameter 100 - 150  $\mu\text{m}$ ) was filled with paraffin wax to prevent liquid from seeping inside around the carbon fibers. The exposed surfaces of the filaments were treated electrochemically before starting the experiments. First, a cathodic potential of - 0.8 V was applied for 40 s, followed by a triangular waveform of 0 to + 3 V for 10 s; finally, an anodic potential of + 1.5 V was applied for 10 s. The reported results correspond to the measurements made for the sweeping rate of 33.3  $\text{mVs}^{-1}$ , the potential step amplitude for the volt coulometric period of measurement was set to - 0.1 V and to 0.1 V for the anodic and cathodic scans, respectively.

### 3. Results

The representative signals measured on the PMPSi samples are in Figs. 3, 4, 5 for the fresh sample and subsequently degraded by the UV in time steps 2, 5 and 10 min. The remarkable increase in hole injection ability of the ITO contact was recorded (Fig.3a). The IQTS signal (Fig. 3b) measured on identical spots shows first neither the bulk relaxation processes or trapping states, on UV degradation gradual development of the hole trap states is observed, with the most expressed signal at  $t_1 = 1.5$  ms for degradation time 10 min. To examine the time dependence of the emitted carriers from the traps, the influence of the extraction voltage ( $U_b$ ), keeping the injecting charge constant (given by  $U_b - \Delta U$ ) were measured (see Fig. 4). The signal shifts to shorter times  $t_1$  with increasing  $U_b$  as expected due to the shorter extraction. On the contrary when applying the injecting voltage on tungsten electrode, it results in virtually no filling of the trapping states and only small IQTS signal is detected.

The steady-state voltammetry and DSVC signals on identical samples of PMPSi are in Fig. 5a for anodic scans (ramp voltage is going from -1.5V to 1.5V) and in Fig. 5b for cathodic scans (from 1.5 V to -1.5 V). Steady-state voltammetry offers potential – current characteristics, where the presence of electrically active centre (defect) is detected by the presence of voltammetric wave, whose amplitude is proportional to the concentration of this centre. Therefore, the increasing current wave near the potential of + 0.8 V depicted in Fig. 5a corresponds to evolution of a defect in PMPSi, which is caused by the exposure of the PMPSi

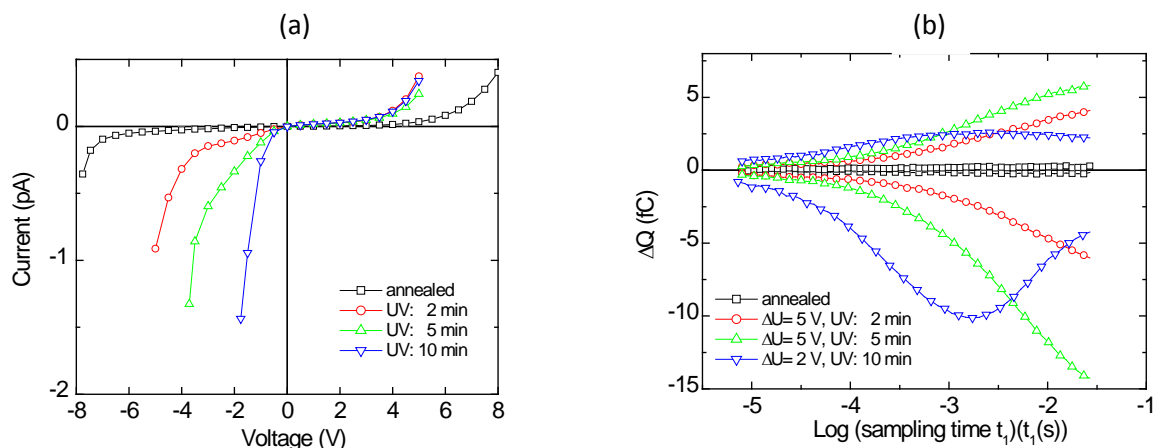


Fig. 3. Evolution of current – voltage characteristics (a) and IQTS spectra (b) of the structure ITO /PMPSi/ W probe with exposition time to UV irradiation. IQTS spectra in upper and lower parts correspond to excitation with positive and negative pulses. Bias voltage,  $U_b = 0$ , the height of excitation pulses takes into account the electrical conductivity of the PMPSi film: 5 V for annealed, 2, and 5 m in for irradiated samples, 2 V for 10 m in irradiated sample. The period and duration of excitation pulses were set to 147 ms and 10 ms, respectively.

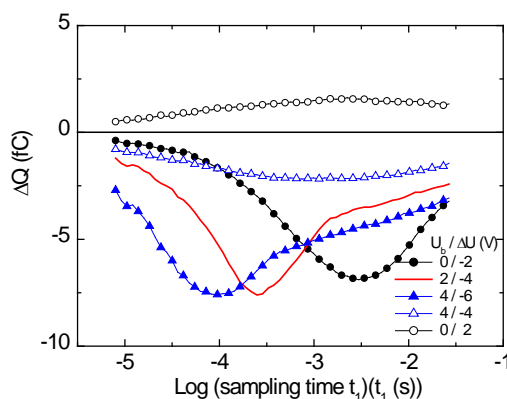


Fig. 4. Effect of bias voltage and the height of excitation pulses on the IQTS peak observed on ITO / PMPSi / tungsten probe structure after 10 min of exposure to UV irradiation. The period and duration of excitation pulses were set to 147 ms and 10 ms, respectively.

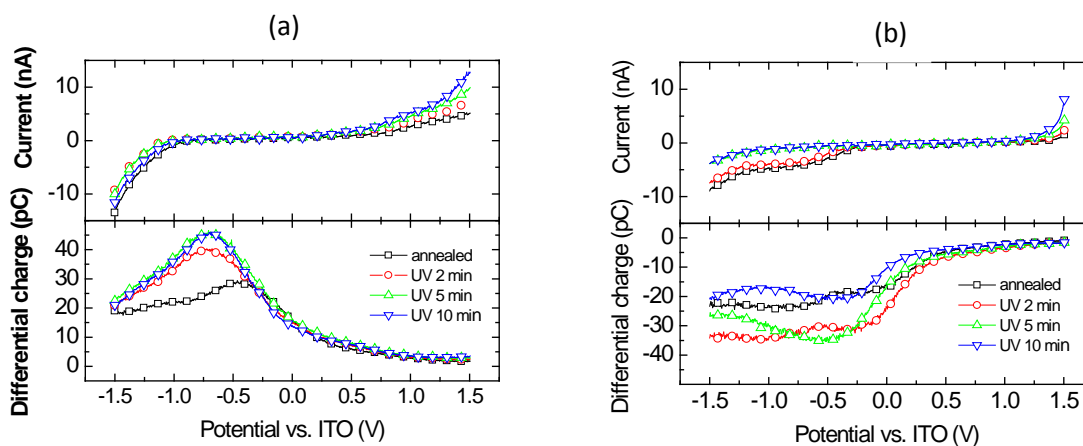


Fig. 5. Voltammetric (upper part) and voltacoulometric (lower part) signals obtained for PMPSi thin film during (a) **anodic scans**, i.e., for the potential swept from -1.5 V to 1.5 V and (b) **cathodic scan**, i.e., for potential swept from 1.5 V to -1.5 V. Individual data sets have been obtained for various exposition times to UV irradiation.

to UV irradiation. The position of volt coulometric peak does not in general match the position of voltammetric wave on the I-V characteristic; the difference depends on the ratio of the apparent diffusion coefficients for the measured charge transfer of capture and emission of electrons or holes. Therefore, the tiny increase of volt coulometric signal observed at potential + 0.5 V (Fig. 5a, lower part) can be related to the voltammetric wave at + 0.8 V.

While the voltammetric wave (anodic scan) in Fig. 5a is caused by the capture of holes by trap or the emission of electrons from trap, voltammetric wave in Fig. 5b (cathodic scan) represents measurement of electron capture or hole emission from the trap. Thus, the discharge of the process at about - 0.5 V (observed on both the voltammetric and volt coulometric signals) can be regarded as drop-out of the ability of the PMPSi to capture electrons or emit holes from a PMPSi matrix after 5-minute exposure to UV irradiation. It should be noted that I-V characteristic and IQTS spectrum of annealed state was recovered by annealing the sample in vacuum at 80°C for 1 hour.

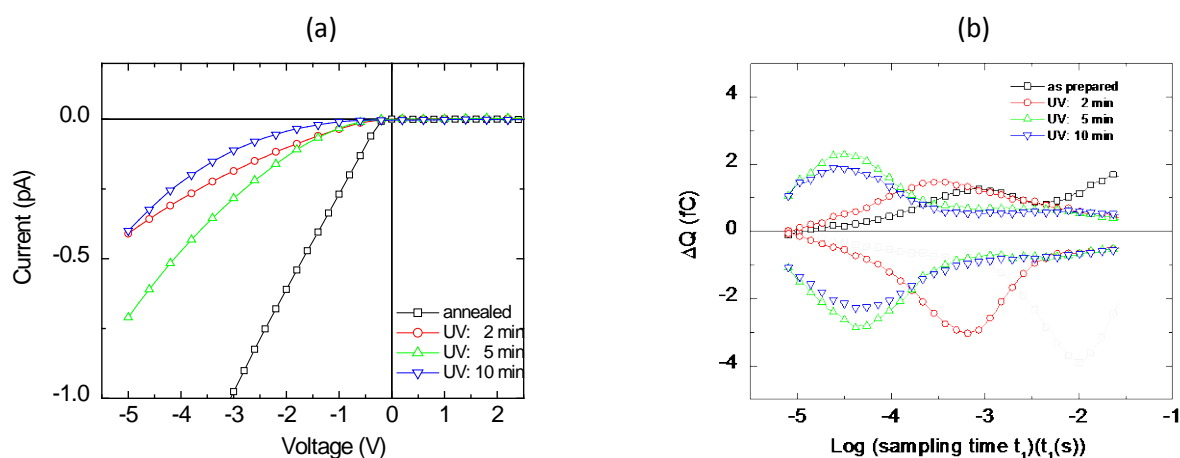


Fig. 6. Evolution of current – voltage characteristics (a) and IQTS spectra (b) of the structure ITO / MEH-PPV / tungsten probe with exposition time to UV irradiation. IQTS spectra in upper and lower parts correspond to excitation with positive and negative pulses. Bias voltage,  $U_b = 0$ , the height of excitation pulses was set to 5 V for annealed and exposed states. The period and duration of excitation pulses were set to 147 ms and 10 ms, respectively.

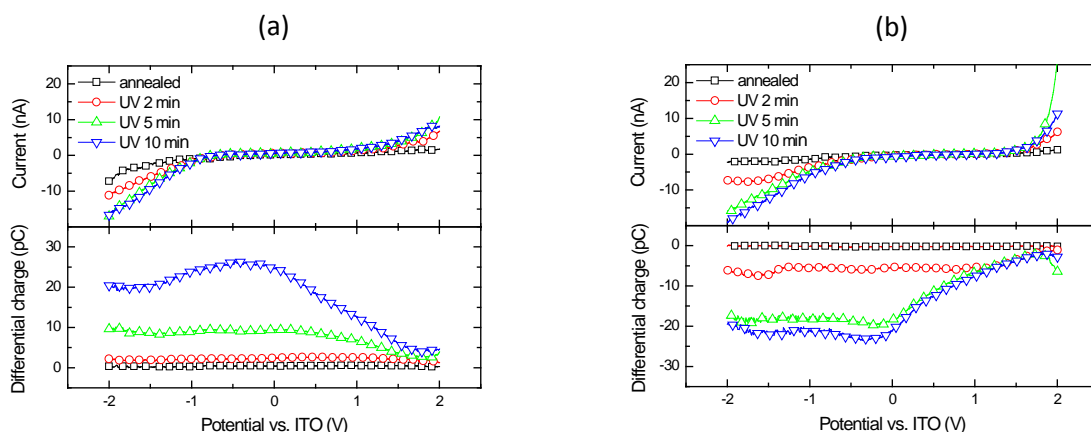


Fig. 7. Voltammetric (upper part) and volt coulometric (lower part) signals obtained on MEH-PPV thin film during (a) **anodic scan**, i.e. for potential swept from -1.5 V to 1.5 V and (b) **cathodic scan**, i.e. for potential swept from 1.5 V to -1.5 V. Individual data sets have been obtained for various exposition times to UV irradiation.

Similarly, the signals in MEH PPV are visible in Fig. 6a (I-V) and Fig. 6b (IQTS). The behavior is quite different, as the injecting properties with UV irradiation decrease, contrary to PMPSi. The IQTS signals depict no trapping, but only bulk relaxation effects, testified by symmetrical signals for both polarities, independent on injection. Also, the DSVCM signals in Fig. 7a (anodic scan) and in Fig. 7b (cathodic scan) give evidence of the evolution of a charge transfer process caused by UV at about  $-1.5$  V.

#### 4. Discussion and conclusions

In Fig. 8 there are the results of post-transit spectroscopy on PMPSi achieved by large signal transient SCLC [1]. The extreme filling of the traps was achieved by laser injection. On UV degradation the Si-Si  $\sigma$  bond breaking leads to the metastable states at about  $0.55$  eV, which are fully reconstructed on annealed [1]. The method is identical to IQTS with much less influence on the sample (UV laser used) due to its extreme sensitivity.

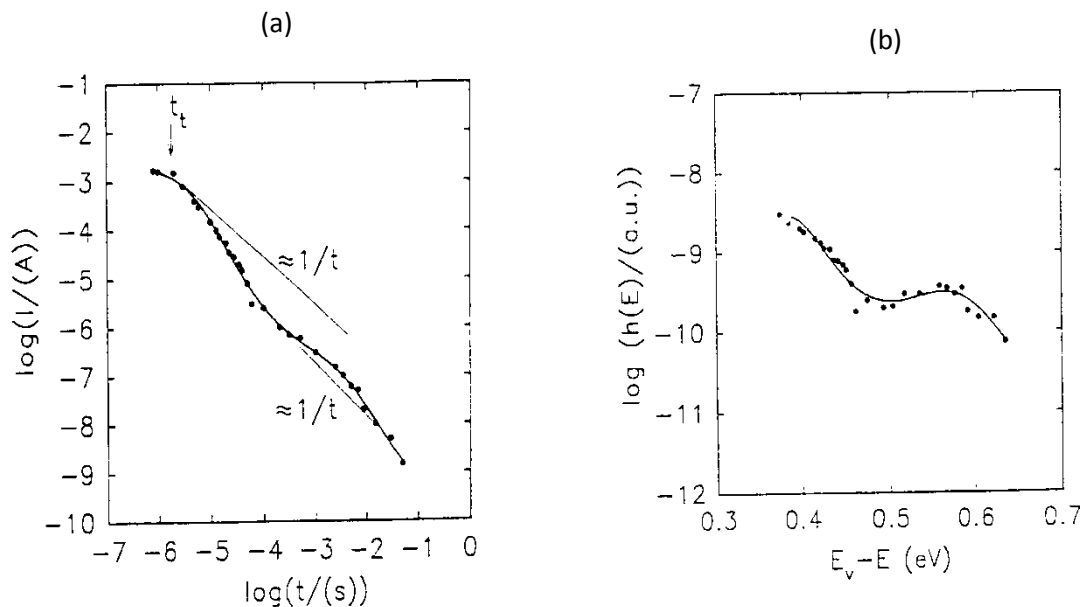


Fig. 8 The post-transit current in large signal SCLC on PMPSi (a), the corresponding DOS distribution (b).

UV irradiation causes bulk modification of both PMPSi and MEH-PPV films under investigation. It is remarkable that the same degradation treatment leads to opposite effect on I-V characteristics. The hole injection in the metal insulator metal (MIM) structure with PMPSi increases but that with MEH-PPV shows decrease of hole injection with degradation. The evolution of corresponding IQTS spectra (Fig. 3b and 6b), voltammetric, and voltacoulometric signals (Figs. 5 and 7) with time exposition to UV irradiation are rather complex. However, some common trends in their behavior can be inferred from the comparison with the evolution of I-V characteristics. Improvement of the hole injection for PMPSi leads to asymmetry of IQTS spectra for negative and positive polarity of excitation pulses. In voltamogram, decay of the current wave at negative potential of  $-0.5$  V is observed and the voltammetric wave at  $+0.8$  V is simultaneously developed. Deterioration of the injection for the structure with MEH-PPV is correlated with the development of symmetric

IQTS peak located at about 50  $\mu$ s and voltammetric wave at about -1.5V. There is a clear two-step increase of this wave and shift in the IQTS peak position.

Steady-state voltammetry offers I-V characteristics, where the presence of electrically active centre (defect) is detected by the presence of voltammetric wave, which amplitude is proportional to the concentration of this centre. Voltammetric wave definitely reveals the presence of redox centers, i.e. electrically active traps. It means that in PMPSi some deep centers (continuum, corresponding to tail of IQTS spectra) decays and a shallower one arises. The increasing current wave near the potential of + 0.8 V depicted in Fig. 3 corresponds to evolution of a defect center in PMPSi caused by the exposure of the PMPSi to UV irradiation, which mediates charge transfer through redox reaction. On the other hand, the process at about - 0.5 V (observed on both the voltammetric and volt coulometric signals) can be regarded as drop-out of other redox centre in PMPSi matrix after 5-minute exposition to UV irradiation + ozone. This process is accompanied with more effective hole injection. In the case of MEH-PPV, voltammetric wave at -1.5 V indicates a redox centre (trap). The IQTS peak position at 50  $\mu$ s supposes relatively shallow trap. The determination of the activation will require IQTS measurements at several temperatures.

### Acknowledgements

The work in Slovak Republic was supported by the ASFEU project Effective control of production and consumption of energy from renewable resources, Activity 4.2, ITMS code 26240220028, supported by the Research & Development Operational Programme funded by the ERDF and by Slovak grant agency VEGA, projects 2/0093/10 and 2/0063/11.

### References

- [1] F. Schauer, Space-charge-limited photoconductivity in polymers, Czech. J. Phys. 49, 1999, p. 871.
- [2] J. Steiger, R. Schmechel, H. von Seggern, Synthet. Metals 129, 2002, p. 1.
- [3] A.J. Campbell, D.D.C. Bradley, E. Werner, W. Brutting, Organic Electr. 1, 2000, p. 21.
- [4] Y.S. Yang, S.H. Kim, J. Lee, H.Y. Chu, L. Do, H. Lee, J. Oh, T. Zyung, Appl. Phys. Lett. 80, 2002, p. 1595.
- [5] C. Renaud, T.P. Nguyen, J. Appl. Phys. 107, 2010, p. 124505.
- [6] I. Thurzo, H. Mendez, D.R.T. Zahn, phys. stat. sol (a) 202, 2005, p. 1994.
- [7] P.J. Kulesza, J.M. Cox, Electroanalysis 10, 1998, p. 73.
- [8] I. Thurzo, K. Gmucová, Rev. Sci. Instrum. 65, 1994, p. 2244.
- [9] Š. Lányi, V. Nádaždy, Ultramicroscopy 110, 2010, p. 685.
- [10] K. Gmucová, M. Weis, M. Della Pirriera, J. Puigdollers, phys. stat. sol. (a) 206, 2009, p. 1404.
- [11] I. Thurzo, K. Gmucová, J. Orlický, J. Pavlásek, Rev. Sci. Instrum. 70, 1999, p. 3723.

## Fabrication of Annealing-Free High Efficiency and Large Area Polymer Solar Cells by Roller Painting Process

Jae Woong Jung, Won Ho Jo\*

*Department of Materials Science and Engineering, Seoul National University, Seoul, Korea*

*\* Corresponding author. Tel: +8228807192, Fax: +8228766086, E-mail:whjpoly@snu.ac.kr*

---

**Abstract:** The polymer solar cells were fabricated by a novel solution coating process, the roller painting. The roller painted film composed of poly(3-hexylthiophene) (P3HT) and [6,6]-phenyl-C61-butyric acid methyl ester (PCBM) has smoother surface than the spin coated film. Since the roller painting is accompanied with shear and normal stresses and is also a slow drying process, the process induces effectively crystallization of P3HT and PCBM. Both crystalline P3HT and PCBM in the roller painted active layer contribute to enhanced and balanced charge carrier mobility. Consequently, the roller painting process results in higher power conversion efficiency (PCE) of 4.6% as compared to that of the spin coating (3.9%). Furthermore, the annealing-free polymer solar cell (PSC) with high PCE were fabricated by the roller painting process with addition of a small amount of 1,8-octanedithiol. Since the addition of 1,8-octanedithiol induces phase separation between P3HT and PCBM and the roller painting process induces crystallization of P3HT and PCBM, the PCE of roller painted PSC is achieved up to 3.8% without post-annealing.

**Keywords:** Roller Painting, Thin Films, Polymer Solar Cells, Device Performance

---

### 1. Introduction

Polymer solar cells (PSCs) provide special opportunities for low cost, printable, light-weight, flexible, and portable energy source [1]. Over the last decade, these advantages of the PSCs have encouraged intensive research on PSCs, and as a result remarkable improvement has been achieved by molecular engineering, morphology control, and device optimization [2-6]. To date, the power conversion efficiency (PCE) over 5% has been obtained by using poly(3-hexylthiophene) (P3HT) or various low-bandgap polymers as a donor and [6,6]-phenyl-C<sub>60</sub>-butyric acid methyl ester (PCBM) as an acceptor [7-10]. Therefore, the P3HT/PCBM combination is one of very promising candidates for commercialization of PSCs.

For commercialization, however, the fabrication process for mass production must be developed [11,12]. Most of the PSCs are manufactured through the spin coating process. Although the spin coating is very useful for fabricating very thin and homogeneous film and for controlling the film thickness [13], the spin coating process has several detrimental problems with mass production. First, the spin coating is not only difficult to scale up but also impossible to fabricate flexible devices. Second, the cost of the process is high, because the spin coating process causes inevitably waste of materials, and furthermore the cost of process increases exponentially as the substrate size increases. Third, as the spin coating is not a continuous process, this process has serious limitation for industrial production.

To overcome these problems, various methods for fabrication of PSCs have been proposed including doctor blading [14,15], ink-jet printing [16], spray coating [17-20], screen printing [21] and brush painting [22]. Although these processes have an advantage for fabrication of large area films and exhibit comparable performance to the spin coating, the thickness control and inhomogeneity of the film still remain unsolved. In spray coating and brush painting, the film uniformity is not satisfactory. Particularly, the quality of thin film in large area cannot be guaranteed through these processes. Therefore, the development of alternative solution process which is low-cost, easy-to-use and continuous is strongly

demanded.

The roller painting process is easy-to-use, high throughput and the most widely used method for conventional painting. The substrate size for the roller painting is limitless, and the process cost is also low since the roller painting is a continuous process. Especially, an advantage of the roller painting compared to other coating processes is easiness to control film thickness and uniformity. Since the roller painting is very promising process for the industry of thin film fabrication, it can be used for fabrication of organic electronics including PSCs. In this work, we report the PSCs fabricated by the roller painting, primarily based on our previous report [23].

Furthermore, the roller painting process has another advantage in development of active layer morphology in PSCs, because the process is accompanied with shear and normal stresses. It is well known that the crystalline polymer such as P3HT can be effectively crystallized when the shear or normal stress such as nano rubbing, molecular reflow and nano imprinting is applied [24]. Particularly, Kim et al. [22] have reported that high efficiency PSCs are fabricated by using the brush painting because the shear stress during the brush painting induces the ordering of P3HT chains. Therefore, it is easily expected that the roller painting process which accompanies both the shear and normal stresses induces effectively the crystallization of P3HT and PCBM, and consequently yields enhanced solar cell performance.

## 2. Experimental

### 2.1. Materials

P3HT (Rieke Metals, 90-93% regioregular) and PCBM (Nano-C, 99.5%) were used as received. Poly(3,4-ethylenedioxy thiophene):poly(styrene sulfonate) (PEDOT:PSS) (Baytron P VP AI 4083) was purchased from H. C. Stark. For the roller painting process, rubber roller (Hwa Hong) was wrapped with thin PET film to give smooth surface.

### 2.2. Fabrication of polymer solar cells

ITO-coated glass ( $15 \Omega/\square$ ) was cleaned with acetone and isopropyl alcohol, and then dried at 200 °C for 30 min. After complete drying, the ITO-coated glass was treated with UV-ozone for 15 min, and then PEDOT:PSS was spin coated with 40 nm in thickness, and the PEDOT:PSS film was annealed at 120 °C for 30 min in a N<sub>2</sub>-filled glove box. P3HT and PCBM (1:1 by weight) were dissolved in o-dichlorobenzene (DCB) with several different concentrations (2-8 wt%) to control the thickness of the roller painted thin film. These solutions were stirred for at least 24 h at room temperature and then were passed through a 0.45 μm PES syringe filter before roller painting. The roller painting was processed at room temperature in N<sub>2</sub>-filled glove box with the roller painting speed of 1 cm/s, and the roller painting was repeated 5 times. The spin coated PSCs were fabricated at 2500 rpm by using the solution with the same concentration as the roller painting. After complete drying of the active layer, Al (100 nm) were thermally evaporated on the top of the active layer under vacuum lower than 10<sup>-6</sup> Torr. The PSC devices were then thermally annealed at 150 °C inside the glove box. The annealing-free PSC devices were fabricated at room temperature by addition of 5 wt% 1,8-octanedithiol as an additive in the solution of active layer materials. LiF (0.7 nm) was thermally evaporated before the evaporation of Al.

### 2.3. Measurement and Characterization

The UV-visible absorption spectra of roller painted or spin coated P3HT:PCBM films were measured by UV-visible spectrophotometer (HP 8452A). The morphology of the active layer films were observed by TEM (JEOL, JEM-1010 and Tecnai F20). The thickness of thin film was measured by AFM. The crystallinity of active layer was investigated by X-ray

diffractometer (M18XHF-SRA). The photovoltaic performance was measured under nitrogen atmosphere inside a glove box. The current density-voltage (J-V) characteristics were measured with a Keithley 4200 source-meter under AM 1.5 G ( $100 \text{ mW/cm}^2$ ) simulated by a Newport-Oriel solar simulator. The light intensity was calibrated using a NREL certified photodiode and light source meter prior to each measurement. The IPCE was measured using a lock-in amplifier with a current preamplifier under short circuit current state with illumination of monochromatic light.

### 3. Results and Discussion

To examine the effect of the coating process on the crystallization of P3HT, we compared the XRD pattern of the film fabricated by the roller painting with the film fabricated by the spin coating. The pristine P3HT film fabricated by the roller painting shows very sharp and intense peak at  $2\theta = 5.6^\circ$  while the spin coated P3HT film exhibits relatively broad and lower peak intensity (see Fig. 1a). Also, the (200) and (300) peaks of as-roller painted P3HT film are more discernible than those of spin coated film, implying that the roller painting process induces higher crystallinity of P3HT than the spin coating process. The P3HT:PCBM blend film prepared by the roller painting also shows stronger and sharper peak than the spin coated films before thermal annealing, as shown in Figure 1b, indicating that P3HT in the blend film is more crystallized in the roller painted film than in the spin coated film. After thermal annealing, the intensity of (100) peak of the spin coated blend film is increased while the (100) peak of the roller painted blend film is nearly unchanged, indicating that P3HT in as-roller painted film is sufficiently crystallized during roller painting and thus the crystallization does not take place significantly during thermal annealing.

Since the diffraction angle at  $2\theta = 5.5^\circ$  corresponds to the (100) packing which is associated with the interdigitation of the alkyl chains of P3HT as shown in Figure 1b [26], the exact interchain spacing between P3HT chains can be determined from the diffraction angle of (100) peak. When the interspacing was calculated by using the Bragg law, the interchain spacings of the roller painted P3HT:PCBM film and the spin coated film are 1.6 nm and 1.7 nm, respectively. One of reasons for higher crystallinity and closer packing of roller painted film is that the normal and shear stress accompanied with the roller painting induces effectively alignment of P3HT chains which induces crystallization. Another reason for higher crystallinity of roller painted P3HT is slower drying of P3HT as compared to the spin coating process, which provides more time for P3HT to crystallize. These closely packed P3HT crystals would have an advantage in hopping and transport of hole carrier.

The effect of roller painting on the chain packing of P3HT was also observed by UV-Vis absorption spectroscopy (see Fig. 2a). Compared to the spin coated P3HT film, the absorption of the roller painted P3HT film is larger in the range of 520–640 nm wavelength. Since the thicknesses of both P3HT films are controlled the same, the larger absorption of the roller painted film is originated from close packing of the roller painted P3HT film [8]. The close packing of the roller painted P3HT is further evidenced by the distinct vibronic shoulder at 600 nm which has been assigned to highly delocalized excitation [26].

The absorption difference between the roller painted film and the spin coated film becomes more prominent in the P3HT/PCBM blend film, as shown in Figure 2b. The roller painted blend film exhibits the maximum absorption at 556 nm with a remarkable vibronic shoulder at 600 nm while the spin coated film does the maximum absorption at 522 nm with a weak vibronic shoulder. Moreover, the absorption intensity of the roller painted blend film is stronger than that of the spin coated film.

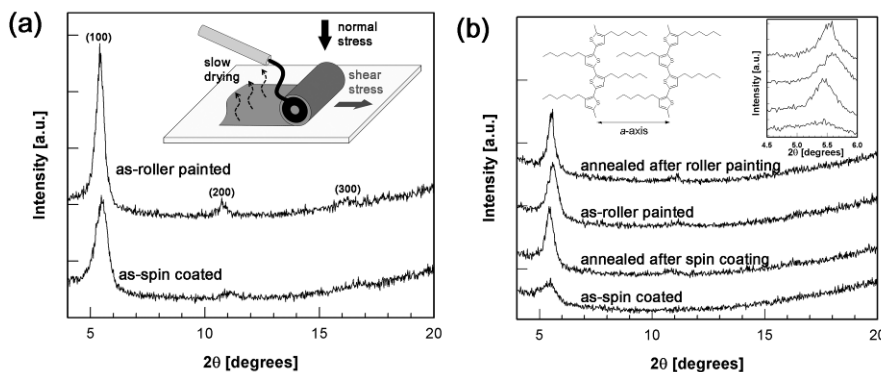


Fig. 1. XRD patterns of (a) P3HT films and (b) P3HT:PCBM films fabricated by the roller painting and the spin coating. Inset of Figure 2b clearly shows the shift of the (100) peak of the roller painted film compared to that of the spin coated film. Schematic illustration in Figure 2b shows the chain packing of regioregular P3HT in crystallite.

When the samples are annealed at 150 °C for 15 min, the absorption intensity of the spin coated film is increased, indicating that thermal annealing induces crystallization of P3HT in the blend film, whereas the absorption spectrum of the roller painted film does not increase significantly after thermal annealing. This result is consistent with the XRD measurement which exhibits almost the same crystallinity before and after annealing in the roller painted blend film (Fig. 1b). This high crystallization arising from the roller painting process without thermal annealing provides a very promising feature for the development of annealing-free PSCs for commercialization.

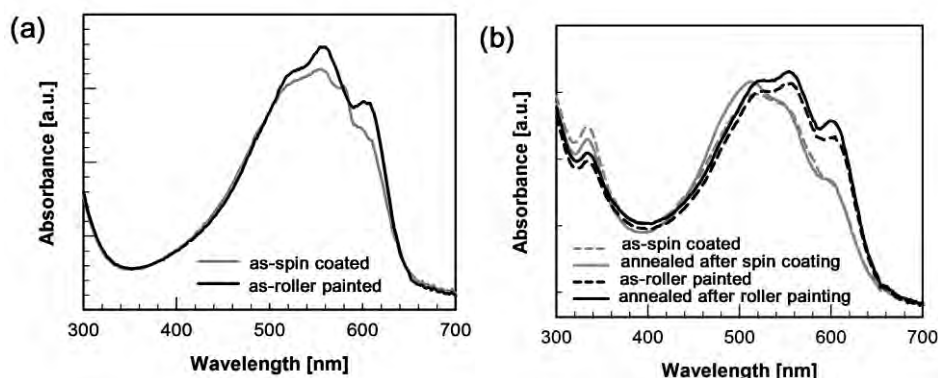


Fig. 2. UV-Vis absorption spectra of (a) pristine P3HT film and (b) P3HT:PCBM blend film fabricated by the roller painting and the spin coating.

The PCEs of the PSCs fabricated by the roller painting process are compared with those of the spin coating process in Table 1, and the corresponding current density-voltage (J-V) curves are shown in Figure 3a. To rationalize the measured values of the short circuit current density ( $J_{SC}$ ), we also calculated  $J_{SC}$  from the incident photon-to-current efficiency (IPCE) measured by using the same device (Fig. 3b). When the  $J_{SC}$  values from IPCE were compared with those of device values of  $J_{SC}$ , it revealed that two values were nearly equal within experimental errors. For the optimization of PCE, the samples are annealed after deposition of Al. The spin coated PSCs show the maximum PCE after thermal annealing for 15-20 min, while the roller painted PSCs show the maximum efficiency after annealing for 6-8 min at 150 °C. The maximum PCE of the roller painted solar cell is 4.6% which is 20% higher than the maximum PCE (3.9%) of the spin coated PSC. Since  $J_{SC}$  is nearly equal to that of the spin coated PSC under the optimum device condition, the main reason for higher PCE of the roller

printed PSC is slightly increased  $V_{OC}$ , and higher fill factor (FF) as compared with that of the spin coated PSC. Although the factors affecting FF are not completely identified yet [27], it has generally been accepted that FF is influenced by the morphology of the active layer, the balance between hole and electron mobility, and the interface of layers in PSC. Since we focused on the balance between hole and electron mobility in this study, we measured the charge transport from the dark current in a single-carrier device.

Table 1. Optimized performance of PSCs fabricated by roller painting or spin coating process. The thickness of the roller painted device and spin coated device are 245 nm and 230 nm, respectively.

Process	Annealing [min]	$V_{OC}$ [V]	$J_{SC}$ [mA/cm <sup>2</sup> ]	FF [%]	PCE [%]	$\mu_h$ [cm <sup>2</sup> /Vs]	$\mu_e$ [cm <sup>2</sup> /Vs]
Roller painting	0	0.57	7.5	0.56	2.4	$5.07 \times 10^{-5}$	$1.75 \times 10^{-4}$
	8	0.63	11.3	0.64	4.6	$1.56 \times 10^{-4}$	$3.90 \times 10^{-4}$
Spin coating	0	0.56	6.6	0.52	1.9	$6.52 \times 10^{-6}$	$4.50 \times 10^{-5}$
	15	0.61	11.1	0.58	3.9	$4.94 \times 10^{-5}$	$1.84 \times 10^{-4}$

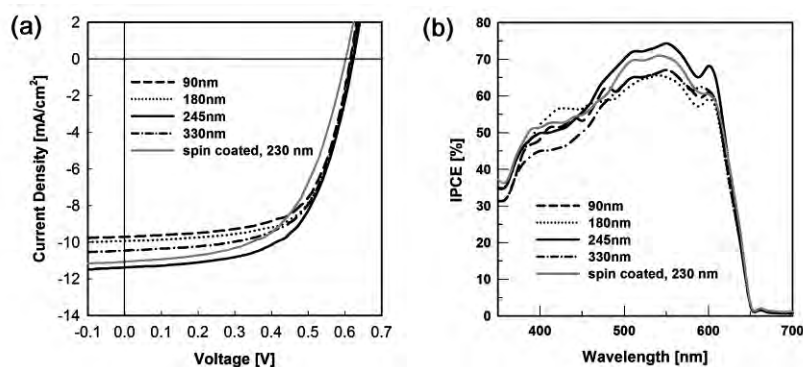


Fig. 3. (a)  $J$ - $V$  curves of PSCs ( $100 \text{ mW/cm}^2$ , AM 1.5G) fabricated by the roller painting with different thickness of active layer and the spin coating process, and (b) the corresponding IPCE spectra. All the devices are thermally annealed at  $150^\circ\text{C}$ .

The hole and electron single-carrier mobilities were measured by the standard methods. In the roller painted device, the values of  $\mu_h$  and  $\mu_e$  are  $5.07 \times 10^{-5} \text{ cm}^2 \text{ V}^{-1} \text{ s}^{-1}$  and  $1.75 \times 10^{-4} \text{ cm}^2 \text{ V}^{-1} \text{ s}^{-1}$ , respectively, before thermal annealing. These values are comparable to those of the spin coated device after thermal annealing. As shown in Figures 1 and 2, the crystallinity of P3HT in the as-roller painted film is almost the same as that of the spin coated film after thermal annealing. Therefore, it is expected that the holes are transported effectively through the network of P3HT crystals in the roller painted film without thermal annealing. After the thermal annealing, the  $\mu_e/\mu_h$  ratio of the roller painted device is decreased from 3.5 to 2.5. As a result, the mobility mismatch between hole and electron transport becomes smaller and thus the space charge effect becomes diminished in the roller painted device. Due to enhanced and balanced charge conduction in the roller painted P3HT:PCBM film, the high FF of 0.64 was achieved in the roller painted device.

When the nanoscale morphology of the active layer is examined by TEM, the as-roller painted film exhibits interesting morphology, as shown in Figure 4a: very dark, cilia-like nanocrystals (width  $\sim 20 \text{ nm}$  and length  $\sim 100 \text{ nm}$ ) are clearly observed. It is more interesting to observe that these nanocrystals are well packed and aligned normal to the rolling direction. This morphological characteristic is more pronounced after thermal annealing (see Fig. 4b). These nanocrystals must be grown from PCBM molecules, because PCBM phase is darker

compared to that of P3HT in bright-field TEM image. The selected area electron diffraction (SAED) pattern also identifies clearly the PCBM nanocrystal [29], as shown in the inset of Fig. 4b. The fact that PCBM nanocrystals can be developed through simple roller painting is remarkable. These well developed PCBM crystals are expected to contribute to the enhancement of electron mobility in the roller painted device. Although the reason for the morphology difference between the roller painted device and the spin coated one is not clear, it is probably because the shear and normal stresses during the roller painting induces the molecular ordering of PCBM along the direction of the roller painting (Fig. 4a).

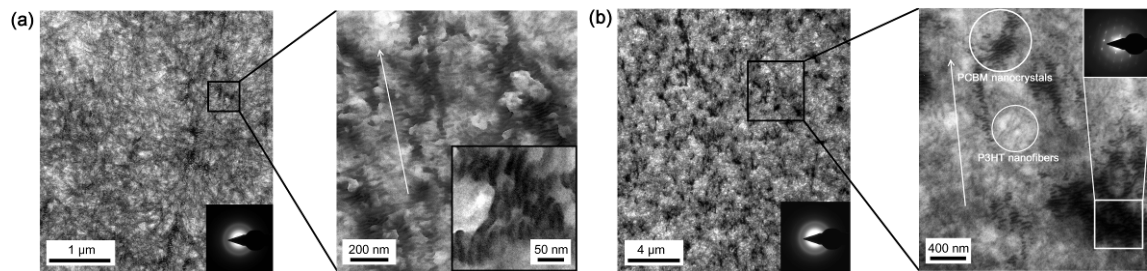


Fig. 4. Bright-field TEM images and the SAED patterns of P3HT:PCBM film fabricated by the roller painting (a) before and (b) after thermal annealing.

Achievement of highly efficient PSC without additional post-treatment is indispensable for industrialization of PSC. However, most of efficient PSCs based on P3HT and PCBM require an additional treatment such as thermal or solvent annealing which induces phase separation and enhances the crystallinity. Since the additional process increases the fabrication cost of PSCs, development of annealing-free PSC is strongly demanded. Furthermore, high temperature for thermal annealing may not be suitable for preparation of flexible PSCs. Recently, the method of simple blending with an additive, which has lower solubility to PCBM than *o*-dichlorobenzene and therefore accelerates phase separation of the blend of P3HT and PCBM, has been reported for achievement of high efficiency without thermal annealing. Although the method has achieved around 3% PCE without thermal or solvent annealing, the PCE value is still lower than the optimized device with annealing process.

We have fabricated the annealing-free large area (5 cm<sup>2</sup>) PSC device by combining the roller painting process with addition of 5 w t% 1,8-octanedithiol. When the performances of annealing-free devices fabricated by the roller painting are compared with those of spin coated device, the  $J_{SC}$  and FF of the roller painted PSC are higher than those of the spin coated PSC while  $V_{OC}$  of both processes are almost the same. The PCE of annealing-free device is 3.8% at the active area of 0.04 cm<sup>2</sup>. To the best of our knowledge, this value is the highest performance of annealing-free PSCs based on P3HT and PCBM.

#### 4. Conclusions

We have fabricated high efficiency PSCs by the roller painting process. Since the roller printing is accompanied with normal and shear stresses and is a slow drying process, it induces effective crystallization of P3HT and PCBM. As a result, the roller painted PSC of P3HT/PCBM has achieved 4.6% PCE, which is 20% higher than that of the device fabricated by the conventional spin coating process (3.9%). This higher efficiency is originated from higher FF and  $J_{SC}$  of the roller painted active layer. By addition of small amount of 1,8-octanedithiol as an additive, annealing-free PSCs were also fabricated by the roller painting. By combining the roller painting and incorporation of additive, the PCE of 3.8% was achieved without any post-treatment. This is because the roller painting process enhances the

crystallization of P3HT and PCBM, and the additive induces phase separation effectively. To the best of our knowledge, this value (3.8%) is the best performance of annealing-free PSC based on P3HT and PCBM. Since the PCE of over 2.7% can be achieved at 5 cm<sup>2</sup> active area by the roller painting without post-treatment, it is concluded that the roller painting process is a very promising method for fabrication of large area solar cells. In short, since the roller painting process follows the basic process of the roll-to-roll processing, this research provides a model study for preparation of roll-to-roll processed organic electronics.

## References

- [1] C. J. Brabec, N. S. Sariciftci, J. C. Hummelen, Plastic Solar Cells, *Adv. Funct. Mater.* 11, 2001, pp. 15-26.
- [2] G. Yu, A. J. Heeger, Charge separation and photovoltaic conversion in polymer composites with internal donor/acceptor heterojunctions, *J. Appl. Phys.* 78, 1995, pp. 4510-4515.
- [3] P. Schilinsky, U. Asawapirom, U. Scherf, M. Biele, C. J. Brabec, Influence of the Molecular Weight of Poly(3-hexylthiophene) on the Performance of Bulk Heterojunction Solar Cells, *Chem. Mater.* 17, 2005, pp. 2175-2180.
- [4] Y. K. Kim, S. Cook, S. M. Tuladhar, S. A. Choulis, J. Nelson, J. R. Durrant, D. D. C. Bradley, M. Giles, I. McCulloch, C. S. Ha, M. H. Ree, A strong regioregularity effect in self-organizing conjugated polymer films and high-efficiency polythiophene:fullerene solar cells, *Nat. Mater.* 5, 2006, pp. 197-203.
- [5] P. W. M. Blom, V. D. Mihailetschi, L. J. A. Koster, D. E. Markov, Device Physics of Polymer:Fullerene Bulk Heterojunction Solar Cells, *Adv. Mater.* 19, 2007, pp. 1551-1566.
- [6] G. Dennler, M. C. Scharber, C. J. Brabec, Polymer-Fullerene Bulk-Heterojunction Solar Cells, *Adv. Mater.* 21, 2009, pp. 1323-1338.
- [7] J. W. Jung, J. U. Lee, W. H. Jo, High-Efficiency Polymer Solar Cells with Water-Soluble and Self-Doped Conducting Polyaniline Graft Copolymer as Hole Transport Layer, *J. Phys. Chem. C* 114, 2010, pp. 633-637.
- [8] G. Li, V. Shrotriya, J. Huang, Y. Yao, T. Moriarty, K. Emery, Y. Yang, . High-efficiency solution processable polymer photovoltaic cells by self-organization of polymer blends, *Nat. Mater.* 4, 2005, pp. 864-868.
- [9] Ma, C. Yang, X. Gong, K. Lee, A. J. Heeger, Thermally Stable, Efficient Polymer Solar Cells with Nanoscale Control of the Interpenetrating Network Morphology, *Adv. Funct. Mater.* 15, 2005, pp. 1617-1622.
- [10] M. Campoy-Quiles, T. Ferenczi, T. Agostinelli, P. G. Etchegoin, Y. Kim, T. D. Anthopoulos, P. N. Stavrinou, D. D. C. Bradley, J. Nelson, Morphology evolution via self-organization and lateral and vertical diffusion in polymer:fullerene solar cell blends, *Nat. Mater.* 7, 2008, pp. 158-164.
- [11] F. C. Krebs, Processing and preparation of polymer and organic solar cells, *Sol. Energy Mater. Sol. Cells* 93, 2009, pp. 394-412.
- [12] F. C. Krebs, Roll-to-roll fabrication of monolithic large-area polymer solar cells free from indium-tin-oxide, *Sol. Energy Mater. Sol. Cells* 93, 2009, pp. 1636-1641.
- [13] Gunes, H. Neugebauer, N. S. Sariciftci, Conjugated Polymer-Based Organic Solar Cells *Chem. Rev.* 107, 2007, pp. 1324-1338.

- [14] C. J. Brabec, F. Padinger, J. C. Hummelen, R. A. Janssen, N. S. Sariciftci, Realization of large area flexible fullerene - conjugated polymer photocells: A route to plastic solar cells, *Synth. Met.* 102, 1999, pp. 861-864.
- [15] P. Schilinsky, C. Waldauf, C. J. Brabec, Performance Analysis of Printed Bulk Heterojunction Solar Cells, *Adv. Funct. Mater.* 16, 2006, pp. 1669-1672.
- [16] C. N. Hoth, S. A. Choulis, P. Schilinsky, C. J. Brabec, . On the effect of poly(3-hexylthiophene) regioregularity on inkjet printed organic solar cells, *J. Mater. Chem.* 19, 2009, pp. 5398-5404.
- [17] D. Vak, S. Kim, J. Jo, S. Oh, S. Na, J. Kim, D. Kim, Fabrication of organic bulk heterojunction solar cells by a spray deposition method for low-cost power generation, *Appl. Phys. Lett.* 91, 2007, 081102.
- [18] C. N. Hoth, R. Steim, P. Schilinsky, S. A Choulis, S. F. Tedde, O. Hayden, C. J. Brabec, Topographical and morphological aspects of spray coated organic photovoltaics , *Organ. Electron.* 10, 2009, pp. 587-593.
- [19] R. Green, A. Morpha, A. J. Ferguson, N. Kopidakis, G. Rumbles, S. E. Shaheen, Performance of bulk heterojunction photovoltaic devices prepared by airbrush spray deposition, *Appl. Phys. Lett.* 92, 2008, 33301.
- [20] K. X. Steirer, M. O. Reese, B. L. Rupert, N. Kopidakis, D. C. Olson, R. T. Collins, D. S. Ginley, Ultrasonic spray deposition for production of organic solar cells, *Sol. Energy Mater. Sol. Cells* 93, 2009, pp. 447-453.
- [21] F. C. Krebs, M. Jorgensen, K. Norrman, O. Hagemann, J. Alstrup, T. D. Nielsen, J. Fyenbo, K. Larsen, J. Kristensen, A complete process for production of flexible large area polymer solar cells entirely using screen printing—First public demonstration, *Sol. Energy Mater. Sol. Cells* 93, 2009, pp. 422-441.
- [22] S. Kim, S. Na, J. Jo, G. Tae, D. Kim, Efficient Polymer Solar Cells Fabricated by Simple Brush Painting, *Adv. Mater.* 19, 2007, pp. 4410-4415.
- [23] J. W. Jung, W. H. Jo, . Annealing-Free High Efficiency and Large Area Polymer Solar Cells Fabricated by a Roller Painting Process, *Adv. Funct. Mater.* 20, 2010, pp. 2355-2363.
- [24] G. Derue, S. Coppee, S. Gabriele, M. Surin, V. Geskin, F. Monteverde, P. Leclere, R. Lazzaroni, P. Damman, Nanorubbing of Polythiophene Surfaces, *J. Am. Chem. Soc.* 127, 2005, pp. 8018-8019.
- [25] H. Sirringhaus, P. J. Brown, R. H. Friend, M. M. Nielsen, K. Bechgaard, B. M. W. Langeveld-Voss, A. J. H. Spiering, R. A. J. Janssen, E. W. Meijer, P. Herwig, D. M. De Leeuw, Two-dimensional charge transport in self-organized, high-mobility conjugated polymers, *Nature* 401, 1999, pp. 685-688.
- [26] R. Osterbacka, C. P. An, X. M. Jiang, Z. V. Vardeny, Two-Dimensional Electronic Excitations in Self-Assembled Conjugated Polymer Nanocrystals, *Science* 287, 2000, pp. 839-842.
- [27] M. Kim, B. Kim, J. Kim, Effective Variables To Control the Fill Factor of Organic Photovoltaic Cells, *ACS Appl. Mater. & Interfaces* 1, 2009, pp. 1264-1269.
- [28] G. Lu, L. Li, X. Yang, Creating a Uniform Distribution of Fullerene C<sub>60</sub> Nanorods in a Polymer Matrix and its Photovoltaic Applications, *Small* 4, 2008, pp. 601-606.

## Bi-layer GaOHPc:PCBM/P3HT:PCBM organic solar cell

I.Kaulachs<sup>\*</sup>, I.Muzikante<sup>2</sup>, L.Gerca<sup>2</sup>, G.Shlihta<sup>1</sup>, P.Shipkovs<sup>1</sup>, G. Kashkarova<sup>1</sup>, M.Roze<sup>3</sup>,  
J.Kalnachs<sup>1</sup>, A.Murashov<sup>1</sup>, G.Rozite<sup>1</sup>

<sup>1</sup>Institute of Physical Energetics, Aizkraukles 21, Riga, Latvia;

<sup>2</sup>Institute of Solid State Physics, University of Latvia, Kengaraga str.8, Riga, Latvia;

<sup>3</sup>Riga Technical University, Azenes 14, Riga, Latvia.

corresponding author : tel. +371 67558666, e-mail kaulacs@edi.lv

**Abstract:** For production organic bulk heterojunction polymer solar cell one of the best materials is regioregular poly-3-hexylthiophene (P3HT), which is widely used as a donor molecule and a hole transporter, with soluble fullerene derivative (PCBM) as acceptor and electron transporter. The main drawback of this highly efficient blend is its limited spectral range, covering only 350-650 nm spectral interval. So main aim of present work was to extend the spectral range of the cell up to 850 nm by adding second bulk heterojunction layer of complementary absorption spectrum to P3HT:PCBM layer. For this purpose hydroxygallium phthalocyanine (GaOHPc) and PCBM blend was used as additional layer because GaOHPc has strong and wide intermolecular charge transfer (CT) absorption band around 830-850 nm. Thus novel organic bi-layer bulk heterojunction system (GaOHPc:PCBM/P3HT:PCBM) has been built by spin coating technique having high charge carrier photogeneration efficiency in 350 – 850 nm spectral range. It was found that thermal annealing in vacuum at 100C increases short circuit photocurrent external quantum efficiency (EQE) values more than 2 – 3 times, and these values reach more than 45% at P3HT absorption band (525 nm) and 25% at GaOHPc band (845 nm) for low light intensities ( $10^{12}$  photon/(cm<sup>2</sup>\*s)).

**Keywords:** Full polymer film, heterojunction, organic solar cell.

### 1. Introduction

At present, crystalline Si solar cells are by far most dominant PVs used, occupying more than 95% of the market [1]. But the main obstacle for the market implementation of these cells is the large production cost of Si-based technologies [2]. A promising approach towards low-cost photovoltaic devices is fabrication of solar cells based on organic materials [3-6]. The bulk heterojunction approach appears to be one of the most promising concepts of creating efficient, low-cost and easily producible solar cells [7,8]. For this purpose one of the best materials is regioregular poly-3-hexylthiophene (P3HT) [8-11], which is widely used as a donor molecule and a hole transporter, with soluble fullerene derivatives as acceptors and electron transporters. Blends of these molecules in PV cells exhibit the efficiency of light power conversion up to 5% [9-11]. Still, it is not sufficient to meet realistic requirements for commercialization. The main drawback of this highly efficient blend is its limited spectral range [7-9], which covers 350–650 nm interval, allowing only ~ 35% of the full solar spectrum energy to be used. In the present work, we tried to extend the spectral range of the cell by additional bulk heterojunction layer of hydroxygallium phthalocyanine (GaOHPc), which has a strong and wide intermolecular charge transfer (CT) band around 830 nm [12,13] and soluble fullerene PCBM. The choice of GaOHPc was dictated by the following reasons: 1) high thermal and chemical stability of phthalocyanines as compared with the most of molecular materials; 2) the NIR absorption providing the possibility to extend the photosensitivity spectral range (up to the NIR region) of the blend; 3) the CT character of the IR absorption band, which promises high efficiency of charge carrier photogeneration [13,14]; 4) the solubility in chloroform, which allows its processing by spin coating [12]. In this work we show, that by adding second bulk heterojunction layer of GaOHPc:PCBM to P3HT:PCBM cell we obtain bi-layer system GaOHPc:PCBM/ P3HT:PCBM which photosensitivity spectrum covers wide spectral range from 350 to 850 nm. It was found that

thermal annealing of cells in vacuum  $10^{-5}$  -  $10^{-6}$  mbar at 100C increases short circuit photocurrent external quantum efficiency (EQE) more than 2-3 times.

## 2. Methodology

For the electron donor and hole transporter in main bulk heterojunction layer we chose regioregular poly 3-hexylthiophene (P3HT) with an average molecular weight of 87000 (Sigma Aldrich) and for acceptor and electron transporter – [6,6]-Phenyl-C61 – butyric acid methyl ester (PCBM) with purity better than 99,5 % (from American Dye Source). The additional bulk heterojunction layer was composed from hydroxygallium phthalocyanine (GaOHPc) as electron donor and PCBM as electron acceptor. The molecules used and cell arrangement is shown in Figure 1.

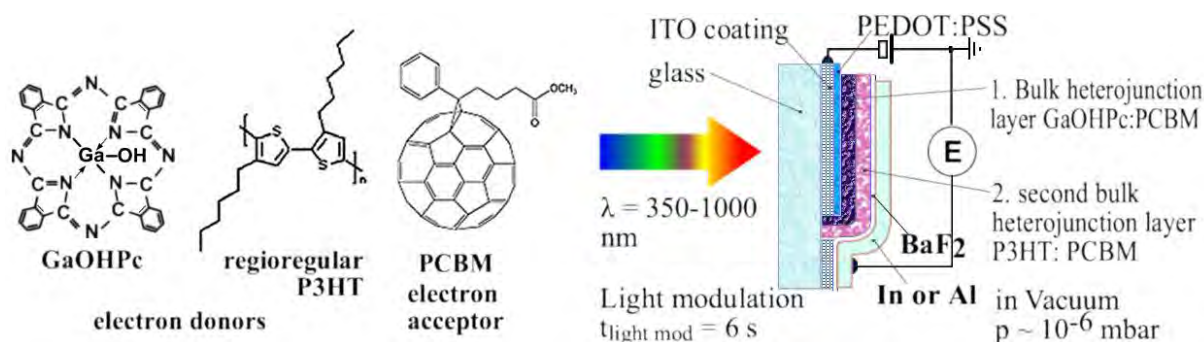


Fig. 1. Molecules used and cell arrangement.

As the sample substrate ITO – covered glass with  $R_{su} = 4\sim 10$  Ohm/Sq was used. The ITO electrode after cleaning and etching anode configuration was covered with a 30 nm thick PEDOT:PSS (Clevios 1000) plus 5% DMSO +5% isopropanol to increase its conductivity [15] by spin coating at 9000 rpm, and dried for 30 min. at 140C in vacuum  $10^{-5}$  mbar. This electrode was covered by GaOHPc:PCBM blend from the solution in chloroform and chlorobenzene mixture by spin coating. This procedure was repeated till optical density of GaOHPc:PCBM layer reaches 0.5 – 0.6 at 840 nm. After drying in vacuum  $10^{-5}$  mbar at 85C this layer was covered by second bulk heterojunction layer of P3HT:PCBM (1:1 by weight) by spin coating from the solution in chlorobenzene. As top electrode the In or Al was evaporated in vacuum of  $10^{-5}$  –  $10^{-6}$  mbar with surface resistance  $R_{su} \sim 10$  Ohm/Sq. In the case of In electrode, the 0.5 – 0.7 nm thick  $BaF_2$  layer was incorporated under In by evaporation in vacuum. The thickness of  $BaF_2$  layer during evaporation process in vacuum was controlled by 20 Mhz crystal oscillator and frequency meter. The photocurrent measurements were carried out at RT and 100C in vacuum of  $10^{-6}$  –  $10^{-5}$  mbar. The samples were illuminated using grating monochromator by chopper modulated monochromatic light through the ITO electrode in the 350 – 1000 nm spectral region with intensity  $10^9$  –  $10^{16}$  photon/( $cm^2 \cdot s$ ) (see Fig.1). Light modulation period was chosen as 6 s long and intensity was controlled by calibrated Si photodiode. The synchro-detection technique with the use of PC controlled data storage equipment [16] was employed for measuring the spectral dependences of photocurrent quantum efficiency:  $EQE = I_{photo}/\Phi$  (where  $I_{photo}$  is the photocurrent (electrons/s) and  $\Phi$  is photon flux (photons/s) incident upon the active area of sample)

## 3. Results and discussion

The spectral dependences of the external quantum efficiency (EQE) of short circuit photocurrent for low incident light intensities  $10^{11}$  –  $10^{12}$  photon/ ( $cm^2 \cdot s$ ) and the optical

properties of novel bi-layer bulk heterojunction system GaOHPc:PCBM/P3HT:PCBM are shown in Fig.2 for top Al electrode and Fig.3 for top BaF<sub>2</sub>/In electrode.

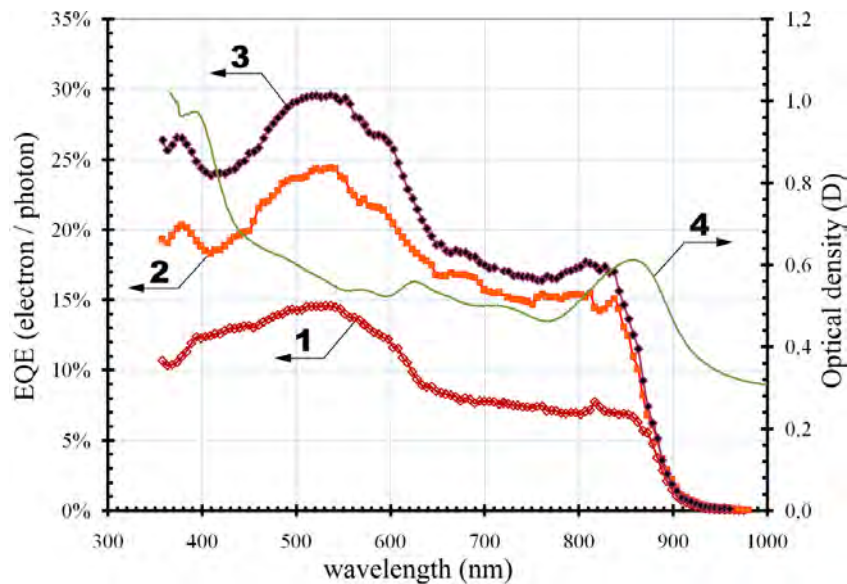


Fig. 2. Spectral dependences of external quantum efficiency (EQE) of short circuit photocurrent at light intensity  $10^{11}$  photon/( $\text{cm}^2 \cdot \text{s}$ ) and optical density for ITO/PEDOT:PSS/GaOHPc:PCBM/P3HT:PCBM/Al cell:

- 1 - EQE at room temperature (RT) for unheated sample;
- 2 - EQE at  $T = 100\text{C}$ ;
- 3 - EQE at RT after sample therm. annealing in vacuum at  $T = 100\text{C}$ ;
- 4 - Optical density of bi-layer system GaOHPc:PCBM/P3HT:PCBM.

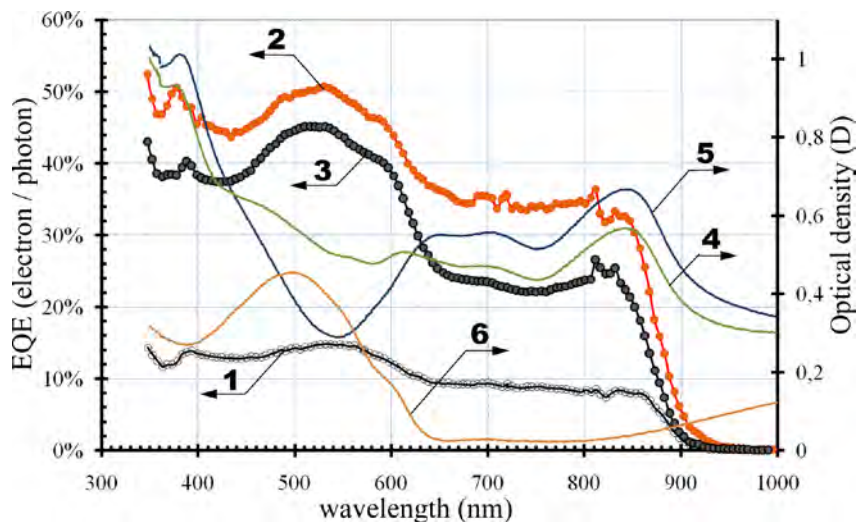


Fig. 3. Spectral dependences of external quantum efficiency (EQE) of short circuit photocurrent at light intensity  $10^{12}$  photon/( $\text{cm}^2 \cdot \text{s}$ ) and optical density for ITO/PEDOT:PSS/GaOHPc:PCBM/P3HT:PCBM/BaF<sub>2</sub>/In cell:

- 1 - EQE at room temperature (RT) for unheated sample;
- 2 - EQE at  $T=100\text{C}$ ;
- 3 - EQE at RT after sample annealing in vacuum at  $T=100\text{C}$ ;
- 4 - Optical density of bi-layer system GaOHPc:PCBM/P3HT:PCBM;
- 5 - Optical density of GaOHPc:PCBM layer;
- 6 - Optical density of P3HT:PCBM layer.

It is seen that absorption spectrum of GaOHPc:PCBM layer (curve 5 in Fig. 3) supplements well the P3HT:PCBM spectrum (curve 6 in Fig.3) enabling practically uniform absorption in 350 – 900 nm region of bi-layer bulk heterojunction system GaOHPc:PCBM/P3HT:PCBM (curves 4 in Fig.2 and Fig.3). Introducing GaOHPc:PCBM layer in the cell extends its photosensitivity spectrum beyond 850 nm (see curves 1 – 3 in Fig.2 and 3), but short circuit photocurrent EQE value for illumination in GaOHPc CT absorption band is 1.7 – 2 times less than for that in the P3HT absorption band possibly due to lower hole polaron mobility in GaOHPc fractal structure than in P3HT. The cell thermal annealing at 100C in vacuum for 48 hours after top electrode deposition significantly increases EQE values for all cells (compare curves 3 and 1 in Fig.2 and 3) due to change of morphology of used organic layers leading to increase of hole, and electron polaron mobilities and also probably by better contact with top electrode [10].

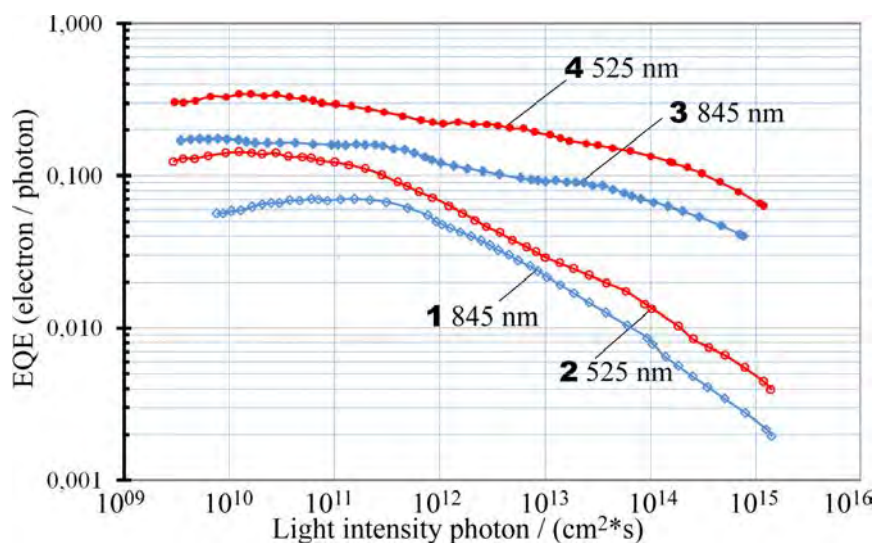


Fig. 4. Short circuit photocurrent external quantum efficiency (EQE) dependence on incident light intensity at room temperature for Al top electrode before annealing (curves 1,2) and after thermal annealing at 100C in vacuum (curves 3,4).

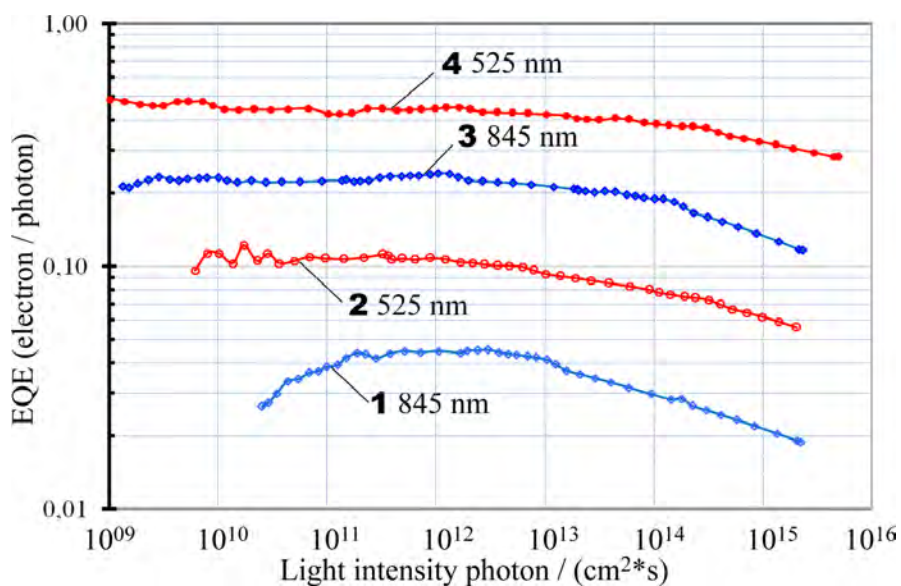


Fig. 5. Short circuit photocurrent external quantum efficiency (EQE) dependence on incident light intensity at room temperature for samples with In/BaF<sub>2</sub> electrode before annealing (curves 1,2) and after thermal annealing at 100C in vacuum (curves 3,4).

Highest EQE values were achieved for cells with top BaF<sub>2</sub>/In electrode which after annealing reached values more than 45% (electron/photon) at P3HT absorption band (525 nm) and 25% (electron/photon) at GaOHPc charge transfer absorption band (845 nm) (curve 3 Fig.3), at room temperature and light intensity 10<sup>12</sup> photon/(cm<sup>2</sup>\*s). By increasing light intensities, EQE values decrease as shown in Fig.4 and Fig.5 probably due to low charge carrier mobilities. This photocurrent sublinear dependence on light intensity diminishes after thermal annealing (compare curves 3,4 with 1,2 in Figs 4 and 5) supporting idea, that improvements by thermal annealing at least partly can be explained by increase of charge carriers mobilities. Comparing curves in Fig.4 and Fig.5, we see that cells with top BaF<sub>2</sub>/In electrodes has more linear photocurrent dependence on light intensity than cell with top Al electrode. Also fill factors (FF) are higher for cells with top BaF<sub>2</sub>/In electrode than Al electrode (compare photocurrent efficiency dependences on applied external voltage in Fig.7 and Fig.6). It possibly can be explained by too thick Al<sub>2</sub>O<sub>3</sub> formation under Al electrode, as spin coating procedure was performed in air and not in glove box with N<sub>2</sub> or argon atmosphere. So prepared organic layers would contain some O<sub>2</sub> in their volume which was not removed in vacuum camera before Al thermal deposition. This O<sub>2</sub> could slowly diffused out towards Al electrode during sample measuring procedure and form isolating Al<sub>2</sub>O<sub>3</sub> layer, as it was discovered by Fan and Faulkner in 1978 [17] even for samples prepared in vacuum by thermal deposition.

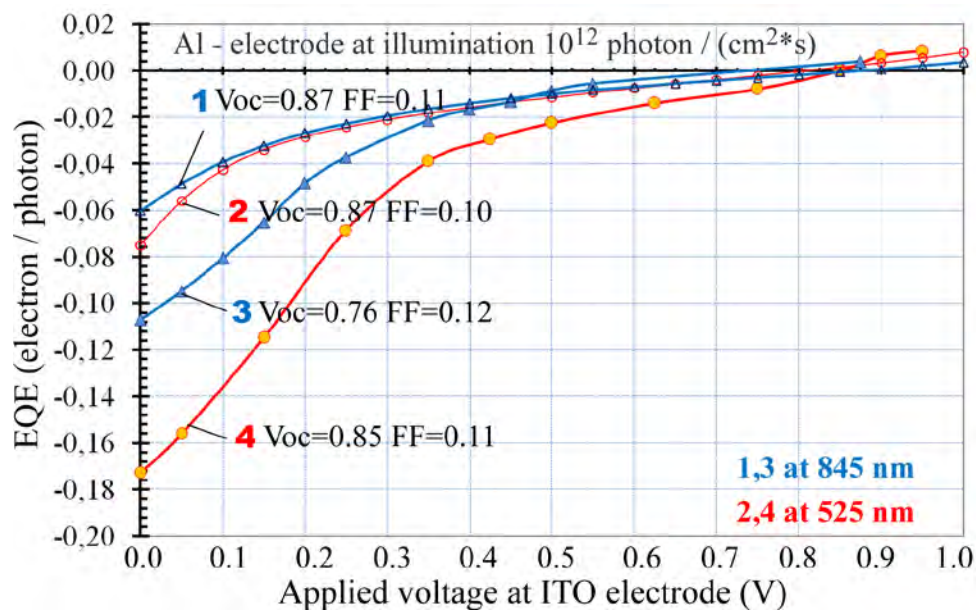


Fig. 6. Photocurrent EQE dependences on applied external voltage for cells with Al electrode at room temperature before annealing (curves 1,2) and after annealing at 100C (curves 3,4), at light intensity 10<sup>12</sup> photon/(cm<sup>2</sup>\*s). Also open circuit voltages (Voc) and fill factors (FF) are shown.

This could be the main reason for extremely low fill factor values (0.10 – 0.12) and high open circuit voltages Voc= 0.76 – 0.85 V for cells with top Al electrode (Fig.6). The cells with top BaF<sub>2</sub>/In electrode exhibit higher fill factor values: 0.21 - before annealing and 0.22 – 0.29 after annealing, but low open circuit voltages: 0.42 V - before annealing and 0.43 – 0.48 V after annealing (see Fig.7). These low FF values could be explained by high electric resistance of GaOHPc:PCBM layer which could be diminished in future by appropriate doping.

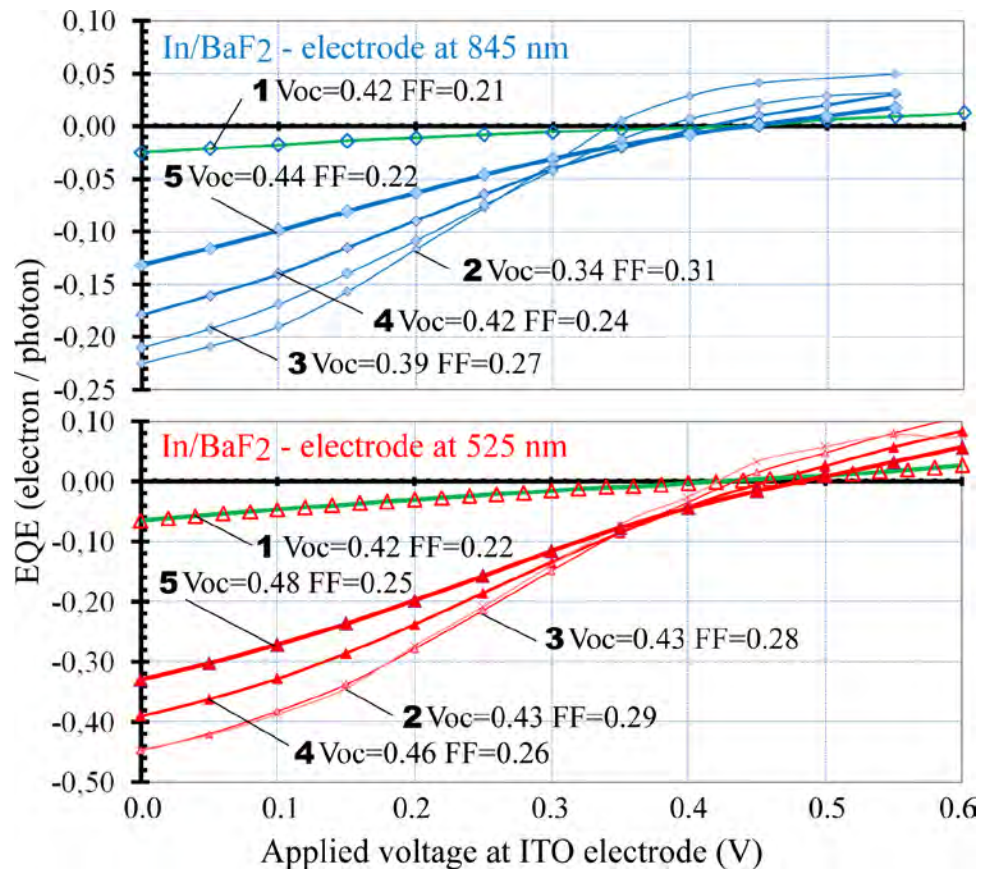


Fig. 7. Photocurrent EQE dependences on applied external voltage for cells with In/BaF<sub>2</sub> electrode at room temperature before annealing at light intensity 10<sup>15</sup> photon/(cm<sup>2</sup>\*s). (curves 1) and after annealing at 100C (curves 2-5), at following light intensities: 2 - 10<sup>12</sup> photon/(cm<sup>2</sup>\*s); 3 - 10<sup>13</sup> photon/(cm<sup>2</sup>\*s); 4 - 10<sup>14</sup> photon/(cm<sup>2</sup>\*s); 5 - 10<sup>15</sup> photon/(cm<sup>2</sup>\*s). Also open circuit voltages (Voc) and fill factors (FF) are shown.

#### 4. Conclusions

- 1) The novel organic bi-layer bulk heterojunction system is built having high charge carrier photogeneration efficiency in 350-850 nm spectral range at low light intensities.
- 2) Thermal annealing significantly increases EQE values for all cells.
- 3) Thermal annealing significantly increases linearity of photocurrent dependences from light intensity.
- 4) Cells with In/BaF<sub>2</sub> electrode have higher EQE values and fill factors, than cells with top Al electrode.

#### 5. Acknowledgments

The authors gratefully acknowledge the kind help of doctor V.Parra for synthesis of GaOHPc.

#### References

- [1] Portman J., and Arkhipov V, Thin Film Solar Cells: Fabrication, Characterization and Applications, John Wiley & Sons Ltd, 2006, pp. 471.
- [2] Lewerenz H. J., and Jungblut H, Photovoltaic – Grundlagen und Anwendungen Berlin, Heidelberg: Springer, 1995.

- [3] Shaheen S.E., Brabec C.J., Sariciftci N.S. Padinger F., Fromherz T., Humalen J.C, 2.5% Efficient Organic Solar Cells Appl. Phys. Lett., 78, 2001, pp. 841–843
- [4] Yu G., Gao J., Hummelen J.C., Wudl F., Heeger A.J, Polymer Photovoltaic Cells: enhanced efficiencies via a network of internal donor-acceptor heterojunctions, Science, 270, 1995, pp. 1789–1791
- [5] Peumans P., Forrest S.R, Very-high-efficiency double hetero-structure copper-phthalocyanine /C60 photovoltaic cells, Appl. Phys. Lett., 80 (2), 2002, pp. 338–338
- [6] Shaheen S.E., Radspinner R., Peyghambrian N., Jabbor G.E, Fabrication of bulk heterojunction plastic solar cells by screen printing, Appl. Phys. Lett. 79(18), 2001, pp. 2996–2998
- [7] Winder C., Sariciftci N.S, Low band gap polymers for photon harvesting in bulk heterojunction solar cells, J. of Materials Chemistry, 14, 2004, pp. 1077–1085
- [8] Al-Ibrahim M., Roth H.K., Zhokhavets U., Gobsch G., Sensfuss S, Flexible large area polymer solar cells based on poly(3-hexylthiophene)/fullerene, Solar Energy Materials & Solar Cell, 85, 2005, pp. 13–20
- [9] Kim J.Y., Kim S.H., Lee H., Lee. K., Ma W., Gong X., Heeger A.J, New architecture for high-efficiency polymer photovoltaic cells using solution-based titanium oxide as an optical spacer, Adv. Mater., 18, 2006, pp. 572–576
- [10] Ma W., Yang C., Gong X., Lee K., Heeger A.J, Thermally stable, efficient polymer solar cells with nanoscale control of the interpenetrating network morphology, Adv. Funct. Mater., 15, 2005, pp. 1617–1622
- [11] M.Lenes, A.H.Wetzelaer, F.B.Kooistra, S.C.Veenstra, J.C.Hummelen, W.M.Blom, Fullerene Bisadducts for Enhanced Open –Circuit Voltages and Efficiencies in Polymer Solar Cells, Adv.Mater, 20, 2008, pp. 2116-2119
- [12] Parra V., Vilar M.R, Battaglini N., Ferraria A.M., Botelho do R ego A.M., Boufi S., Rodríguez-Méndez M.L., Fonavs E., Muzikante I., Bouvet M, New Hybrid Films Based on Cellulose and Hydroxygallium Phthalocyanine: Synergetic Effects in the Structure and Properties, Langmuir 23 7, 2007, pp. 3712–3722
- [13] Yamasaki K., Okada O., Inami K., Oka K., Kotani M., Yamada H, Gallium Phthalocyanines: Structure Analysis and Electroabsorption Study, J. Phys. Chem., 101, 1997, pp. 13–19
- [14] Saito T., Sisk W., Kobaysashi T., Suzuki S., Iwayanagi T., Photocarrier Generation Processes of Phthalocyanines Studied by Photocurrent and Electroabsorption Measurements, J. Phys. Chem., 97, 1993, pp. 8026–8031
- [15] H.Do, M.Reinhard, H.Vogeler, A.Puetz, F.G.Klein, W.Schabel, A.Colsmann, U.Lemmer, Polymeric anodes from poly(3,4-ethylenedioxythiophene):poly (styrenesulfonate) for 3,5% efficient organic solar cells, Thin Solid Films, 517, 2009, pp. 5900-5902.
- [16] I.Kaulach., E.Silinsh. Molecular Triplet Exciton Generation via Optical Charge Transfer States in  $\alpha$  – Metal Free Phthalocyanine, Studied by Magnetic Field Effect, Latv. J. Phys. Tech. Sci., 5, 1994, pp. 12–22.
- [17] F.R.Fan, L.R.Faulkner, Photovoltaic effects of metal-free and zinc phthalocyanines, J.Chem.Phys. 69 (7), 1978, pp. 3334-3349.

## Pulse and direct current electrodeposition of zinc oxide layers for solar cells with extra thin absorbers

G. Khrypunov<sup>1,\*</sup>, N. Klochko<sup>1</sup>, N. Volkova<sup>2</sup>, V. Kopach<sup>1</sup>, V. Lyubov<sup>1</sup>, K. Klepikova<sup>1</sup>

<sup>1</sup>National Technical University “Kharkiv Polytechnic Institute”, Kharkiv, Ukraine

<sup>2</sup>National Aerospace University “Kharkiv Aviation Institute”, Kharkiv, Ukraine

\*Corresponding author. Tel: +380-572-971928, E-mail: khrip@ukr.net

---

**Abstract:** The feasibility of one-dimensional (1D) nanostructured zinc oxide array pulse plating has been presented. An effect of the electrolyte composition, deposition regime and subsequent annealing on structure and optical properties of the electrodeposited ZnO layers has been approved by X-ray diffraction and spectrophotometric analysis. We have determined that for obtaining of ZnO arrays with strong (002) preferable growth orientation in the c-axis direction it is necessary to diminish adsorption of hydrogen and Cl<sup>-</sup> ions. It has been shown that such conditions are created in electrolyte that contains 0.05 M Zn(NO<sub>3</sub>)<sub>2</sub> and 0.1 M NaNO<sub>3</sub> during electrodeposition on FTO-coated glass substrates in pulse plating regime with rectangular impulses of cathode potential (20 ms on-time at U<sub>on</sub> = -1.4 V and 30 ms off-time at U<sub>off</sub> = -0.8 V). Therefore, in this work we for the first time have demonstrated the successful growth of 1D ZnO nanostructures by pulse plating without using of templates. The novel electrodeposition technique gives possibilities for the manufacture of the ZnO arrays suitable for solar cells with extra thin absorbers.

**Keywords:** Electrodeposition, Zinc oxide, Pulse plating

---

### 1. Introduction

Zinc oxide (ZnO) has attracted a lot of research interest in recent years due to its unique optical and electronic properties and low cost of materials and fabrication. A wide variety of ZnO crystallite morphologies are observed for both precipitates and thin films including columnar grains, rods, stars and spherical habits [1-4]. Now highly transparent conducting ZnO windows are important components of photovoltaic devices and displays. Recently, solar cells with extra thin absorbers (ETA SC) have shown high potential of ZnO arrays as semiconductor covered electrodes and dye-sensitized photoanodes, particularly, ZnO nanorods proved to be suitable for application in organic photovoltaic devices [5, 6]. An assortment of ZnO nanostructures, such as whiskers, nanowires, nanorods, nanotubes, nanorings and nano-tetrapods have been successfully grown via a variety of methods including chemical vapor deposition, thermal evaporation, and electrodeposition. But despite numerous studies, there is little understanding of the mechanisms and factors that govern the observed morphology [1]. Among other deposition techniques electrodeposition has various advantages, viz. low processing cost, large scale, no vacuum system need, high deposition speed and no use of toxic gases. Effects of electrolyte formula, namely anionic composition [4] and presence of the different organic additives [6], deposition temperature and deposition time [7] and even gravitational level effects [9] on structure and properties of the electrodeposited ZnO nanowire arrays are studied extensively. Nevertheless, there are only rare attempts to employ a pulsed potential technique for ZnO electrodeposition [10]. On the same time, the use of pulse plating is well-known promising way to perfect properties of the electrodeposited layers. That's why purpose of this work is a comparative study of influence of direct current and pulse plating conditions, electrolyte composition and subsequent air annealing on ZnO film structure and optical properties in order to reveal means for obtaining of one-dimensional (1D) zinc oxide nanostructured layers applicable for ETA SC.

## 2. Methodology

ZnO arrays were electrodeposited on transparent indium tin oxide (ITO) or fluorine doped tin oxide (FTO) covered glass (Pilkington) cathodes in aqueous electrolytes contained ZnSO<sub>4</sub> or Zn(NO<sub>3</sub>)<sub>2</sub>, KCl and NaNO<sub>3</sub> (Table 1) in three-electrode cell with platinum counter-electrode and saturated Ag/AgCl reference electrode. Electrodeposition of each ZnO layer sample was carried out during 1 hour at 70 °C under potentiostatic conditions (at constant cathode potential U) or under pulse plating regimes with rectangular impulses of cathode potential (20 ms on-time at U<sub>on</sub> and 30 ms off-time at U<sub>off</sub>). All potential values in Table 1 are given versus saturated Ag/AgCl reference electrode. In some experiments electrolyte was magnetically stirred (marked + in Table 1). A following treatment of some ZnO layers was fulfilled by air annealing at 200 °C, 300 °C and 400 °C for 1 hour each.

Phase composition and structure of the deposited films were determined by XRD-method using an X-ray diffractometer DRON-4M with CoK<sub>α</sub> radiation according to θ-2θ- scheme. Preferable orientations of the films were researched by analytical treatment of the X-ray diffractions by means of obtaining of texture factor P<sub>i</sub> [11]:

$$P_i = \frac{(I_i/I_{0i}) \cdot N}{\sum_1^N I_i/I_{0i}} \quad (1)$$

where I<sub>i</sub> – experimental intensity of maximum; I<sub>0i</sub> – intensity of this line in accordance with JCPDS card; N – total number of X-ray reflections.

Angles φ between texture axis and surface normal for all reflection planes and P<sub>i</sub> values have been calculated according to relation [11]:

$$\cos \varphi = \frac{hh_i + kk_i + \frac{1}{2}(hk_i + h_i k) + \frac{3}{4} \frac{a^2}{c^2} l_i l}{\sqrt{h^2 + k^2 + hk + \frac{3}{4} \frac{a^2}{c^2} l^2} \sqrt{h_i^2 + k_i^2 + h_i k_i + \frac{3}{4} \frac{a^2}{c^2} l_i^2}} \quad (2)$$

A shape of function P = f(φ) allow [11] to distinguish degree of texture perfection: the texture is perfect if P decreases rapidly. When the function P = f(φ) has two or more vertexes, then the structure has two or some texture axes. Average crystalline sizes t (i. e. X-ray domains defined as volumes that diffract coherently) and lattice strains Δd/d of the electrodeposited ZnO arrays were determined by the Williamson-Hall formula for adherent deposits [12]. ZnO lattice characteristics a and c were calculated using the formula [11]:

$$\frac{1}{d^2} = \frac{4}{3} \frac{h^2 + hk + k^2}{a^2} + \frac{l^2}{c^2} \quad (3)$$

Table 1. Electrolytes and electrolysis regimes used for deposition of ZnO.

Sample number	Electrolyte	Deposition regime	Cathode potential (V)			Magnetic stirring	Current density $j$ (mA/cm <sup>2</sup> )	Charge-area ratio $q$ (C/cm <sup>2</sup> )
			U	U <sub>off</sub>	U <sub>on</sub>			
1 6.1	7·10 <sup>-4</sup> M ZnSO <sub>4</sub>	Potentiostatic	-1.3	-	-	-	+	2→1.4
2	0.1 M KCl	Pulse	-	-0.9	-1.5	+	+	1.3→0.5
3	0.05 M NaNO <sub>3</sub>	Pulse	-	-1.0	-1.6	+	+	2.6→1.5
4	7·10 <sup>-4</sup> M ZnSO <sub>4</sub> 0.1 M KCl 0.001 M NaNO <sub>3</sub>	Pulse	-	-0.9	-1.5	+	+	0.6→0.4
5	0.05 M Zn(NO <sub>3</sub> ) <sub>2</sub>	Potentiostatic	-1.1	-	-	-	-	1.1
6 2.3	0.1 M NaNO <sub>3</sub>	Pulse	-	-0.8	-1.4	-	-	0.5→0.8

The transmittance spectra of ZnO layers were measured by double beam spectrophotometer SF-46 in the spectral range 0.4 – 0.9 μm, when the sample ZnO/FTO/glass was put into working canal and FTO/glass or ITO/glass one was placed in reference canal.

### 3. Results

As-electrodeposited films were high adherent, semitransparent and scattered visible light. Samples 1 and 2 were grayish in color, but others were white. Figure 1 shows the transmittance spectra (T vs. wavelength λ) for the as-grown and air annealed ZnO layers. As it can be seen, from the one side, the grayish layers increase their transmittance after the annealing (they became white, probably owing to oxidation of Zn traces). From the other side, according to transmittance data, irrespective of electrolyte stirring, sample 3 offers the thinnest near transparent film, samples 1, 2 and 4 were thicker, samples 5 and 6 (not presented in Fig. 1) were the thickest. Assuming ZnO to be typical direct band gap semiconductor, the corresponding optical band gap has been estimated by the zero-crossing of the rising edge of the  $[-\ln T) \times hv]^2$  vs.  $hv$  curve [8] (Fig. 1, inset). All obtained band gap values as before such as after annealing correspond to ZnO ( $E_g$  near 3.2 - 3.3 eV) [2, 3, 9].

Investigation of structure of zinc oxide arrays electrodeposited in electrolytes and regimes presented in Table 1 has shown (Fig. 2) that all diffraction peaks match the hexagonal structure of wurtzite ZnO (with the exception of reflections assigned to FTO-glass or ITO-glass substrates). Comparative analysis of XRD patterns of the electrodeposited ZnO layers has revealed that, from the one side, the intensity of ZnO diffraction peaks is in direct proportion to concentration of NO<sub>3</sub><sup>-</sup> ions in the electrolyte that allows us to conclude that thicknesses of ZnO layers grow when amounts of nitrates increase.

From the other side, a deviation of cathode potential towards more negative values (U = -1.3 V for electrodeposited in potentiostatic regime sample 1 and 20 ms on-time at U<sub>on</sub> = -1.6 V and 30 ms off-time at U<sub>off</sub> = -1.0 V for pulse plated sample 3) result in the obtaining of very thin near amorphous ZnO layers, in spite of their large current densities and charge-area ratios of the electrodeposition processes. To our opinion, the reason for that is a most probable intense additive cathode reaction of hydrogen generation in aqueous electrolytes for ZnO deposition that fulfilled at comparatively negative potentials according to relation [13]:

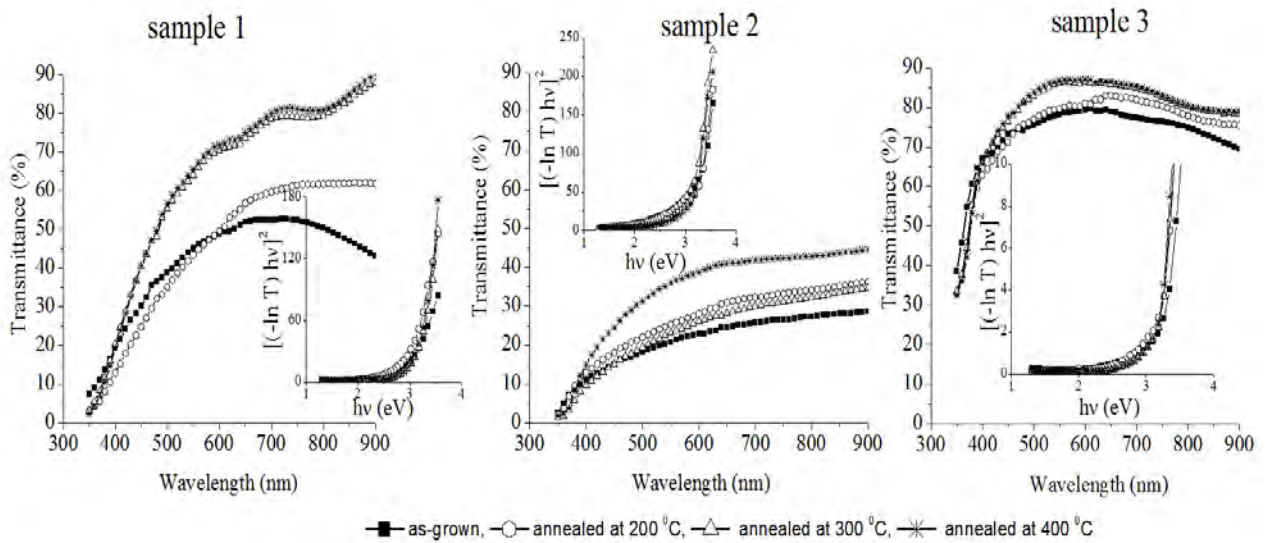
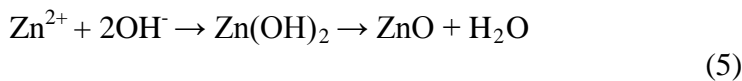


Fig. 1. Optical transmittance spectra and the corresponding band gap spectra (insets) of as-electrodeposited and air annealed ZnO arrays.

Probably, hydrogen beads adsorbed on the surfaces of substrates or on the growing ZnO crystals suppress adsorption of  $\text{Zn}^{2+}$  and  $\text{OH}^-$  ions and therefore inhibit growth of zinc oxide arrays, which could be carried out as follows:



At less negative cathode potentials ( $U = -1.1 \text{ V}$  for electrodeposited in potentiostatic regime sample 5 and  $U_{\text{on}} = -1.5 \text{ V}$  and  $U_{\text{off}} = -0.9 \text{ V}$  for pulse plated sample 2 and more clearly for sample 6 deposited in the pulse regime at  $U_{\text{on}} = -1.4 \text{ V}$  and  $U_{\text{off}} = -0.8 \text{ V}$ ) current efficiency of the ZnO electrodeposition process increases, that can be seen from comparison of overall intensities of ZnO diffraction peaks for this samples (Fig. 2) and their current densities and charge-area ratios (Table 1).

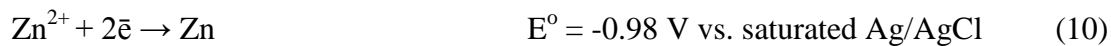
Required for acceleration of ZnO synthesis cathode reductions of nitrate-ions with creation of  $\text{OH}^-$  groups can be realized according to [13] as follows:



To our opinion, the most useful for ZnO deposition is cathode reaction Eq. (6), because processes Eq. (7) and Eq. (8) produce gaseous compounds whose adsorption can suppress

growth of ZnO, and reaction Eq. (9) is undoubtedly sophisticated multistage process as such as it consumes eight electrons. Therefore, high amount of  $\text{NO}_3^-$ -ions is a cause of the elevated thicknesses of samples 5 and 6. Enhanced structure of sample 2 as compared with sample 1 is evidently a result of such advantage of pulse electrolysis as suppression of additive cathode reaction Eq. (4), because it is impossible at  $U_{\text{off}}$ , but during off-time ions  $\text{NO}_3^-$  and  $\text{Zn}^{2+}$  can diffuse to the cathode and can be realized processes Eq. (6), Eq. (8) and Eq. (9) which are useful for creation of ZnO.

Moreover, at on-time electrochemical reaction Eq. (7) and reduction of  $\text{Zn}^{2+}$  are doubtless:



So, during off-time internal electrolysis is additive possible way for creation of ZnO arrays through following heterogeneous chemical reaction:

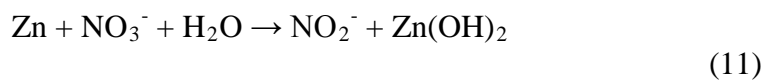


Table 2 shows structure characteristics of thicker ZnO layers. All ZnO arrays are nanostructured and characterized by little compressive stress (samples 2 and 5) or tension (sample 6). Lattice constants  $a$  are near value for single crystal ZnO of hexagonal modification, but the electrodeposited ZnO grains were elongated along  $c$  axis (according to JCPDS 36-1451,  $a = 3.250$ ,  $b = 5.207$ ).

Table 2. Structure characteristics of the electrodeposited ZnO arrays.

Sample number	Lattice constant (Å)		Average crystalline size $t$ (nm)	Lattice strain $\Delta d/d \times 10^4$
	$a$	$c$		
2	3.251	5.228	27	14.5
5	3.249	5.226	54	3.5
6	3.253	5.220	16	-36.8

Comparison of preferable orientations has revealed (Fig. 3) that ZnO layer prepared in electrolyte with low concentration of nitrates (sample 2) has crystallites with random orientation. There seems to be main reason for such structure that the polar (002) crystal plane of the ZnO is capped by  $\text{Cl}^-$ -ions (from the KCl supporting electrolyte), which [1, 4] redirect the growth of ZnO. Sample 5 plated at direct current in  $\text{NO}_3^-$ -enriched electrolyte has two preferable orientations (002) and (103), probably because of influence of cathode reaction of hydrogen evolution by Eq. (4). Only sample 6 electrodeposited in electrolyte, which contains large concentration of  $\text{NO}_3^-$ -ions at pulse plating conditions has strong (002) preferable growth orientation in the  $c$ -axis direction. According to [1], increase of (002) reflection in relative intensity is consistent with formation of ZnO rod crystallites along  $c$ -axis. In [2-4, 6] judgment, such preferential growth in the (001) plane results in 1D nanostructure of ZnO arrays, e.g. nanowires, nanorods or nanopillars, that grow along the direction perpendicular to the substrate.

#### 4. Discussion and Conclusions

We have determined that for obtaining by electrodeposition of ZnO arrays preferential grown in the (001) plane it is necessary to diminish adsorption of Cl<sup>-</sup> ions and hydrogen beads on this plane.

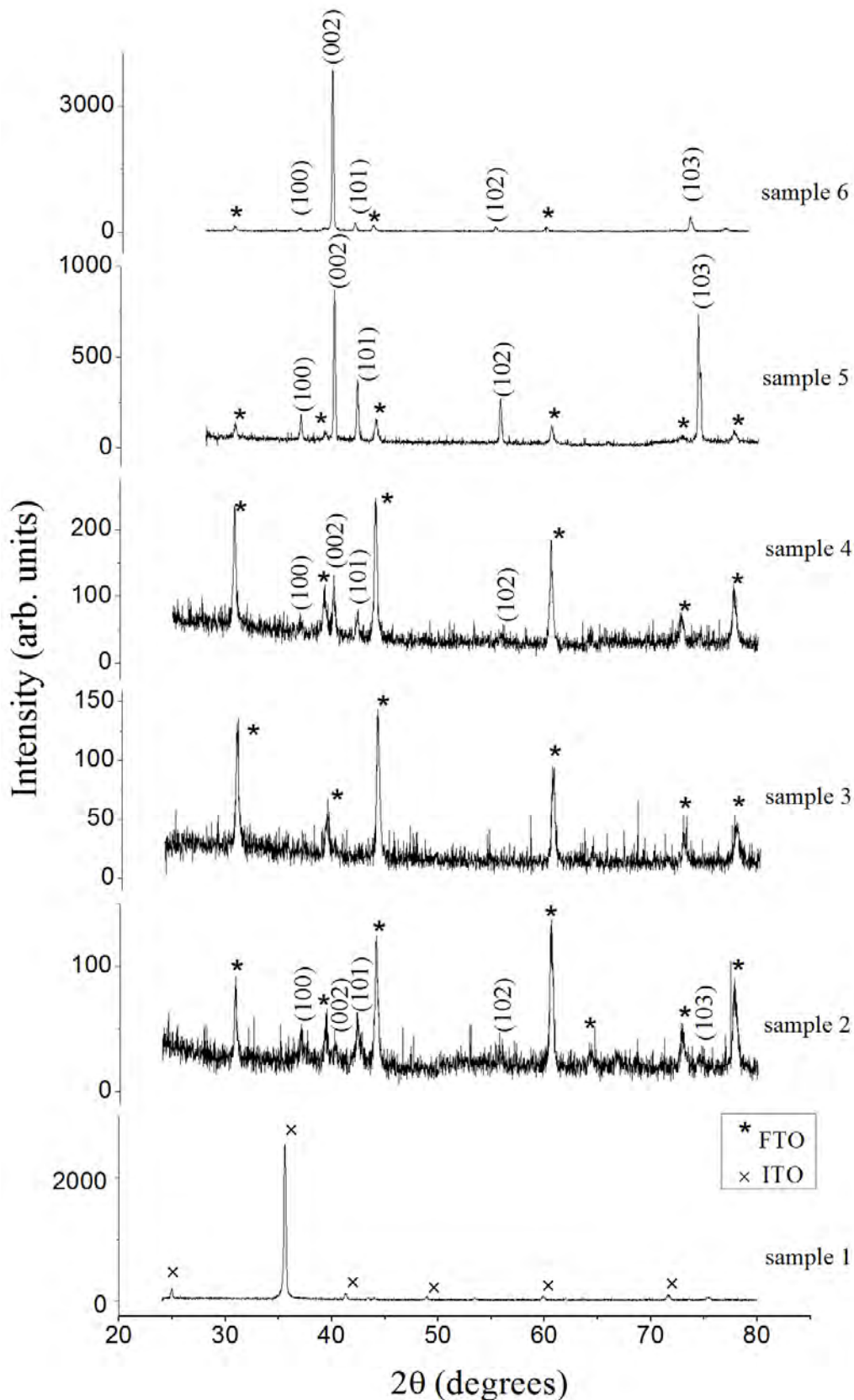


Fig. 2. XRD patterns of ZnO layers electrodeposited onto transparent conducting oxide coating glass substrates (\* – FTO, × – ITO).

It has been shown that such conditions are created in electrolyte that contains 0.05 M  $\text{Zn}(\text{NO}_3)_2$  and 0.1 M  $\text{NaNO}_3$  during electrodeposition in pulse plating regime with rectangular impulses of cathode potential (20 ms on-time at  $U_{\text{on}} = -1.4$  V and 30 ms off-time at  $U_{\text{off}} = -0.8$  V) on FTO-coated glass substrates. Therefore, in this work we for the first time have demonstrated the successful growth of 1D ZnO nanostructures by pulse plating without using of templates. The obtained ZnO arrays have to be the suitable layers for solar cells with extra thin absorbers.

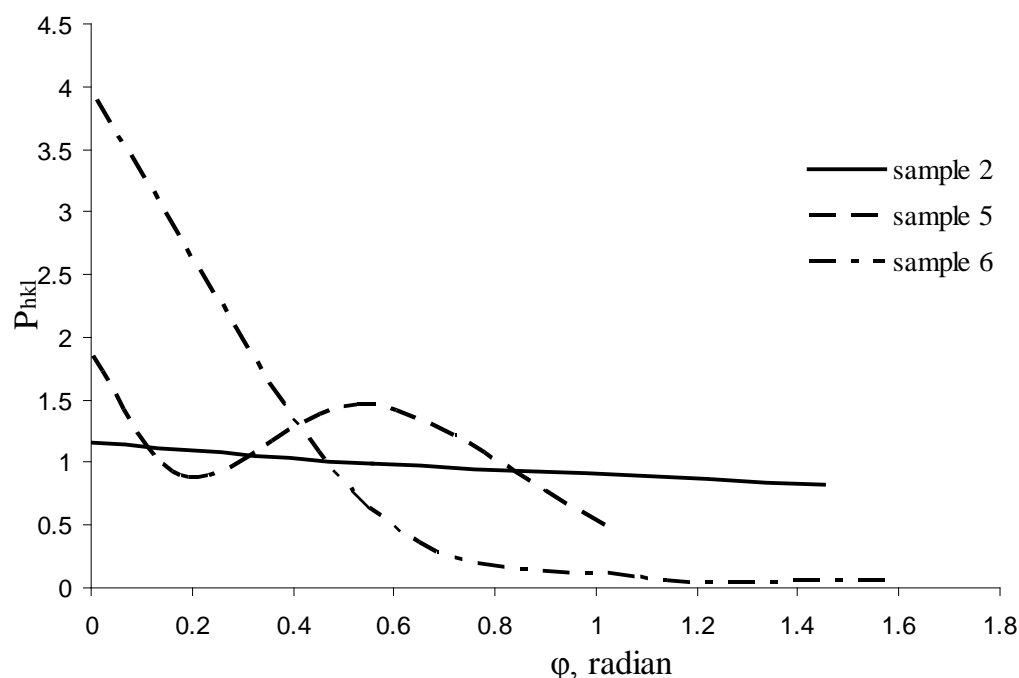


Fig. 3. Degree of texture perfection of electrodeposited ZnO arrays.

### Acknowledgments

The work was supported by STCU under Project 4301.

### References

- [1] K. Govender, D. S. Boyle, P. B. Kenway, P. O'Brein, J. Mater. Chem. 14, 2004, pp. 2575-2591.
- [2] C. X. Xu, X. W. Sun, Z. L. Dong, G. P. Zhu, Y. P. Cui, Appl. Phys. Lett. 88, 2006, pp. 093101.
- [3] X. Hu, Y. Masuda, T. Ohji, K. Kato, Journal of the Ceramic Society of Japan 116 (3), 2008, pp. 384-388.
- [4] D. Pradhan, M. Kumar, Y Ando, K. T. Leung, J. Phys. Chem. C 112, 2008, pp. 7093-7096.
- [5] A.M. Peró, P. Ravirajan, K. Govender, D.S. Boule, P. O'Brein, D. D. C. Bradley, J. Nelson, J. R. Durrant, J. Mater. Chem. 16, 2006, pp. 2088-2096.

- [6] X. Ju, W. Feng, X. Zhang, V. Kittichungchit, T. Hori, H. Moritou, A. Fujii, M. Ozaki, *Solar Energy Materials and Solar Cells* 93, 2009, pp.1562-1567.
- [7] E. Michaelis, D. Wöhrle, J. Rathousky, M. Wark, *Thin Solid Films* 497, 2006, pp.163-169.
- [8] D. Pradhan, K. T. Leung, *J. Phys. Chem. C* 112, 2008, pp. 1357-1374.
- [9] Y. Fukunaka, K. Kuribauashi, *Space Utiliz. Res.* 24, 2008, pp. 27-30.
- [10] M. Gupta, D. Pinisetty, J.C. Flake, J. J. Spivey, *Journal of the Electrochemical Society* 157, 2010, pp. D473-D478.
- [11] *Structura i fizicheskie svojstva tverdogo tela* /edited by L.S. Palatnik, Kiev, Visshaja shkola, 1983, p.284 [in Russian].
- [12] A. Malik, B.C. Ray, *Thin Solid Films* 517, 2009, pp. 6612-6616.
- [13] Y. Y. Lurje, *Spravochnik po analiticheskoy himiji*, Moscow, Himija, 1989, p.448 [in Russian].

## Rope-pump System Modelling using Renewable Power Combinations

Cai Williams<sup>1</sup>, Andrew Beattie<sup>1</sup>, Tim Parker<sup>1</sup>, Jo Read<sup>1</sup>, Julian D. Booker<sup>1\*</sup>

<sup>1</sup>University of Bristol, Bristol, UK

\*Corresponding author. Tel: +44 117 331 5905, Fax: +44 117 929 4423, E-mail: j.d.booker@bristol.ac.uk

**Abstract:** Rope-pumps are a highly successful method of lifting water by hand in developing countries. The primary aim of this work was to develop a validated methodology to decide the most cost effective renewable power sources in order to fully automate the operation of the rope-pump for given well depth, volume of water required and environmental conditions in the proposed installation location. The renewable energy sources considered were a 150W photovoltaic (PV) panel and a 100W wind turbine, either used in isolation or in combination with a battery and motor, or direct drive to a motor, providing five viable systems for further consideration. All system elements and the rope-pump itself were fully characterised through experimental testing. Computer-based simulations incorporating environmental conditions for Lilognwe, Malawi, were used to provide a 15 year lifecycle analysis. Results show that the use of PV powered system can deliver water reliably, at the lowest cost. For validation purposes, each rope-pump system was also analysed with the environmental conditions found in Bristol, UK providing comparison results, indicating the approach is systematic and rigorous enough to provide an effective decision making tool for the installation of rope-pumps anywhere, provided environmental data is available.

**Keywords:** Rope-pump, renewable power, system modelling, system selection.

### 1. Introduction

The rope-pump is a very simple type of water lifting device. The almost intuitive design is known by many other names including the paternoster (after the beaded prayer chain it resembles), liberation or rope-and-washer pump. It is a relatively recent development of the ancient chain-and-washer pump, which dates back two thousand years to feudal China [1]. In the 1980s the basic design was developed by numerous individuals [2, 3], taking advantage of low cost and versatile modern plastics to produce the modern rope-pump design, shown schematically in Fig.1. The rope-pump consists of a continuous loop of rope with plastic pistons spaced evenly along its length. When the rope is pulled up through the rising-main by a drive wheel located at ground level, the close fit of the pistons in the cylinder draws water up to a height of 30m potentially.

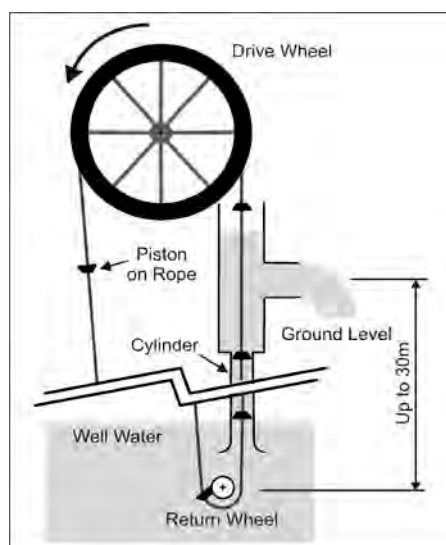


Fig.1. Schematic of a Rope-pump Powered Manually using a Drive Wheel.

The hand powered rope-pump has been highly successful across Africa and South America mainly due to attributes such as a high achievable head, low starting torque, low installation cost, ease of manufacture and minimal maintenance. These attributes identify the rope-pump as the most appropriate type of pump for automation, providing the remaining system components for automation still allow water to be delivered reliably at low cost. An affordable automated pump would allow a greater amount of water to be extracted than would be possible by hand alone, and this has many implications societally and economically for its users in developing countries. The extra water could be used to improve levels of sanitation and increase crop yields. This in turn would improve nutritional levels and provide a potential income from the sale of excess produce. It would also free up the time of users, which would otherwise be spent manually lifting limited amounts of water. This time could then be used for education and other income generating activities [4]. Various types of power supply for the rope-pump have previously been explored in order to replace manual operation, including: water wheel, pack animal, internal combustion engine and wind-turbine. This research aimed to simulate the performance of a range of automated systems with two renewable energy power sources (PV panel and wind turbine) in order that an economically viable rope-pump solution can be selected for any specific location and given set of environmental conditions.

## 2. Methodology

Economic, social and environmental factors associated with technical hardware prove to be crucial to the success or failure of the final rope-pump systems. Frequent maintenance and additional control systems required are likely to make the system impractical in locations where the necessary resources are unlikely to be available. The importance of a simple system, with a minimal demand on local expertise and supply chains and one that is appropriate to both the hydrological, geographical and social environment is crucial, a point stressed by industrial contacts and made clear from reviewing existing rope-pump systems.

A literature review, in combination with a dialogue with representatives of Solar-Aid (the main industrial contact on the project) identified the requirements of an automated rope-pump system, which were then summarised in a product design specification (PDS). Five system configurations capable of fulfilling this PDS were identified through a team-based exercise with all project stakeholders. These systems are shown schematically in Fig.2, and are a) direct connection of the motor to a PV panel; b) direct connection of the motor to a wind turbine; c) connection of the motor to a PV panel via a battery; d) connection of the motor to a wind turbine via a battery; and e) connection of both a PV panel and a wind turbine to the motor via a battery. The common component of all the system configurations devised is a suitably geared motor, but it would still be possible to decouple the motor from the rope-pump drive axle and provide manual operation through a hand-crank.

First, a theoretical force model for the rope-pump was developed based on a complete analysis of the frictional loads and energy flows present within the rope-pump. This could then define the electrical power and speed (gearing) requirements of the motor drive. Force and flow models were investigated empirically using a custom built motor driven rope-pump rig, designed to measure the rope tension, rope velocity and the discharge flow-rate, for two different pipe diameters and a range of heads up to 8m. The force model developed was found to be significantly more accurate than models proposed in previous literature, and the dependency of the flow-rate of the rope-pump on head and rising-main diameter was empirically confirmed to match an improved version of the model [5, 6]. The comprehensive treatment and analysis of frictional loads and energy flows within the rope-pump produced a key component of the system model performance model.

The remaining specific characteristic parameters of all system components were identified empirically from experimental testing; designed and built to accurately simulate the duty cycles of the components. The renewable energy power sources were chosen as a 150W PV panel (two RSM-75 from Shell Solar) and a 100W wind turbine with an axial flux generator, hand-built Hugh Piggott turbine type [7]. These system components were chosen due to availability and comparable (full) power rating to that of a human male, assuming a working duration of one hour. The wind turbine was fully characterised at different load conditions and wind speeds using a wind-tunnel providing new performance data for this turbine. Models of the motor, battery and PV panel were also identified and supported along with the turbine by empirical observations of their characteristics. The complete solar powered systems were tested under the local environmental conditions in Bristol, UK, but due to limiting wind speeds and radiation from the sun, the combined power sources had to be replicated using a power supply unit. A detailed description of the governing analytical equations and experimental characterisation for all system components is provided in [5] and [8].

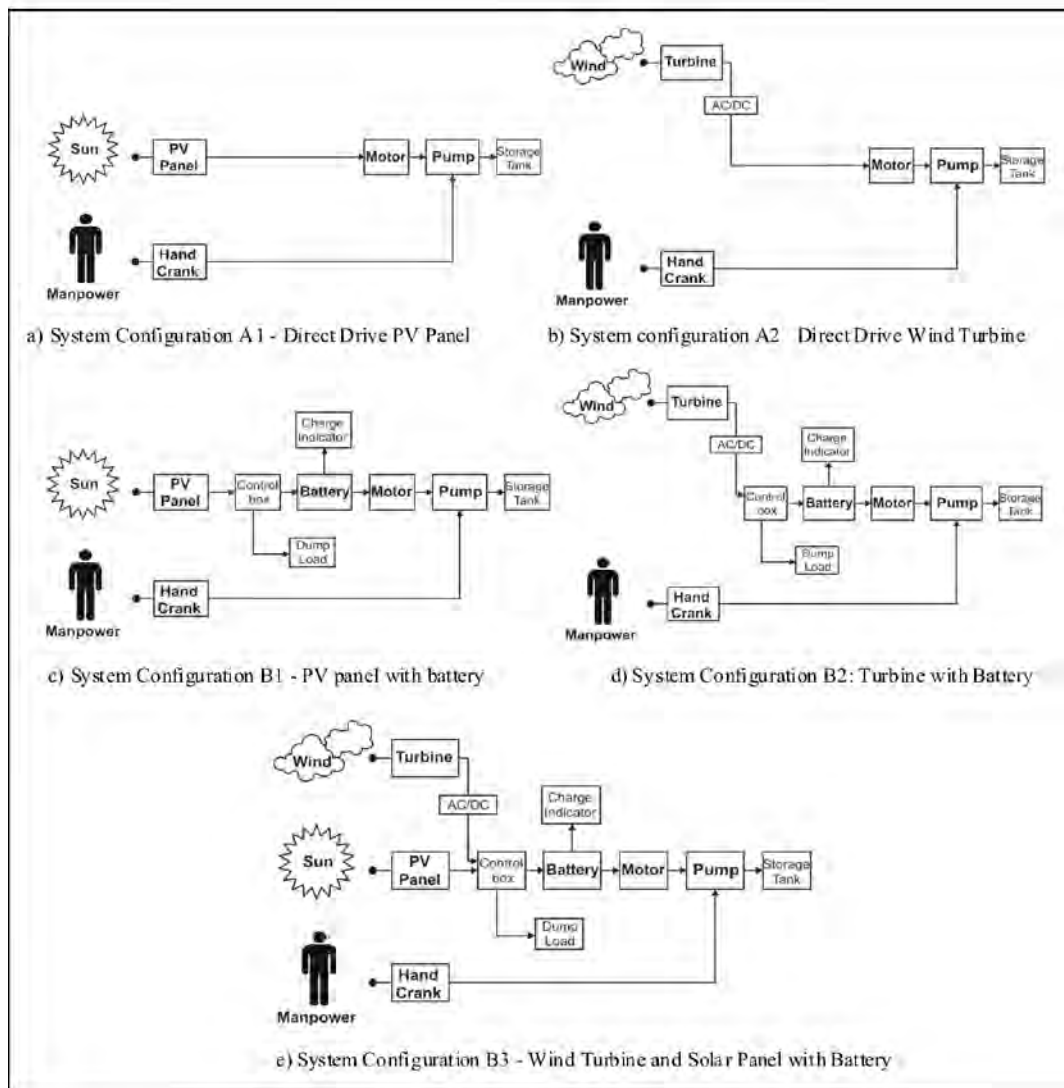


Fig.2. Five Automated Rope-pump System Configurations Considered for Simulation Studies.

From the comprehensive rope-pump system model, two computer programmes using MATLAB programming software were coded in order to investigate more efficiently a wide range of operational requirements for those systems with a battery and those without a battery,

as the computational stages are quite different for each. The computer programmes are provided in flowchart form (for one time-step) in Fig.3a) for those system configurations that use a battery, and Fig.3b) for those that do not i.e. directly driven by a motor, respectively. Together, these programmes are able to replicate the complete rope-pump system in direct drive or battery configurations, utilising a PV module and/or wind turbine as power inputs.

The PV panel model is based on the characteristic equations, and only requires inputs which are available on standard datasheets as this allows for easy comparison of alternative modules within the system. The wind turbine was modelled by directly uploading results from the turbine characterisation testing into the computer program. The program inputs are the independent local parameters (such as head and local weather data) and parameters which determine the size of the system (such as pipe diameter and number and characteristics of solar panels). This allows for the flow rate, and therefore the water volume lifted, to be estimated based on the capital cost available, as capital cost was identified as the a key differentiating requirement in the PDS.

A rigorous test regime showed the flow rates predicted by the computer model to be accurate to within 7% compared to the results from the experimental rope-pump. This is considered acceptable considering the unavoidable sources of error which would occur were the computer program to be used to size rope-pumps for use in the field. There are considered to be two major and unavoidable sources of error: firstly, the variation of local weather conditions from the average conditions used as program inputs will lead to the available power differing from the predicted values. For example, a decrease in the insolation available by 10% leads to a 4% decrease in the volume of water lifted for a direct drive PV powered system. Secondly, the empirical values derived for the pump and motor in the characterisation stage will not be identical for each rope-pump built. This is particularly true of the friction coefficient over the bottom guide, for which an increase from 1N to 10N leads to a 10% decrease in the volume water lifted for a head of 10m for a given internal rising-main diameter.

### **3. Results**

The town of Lilongwe, Malawi and the city of Bristol, UK, are used as case examples for results analyses. Lilongwe is where the main industrial contact of the project, Solar-Aid, is based. Bristol is used to provide comparison data for presentation of the results and in order to demonstrate the robustness of the simulation software for a very different set of environmental conditions. The rope-pump is to be used to lift 1 to 10m<sup>3</sup> of water per day from a well 10m deep. This is a volume that is more than can be reasonably lifted by hand and a suitable amount for a typical small rural institution such as a school or hospital in Malawi. The environmental data used in the simulations were taken from a number of online sources [9-11].

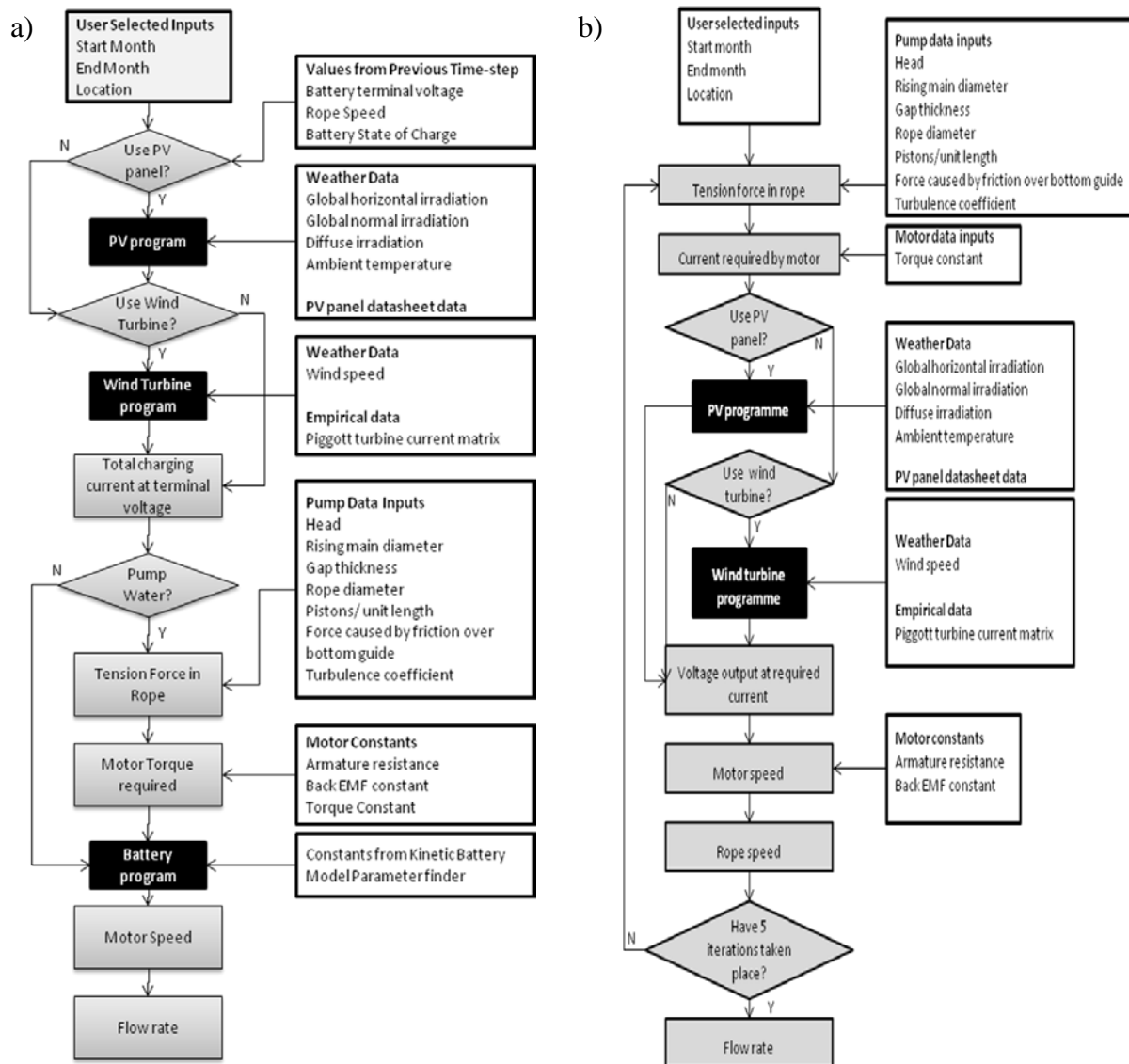


Fig.3. Simulation Flowcharts for Automated Rope-pump Configurations, a) battery systems, b) direct drive systems.

A 15 year life-cycle analysis was carried out for each of the five system configurations, including an additional variant of the direct driven rope-pump using a PV panel, called “A1-tilt”, where the PV panel is manually oriented towards the direction of the sun periodically. The results of this life-cycle analysis for both Lilongwe and Bristol locations are shown in Fig.4. Where wind velocities are sufficient, the direct drive wind turbine rope-pump system has the potential to deliver water for the lowest cost (0.03US\$/m<sup>3</sup> from 10m) in Lilongwe. However, the starting speed of the tested wind turbine was 3m/s, and makes this wind turbine component unsuitable for use in Malawi. The cost per m<sup>3</sup> of water lifted is capped at \$0.14/m<sup>3</sup> for all rope-pump system configurations, and as Fig.4 shows, those systems using wind turbines in Lilongwe are the most costly. The use of a direct drive PV powered rope-pump system is then preferable as indicated by the low cost of A1. It is estimated that a direct drive PV system in Malawi weather conditions can deliver water at a cost of 0.05US\$/m<sup>3</sup>, again from 10m well. This cost can be reduced further with the A1-tilt system, although this system is not fully automated. In all cases the use of a battery was found to increase the cost per cubic meter of water lifted despite the increased volume of water delivered. For the PV powered rope-pump system, the cost was increased by 20%, for example.

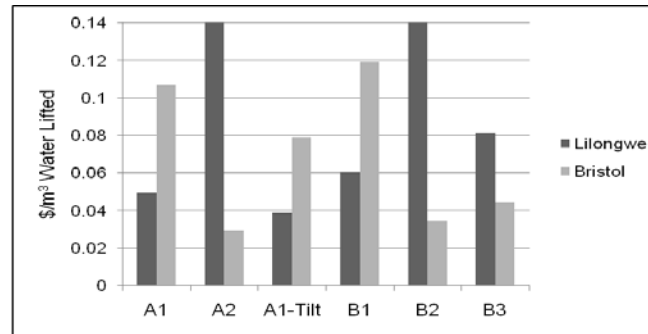


Fig.4. Cost of Water Lifted for Each Rope-pump Configuration in Lilongwe, Malawi and Bristol, UK.

Further results from the simulations are shown in Fig.5, where a daily volume of water in  $m^3$  is provided for given inputted environmental data for a calendar year. These results are cost independent, and are purely performance based. Again, the solely wind turbine powered rope-pump systems A2 and B2 are determined as non-viable configurations for Lilongwe, as they do not appear on this chart at all. Systems B1 and B3 seem competitive in terms of water lifted, but B3 uses the wind turbine, and therefore it does not contribute to the system power due to a 3m/s starting wind speed, and should be disregarded. Similarly, B1 uses a battery and therefore is more costly overall for initial investment and long-term servicing, as previously estimated.

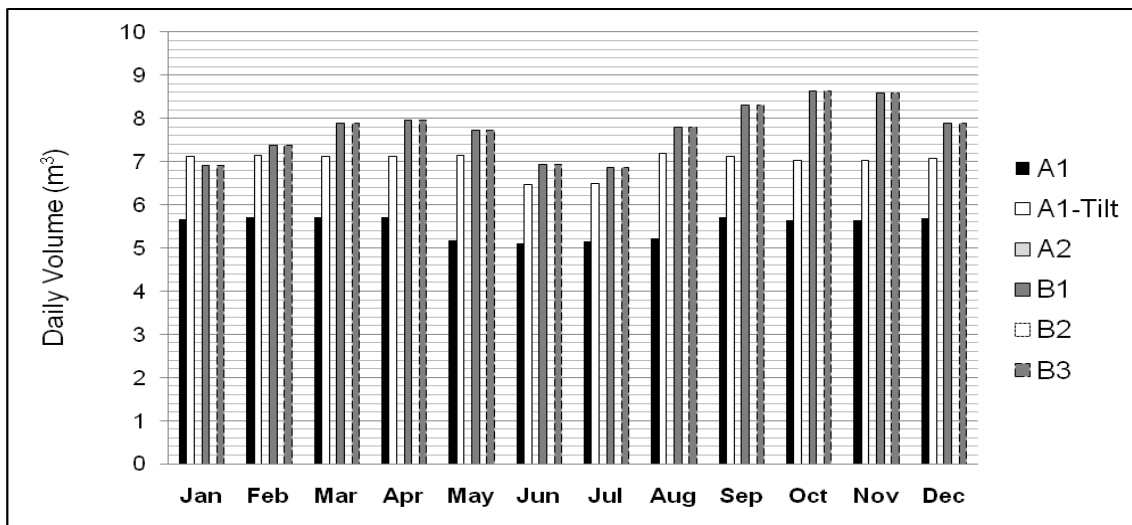


Fig.5. Daily Volume of Water from the Different Rope-pump Configurations for Lilongwe, Malawi Location (wind speeds in Lilongwe are lower than the cut in wind speeds for the tested turbine and so configurations A2 and B2 lift no water).

The results for Bristol are demonstrative of the range of location conditions that the simulation software can accommodate, with the only requirement of satisfactory data sets used for cost and environmental parameters. Overall, the results are very different to Lilongwe, as expected. All system configurations are technically viable at some part of the year, as indicated by Fig.6. A direct drive (A2) or battery powered (B2) wind turbine rope-pump configurations are the most cost effective as shown originally in Fig.4.

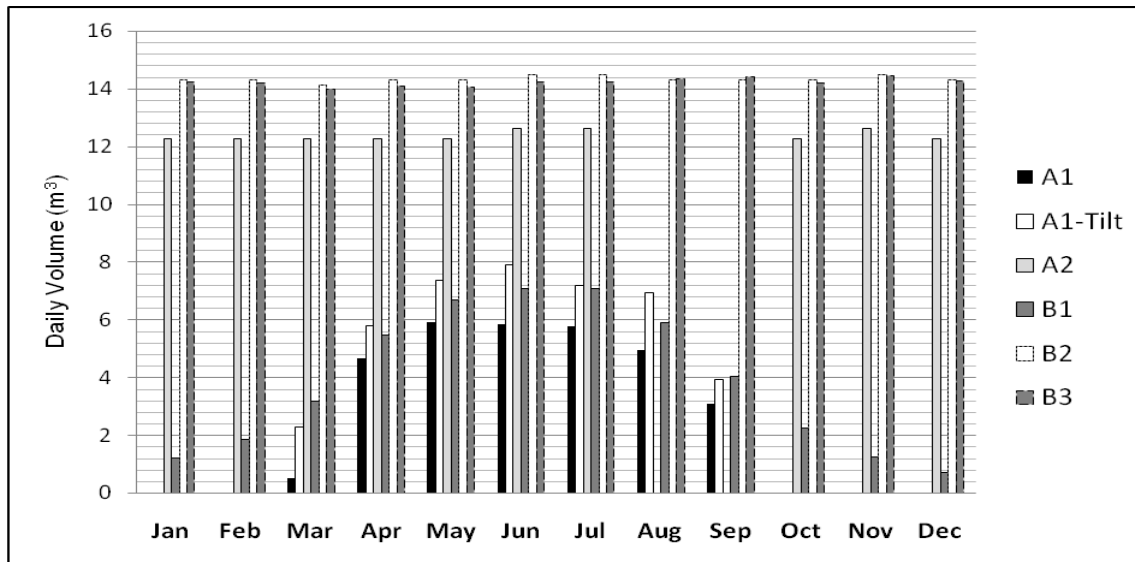


Fig.6. Daily Volume of Water from the Different Rope-pump Configurations for Bristol, UK Location.

#### 4. Conclusions

Fully parameterised software, together with scalable hardware for physical testing of a variety of rope-pump systems has been produced in order to provide a decision making tool to select the most appropriate combination of system elements for technical and economic viability. The results shown confirm the simulation software has the flexibility to be applied to a variety of environments, duty cycles and rope-pump delivery requirements. An improved model for the rope-pump mechanical loads and flow-rates enables detailed specifications of sub-systems based around the rope-pump to be made, when previously a significant degree of trial and error was required. The method has been applied to different areas of the world to show the acceptability of other systems given their environmental data.

The use of a battery as the primary load on the PV module or wind turbine allowed for the efficient matching of the IV curves of the power source with the IV curves of the load, leading to an average of 40% more water pumped per annum for PV powered systems. However, the inherently short life-span of the battery leads to high capital and component replacement costs which lead to the cost per litre of water lifted being an average of 20% higher for systems utilising a battery than for the direct drive rope-pump systems. In locations where water source reliability is a concern, a reservoir should be used instead of storing energy in a battery, if installation costs permit. There has been considerable interest in the solar powered rope-pump for use in countries that have high-average sunshine levels, since its conception in 2007 [4]. The simulation has confirmed that a battery is not necessary for such locations. Based on other findings of the project, the possibility of integrating a wind turbine with a rope-pump may be given greater investigation for certain locations for installation, but requires a range of alternative turbine types to be evaluated. For example, the use of a small vertical axis wind turbine may offer a promising alternative to the one tested in this study.

There is potential for the computer program to be used by individuals and companies charged with the design and distribution of rope-pump systems. For this to be possible, the program would need to be loaded with weather data for a wide range of locations, and with power curves for a selection of available wind turbines. The process of selecting a PV module could also be improved if the program were linked to an available database of PV modules, such as that compiled by Sandia [12] removing the need to input a large amount of data from

datasheets. The program would be of most use in the early system design stages, to carry out feasibility studies for a number of system configurations. This will allow the user to determine the most suitable system for the location, which could then be designed in detail, with consideration given to the realities of component sourcing and maintenance. The modular nature of the program makes it possible to add additional 'modules'. Any component which can be fully characterised could be added. A suitable module would be a small grain mill: an item commonly used in developing countries which requires large amounts of man power to operate and has the potential to be powered by alternative sources. There is also potential for adding additional power source modules, for example, a diesel engine.

### Acknowledgements

The authors would like to thank. Mark O'Riordan from Partners in Development, Bobby Lambert, Cardiff University and Solar-Aid, the project's industrial contact.

### References

- [1] P. Fraenkel and J. Thake, *Water Lifting Devices: a handbook for users and choosers*, Rugby: Intermediate Technology Publications Ltd, 3<sup>rd</sup> Ed., 2006.
- [2] R.A. Lambert, *How to Build a Rope-and-Washer Pump*, Intermediate Technology Design Group, London, 1990.
- [3] J.H. Alberts, *The Rope-Pump: an example of technology transfer*, *Waterlines*, 22(3), 2004, pp. 22-25.
- [4] R.A. Lambert, *Jumemaji: Solar Pumping for Sustainable Food Production Concept Paper*, 2007 [Available from: [bobby@bobbylambert.eu](mailto:bobby@bobbylambert.eu), 5<sup>th</sup> July 2007].
- [5] A. Blanken, *Measurements and Analysis on the Performance of the Rope-pump*, University of Technology, The Netherlands, 2009 [<http://www.msabi.org/docs/ropepump>, viewed online 08/12/10].
- [6] P. T. Smulders and R.P.P. Rijs, *A Hydrodynamic Model of the Rope-pump*, Veldhoven, The Netherlands, 2006 [[http://www.arrakis.nl/reports/060923\\_Roepump\\_Smulders-Rijs\\_lr.pdf](http://www.arrakis.nl/reports/060923_Roepump_Smulders-Rijs_lr.pdf), viewed online 08/12/10].
- [7] H. Piggott, *A Wind Turbine Recipe Book* [<http://www.scoraigwind.com>, viewed online 13/12/10].
- [8] A. Beattie *et al*, *Rope-pump System Modelling using Alternative Power Combinations*, UK, 2009 [<http://www.msabi.org/docs/ropepump>, viewed online 08/12/10].
- [9] European Commission, *Photovoltaic Geographical Information System (PVGIS)* [<http://re.jrc.ec.europa.eu/pvgis>, viewed online 08/12/10].
- [10] R. Hoare, *World Climate* [<http://www.worldclimate.com>, viewed online 08/12/10].
- [11] The Weather Network, *Statistics: Chitedze, Malawi* [<http://www.theweathernetwork.com/index.php?product=statistics&pagecontent=C0179>, viewed online 08/12/10].
- [12] Sandia National Laboratories, *Photovoltaic System Research and Development* [<http://photovoltaics.sandia.gov>, viewed online 08/12/10].

## Machine learning approach for next day energy production forecasting in grid connected photovoltaic plants

L.Mora-López<sup>1,\*</sup>, I.Martínez-Marchena<sup>1</sup>, M.Piliouginé<sup>2</sup>, M.Sidrach-deCardona<sup>2</sup>

<sup>1</sup> Dpto. Lenguajes y Ciencias de la Comunicación. Universidad de Málaga. Málaga, Spain

<sup>2</sup> Dpto. Física Aplicada II. Universidad de Málaga, Málaga, Spain

\* Corresponding author. Tel: +34 952250362, Fax: +34 952131397, E-mail: llanos@uma.es

---

**Abstract:** This paper presents a model for predicting the next-day energy production of a photovoltaic solar plant. The model is capable of forecasting the next-day production profile of such a system, merely by using the information obtained from the plant itself and the solar global radiation values for the previous operation days. This prediction is key in many photovoltaic systems in order to interact with conventional electrical grids. For example, Spanish legislation requires this type of information for large photovoltaic plants. In fact, the deviations from the predicted values are financially penalized. A three-stage procedure is used to build the model, which is capable of learning specific information about each facility and of using this information to fit the prediction. This model binds the use of regression techniques and the use of a special type of probabilistic finite automata developed from machine learning. The energy prediction yearly error is less than 20 percent which is a significant improvement over previous proposed models, whose errors are around 25 percent.

**Keywords:** short term forecasting, photovoltaic energy production, machine learning

---

### 1. Introduction

Process forecasting has become a key tool in many areas, such as competitive electricity or economic markets. In the short term, forecasting the expected values of certain variables can be an important tool for optimal systems management and to decide on the best operation strategies. Forecasting energy production by large plants has thus become a requirement in competitive electricity markets. In the short term, expected produced energy can help producers to achieve optimal management and can also help to implement efficient operation strategies based on the best way of interacting with conventional grid. For example, since 1998, the Spanish electricity market has moved from a centralized operational approach to a competitive one. It encourages the deployment of solar plants with a financial penalty for incorrect prediction of solar yields for the next day. In this global market, energy generated by these systems for the grid needs to be predicted as accurately as possible in order to ensure that solar energy systems are truly penetrated in the electricity market. Forecast regarding energy production is necessary to manage and schedule electricity grids. This prediction will facilitate the use of these systems as distributed generators in grid connected photovoltaic systems.

Estimating the energy generated by solar plants is difficult mainly due to its dependence on meteorological variables, such as solar radiation and temperature. In fact, photovoltaic production prediction is mainly based on global solar irradiation forecasts. The behavior of this variable can change quite dramatically on different days, even on consecutive days. This is because global solar radiation is not a deterministic variable due to the climatic conditions. Although the extraterrestrial solar irradiation -defined as the solar irradiation that reaches the extra atmospheric zones of the earth- is deterministic, once this irradiation penetrates in the atmosphere, different variable phenomena come into play and only a fraction of the extraterrestrial solar irradiation therefore reaches the surface of the earth. This fraction is known as solar global radiation. These phenomena include the presence of clouds in the atmosphere that can significantly reduce the solar irradiation reaching the earth. Accurately

forecasting the energy generated by these systems is difficult as solar radiation is the energy source of solar systems.

In general, a wide range of statistical and artificial intelligence techniques have been developed for process forecasting. Statistical time series methods are based on the assumption that the data have an internal structure that can be identified by using simple and partial autocorrelation, [1], [2], [3], [4]. Time series forecasting methods detect and explore such a structure. In particular, ARMA (autoregressive moving average), ARIMA (autoregressive integrated moving average) models have been widely used. Artificial intelligence techniques and, in general, machine learning models have been also used for process forecasting, [5], [6], [7], [8], [9]. Different approaches have likewise been specifically developed for forecasting global solar irradiation, [10], [11], [12], [13], [14].

We propose a model that is capable of learning the important facts in the prediction of photovoltaic plants energy production. A new approach based on the use of probabilistic finite automata and multivariate regression analysis is proposed here for short-term forecasting of the production of solar plants. The forecasting model is built in three stages and has been previously used for short-term forecasting of hourly global solar radiation, [15], [16]. The first and second stages of the procedure are used to identify and capture the significant information for predicting the production of a photovoltaic plant and to build the model using this information. In the first stage, the most significant independent variables are selected by using a multivariate regression analysis. In the second stage, probabilistic finite automata are built using the significant variables obtained in the first stage. The next values of the dependent variable are predicted using an algorithm for short term forecasting which is based on the information stored in the built model. In the third stage, the next-day solar energy production forecasting is calculated using the estimates values in the second step and the parameters of each solar photovoltaic plant. The methodology and the proposed model are described in the second section. In the third section, the results obtained when the model is used for next-day energy production forecasting in photovoltaic plants are presented. The conclusions of the paper are presented in the last section.

## **2. Methodology**

This paper seeks to propose a model for forecasting next-day energy production in grid connected photovoltaic plants. The model is based on the model developed for short-term forecasting of hourly global solar radiation described in [15]. We propose the use of several independent variables to build the model; these variables are usually available in large photovoltaic solar plants: irradiation values and temperature. Moreover, specific parameters of the plant, such as power installed, orientation and tilt of the panel arrays, have been included in the final model. The model is built in three stages.

In the first stage, statistical techniques are used to determine the most significant information among the independent variables used. Using this information, the data are divided into different groups and for each group the new significant variables are determined. In the second stage, a special type of probabilistic finite automata is built for each group taking into account the significant variables of the group. In the third stage, the model of prediction is used for forecasting the energy produced by the photovoltaic solar plants for the next day.

The mathematical model proposed to store the information contained in solar irradiance is based on the use of a special type of probabilistic finite automata (PFA). The use of this mathematical model is envisaged to select both the most meaningful information included in a

stationary continuous time series and the information obtained from other sources. A detailed description of this model can be found in [15].

The power generated at the output of the inverter,  $P_{AC}$  can be estimated using the expression:

$$P_{AC} = \eta_{inv} * P_m^{STC} * \frac{G_{\beta}}{1000} * (1 + \gamma * (T_{mod} - 25)) \quad (1)$$

where,  $\eta_{inv}$  is the efficiency of the inverter,  $P_m^{STC}$  is the power generated by the photovoltaic generator in standard conditions of radiation and temperature (1000W/m<sup>2</sup>, 25°C),  $G_{\beta}$  is the global irradiance on the surface of the modules (W/m<sup>2</sup>) –  $\beta$  is the inclination of the modules,  $\gamma$  is the temperature coefficient of  $P_m$ , and  $T_{mod,t}$  is the module temperature. In the case of monocrystalline silicon, the value of the coefficient  $\gamma$  is 0.48%/°C (these type of modules are used in all the facilities analyzed).

The irradiance on the surface of the modules is the most difficult parameter to estimate using Eq.(1). Moreover, this parameter presents a seasonal trend due to the changes in the relative sun-earth position. Using the values of clearness index is proposed to remove this seasonal trend. This parameter is estimated using the following expression:

$$k_t = \frac{G_t}{G_{0,t}} \quad (2)$$

where  $G_t$  is the global irradiance (Wh/m<sup>2</sup>) at time  $t$  and  $G_{0,t}$  is the extraterrestrial solar irradiance at time  $t$  (Wh/m<sup>2</sup>); the expression for estimating  $G_{0,t}$  can be found in [17].

### 2.1. First stage

In the first stage, the following linear regression model is estimated using ordinary least squares :

$$k_{t,d} = \beta_0 + \beta_1 k_{t,d-1} + \beta_2 k_{t,d-2} + \beta_3 k_{t,d-3} + \beta_4 S_{1,t,d} + \beta_5 S_{2,t,d} + \beta_6 S_{3,t,d} + Error \quad (3)$$

where  $t$  means time,  $d$  means day and  $S_i$ ,  $i=1,2,3$ , are three dummy variables to represent the season to which the observation  $k_{t,d}$  belong (only three dummy variables are used to avoid multicollinearity problems). Among these independent variables, the most significant variable for predicting the next value of clearness index is used for splitting the observation into  $G$  groups. For each one of these groups, the Eq.(3) is again estimated to determine the significant variables of the group.

### 2.2. Second stage

For the observations of each group, a special type of probabilistic finite automata is built using the significant variables of the group. The continuous variables need to be discretized to use this model. A static discretization method has been used. The range of each continuous variable has been divided into  $q$  equals intervals. Several values of  $q$  have been proved for each group in order to select the best discretization, taking into account the performance of the probabilistic finite automata in the short-term forecasting of clearness index. The proportional mean prediction error ( $PMPE$ ) has therefore been estimated, i.e.

$$PMPE = \sum_{t=1}^N \frac{|k_{t,d} - k_{t,d}^*|}{k_{t,d}} \quad (4)$$

where  $N$  are the number of observations in each group and  $k_{t,d}^*$  is the predicted value of clearness index.

### 2.3. Third stage

In the third stage, the values of solar irradiance  $G_t$  are estimated from the values of clearness index predicted using the PFAs built in the second stage. With these values, the power generated at the output of the inverter is estimated using the Eq. (1). For evaluating the model, the mean prediction error for these values has been estimated, i.e.:

$$MPE = \frac{\sum_{t=1}^N |P_{AC,t} - P_{AC,t}^*|}{\sum_{t=1}^N P_{AC,t}} \quad (5)$$

## 3. Data

The data used have been recorded from four photovoltaic plants installed in different Spanish locations. The data used for these facilities are the following: power generated at the inverter output, irradiance on the surface of the modules and modules temperature. Moreover, the season to which each observation belongs has been included. Table 1 sets out a summary of the characteristics of each facility.

Table 1. Description of the data used.

Location	Latitude/Longitude	Peak power (kW)	Inclination of modules	Data
Location 1	43.30/-1.95	14.08 kW	20	01/10/2009-10/12/2010
Location 2	43.18/3.00	13.86 kW	20	01/10/2009-10/12/2010
Location 3	43.37/-1.85	20.16 kW	30	01/11/2009-10/12/2010
Location 4	43.37/-1.85	20.16 kW	30	01/11/2009-10/12/2010

## 4. Results

In the first stage, the linear regression model, Eq. (3), has been estimated using the ordinary least square (OLS) for the data of each location. In all cases, the most significant variable proves to be  $k_{t,d-1}$ , that is the clearness index for the same hour at the previous day (significance level=0.05).

Using this variable, the observations of each location have been split into 5 different groups depending on the value of this variable. The model, Eq. (3), has been estimated by OLS for each group.

Table 2 summarizes the significant variables for each group, taking into account the values of the t-statistic for a significance level of 0.05, for Location 3. As can be observed, these variables differ depending on the group. This result is similar for all locations.

Table 2. Significant variables for each group of observations (Eq.1, significance level=0.05) for Location 3

Interval	Significant variables
[0.0-0.2[	$K_{t,d-2}, K_{t,d3}, S_{3,t,d}$
[0.2-0.4[	$K_{t,d-2}, K_{t,d-1}, S_{3,t,d}$
[0.4-0.6[	$K_{t,d-2}, S_{3,t,d}$
[0.6-0.8[	$K_{t,d-2}, S_{1,t,d}$
[0.8-1.0]	$K_{t,d-1}, K_{t,d-2}, S_{1,t,d}$

A probabilistic finite automata (PFA) has been built for each location and group of observations using the significant variables and the procedure described in [15]. Using these PFAs, the values of clearness index have been estimated. The values of irradiance at the surface of the modules are also obtained using these estimates and the Eq.(2) . Finally, Eq.(1) is used to calculate the power generated at the inverter output for each instant and the daily profiles are also obtained. The mean prediction error has been estimated using Eq.(5) for the power generated at the output of the inverter for each location. These values are reported in Table 3.

Table 3. Mean prediction error of the proposed model.

Location 1	Location 2	Location 3	Location 4
0.18	0.14	0.17	0.16

## 5. Conclusions

We have developed a model to predict the energy that a photovoltaic solar plant will produce for the next day. This model only uses the information obtained in the own plant and the values of solar global radiation for the previous operation days. A three stage procedure was used to build the model. The model is estimated using the data from each facility and is capable of learning specific information about each facility and of using this information to fit the predictions.

This model binds the use of regression techniques and the use of a special type of probabilistic finite automata developed from machine learning. The mean prediction error of the energy predictions is less than 20 percent which is a significant improvement over previous proposed models, whose errors are about 25 percent.

Further research would lead to further information that is usually available at large grid-connected photovoltaic plants being included in the model

## References

- [1] G.E.P. Box, G.M. Jenkins, Time Series Analysis forecasting and control. USA. Prentice Hall, 1976.
- [2] J.G. Gooijer, R.J. Hyndman, 25 Years of IIF Time Series Forecasting: A Selective Review," Tinbergen Institute Discussion Papers 05-068/4, Tinbergen Institute, 2005.
- [3] P.J. Brockwell, A.D. Richard, Introduction to Time Series and Forecasting, Springer Texts in Statistics, 2002.
- [4] J. Hwang, S.M. Chen, C.H. Lee, Handling forecasting problems using fuzzy time series. Fuzzy sets and Systems, 100, 1998.

- 
- [5] J.J. Guo, P.B. Luh, Selecting input factors for clusters of Gaussian radial basis function networks to improve market clearing price prediction, *IEE Trans Power Syst*, 18 (2), 2003, pp. 665-672.
- [6] C.H.Wang, L.C. Hsu,. Constructing and applying an improved fuzzy time series model: Taking the tourism industry for example. *Expert Systems with Applications* 34, 2008.
- [7] Q. Song, B.S. Chisson, Forecasting enrollments with fuzzy time series. Part I. *Fuzzy Sets and Systems*, 54, 1993.
- [8] Q. Song, B.S. Chisson, Forecasting enrollments with fuzzy time series. Part II. *Fuzzy Sets and Systems*, 54, 1993.
- [9] J. Hwang, S.M. Chen, C.H. Lee, Handling forecasting problems using fuzzy time series. *Fuzzy sets and Systems*, 100, 1998.
- [10] R. Perez, K. Moore, P. Stackhouse, Forecasting solar radiation Preliminary evaluation of an approach based upon the national forecast database, *Solar Energy*, vol. 81, no. 6, 2007, pp. 809-812.
- [11] L. Mora-Lopez, J. Mora, M. Sidrach-de-Cardona, R. Morales-Bueno, Modelling time series of climatic parameters with probabilistic finite automata. *Environmental modelling and software*, 20(6), 2005, pp. 753-760.
- [12] B. Viorel (Ed). *Modeling Solar Radiation at the Earths Surface. Recent Advances.* Springer, 2008.
- [13] R.A. Guarnieri, E.B. Pereira, S.C. Chou, 2006, Solar radiation forecast using artificial neural networks in South Brazil, in *Proc. 8 ICSHMO*, Foz do Iguau, Brazil, Apr. 2428, 2006, 17771785, INPE.
- [14] D. Heinemann, E. Lorenz, M. Girodo, Forecasting of solar radiation, *Solar Energy Resource Management for Electricity Generation From Local Level to Global Scale*, Hauppauge, NY: Nova, 2005.
- [15] L. Mora-Lopez, J. Mora, M. Piliouquine, M. Sidrach-de-Cardona. "An Intelligent Memory Model for Short-Term Prediction: An Application to Global Solar Radiation Data". *LNAI* 6098, 2010, pp. 596–605.
- [16] L. Mora-López, M. Piliouquine, J.E. Carretero, M. Sidrach-de-Cardona. Integration of Statistical and Machine Learning Models for Short-term Forecasting of the Atmospheric Clearness Index. *International Congress on Environmental Modelling and Software Modelling for Environment's Sake, Fifth Biennial Meeting*, Ottawa, Canada, Julio, 2010.
- [17] M. Iqbal, *An introduction to solar radiation.* Academic Press Inc. New York – London, 1984.

## PSpice Model for Optimization of battery Charging using Maximum power point Tracker

\*<sup>1</sup>Md. Fahim Ansari, <sup>2</sup>Anis Afzal, <sup>1</sup>S.Chatterji, <sup>2</sup>Atif Iqbal, <sup>3</sup>N.K Nautiyal and <sup>4</sup>Padmanabh Thakur

1. NITTTR Chandigarh,

2.AMU Aligarh, ,

4 MNNIT Allahabad

3,GEU Dehradun,

\* Corresponding author. Tel: +919761866637, E-mail: fahim402001@yahoo.co.in

**Abstract;** the goal of this paper is to use the solar power to charge Lithium-ion (Li-ion) batteries, pulse width modulator (PWM) control method is implemented to design and build a solar battery charger prototype. Maximum power point tracking (MPPT) is used in the photovoltaic (PV) system to maximise the PV output power, irrespective of the temperature and irradiation conditions. MPPT system, consisting of a buck-type dc-dc converter, which is controlled by a microcontroller unit, is implemented. It is presented a model for the lithium-ion battery (Li-Ion) that is suitable for computer simulation. The used model can be easily modified to fit data from different batteries. The simulation results achieved by using *Pspice* programs and are in good agreement with the experimental results. These results allowed demonstrating the reliability and validity of the proposed MPPT technique. The battery charger prototype was tested and the results obtained allowed to conclude about the conditions of permanent control on the battery charger.

**Keywords:** dc-dc converter, maximum power point tracking, microcontroller, photovoltaic systems, solar battery charger

### 1. Introduction

Photovoltaic sources are used today in many applications such as battery charging [1], light sources [2], water pumping [3], satellite power systems [4], etc. Since PV modules still have relatively low conversion efficiency, the overall system cost can be reduced using high efficiency power trackers which are designed to extract the maximum possible power from the PV module (maximum power point tracking, MPPT) [5]. The main goal of this paper is to study the use of solar power to charge lithium-ion batteries. In the literature, many battery charging techniques are investigated and proposed [6]-[7]. These methods use a variety of battery characteristics like voltage and temperature to achieve a safe and fast charging process. However, in this paper a simple maximum power point tracking technique, known as Voltage MPPT (VMPPT) [8], is simulated and constructed. The implementation and simulation of the proposed method uses a low-cost, low-power consumption microcontroller, which controls a buck type dc-dc converter and performs all control functions required by the MPPT process and battery charging.

Due to their high energy densities and long life times, Li-Ion batteries are increasingly used in systems such as portable electronics, electric vehicles [9], etc.

### 2. Description of system

The photovoltaic charger system consists of four subsystems, each with its own function. These four subsystems are connected in accordance with the block diagram shown in Figure 1. The first subsystem consists of solar panel of polycrystalline PV module from Solarex. This PV module has a rated power of 12 Watt and is formed by 18 photovoltaic cells connected in series. Second subsystem is charger unit which includes a dc-dc converter controlled by a PWM signal. Dc-dc converter is formed by two switches and an input and output filter [10].

Third subsystem (control unit), consists of a programmable interface circuit (PIC) microcontroller, model PIC18F4585, and an integrated circuit (IC), SG3524. PIC microcontroller is a high performance 8-bit reduced instruction set code (RISC) architecture, operates from 2V to 5.5V belonging to 40 pins family and IC is a 16 pin PWM switching regulator.

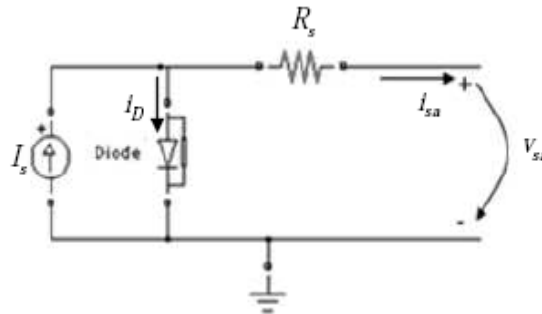


Fig.1. Equivalent circuit of solar cell

However, when it is connected to an external supply a current  $i_D$  called diode current will be present. A solar cell is usually represented by an electrical equivalent one-diode model [3] with a series resistance, as shown in Fig.1. The model contains a current source  $I_s$  one diode and a resistor  $R_s$ . The net current is the difference between the photocurrent  $I_s$  and the normal diode current  $i_D$ . The diode current is given by equation (1).

$$i_D = I_0 \times \left\{ e^{\frac{V_{sa} + R_s}{m \times V_T}} - 1 \right\} \quad (1)$$

Where:

$I_0$  = diode current (strongly dependent on temperature);

$V_{sa}$  = voltage imposed across the cell;

$m$  = Ideal factor (ideal:  $m=1$ ; real:  $m > 1$ );

$V_T$  = Thermal potential =  $\frac{K \times T}{q}$

$R_s$  = Series cell resistance;

Where

$K$ : Boltzmann constant,  $K = 1.38 \times 10^{-23} \text{ J / K}$ ;

$T$  : cell temperature in  $K$

$q$  : electric charge of electron,  $q = 1.6 \times 10^{-19} \text{ C}$ .

hence net current  $i_{sa}$  is given by

$$i_{sa} = I_s - I_0 \times \left\{ e^{\frac{V_{sa} + R_s}{m \times V_T}} - 1 \right\} \quad (2)$$

### 2.1. Charger Circuit

Fig.2 gives a general description of the charging unit block. A dc-dc converter consists of a number of storage elements and switches that are connected in a topology such that the periodic switching controls the dynamic transfer of power from the input to the output, in order to produce the desired dc conversion. The two fundamental topologies of dc-dc converters are the buck and the boost converter as described [11]. The purpose of the dc-dc

converter is to transform a DC voltage from one level to another. This is done by varying the duty cycle,  $\delta$ . Dc-dc converters have two distinct operating modes; continuous conduction mode (CCM) and discontinuous conduction mode (DCM). The paper takes the advantage of dc-dc converter working in CCM.

The low pass filter (LPF) is a simple RC filter where the capacitor is in parallel with the load. The combination of resistance and capacitance gives the time constant of the filter:

$$\tau = RXC \quad (3)$$

The cut off frequency is given by

$$f_c = \frac{1}{2\pi RC} \quad (4)$$

## 2.2. Electrical Model for Li-ion Battery

The duration of the battery cycle is the total amount of discharge-charge cycle that a battery relieves before more power cannot be hold. The energy of the battery, expressed in Watt-hour,  $Wh$ , is the product of the capacity and the voltage of the battery,  $V$ . Fig.2 represents an intuitive and comprehensive electrical battery model.

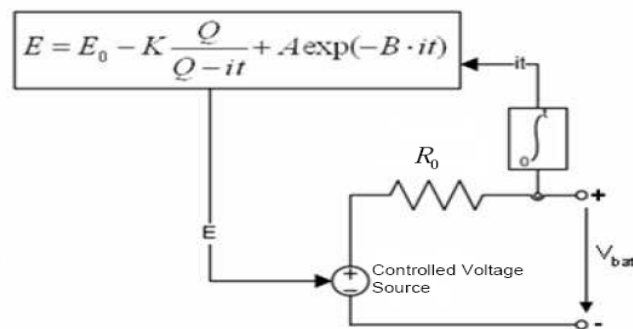


Fig.2 Equivalent circuit models of Li-ion battery

Where,

$E$  = Internal voltage, V;

$E$  = Constant voltage, V;

$K$  = Polarization voltage, V;

$Q$  = Battery capacity, Ah;

$A$  = Exponential Voltage, V;

$B$  = Exponential Capacity,  $Ah^{-1}$

The terminal voltage  $V_{batt}$  is given by equation 5

$$V_{batt} = E - I_{batt} \times R_0 \quad (5)$$

## 3. Simulation results in Pspice

The use of Pspice is very useful in cases where there is the need to determine the values of voltage and current circulating in the circuit, in order to investigate the range of values of some components, or even just to make changes in topology. With the help of this simulation program it was possible to build a basic circuit of a step-down switching regulator with duty

cycle ratio control. The circuit is depicted in Fig.3 and allows the modulation of the dc-dc converter. Specification of the used components may be consulted in as shown below;

**Voltage source**

$$V_0=V_1=V_2=10V_{dc}$$

**Resistances**

$$\begin{aligned} R_1=4k\Omega & \quad R_4=5k\Omega \\ R_2=4k\Omega & \quad R_5=5k\Omega \\ R_3=15k\Omega & \quad R_{PV}=15\Omega \end{aligned}$$

**DC-DC Converter components**

$$\begin{aligned} C_1=10\mu F \\ L_1=300\mu H \\ C_2=100\mu F \\ Q_1 \text{ -MOSFET 2N6660} \\ \text{Diode - D1N5817} \end{aligned}$$

**IC SG3524 components**

$$\begin{aligned} C_3=5nF \\ C_4=100nF \end{aligned}$$

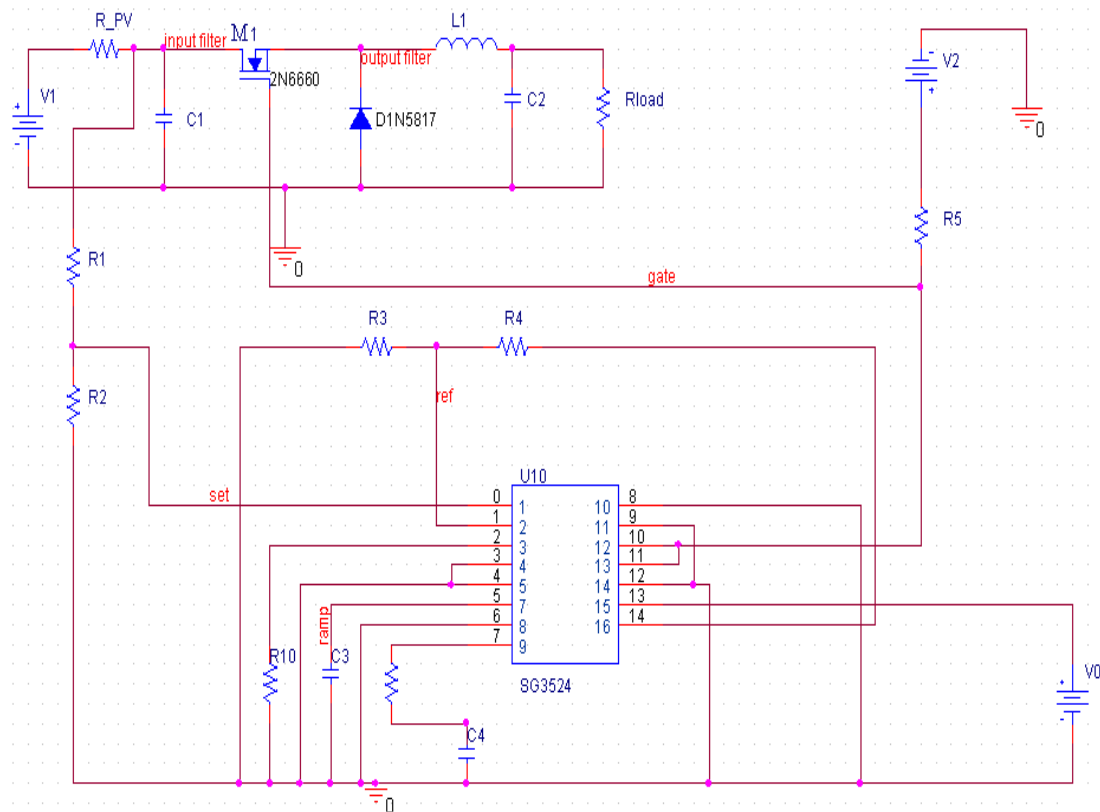


Fig.3–Step-down switching regulator circuit

Two schemes were simulated for both  $R_{load} = 20 \Omega$  and  $R_{load} = 40 \Omega$ . It is assumed that the circuit is working on the MPPT point and that all the results obtained depend of it. The value of  $V_{set}$ , output voltage of the solar panel is tending to this operation point which allows predicting that the circuit is being controlled: without knowing the value of the output voltage

and current the system evolves to the maximum power rate that the PV model allows VMPPT algorithm. There is a permanent control of the system duty cycle ratio control. Another important aspect worth to look at is the ripple value of the  $V_{set}$  voltage corresponds to the solar panel output voltage. In Fig.4 the maximum ripple obtained is nearly 3% of the voltage value  $\Delta V_{C_1} = 0.1V = V$ , which means that capacitor,  $C_1$  is well dimensioned.

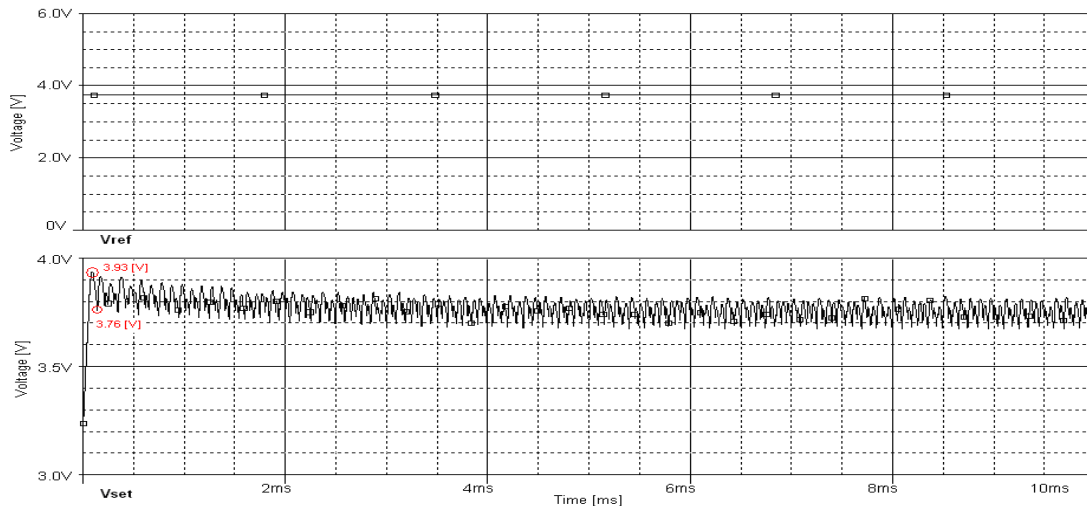


Fig.4 variation of  $V_{set}$  and  $V_{ref}$  for  $R_{load} = 20 \Omega$

Fig.4 presents the result of the difference between  $V_{ref}$  and  $V_{set}$ . The PWM signal gives us the final idea that the system is, in fact, being controlled. Variation of  $V_{set}$ ,  $V_{ref}$  and  $V_{gate}$  are given in Fig.5

Fig.5 presents the voltage and current that is present in the load ( $R_{load} = 20 \Omega$ ), this resistive load reflects the ideal conditions for the charging process, taking into account the technical specifications of the chosen battery, presenting very good values for voltage  $V_{R_{load}} = 4.1V$  and current  $i_{load} = 205mA$ . The initial conditions ( $V_{R_{load}} = 4.8V$  and  $i_{load} = 240mA$ )

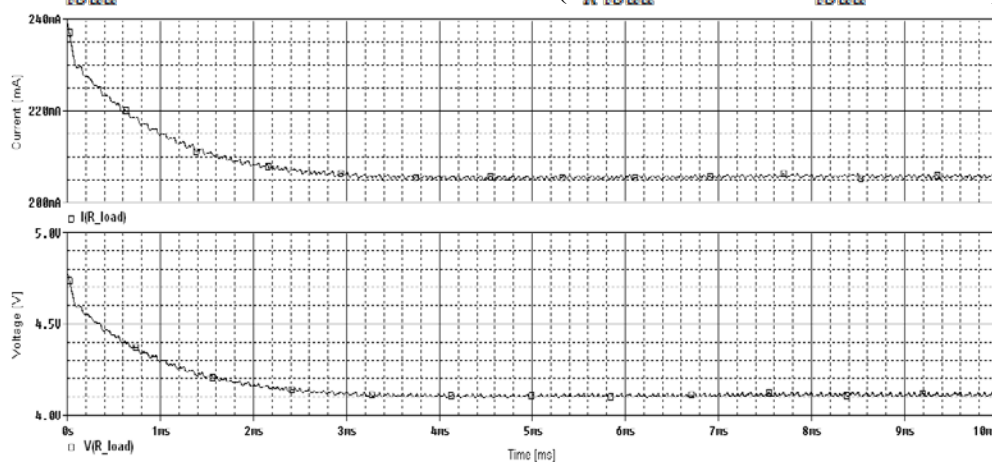


Fig.5 variation of  $I(R_{load})$  and  $V(R_{load})$  at  $R_{load} = 20 \Omega$

Fig.6 presents current in inductor  $L_1$  and voltage across diode for  $R_{load} = 40 \Omega$ . Current in inductor is always  $i_{L_1} > 0$  the converter is in CCM. When current in inductor decreases, the

diode is forward biased and hence converter is working correctly. This figure shows that current in the circuit is well dimensioned: current  $i_{L_1}$  does not go to complete zero which allows the circuit to work in CCM.

Fig.7 presents voltage across the resistance  $R_{load} = 40 \Omega$ . Although the voltage is too high for the conditions stated in this paper and so the system is no longer controlling the ratio power between the input voltage sources which simulates the solar panel for the resistive load.

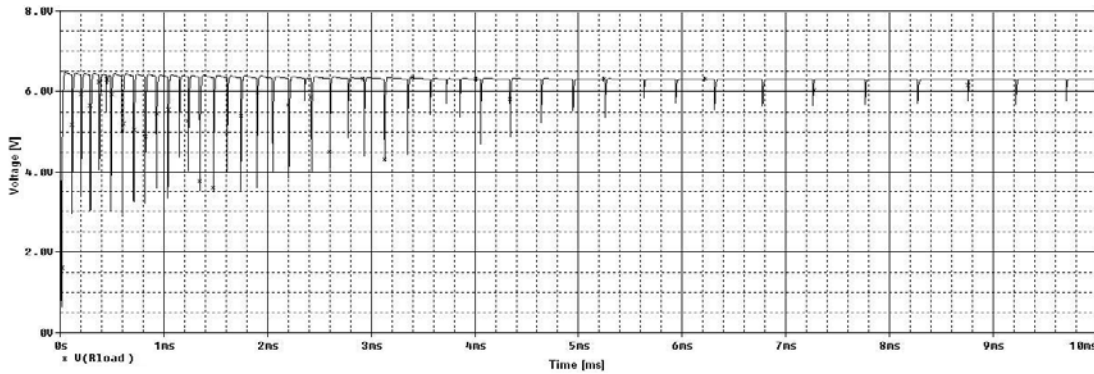


Fig.7 Voltage across load resistance  $R_{load} = 40 \Omega$

Fig.8 presents the situation where the system is being controlled for  $R_{load} = 20 \Omega$  contrasting to Fig.9 where  $R_{load} = 40 \Omega$ , the control is practically inexistent. If current  $i_L$  is lower than 150mA the system loses  $V_{gate}$  control and starts deficient control which shows that the current limit for control is achieved.

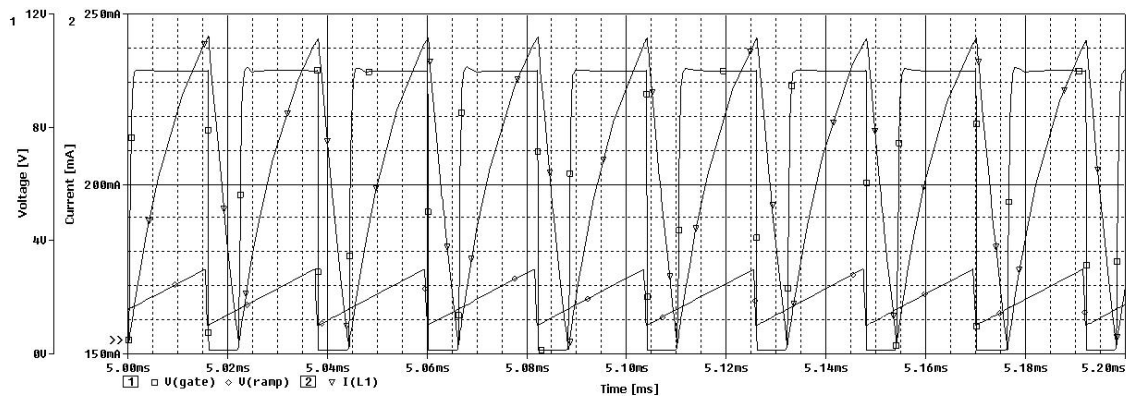


Fig.8 variations of  $V_{gate}$ ,  $i_L$  and  $V_{rampSG3524}$   $R_{load} = 20 \Omega$

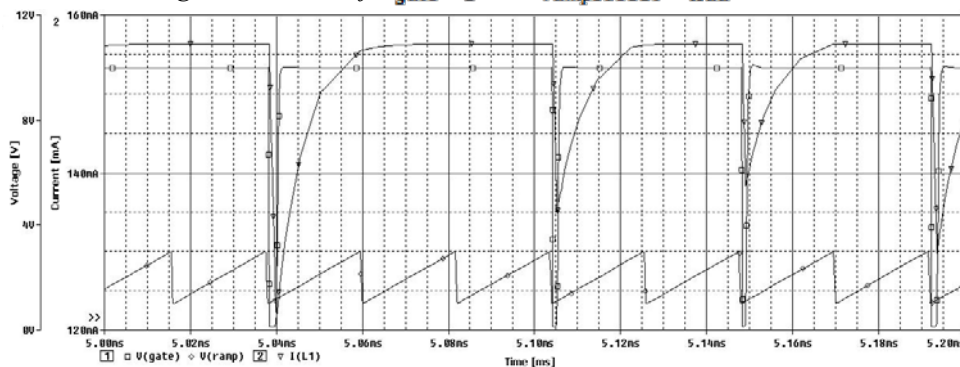


Fig.9 variations of  $V_{gate}$ ,  $i_L$  and  $V_{rampSG3524}$   $R_{load} = 40 \Omega$

Fig.10 presents the maximum power transfer rate that operating in the maximum power point the solar panel provides, more or less  $P_{\max pv} \approx 1.2W$ . Therefore, the representation of the solar panel by an ideal voltage source and resistance is reliable for this system.

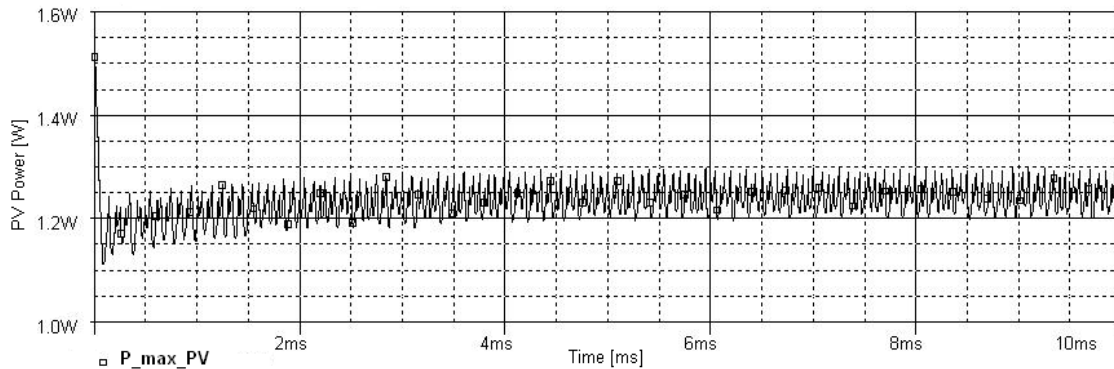


Fig.10 PV Output Power

Fig.11 and Fig.12 presents the power across the  $20 \Omega$  and  $40 \Omega$  load, respectively. In the individual graphs it is possible to look at the power loss:  $R_{load} = 20 \Omega$  the system presents a power loss for  $20 \Omega$  load resistance  $\approx 1.2-0.85=0.35W$  and power loss for  $40 \Omega$  load resistance  $\approx 1.2-0.89=0.31W$ . With these results it is possible to conclude that the system is not ideal, even referring to a simulation program. Nevertheless, regardless of the load value, the system presents power conservation: the final power value achieved is very similar in both cases even if the system with  $R_{load} = 40 \Omega$  loses control.

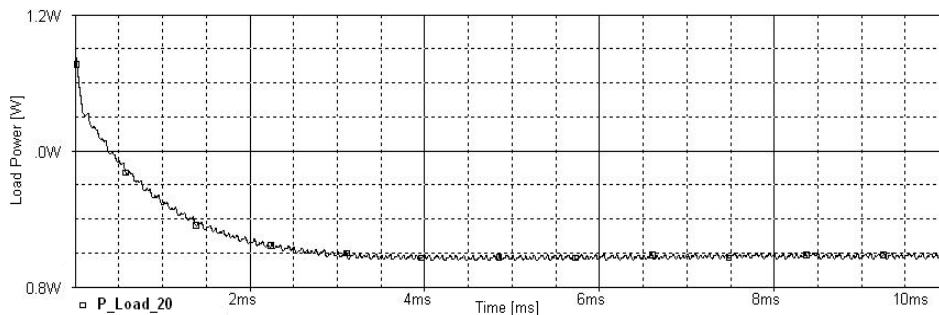


Fig.11 Load Power  $R_{load} = 20 \Omega$

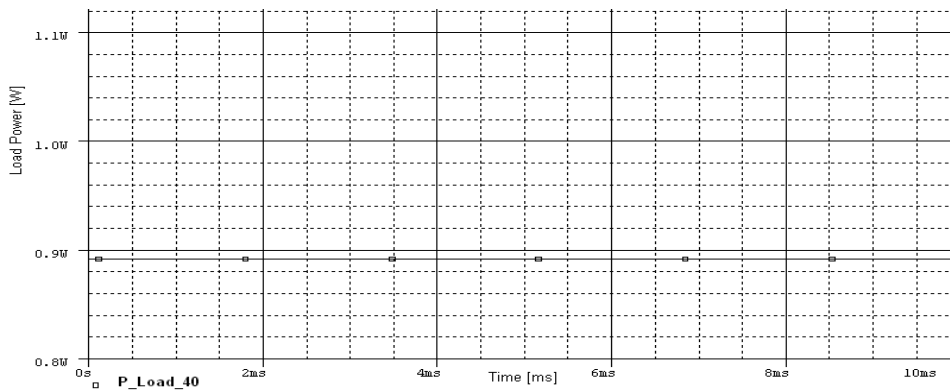


Fig.12 Load Power  $R_{load} = 40 \Omega$

#### 4. Conclusions

The use of *Pspice* simulation program allows a better understanding of the system behavior when in the presence of variable loads. It can be generally stated that while the system is represented by a load of  $R_{load} = 20 \Omega$ , it allows a controllable system. The duty cycle ratio control is a constant premise. For this reason the values obtained at the output of the system voltage and current are the ideal ones for an optimum battery charger in this case, optimum values for the type of battery chosen. Although the losses presented in the system, probably due to losses of the transistor switching and internal resistance, the system presents a very good behavior and a faithful representation of what will happen in reality. Since system is very sensitive to load variations. The system starts losing control for load values above  $40 \Omega$  presenting a load voltage higher than the one allowed to correctly charging the Li-Ion battery. The maximum voltage value in the load that allows the duty ratio control of this system is close to 5.2V.

#### References

- [1] Mohamad A. S. Masoum, Seyed Mahdi Mousavi and Ewald F. Fuchs, “Microprocessor-Controlled New Class of Optimal Battery Chargers for Photovoltaic Applications”, IEEE Transactions on Energy Conversion, Vol. 19, No.3, Sep. 2004.
- [2] Md.Fahim Ansari,S.Chatterji and Atif Iqbal“AUTOMATIC PEAK POWER TRACKER FOR SOLAR PV MODULES USING d SPACE SOFTWARE”. International Journal of Sustainable Energy,Taylor and Francis Vol. 29 No. 3 September2010 pp 151-163,
- [3] Md.Fahim Ansari,S.Chatterji and Atif Iqbal “A FUZZY LOGIC CONTROL SCHEME FOR SOLAR PHOTO VOLTAIC SYSTEM FOR MAXIMUM POWER POINT TRACKER” International Journal of Sustainable Energy,Taylor and Francis 29: 4, 245 — 255,December 2010.
- [4] K. Tanaka, E. Sakoguchi, Y. Fukuda, A. Takeoka, and H. Tokizaki, “Residential solar powered air conditioner”, in Proc. Eur. Power Electronics Conf., Brighton, U.K., Apr. 1993, pp.127-132.
- [5] E. Koutroulis and K. Kalitzakis, “Novel battery charging regulation system for photovoltaic applications”, IEE Proc.-Electr. Power Appl, Vol. 151, No. 2, March 2004.
- [6] Lijun Gao, Shengyi Liu, and Roger A. Dougal, “Dynamic Lithium-Ion Battery Model for System Simulation”, IEEE Transactions on Components and Packaging Technologies, Vol. 25, No.3, Sep. 2002, pp1521-3331.
- [7] Wei Zhang, Dale Skelton and Robert Martinez, Modelling and Analysis of an Off-line Battery Charger for single Cell Lithium Batteries”, IEEE, Sep. 2004.
- [8] Mohamad A. S. Masoum, Hooman Dehbonei and Ewald F. Fuchs, “Theoretical and Experimental Analyses of Photovoltaic Systems With Voltage and Current Based Maximum Power Point Tracking”, IEEE Transactions on Energy Conversion, Vol. 17, No.4, Dec. 2002.
- [9] <http://www.mathworks.com/toolbox/phymod/powersys/ref/battery.html>, Apr. 2008.
- [10] Min Chen and Gabriel A. Rincón-Mora, “Accurate Electrical Battery Model Capable of Predicting Runtime and I-V Performance”, IEEE Transactions on Energy Conversion, Vol. 21, No.2, June 2006.
- [11] José Fernandes Alves da Silva, Sistemas de Energia em Telecomunicações: Texto de Apoio, Set 05-06, Instituto Superior Técnico, Área Científica de Energia, Portugal, May. 2006.

## Photovoltaic for Rural Development: A study of policy impact and scope of market development in South Asian Region

Siddha Mahajan<sup>1,\*</sup>, Shirish Garud<sup>2</sup>

<sup>1</sup> The Energy and Resources Institute, New Delhi, India

<sup>2</sup> Greenergy Renewables Pvt Limited, Mumbai, India

\* Corresponding author. Tel: +91 1124682100, +91 9873846092, Fax: +91 1124682144, E-mail: siddha.mahajan@teri.res.in

---

**Abstract:** Growing energy demand, increase in carbon emissions due to increase in fossil fuels it becomes imperative for developing regions like South Asia to switch to non-conventional sources of energy. Being naturally blessed with the renewable energy resources it becomes easy for these countries to switch. The best resource to be harnessed in the region is the solar energy through Photovoltaic technology. The best part about this technology is its suitability for remote area rural electrification which is the need of hour in the region. Access to electricity is essential to bring about equitable economic development in sustainable manner. But, there exist barriers which hold back the development of renewable energy resources. While some countries in this region like India, Sri Lanka and Bangladesh have been able to develop the markets for PV, other countries in the region are yet to develop policies and programs. Financial initiatives as a result of policy push have major role to play in developing the market. Un-electrified rural population being very high in this region, the countries like Nepal, Bhutan Pakistan and Maldives which seeks to develop the market can learn from the success stories of these countries.

**Keywords:** Photovoltaic, South Asia, Policy, Rural development

---

### 1. Introduction

Energy consumption is an indicator of socio-economic development of the country. With the increasing energy demands coupled with global warming and energy security issues, it becomes imperative for all the countries to switch from conventional carbon based fuels to low carbon sources of energy. This is especially important for the developing countries which are on development path. South Asia is one such region. It is on one hand, one of the major economic hubs of the world, and on the other, is home to a quarter of total world's population, majority of them in rural areas. Major portion of the population of this region still remains devoid of electricity due to infrastructural in-capabilities, high investments required for the development of infrastructure. This holds back the development of this part of world. Abundance of sunshine throughout the year makes Photovoltaic (PV) technology a suitable and viable option to provide off-grid and decentralized electricity solutions is a long term cost effective solution that can help in equitable development. It also gives added advantages like rural employment, future energy security, and clean environment. Governments in India, Bangladesh and Sri Lanka have taken several steps ahead to create markets for this technology, through policy intervention in rural areas and there have been successful stories as well. While, Bhutan, Nepal and Maldives are still far behind in the development of market for the technology and can learn from successful stories of neighboring countries to develop a self sustaining market in their regions.

The purpose of this study is to bring out the advantages and impacts of policies on photovoltaic technology through various successful stories that can help in rural development. Also, to understand what are the various financing mechanisms developed for creating market. To achieve this purpose the objectives of this paper are:

- To conduct a cost-benefit analysis of the technology with the conventional sources
- To understand the existing PV deployment in the rural regions of South Asia

- To learn about the available financial incentives and schemes for its deployment.
- To understand the barriers in market development

## 2. South Asia

### 2.1. Current scenario

The South Asian region, which comprises of Bangladesh, Bhutan, India, Maldives, Nepal, Pakistan, and Sri Lanka<sup>1</sup> is home to more than 1.5 billion people, reaching almost close to a quarter of the world's population [1]. This geographical region is currently experiencing a rapid growth in energy demand, associated with economic growth and industrialization. Despite, such a growth, there is a huge gap between demand and supply of electricity. Table 1 and figure 1 together summarizes the current scenario. Nearly 613.9 million people in this region are un-electrified in this region (IEA/OECD 2009) consisting mainly of the rural region. This issue, further, is strongly linked to other major issues of poverty, education, and health and hygiene. The electricity production in this region is through coal, petroleum and crude oil imports [2]. Countries like Bangladesh and India do have substantial reserves of natural gas, coal and petroleum, despite that substantial amount is imported for sustaining the commercial and industrial sector for meeting the growing demands. Maldives, on the other hand, rely 100% on imported refined petroleum. Pakistan, Nepal and Bhutan, derive most of its energy needs through hydro and biomass. Pakistan is still heavily dependent on oil imports. All over in the region, hydro is mainly deployed for commercial power generation; biomass obtained from forests supplements the household energy needs of rural population. This is followed by small hydro and very miniscule amount of solar PV. Conventional fuels that are common among rural population are kerosene and diesel that are offered at highly subsidized rates. A study by UNDP shows that this region has medium to high Oil Price Vulnerability Index (OPVI)<sup>2</sup> point for all the countries. It has been found that the divergence of large amount of national investments towards the fuel imports side-lines the social development. Also, huge dependence on the foreign oil imports leads to insecurity of energy.

Table 1: Summary of South Asian countries energy scenario[3,4,5,6,7]

Country	Land area (sq. km)	Total Population (million)	Energy production (Mtoe)	Population without electricity (millions)	OPVI Index
Bangladesh	1, 47, 570	158	21.26	95.7	High
Bhutan	38,394	0.6	0.6804	NA	Medium
India	32,87, 263	1123	450.92	403.7	Medium
Maldives	8, 59, 000	0. 3	NA	NA	High
Nepal	1, 47, 181	28	8.53	16.5	High
Pakistan	8, 03, 950	162	63.64	68	High
Sri Lanka	65, 610	19	5.08	4.7	High

### 2.2. Solar energy deployment

South Asia being a tropical region is abundantly rich in solar energy, receiving an average solar radiation of 4-4.9 kWh/m<sup>2</sup> [8]. The most important contribution of this source is in the decentralised and off-grid power supply to the remote rural areas where grid connectivity is not possible. This will not only contribute to the rural development but also the equitable

<sup>1</sup> Afghanistan, though a part of South Asia has not been considered due to unreliability of data

<sup>2</sup> Oil price vulnerability index (OPVI). It is calculated with the help of three indices economic strength, economic of performance and economic growth with low share of oil

social and economic development of the rural parts, thus contributing to the overall development of the country as a whole.

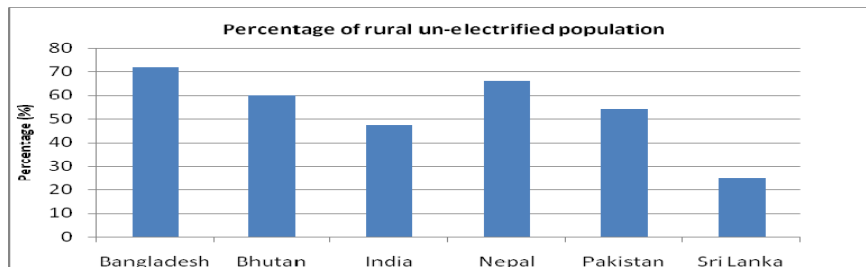


Fig. 1: Graph showing the total un-electrified population in South Asia. Data for Maldives is unavailable [9]

### 2.3. Photovoltaic technology

Photovoltaic (PV) is the technology through which the solar power can be harnessed. Photovoltaic is the array of cells, commonly known as solar cells, which convert solar energy into electricity. The commonly used end use applications of solar PV in rural areas are Solar Home Lighting Systems/Solar Home Systems, Solar Lanterns, Solar Street Lighting Systems, Solar PV Water Pumping system. These applications are put in use for various purposes like residential, rural communities, schools and hospitals electrification, for micro enterprises, water pumping, signalling remote telecommunication, captive power generation, back up power generation, urban applications, highway lightings and many more.

### 2.4. Choice of Solar PV as preferred technology

Harnessing of this resource is suggested above other resources because of the reliability, modularity and free and easy availability of the resource in the region, unlike wind, biomass and hydro energy which are highly site specific. The two most important benefits are:

1. It can be used for rural electrification in remote areas. This is the most potential reason for the South Asian countries to adopt this technology.
2. The fuel cost is zero and no fuel supply linkages are required as in biomass [Refer to Table 1].

This reduces the dependence on the fossil fuels and the large drain of money due to imports of fuels. Besides these, it is a silent process of energy generation and the installation of the technology does not require large space. In case of roof-tops it uses the unused spaces on the roof. It is easy to install and maintain; produced and consumed at the same place so no translocation charges. PV modules can be added to increase the capacity as needs grow.

## 3. Methodology

Literature study was done firstly to understand the basic energy scenario in each country through primary and secondary research. Stakeholder discussions and sector knowledge of the experts was also taken as secondary research that provided the dynamic of the sector. Open ended structured questionnaires were prepared and were mailed to the organizational heads in different countries. Questionnaires prepared for the countries were based on the current situation and the literature survey done during previous research. Two sets of questionnaires were prepared. One set was for India, Sri Lanka and Bangladesh and another set was for Pakistan, Bhutan, Maldives and Nepal. 13 respondents were mailed the questionnaire, out of which only three responded. These respondents belonged to Nepal, Bangladesh and Sri Lanka. Due to weak responses to the questionnaire the analysis for Bhutan, Pakistan and Maldives was based on the data collected during literature survey and stakeholder consultation.

The values taken for conducting cost benefit analysis has been mainly taken from the Indian market since the facts say that the market is most developed in India. The calculations are based on the study done by International Energy Studies in 2004 [10]. The results obtained would be used as a representative data for the region to understand the cost and benefits of the technology. The calculations have been carried out in USD with the conversion factor of 44.45, as per the currency conversion rate in April, 2010.

Thus, results produced are primarily based on the articles, reports, research papers, publications, stakeholder discussions and sector knowledge of experts. Various international conference presentations by national experts of different countries were also used in understanding, documenting, analyzing the PV market. The results have been produced in both quantitative and qualitative form.

## 4. Results and Discussions

### 4.1. Cost-benefit analysis of the technology with the conventional sources

The Cost Benefit Analysis (CBA) has been carried out between the off-grid solar PV rooftop and conventional power plants (thermal power plant, diesel and natural gas power plant) that would be providing the electricity to the un-electrified region through grid connection.

#### 4.1.1. Total Cost of generation

Figure 2 compares the total cost of generation (TCoG) from four different fuel plants. TCoG for off-grid PV is found to be greatest among the four i.e. \$ 0.4719/kWh followed by Diesel power generation and natural gas. It has come least for the coal generated power i.e. \$ 0.0509/kWh. Higher TCoG of solar PV is mainly because of high capital cost of the technology.

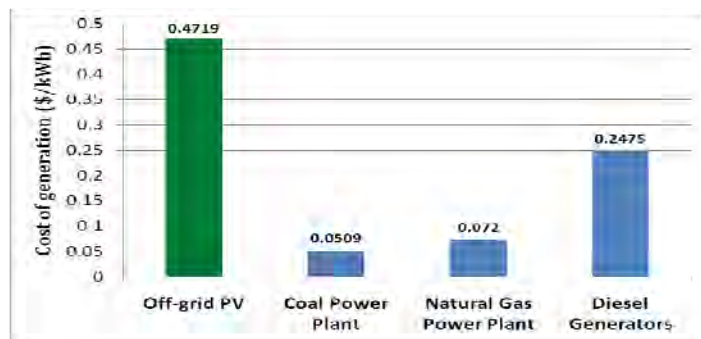


Fig. 2: Comparison of cost of electricity generation profit

#### 4.1.2. Net Profits

Figure 3 and 4 compares the net profits on the cost of generation for electricity derived from the conventional and PV power plants before and after internalising the environmental cost, respectively. The costs have been calculated over the useful life of the plants. The useful life of Off-grid PV, coal power plant and natural gas power plant is 25 yrs [11]. It is found that that net profits over the remains positive in all the cases but it is higher by investing in off grid solar PV. Long-term profits further decrease in case of investments in conventional plants when environmental cost is internalized. Diesel power plant could not be assessed due to the lack of data but it can be understood with the combustion properties of diesel the NPV tends to come down if environmental cost in internalized.

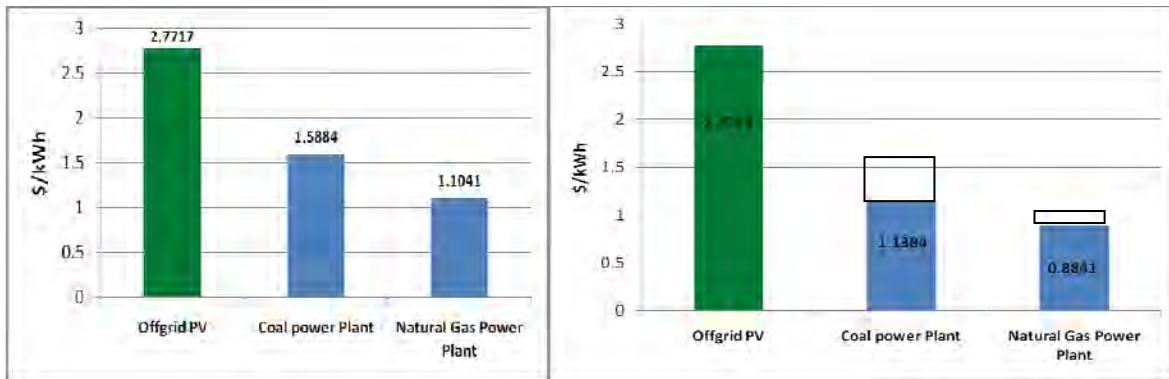


Fig. 3: Net profit before internalizing environment cost; Fig 4: Net Profit after internalising the environment cost

#### 4.1.3. Net present value

Figure 5 shows that the net returns of today's investment in the PV project. Results show that investments in PV deployment would fetch greater returns than investments today in conventional plants.

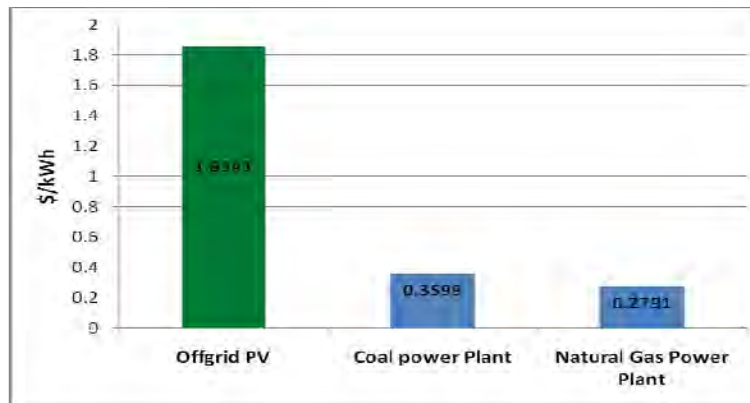


Fig. 5: NPV of various power generators

## 4.2. PV deployment

Table 3 and figure 6 are the summary of the PV installations done in South Asia. Out of all the PV off-grid installations, the most popular end use application is the Solar Home lighting Systems (SHSs). It has been installed in almost all the countries in South Asia. It is followed by the distribution of solar pumps. It is used in India, Bangladesh and Nepal. It is followed by solar lanterns distributed mainly in the rural areas which are un-electrified. Street lighting systems which has found more urban application is in use in India. In Bangladesh, it is still in the discussion phase. Over the years, with the developing market the number of installations has also increased. Thus it can be concluded from the above table and graph that PV market is most developed in India, followed by Bangladesh and Sri Lanka

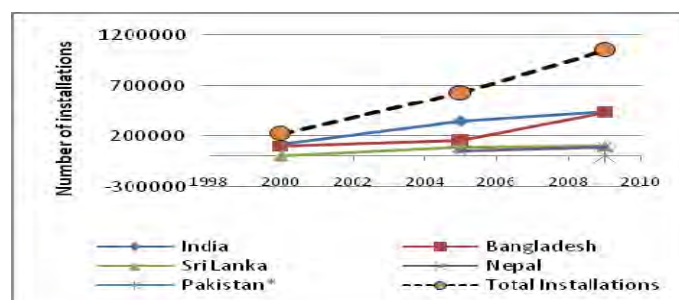


Fig 6: Total SHS installations in South Asia

Table 3: Various end use applications of PV

Country	Solar Home lighting Systems (SHS)	Solar Lanterns	Solar Street lighting systems	Solar Pumps
Bangladesh				
India				
Sri Lanka				
Pakistan				
Bhutan				
Nepal				
Maldives				

System installed In demonstration phase Not installed Data unavailable

### 4.3. Financial incentives available

Table 4 summarises various financial incentives offered in the South Asia region. The PV market set up in South Asia so far has been set up mainly in three countries: India, Sri Lanka and Bangladesh. Although, the market is small yet, it is growing up. The majority of the market share is that of off-grid installations. The two main financial mechanisms which have been effective in this market segments are :

Table 4: Off-grid financial schemes for PV

Country	Off-grid Schemes		
	Micro credit System	Capital Subsidy	Interest Subsidy
Bangladesh			
India			
Sri Lanka			
Nepal			
Bhutan			
Pakistan			
Maldives			

Practiced Being discussed Not practiced Data unavailable

**Micro-credit System:** This is mainly practiced in Bangladesh and has been successful in creating the rural market in the country. A community participation initiative taken on the basis of trust to make repayments of loans has been very successful in developing rural sector of the country (See figure 7). Initiative taken by the Grameen Bank in Bangladesh has helped the rural market to grow rapidly. It is interesting to note that today the villagers have 90% shareholding whereas; the government has 10% share holdings.

**Capital Subsidy:** This financial mechanism is practiced in India and Sri Lanka (See figure 8). While in case of India the subsidy given is supported by the Government, in Sri Lanka the subsidy given is supported mainly by the international support. The international support given to Sri Lanka for the promotion of Solar Home Lighting Systems had actually crossed the target set for installations and has been a major reason of success in the rural sector.

The above two financial models have been succesful in revolutionising SHSs in the respective countries and creating the market. Soft loans have also been extended to the consumers for achieving the targets of SHSs installations in Sri Lanka and India. Soft loan scheme is a interest subsidy scheme where interest charged on loan is lower than the prevailing market interest rate. It was introduced in India in the year 2002-2003 for financing the purchase of

solar photovoltaic systems by various categories of users. This is slowly replacing the upfront capital subsidy schemes which need huge budgetary support from the government.

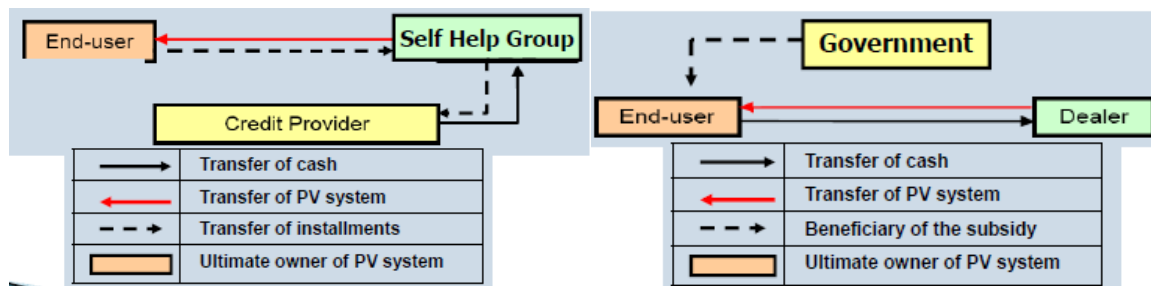


Fig 7: Micro-credit model

Fig 8: Capital Subsidy Model

#### 4.4. Barriers

Table 5 summarises various barriers country wise. The two common barriers in the promotion of PV market in the South Asian countries are lack of R&D sector focussed on solar energy development and the funds availability. Also the people awareness and the availability of technologies are other barriers which hold back the growth of the market. Political inconsistency is one of the prime concerns of the funding given by the international funding agencies. But, with a successful example of Bangladesh one can learn that with more of people's willingness and interest in taking initiatives market could be created. Lack of information about the resource, needs, appropriate technologies are also major issues in developing the markets especially in Bhutan, Nepal, Maldives and Pakistan. Lack of suitable financing schemes has also held back the development of PV market in countries like Bhutan, Maldives and Pakistan.

Table 5: Barriers in various countries for PV

Barriers	Bangladesh	Bhutan	India	Maldives	Nepal	Pakistan	Sri Lanka
Financing schemes							
R&D							
Lack of Information							
Funds availability							
Institutional Framework							
Political instability							

Barrier Exist    Barrier doesn't exist    Information unavailable

In all these countries though the PV technology is used for the off- grid power generation yet, either the contribution compared to grid power is miniscule or nearly zero. SHSs have found easy way in the market because of affordable incentive schemes and favourable policy environment. In Bangladesh because of its properties like modularity, easy maintenance and with Self Help Group (SHG) practice in Bangladesh, the banks have been ready to provide loans for installation. The main policy push comes from the government, thus government plays a major role in penetration of the technology. The financial schemes to create and support the off-grid market like capital subsidy in India and Sri Lanka and microcredit system of Bangladesh made it easy for the rural consumers to meet their power demands and easy down payments have been supported by government. Central funding is still an issue as many countries are not able to afford the same. Besides, it is also seen the government does not allocate the funds for the development of solar energy technology and its harnessing.

## 5. Conclusion and Recommendation

The policies initiatives for flexible and easy flow of cash have a major role to play in the proliferation of PV technology into the market, especially when the market development is in the nascent stage and is dominated by the rural population. While in case of India and Sri Lanka, capital subsidy and soft loans succeeded to generate the market for Solar Home lighting installations, micro-credit system model succeeded in Bangladesh to develop market among rural sector. This has also helped in generating rural employment and averting poverty by promoting cottage industries. This, keeping into consideration the large un-electrified population, and increase in PV market through installations of SHS in India, Bangladesh and Sri Lanka, it is very much possible for other countries in South Asia to learn from the neighboring countries and work towards development of market. There are several disadvantages considered for the technology like it cannot be used during cloudy and rainy seasons and that its output is not comparable to the conventional sources but it is the government through policy should encourage capacity building and R & D to overcome barriers. Also, at the initial stage government should also provide lucrative offers to bank to promote adoption of PV at easy interest rates. This would not only help in building rural market but would also boost rural employment and avert other social issues.

## References

- [1] South Asia Environment Outlook 2009  
<http://www.roap.unep.org/publications/SAEO%202009.pdf> [Accessed 12 November 2010]
- [2] United Nations Development Programme, 2007. Overcoming vulnerability to rising oil prices options for Asia and the Pacific, Thailand.
- [3] Energy and the Poverty in the Maldives, UNDP Report, Challenges and the way forward, 2007
- [4] Development Effectiveness Brief Report of Bhutan, Asian development Bank
- [5] Overview of Energy policies in Bhutan, Department of Energy, Ministry of Economic Affairs, RGoB March 2009
- [6] International Energy Outlook, International Energy Agency, 2009
- [7] <http://tonto.eia.doe.gov/cfapps/ipdbproject/IEDIndex3.cfm?tid=2&pid=2&aid=2>  
[Accessed 22 February 2010]
- [8] <http://www.oksolar.com/abctech/solar-radiation.htm>
- [9] [http://www.worldenergyoutlook.org/database\\_electricity/electricity\\_access\\_database.htm](http://www.worldenergyoutlook.org/database_electricity/electricity_access_database.htm)  
[Accessed 22 February 2010]
- [10] Sayathe, J. & Phadke, A., 2004. Cost and carbon emissions of coal and combined cycle power plants in India: Implications for costs of climate mitigation projects in a nascent market, International Energy Studies, Berkeley, USA
- [11] CERC (Terms and Conditions of Tariff) Regulations, 2009
- [12] Summary report of the study “ Post-Clearance Environment impacts and Cost benefit analysis for Power Generation in India” Conducted by National Environment Engineering Institute (2006) Available at:  
[http://www.mospi.gov.in/research\\_studies\\_post\\_clearance.htm](http://www.mospi.gov.in/research_studies_post_clearance.htm)

## Case Study: Modelling and sizing stand-alone PV systems for powering mobile phone stations in Libya

Salem Ghozzi<sup>a\*</sup>, Khamid Mahkamov<sup>b</sup>

<sup>a</sup>*Al madar Al jadid, Almadar Aljadeed Building, Gorgi Area, P.O. Box 83792, Tripoli Libya*

<sup>b</sup>*School of Comp., Eng. and Inf. Sciences, Northumbria University, Newcastle upon Tyne, NE1 8ST, UK*

\* *Corresponding author. Tel: +218 91-919-0500, E-mail: [s.ghezzi@almadar.ly](mailto:s.ghezzi@almadar.ly)*

---

**Abstract:** A mobile telecommunication sector has experienced a rapid growth in Libya and Al-Madar Al-Jadid is one of largest companies providing services in this sector. Currently, PV systems are widely used for powering remote GSM communication stations in the country and number of Al-Madar Al-Jadid communication stations powered by such stand-alone PV systems was about 135 in 2009. A Simulink Matlab model was built to dynamically simulate the operation of the stand alone PV system powering one of Al Madar Al Jadid remote communication stations in desert conditions, taking into account variation of insolation and ambient temperature during a day. The results of mathematical modelling on the producible and produced power, charging and discharging battery power and the state of charge of the battery bank are in a good agreement with real experimental data recorded on the station with the use of a data-logger. Results obtained clearly indicated that the existing system, including PV panels and the electrical storage, is excessively large for the current electrical demand on the station and therefore could be reduced in the size by a factor of two.

**Keywords:** *Stand alone PV systems, Modeling stand alone PV systems, Powering mobile phone stations by stand alone PV systems.*

---

### 1. Introduction

The use of PV systems for powering remote communication stations is rapidly expanding in both developed and developing countries [1]. In Libya the photovoltaic power has been in use for the stations of communication networks since 1979. The use of the PV technology instead of diesel-generators reduces operational costs, since there is no need for fuel transportation, and is exhaust gas emissions (CO<sub>2</sub> and NO<sub>x</sub>) free.

A typical PV system generally consist of an array of PV panels (a solar generator), an energy storage, which is very important for stand-alone systems, a power conversion system made of DC/DC converters and inverters, and an associated power flow control.

Dynamic modelling the operation and interaction of all system components, especially the PV generator and the electrical storage, is very important for the system assessment and its sizing. Mathematical models should be validated against the performance of the actual system in order to evaluate its accuracy and then can be used with a confidence to predict the overall performance of similar systems with different sizes. In this study, the PV generator and the electrical storage made of battery banks have been modelled in the Libyan environment using Simulink Matlab software and then the model results were compared to experimental data collected in one of Al-Madar Al-Jadid standalone communication stations.

### 2. Methodology

#### 2.1. Modelling of the stand-alone PV system

The system model combines two sub-system models, the PV model and the battery storage system model, see *figure 1*. The model does not take into account the influence of air flow, due to its complexity, and calculates the DC output power of the PV array ( $P_{PV}$ ) in watts as function of the solar irradiance, the PV cells temperature and the ambient temperature. The DC power output of the PV array is used as input data in the battery storage model. The

battery model simulates a lead-acid battery bank and calculates the electricity flow for situations when batteries are charged or discharged and also the surplus and deficient power values.

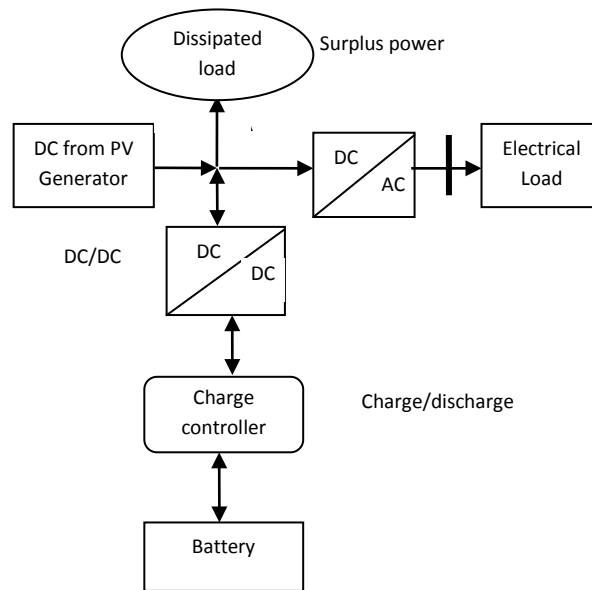


Fig. 1. The schematic of the electrical storage and electrical interface model

## 2.2. PV generator model

In order to achieve the best performance the PV modules must operate at the maximum power point (MPP). There are several methods to calculate DC power generated by the PV system and in this work this value was calculated as [2]:

$$P_{PV} = \eta_g \times N \times A_m \times G_T, \quad (1)$$

where  $\eta_g$  is the instantaneous efficiency of the PV system,  $A_m$  is the area of a single PV module ( $m^2$ ),  $G_T$  is the global irradiance incident on the titled plane ( $W/m^2$ ) and  $N$  is the number of modules.

In the modelling it was assumed that connection and wiring losses and all other energy losses in the PV system are negligible.

The instantaneous efficiency of the PV generator is given as

$$\eta_g = \eta_r \times \eta_{TR} [1 - B_T (T_c - T_r)]. \quad (2)$$

Here  $\eta_r$  is the PV generator reference efficiency,  $\eta_{TR}$  is the efficiency of the maximum power point tracker (MPPT),  $T_c$  is the solar cell temperature ( $^{\circ}C$ ),  $T_r$  is the solar cell reference temperature ( $^{\circ}C$ ) and  $B_T$  is the temperature coefficient, ranging from 0.004 to 0.006 per  $^{\circ}C$  for a silicon cell.

The PV cell temperature is expressed as [3]:

$$T_c = T_a + G_T \left( \frac{\tau \times \alpha}{U_L} \right), \quad (3)$$

where  $T_a$  is the ambient temperature ( $^{\circ}\text{C}$ ),  $U_L$  is the overall heat loss coefficient ( $\text{W}/\text{m}^2\text{ }^{\circ}\text{C}$ ),  $\tau$  and  $\alpha$  is the transmittance and the absorbance coefficients, respectively, of the PV cell.

In this investigation the simplified mathematical model of the PV generator has been adopted in Simulink Matlab in order to calculate the DC power output and this model is based on the following equation [4]:

$$P_{PV} = \eta_{PV} \times S \times A_{PV} (1 + \sigma_T (T_c - T_{c\_ref})) \times \eta_{MPP\_PV}, \quad (4)$$

where  $P_{PV}$  is the DC power output of the PV generator,  $S$  is the solar irradiance incident on the surface of the solar cell,  $\eta_{PV}$  is the efficiency of the PV generator,  $A_{PV}$  is the area of the PV modules,  $\sigma_T$  is the temperature coefficient,  $T_c$  is the solar cell temperature,  $T_{c\_ref}$  is the reference solar cell temperature and  $\eta_{MPP\_PV}$  is the efficiency of the MPP tracker.

The input data for the Simulink Matlab model consists of the irradiance, the ambient temperature, the temperature of the cell, the area of the modules and the reference solar cell temperature. The Simulink Matlab model simulates the PV generator when it is working at the MPP.

The temperature of the PV cells is a function of the weather conditions and the PV cells characteristics. The PV cell temperature ( $T_c$ ) is given as [4]:

$$T_c = T_a + \frac{S}{S_{ref}} \times (T_{c\_ref} - T_{a\_ref}) \times \left(1 - \frac{\eta_{PV}}{0.9}\right), \quad (5)$$

where  $S_{ref}$  is the reference solar irradiance and  $T_{a\_ref}$  is the reference ambient temperature.

### 2.3. Electrical storage system model

The battery storage system, shown in *figure 1*, has been adopted from [6]. It is relatively simple model but is sufficient to achieve the purpose of these investigations, which is evaluation of the power flow between the PV generator and the load and batteries and between batteries and load when it is necessary to compensate the shortage in the power production. The model is based on a time resolution of 60 minute to simulate the generated power, the load demand, the electrical storage and the power losses in the inverters and the power electronic equipment. The model is a generic and can simulate different sizes of the electrical storage system by changing the nominal voltage of the system  $V_B$  and the storage capacity  $C_O$ .

The nominal DC voltage output  $V_B$  of the battery in the model is set to be 48 V to match the battery used in the Al Madar Al Jadid telecommunication station. The storage capacity  $C_O$  of battery bank of PV system used in the stations of Al Madar Al Jadid is 5964 Ah. The state of charge SOC can be defined from documentation provided by the manufacturer. It is recommended not to discharge the battery completely in order to increase the life span of the battery and to avoid the very high drop of the battery voltage. Manufacturers commonly recommend the SOC from 20% to 80% of the storage capacity  $C_O$ . However, in this model,  $\text{SOC}_{\max}$  and  $\text{SOC}_{\min}$  are taken as 100% and 20% of  $C_O$ , respectively, to guarantee an acceptable battery's lifetime (i.e.  $\text{SOC}_{\max}=5964$  Ah and  $\text{SOC}_{\min}= 4771.2$  Ah). It is recommended in the provided technical documentation that the maximum allowable discharging current should be equal to  $C/5$  and that the maximum charging current should be

equal to  $C/10$ . Thus, in the battery bank the maximum allowable discharging current  $I_{Dmax}$  and the maximum allowable charging current  $I_{Cmax}$  are 1192.8 and 596.4 A, respectively.

Charging and discharging currents at any time ( $t$ ) vary depending on the shortage or surplus in the available DC power from the PV generator, though, in order to ensure efficient performance of the battery, a charge controller limits these currents to the maximum and minimum amounts,  $I_{Dmax}$  and  $I_{Cmax}$ , respectively [5].

The surplus power  $P_+$  at any time is the difference between the power of the PV generator ( $P_{PV}$ ) and the electricity demand of the load  $P_{Load}$  at the same time [5]:

$$P_+ = P_{PV} - P_{Load}, \quad P_{PV} > P_D \quad (6)$$

where  $P_D$  is the electricity demand of the site at any time.

However, when the power produced by the PV generator  $P_{PV}$  is less than the demand, then a shortfall in power  $P_-$  can be calculated as follow:

$$P_- = P_{Load} - P_{PV}, \quad P_D > P_{PV} \quad (7)$$

The surplus power produced by the PV modules is used to charge the battery bank, unless it is already fully charged; the batteries charging current ( $I_{CO}$ ) is limited by the charge controller to the maximum allowable charging current  $I_{Cmax}$  and SOC must be equal to or less than  $SOC_{max}$ . The charging current  $I_{CO}$  is calculated as [5]:

$$I_{co} = \frac{(P_+ \times \varepsilon_c \times \varepsilon_{B1})}{V_B}, \quad (8)$$

where  $\varepsilon_C$  is the charge controller efficiency (it is constant and equal to 0.98 in the model) [5];  $\varepsilon_{B1}$  is the AC/DC converter efficiency, though it varies insignificantly with the load, it is assumed to be constant at 0.9;  $V_B$  is the system and the batteries voltage and equals to 48 V.

In the event when the power required by the demand exceeds the generated power the current from the battery  $I_{DO}$  contributes to compensate this shortfall power.  $I_{DO}$  is

$$I_{DO} = \frac{P_-}{(V_B \times \varepsilon_C \times \varepsilon_{B2})}, \quad (9)$$

Here  $\varepsilon_{B2}$  is the efficiency of the DC/AC converter or inverter [5].

The change in the battery capacity  $C_D$  with a period of time of  $\Delta t$  can be calculated as:

$$\Delta C = (I_C \times \Delta t) - C_D, \quad (10)$$

The battery state of charge SOC at any time  $t$  is calculated by the following equation:

$$SOC_t = SOC_{(t-1)} + \Delta C, \quad (11)$$

where  $SOC_{(t-1)}$  is the battery's SOC at the time earlier than  $t$ , which is limited by the values of  $SOC_{min}$  and  $SOC_{max}$ .

The PV generator sources the load and charges the batteries during the day. In sunny periods, when the batteries are fully charged there will be more power produced than it is required. Therefore, the surplus power is dissipated in the Simulink model. The power demand supplied by the batteries at any time is calculated as [5]:

$$P_{batt} = I_D \times V_B \times \varepsilon_{B2} \times \varepsilon_C \quad (12)$$

On the other hand, if there is surplus power  $P_+$  and  $SOC = SOC_{max}$  or  $I_{CO} > I_{Cmax}$ , the dissipated power  $P_{diss}$  will be determined as

$$P_{diss} = \left[ \frac{I_{CO}}{\varepsilon_{B1} \times \varepsilon_C} - I_C \right] \times V_B \quad P_{diss} = \left[ \frac{I_{CO}}{\varepsilon_{B1} \times \varepsilon_C} - I_C \right] \times V_B \quad \text{For } I_{CO} > I_C \quad (13)$$

The model calculates the SOC for every minute taking into account the charging and discharging currents determined in equations 8 and 9, the maximum and minimum limits of the charge,  $SOC_{max}$  and  $SOC_{min}$ , respectively. The power drawn from the battery  $C_D$  at any time estimated by multiplying  $I_D$  by  $\Delta t$  in hours. However, the efficiency of discharge at high rates is considerably lower than 100%, so the accurate discharge efficiency can be calculated as [6]:

$$C_D = \frac{I_D \times \Delta t}{\alpha}, \quad C_D = \frac{I_D \times \Delta t}{\alpha}, \quad 0 \leq \alpha \leq 1 \quad (14)$$

where  $\alpha$  is the discharge efficiency determined as [5]:

$$\alpha = \frac{13.3 \times \ln\left(\frac{C_D}{I_D}\right) + 59.8}{100}, \quad 0 \leq \alpha \leq 1 \quad (15)$$

It has been assumed in the model that the value of  $\alpha$  cannot exceed the value which guarantees that the maximum charge removed from that battery at any time period  $\Delta t$  does not exceed the product ( $I_D \cdot \Delta t$ ).

Although the same phenomenon is present during charging process, it does not significantly affect the efficiency of charging, especially with the charge current limited to  $C/10$  (as highlighted earlier). So, such the effect has been neglected in the model. Consequently, the change in battery capacity  $C_D$  during any time period  $\Delta t$  is calculated as

$$\Delta C = (I_c - \Delta t) - C_D \quad (16)$$

Thus, the battery SOC at any time  $t$  is calculated using the following equation:

$$SOC_t = SOC_{(t-1)} + \Delta C, \quad (17)$$

Here  $SOC_{(t-1)}$  is the battery's SOC at the time earlier than  $t$  and is limited by the values of  $SOC_{min}$  and  $SOC_{max}$ .

### 3. Experimental Part

Al Madar Al Jadid Company started using PV panels for power supply of stations in 2005, when 6 new stations were built in a rural areas and the General Company of Electricity refused to power these new sites since some of them were away from the national grid and the grid network in the vicinity of others were not powerful enough. The PV systems were supplied and installed by Total Company using Ericsson a sub-contractor. The PV systems and batteries with the voltage of 24Vdc were used to power the stations directly without DC/AC conversion. Recently, the network of Al Madar Al Jadid Company has expanded to cover rural regions, oil company sites and roads in the desert area. A project to built 350 stations including 135 sites powered by PV panels, was developed and accepted in 2009. The new stations will have AC air conditioning, so it is necessary to use DC-AC inverters.

The GSM station which was chosen to be used for evaluation in this study is located in the vicinity of the main road connecting country's north and south parts and is about 50 km away from the national grid. The actual data used in this study is acquired at the location of the station using a laptop base data acquisition system. The data has been collected over three times periods, namely in January, April and July.

### 4. Results and discussion

During numerical investigations the average hourly performance of the PV system was modeled for three periods, namely January, April and July, and then the theoretical results were compared with the corresponding experimental data. The climatic conditions were taken from NACA collected data and the highest discrepancy between theoretical and experimental results was observed in modeling of operation in January period. Even so, the theoretical model provides acceptable accuracy in simulation the performance of the PV system.

The load entered into the Simulink Matlab model is an actual load for the real PV generator operating in Libyan winter conditions.

Although the solar radiation on a horizontal surface in winter, particularly, in January and December is not high, the solar radiation on an inclined surface is fair and at noon reaches the level of about  $700\text{W}/\text{m}^2$ . The high value of the geometric factor for January and December months causes an increase in the solar radiation on inclined surfaces.

*Figure 2* illustrates the DC power that can be produced by the PV generator. Overall, the both theoretical and experimental curves have the same trend and the output power, which is represented by the area under the curves, is almost equal. The main difference is that the curve of the experimental output power is shifted in time and the PV system starts to generate power at about 8:30 am and not at 7.30 as predicted by simulations. This is because of satellite data on solar irradiance used in this study which is hourly data for a fixed period from 7:30 to 16:30 for 12 months of the year.

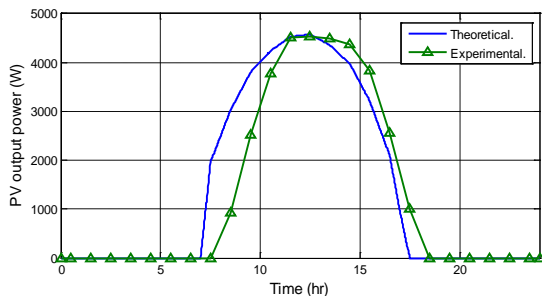


Fig. 2. Producing PV power

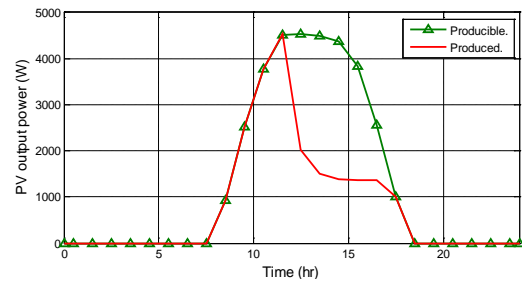


Fig. 3. Producing and produced PV power

Figure 3 shows the actual power produced by the PV generator and how much power is lost as a result of over sizing the PV system. The sum of the power consumed by the load and received by the electrical storage is about a half of the total producible power.

It can be seen in figure 4 that the simulated battery charging curve is very similar to that of the experimental results. In both theory and experiment the batteries receive power as soon as it is started to be generated by the PV panels and it demonstrates that the power consumed by the load is very small compared to the power generated. On the other hand, the batteries are fully charged within few hours, because of the low power discharge, which is result in the huge capacity of the battery bank comparing with the load consumption. However, it can be observed from the experimental curve in figure 4 that the batteries charging is continued until the end of the day to compensate battery self-discharging process.

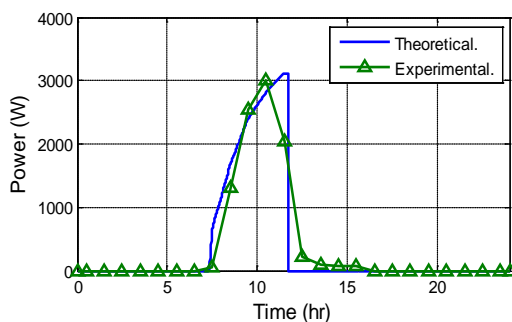


Fig. 4. Charging power

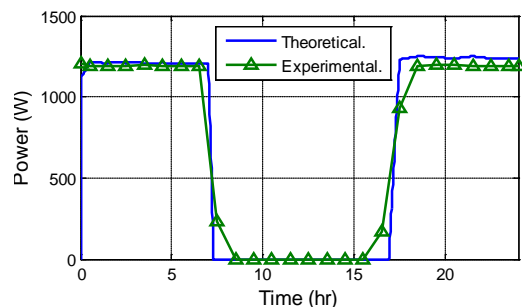


Fig. 5. Discharging power

Figure 5 presents the theoretical and experimental results on the battery discharging. As it can be seen from this figure, the curves are close, except at the beginning and the end of the day. Theoretically, the load is supplied either by the PV generator or the electrical storage; while in the real system, the shortage in the power from the PV generator is compensated by the power from the battery and this is reason for discrepancy between theoretical and experimental curves.

Figure 6 shows the SOC and processes of charging and discharging power in the summer period. It can be observed in this figure that, the batteries are fully charged within few hours, due to the small power drawn by the load during the night time. That emphasizes the excessive capacity of the battery bank compared with the load consumption.

As it is highlighted above, the power produced by the PV panels is disproportionately large when compared to the load consumption and the electrical storage. On the other hand, the capacity of the electrical storage is also very large with respect to the power consumed by the load. As a result, the deficit in the power is always zero. The dissipated power, which is represented by the red colour section in figure 7, is approximately two thirds of the total power that can be produced if the capacity of the battery bank is large enough, whereas the

produced power, which is represented by the blue colour section, is only about one third of the total power.

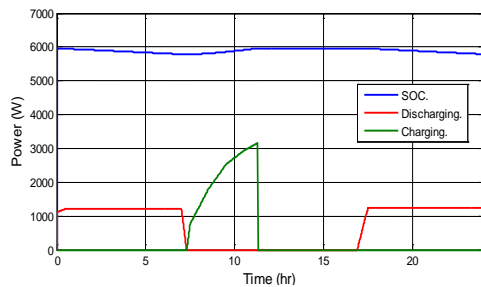


Fig. 6. State Of Charge of the battery bank

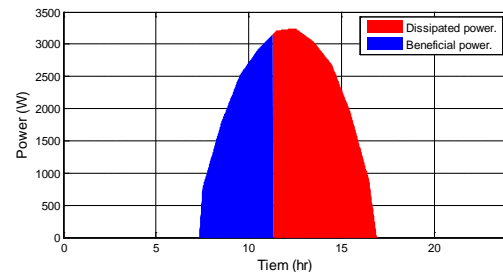


Fig. 7. The beneficial and the dissipated power

## 5. Conclusion

In this study the performance of standalone PV systems in telecommunication stations has been numerically evaluated. The simulation results illustrated that there is a considerable amount of the producible power is dissipated due to the over sized PV panels which can produce much more electricity than that could be stored in batteries bank. On other hand, the power drawn from the battery bank at the normal rate is small and does not exceed 3% of the total stored power, which demonstrates the excessively large capacity of the electrical storage. Although zero solar radiation situations are very unlikely to have place such scenario taking place for 24 hours was simulated in order to calculate the power supplied by the battery and the SOC of the battery bank. The results from the simulation of such the scenario showed that only 10% of the total stored power is drawn from the battery in the winter, autumn and spring seasons, and in summer period this value is 11% of the total stored power. These results emphasize the large capacity of the battery bank. As a result of series calculations, it is found that the 60% of the existed PV modules area and 50% of the electrical storage capacity would be sufficient for powering the station. This would also result in significant reduction (by about 50%) of the capital cost of the PV system.

## References

- [1] Kaldellis, J.K. Optimum Hybrid Photovoltaic-based Solution for Remote Telecommunication Stations, *Renewable Energy*, Vol. 35, October 2010, PP 2307-2315.
- [2] Markvart, T. *Solar Electricity*, 2<sup>nd</sup> edition, John Wiley & Sons, 2000, pp. 6-132.
- [3] Diaf, S. Diaf, D. Belhamel, M. Haddadi, M. and Louche, A. A methodology for Optimal Sizing of Autonomous Hybrid PV/Wind System, *Renewable Energy*, Vol. 35, November 2007, pp 5708-5718
- [4] Ashraf, A. Ran, Li Bumby, J. Sizing and Best Management of Stand Alone Hybrid PV-Wind System Using Logistical Model, 2009, The University of Durham.
- [5] Jenkins, D.P. Fletcher, J. and Kane, D. Model for Evaluating Impact of Battery Storage on Micro Generation Systems in Dwellings, *Energy Conversion and Management*, Vol. 49, August 2008, pp 2413-2424.
- [6] Peacock, A.D. and Newborough, M. Effect of Heat-Saving Measures on the CO<sub>2</sub> Savings Attributable to Micro-Combined Heat and Power ( $\mu$ CHP) Systems in UK Dwellings, *Energy*, Vol. 33, April 2008, pp 601-612.

## Designing a Photovoltaic Solar Energy System for a Commercial Building Case Study: Rosa Park Hotel in Khartoum-Sudan

Asim M. Widatalla<sup>1,\*</sup>, Heimo Zinko<sup>2</sup>

<sup>1</sup> Linköping University, Dept. of Thematic Studies, Water and Environmental Studies, Linköping, Sweden.

<sup>2</sup> Linköping University, Department of Management and Engineering, Energy Systems, Linköping, Sweden

\* Corresponding author. Tel: +46 707165268, E-mail: asiwi224@student.liu.se

**Abstract:** Instability of electricity supply in Sudan is an increasing problem, especially in the capital and other larger cities. Commercial users such as hotels are looking for alternative solutions in order to be able to deliver adequate standards to their guests. In this study we investigate and optimize combined PV/Diesel system as a main electricity source for a hotel. There is significant potential for the use of the photovoltaic solar energy in countries like Sudan which receive abundant amounts of solar radiation around the year; the present work aims to design a rooftop photovoltaic solar system, or a hybrid system (Solar and Diesel) to produce 88100 kWh/yr of electricity for Rosa Park Hotel in Khartoum. The aim of this feasibility study was to find economic and useful combinations between Diesel and PV systems based on actual electricity consumption data of the hotel, taking into consideration both economic and environmental system aspects.

The study shows that, the PV systems can be used independently or together with the Diesel generator as a replacement energy resource. Due to the high initial cost of the installation of a PV stand-alone systems, the economic optimizations shows that a combination of a relatively small Diesel aggregates with a PV system can result in low system costs taking advantage of free and clean solar energy of PV and the system flexibility of a Diesel system.

**Keywords:** HOMER, Hybrid system, Photovoltaic Solar Energy, Renewable Energy, Sudan.

### 1. Introduction

Sudan Fig.2 is a country located in northeastern of Africa, with high solar radiation, according to Abdeen, (1997), the average sunlight hours in the capital– Khartoum - range between 8.7 hours per day in July and 10.5 hours per day in February [1], this gives a yearly average of sunlight hours 9.92 per day, and around 3600 hours/year. On the real side: the country faces a serious problem of instability of electricity supply especially in the capital and the main big cities. The hydro-power generators could not feed their rated electricity supply mainly in the rainy season - April to October - because of the accumulation of the mud in the dams. There are some other factors that make the problems of electricity supply and demand in urban areas bigger than similar problems in rural areas, such as the constant increase of population and building density.



Figure 1: Map of Sudan [2]

The aim of this study is to find out how the solar energy can be used to produce electricity for a hotel in Sudan, the task is to design a stand-alone PV system, and a Solar/Diesel system, and then to compare those regarding cost-effectiveness and environment.

### 1.1. Rosa park hotel

Rosa Park Hotel is a new four stars hotel located at the city center of Khartoum, there are 66 rooms spread across five floors, In addition to the health club service and fitness center.



Figure 2: Photos from Rosa Park Hotel. [3]

### 1.2. Photovoltaic System

For this study, a commercial polycrystalline silicon solar cell was chosen at offered fixed price for the installation. Besides the solar cells, there are other important components in the PV-system, such as the inverter that is used to convert the direct current DC from the solar modules to alternating current AC, in our case synchronous with the grid. Furthermore, due to the variability of sunshine on both daily and seasonable basis, the mismatching between the production and the consumption of the electricity must be balanced by a battery system. [4].

### 1.3. Methodology

The methodology that we used for this study included the preparation of the inputs and calculations that are required for the simulation process. These inputs can be technical specifications of the PV panels, batteries, generators, etc., or the characteristics of the plant size, such as the weather data of the area where the system will be build on, the solar radiation density to which the plant site is exposed and the annual average temperature of the specific area. Also the economical inputs such as the capital costs and costs for replacement, operation and maintenance of the different equipment are of great importance for the financial evaluation.

A commercial software HOMER (Hybrid Optimization Model for Electric Renewables) was chosen for simulation purposes. HOMER is a computer model first developed by National Renewable Energy Laboratory, (USA-DOE). It is based on hour to hour simulation and this gives possibilities to control the battery status and to determine the sizing of the batteries [5]. The program determines the energy production for a given system over a defined period and calculates investment and operational costs. Because of the possibility of handling multiple inputs, HOMER can in short time calculate a multitude of optional system solutions and by that way an optimal system solution can be found.

## 2. Energy specifications

### 2.1. Electrical loads

The primary load distribution is essential for the designing process because the variation of the load through the day and night will affect the number of PV panels, and hence the capacity of storage battery and inverter:

- There are different loads for different seasons, the load will be 300 kWh/day for the tourists season (from October till February), and 200 kWh/day for the normal season (from March till September).
- The power consumption will vary according to the daily activities, for example; most of the work in the kitchen, rooms cleaning and the laundry used to be during the day.

The following tables show the loads for the two seasons per hour during day and night.

Table 1: The load of the tourist season

Time	Load kW	Time	Load kW	Time	Load kW	Time	Load kW
00:00 - 01:00	3.0	06:00 - 07:00	7.0	12:00 - 13:00	20.0	18:00 - 19:00	15.0
01:00 - 02:00	3.0	07:00 - 08:00	10.0	13:00 - 14:00	25.0	19:00 - 20:00	15.0
02:00 - 03:00	3.0	08:00 - 09:00	15.0	14:00 - 15:00	25.0	20:00 - 21:00	10.0
03:00 - 04:00	3.0	09:00 - 10:00	15.0	15:00 - 16:00	25.0	21:00 - 22:00	8.0
04:00 - 05:00	3.0	10:00 - 11:00	15.0	16:00 - 17:00	25.0	22:00 - 23:00	6.0
05:00 - 06:00	3.0	11:00 - 12:00	20.0	17:00 - 18:00	20.0	23:00 - 00:00	6.0

Table 2: The load of the normal season

Time	Load kW	Time	Load kW	Time	Load kW	Time	Load kW
00:00 - 01:00	2.0	06:00 - 07:00	3.0	12:00 - 13:00	13.0	18:00 - 19:00	10.0
01:00 - 02:00	2.0	07:00 - 08:00	6.0	13:00 - 14:00	18.0	19:00 - 20:00	10.0
02:00 - 03:00	2.0	08:00 - 09:00	10.0	14:00 - 15:00	18.0	20:00 - 21:00	8.0
03:00 - 04:00	2.0	09:00 - 10:00	10.0	15:00 - 16:00	18.0	21:00 - 22:00	4.0
04:00 - 05:00	2.0	10:00 - 11:00	10.0	16:00 - 17:00	18.0	22:00 - 23:00	3.0
05:00 - 06:00	2.0	11:00 - 12:00	13.0	17:00 - 18:00	13.0	23:00 - 00:00	3.0

## 2.2. Solar radiation

The average global solar radiation on the horizontal surface for each hour of the year will be needed for designing a PV system in a specific location. Here for this study, the solar plant was suggested to be located in Khartoum in Sudan at a location of 15° 31' N latitude and 32° 35' E longitude. The hourly solar radiation data was obtained from the NASA Surface Meteorology and Solar Energy web site [6]. The annual average of the daily solar radiation on a horizontal surface for this area is 6.31 (kWh/m<sup>2</sup>/d).

## 3. Optimization

By feeding the software with the required basic input data, HOMER starts the work by running an hourly simulation of all possible configurations of different system types, and performs energy balance calculations for each hour in the year. The optimization process generates a list of configurations, sorted by net present cost, which can be used for the comparison of the different system design options [7]. An example is shown in Figure 3.

Three main types of system solutions have been investigated: PV stand-alone system, Hybrid system (PV + Diesel) and Diesel generator system (reference case). The size of PV system, Battery system and inverter system is depicted in Figure 3.

Sensitivity Results		Optimization Results												
Double click on a system below for simulation results.														
Categoriz														
		PV (kW)	engin (kW)	H3000	Conv. (kW)	Initial Capital	Operating Cost (\$/yr)	Total NPC	COE (\$/kWh)	Ren. Frac.	Diesel (L)	engin (hrs)	Batt. Lf. (yr)	
		20	10	12	20	\$ 137,703	11,083	\$ 279,380	0.251	0.42	18,481	5,629	8.3	
			20	12	20	\$ 47,430	18,559	\$ 284,672	0.251	0.00	32,372	5,082	6.4	
		20	20		20	\$ 134,374	20,225	\$ 392,918	0.348	0.36	48,390	8,732		
			30			\$ 29,181	29,745	\$ 409,424	0.361	0.00				
		61		48	40	\$ 387,064	3,650	\$ 433,729	0.399	1.00			13.8	

Figure 3: Optimization results generated by Homer.

The headers in Figure 3 have the following meanings: *engin* - diesel engine, *H3000* means 1 set of storage battery type of Hoppecke 24 OPzS (3000 Ah), *Conv.* is for converter, *Ren. Frac.* is for Renewable fraction of generated electricity, and *Batt. Lf.* is for battery lifetime, besides the symbols of PV panel, diesel engine, battery and converter are also included.

### 3.1. Economic parameters

The investment costs are described in Table 3. The costs include the hardware, the installation on the site and the connection to the grid. Beside the initial investment, we have to take into account replacement of equipment which is worn out. Hence replacement costs are added to the generation cost, when the lifetime of equipment has been reached. For batteries, the life time is different depending on the number of charging cycles and depth of the discharge. This is the reason for varying battery lifetimes in different systems. The time frame of the financial analysis of this project is 25 years. The interest rate was taken to 6 %.

The economical evaluation of the project can be calculated based on the inputs of financial aspects, which include the cost of the system components that the hotel's owner will pay, and on the other hand the benefits that the owner will earn from the projects.

- *Projected Benefits = Value of Generated Electricity + Value of Excess Energy + Value of CO<sub>2</sub> Reduced*
- *Electricity Costs = Capital Costs + Replacement Costs + Periodic Costs.*

The annuity calculations of all the benefits, the costs and also the Net Present Value were done based on assumed 25 years lifetime of the PV panels. The lifetime of the batteries is varying according to their use (see sect. 3.2.2) and the life time of the inverter is 15 years. Replacement costs are shown in Table 4.

#### 3.1.1. Value of electricity

For the evaluation purpose of this system, we will use the electricity price that is achieved by the Diesel generator as a reference in order to calculate the projected benefit – because Diesel generators are widely used to produce the electricity in the areas of instable electricity supply. Therefore, According to the summary of the results in Table 7 the annual saving due to the electricity production is:

$$= \text{the generated electricity through the year (kWh/yr)} * \text{Diesel generated electricity price (\$)}$$

$$= 88100 \text{ kWh/yr} * 0.251 (\$/\text{kWh}) = 22113.1 (\$/\text{yr}).$$

Eventual excess energy (which is produced by the stand-alone system) is assumed to be sold to neighbors for the price of diesel-electricity.

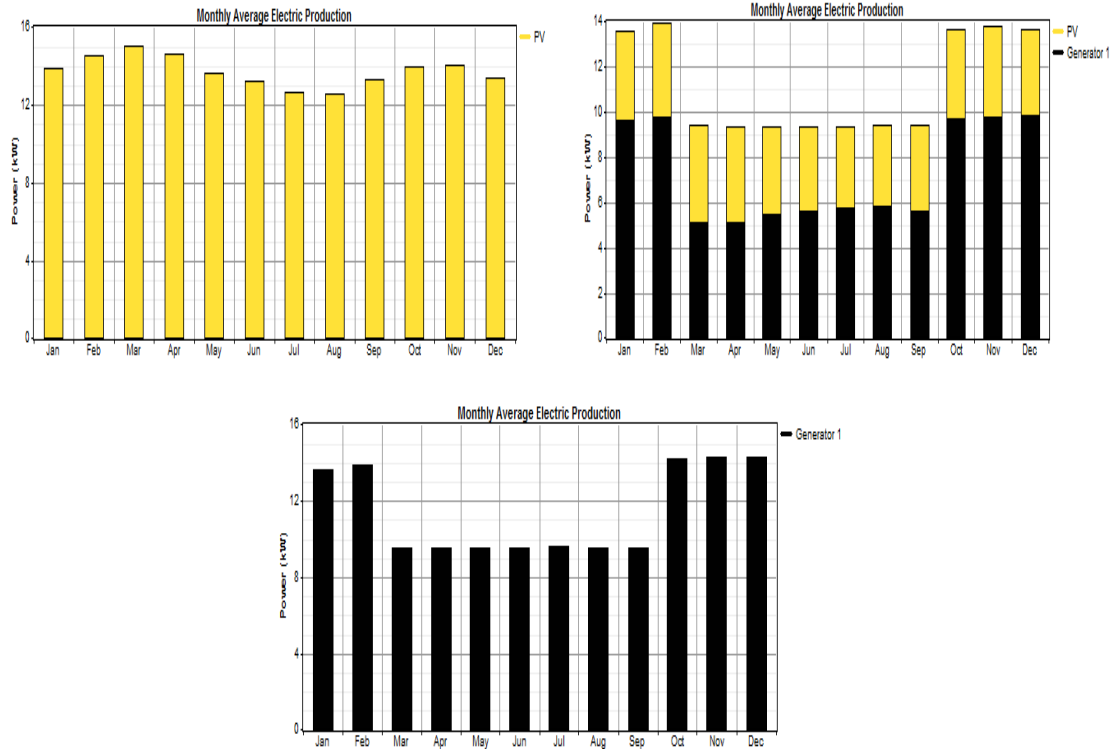


Figure 4: Monthly Average Electric Production for the three different System solutions.

### 3.1.2. Value of emitted CO<sub>2</sub>

The reduced amount of CO<sub>2</sub> by the energy system has an economical value, due to the taxes that will be paid for each kg of CO<sub>2</sub> that is emitted, even if there are at the moment no policies that control the emission of CO<sub>2</sub> in Sudan. The value for the CO<sub>2</sub> reduction is set to 15 \$/ton.

### 3.1.3. Capital cost

Table 3 below shows the capital cost or the specific purchase price of the different components of the system (PV systems, Storage Batteries, Inverters and Diesel Generator):

Table 3: The Capital Cost

Unit	Size	Capital Cost	Ref.	Unit	Size	Capital Cost	Ref.
PV panels	1.0 kW	5000 \$	[8]	Inverters	1 kW	746.4 \$	[10]
Diesel Generator	1.0 kW	972.7 \$	[9]	Batteries	1 set (3000 Ah)	1088.2 \$	[11]

The PV panel's cost that mentioned above is the total cost of the system including panel, installation, connection to the house and so on, the panel's cost is about half of that.

### 3.1.4. Cost of Replacement, Maintenance and Fuel

The replacement cost is the cost of equipment that is purchased to replace a component when its lifetime is shorter than the project time set for this financial analysis. The solar cells have not to be replaced, but the inverters will be replaced after 15 years, battery's lifetime indicated in Figure 3. Battery's lifetime is greater when using PV standalone than the other systems because the number of batteries that used is four times greater, also the battery's annual throughput (the amount of energy that cycled through the battery bank /year) of this system is two times greater. Table 4 shows the replacement cost of the different components:

Table 4: The inputs of the specific Replacement Cost

Unit	Size	Replacement Cost	Unit	Size	Replacement Cost
PV panels	1.0 kW	0	Inverters	1.0 kW	\$ 746.4
Diesel Gen.	1.0 kW	\$ 680.9	Batteries	1set (3000 Ah)	\$ 1088.2

The operating and maintenance (O&M) cost of the PV panel is expected to be \$0.45 per m<sup>2</sup>/year, [12], Table 5 shows the maintenance cost for the rest of the components:

Table 5: The Inputs of the Periodic Maintenance Cost

Unit	Size	O&M Cost \$	Unit	Size	O&M Cost
PV panels	1.0 kW	\$4.09/yr	Inverters	1.0 kW	0
Diesel Gen.	1.0 kW	\$0.078/hr	Storage Batteries	1set (3000 Ah)	\$20/yr

The total operating cost is the sum of the annual operation and maintenance cost, and the annualized replacement cost for remaining time of the equipment. The price of Diesel used in this study was selected based on the actual market price of 2006, for gasoline and Diesel in northern Kurdufan which was approximately (1.35 \$/gallon), while the cost in villages is about (1.44 \$/gallon) [13]. The total annual O&M costs are shown in Figure 3, showing the large difference between PV stand-alone at the Diesel system.

#### 4. Results

A summary of the optimized results of the different categories are listed in Table 6. Based on the results, the selected economical evaluation methods will be discussed as shown below. It is interesting to note, that the Hybrid system shows the lowest Net Present Value of all the systems investigated. The systems are compared by means of three types of cost analysis, all three calculated using standard methods and standard definitions:

- *Net Present value NPV*
- *Payback Period (straight payback)*
- *Levelized Cost of Energy (COE)*

Table 6: Summary of the Simulation Results

System	Ann. Saving \$	NPV \$	Payback period	Levelized COE (\$)	Excess Electricity	CO <sub>2</sub> Emission kg CO <sub>2</sub> /kWh
PV Stand-alone	29774.1	433729	13.1 yr	0.399	18.6 %	0
Hybrid System	24031.8	279380	8.3 yr	0.251	0	0.507
Diesel Gen.	22113.1	284672	5.0 yr	0.251	0	0.879

The annual saving is based calculated from the amount of the electrical energy produced per year and delivered to the hotel and in the case of the stand-alone system also to the neighbors. This is multiplied by the cost of electricity produced by the Diesel system (which is 0,251 \$/kWh).

##### 4.1. Net Present Value NPV

As shown in Table 7, the initial cost of the PV Stand-alone system is the highest among all the systems-almost 3 times compared with the hybrid system, and more than 8 times compared with the Diesel system. However, the PV system uses no fuel, and the other systems pay from \$7000 and \$12000 per year, respectively. Also, Diesel generators need to be replaced approximately 4 times during the project's lifetime. The storage battery holds for about 14 years in the stand-alone system; it needs to be changed 2 times at least for the other systems.

At the end of the project's economic running time, the total NPV of the PV stand-alone system is only about 1.5 times of both the hybrid and the diesel systems total NPV cost.

Table 7: The details of the NPV cost.

	Initial Capital \$	O&M Cost \$	Annual Fuel \$	Total NPV \$
PV Stand-alone system	387 064	1 204	0	433 729
Hybrid System	137 703	335	7 014	279 380
Diesel Generator	47 430	266	12 285	284 672

It can be seen that the NPV-analysis has a limited effect on the economical evaluation on the two systems (stand-alone and the hybrid), in spite of the big difference in the initial costs.

#### 4.2. Payback period

The payback period can give an indication to the investor how fast he can get his money back. From the data of Table 6, one can notice that while the minimum time that is needed to recover the investment cost of the hybrid system and the Diesel generator system are 8.3 and 5 years respectively, the stand-alone PV system needs 13.1 years to recover its cost.

#### 4.3. The Levelized Cost of Energy COE

The levelized cost of energy COE gives the average cost of producing one kWh of electricity, including all the different cost contributions. Table 7 shows that the PV stand-alone system has the highest COE per kWh (\$ 0.399), while the COE of both Diesel and hybrid systems are the same (\$0.251). This seems to be reasonable in respect to the NPV-levels of the systems.

#### 4.4. Sensitivity analyses

In such analyses, the results are strongly influenced by the quality of the input. Therefore, sensitivity analyses can illustrate this influence. In our study, we have increased the oil price by 20 % , and reduced the PV panels cost by 20 %. In all cases, there was no change of the ranking of the three types of systems, but of course the gap becomes smaller. The Hybrid system turns out to be the system with lowest COE (0.25 \$/kWh) in both cases, the PV stand-alone system remaining the system with the highest COE (0.359 \$/kWh).

### 5. Discussion and/or Conclusions

Three categories of the power systems are suggested by this study to solve the instability of the power supply of Rosa Park Hotel in Khartoum, and to replace the grid/Diesel current options. From the simulation results, and the analysis of the annuity calculations, one can notice that both the stand-alone and hybrid PV/Diesel systems can be used and both of them sound profitable, with a straight payback period less than 9 years for the hybrid system, and less than 14 years -which is almost half of the project's lifetime- for the stand-alone system.

The study shows also that, the PV solar energy can be use separately or together with the Diesel generator as a replacement energy resource, to solve the power supply problems, and also to reduce the need of carbon-based energy. Due to the high initial cost of the installation of the stand-alone system, based on the economical evaluation of the systems, we think, the hybrid system is more viable option compared to the use of the Diesel generator separately. However, the selection of such system should not be evaluated based only on the economic feasibility; also the expected environmental and social benefits need to be considered, since the three elements are important for the sustainable development assessment of any project.

From the economical analysis it is easy to notice that, the stand-alone PV is the most expensive way to generate electricity among the three systems, but in terms of carbon dioxide emissions, it is more environmentally sound because the system emits no CO<sub>2</sub> during the electricity production, while both the Diesel generator system and the hybrid system emit considerable amounts of the greenhouse gas, about 0.879kg of CO<sub>2</sub>/kWh and 0.507kg of CO<sub>2</sub>/kWh respectively. According to Simon, these emissions from fossil fuel-powered generators present a 'cost' that should be factored into energy system choices [14]. This might be difficult to be achieved in developing countries such as Sudan, but if the government would make the cost per kWh from the power generator more transparent and would remove the fuel subsidy, PV systems would be a competitive option also in this country [13].

## References

- [1] O. Abdeen, Compilation and Evaluation of Solar and Wind Energy in Sudan, Renewable Energy Vol. 12 (No.1), 1997, pp 47.
- [2] Greenwich Mean Time website, (sited 29-10-2009, 21.58)
- [3] Rosa Park Hotel website (sited 24/08/2010) <http://www.rosaparkhotels.com/Photos.html>
- [4] (EUREC), PV in Building: The Art of Merging, the European Renewable Energy Research Centres Agency, 1997.
- [5] Vangaard, Morten Eghøj, Lund, Dan Toste, Design of a standalone PV system for Greenland, Dep. of Civil Engineering, Danmarks Tekn. Univ. (DTU), 2009, M.Sc: 7&8.
- [6] The NASA Surface Meteorology and Solar Energy web site - [http://eosweb.larc.nasa.gov/cgi-bin/sse/homer.cgi?email=asim214@yahoo.com&step=1&lat=15+31&lon=32+35&submit=Submit&ms=1&ds=1&ys=1998&me=12&de=31&ye=1998&daily=swv\\_dwn](http://eosweb.larc.nasa.gov/cgi-bin/sse/homer.cgi?email=asim214@yahoo.com&step=1&lat=15+31&lon=32+35&submit=Submit&ms=1&ds=1&ys=1998&me=12&de=31&ye=1998&daily=swv_dwn)
- [7] National Renewable Energy Lab., Getting started Guide for HOMER Vers. 2.1,2005.
- [8] Wholesale Solar Company website: sited 16/08/2010  
<http://www.wholesalesolar.com/products.folder/module-folder/bp/bp380U.html>.
- [9] Just Generators website: sited 16/08/2010  
[http://www.justgenerators.co.uk/pages/Stephill\\_SSDX11\\_3phase.htm](http://www.justgenerators.co.uk/pages/Stephill_SSDX11_3phase.htm).
- [10] Wholesale Solar Company website: sited 16/08/2010.  
<http://www.wholesalesolar.com/products.folder/inverter-folder/XP1100-12.html>
- [11] Wind & Sun company website: sited 16/08/2010.  
[http://www.windandsun.co.uk/Prices/prices\\_batteries.htm](http://www.windandsun.co.uk/Prices/prices_batteries.htm)
- [12] Joan M. Ogden, Cost and performance sensitivity studies for solar photovoltaic / electrolytic hydrogen systems, Solar Cell, 30, 1991 pp 517.
- [13] B. Croxford, M. Rizig, Is photovoltaic power a cost-effective energy solution for rural peoples in western Sudan? Solar 2006: renewable energy, key to climate recovery, American Solar Energy Society.
- [14] International Energy Agency (IEA), Guidelines for economic evaluation of building integrated PV, Report IEA PVPS T7-05: 2002 p.12.

## Analytical model and experimental validation of the heat transfer and the induced flow in a PV cooling duct in environmental conditions

R. Mazón<sup>1,\*</sup>, A.S. Káiser<sup>1,\*</sup>, B. Zamora<sup>1</sup>, J.R. García<sup>1</sup>, F. Vera<sup>1</sup>

<sup>1</sup> Thermal and Fluid Engineering Department, Technical University of Cartagena, Doctor Fleming, s/n 30202, Cartagena, Murcia, Spain

\* Tel: 34 96832594 rmh@alu.upct.es

\*Tel: 34 968325984, antonio.kaiser@upct.es

**Abstract:** This paper describes a model to account for the heat transfer and the convective flow induced in the interior of a channel inclined 35° with respect to the horizontal, formed by a photovoltaic panel and an adiabatic plate. The model developed is validated experimentally by measurements made on an experimental prototype. The solar installation consists of two photovoltaic panels integrated with air ducts on the top of a building in southern Spain. The objective is to determine the temperature reached by the photovoltaic module in this configuration. This model considers the processes of heat transfer by radiation and convection on the outside for several atmospheric conditions (wind speed, ambient temperature and incident radiation) and for different geometrical and physical characteristics of the PV cooling duct (plate area, module performance, emission and absorption coefficients). Good agreement has been obtained between the experimental data and the results of this model.

**Keywords:** PV cooling duct, solar experimental facilities, efficiency solar panels.

### 1. Introduction

The performance of PV implemented on the top of a building depends on the panel temperature in addition to other factors such as insulation and shading. High panel temperatures resulting from overheating could occur due to low wind cooling effect compared with free standing installation. One cost effective method to regulate the temperature of rooftop integrated photovoltaic (PV) panels is to provide an open air channel underneath the panel.

To determine the equilibrium temperature of the modules, for different atmospheric conditions, it is necessary to solve simultaneously the heat transfer processes between the PV modules and the exterior and interior of the air duct, and the convective flow induced by buoyancy effects and by the suction of the external wind. Various studies have been carried out to assess the performance of roof-mounted solar (thermal or photovoltaic) panels. Some authors centered their research on the effect of the air gap between a solar panel and a roof [1], others suggested that a reasonable air gap for solar thermal collectors would be between 0.1 and 0.14 m [2] and also derived expressions for the mass flow rate, velocity and temperature rise in the air gap behind solar cells considering the effect of the geometry (aspect ratio of the channel) and location of these solar cells [3]. Other authors presented procedures of the heat transfer and the convective flow through a PV cooling duct to determine the equilibrium temperature of the module [4].

This work initially raises the set of equations that characterize the thermal and fluid dynamic process in the air gap behind the solar cells. Subsequently a selection of the characteristic values is made of the input variables in this model, based on the existing literature and the available data on the experimental prototype presented in this work. Once estimated the solution of the equations system is presented, with particular emphasis on how the temperature of the module changes as the incident radiation and the external wind change. To

solve this system of equations the ESS software has been used. The model is validated with experimental measurements obtained on the configuration under study.

## 2. Experimental facility

The solar installation consists of two photovoltaic panels arranged as shown in figure 1, first panel (panel A) is used as reference panel. Panel temperature at different points, voltage, and current are measured to understand the panel behavior under normal operating conditions and to compare with another one (panel B) which is modified to test different ducts with different cross sections. In this second panel, surface temperature at different points, voltage, and current are also measured jointly with the air temperature and air flow rate. In the solar panels, temperatures are measured with RTD, and duct air speed with hot film anemometers [5].



Fig. 1. Solar panels. Left panel (A), right panel (B).

The horizontal components of solar radiation are measured by two pyranometers. Other environmental conditions such as temperature, pressure, humidity and wind speed are measured with a meteorological station place on our laboratory roof just beside the experimental facility. All data is registered and recorded by means of a data logger.

## 3. Analytical model

### 3.1. The incoming heat flow to the channel

As mentioned, the procedure requires the simultaneous solution of two heat transfer equations. On one hand it has to solve the external equation, which represents the transfer of heat to the surroundings from the top face of the module and on the other hand the internal equation, which represents the transfer of heat into the duct. The module temperature links up both equations. In general, there may be a temperature difference between the two faces of the photovoltaic module, which is given by the expression [6]

$$T_o - T_m = \frac{E}{E_o} \Delta T \quad (1)$$

where  $T_o$  is the cell temperature inside the module,  $T_m$  the lower face temperature,  $E$  is the irradiance measured,  $E_o$  is reference solar irradiance on the module ( $1000 \text{ W/m}^2$ ) and  $\Delta T$  the temperature gap between cell and back surface measured with  $E_o = 1000 \text{ W/m}^2$ , whose value

depends on the module rear ventilation (in this case is usually 2-3 ° C). In the approach of our model we consider in the first instance that there is no temperature difference between the two sides of the module.

The external equation requires the following energy balance. At any point of the module, the heat flux that goes into the channel is given by the difference between the absorbed solar radiation minus the electrical output and losses to the surroundings. These losses are due on one hand, to the reflected and emitted radiation, and on the other hand to the external convection:

$$q = (\alpha_s - \eta) \cdot q_s - U_a (T_o - T_a) \quad (2)$$

being  $\alpha_s$  the absorption coefficient,  $\eta$  the electrical efficiency,  $U_a$  the external loss coefficient and  $T_a$  the ambient temperature, and  $q_s$  the solar flux or irradiance. As guide values for electrical efficiency and the absorption coefficient we've considered  $\alpha_s = 0,85$  and  $\eta = 0,12$  [7]. Other authors suggest a value of  $\alpha_s - \eta = 0.8$  and regarding the external loss coefficient ( $U_a$ ), they also propose  $U_a = h_{re} + h_{ce}$  [8] where

$$h_{re} = 4\varepsilon\sigma \left[ \frac{T_o + T_a}{2} \right]^3 \quad (3)$$

$$h_{ce} = 1,3(T_o - T_a)^{1/3} + 4 \cdot V_{10} \quad (4)$$

with  $h_{re}$  as the radiation loss coefficient (where we assume that the surroundings are a cavity of adjacent air temperature and that the panel has an emittance of  $\varepsilon$ ),  $h_{ce}$  is the external convection coefficient (it takes into account the existing exterior wind and it has been adjusted for the location of our facility studied considering the results of Palyvos [9]) and  $V_{10}$  is the external wind speed at the height of 10 meters. It is obvious that in general the heat flow  $q$  is not uniform over the surface of the module. However, as  $U_a$ , is usually taken as uniform, so the heat flow will be also in our model over the PV module.

The formulation of the equation of heat transfer inside the duct initially requires determining the buoyancy-induced flow and wind effects inside the channel when the photovoltaic module is subjected to a uniform solar radiation. In this process, the output variables are the wall temperatures,  $T_o$  (module temperature) and  $T_b$  (temperature of adiabatic wall) and its variation along the panels. The process requires an iterative calculation, given the existing degree of coupling.

### 3.2. The mass flow rate induced inside the channel

According to the investigations of Brinkworth [8], considering a constant heat flow in the module, determining the flow induced in the interior, is decoupled from the temperature of the channel walls, and can therefore be obtained separately. Therefore, we will raise the problem as decoupled and initially we will solve the induced mass flow (and hence the average speed) and then, based on this result, the heat transfer and temperature of the plates. To obtain the induced mass flow inside the channel, it is necessary to consider a balance of global forces on the air mass inside the same channel. The flow inside the duct is the result of driving forces (buoyancy-induced by natural convection and wind suction) and resistant forces (friction and

other hydraulic losses in the inputs and outputs). Below, this paper describes each of these forces.

### 3.3. Driving forces

The drop in pressure to conduct the air through the duct is the sum of buoyancy and wind effect [10]:

$$\Delta p_d = \Delta p_b + \Delta p_w \quad (5)$$

For flows that meet certain conditions, Boussinesq suggested that variations in fluid density can be neglected except in the gravitational term of the equation of conservation of momentum in the vertical direction, in which density appears multiplied by the gravity acceleration ( $g$ ). This approach assumes that other fluid properties such as dynamic viscosity, conductivity and specific heat are constant. Supposing that the compressibility effects are small, so that density variations are due solely to the temperature changes, we can use the Boussinesq approximation, if the temperature variations in the fluid are small. Considering the Boussinesq's hypothesis the buoyancy term can be expressed as the difference between the base and the end point of the fluid column with a height of  $L \sin \theta$ :

$$\Delta p_b = \rho g \beta (T_{media} - T_i) L \sin \theta = \rho g \beta S (T_e - T_i) L \sin \theta \quad (6)$$

where  $S(T_e - T_i)$  is the average increases of the temperature reached in the duct. The value of  $S$  depends on the temperature profile along the duct. For a linear increase in temperature, its value is about 0.5. This value is what we consider in this study as a starting point. On the other hand, the value of  $(T_e - T_i)$  can be expressed in terms of incoming heat as

$$qA = \dot{m} C_p (T_e - T_i) \quad (7)$$

If we solve eq. (7) for  $(T_e - T_i)$ , expressing the mass flow-rate,  $\dot{m}$ , in terms of the density,

$$(T_e - T_i) = \frac{qL}{\rho U H C_p} \quad (8)$$

and substituting in equation (6)

$$\Delta p_b = \frac{g \beta S q L^2 \sin \theta}{U H C_p} \quad (9)$$

where  $\beta$  is the coefficient of thermal expansion,  $L$  the channel length,  $U$  the average velocity of induced flow,  $C_p$  the specific heat of air and  $H$  the depth of the channel. The channel width is taken to be 1m.

As already mentioned, the external wind exerts a suction force on the channel so the mass flow increases. The pressure difference induced by wind can be represented by

$$\Delta p_w = C_{pi} \left( \frac{\rho V_{wi}^2}{2} \right) - C_{pe} \left( \frac{\rho V_{we}^2}{2} \right) \quad (10)$$

being  $C_{pi}$  and  $C_{pe}$  the wind pressure coefficients at the entrance and exit of the duct, and  $V_{wi}$  and  $V_{we}$  are the values of wind speed at the inlet and outlet of the duct. According to Brinkworth [8], assuming that the position of the duct is such that the wind causes an increase in mass flow, we can estimate the combined effect of wind on the channel as:

$$\Delta p_w = (+0.5) \frac{\rho V_{10}^2}{2} \quad (11)$$

with  $V_{10}$  the wind speed at the height of 10 meters above the channel (the coefficient of +0.5 is included in eq.11 to adjust experimentally the effect of the surroundings).

### 3.4. Resistant forces

The flow resistance expressed in terms of pressure differences ( $\Delta p_r$ ) is given by the sum of the pressure drop due to friction ( $\Delta p_f$ ) and other hydraulic losses ( $\Delta p_h$ ). Friction losses can be expressed by the Darcy's equation

$$\Delta p_f = f(L/D) \frac{\rho U^2}{2} \quad (12)$$

where  $f$  is the friction factor in a duct of length  $L$  and the hydraulic diameter of the cross section is  $D = 2H$ , due to the width is 1m and  $H \ll 1$ . In general, the factor  $f$  is a function of the aspect ratio ( $L/D$ ) and of the Reynold number ( $Re_D = UD/\nu$ ). In the case of a channel the following expression is proposed:

$$f = f_o + \frac{f_1}{L/D} + \frac{f_2}{Re^n} \quad (13)$$

With  $n \approx 1$ ,  $f_0 \approx 0$ ,  $f_1 \approx 1$  and  $f_2 \approx 64$ . Given these values, the expression  $f(L/D)$  approaches to 1. On the other hand, the pressure drop due to hydraulic losses can be expressed in terms of coefficients  $K_h$  of the dynamic pressure in the form

$$\Delta p_h = \left( \sum k_h \right) \frac{\rho U^2}{2} \quad (14)$$

When there is a heat flow asymmetry on both walls in the channel. We may assume  $\sum k_h \approx 1.5$  [10]. If we propose the balance of forces, the equation obtained is:

$$\frac{2gqSL^2 \sin \theta}{T_a \rho H C_p} = \left( f \frac{L}{D} + \sum k_h \right) U^3 - \left( \frac{2\Delta p_w}{\rho} \right) U \quad (15)$$

which is a cubic function of the average velocity induced in the channel.

$$A \cdot U^3 + B \cdot U^2 + C \cdot U + X = 0 \quad (16)$$

With  $A=1+\sum k_h$ ,  $B=0$ ,  $C=-V_{10}^2$  and  $X=-2gqSL^2 \sin \theta / T_a H \rho C_p$ .

### 3.5. The heat transfer inside the duct

The incoming heat flow  $q$  is transferred to the air through the convection at the two walls of the channel and may be expressed by  $q = q_o + q_b$ . The first term,  $q_o$ , regards to the heat flow for convection of the PV module to channel air. This is given by

$$q_o = (T_o - T_m) \cdot h_o \quad (17)$$

where  $h_o$  the convection coefficient of this panel,  $T_o$  temperature of the panel at a distance of the channel input in longitudinal direction and  $T_m$  the average temperature of the air-flow at this point. The second term,  $q_b$ , represent the heat flow for convection from the adiabatic module. This heat came from the radiation heat flow issued over this panel for the PV module. It can be represented with the next equation.

$$q_b = (T_b - T_m) \cdot h_b \quad (18)$$

This radiation heat flow can be well represented for an interchange direct equation that considers local temperature of the two facing surfaces, with a heat transferred coefficient linearized  $h_r$ , described by [8],

$$h_r = 4 \cdot \varepsilon_{eff} \cdot \sigma \left( \frac{T_o + T_b}{2} \right)^3 \quad (19)$$

In this case, we assume that the plate facing the module is adiabatic and that the energy that it receives by the radiation is entirely transferred for convection to the flow. So, the average air temperature in the duct at a distance  $x$  from the input is given by

$$(T_m - T_b) = \frac{q x}{\rho_a C_p U H} \quad (20)$$

From the above equations, you can get the temperatures of the two walls thanks to the expressions (23) and (24). The convection coefficients  $h_o$  and  $h_b$  can be obtained from the following expressions

$$h_o \cdot (1 - n \hat{\theta}) = h_c \quad (21)$$

$$h_b \cdot (1 - \hat{\theta} / n) = h_c \quad (22)$$

where  $h_c$  is the coefficient of convective heat transfer on the hot wall of a channel in where the other wall is adiabatic and we assume there is not heat flow by radiation.  $\hat{\theta}$  is the influence coefficient which depends on the shape of the temperature profile of the plate that the duct is only heated on one side. The variable  $n$  is the ratio of heat flux between two walls

$$n = \frac{q_b}{q_o} = \frac{h_r (T_o - T_b)}{h_o (T_o - T_m)} \quad (23)$$

To close the system, we need information about  $h_c$  (or of  $Nu_c$ ) and  $\hat{\theta}$ . For turbulent flow in a channel with heat flow in a plate and the other being adiabatic, the following expression is referenced, where  $Re_D$  is the Reynolds number based on the hydraulic diameter:

$$h_c = 0,0186 Re_D^{0,787} k / D \quad (24)$$

With regards to the value of  $\hat{\theta}$ , we have estimated it, correlating the presented values for the case of  $Re_D = 10,000$  according [11]

$$\hat{\theta} = 0,0452 \ln(L / D) + 0,0178 \quad (25)$$

In spite of these values assumed by  $h_c$  (or by  $Nu_c$ ) and of  $\hat{\theta}$ , there is no criteria in bibliography to determine them. Therefore, a future task is to numerically determine its values for different conditions of heat flow between both walls and different angles of incidence.

#### 4. Experimental validation of the model and results

The equation model proposed to resolve the heat transfer and the induced flow has been solved by means of the EES software used, for different real cases which have been measured experimentally in our solar facility. The following starting parameters have been considered:  $C_p = 1007 \text{ J/kg K}$ ,  $D_h = 0.27 \text{ m}$ ,  $\varepsilon = 0.88$ ,  $\varepsilon_{eff} = 0.3$ ,  $g = 9.8 \text{ m/s}^2$ ,  $\eta = 0.1353$ ,  $H = 0.165 \text{ m}$ ,  $\alpha_s = 0.85$ ,  $K_h = 1.5$ ,  $L = 1.956 \text{ m}$ ,  $\sigma = 5.670 \times 10^{-8} \text{ W/m}^2\text{K}^4$ ,  $\mu_a = 0.00001834 \text{ kg/ms}$ ,  $V_w = 1,86 \text{ m/s}$ ,  $Re_{Dh} = 17,351$ ,  $\rho_a = 1.197 \text{ kg/m}^3$ ,  $S = 0.5$  y  $\theta_p = 35^\circ$ .

Figure 2 compares the experimental data of the temperatures of the module ( $T_o$ ) and the adiabatic wall ( $T_b$ ) as a function of the irradiance, with those obtained by the analytical model. Taking into account that the experimental data has been obtained varying the atmospheric temperature (between 298 and 303 K), the results of the analytical model have been presented for different atmospheric temperature conditions. Experimental correlations for module and adiabatic wall temperature have been also printed in the Fig. 2. On the other hand, it has been also studied experimental and analytically the effect of the air gap between the module and the adiabatic wall. It has been tested that its effect is not very important in the performance of the module, once a minimum value of the aspect ratio has been reached ( $H/L \approx 0.1$ ).

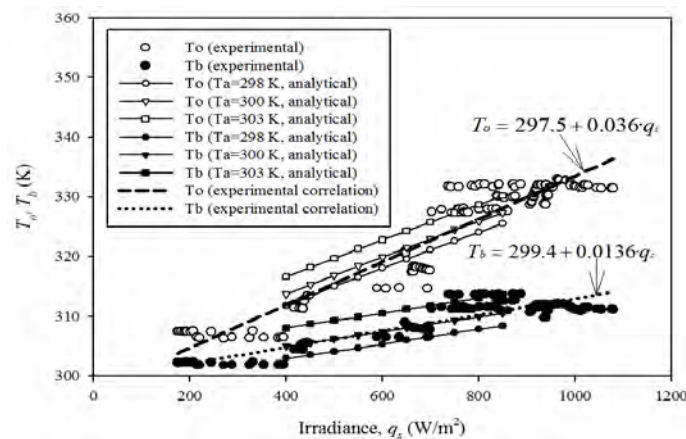


*Fig.2. Experimental validation of the analytical model for different atmospheric temperatures and the experimental correlation of the photovoltaic plate temperatures.*

## 5. Conclusions

A solar installation consisted of a photovoltaic panel and adiabatic plate in an inclined channel configuration has been experimentally tested. Experimental correlations have been proposed for the temperature of the module and the temperature of the adiabatic plate as a function of the irradiance, for an average wind velocity of 2 m/s and an average atmospheric temperature of roughly 300 K.

An analytical model of this configuration to study the heat transfer and the convective flow induced in it has been carried out and solved by EES software, considering some previous models of the bibliography and particular aspects of this experimental facility. The experimental measurements have been used to validate this analytical model. It has been tested that the effect of the air gap between the module and the adiabatic wall is not very important in the performance of the module, once a minimum value of the aspect ratio has been reached ( $H/L \approx 0.1$ ).

## Acknowledgements

The authors thank the local association Fundacion Seneca for its cooperation in this study, which has been supported by the company Apia XXI, so we'd like to show our gratitude to them.

## References

- [1] J. Khedari, J. Hirunlabh, T. Bunnag, Experimental study of a roof solar collector towards the natural ventilation of new habitations. *Energy and Buildings* 26, 1997, pp. 159–164.
- [2] J. Hirunlabh, S. Wachirapuwadon, N. Pratinthong, J. Khedari, New configuration of a roof solar collector maximizing natural ventilation. *Building Env.* 36, 2001, pp. 383–391.
- [3] M. Sandberg, B. Moshfegh, Buoyancy-induced air flow in photovoltaic facades. Effect of geometry of the air gap and location of solar cell modules. *B. Env.* 37, 2002, pp. 211–218
- [4] B.J. Brinkworth, R.H. Marshall, Z Ibarah, A validated model of naturally ventilated PV cladding. *Solar Energy* 69 (1), 2000, pp. 67–81.
- [5] R. Mazón, JR García, F Vera, A S. Kaiser, B Zamora, Development of an installation to reduce the temperature of photovoltaic modules and improve their efficiency, ICREPQ'10, 2010.
- [6] D.L. King, W.E. Boyson, J.A. Kratochvil, Photovoltaic array performance model, Sandia National Laboratories, 87185-0752, 2004.
- [7] F. Sarhaddi, S. Farahata, H. Ajama, A. Behzadmehra and M. Mahdavi Adelia, An improved thermal and electrical model for a solar photovoltaic thermal (PV/T) air collector, *Applied Energy* 87, 2010, pp. 2328-2339.
- [8] B.J. Brinkworth, M. Sandberg, Design procedure for cooling ducts to minimize efficiency loss due to temperature rise in PV arrays, *Solar Energy* 80, 2006, pp. 89-103.
- [9] J.A. Palyvos, A survey of wind convection coefficient correlations for building envelope energy systems modeling, *Applied Thermal Engineering* 28, 2008, pp. 801-808.
- [10] B.J. Brinkworth, Estimation of flow and heat transfer for the design of PV cooling ducts, *Solar Energy* 69, 2000, pp. 413-420.

- [11] B.J. Brinkworth, Coupling of convective and radiative heat transfer in PV cooling ducts, ASME 124, 2002, pp. 250-255.

## Design, fabrication and testing of micro-channel solar cell thermal (MCSCT) tiles in indoor condition

Sanjay Agrawal<sup>1,\*</sup>, S. C. Solanki<sup>1</sup>, G. N. Tiwari<sup>1</sup>

<sup>1</sup>Centre for Energy Studies, Indian Institute of Technology Delhi, New Delhi, India

\* Corresponding author. Tel: +91 9911428863, Fax: +91 1126591251, E-mail: [sanju.aggrawal@gmail.com](mailto:sanju.aggrawal@gmail.com)

**Abstract:** In this paper design, fabrication and testing of micro-channel solar cell thermal (MCSCT) tiles has been discussed. Solar simulator for an indoor testing of micro-channel solar cell thermal tiles has also been developed. Fabricated MCSCT tile consists of single solar cell, micro-channel and fan for extraction of heat from bottom of solar cell. Single MCSCT tile has been termed as case-I. Similarly, two MCSCT tiles which are connected in series have been termed as case-II. The performance evaluation in terms of electrical efficiency, thermal gain, overall thermal energy and overall exergy of both cases has been carried out in indoor conditions on various intensities. It has been also found that the electrical efficiency is higher in case-I as compared to case-II. On the other hand the thermal out put of case-II is higher than case-I on same intensity and mass flow rate. It has been found that the average electrical and thermal efficiency of newly designed and fabricated MCSCT tile is 12.4% and 35.7% respectively. This economical solar simulator can be used by manufactures for testing of different type of photovoltaic tile as well as photovoltaic modules.

**Keywords:** Full Photovoltaic thermal tile, Micro-channel, Solar simulator.

### Nomenclature

$A_c$ Area of MCSCT tile ..... $m^2$	$T_{foN}$ Outlet fluid i.e air temperature of $N^{th}$ tile..... $^{\circ}C$
$E$ Electrical power ..... $W$	$T_{fi}$ Inlet fluid i.e air temperature ..... $^{\circ}C$
$\dot{E}x$ Exergy ..... $kW$	$T_a$ Ambient temperature ..... $^{\circ}C$
$I(t)$ Intensity..... $Wm^{-2}$	
$\dot{m}_f$ Mass flow rate of ..... $Kg s^{-1}$	<b>Subscript</b>
$C_f$ Specific heat of air..... $Jkg^{-1} K^{-1}$	$n$ number of MCSCT tile
$\dot{Q}_u$ Rate of useful energy ..... $kW$	$f$ Fluid
$V$ velocity of air inside micro-channel ..... $m.s^{-1}$	$c$ solar cell
$V_{oc}$ Open circuit voltage ..... $Volt$	$o$ outlet
$V_L$ Load voltage ..... $Volt$	<b>Greek letter</b>
$I_{sc}$ Short circuit current ..... $Amp$	$\eta_e$ Electrical efficiency
$I_L$ Load current ..... $Amp$	$\eta_{th}$ Thermal efficiency

### 1. Introduction

Photovoltaic technology (PV) is commonly known as one of the promising renewable energy technologies. It is well known fact that electrical efficiency falls as the temperature of the photovoltaic cells rises. The efficiency of the system falls about 0.0045 when cells temperature increased by  $1^{\circ}C$  [1]. The generation of both thermal and electrical energy simultaneously is known as hybrid photovoltaic thermal technology (PVT). Solar hybrid PVT system can generate more energy per unit area compared to the system of solar panel and thermal collector separately side by side [2]. Sopian et al. [3] and Prakash[4] have analyzed single pass solar collector with open channel absorber. The double pass solar collector with upper and lower channels has been fabricated by Garg et al. [5] and cox et al. [6]. Erdil et al. [7] fabricated a hybrid system consisting of a PV module and a solar thermal collector and tested it for energy collection in Cyprus. They found out that the ratio of gain to losses for

thermal energy is 50 times the electrical energy, which was measured between the periods of 12:00 and 16:00 hour.

An experiment to compare the efficiency of an integrated photovoltaic thermal solar (IPVTS) system with conventional solar water heater was carried out by Huang et al.[8]. Tonui and Tripanagnostopoulos [9] reported a cheap and simple method to cool the photovoltaic thermal (PVT) system. Sopian et al. [10] developed and tested a double pass PVT solar collector, which is suitable for solar drying purposes. Design, development and performance monitoring of a photovoltaic-thermal (PVT) air collector has been studied by Niccolo et al. [11] and they found that the simulation model, developed under this program predicts quite well the thermal and electrical performance of a PVT collector. The model, in general, can be utilized for any set of design and operational parameters for evaluating the performance of front cover direct flow PVT air collector, semitransparent with different solar cell density (i.e. the ratio between the area of the cells and the total laminate surface) or completely opaque (e.g. standard PV laminate like those employed in the experimental campaign presented). The relations between energy and exergy, energy and sustainable development, energy policy making, exergy and the environment and exergy in detail are reported by Dincer [12]. Energy and exergy analysis of hybrid micro-channel photovoltaic thermal module has been carried by Agrawal and Tiwari [13] and they concluded that micro-channel photovoltaic thermal module gives better results.

Till now, most researchers have carried out the electrical and thermal performance analysis on PVT system consisting of PV module and a duct. The objective of this study is to develop a micro PVT system known as MCSCT tile and solar simulator for testing of MCSCT tile. The performance evaluation of MCSCT tiles has been carried out on various intensity and constant mass flow rate. Comparative studies have been carried out between single MCSCT tile (case I) and two MCSCT tile connected in series (case II).

## **2. Experimental setup**

Experimental test rig consisting of MCSCT tiles and solar simulator to test the performance of the MCSCT tiles on various operating parameter.

### **2.1. Micro-channel solar cell thermal tile**

The MCSCT tile as shown in Fig. 1a consists of a single solar cell, rated at 2.2 Wp having 0.125m width and 0.125 m length and mounted on a rectangular wooden channel. The channel has a dimension 0.125m in length, 0.125m in width and 0.005m in depth. Small holes are provided at the cross edge of the channel to pass the hot air for utilization and also to connect other the MCSCT tile in series combination. The wooden micro-channel has been sealed with putty and adhesive tape to avoid air leakage. Similarly, another one MCSCT tile are fabricated and connected in series through PVC pipe. MCSCT tile are arranged in such a manner that outlet of first tile is inlet of second. The MCSCT tile have been placed on a mild steel platform with a mechanism for up and down movement for varying the light intensity. A DC fan of 6.0 V and 0.1A has been used for forced mode of operation to make flow the air through the channel of tile.

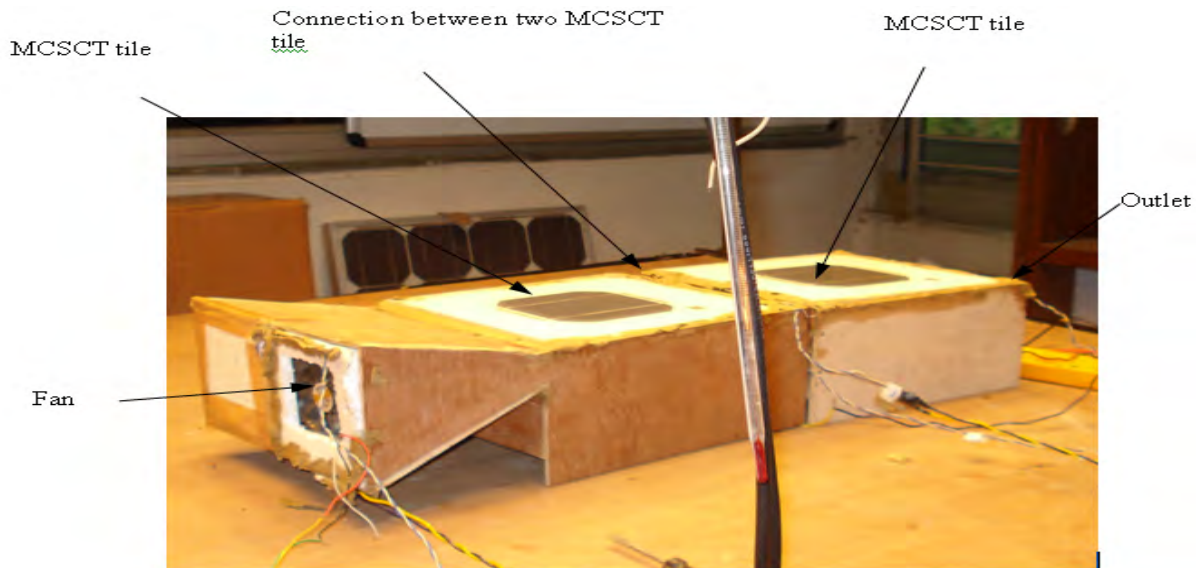


Fig.1a. Photograph of hybrid micro-channel solar cell thermal (MCSCCT) tiles

## 2.2. Solar simulator

A solar simulator (Fig.1b) with a 3-phase lamp array is employed to imitate the necessary solar irradiation in the testing of micro-channel solar cell thermal tile. The solar simulator has 28 tungsten halogen lamps (Philips manufactured; Model: 392472) each having 500W, 9000 lumens and rated at 240V and 11A. The halogen lamps are arranged in  $7 \times 4$  matrices for uniform distribution of irradiance on the MCSCCT tile. An exhaust fan has also been provided in the laboratory wall to avoid the overheating of cell by withdrawing the thermal energy associated with it. The available area for testing is  $1 \times 2$  m. The height of the simulator from the floor is 200 cm. The distance between platform and halogen lamp is 100 cm. Intensity of simulator can be varied between  $300 \text{ W/m}^2$  to  $1000 \text{ W/m}^2$  by decreasing the gap of halogen lamp and platform.



Fig.1b. Photograph of solar simulator with micro-channel hybrid MCSCCT tiles

## 2.3. Instrumentation

The following instruments have been used during the experimentation:

(i) *Thermocouples*: A calibrated copper-constantan thermocouples and a digital temperature indicator are used to measure the temperature of several locations, namely, back surface, inlet and outlet air temperature of each collector and final outlet air temperature. Digital temperature indicator has least count of 0.1°C.

(ii) *Solarimeter*: The intensity of solar radiation is measured by the solarimeter having a least count of 20W/m<sup>2</sup>, manufactured by CEL, India Ltd, Sahibabad (UP), India. The solarimeter has been calibrated with the standard pyranometer.

(iii) *Anemometer (Lutron-AM4201)*: It is a conventional instrument used to measure the velocity of flowing air. The least count of the instrument is 0.1 m/s.

(iv) *Infrared thermometer*: The infrared thermometer is used to measure the top surface temperature of PV module. The least count of the instrument is 0.1°C.

(v) *Clamp meter*: It is used for measurement of a current and voltage. The least count of the instrument is 0.1A and 0.1V.

### 3. Methodology

The experiments have been conducted on various intensity namely 600,700 and 800 W/m<sup>2</sup> and maintaining the constant mass flow rate (0.000145 kg/s) to observe the effect of intensity on different performance parameters of single MCSCT tile (case-I) and two MCSCT tile connected in series (case-II). The following mathematical expressions have been used for analysis:

#### 3.1. Electrical efficiency

The electrical efficiency of micro-channel solar cell thermal (MCSCT) tile can be obtained as, Tiwari [14],

$$\eta_e = \frac{FF \times V_{oc} \times I_{sc} - I_L \times V_L}{N \times A_c \times I(t)} \quad (1)$$

where fill factor (FF) is a measure of sharpness of the *I-V* curve. It indicates how well a junction was made in the cell and how low is the series resistance. It can be lowered by the presence of series resistance and tends to be higher whenever the open circuit voltage is high

#### 3.2. Instantaneous thermal efficiency

An instantaneous thermal efficiency of hybrid micro-channel solar cell thermal tile can be obtained as, Tiwari [14] and Duffie and Beckman [15],

$$\eta_{th} = \frac{\dot{Q}_{U,N}}{NA_c I(t)} \quad \text{where } \dot{Q}_{U,N} = \dot{m}_f C_f (T_{foN} - T_{fi}) \quad (2)$$

#### 3.3. Over all thermal energy

The energy analysis is based on the first law of thermodynamics, and the expression for overall thermal gain can be defined as,

$$\sum \dot{Q}_{u,overall} = \sum \dot{Q}_{u,thermal} + \frac{\sum \dot{Q}_{u,electrical}}{\eta_{cpower}} \quad (3)$$

where  $\eta_{cpower}$  is a conversion efficiency of thermal power plant which depends upon quality of coal ( $\eta_{cpower} = 0.38$  for good quality of coal). The range of  $\eta_{cpower}$  is varying between 0.20-0.40. This electrical energy has been converted to equivalent thermal by using electric power generation efficiency conversion factor as 0.20-0.40 for a conventional power plant, Huang et al. [8] and it depends on quality of coal. Usual value of this factor is taken as 0.38 for conversion

### 3.4. Overall exergy

The exergy analysis is based on the second law of thermodynamics, which includes accounting the total exergy inflow, exergy outflow and exergy destructed from the system.

$$\dot{E}x_{overall} = \dot{E}x_{thermal} + \dot{E}x_{electrical} \quad (4)$$

Where  $\dot{E}x_{thermal} = \dot{Q}_{U,N} \left[ 1 - \frac{T_a + 273}{T_{fo} + 273} \right]$  and  $\dot{E}x_{electrical} = \left[ \frac{\eta \times A_c \times I(t)}{1000} \right]$

## 4. Results and discussions

In a series of experiments conducted, data have been recorded at different intensity for comparative evaluation for case-I and case-II. The experimental results of outlet air temperatures for both configurations (case-I and case –II) at various intensities 600 W/m<sup>2</sup>, 700 W/m<sup>2</sup> and 800 W/m<sup>2</sup> have been shown in Fig. 2. It has been observed that outlet air temperature of case-II is higher as compared to case-I at same intensity and constant mass flow rate (0.000145 kg/s) and  $T_{fi} = 38$  °C. The Effect of intensity on outlet air temperatures of MCSCT tiles has also been shown in Fig. 2. One can be concluded that as intensity increases, the outlet air temperature increases for case-I. Similarly trends have also been observed for case-II. It has also been observed that as there is increase in duration of time, outlet air temperature is increased and approaches the steady state condition after approximately two hours. The maximum outlet air temperature of 90<sup>0</sup> C and 89<sup>0</sup> C on intensity of 800 W/m<sup>2</sup> have been observed for series combination and single MCSCT tiles respectively.

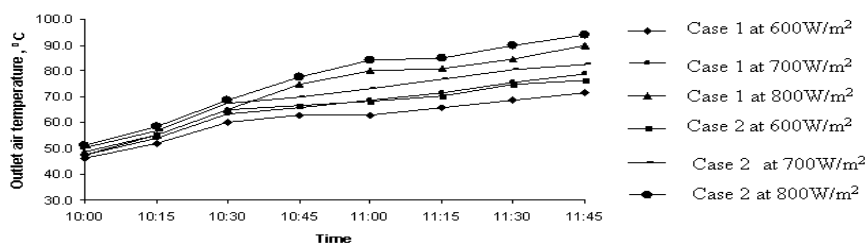


Fig. 2 . Variation of outlet air temperature at various intensity

Fig. 3 shows the time variation of solar cell temperature at different intensities 600 W/m<sup>2</sup>, 700 W/m<sup>2</sup> and 800 W/m<sup>2</sup> for both cases. It can be seen that solar cell temperature of case-II is

significantly higher than case-I at lower intensity ( $600 \text{ W/m}^2$ ) but at higher intensity ( $700$  and  $800 \text{ W/m}^2$ ) the solar cell temperature of both cases are nearly same. It is obviously due to very small heat carrying capacity of air.

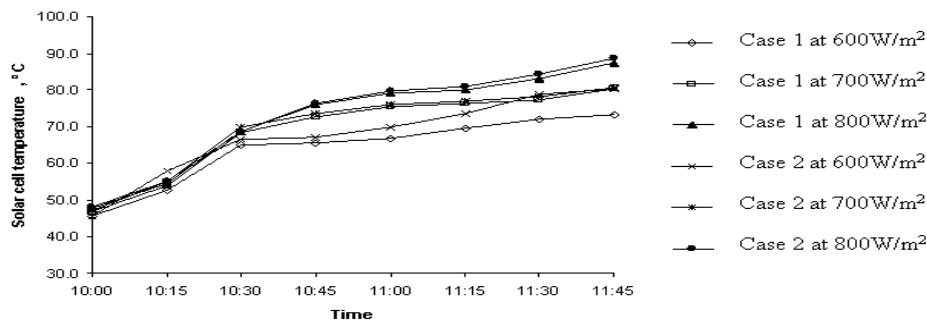


Fig. 3. Variation of solar cell temperature at various intensity

The electrical and thermal efficiency have been calculated with help of Eq. (1) and Eq. (2) for both cases at various intensities. Variations of electrical and thermal efficiency with respect to time have been shown in Fig. 4 and Fig. 5, respectively. It has been found that as intensity increases, electrical efficiency decreases because of rise in cell temperature and this result is in accordance with result reported by earlier researchers, Zondag et al.[1]. The electrical efficiency for case-I is higher than case-II at lower intensity due to lower cell temperatures. Electrical efficiency in the range of 13.6 % to 11.7% and 13.6 % to 11.1% has been observed for case-I and case-II respectively. It has been found that as intensity increases, outlet temperature of MCSCT tile also increases and due to increase in outlet temperature, thermal efficiency is increased because inlet temperature  $T_{fi} = 38 \text{ }^\circ\text{C}$  is maintained constant.

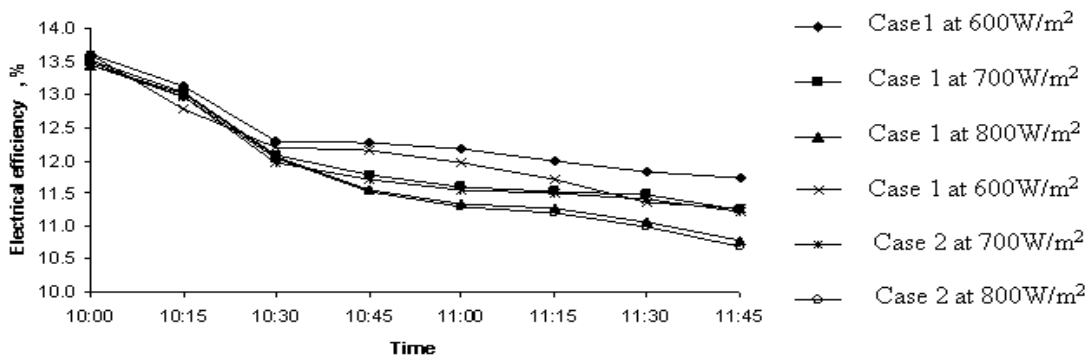


Fig. 4. Variation of electrical efficiency at various intensity

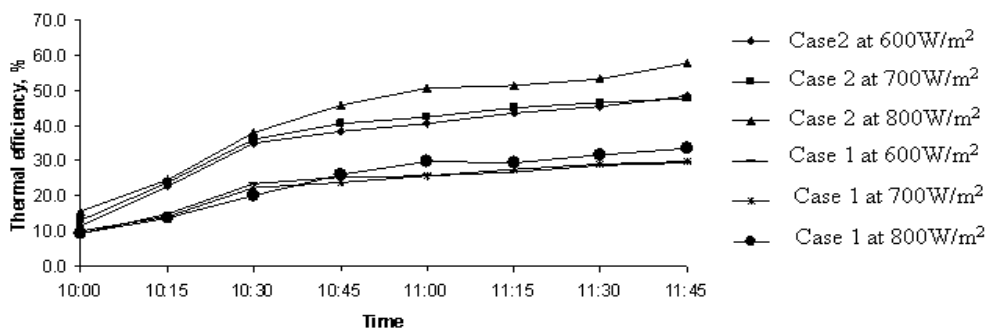


Fig.5. Variation of thermal efficiency at various intensity

Overall thermal energy and overall exergy have been calculated with help of Eq. (3) and Eq. (4) for both cases at various intensities Fig.6 shows that the variation of overall thermal energy at various intensities. It has been observed that increase in intensity will increase the overall thermal energy for MCSCT tiles for both cases and one can also conclude that overall thermal energy of series connected MCSCT tiles (case II) is significantly higher than single MCSCT tile (case I). Similarly trends has also seen for overall exergy for both case as shown in Fig. 7.

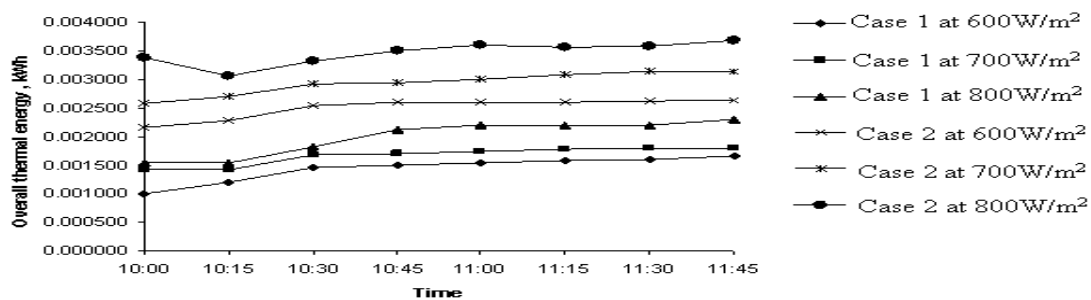


Fig. 6. Variation of overall thermal energy at various intensity

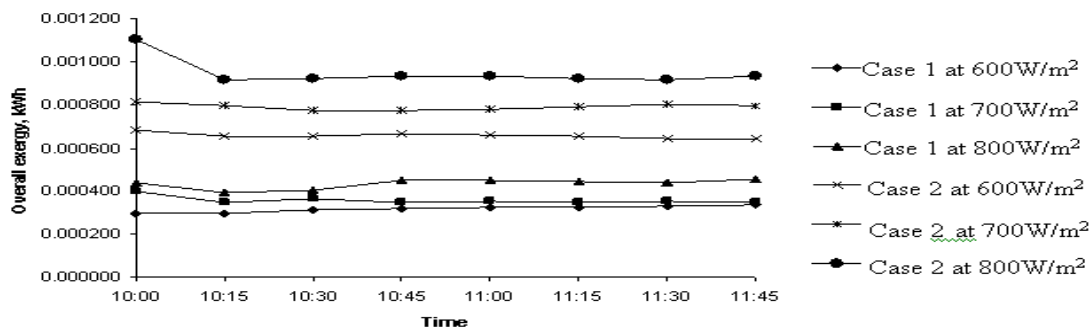


Fig. 7. Variation of overall exergy at various intensity

## 6. Conclusions

It has been concluded that the average electrical and thermal efficiency of newly designed and fabricated MCSCT tile is 12.4% and 35.7% respectively. This new present setup would have beneficial effect of permitting much less expensive installation for testing of PV tile. Hence the test procedure can be used by manufacturers for testing of different type of PV tiles and combination of PV tiles in order to optimize its products for better efficiency. The Limitations of MCSCT tile are ohmic losses in solar cell, temperature gradient along the thickness of solar cell.

## References

- [1] H. A. Zondag, D. W. de Vries, W. G. J. van Helden, R. J. C. van Zolingen, A. A. van Steenhoven, The thermal and electrical yield of a PV thermal collector, Solar Energy, 72 (2), 2002, pp.113–128.
- [2] P.G. Charalambous, G.G. Maidment, S.A. Kalogirou, K. Yiakoumetti, Photovoltaic Thermal (PVT) collectors: A review, Applied Thermal Energy 27, 2007, pp. 275- 286.

- [3] K. Sopian, K.S. Yigit, H. T. Liu, S. Kakac , T. N. Veziroglu, Performance analysis of photovoltaic thermal air heaters, *Energy Conversion and Management* 37,1996, pp. 1657-1670.
- [4] J. Prakash, Transient analysis of photovoltaic thermal solar collectors for cogeneration of electricity and hot air/water, *Energy Conversion and Management* 35, 1994, pp. 967-972.
- [5] H. P Garg, R. K Agarwal, A. K. Bhargava ,Study of a hybrid solar system-solar air heater combined with solar cells, *Energy Conversion and Management* 31, 1991, pp. 471-479.
- [6] C. H. Cox III, P. Raghuraman, Design considerations for flat-plate photovoltaic/thermal collectors, *Solar Energy* 35, 1985, pp. 237-242.
- [7] E. Erdil, M. Ilkan, F . Egelioglu , Renewable energy resources as an alternative to modify the load curve in Northern Cyprus, *Energy* 33, 2008, pp.1241 -2008.
- [8] B. J. Huang, T. H. Lin, W. C. Hung, F S. Sun,Performance evaluation of solar photovoltaic/thermal systems, *Solar Energy* 70, 2001, pp 443–448.
- [9] J. K. Tonui, Y. Tripanagnostopoulos , Air-cooled PVT solar collectors with low-cost performance improvements, *Solar Energy* 81, 2007,pp. 498–511.
- [10]K. Sopian, H. T. Liu, S. Kakac, T. Veziroglu, Performance of a Double Pass Photovoltaic Thermal Solar Collector Suitable for Solar Drying Systems, *Energy Conversion and Management* 41, 2000, pp. 353 – 365.
- [11]Niccolo, C. Giancarlo, V. Francesco, Design, development and performance monitoring of a photovoltaic-thermal (PVT) air collector, *Renewable energy* 33, 2007,pp. 914-927.
- [12]Dincer, The role of exergy in energy policy making, *Energy Policy* 30, 2002, pp. 137-149.
- [13]S. Agrawal, G. N. Tiwari, Energy and exergy analysis of hybrid micro-channel photovoltaic thermal module, *Solar Energy*, 85, 2011, pp 356-370.
- [14]G. N. Tiwari, *Solar Energy: Fundamentals, Design, Modeling and Applications*. Narosa Publishing House New Delhi, 2004.
- [15]J. A. Duffie, W. A. Beckman, *Solar Engineering of Thermal Processes*, John Wiley and Sons, New York, 1991

## Using structured aluminum reflectors in flux scattering on module performance

Joseph Simfukwe \*<sup>1</sup>, Sylvester Hatwaambo<sup>1</sup>, Kabumbwe Hansingo<sup>1</sup>

<sup>1</sup>University of Zambia, Department of Physics, Box 32379, Lusaka, 10101, Zambia.  
\* Corresponding Author: Tel: +260 211 293343, Email: josephsimfukwe@yahoo.com

---

**Abstract:** The current energy production from fossil fuels and nuclear energy has environmental drawbacks. These drawbacks include the creation of nuclear waste, and the pollution associated with fossil fuels which lead to global warming and climate change. It is apparent that an alternative and sustainable source of energy must be found. A potential solution to this problem is solar electricity. Currently, solar panels are expensive and hence un-economical for most buyers. The use of solar concentrators creates a potential for less expensive electricity because concentrators raise the amount of incident radiation over a relatively small area of the absorber. The reduction in cost is achieved by reducing the module area and the use of low-cost reflectors. However, specular reflectors cause high concentrated heating and form hot spots on the solar module cells. These hot spots are a result of uneven concentration of radiation. The overall effect is the reduced fill-factor and overall efficiency of the system. In this paper, we report an alternative solution to the problem of non-even illumination by using locally available low-cost semi-diffuse reflector with four different groove orientations scribed on it so as to scatter the radiation flux onto the module. The groove orientations were plain sheet (NG), horizontal grooves (HG), vertical grooves (VG), and the crisscross groove (CG) orientations. Our results show that the locally purchased semi-diffuse aluminium structure can be used as a booster reflector compared with the commercial high specular reflector.

**Keywords:** Semi-diffuse, specular, fill-factor, non-even illumination, low-concentration

---

### 1. Introduction

The costs of solar panels compared to the amount of power they produce make their purchase un-economical for most end-users. The use of solar concentrators create a potential for producing less expensive electricity by replacing expensive solar cell area with inexpensive optical materials such as plastic refractors or metal reflectors. Currently, mirror-like reflectors (specular materials) are used for solar thermal applications while lenses are used in photovoltaic systems. The use of lenses in photovoltaic (PV) may not reduce the cost of electricity to affordable levels because they are expensive. Highly specular materials have high reflectance and are good in imaging optics for high concentration, whereas semi-diffuse reflectors are preferred in non-imaging optics for flux scattering. The module cost could be reduced if low-cost materials are used to concentrate solar energy flux across a small module area [1,2]. In this paper we address two of the problems faced with concentrating photovoltaic systems namely; non-even illumination and use of expensive lenses and specular materials as reflectors by designing, constructing and evaluating a low concentrator system, using locally available low-cost semi-diffuse aluminium structure reflector with four different groove orientations scribed on it to improve on the fill-factor (FF) of the module for low cost electricity. Fill-factor is an important parameter that tells the overall performance of the solar module. A solar module with a high fill-factor is able to produce high power for a longer period of time. Therefore, by improving the FF of the module we are increasing both the power output and the durability of the module [3].

### 2. Methodology

#### 2.1. Design and construction of the compound parabolic concentrator (CPC)

We first designed the Compound Parabolic concentrator (CPC) using the standard polar co-ordinate system proposed by Winston [4,5]. The value of  $a$  which is the half width of the

exit aperture was determined after deciding on the size of the solar module string to be used after which the acceptance half angle  $\theta$  of the CPC was decided while  $\Phi$  varied from  $5^\circ$  to  $107^\circ$  in our case. The determined values of  $a$  and  $\theta$  in this case were ( $a=5\text{cm}$  and  $\theta=15^\circ$ ) which we then used in equations (1) and (2) to generate the  $X$  and  $Y$  co-ordinates. These co-ordinates were then plotted on the graph paper to design the CPC which was later constructed .Figure 1 shows the CPC designed (a) and the actual constructed Compound Parabolic Concentrator (b) used for the current-voltage (I-V) measurements.

$$x = \frac{2f \sin(\phi - \theta)}{1 - \cos \phi} - a \quad (1)$$

$$y = \frac{2f \cos(\phi - \theta)}{1 - \cos \phi} \quad (2)$$

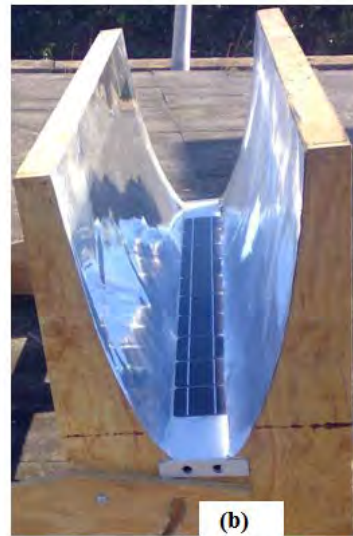
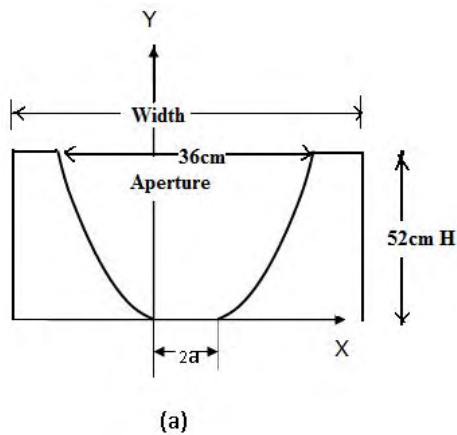


Fig 1. Shows the CPC design from polar co-ordinates into the X-Y co-ordinates system (a) and the actual compound parabolic concentrator constructed (b).

## 2.2. Spectral reflectance of structured aluminium

An ideal reflector material for solar electricity production should have a relatively high reflectance in visible and ultra violet regions of the solar spectrum and to maintain this relative high reflectance for the entire life of the solar system [6].

In this experiment we used one reflector material (semi-diffuse aluminium structures), but with four different orientations of the grooves namely; plain (NG) (no grooves), horizontal grooves (HG) vertical grooves (VG) and criss-cross groove (CG) orientations as shown in Figure 2. The groove sizes ranged between 2mm to 3mm. Our aim was to determine which of these four orientations was able to provide uniform illumination and a better fill-factor improvement using the named reflector .The optical properties of this reflector material were obtained from the Perkin Elmer spectrophotometer lambda 900. The total integrated

reflectance (TIR) was calculated from equation (3). The TIR gives the overall reflectance of the material the property that shows how much flux the material is able to scatter.

$$R_s = \frac{\sum_{305nm}^{2450nm} R(\lambda).G(\lambda).\Delta\lambda}{\sum_{305nm}^{2450nm} G(\lambda).\Delta\lambda} \quad (3)$$

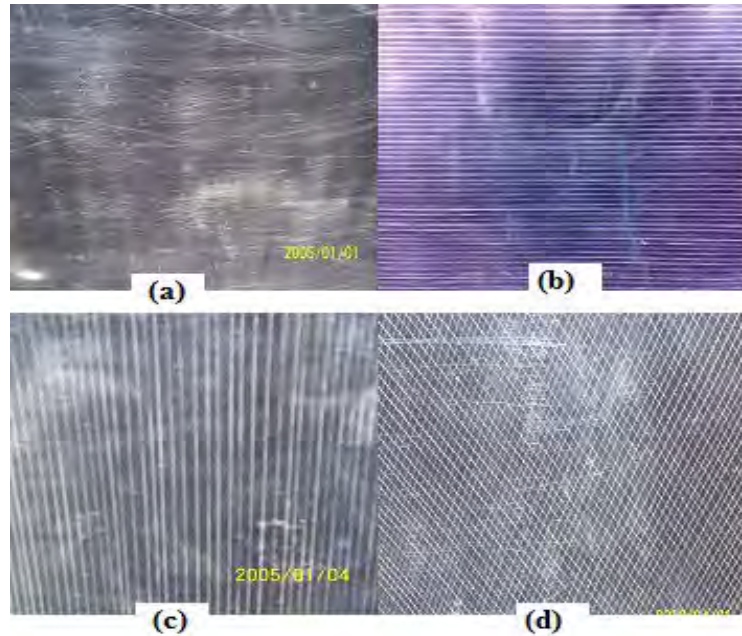


Fig 2. Showing the four different orientations of the grooves on the semi-diffuse structured aluminium:(a) plain sheet (NG) (b) horizontal grooves (HG) (c) vertical grooves (VG) and (d) criss-cross grooves (CG)

### 2.3. Current-voltage (I-V) curve measurement.

The current and voltage generated by the module under concentration was measured using the current-voltage tracker instrument obtained from Vattenfall, Sweden .The short-circuit current  $I_{sc}$ , the open-circuit voltage  $V_{oc}$ , the power maximum  $P_m$ , the maximum current  $I_m$ , and the maximum voltage  $V_m$  were extracted from each I-V curve. The fill-factor (FF) was evaluated from equation (4).

$$FF = \frac{I_m \cdot V_m}{I_{sc} \cdot V_{oc}} = \frac{P_m}{I_{sc} \cdot V_{oc}}. \quad (4)$$

### 3. Results

#### 3.1. Measurement of Total Integrated Reflectance(TIR)

Table 1 shows that the plain sheet (NG) was a better reflector with TIR of 89% followed by the criss-cross grooves (CG) orientations with 88%, the horizontal grooves (HG) orientation was the third best with 85% while the vertical orientations of the grooves on the aluminium structure was the least with 82%, as measured by the integrating sphere in the lab.

Orientation	Total Integrated Reflectance (TIR)
NG	89%
HG	85%
VG	82%
CG	88%

#### 3.2. Fill-factor comparison at 0° (normal)

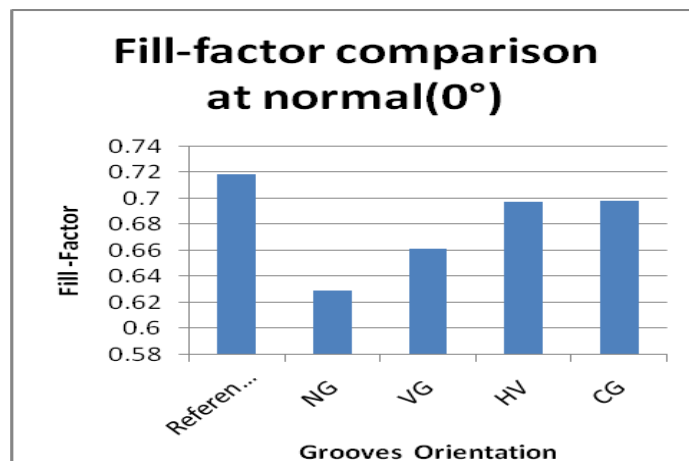


Fig.3 Fill-factor comparison at 0°

The results for the fill-factor comparison revealed that the criss-cross grooves (CG) gave the highest fill-factor followed by the horizontal grooves (HG) and then the vertical grooves (VG). The plain sheet had the least fill-factor. The results also shows that the drop in the fill-factor from the reference for the criss-cross grooves and the horizontal grooves orientations was about 3%, while that of the vertical grooves (VG) and the plain sheet was 8% and 12% respectively. The better results of fill-factor for the criss-cross grooves and the horizontal grooves can be attributed to the fact that, the orientation of the grooves in this manner provided evenly scattering of the solar flux on the module thereby reducing the hot spot formation and causing an even distribution of current within the solar cell . On the other hand, the reduced fill-factor for the plain sheet and the vertical grooves can be explained in terms of the non-uniform irradiance leading to non even distribution of current within the solar cell. This causes hot-spot formation that leads to the overall degradation of the module.

### 3.3. Power comparison at 0° (normal)

Figure 4 shows the comparison of power at 0° with VG and NG giving the highest power output, but these are a result of high currents which cause hot spots and an overall reduction in the performance of the module. Hot-spot heating occurs when a large number of series connected cells cause a large reverse bias across the shaded cell, leading to large dissipation of power in the poor cell. Essentially the entire generating capacity of all the good cells is dissipated in the poor cell. The enormous power dissipation occurring in a small area results in local overheating, or "hot-spots", which in turn leads to destructive effects, such as cell or glass cracking, melting of solder or degradation of the solar cell[3].

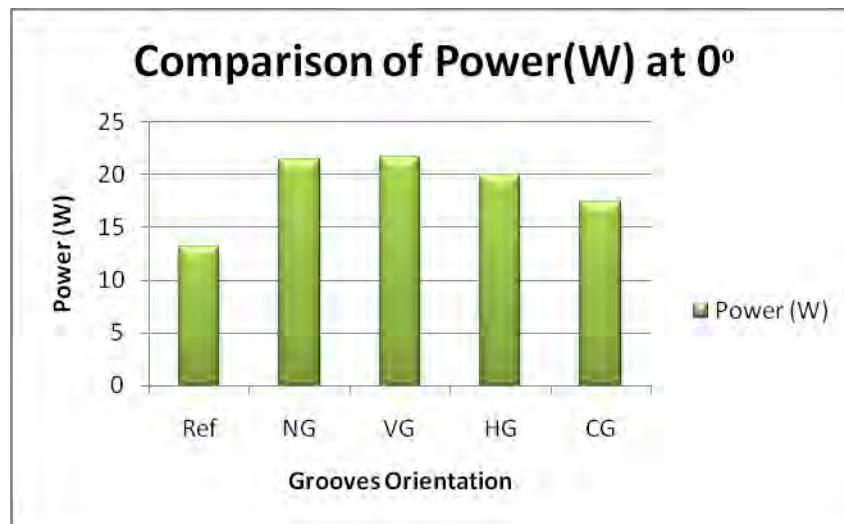


Fig. 4 bar charts showing comparison of the power for the four different grooves orientations and the reference (Ref) (without concentration).

## 4. Discussion and Conclusions

The performance of the CPC constructed using the locally available materials has been analysed and the results show that the locally purchased semi-diffuse aluminium structure can be used as a booster reflector in low cost photovoltaic system. The results also show that the criss-cross groove and the horizontal groove orientations were found to be the best orientations for the fill-factor improvement since they had only a 3% drop in fill-factor from the reference. The two orientations were able to scatter the solar flux evenly across the solar cell module. It is the even scattering that causes uniform distribution of currents within the solar cell thus reducing the hot spot formation. However, between the two orientations we would recommend the horizontal grooves(HG) because it is less costly when making the grooves but it gives a better fill-factor as much as that of the criss-cross grooves. The horizontal grooves also gave a higher power increase of 52% compared to 33% for the criss-cross grooves.

### Acknowledgements

My deep and heartfelt appreciation to my supervisors:

**Dr. Sylvester Hatwaambo** and **Dr. Kabumbwe Hansingo** under whose guidance, patience, and genuine criticism, this work was successfully done. I am also indebted to the Solar Energy Materials (SEM) Project in the Department of Physics at the University of Zambia (UNZA) in conjunction with the International Science Programme (ISP) of the Uppsala

University in Sweden for granting me a scholarship. Many thanks to **Dr.H.V. Mweene**, The Head of Physics Department for taking care of our welfare.

## **References**

- [1] S. Hatwaambo et al, “Angular Characterization of low concentrating PV-CPC Using low cost reflectors,” *Solar Energy Materials & Solar Cells* Vol. 92,1347-1351.(Elsevier, 2008).
- [2] S. Hatwaambo, H.Hakansson, A.Roos and B. Karlson ,Mitigating the non-uniform illumination in low concentrating CPCs using structured reflectors,” *Solar Energy Materials & Solar Cells* Vol. 93,202-2024 (Elsevier, 2009).
- [3] <http://pvcdrom.pveducation.org/MODULE/Hotspot.htm>
- [4] W. T. Welford and R. Winston, *High Collection Non-imaging Optics*, (Academic Press,1989).
- [5] R. Winston, J. C. Miñano and P.Benitez , *Non-imaging Optics*, (Elsevier Academic Press,2005).
- [6] Brogren, M., “Optical Efficiency of Low –Concentrating Solar Energy Systems with Parabolic Reflectors,” (PhD. Thesis, Uppsala University, Sweden, 2004).

## Semi-Virtual laboratory design for photovoltaic generator characterization performance

Hocine Belmili<sup>1,\*</sup>, Mourad Haddadi<sup>2,\*\*</sup>, Salah Med Aitcheikh<sup>2</sup>, Ahmed Chikouche<sup>1</sup>

<sup>1</sup>Group of research: Photovoltaic system, Unit of Development of Solar Equipments (UDSE)  
National road N°: 11 Bou-Ismaïl LP 365, Tipaza 42415, Algiers,

<sup>2</sup>Laboratory of communication devices and photovoltaic conversion (LCDPVC), Polytechnic National School, 10 Avenue Hacén Badi El Harrach Algiers,  
\*belmilih@yahoo.fr, \*\*mourad\_haddadi@yahoo.fr

**Abstract:** This paper presents a study of the photovoltaic generator (PVG) performance. It is based on a comparison between characterizations obtained in real time test and simulated ones using mathematical models. This study is evaluated by the design of a semi-virtual laboratory, which is composed of a hardware support based on the developed data acquisition system in real operating conditions and a software support based on mathematical models descriptions. This laboratory permits to identify PVG parameters using correlation between measurements and simulated characteristics.

**Keywords:** Simulation, photovoltaic generator, characterization, performance, hardware, software.

### 1. Introduction

PVG or PV modules in general are formed by a combination of parallel and series connections of solar cells. The electrical characteristics of PV modules are rated at standard irradiance and temperature conditions. The standard conditions are AM1.5 spectrum, 1000 W/m<sup>2</sup> at 25°C cell temperature, for terrestrial applications, whereas for the extraterrestrial standard conditions it is AM0 (1353 W/m<sup>2</sup>) at 25°C [1]. Therefore the user knows only the electrical parameters nominal values of the PV module, which may be different from the values during the operating conditions. The variation of the characteristics from one set of conditions to another is a problem faced by designers and users, who want to know the outputs of a PV installation in real conditions rather than those given by the manufacturer in standard conditions [2]. Several environmental factors act to influence the performance of photovoltaic devices such as the temperature, the solar angle of incidence, the total irradiance level, the irradiance spectrum and optical effects due to shading. Numerous performance analysis studies have been carried out to assess the magnitudes of these effects, yet there is still some debate about the relative importance of each factor. Due to strong correlations between each environmental driver, their separation for quantification has proved a major challenge that has not yet been met conclusively [3]. Figure 1 represents the block diagram of the semi-virtual laboratory design.

### 2. PVG model description

There are several description models for PVG. Some themes are analytical models; the other ones are empirical and semi-empirical model. In this context we present two PVG model descriptions. The first one is an analytical model based on one-diode model and the second one is an empirical model which is developed by Sandia Laboratory.

#### 2.1. One-diode PVG model

One-diode model of PVG is presented as an electrical circuit as shown in the figure 2.

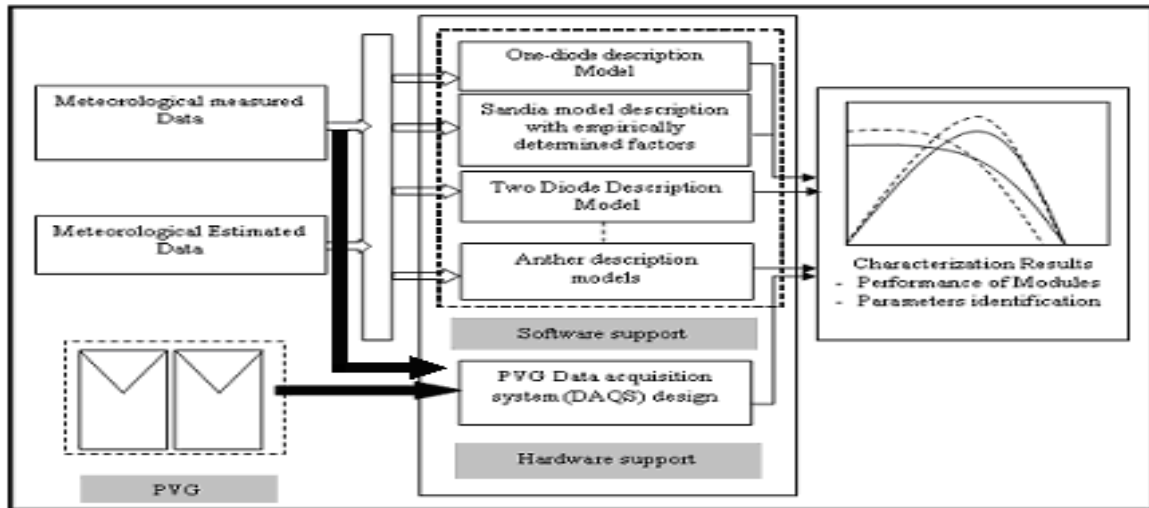


Fig.1: Semi-virtual laboratory design for PVG characterization performance.

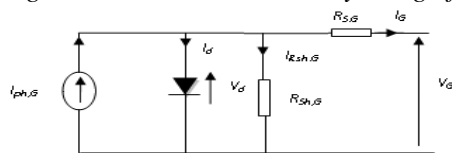


Fig. 2: one-diode equivalent circuit model.

At a fixed temperature and solar irradiation, the I-V curve of this circuit is given by equation:

$$I_G = I_{ph,G} - I_s \left[ \exp\left(\frac{q(V_G + R_{s,G} \cdot I_G)}{n n_s kT}\right) - 1 \right] - \frac{V_G + R_{s,G} \cdot I_G}{R_{sh,G}} \quad (1)$$

The parameters for this model, described elsewhere [4], can be found by either numerical or analytical methods. It has been shown that the circuit parameters  $I_{ph}$ ,  $R_{sh}$ ,  $R_s$ ,  $I_s$  and the diode ideality factor ‘n’ at a particular temperature and irradiation can be computed from the  $V_{oc}$ ,  $I_{sc}$ ,  $V_m$ ,  $I_m$ ,  $R_{so}$  and  $R_{sho}$  values measured from the I-V characteristic. Several researchers have either investigated or developed numerical algorithms to determine the solar cells parameters by fitting measured I-V curves [5]. The difficulty to obtain the PV parameters, from the measured I-V curves, resides in the implementation of complex computer algorithms since the estimation of these parameters, somehow, are restricted to specific research laboratories as those studying fundamental physics device. However, analytical methods can be used as a design tool to derive the parameters from the basic data given by PV module manufacturers, or other readily available data. Under Simulink we present this model as following

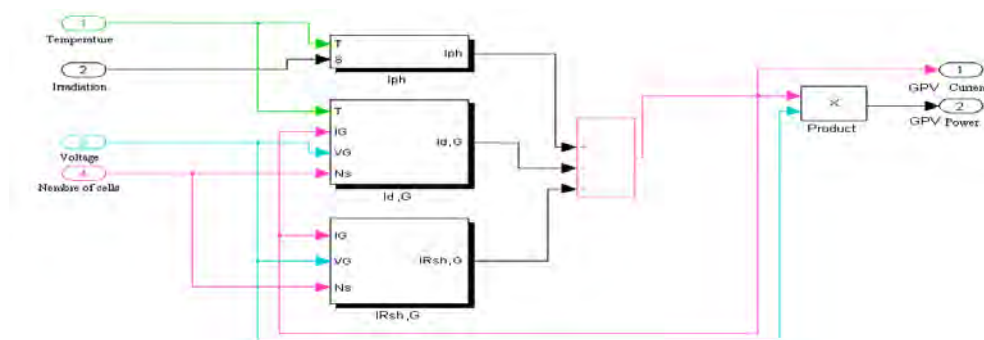


Fig.3: One-diode PVG model simulation under Simulink.

2.2. SNL model description

SNL (Sandia National Laboratory) performance model is an empirically based method. It achieves its versatility and accuracy from the fact that individual equations used in the model are derived from individual solar cell characteristics. The versatility and accuracy of the model has been demonstrated for different photovoltaic and concentrator modules, as well as for large arrays of modules. This model takes account of electrical, thermal, solar spectral and optical effects for photovoltaic modules [6]. The performance modeling approach has been well validated through extensive outdoor module testing, and through inter-comparison studies with other laboratories and testing organizations [7]. Recently, the performance model has also demonstrated its value during the experimental performance optimization of off-grid photovoltaic systems [8]. The following equations define the model used by the Solar Technologies Department at Sandia for the analysis and the modelling of the photovoltaic modules performances. The equations describe the electrical performances for individual photovoltaic cells, modules, and arrays. The solar resource and weather data required by the model can be obtained from tabulated databases [9] or from direct measurements.

$$\begin{cases}
 I_{sc}(E, T_c, AM_a, AOI) = \left(\frac{E}{E_0}\right) f_1(AM_a) \cdot f_2(AOI) \{1 + \alpha_{isc} \cdot (T_c - T_0)\} \\
 Ee = I(E, T_c = T_0, AM_a, AOI) / I_{sc0} \\
 V_{oc}(E, T_c) = V_{oc0} + C_3 \cdot \ln(E_e) + \beta_{V_{oc}} \cdot (T_c - T_0) \\
 V_{mp}(E, T_c) = V_{mp0} + C_3 \cdot \ln(E_e) + C_5 \cdot \{\ln(E_e)\}^2 + \beta_{V_{mp}} \cdot (T_c - T_0) \\
 I_m(E_{ea}, T_c) = C_1 + Ee \{C_2 + \alpha_{I_{mp}} \cdot (T_c - T_0)\} \\
 P_{mp} = I_{mp} \cdot V_{mp} \\
 FF = P_{mp} / (I_{sc} \cdot V_{oc})
 \end{cases}
 \quad (2)$$

The following figure represents Simulink simulation of this model.

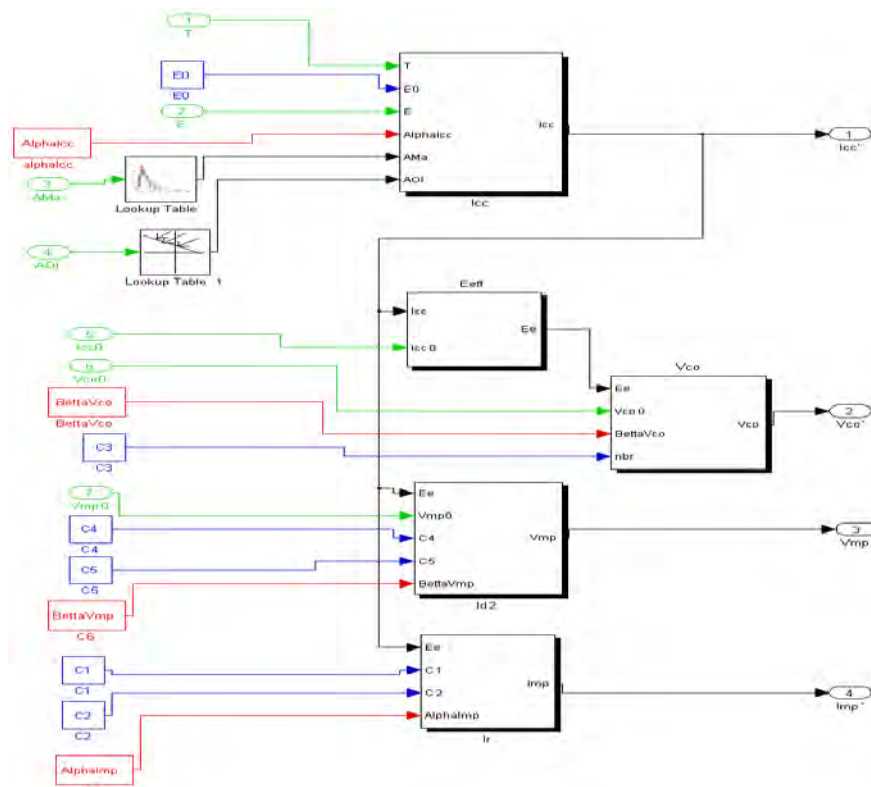


Fig.4: Sandia PVG model simulation under Simulink.

### 3. Hardware design and development of a real-time PVG characterizer

The Hardware part is based on a development of a data acquisition system for real time PVG characterization. The data acquisition system (DAQS) is an important part of the experimental setup. A good experiment can be completely ruined if the data is not collected with the necessary precision and repetition. Figure 5, shows the block diagram of the developed system. The DAQS is linked to a graphical user interface. The developed hardware parts basic element is the electronic load [10]. This electronic load can characterize an array of one or two solar modules connected in serial or in parallel, protected with a by-pass diode. Figure 5 show the block diagram of the developed hardware PVG testing unit.

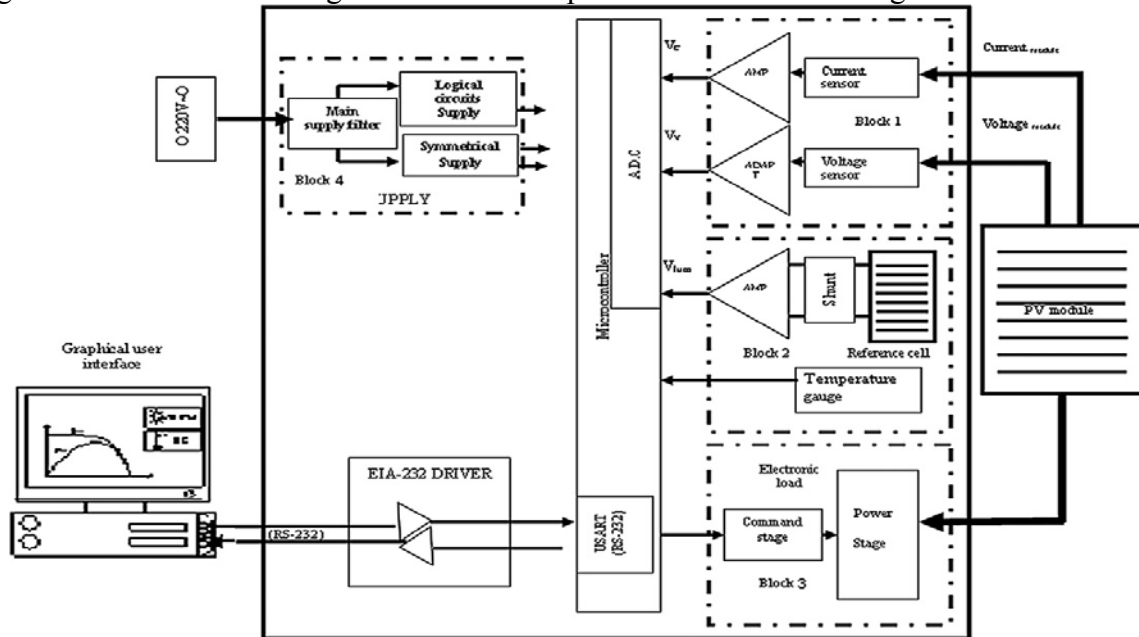


Fig.5: Block diagram of PVG testing unit.

### 4. Software design

The software has been developed using Object-Oriented Programming (O.O.P) under windows. This software based on the development of a three principal programs (figure 6). The first one to estimate irradiation on PVG captor, the second to extract PVG parameters from manufactures data sheet and from other temperature and irradiation inputs and the third one we permits to identify PVG parameters using correlation between measured and estimate characteristics.

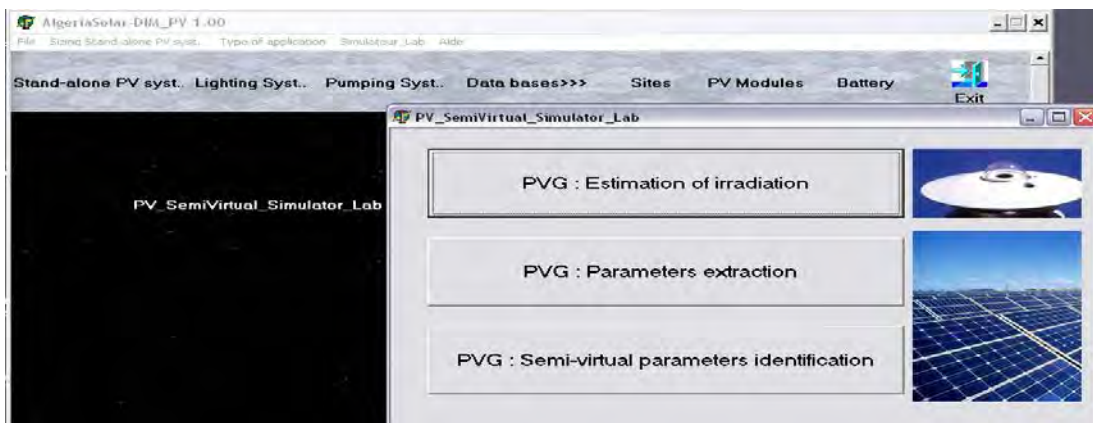


Fig. 6: software design.

#### 4.1. Estimated irradiation program

In this context the developed software is based on a specific algorithm for irradiation simulation [11]. Figure 7 represent the input data window of the developed software for the daily and annual estimation irradiation for different locations. In the present window, sites are identified by the geographical location (latitude, longitude and altitude). With this program, we simulate global horizontal and inclined irradiation. The Albedo represents the diffusion coefficient. Its value belongs to [0.1, 0.9]. The user introduces the year day number and the angle of incidence (AOI) of the irradiation on the module. This software has a data base of different sites in the world. The user can introduce other sites, not configured in the data base, by introducing its geographical location. He, then, can estimate the global and inclined, daily and annual irradiation of the introduced site. The daily sunshine duration is also calculated when the user start execution of daily irradiation simulation.

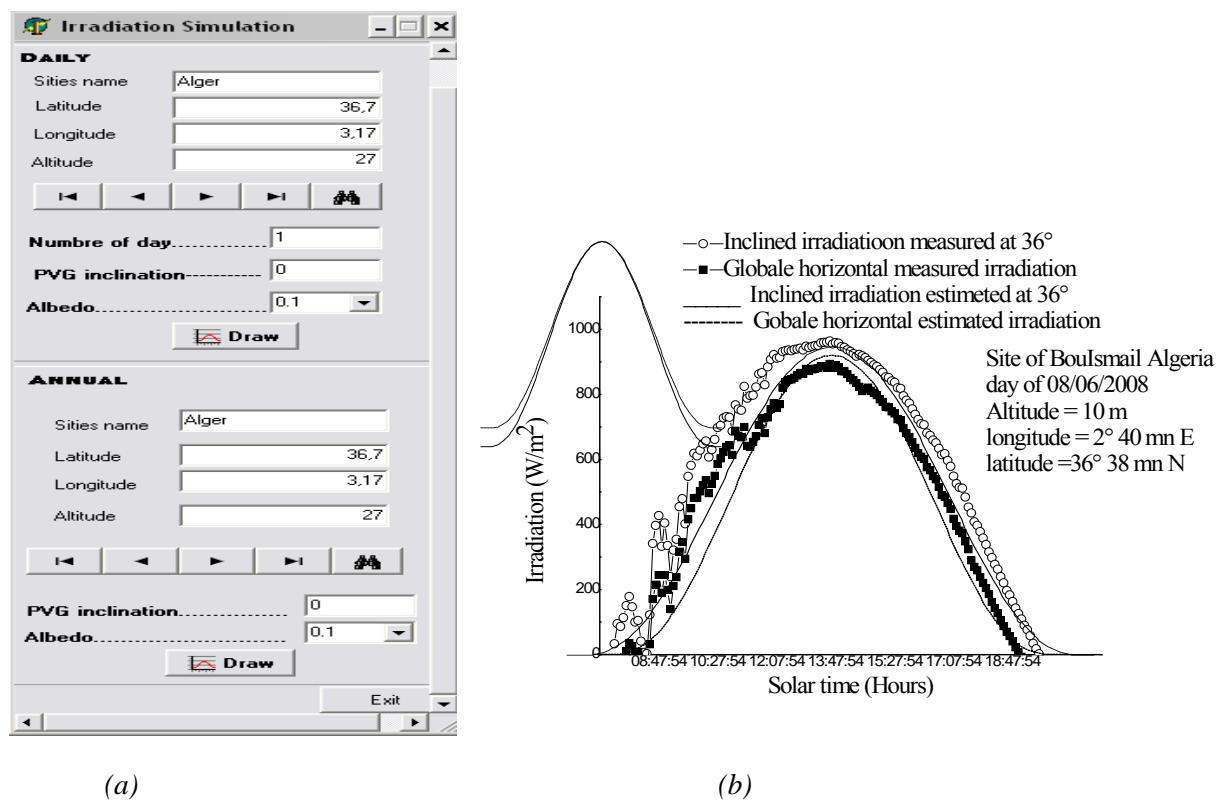


Fig. 7: (a) Inputs data (latitude, longitude and altitude) window for daily and yearly irradiation simulation for sites characterization, (b) Measured and estimated irradiation comparison results.

#### 4.2. Developed software for PVG Parameter extraction

Figure 8 shows the input/output data window for the PVG characterisation under STC conditions and under measured irradiation and temperature conditions. This software disposes of a user-friendly PV modules database for different manufacturers. Using one-diode description model for PV module, this program can identify the five parameters models: ideal factor, serial resistance, shunt resistance, saturation current and photocurrent. The modules in the database are identified by the manufacturer reference and by their STC condition characteristics:  $I_{sc}$ ,  $V_{oc}$ ,  $I_m$ ,  $V_m$  and  $P_m$ . Besides, thru this software, we can add in the database other commercial modules and carry out their characterization, figure 8.

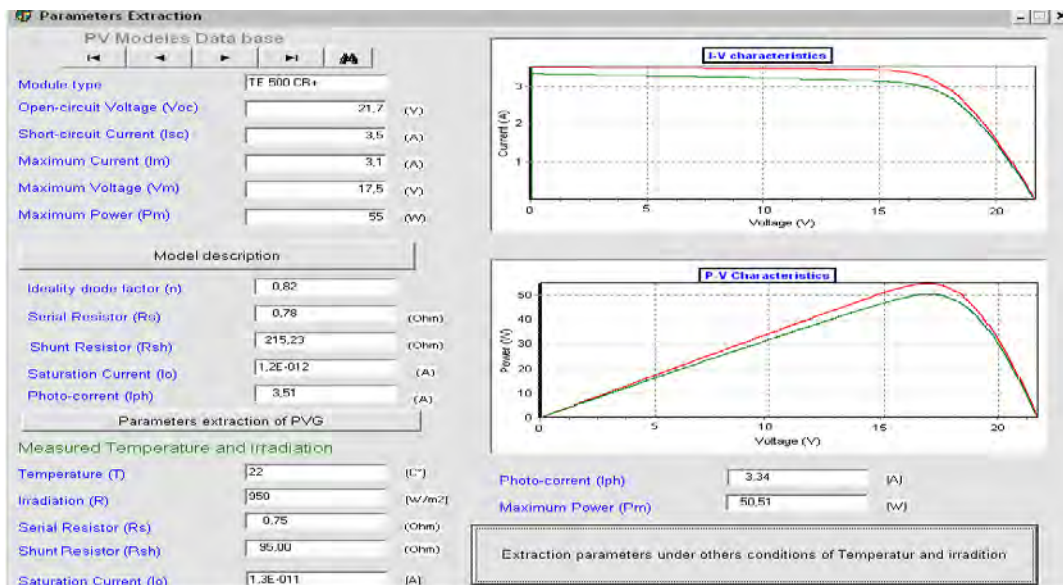


Fig.8: PVG parameter extraction from manufacture data in STC and from authors temperature and irradiation values.

### 4.3. PVG parameter identification platform using correlation with measured characteristics

After developing the data acquisition system for PVG characteristics measurements, we are very interested by the developing of software which permits the identification of PVG parameters in correlation with the measurements characteristics. The identification algorithm is based on the calculation of the correlation factor named “R<sup>2</sup>” between measurements and simulated characteristics. This coefficient is given by the equation number (3).

$$R^2 = 1 - \frac{\sum (X_{exp} - X_{sim})^2}{\sum (X_{exp} - X_{exp})^2} \quad (3)$$

The following figure shows this software. This software permits also the identification of the current and voltage coefficients of temperature.

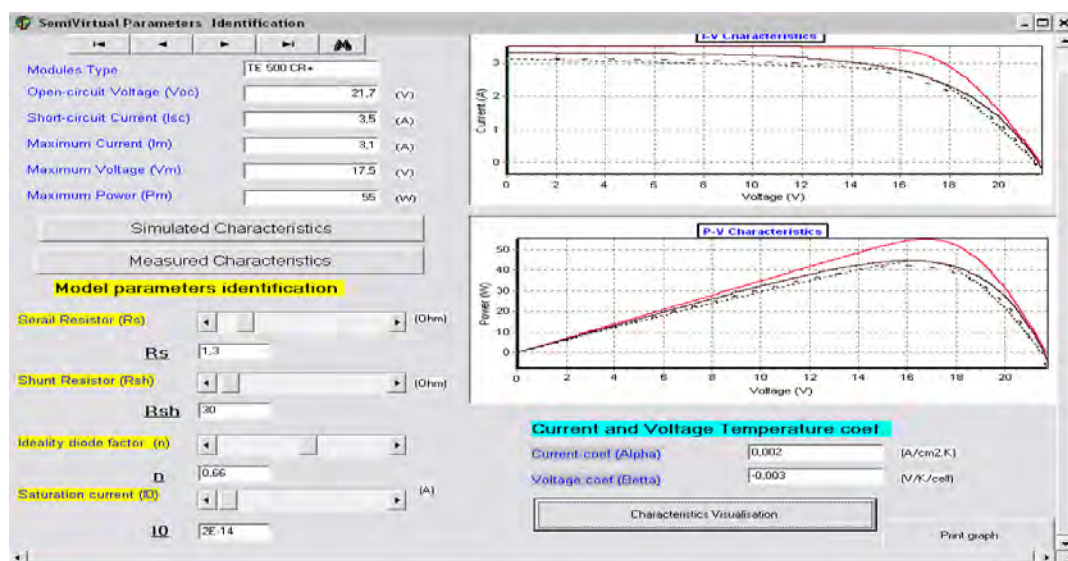


Fig.9: Software of PVG parameters identification using correlation between measurement and simulated characteristics.

### 5. Example for commercial PVG characterization

This example is study the PV commercial module “TE500CR+”. It is multi-crystalline technology [12]. The following figure, shows the I-V and P-V characteristics for the SNL, one diode model and experimental measurement at  $T = 20^{\circ}\text{C}$ ,  $I_r=820\text{W/m}^2$  and  $W_s= 3.5 \text{ m/s}$ .

Table 2: Results of TE 500 CR+ module characterization

Manufactures results (STC conditions)		Isc(A)		Voc (V)		Pm (W)		Im (A)		Vm (V)		
		3,50		21.70		55		3,10		17,50		
Real Meteorological data measurement	Model used	Isc	E <sub>Isc</sub> (%)	Voc	E <sub>Voc</sub> (%)	Pm	E <sub>Pm</sub> (%)	Im	E <sub>Im</sub> (%)	Vm	E <sub>Vm</sub> (%)	
T = 20°C I <sub>r</sub> =820W/m <sup>2</sup> W <sub>s</sub> = 3.5 m/s	Measured results	3.406		19.463		46.64		2.88		14.78		
	RMSE	Measured results/ One diode model prediction									0,69	
		Measured results/ Sandia model approximation prediction									0.63	
FF	Manufactures results (STC conditions)										0.72	
	Measured results										0.64	
	One diode model prediction										0.70	
	Sandia approximation model prediction										0.67	
One-diode PVG model parameters identification												
TE 500CR+ module	Model parameters identification using correlation with measured values with R <sup>2</sup> = 0,98					Model parameters extracted using manufactures data						
	I <sub>ph</sub> (A)	I <sub>0</sub> (A)	R <sub>s</sub> (Ω)	R <sub>sh</sub> (Ω)	n	I <sub>ph</sub> (A)	I <sub>0</sub> (A)	R <sub>s</sub> (Ω)	R <sub>sh</sub> (Ω)	n		
	3.10	2e-14	1,3	30	0.66	3.51	1.2e-12	0.78	215,23	0.82		

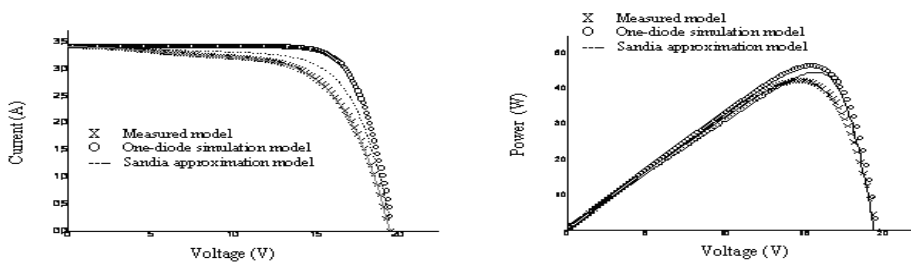


Fig.10: I-V and P-V TE500CR+ module characteristics comparison between Sandia approximations, One-diode estimated model and experimental results.

### 6. Conclusion

This work described the functioning of the designed semi-virtual laboratory for PVG performance characterization methodology. This laboratory based on the comparison between the predicted models results and experimental ones. I-V and P-V, characteristics are obtained and compared, in one hand. In the other hand the PVG parameters are obtained using predict models and experimental results for real and estimated meteorological data. The present example for measurement and modeling applied for the TE500CR+ modules can be used for characterized different PV commercial modules. The final objectives is to duplicated this results and choose modules gives good response when they are introducing in the PV installation and gives either a best installation dimensioning. In perspectives of this research is to introduce other PVG models in this semi-virtual laboratory and its compared with the studied ones

### References

[1] Test Method for Photovoltaic Module Power Rating, FSEC Standard 202-05, Research institute of the university of central Florida, May 2005

- 
- [2] David L. King, William E. Boyson and al, “Application and Validation of a New PV Performance Characterization Method”, 26<sup>th</sup> IEEE Photovoltaic Specialists Conference, September 29 October 3, 1997, Anaheim, California.
- [3] W. Durisch ,J. Urban and G. Smestad, “Characterisation of solar cells and modules under actual operating conditions” California 93955-8001, California, U.S.A. WREC 1996
- [4] Ali Nacer celik and Nasir Acikgoz, “Modeling and experimental verification of the operating current of mono-crystalline photovoltaic modules using four and five parameter models”, Elsevier, Applied energy pp 84 (2007)1-15.
- [5] D. S. H. Chan, J. R. Philips and J. C. H. Phang, “A comparative study of extraction methods for solar cell model parameters”, Solid-State Electronics Vol. 29, No. 3. pp. 329-337, 1986.
- [6] D. L. King et al, Photovoltaic system performance characterization methodologies, NREL/CD-520-33586, 543-546.
- [7] A. Hunter Fanney, and al, «Comparison of Photovoltaic Module Performance Measurements”. 152 / Vol. 128, MAY 2006 Copyright © 2006by ASME Transactions of the ASME
- [8] D.L. King, J.A. Kratochvil, W.E. Boyson, and W.I. Bower, “Field experience with a new performance characterization procedure for photovoltaic arrays” , 2<sup>nd</sup> World Conference and Exhibition on Photovoltaic Solar Energy Conversion, 6-10 July 1998, Vienna, Austria.
- [9] <http://www.sandia.gov/pv/>
- [10] Hocine Belmili, Salah Med Aitcheikh, Mourad Haddadi, Cherif Larbas “Design and development of a data acquisition system for photovoltaic modules characterization” Elsevier Renewable energy 35(2010)1484-1492.
- [11] Piedallu, C. and Gégout, J.C. “Multiscale computation of solar radiation for predictive vegetation Modeling”. Annals of Forest Science, 64: 899-909. 2007.
- [12] TE 500 CR+ Modules. [www.total-energie.com](http://www.total-energie.com).

## Two Phase Change Material with Different Closed Shape Fins in Building Integrated Photovoltaic System Temperature Regulation

M. J. Huang<sup>1,\*</sup>

<sup>1</sup> University of Ulster, Newtownabbey, Co. Antrim, N. Ireland, UK

\* Corresponding author. Tel: +44 28 90366037, E-mail: m.huang@ulster.ac.uk

**Abstract:** Photovoltaics (PVs) operate at around 40°C above ambient temperature in full sun. On a cold day in Europe the cell temperature will be at 30°C and compared to a summer temperature of up to 80°C. As each ten temperature increases the efficiency of the crystal silicon photovoltaic will reduce 10%. So considering the whole year, running at 25°C for Building Integrated Photovoltaic (BIPV) will be an ideal temperature target to achieve in order to keep PV cells at their peak efficiency in Europe. Passive heat removal technique was applied for thermal regulation of PV using Phase Change Material (PCM) integrated on the back of the PV. The temperature in PV can be effectively regulated, but the low thermal conductivity of the PCMs is one of the main problems for this application. This paper details the results of a theoretical investigation and analysis of PV temperature control and solar thermal energy storage achieved using phase change materials with different types of fins, structure and PCMs. The predicted performance provides an insight into the effects of using various quantities of different PCM materials with different types of fins and thermal storage for selected ambient conditions of temperature and insolation. From this parametric study, optimum arrangements of the PV/PCM system with different type of fins are proposed, thereby improving the efficiency of the PV/PCM system.

**Keywords:** phase change materials, Photovoltaic and Building Integrated Photovoltaics

### Nomenclature

$C$	Specific heat capacity ..... $Jkg^{-1} K^{-1}$	$T_{amb}$	Ambient temperature ..... $^{\circ}C$
$E$	Thermal energy ..... $Jkg^{-1}$	$T_m$	PCM Melt temperature ..... $^{\circ}C$
$H$	Heat transfer coefficient ..... $Wm^{-2} K^{-1}$	$U_L$	Overall heat loss coefficient, $Wm^{-2} K^{-1}$
$H$	Latent thermal energy..... $Jkg^{-1}$	$\eta_c$	PV Electrical conversion efficiency
$I_T$	Insolation incident on photovoltaic cell $Wm^{-2}$	$\tau$	Transmittance of PV cover
$K$	Thermal conductivity ..... $Wm^{-1} K^{-1}$	$\alpha$	Absorptance of PV
$T$	Time .....	<i>Subscripts</i>	
$\Delta t$	Time step.....	$L$	liquid phase
$T$	Temperature ..... $^{\circ}C$	$S$	solid phase
$\Delta T$	Transition temperature of PCM $^{\circ}C$		
$T_{PV}$	PV Temperature ..... $^{\circ}C$		

### 1. Introduction

Building integrated photovoltaic systems (BIPVs) are widely recognised as the most cost effective form of PV power generation [1]. As well as producing electricity, BIPV panels can replace some of the conventional wall cladding and roofing materials, therefore reducing the net costs of the PV system. The elevation of the PV temperature reduces solar to electrical energy conversion efficiency by 0.4-0.5%K<sup>-1</sup> for crystal silicon PV when it rises above the characteristic power conversion temperature of 25°C [2] [3]. Maintaining the silicon PV's temperature at a low temperature, preferably lower than or around 25°C will retain the maximum conversion efficiency of the PV for practical applications. Active and passive heat dissipations have been studied for decade [4] [5] [6].

PCM can absorb a large amount of energy during the phase change, and is therefore widely investigated for thermal storage. A review on thermal energy storage with phase change materials and application has been carried by Sharma, et al. [7] and Agyemin et. al. [8]. An

investigation of a system which uses PCMs to absorb energy as latent heat at a constant phase transient temperature and to regulate the rise in PV temperature (PV/PCM) has been carried out recently ([6], [9] and [10]). It was found that the PCM thermal conductivity and volume expansion during melting are the main barriers for this application. A series of arrangements with different types of fins inserted inside the PV/PCM system was also carried out experimentally [6]. Although the metal fins inserted inside the PCM can improve the heat transfer inside the PV/PCM system, the thermal regulation period declines as the volume of the PCM is substituted by the metal mass of the PV/PCM system. It was also found that during crystallisation the air cavity formed inside the PCM will increase the thermal resistance when used for temperature regulation during the day time. The further studies using different types of PCMs for the PV/PCM application, including a eutectic mixture of capric-lauric acid (CL), a commercial blend of salt hydrate and paraffin phase change material (SP22), a eutectic mixture of Capric Palmitic acid (CP) and a Calcium Chloride hexa hydrate ( $\text{CaCl}_2$ ), have been carried out [11]. Eutectic Mixture of Capric-Palmitic Acid and  $\text{CaCl}_2 \cdot 6\text{H}_2\text{O}$  with higher thermal conductivities than paraffin wax have a better thermal regulation performance on BIPV for indoor conditions and the outdoor climates of Ireland and Pakistan [11]. Further investigation on the corrosion of the container needs to be conducted.

In this paper an experimental validated numerical simulation model [9] has been modified to suit for two phase change materials for PV/PCM modeling. The thermal regulation of the PV/PCM system in triangular shaped cells and circular shaped cells (which optimise for reducing stress due to PCM expansion) have been studied. A range of different phase transient temperature PCMs under static state and realistic conditions have been discussed in this paper.

## 2. Methodology

The simulation model used in this work is a two dimensional temperature-based finite volume based conjugated heat transfer numerical model to moderate the temperature rise in BIPVs in a PV/PCM system. This model is based on the previously developed and experimentally validated model for a single PCM with straight fins in the PV/PCM system by the authors [9]. The non-linear transient model uses Boussinesq's approximation and allows convection and diffusion to be simulated. The developed model can be used to predict the transient temperature distribution and fluid flow field within a two-dimensional region in the PV/PCM system for different insolation, ambient temperatures, convective and radiative heat transfer boundary conditions ([9] and [10]). The modified PV/PCM model can be used for multiple PCMs with different transient temperatures and for triangular shaped PCM cells. The following assumptions are made:

- (i) The heat conduction in the PV/PCM combined system is two-dimensional and the end sides at the top and bottom are adiabatic.
- (ii) The thermal conductivity of the aluminum frame and PCMs in the solid and liquid phases are constant and do not vary with respect to temperature.
- (iii) The PCM is homogeneous and isotropic.
- (iv) The convection effect in the molten PCM is neglected for the thermal performance comparison, but has been considered for special case.
- (v) The interfacial resistances are negligible.
- (vi) The specific heat capacity " $C_p$ " value of the PCM is considered as uniform during phase change process, though in actual practice, there is variation in  $C_p$  value within the small temperature range.

A brief summarization is as follows.

The energy equation for melt [9]:

$$\rho_L c_L \frac{\partial T}{\partial x} + \frac{\partial}{\partial x} (\rho_L c_L \bar{u} T - k_L \frac{\partial T}{\partial x}) + \frac{\partial}{\partial y} (\rho_L c_L \bar{v} T - k_L \frac{\partial T}{\partial y}) = 0 \quad (1)$$

The energy equation for solid:

$$\rho_s c_s \frac{\partial T}{\partial t} + \nabla \cdot (k_s \nabla T) = 0 \quad (2)$$

Where the same equations hold good for all the frame and cell wall material and PCMs by incorporating suitable  $k$ ,  $\rho$ ,  $C_p$  values. The instantaneous continuity of heat flux and temperature at the interfaces of frame and cell with PCMs are preserved.

In the exterior front boundary, where the PV/PCM system is exposed to solar radiation, the boundary condition is,

$$k \frac{\partial T}{\partial x} \Big|_{x=0} = S + h_0 (T_{amb} - T_{x=0})$$

In the exterior back layer of the PV/PCM system  $x=L$ , the boundary condition is

$$k \frac{\partial T}{\partial x} \Big|_{x=L} = h_L (T_{x=L} - T_{amb})$$

Where  $h_0$  and  $h_L$  are the heat transfer coefficients from the front and back surfaces of the PV/PCM system to the surroundings.  $S$  is the heat received by the PV/PCM system on the front surface from the incident solar energy.

Table 1. Thermophysical properties of RT21, RT27, RT31 [13]

	RT21	RT27	RT31	Aluminium
Melting temperature	21	27	29	N/A
Latent heat (kJ kg <sup>-1</sup> )	134	184	169	N/A
Density (kg m <sup>-3</sup> )				
Liquid	760	750	770	N/A
Solid	840	840	890	2675
Thermal conductivity (Wm <sup>-1</sup> K <sup>-1</sup> )	0.2	0.2	0.2	160
Viscosity (mm <sup>2</sup> s <sup>-1</sup> )	25.71	26.32	28.57	N/A

The most significant thermal characteristics affecting the performance of the PV/PCM system are (a) the PCM heat capacity, (b) the phase transient temperature, (c) the location of the PCM and (d) the mass in the system fins arrangement. In this paper, the PV/PCM system has been designed with small metal cells to hold two types of PCMs considered to enhance heat transfer. The triangular and circular cell shapes are good for directing the bubbles produced during the melting process and thereby dissipates the stress due to the volume expansion which challenges many PCM applications. The schematic of the PV/PCM with metal cells is illustrated in Figure 1. The vertical position is used to mimic building integrated PV. The study here is just concentrated on the building wall integrated PV, the inclined PV systems beyond these limits. The 4 mm aluminium front/ back walls and the 1 mm aluminium alloy fins of the PV/PCM test system provided a high rate of heat transfer to the PCM. The interior dimensions of the containers were 0.132m high by 0.04m depth. The upper and lower ends of the PV/PCM system were assumed adiabatic. The incident energy  $I_T$  absorbed by the PV as heat is conducted through the high heat transfer cell wall to the PCM and dissipated from the rear of the PV/PCM system. The different thermal regulation characters of the PCMs can hold PV temperature at lower levels for longer periods. The PCMs that are commercially available

with different phase transient temperatures from 21 to 60°C are combined to regulate the PV temperature rising in the PV/PCM system. Different combinations of the PCMs used to augment the PV/PCM system are analysed for static conditions and realistic diurnal temperature and insolation boundary conditions in the England summer period and the heat transfer and temperature distribution are predicted. The thermal properties of the aluminium alloy and the four PCMs that can be combined into the types of PCMs from RUBITHERM [13] used as input data in the simulations are presented in Table 1.

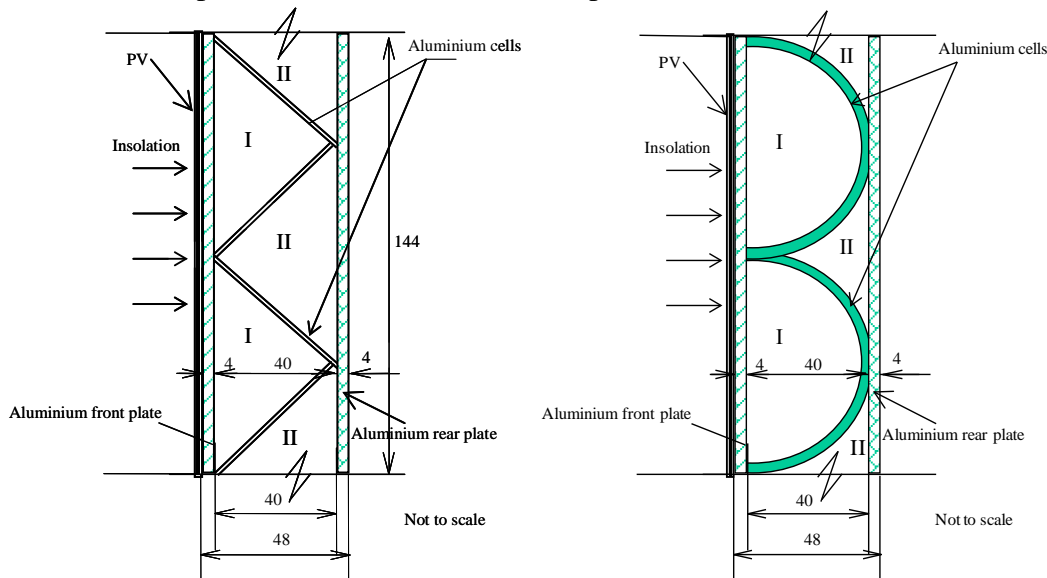


Figure 1. Schematic diagram of PV/PCM system with metal cells for different PCMs

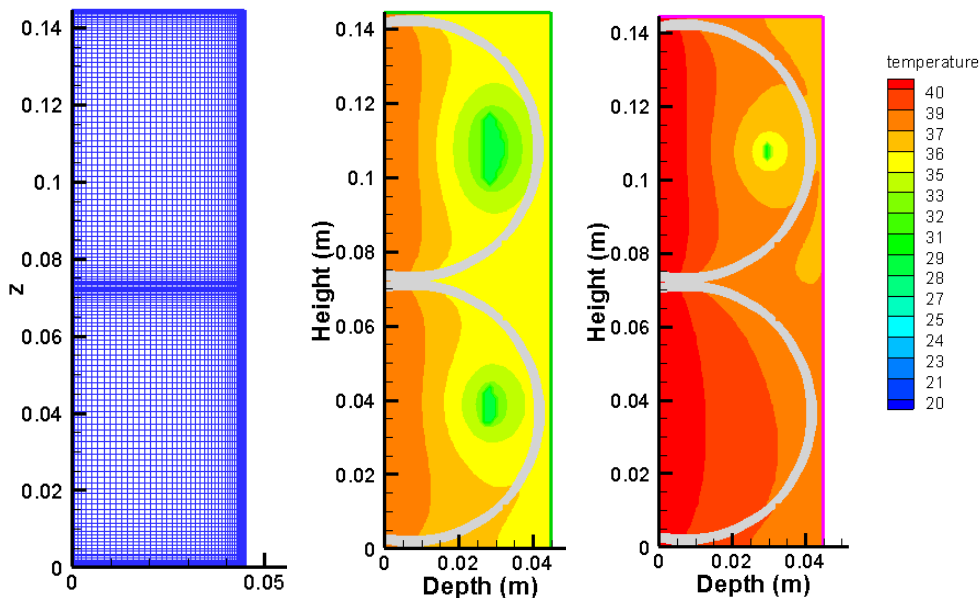


Figure 2. Grid and isotherms of circular cells with two phase change materials in PV/PCM system

The heat transfer coefficients from the front and back surfaces of the PV/PCM system are set at  $10 \text{ Wm}^{-2}\text{K}^{-1}$  and  $5 \text{ Wm}^{-2}\text{K}^{-1}$  (to simulate natural ventilation conditions) and the top and bottom boundaries of the system are assumed to be adiabatic. A fixed grid space of 1mm square for straight fins and variable grid for circular cell fins simulation with finite volumes and a variable time step with a minimum value of 0.0125 s are used for all the simulations. The total number of grid is 144x48 for simulation.

Simulating the behaviour of the PV/PCM system with the two different phase transient temperature PCMs is carried out under the static state and realistic conditions. In real thermal applications it is subject to the cyclic melting and solidification boundary conditions. To predict long-term temperature control, three days are simulated using weather data for the 21<sup>st</sup> June for the SE of England [14] on the vertical south-east oriented PV/PCM system when the insolation was greater than  $120 \text{ Wm}^{-2}$ . For the simulations, realistic ambient temperatures and insolation boundary conditions are regarded as invariant over 5 minute intervals. The simulation temperatures within the PV/PCM system are all initially set to the outdoor ambient temperature at 00:00 hr for the transient applied boundary condition.

### 3. Results and Discussions

In order to evaluate the PV/PCM performance, predictions of the temperature development with the two phase materials, a single PV plate is predicted as a reference for performance comparison. The predicted reference temperature is at  $68.45^\circ\text{C}$  with insolation  $1000 \text{ W/m}^2$  and ambient temperature  $20^\circ\text{C}$ . The following four cases using different combinations of two PCMs with different melting temperatures and two shapes of fins (triangle and half circular fins) were simulated on setting static conditions of (a) insolation  $1000 \text{ W/m}^2$  and ambient temperature  $20^\circ\text{C}$  and (b) realistic three days ambient conditions with repeating data on 1<sup>st</sup> June [14].

- RT27 with RT21 (triangle cells)
- RT27 with RT27 (triangle cells)
- RT31 with RT27 (triangle cells)
- RT31 with RT27 (half circular cells)
- RT60 with RT21 (triangle cells)

The variable grids of the simulation for the circular cell is listed in Figure 2 along with the isotherms of the circular cells in different time. The insolation absorbed on the front surface of the PV/PCM system and conducted through the PV increases the temperature of the metal cell wall. The metal wall of the cell provides good thermal transfer to the two PCMs. Similar situations can be seen on the triangle fins in Figure 3. As time elapses, it can be seen that the temperature on the front surface of the PV/PCM system has a lower temperature rise for the system with RT27-RT21 than that with the RT27-RT27 and RT31-RT27 filled system, and the thermal regulation period is shorter. It is easy to understand that the lower melting PCM can have better thermal regulation compared with the higher melting PCM. This can be observed from the predicted isotherms for the PV/PCM system cross-sections as shown in Figure 3. Metal fins in the PCM increase the heat transfer inside of the PCMs by increasing the surface area over which heat transfer to the PCM occurs and also act as a pressure release pathway for the melted PCM. After the first 30 minutes the temperature inside the system with RT27-RT21 is relatively lower than the RT27-RT27 and RT31-RT27 cases. After 60 minutes the front temperature on RT27-RT21 increases more rapidly to the insolation intensity than the RT27-RT27 and RT31-RT27 cases do, and the thermal regulation period is less. The position of the PCMs is an important factor in thermal regulation. When combined with low phase change transient PCM the temperature on the front surface of the PV/PCM system has a lower temperature rise.

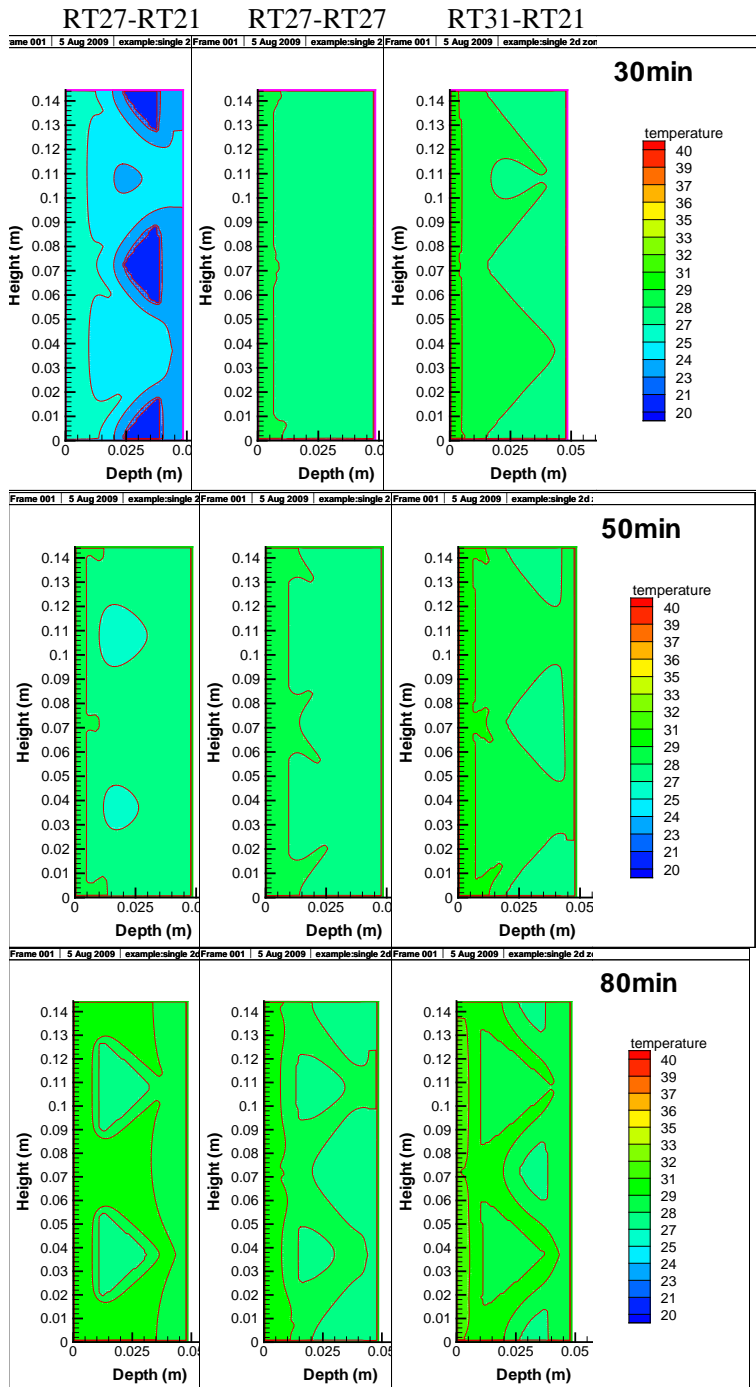


Figure 3. Predicted isotherms for the PV/PCM system with four cases of RT27-RT21, RT31-RT27 during the PCM phase change process

A three day simulation using the weather data on 21<sup>st</sup> of June has been undertaken to predict the heat accumulation in the PV/PCM system with a combination of two PCMs and is presented in Figure 4. The temperatures of the system respond more rapidly to the insolation than to the ambient temperatures. When no insolation is involved, it can be found that the temperature on the front surface of the system decreases with phase change properties. The temperature of the PV/PCM systems follows the incident insolation but lags with the properties of PCMs by more than 20 minutes. Absorbed solar energy is stored in the PCMs during high daytime temperatures and subsequently released to the ambient in the evening. The predicted temperatures for the second and third days for all the cases are the same, the

PCM has thus released all its latent heat to the ambient environment at night and returned to its solid phase at the start of each period of insolation. The RT31-RT27 system with triangle and circulate close fins can efficiently control the temperature on the PV under 30°C for the whole test period. For two different PCMs the lower phase transient PCM dominates the whole system performance. The phase transient performance is clear in the cooling stage.

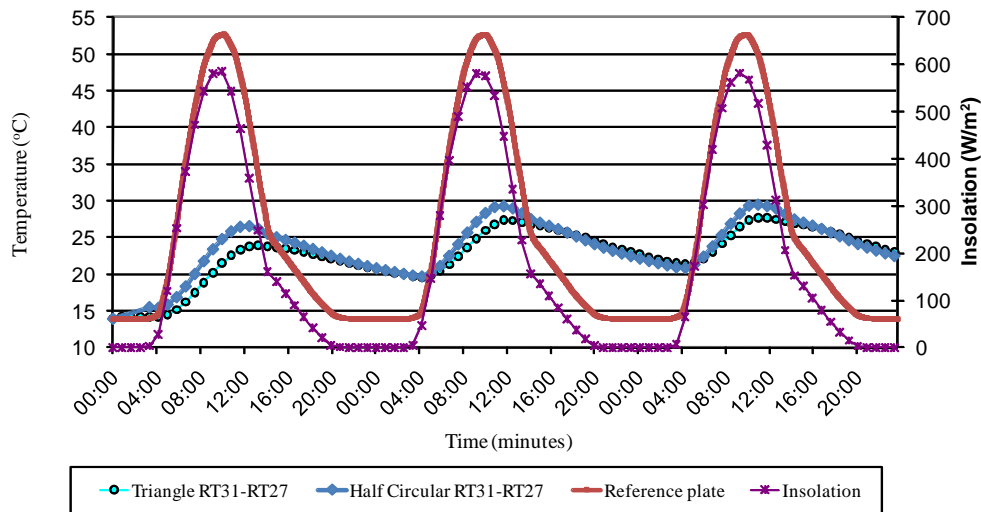


Figure 4 Average temperature evolution at the front surface of the PV/PCM system with the RT31 and RT27 combination for a three day simulation using the weather data on 21<sup>st</sup> of June SE England

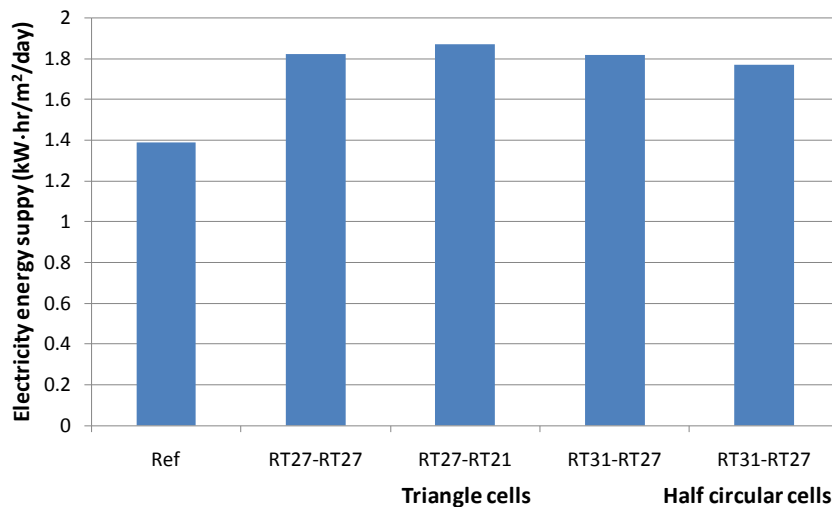


Figure 5 Electricity energy supply on the selected day in 23th June in SE England per square metre for different PCMs combine PV/PCM system along with reference PV module

The temperature regulation may be quantified in terms of the electricity supplied in a typical day in summer. Assuming that the useful electricity power can be produced only after the insolation is over  $200 \text{ Wm}^{-2}$ . Figure 5 shows the comparison of the electricity energy provided by the two PCMs combined PV/PCM systems with the reference PV module during one day's performance in 21<sup>st</sup> June in SE England. The PV/PCM systems with half circular cells and triangle cells have been compared as well. The effect of temperature regulation by PV/PCM combined system is clear. The difference between using the triangle and half circular cells is not significant with the selected PCMs combination.

#### 4. Conclusions

The thermal performance of using two PCMs to regulate the temperature rising on PV/PCM system is studied. The PCMs with different transient temperatures can maintain the PV at operating temperature closer to its characteristic value of 25°C and thus lead to an improvement in solar-to-electrical conversion efficiency. The different thermal regulation characters of the PCMs can keep PV temperature at lower levels for longer periods. The PCMs evaluated at different combinations show that the thermal regulation performance of the PV/PCM depends on (a) the thermal mass of PCMs, (b) the positions of the PCMs inside the PV/PCM system and (c) the thermal characteristics of both the PCMs and the PV/PCM systems structure. Comparing different combinations, RT27-RT21 achieves the highest temperature reduction during the daily operation.

#### References

- [1] NREL, (2008). National Renewable Energy Laboratory, A National Laboratory of the US Department of Energy Office of Energy Efficiency & Renewable Energy, [http://www.nrel.gov/pv/building\\_integrated\\_pv.html](http://www.nrel.gov/pv/building_integrated_pv.html).
- [2] Ingersoll J. G., (1986). Simplified calculation of solar cell temperatures in terrestrial photovoltaic arrays. *ASME J. Solar Energy Engineering* 108, 95-101
- [3] Krauter S., Hanitsch R. and Wenham S. R., (1994). Simulation of thermal and optical performance of PV modules, *Renewable Energy*, 5, 3, 1701-1703
- [4] Tonui, J.K. and Tripanagnostopoulos, (2007). Air cooled PV/T solar collectors with low cost performance improvements. *Solar Energy* 81, 498-511.
- [5] Fossa, M., Ménézo, C., Leonardi, E., (2008). Experimental natural convection on vertical surfaces for building integrated photovoltaic (BIPV) applications, *Experimental Thermal and Fluid Science* 32, 980-990.
- [6] Huang M.J., Eames P.C. and Norton B., (2006). Experimental Performance of Phase Change Materials for Limiting Temperature Rise Building Integrated Photovoltaics, *Journal of Solar Energy*, 80, pp. 1121-1130.
- [7] Sharma, A., Tyagi, V. V., Chen, C. R. and Buddhi, D. (2009). "Review on thermal energy storage with phase change materials and applications." *Renewable and Sustainable Energy Reviews* 13(2): 318-345.
- [8] Agyenim, F., Hewitt, N., Eames, P. and Smyth, M. (2010). "A review of materials, heat transfer and phase change problem formulation for latent heat thermal energy storage systems (LHTESS)." *Renewable and Sustainable Energy Reviews* 14(2): 615-628.
- [9] Huang M.J., Eames P.C. and Norton B., (2004). Thermal Regulation of Building-Integrated Photovoltaics Using Phase Change Materials, *International Journal of Heat and Mass Transfer*, 47, Pages 2715-2733
- [10] Huang M.J., The Application of CFD to Predict the Thermal Performance of Phase Change Materials for the Control of Photovoltaic Cell Temperature in Buildings, PhD Thesis, University of Ulster, UK, 2002.
- [11] Hasan, A. (2010), Phase Change Materials for Thermal Regulation of Building Integrated Photovoltaics, PhD thesis, Dublin Institute of Technology.
- [12] Duffie J.A. and Beckman W.A., (1991). *Solar Engineering of Thermal Processes*, Wiley & Sons, Inc., USA.
- [13] Anon, RUBITHERM data sheets for RT21, RT27, RT31 and RT60, RUBITHERM GmbH, Schumann company. (2011).
- [14] CIBSE, (2006). *CIBSE Guides A*, Chartered Institute of Building Services Engineers, London, UK.

## Performance-based analysis of a double-receiver photovoltaic system.

Alaeddine Mokri, Mahieddine Emziane

*Solar Energy Materials and Devices Lab,  
Masdar Institute of Science and Technology, Masdar City, PO Box 54224, Abu Dhabi, UAE  
E-mail: amokri@masdar.ac.ae, memziane@masdar.ac.ae*

---

**Abstract:** Concentrating photovoltaic (CPV) systems with three-junction solar cells are already in the market. In the CPV market, photovoltaic systems with four cells are needed to make CPV more cost competitive. This is because systems with four cells have more yield than the existing three cell systems. Technically, making a stack of four cells imposes constraints on the choice of the materials (i.e. energy bandgap and lattice constant) and it involves complex and costly fabrication techniques. This paper suggests a design of a CPV system with two separate double-junction solar cells (i.e. four PV cells). The system proposed enables the operation of the four cells independently. It also offers high flexibility in the choice of the materials for making the solar cells. The system described in this paper involves a double-junction cell made of AlGaAs/Si; and another double-junction cell made of: InGaAsP/InGaAs. This paper presents the modeling approach and the response of the system under the standard conditions.

**Keywords:** photovoltaic, beam splitting, concentrating photovoltaic system.

---

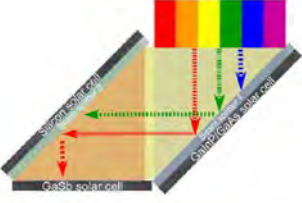
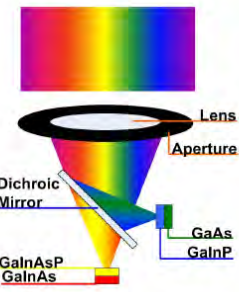
### 1. Introduction

Recently, efficiencies as high as 41.6 % have been measured on concentrating photovoltaic systems (CPV) with a three junction solar cell made of InGaP/InGaAs/Ge [1, 2]. Such converters are already in the PV market for terrestrial applications but with a share of less than 1%, while the other photovoltaic technologies (i.e. silicon and thin films) dominate the market [3, 4]. Though the performance of CPV systems with three cells is high, further improvements are still needed to bring down the cost of power from CPV systems and make it cost competitive with the other technologies, namely: silicon based technologies, thermal concentrating solar power and thin-films. One way to improve the response of CPV systems is to involve four-junction solar cells which are not in the market yet. As a matter of fact, the company Emcore is planning to use four-junction cells in their modules from the second quarter of 2011 to achieve 30% outdoors efficiency [5]. Theoretically, the limiting efficiency of a series connected solar cell with four sub-cells is 67.9% under the direct solar spectrum [6]. Making monolithic 4-junction solar cells is technically challenging imposes constraints on the choice of the material because the four cells need to have specific lattice constants and specific energy bandgaps for an optimum response. However, making 2-junction solar cells is relatively simple and can be made with less constraints.

In this work, we suggest a design to involve four cells to achieve a high efficiency with less constraints by using optical techniques. The idea is to design a multi-receiver system in which the cells are kept apart and the sunlight is split into different sub-beams. This type of multi-receiver systems tends to be complex shape-wise which makes wiring, mounting and cooling more complex. In the literature, many CPV systems with beam-splitting features are reported; however, three CPV systems only involve four solar cells [7-11]. United Innovations Inc. proposed a cavity receiver with four mono-junction cells coated with optical filters: InGaP, GaAs, InGaAsP and InGaAs (see configuration 1 in Table 1). The efficiency was calculated and estimated at 48.32 % under 100 suns [8]. Another receiver with four cells was demonstrated at the Fraunhofer ISE in Freiburg, Germany (see configuration 2 in Table 1) [9]. Two of the cells were made of InGaP and GaAs, and they were stacked together. The other mono-junction cells were made of Si and GaSb. An efficiency of 34% was measured [9, 11].

In configuration 3 in Table 1, a system built at the University of Delaware is shown. The system was tested under outdoors site-specific conditions and an efficiency approaching 40% was measured [10].

Table 1: Photovoltaic systems with four cells and beam-splitting features.

Configuration	Solar cells	Efficiency	Reference
 <p>Configuration 1</p>	InGaP, GaAs, InGaAsP, InGaAs	48.32 % under 100 suns (calculated)	Ref. 8
 <p>Configuration 2</p>	GaInP/GaAs, Si, GaSb	34 % (measured)	Ref. 9
 <p>Configuration 3</p>	InGaAsP/InGaAs, GaAs/InGaP	39.5 % under 30 suns and DNI = 360 W/m2 (not standard conditions)	Ref 10

We have looked at several systems with beam-splitting features, and based on the lessons learned from the designs proposed in the literature, we are proposing a design with four solar cells. Our system has concentration features. This is because concentration improves the response of solar cells and their yield. Also, concentrating systems use a small cells which reduces the amount of material required for making the solar cells; thus, reducing their cost. The proposed system has only two separate receivers in order to avoid multiple reflections, which is not the case in configurations 1 and 2 in Table 1. Having a system with four solar cells and two receivers imply that each receiver holds a double-junction tandem solar cell.

In this paper, the proposed system is presented. A modeling approach has been developed to estimate the response of the system under the standard conditions.

## 2. Description of the system

The proposed system is displayed in figure 1 and it is composed of a parabolic mirror, a plano-convex lens coated with a short-pass optical filter, and two tandem photovoltaic cells. The setup has two separate receivers: one receiver holds a double junction solar cell made of AlGaAs/Si and the other receiver holds an InGaAsP/InGaAs double-junction cell.

For the dimensions of the receiver, the diameter of the dish is 112 mm. The cells have circular shapes. The AlGaAs/Si cell has a radius of 7 mm; however, the cell at the opposite receiver has a radius of 10 mm.

The dish concentrates sunlight on the lens. The plano-convex lens is made of fused silica and it is coated with a short-pass multilayer optical filter. Ideally, the filter transmits photons with energies higher than the energy bandgap of Silicon and reflects photons with energies shorter than the energy bandgap of Silicon. We should remind that AlGaAs and Si have the following energy bandgaps of 1.817 eV and 1.124 eV. Therefore, photons with energies higher than 1.124 eV only can be absorbed and converted and those with energies lower than 1.124 eV are reflected to the InGaAsP/InGaAs solar cell. In<sub>0.57</sub>Ga<sub>0.43</sub>AsP and InGaAs have energy bandgaps of 1.0 eV and 0.74 eV respectively. Therefore, photons with energies higher than 0.74eV and shorter than 1.124 eV can be absorbed and potentially converted.

For the sake of developing an accurate model, realistic optical properties for the reflective coating on the mirror and the short-pass coating on the lens for commercialized products were used in our model. The transmittance of the multilayer optical filter is presented in figure 2. The spectrum incident on each receiver is presented in figure 3.

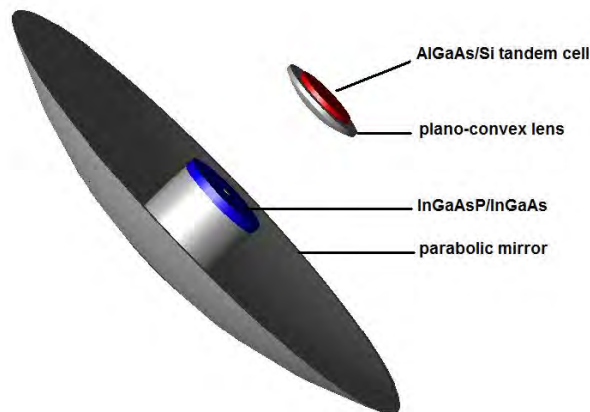


Fig. 1. Configuration of the proposed double-receiver system.

## 3. Modeling approach

To the best of our knowledge, there is no package dedicated to the modeling of CPV systems with multiple receivers. Therefore, we had to devise a multi-step procedure for modeling the different parts of the system: the light source, the opto-mechanical system, and the solar cells. For the details of the modeling procedure, reference [12] is recommended.

### 3.1. Modeling the light source:

For modeling the light source, the package SMARTS was used for generating a file for the standard solar spectrum AM1.5 D ASTM G173-03 [13, 14]. The output of the package consists of the wavelengths and the corresponding flux values in  $\text{W}/\text{m}^2/\text{nm}$  in the other column. As we are modeling a concentrating photovoltaic system, only photons coming directly from the source (i.e. the sun) can be tracked. For this reason, spectrum of sunlight coming directly from the sun was generated (i.e. AM1.5D). To cover the maximum of the spectrum, we generated spectrum for wavelengths starting from 280 nm to 4000 nm. The spectrum is presented in figure 3.

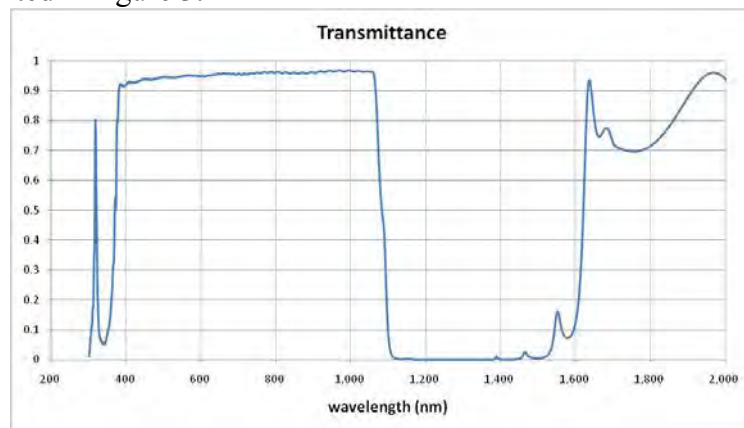


Fig. 2. Transmittance of the short-pass optical filter.

### 3.2. Modeling the opto-mechanical system:

The values obtained from SMARTS were used for modeling the light source in the ray tracing package TracePro Expert [15]. We used the ray tracing program to determine the flux received at the two receivers. The system presented in figure 1 was built in TracePro Expert and one million rays were launched from the source to find the power incident on each one of the two receivers. Though the acceptance angle should theoretically be  $32^\circ$ , in our model, we considered it to be  $0^\circ$ .

### 3.3. Modeling the solar cells:

After determining the flux incident on the receivers and the spectrum absorbed by the two solar cells, the cells were simulated in PC1D. PC1D is a package dedicated to modeling photovoltaic solar cells [16]. That is, two PC1D models were developed: one for the AlGaAs/Si solar cell and one for the InGaAsP/InGaAs solar cell, and both are double junction tandem cells. Numerical optimization of the cells is the subject of our previous studies [17, 18].

In PC1D, two spectrum files were generated to model the two solar cells. These files were obtained by modifying the spectrum files that correspond to AM1.5D. For each wavelength in the AM1.5D file, the value of the flux was multiplied by reflectance of the reflective coating and then multiplied either by transmittance (or reflectance) to obtain the flux incident on the AlGaAs/Si cell (or the InGaAsP/InGaAs cell).

After preparing the spectrum files in PC1D and after determining the flux incident on the two solar cells by using TracePro Expert, the PC1D model was run and the final results were obtained.

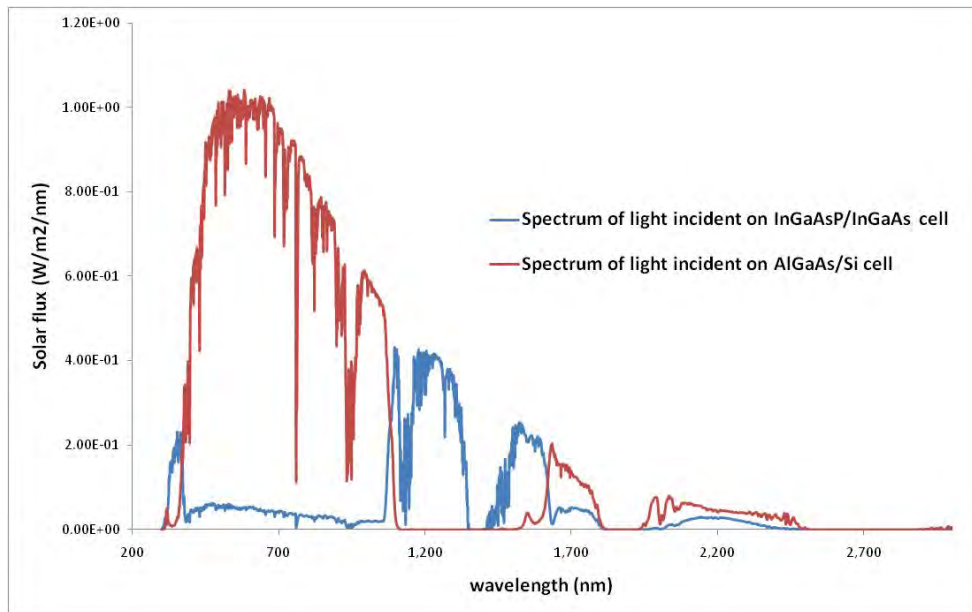


Fig. 3. Spectrum of light incident on the two receivers.

Table 2: Response of the cells in the system.

	AlGaAs	Si	InGaAsP	InGaAs
Energy bandgap (eV)	1.817	1.12	1.00	0.74
Isc (mA/cm <sup>2</sup> )	717	470	77.1	339.5
Voc (Volts)	1.352	0.752	0.624	0.425
Efficiency (%)	15.5	5.6	1.47	4.21

#### 4. Response of the system:

After running the model, we found that under the standard conditions where the total flux incident on the dish is 850 W/m<sup>2</sup> (i.e. a power of 8.374 W is received by the 112 mm wide receiver), 5.716 Watt of concentrated sunlight is received by the InGaAs/Si tandem cell and another 1.712 Watt of concentrated sunlight is received by the InGaAsP/InGaAs tandem cell. These values correspond to power densities of 37.13 kW/m<sup>2</sup> and 5.45 kW/m<sup>2</sup> on the AlGaAs/Si and InGaAsP/InGaAs cells, respectively. These numbers show that the optical efficiency of the system is 88.7 %. The response of the solar cells is summarized in Table 2.

The results in table 2 show that the overall efficiency of the system is 26.8 %. Under the standard conditions, this corresponds to a power density of 227.6 W/m<sup>2</sup>. This also means that one dish generates 2.24 W under the standard conditions.

## 5. Conclusions

In this paper, a system with four solar cells was modeled under the standard conditions. The system involved four solar cells made of the following materials: AlGaAs (1.817 eV), Si (1.124 eV), InGaAsP (1.0 eV) and InGaAs (0.74 eV). The system has beam splitting features and an optical concentration of 63 suns. For modeling the system, we proposed a multi-step modeling procedure. The modeling results show that the efficiency of our proposed system is 26.8 % which corresponds to a power output of 2.24 W. Comparatively with systems with four solar cells reported in the literature, the efficiency of the system is low because of two reasons:

- The combination of the energy bandgaps is not optimum: changing the distribution of the energy bangaps can be done either by using other materials or by changing the composition of the materials used in this study. The optimum energy bandgaps can be determined by changing the cells.
- The optical concentration ratio: the concentration ratio of the system is 63 s uns. Increasing this efficiency to very high values above 300 s uns would enhance the efficiency of the system.

## References

- [1] M. A. Green, Keith Emery, Yoshihiro Hishikawa, Wilhelm Warta, “Solar cell efficiency tables (version 36),” *Progress in Photovoltaics: Research and Applications*, 2010, 18:346–352.
- [2] R.R. King, A. Boca, W. Hong, X.-Q. Liu, D. Bhusari, D. Larrabee, K.M. Edmondson, D.C. Law, C.M. Fetzer, S. Mesropian, N.H. Karam,” *Band-Gap-Engineered Architectures for High-Efficiency Multijunction Concentrator Solar Cells*,” in *Proceedings of the 24th European Photovoltaic Solar Energy Conference*, 21-25 September 2009, Hamburg, Germany.
- [3] International Energy Agency Report,” *Technology roadmap: solar photovoltaic energy*”, 2010.
- [4] A. Extance, C. Marquez, “The Concentrated Photovoltaics Industry Report 2010,” *CPV Today*, 2010.
- [5] D. Buie, R. Hoffman, P. Blumenfeld, J. Foresi, J. Nagyvary, C. Dempsey, “A Review of Emcore’s Third Generation Utility Scale CPV System,” In the proceedings of the 6<sup>th</sup> International Conference on Concentrating Photovoltaic Systems, 07-09 April 2010, Freiburg.
- [6] M. A. Green, “Third Generation Photovoltaics: advanced solar energy conversion”, Springer, 2003, pp 59-68.
- [7] A.G.Imenes, D.R.Mills, ”Spectral beam splitting technology for increased conversion efficiency in solar concentrating systems: a review”, *Solar Energy Materials & Solar cells* 84 (2004) 19-69.
- [8] U. Ortabasi, A. Lewandowski, R. McConnell, D. J. Aiken, P. L. Sharps, B. G. Bovard “Dish photovoltaic cavity converter (PVCC) system for ultimate solar-to-electricity conversion efficiency general concept and first performance predictions,” proceedings of the 29<sup>th</sup> Photovoltaic Specialists Conference 2002, pp 1616-1620.

- [9] B. Groß, G. Peharz, G. Siefert, M. Peters, J.C. Goldschmidt, M. Steiner, W. Guter, V. Klinger, B. George, F. Dimroth, "Highly efficient light splitting photovoltaic receiver," In the proceedings of the 24<sup>th</sup> European PV Solar Energy Conference and Exhibition, 21-25 September 2009, Hamburg, Germany.
- [10] X. Wang, A. Barnett, "One lateral spectrum splitting concentrator photovoltaic architecture: measurements of current assemblies and analysis of pathways to 40% efficient modules", proceedings of the 35th IEEE Photovoltaic Specialists Conference, Honolulu, Hawaii, June 20-25, 2010.
- [11] B. Mitchell, G. Peharz, G. Siefert, M. Peters, T. Gandy, J. C. Goldschmidt, J. Benick, S. W. Glunz, A. W. Bett, F. Dimroth, "Four-Junction Spectral Beam-Splitting Photovoltaic Receiver with High Optical Efficiency," *Progress in Photovoltaics: Research and Applications*, n/a. doi: 10.1002/pip.988.
- [12] Mokri A., Emziane M., "An approach for modeling and optimizing multi-receiver photovoltaic systems with optical filters", *Proceedings of the IEEE International Energy Conference*, Manama, Bahrain, 18-21 December 2010.
- [13] Gueymard, C., "Parameterized Transmittance Model for Direct Beam and Circumsolar Spectral Irradiance", *Solar Energy*, Vol. 71, No. 5, pp. 325-346, 2001.
- [14] Gueymard, C., "SMARTS, A Simple Model of the Atmospheric Radiative Transfer of Sunshine: Algorithms and Performance Assessment". Professional Paper FSEC-PF-270-95. Florida Solar Energy Center, 1679 Clearlake Road, Cocoa, FL 32922, 1995.
- [15] TracePro Expert - 6.0.4 Release, Lambda Research Corporation.
- [16] PC1D, Version 5.9, © School of Photovoltaic and Renewable Energy Engineering at the University of New South Wales, Australia.
- [17] M. Emziane, R. J. Nicholas, D. C. Rogers, J. Dosanjh, "Investigation of InGaAsP-based solar cells for double-junction photovoltaic devices," *thin solid films* 516 (2008) 6744-6747.
- [18] M. Emziane, R. J. Nicholas, "Optimization of InGaAs(P) photovoltaic cells lattice matched to InP," *Journal of Applied Physics*, 101, 054503 (2007).

## Improving the performance of solar panels by the use of phase-change materials

Pascal Biwolé<sup>1,\*</sup>, Pierre Eclache<sup>2</sup>, Frederic Kuznik<sup>2</sup>

<sup>1</sup> University of Nice Sophia-Antipolis, Nice, France

<sup>2</sup> University of Lyon, Villeurbanne, France

\* Corresponding author. Tel: +33 492965029, Fax: +33 492965071, E-mail: phbiwole@unice.fr

**Abstract:** High operating temperatures induce a loss of efficiency in solar photovoltaic and thermal panels. This paper investigates the use of phase-change materials (PCM) to maintain the temperature of the panels close to the ambient. The main focus of the study is the CFD modeling of heat and mass transfers in a system composed of an impure phase change material situated in the back of a solar panel (SP). A variation of the enthalpy method allows simulating the material thermo-physical change of properties. The buoyancy term in Navier-Stokes' momentum conservation equation is modified through an additional term which forces the velocity field to be non-existent when the PCM is solid. For validation purposes, isotherms and velocity fields are calculated and compared to those from an experimental set-up. Results show that adding a PCM on the back of a solar panel can maintain the panel's operating temperature under 40°C for around two hours under a constant solar radiation of 1000W/m<sup>2</sup>.

**Keywords:** Solar Panel, Operating Temperature, Phase Change Material

### Nomenclature

$C_p$	specific heat..... $J\ kg^{-1}\ K^{-1}$	$P$	pressure..... $Pa$
$g$	gravitational constant..... $m\ s^{-2}$	$T_m$	mean melt temperature..... $K$
$H$	PCM container height..... $m$	$u$	velocity..... $m\ s^{-1}$
$k$	thermal conductivity..... $Wm^{-1}K^{-1}$	$\Delta T$	half range of melt temperatures..... $K$
$L_F$	Latent heat of fusion..... $J\ kg^{-1}$	$\beta$	coefficient of thermal expansion..... $K^{-1}$
$L$	PCM container internal width..... $m$	$\rho$	density..... $kg\ m^{-3}$
$m$	mass..... $kg$	$\mu$	dynamic viscosity..... $kg\ m\ s^{-1}$

### 1. Introduction

The efficiency of solar panels depends on three factors: the intensity of the solar radiation flux, the quality of the semi conductor in use, and the operating temperature of the semi conductor cell. The variations of solar radiation cannot be controlled. Therefore the ongoing research focuses either on new material like copper, indium diselenium, cadmium tellurium and chalcopyrites, or on maintaining low operating temperatures. For PV panels, high operating temperatures create a drop in the conversion rate of about 0.5% per Celsius degree over the nominal cell operating temperature of 25°C [1], as defined by the industry standard STC (Standard Test Conditions). In summer, panel's temperature typically ranges from 40 to 70°C which makes a 7.5 to 22.5% drop in the conversion rate. In the same way, the efficiency of solar thermal panels decreases mainly because of radiation losses when their operating temperature is above the ambient.

To lower the operating temperature, one can either improve the free cooling on the back of the panel thanks to natural or forced convection, or try to absorb the excess heat by modifying the panel's architecture. The latter solution includes the use of PCMs situated on the back of solar panels. PCMs are materials that undergo reversible transition of phase depending on their temperature. They absorb or reject heat in the process. Only a few studies have been specifically devoted to passive cooling of solar panels by SP/PCM architectures. The hypothesis driving the research is simple: when the panels' temperature rises, the excess heat

must be absorbed until the PCM has completely melted. When the panel's temperature decreases, the solidification of the PCM should provide additional heat for the operating liquid in solar thermal panels, provide heat to the building or act as an insulation material. The SP/PCM solution is expected to be very useful for roof or facade integrated panels where space for ventilation is limited.

Huang et al. [2] studied the melting of PCMs in an aluminum container submitted to a solar radiation of 750 to 1000W/m<sup>2</sup>. They used a finite volume model to resolve both the heat transfers diffusion and the Navier-Stokes equations. They later included cooling fins in the tank to improve the PCM bulk thermal conductivity [3] [4]. They found that the temperature rise in the system could be reduced by more than 30°C for 130 minutes. Cellura et al. [5] resolved the same architecture using a finite element PDE solver. However, they considered the PCM as pure, meaning that the PCM melting temperature is unique and does not change while the PCM is still melting. This property is not valid for most commercial PCMs which are generally mixtures of several different materials. By resolving only the heat transfers diffusion equation, they showed that a PCM with a melting temperature between 28°C and 32°C can improve the energy conversion efficiency by around 20% in summer time. Jay et al. [6] experimentally studied a layout where PCM were contained in a honeycomb grid to improve conduction in the container. They showed that after 6 hours and 30min of experiment under an artificial insulation of 800W/m<sup>2</sup> on real PV panels, the temperature of a PV/PCM system was still lower than that of a single panel, with a mean temperature difference of 24°C. They also found that the panel's temperature drop using a PCM with a melt temperature at 27°C was higher than using a PCM with a melt temperature at 45°C.

In this study, we consider the same geometry as [2]. The transient conduction and convection heat transfers as well as the Navier-Stokes equations are simultaneously resolved in the PCM domain using a finite element model on a fixed grid. The buoyancy term in Navier-Stokes' momentum conservation equation is modified through an additional term to force the velocity field to be zero when the PCM is solid. This scheme is validated using an experimental set-up. The model is then used for a parametric study of the SP/PCM architecture performances.

## 2. Methodology

### 2.1. Numerical case description

The geometry of the model is presented in Fig. 1. The thermo-physical properties of the simulated materials are presented in Table 1.

Table 1. Thermo-physical properties of RT25 and aluminum.

	Cp	k	ρ
Solid RT25	1800	0.19	785
Liquid RT25	2400	0.18	749
Aluminum	903	211	2675
Constant properties of RT25:			
$L_F$ :	232000 J kg <sup>-1</sup>		
$T_m$ :	26.6°C, ΔT=1°C		
$\beta$ :	1e-3K <sup>-1</sup>		
$\mu$ :	1.7976e-3 m <sup>2</sup> .s <sup>-1</sup>		

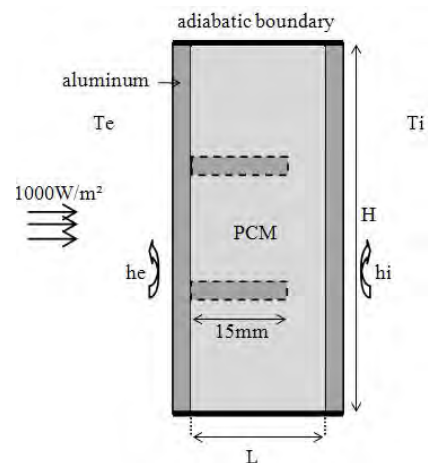


Fig. 1. Geometry of the numerical model.

## 2.2. Mathematical model

### 2.2.1. Modeling heat transfers

Over the front plate surface, we considered conduction, convection and radiation heat transfers as shown in Eq. (1). Long wave radiation with the sky was neglected in the model.

$$\rho C_p \frac{\partial T}{\partial t} = -k \frac{\partial T}{\partial x} + h_e(T_e - T) + \alpha E(t) \quad (1)$$

where  $\alpha$  is the aluminum thermal absorptivity and  $E$  the solar radiation intensity. The heat transfers diffusion equation applies over the PCM, the air layer and the aluminum domains:

$$\rho C_p \frac{\partial T}{\partial t} + \nabla \cdot (-k \nabla T) + \rho C_p \vec{u} \cdot \nabla T = 0 \quad (2)$$

The velocity field  $\mathbf{u}$  in Eq. (2) is given by Navier-Stokes equations for incompressible fluids. To model the changes in PCM RT25 thermo-physical properties occurring during the phase transition, we define function  $B_0$  as the liquid fraction in the PCM domain. Let be  $T_m$  the mean melt temperature and  $\Delta T$  the half range of melt temperatures:

$$B_0(T) = \begin{cases} 0 & , \quad T < (T_m - \Delta T) \\ (T - T_m + \Delta T) / (2\Delta T) & , \quad (T_m - \Delta T) \leq T < (T_m + \Delta T) \\ 1 & , \quad T > (T_m + \Delta T) \end{cases} \quad (3)$$

Eqs. (3) show that  $B_0$  is zero when the PCM is in solid and 1 when it is in liquid phase.  $B_0$  linearly grows from zero to 1 between the two states. To ensure second order continuous differentiability of the liquid fraction over the temperature domain and to help numerical convergence,  $B_0$  is approximated by a second order differentiable function  $B_1$ .  $B_1(T)$  is the sixth-degree polynomial whose coefficients are calculated using the following conditions:

$$\begin{cases} B_1(T_m - \Delta T) = 0 & ; & B_1'(T_m - \Delta T) = 0 & ; & B_1''(T_m - \Delta T) = 0 & ; & B_1(T_m) = 0.5 \\ B_1(T_m + \Delta T) = 1 & ; & B_1'(T_m + \Delta T) = 0 & ; & B_1''(T_m + \Delta T) = 0 \end{cases} \quad (4)$$

where  $B_1'$  and  $B_1''$  are  $B_1(T)$  first and second derivatives.  $B_1$  is used to model the changes in the PCM thermo-physical properties as follows:

$$\rho(T) = \rho_{solid} + (\rho_{liquid} - \rho_{solid}) \cdot B_1(T) \quad (5)$$

$$k(T) = k_{solid} + (k_{liquid} - k_{solid}) \cdot B_1(T) \quad (6)$$

The modeling of the specific heat includes an additional term representing the latent heat of fusion absorbed during the melting process:

$$C_p(T) = C_{p,solid} + (C_{p,liquid} - C_{p,solid}) \cdot B_1(T) + L_F \cdot D(T) \quad (7)$$

Where

$$D(T) = e^{\frac{-T(T-T_m)^2}{\Delta T^2}} / \sqrt{\pi \cdot \Delta T^2} \quad (8)$$

Function D is a smoothed Delta Dirac function which is zero everywhere except in interval  $[T_m - \Delta T, T_m + \Delta T]$ . It is centered on  $T_m$  and its integral is 1. Its main role is to distribute the latent heat equally around the mean melting point.

### 2.2.2. Modeling mass transfers

We assumed that the PCM in the liquid phase is a Newtonian fluid. The mass, momentum and energy conservation equations were resolved simultaneously with the heat transfers diffusion equation. However, to model the phase transition, the momentum conservation equation was modified as follows:

$$\rho \frac{\partial \vec{u}}{\partial t} + \rho(\vec{u} \cdot \nabla) \vec{u} - \mu \nabla^2 \vec{u} = -\nabla P + \vec{F}_b + \vec{F}_a \quad (9)$$

where  $\vec{F}_b$  is buoyancy force given by the Boussinesq approximation:

$$\vec{F}_b = -\rho_{liquid} (1 - \beta(T - T_m)) \vec{g} \quad (10)$$

$$\text{And } \vec{F}_a = -A(T) \cdot \vec{u} \quad (11)$$

$$\text{with } A(T) = \frac{C(1 - B_1(T))^2}{(B_1(T)^3 + q)} \quad (12)$$

The expression of A is inspired from the Carman-Kozeny relation in a porous medium where the value of C depends on the morphology of the medium. If we assume that the flow is laminar:

$$\nabla(P) = \frac{-C(1 - B(T))^2}{B_1(T)^3} \cdot \vec{u} \quad (13)$$

In this study, C is given the constant value  $10^5$ . This value is chosen arbitrarily high. Constant q is chosen very low in order to make Eq. (12) valid even when  $B_1(T)$  is zero. The value of q was fixed at  $10^{-3}$ . When the temperature of the MCP is higher than  $T_m + \Delta T$ , the PCM is completely liquid. Therefore,  $B_1$  is 1 and consequently, A and  $\vec{F}_a$  are zero. In this case, the usual momentum conservation equation applies. During the transition state,  $0 < B_1(T) < 1$ . A(T) increases along with the melting process until the added force  $\vec{F}_a$  becomes greater than the convection and diffusion terms in Eq. (9). The momentum conservation equation becomes similar to the Darcy law for fluid flow in porous medium:

$$\vec{u} = -\frac{K}{\mu} \nabla(P) \quad (14)$$

where the permeability K is a function of  $B_1(T)$ . When  $B_1(T)$  diminishes, the velocity field also diminishes until it reaches zero when the PCM becomes completely solid. At that point, the MCP temperature is lower than  $T_m - \Delta T$ . Therefore,  $B_1$  is 0. Eq. (12) shows that the value of A(T) becomes very high. Consequently, all the terms in the momentum conservation equation are dominated by the added force. The only solution of the Navier-Stokes equations is  $\mathbf{u}=\mathbf{0}$  which corresponds to a solid medium.

### 2.2.3. Numerical method

A 2D finite element model was used. To satisfy the Brezzi-Babuska condition [7] three degrees of freedom were used on each element to approximate the pressure field and an additional degree of freedom was used by adding a node at the center of mass of each triangular element to approximate the velocity field. The maximum mesh size was  $4.10e-4$ m. The final mesh had 135 240 elements and 465 857 degrees of freedom. No significant change of the results was observed when using a finer mesh. A Galerkin least-squares stabilization method was employed.

### 2.3. Elements of validation

#### 2.3.1. Experimental set-up

The experimental set-up consisted of a 167mm x 167mm x30mm-large Plexiglass container without cooling fins and filled with a PCM. An air layer was left at the top of the tank to prevent it from breaking due to the PCM thermal expansion. A fixed temperature of  $T_e = 20^\circ\text{C}$  and  $T_i = 40^\circ\text{C}$  was imposed on each side of the tank thanks to heating plates. The transient two-dimensional velocity field in the tank was measured thanks to a PIV apparatus including a Nd-Yag laser.



Fig. 2. Comparison of the simulated (left) and the experimental (right) liquid-solid moving boundary location

The experimental validation consisted of: firstly, a transient comparison of the moving liquid-solid boundary location (Fig. 2); secondly, a comparison of the simulated and measured velocity fields in the completely melted PCM (Fig. 3). Some discrepancies were noted between the simulated and the measured velocity fields. This may be due to the very low velocities in the tank which are of the order of  $10e-4$ m/s. However, the transient locations of the simulated moving boundary closely matched the experimental one.

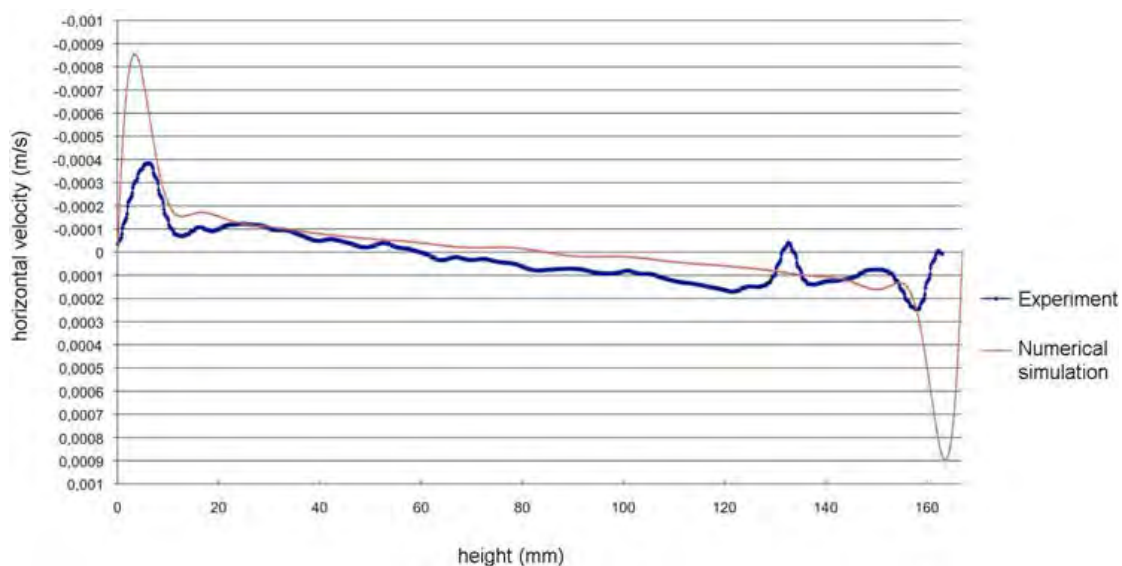


Fig. 3. Comparison of the PIV-measured and simulated velocity in the vertical mid cross-section of the PCM domain.

### 3. Results

All the simulations were conducted using  $h_e=10\text{W/m}^2\cdot\text{K}$ ,  $h_i=5\text{W/m}^2\cdot\text{K}$  and  $E = 1000\text{W/m}^2$ .

#### 3.1.1. Temperature and velocity fields

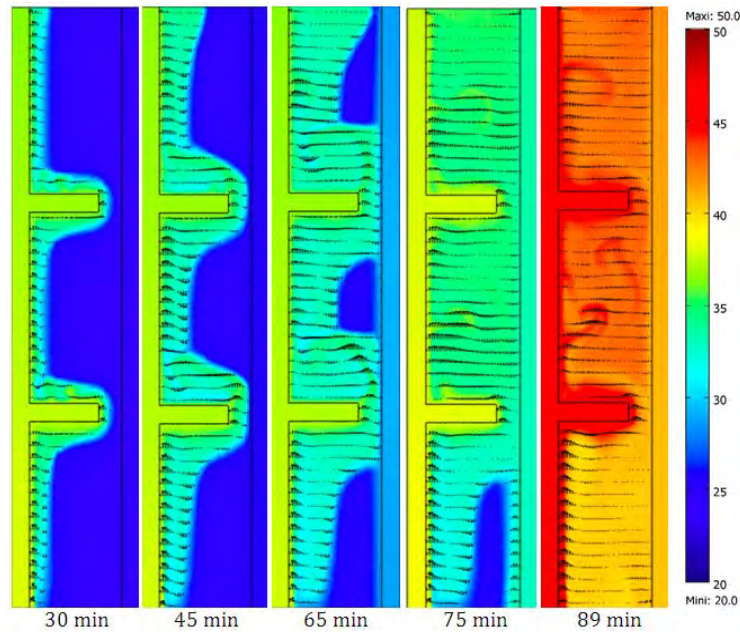


Fig. 4. Simulated transient isotherms and velocity fields in the SP/PCM system.  $H=132\text{mm}$ ,  $L=20\text{mm}$ .

#### 3.1.2. Parametric study

Table 2. List of simulated cases.

	(a)	(b)	(c)	(d)
<b>L(m)</b>	0	20	20	20
<b>H(m)</b>	132	132	40	132
<b>Cooling fins</b>	no	yes	no	no

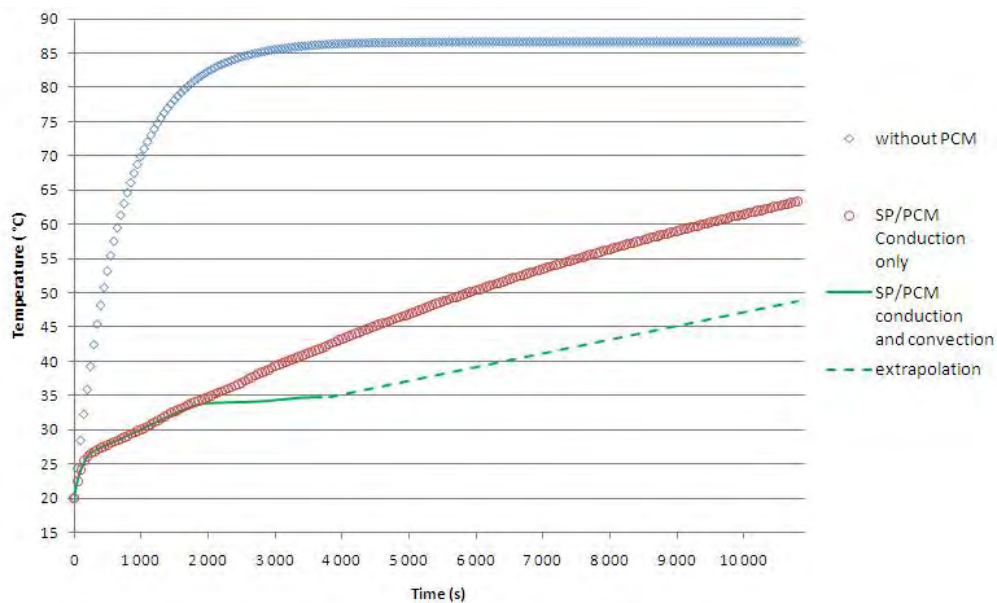


Fig. 5. Impact of convection heat transfers in the PCM on the panel's operating temperature.  $H=0.132\text{m}$  and  $L=0.049\text{m}$ .

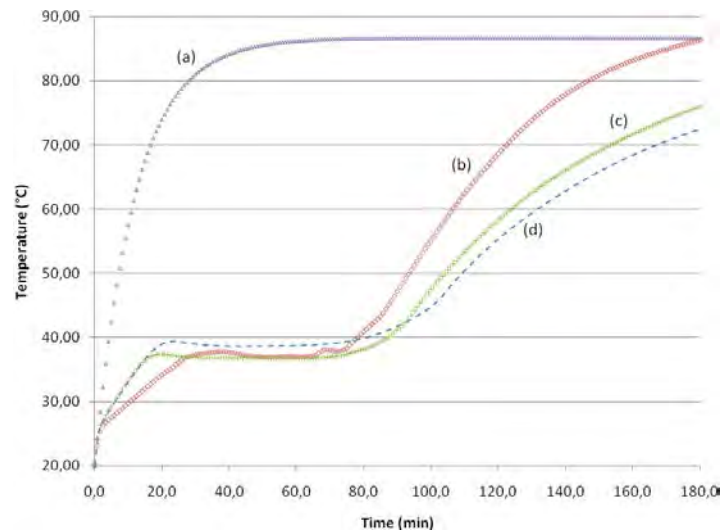


Fig. 6. Impact of the SP/PCM size on the panel's operating temperature.

#### 4. Discussion and conclusion

The first limitation of this work rises from the representation of the solar panel by an aluminum plate. This simplification does not take into account the bulk specific capacity of real panels. The second limitation comes from the fact that the impact of sky temperature was not included in the numerical model, due to experimental validation difficulties. Despite those limitations, the following observations remain relevant:

The velocity field in Fig. 4 shows a circulation of the liquid PCM through the three parts of the container. Convection of the liquid PCM is observed upward close to the heated panel, and downward close to the liquid-solid boundary. The Rayleigh number in the liquid PCM was between  $10^5$  at melt start and  $10^6$  at melt end. This result is coherent with our initial assumption of a laminar flow and confirms the observation of [4]. Like [4], we also numerically observe a suspended solid PCM mass when the melting is nearly over.

Over the range of simulated sizes for the SP/PCM system, the temperature of the front plate always remains lower than  $50^\circ\text{C}$  after 89min under a constant radiation of  $1000\text{ W/m}^2$ . The better performance is obtained with a  $13.2 \times 4.9\text{ cm}$  large PCM container. In this case, the panel's temperature is  $34.9^\circ\text{C}$  after 1 hour. The same temperature is reached after 5min without PCM (Fig. 5). These observations are in good agreement with [3] and [5]. Three inflexions points can be observed on the transient operating temperature profile. The first one happens at the PCM melt temperature. After a steep increase, the panel temperature rises much more slowly from that point because of the start of the melting process.

Between the first and the second inflexion point, the PCM acts like an insulation material for the panel and heat transfers are dominated by conduction (Fig. 5). The second inflexion point indicates the start of the convection heat transfers which balances conduction heat transfers in the PCM. Fig. 5 shows that the simulated panel temperature may be overestimated by 20% after 3600s when conduction only is considered in the numerical model. On Figs. 5 and 6, the operating temperature remains more or less constant until the PCM has completely melted. The last inflexion point marks the end of the melting process. Heat transfers in the container are dominated by convection. Afterwards, the temperature rises more slowly than before the start of the melt because of the higher specific heat capacity of the liquid PCM.

The parametric study also shows that the operating temperature drops proportionally to the increase of the PCM width: after 3600s,  $T = 34.9^{\circ}\text{C}$  when  $L = 0.049\text{m}$  whereas  $T=37^{\circ}\text{C}$  when  $L = 0.02\text{m}$ . Comparing curves (c) and (d) shows that the same trend is observed when the panel height is increased but only when the PCM has completely melted. In brief, it is better to increase the PCM width than its height to lower the panel's temperature. Adding cooling fins in the PCM tank provides a faster attenuation of the operating temperature because the PCM bulk conductivity is increased. But this layout accelerates the phase transition too. When the PCM has completely melted, the operating temperature rises faster than for all other SP/PCM architectures (Fig. 6). This fact moderates the idea that adding cooling fins makes SP/PCM systems more efficient [4].

To conclude, adding PCM on the back of solar panels is an efficient way of improving panels' performance. Their operating temperature can be substantially decreased using that technology. Future work should include experimental validations of this first numerical model using real solar panels under real climate.

## References

- [1] K. Emery, J. Burdick, Y. Caiyem, D. Dunlavy, H. Field, B. Kroposki, T. Moriarty, Temperature dependence of photovoltaic cells, modules and systems, Proceedings of the 25th IEEE PV Specialists Conference, Washington DC, USA, May 13–19, 1996, pp. 1275–1278.
- [2] M.J. Huang, P.C. Eames, B. Norton, Thermal regulation of building integrated photovoltaics using phase change materials, *International Journal of Heat and Mass Transfers* 47, 2004, pp. 275-2733.
- [3] M.J. Huang, P.C. Eames, B. Norton, Phase change materials for limiting temperature rise in building integrated photovoltaics, *Solar Energy* 80 (9), 2006, pp. 1121-1130.
- [4] M.J. Huang, P.C. Eames, B. Norton, Comparison of a small-scale 3D PCM thermal control model with a validated 2D PCM thermal control model, *Solar Energy Materials and Solar Cells* 90 (13), 2006, pp. 1961-1972.
- [5] M. Cellura, G. Ciulla, V. Lo Brano, A. Marvuglia, A. Orioli, Photovoltaic panel coupled with a phase changing material heat storage system in hot climates. In: Proceedings of the 25th Conference on Passive and Low Energy Architecture, Dublin, Ireland, October 22-24, 2008.
- [6] A. Jay, S. Clerc, B. Boillot, A. Bontemps, F. Jay, Utilisation de matériaux à changement de phase pour réduire la température de panneaux PV intégrés au bâti, Proceedings of the International Building Performance Simulation Association conference, Moret sur Loing, France, November 9-10, 2010.
- [7] D. N. Arnold, F. Brezzi, M. Fortin, A stable element for the Stokes equations, *Calcolo* (21), 1984, pp. 337-344.

## Assessing the impact of micro generation in radial low voltage distribution networks taking into consideration the uncertainty

Alvaro Gomes<sup>1,2,\*</sup>, Luís Pires<sup>1</sup>

<sup>1</sup>Department of Electrical Engineering and Computers – University of Coimbra, Coimbra, Portugal

<sup>2</sup>INESC Coimbra, Coimbra, Portugal

\* Corresponding author. Tel: +351 934262925, Fax: +351 239796247, E-mail: agomes@deec.uc.pt

---

**Abstract:** The increasing penetration of micro generation units in low voltage distribution networks and the need for evaluating the potential benefits and also the potential negative impacts of such penetration ask for detailed assessment tools and methodologies. The impacts of a single small-scale unit (<5,75kW) is, probably, negligible. However, the aggregate contribution of many small capacity units can be significant and an adequate assessment of the impacts is needed in order to prevent some undesirable effects and in order to accurately compute the benefits of such units. This paper presents a methodological approach that allows an adequate assessment of micro generation impacts on radial distribution networks based on Monte Carlo simulations to reproduce both demand and generation behavior, and using scenarios to deal with the uncertainty about micro generators placement. Besides, the use of both generation and demand diagrams of high resolution allows to adequately assess the voltage values variability in different buses.

**Keywords:** Micro-generation, LV radial distribution networks, Losses and voltage profile assessment

---

### 1. Introduction

In traditional power systems, without distributed generation or micro-generation units, power flows from substation to the end-user loads and power systems are designed for such behavior. The utilization of micro-generation units might, however, impact the flow of power and voltage levels and eventually cause reverse power flows. Thus, some problems may arise and should be taken into consideration when promoting this type of generation. For a given load and generation levels the impacts of micro generation on distribution networks depend, among others, on both the location and size of micro generation systems. Several methodologies dealing with different issues raised by the dissemination of micro-generation have been proposed in the literature [1]-[9]. However, load demand and the output of micro generation units vary widely over the time and typically micro generation systems location is not known in advance. The uncertainty associated with both generation systems location and load/generation levels makes hard an accurate assessment of the impacts of those generation systems on the radial distribution networks. Namely, the impacts on the voltage profile and power losses, but also eventual changes in power flows direction should be carefully accounted for. On the other hand, an adequate assessment of the impacts on voltage profiles asks for both an adequate time resolution in the representation of demand and generation and the usage of real load and generation diagrams not averaged ones. Averaged load diagrams and inadequate time resolution of load diagrams do not allow capturing the real impact on buses voltage profile. Even 15 minutes time resolution may provide only indicative values for changes in voltage profiles provoked by micro generation systems.

The main contribution of this work is the capability of making a daily basis analysis with a proper time resolution allowing for an adequate assessment of voltage impacts and the ability to deal with uncertainties that exist at both available generation and at the demand level.

The structure of the paper is as follows. In section 2 the methodological approaches to compute power flow and the demand and generation models are presented. Also, the different scenarios used to deal with the possible different locations of micro-generation units are

presented. Follows, in section 3, the case study while, in section 4, the results are shown. Finally, in section 5, some conclusions are drawn.

## 2. Methodology

In order to properly assess the impacts of micro-generations units on voltage profile and on the losses in a radial low voltage (LV) network, suitable demand and generation models and adequate power flow algorithms are necessary. Demand and generation models should be able to tackle the uncertainty that exist in both generation and in the demand, and the power flow algorithms need to take into consideration the intrinsic characteristics of distributions circuits which typically are unsymmetrical and unbalanced. Some proposals for dealing with some of these issues can be encountered in the literature [10][11]. However, a detailed analysis at the LV network level taking into consideration demand and generations variability is not available. The methodological approach followed in this work allows such detailed analysis, namely regarding the impacts on voltage levels and on power losses, while taking into consideration the uncertainties associated with both the demand and the generation. In order to deal with the uncertainty of both the demand and generation we use Monte Carlo simulations to generate all possible realistic load/generation diagrams. The Monte Carlo simulations carried out to obtain demand diagrams, different for each customer, were based on information collected from load profiles obtained during monitoring campaigns. Namely, for each time interval, a probability density function characterizing the behavior of the demand was identified and used in the Monte Carlo simulations. For every customer (bus) different load profiles, obtained from field surveys, are considered. In the study carried out, in order to account for different possible amounts (number) and locations (buses) of micro generation units several scenarios have been simulated. The developed software tool allows the use of any time resolution to represent load profiles and generation.

The variability of the demand is, most of times, associated with the utilization of energy services (heating, cooling, tv, computers, lighting, etc) according to the needs of the end-user. Consequently, energy consumption varies throughout the day and is different for different days (Figure 1). Adequate models for reproducing the demand taking into account such variability must produce realistic load curves and not averaged load curves and should have a proper time resolution that allowing capturing the impacts on the voltage levels. Therefore, average demand curves with a time resolution too high, for instance hourly demand models (Figure 2), are not adequate for such evaluation. In order to run Monte Carlo simulations, for every time interval adequate probability distributions have been identified based on data collected, thus allowing the generation of realistic load diagrams for different days of the week and different periods of the year. The uncertainty associated with the photovoltaic and wind generation is modeled also by using Monte Carlo simulations with normal distribution probability. Several scenarios regarding the number of micro-generation units and location have been analyzed. "A" is the scenario with no micro-generation units (MGU); in scenario B there are only 5 MGU, for evaluating the impacts of a low level MG penetration; in scenarios C – G there 10 MGU, located in different buses. In scenario C MGU distributed throughout the network; in scenario D (E) MGU are preferably located in buses far (near) from the distribution transformer (DT), allowing to evaluate the impacts as a function of the distance from DT; and in scenario F(G) MG units are mainly in the phase with higher (lower) demand, allowing to assess the impacts as a function of the demand level. These scenarios are summarized in Table 2. The implemented algorithm for computing power flows is the forward/backward sweep method based on successive sweeps until the convergence is achieved [12]-[15].

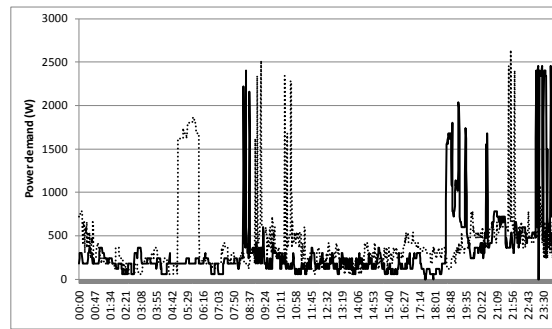


Figure 1- Energy consumption patterns in two consecutive days for the same residential consumer.

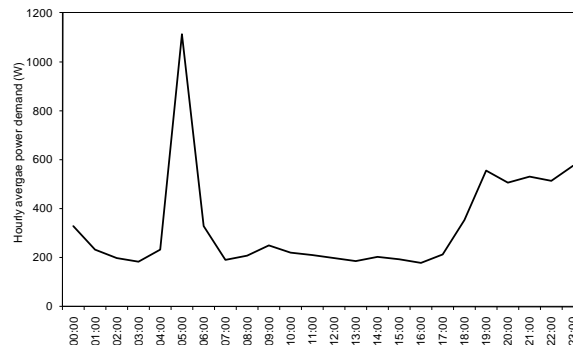


Figure 2- Hourly averaged load diagram for the residential consumer of Figure 1.

### 3. Case study

A real urban low voltage radial distribution network data has been used in this case study. The network has 38 buses, 28 feeding residential consumers and 8 distribution buses (points of connection). There are no losses at the distribution buses and the neutral is grounded in every bus. The distribution transformer is a 30kV / 400V-230V 160 kV A transformer. Figure 3 shows the layout of the network. Besides residential consumers we have also street light.

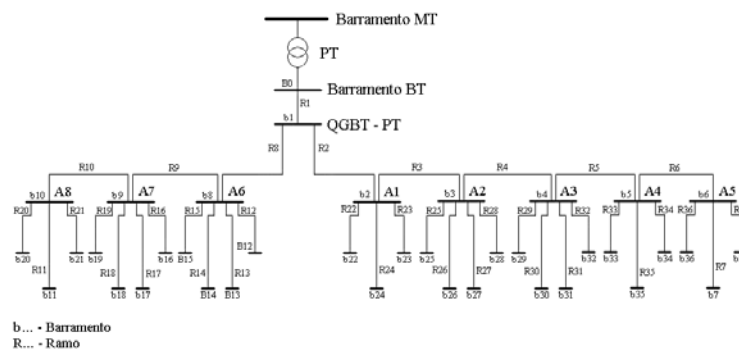


Figure 3- LV distribution network being analyzed.

Most residential customers are single-phase consumers. In Table 1 the contracted power and the phase for every consumer are shown. Phase “A,B,C” means a three-phase consumer. According to the Portuguese legislation (decree-law 363/2007) the aggregated power of all micro-generation units installed in a LV distribution network cannot exceed 25% of the distribution transformer capacity and in order to access special-regime (premium) of the PV feed-in-tariff scheme the individual capacity of the micro-generation units is limited to 3.68 kW, meaning that in this LV network can be installed at most 10 units. In this work all MG units have 3,68 kW capacity and are consumer owned.

Table 1- Placement of microgeneration units.

Bus	Phase	Contracted Power	Bus	Phase	Contracted Power
1	A	6,9 kVA	24	C	6,9 kVA
7	A	6,9 kVA	25	B	6,9 kVA
11	A	6,9 kVA	26	A,B,C	10,35 kVA
12	C	6,9 kVA	27	C	6,9 kVA
13	A	6,9 kVA	28	A	6,9 kVA
14	C	6,9 kVA	29	C	13,8 kVA
15	B	10,35 kVA	30	A	6,9 kVA
16	A,B,C	10,35 kVA	31	B	6,9 kVA
17	B	10,35 kVA	32	B	10,35 kVA
18	C	10,35 kVA	33	C	10,35 kVA
19	A	6,9 kVA	34	B	6,9 kVA
20	C	10,35 kVA	35	A	10,35 kVA
21	B	10,35 kVA	36	C	10,35 kVA
22	B	6,9 kVA	37	B	6,9 kVA
23	A	10,35 kVA			

In order to deal with the uncertainty of demand and of the generation, 300 simulations per interval of time have been done. Total computer time was 1200 seconds. Regarding the location of micro-generation units (MGU) 7 scenarios have been analyzed, as described in Table 2.

Table 2- Different scenarios for the placement of micro-generation units

Scenario	Characteristics
A	Reference scenario, with no micro-generation units.
B	5MGU, to assess the impact of low level MGU penetration.
C	10 MGU spread throughout the circuit.
D	10 MGU mainly connected in remote buses.
E	10 MGU mainly connected in buses near the distribution transformer.
F	10 MGU connected mainly in highly loaded phase (B).
G	10 MGU connected mainly in phase with lower demand (C).

## 4. Results

### 4.1. Power Flows

In the following table the average active and reactive power flows at the DT and the amount of energy drawn from the grid to feed the consumers are shown. The difference between each alternative scenario (B-G) and the reference scenario (A) is also presented. One can see the reduction of power drawn from the grid through power transformer as a result of micro generation units

In Figure 4 the power flows at DT for scenarios A-C are shown. Negative values mean that reverse power flows exist, as in scenario C (high photovoltaic penetration). Dealing with photovoltaic units means the main changes regarding the reference scenario occur during the day. As MGU are operating at unity power factor there are no differences regarding the reactive power flows.

Table 3- Power flow at the distribution transformer and energy drawn from the grid.

	Sc. A	Sc. B	Sc. C	Sc. D	Sc. E	Sc. F	Sc. G
Hourly averaged active power (kW)	17,96	13,89	9,81	9,81	9,80	9,82	9,81
Daily active energy (kWh)	430,99	333,28	235,48	235,55	235,20	235,74	235,38
Differences regarding scenario A(%)	0	-22,67	-45,36	-45,35	-45,43	-45,30	-45,39
Hourly averaged reactive power (kVAr)	12,99	13,01	13,02	13,03	13,01	13,04	13,20
Daily reactive energy (kVArh)	311,66	312,16	312,58	312,66	312,27	312,86	312,48
Differences regarding scenario A(%)	0	0,163	0,298	0,321	0,197	0,388	0,264

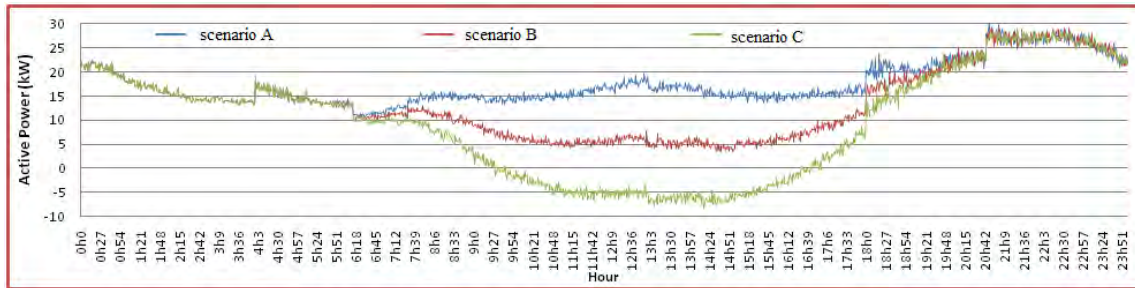


Figure 4- Active power flow at distribution transformer (scenarios A-C).

#### 4.2. Power Losses

In Table 4 the active and reactive power losses are presented as well as the differences regarding the reference situation (scenario A). For low level MGU penetration (scenario B) there is a reduction in losses. However, when MGU penetration increases losses depend on the location of MGU. Typically there is a reduction in losses, not as big as in scenario B, but some situations, like in scenarios D and G, might present higher losses. In scenario G, MGU are connected mainly in the phase with lower demand (phase C) resulting in a strong current flow increase in this phase and thus an increase in losses. In scenario D, MGU are mainly connected at remote buses resulting in longer distances for power flows and thus higher resistance. An interesting situation that may occur when MGU penetration increases is that the power losses maximum value can occur during the higher outputs from MGU and not in the periods of higher demand.

Table 4- Losses for the different scenarios

	A	B	C	D	E	F	G
Active power losses (W)	87,78	79,77	83,65	88,92	85,05	84,60	93,70
Daily active losses (kWh)	2,107	1,914	2,008	2,134	2,041	2,030	2,249
Variation regarding A (%)	0	-9,13	-4,70	1,30	-3,11	-3,62	6,75
Reactive power losses (VAr)	23,81	21,05	21,73	22,90	22,03	22,29	24,93
Daily reactive losses (kVArh)	0,571	0,505	0,522	0,550	0,529	0,535	0,598
Variation regarding A (%)		-11,58	-8,72	-3,84	-7,48	-6,40	4,70

#### 4.3. Voltage

Following figures show the voltage values in the 38 buses of the network at 12:00h, for the different scenarios. In general voltage profile improves when MGU are connected. Typically, higher voltage increase occurs in the buses and in the phases where MGU are connected. There is, however, a decrease in voltage values in phase B in buses 8, 9 and 10. These decrease might be due to the introduction of MGU in buses 11 (phase A) and 18 (phase C)

reducing the magnetic coupling between phases A and C and the phase B thus leading to a higher voltage drop in phase B. From Figure 6-scenario D) to Figure 6-scenario G) one can see that the voltage profile in the network is highly dependent on the location of MGU. When the MGU are located in remote buses (scenario D) the impact on voltage level is higher compared with the scenario in which MGU are connected near the DT (scenario E). When MGU are mainly located in a single phase (scenario F – phase B, high demand; scenario G – phase C, low demand) the voltage value in the phase increases strongly but is higher when MGU are located in the low loaded phase (scenario G).

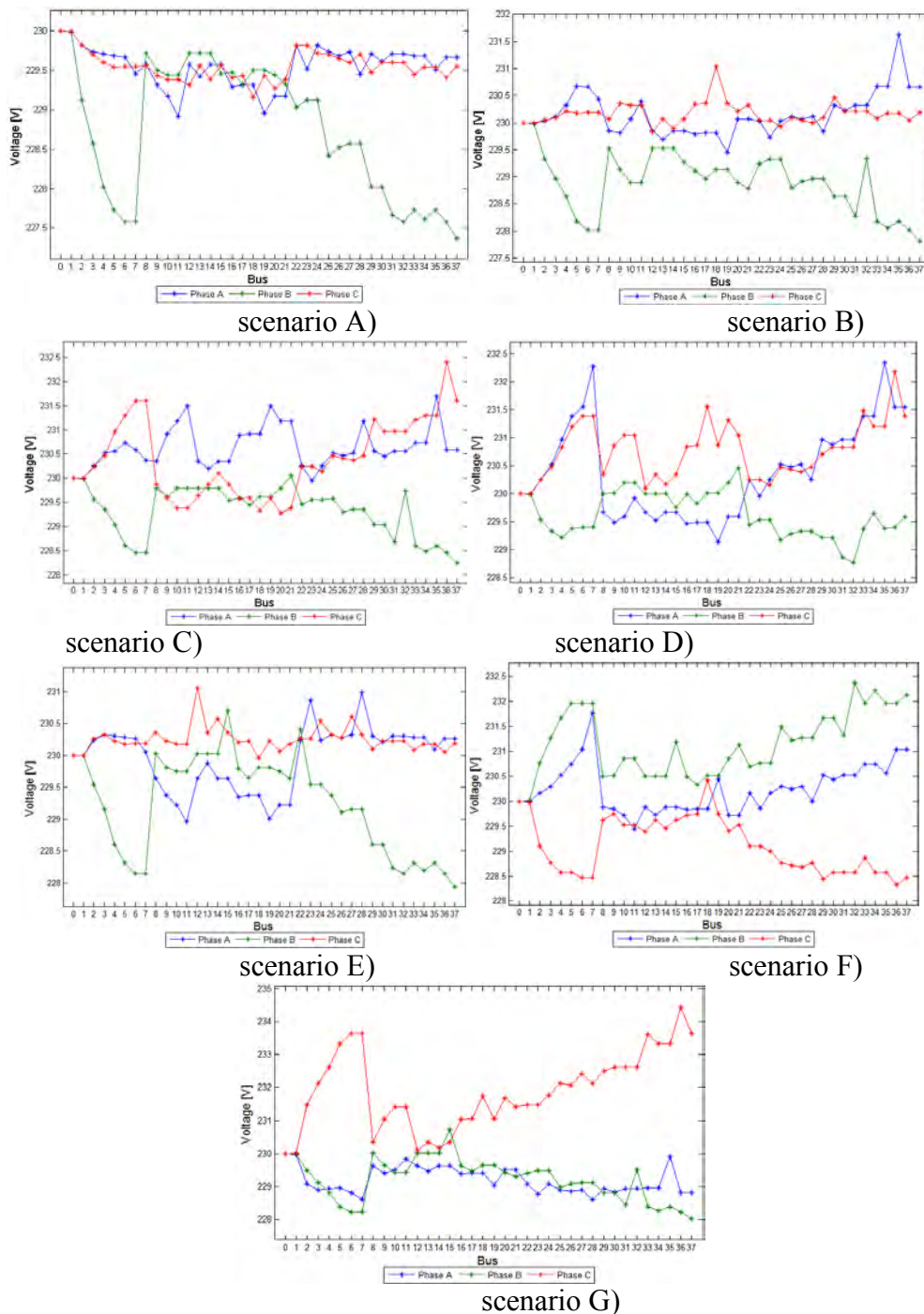


Figure 5- Voltage values at the different buses for all the scenarios

Figure 6 shows the variation in voltage profiles due to the variability of demand or/and micro-generation. For example, according to the collected data, voltage in bus 35 may vary between 229,6V and 234V. In some buses the voltage variation range is much higher (for example, in buses 7, 11, 35) than in other buses (for example, 8, 12, 14, 15). In figure 6 circles show the average voltage values in each bus.

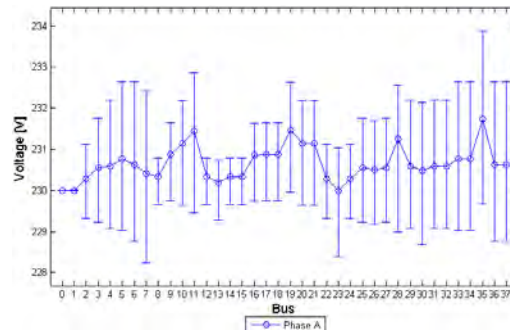


Figure 6- Variation of voltage profile at 12h in phase A due to demand uncertainty and micro-generation variability.

The single-phase nature of both most end-use loads and of micro-generation units at residential level together with the unsymmetrical nature of the LV distribution networks may result in unbalanced voltages. In Figure 7 the unbalance of voltage at bus 36 for the different scenarios is shown. G is the scenario presenting the highest voltage unbalance, resulting from micro-generation occurs mainly in the phase with the lower demand/higher voltage.

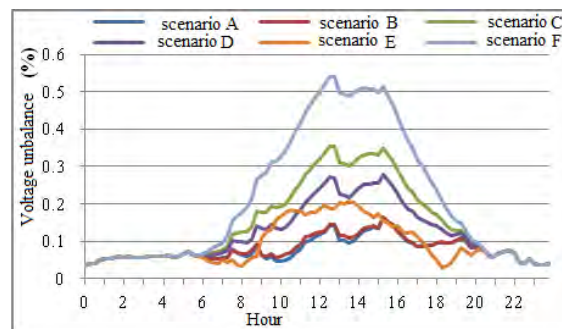


Figure 7- Voltage unbalance at bus 36.

## 5. Conclusions

The increasing penetration of micro-generation on LV distribution networks will impact the flow of power, with possible reverse flows, and voltage levels on the network. It is clear that besides the detailed assessment of those impacts, the accurate calculation of benefits pointed out to this type of generation, such as losses reduction, needed to be carried out. In this work Monte Carlo models have been used to reproduce the demand and available micro-generation in a LV distribution network, taking into account the uncertainty associated with both the demand and generation, in order to allow a detailed assessment of the impacts of MGU in the power flows, voltage levels and unbalance and in the power losses. By using load diagrams developed from interval metering in each consumer and Monte Carlo simulations it is possible to use realistic demand patterns with adequate time resolution.

## References

- [1] P. Costa, M. Matos, Avoided losses on LV networks as a result of microgeneration, *Electric Power Systems Research*, 79, 2009, pp. 629-634.

- [2] E. Carpaneto, G. Chicco, J. Akilimali, Loss Partitioning and Loss Allocation in Three-Phase Radial Distribution Systems With Distributed Generation, *IEEE Transactions on Power Systems*, Vol. 23, No. 3, August 2008, pp.1039-1049.
- [3] P. Trichakis, P.C: Taylor, P.F. Lyons, R: Hair, Predicting the technical impacts of high levels of small-scale embedded generators on low-voltage networks, *IET Renewable Power Generation*, 2008, Vol. 2, No. 4, pp. 249-262.
- [4] D. Zhu, R. Broadwater, K.-S. Tam, R. Seguin, H. Asgeirsson, Impact of DG placement on reliability and efficiency with time-varying loads, *IEEE Transactions on Power Systems*, Vol. 21, No. 1, February 2006, pp.419-427.
- [5] V. Quezada, J. Abbad, T. Román, Assessment of Energy Distribution Losses for Increasing Penetration of Distributed Generation, *IEEE Transactions on Power Systems*, Vol. 21, No. 2, May 2006, pp. 533-540.
- [6] P. Barker, R. Mello, Determining the Impact of Distributed Generation on Power Systems: Part 1 – Radial Distribution Systems, *Power Engineering Society Summer Meeting*, 2000, IEEE.
- [7] J.-H. Teng, Modelling distributed generations in three-phase distribution load flow, *IET Generation, Transmission & Distribution*, 2008, Vol. 2, No. 3, pp. 330-340.
- [8] M. Begović, A. Pregelj, A. Rohatgi, D. Novosel, Impact of Renewable Distributed Generation on Power Systems, *Proceedings of the 34th Hawaii International Conference on System Sciences – 2001*.
- [9] P. Sritakaew1, A. Sangswang, K. Kirtikara, On the Reliability Improvement of Distribution Systems Using PV Grid-Connected Systems, *ECTI Transactions on Electrical Eng., Electronics, and Communications* Vol.5, No.1 February 2007.
- [10] W. H. Kersting, The computation of neutral and dirt currents and power losses. s.l: *IEEE Power Systems Conference and Exposition*, 2004, pp. 213 - 218 (vol. I).
- [11] W. H. Kersting, and Phillips, W.H, Distribution feeder line models, *IEEE Transactions on Industry Applications*, 1995, pp. 715 – 720.
- [12] A. G. Bhutad, S. V. Kulkarni, S. A. Khaparde, Three-phase load flow methods for radial distribution networks. *IEEE TENCON 2003, Conference on Convergent Technologies for Asia-Pacific Region*. pp. 781-785, Vol. 2.
- [13] G. W. Chang, S. Y. Chu, H. L. Wang, A Simplified Forward and Backward Sweep Approach for Distribution System Load Flow Analysis, *IEEE PowerCon 2006, International Conference on Power System Technology*. pp. 1–5.
- [14] J. Nanda, et al., New findings on radial distribution system load flow algorithm, *IEEE Power Engineering Society Winter Meeting*, 2000, pp. 1157 - 1161, Vol.2.
- [15] R. M. Ciric, A. P. Feltrin, L. F. Ochoa, Power flow in four-wire distribution networks-general approach, 2003, *IEEE Transactions on Power Systems*. pp. 1283-1290.

## Optimal Sizing of an Islanded Micro-grid for an area in north-west Iran Using Particle Swarm Optimization Based on Reliability Concept

H. Hassanzadehfard<sup>1,\*</sup>, S.M.Moghaddas-Tafreshi<sup>1</sup>, S.M.Hakimi<sup>1</sup>

<sup>1</sup> Faculty of Electrical Engineering, Khajeh Nasir Toosi University, Iran, Tehran

\* Corresponding author. Tel: +989124798639 Fax: +982188462066, E-mail: sm\_hakimi@iee.org

**Abstract:** In islanded micro-grid design, a proper Distributed Energy Resource (DER) selection, sizing and effective coordination between resources are important and challenging optimization tasks. The types and sizes of renewable energy sources such as wind turbines, photovoltaic panels, fuel cell and the capacities of battery bank and the other distributed generators must be optimized in islanded micro-grid design. In this paper, the problem is formulated as a nonlinear integer minimization problem which minimizes the sum of the total capital, operational and maintenance and replacement cost of DERs, subject to constraints such as energy limits of each DER. This paper proposes Particle Swarm Optimization (PSO) for solving this minimization problem. The proposed methodology was used to design micro-grid for northwest of Iran. The simulation studies have shown that the proposed methodology provides excellent convergence and feasible optimum solution for sizing of islanded micro-grids using particle swarm optimization. In this paper some notions of reliability are considered for micro-grid, and the effect of reliability on total cost of micro-grid is evaluated.

**Keywords:** Micro-grid, Optimal sizing, Particle swarm optimization, Reliability

### Nomenclature

$P_{wind}$ power generated by wind turbines..... kW	$E_{bat}$ stored energy in battery banks ..... kWh
$P_{PV}$ power generated by PV generators ..... kW	$R$ lifetime of project ..... year
$P_{FC}$ power generated by fuel cells ..... kW	$L$ lifetime of each component..... year
$P_{Load}$ ..... load power	$ir$ Interest rate ..... %

### 1. Introduction

The increase in penetration of distributed generation depth and the presence of multiple distributed generators in electrical proximity to one another have brought about the concept of the micro-grid [1, 2]. Micro-grids comprise low voltage distribution systems with distributed energy sources, storage devices, and controllable loads, operated either islanded or connected to the main power grid in a controlled, coordinated way. Refs. [3, 4] introduce the benefits of micro-grid, such as, enhance local reliability, reduce feeder losses, support local voltages, provide increased efficiency through using waste heat combined heat and power, voltage sag correction or provide uninterruptible power supply functions. Proper selection of distributed energy resources and optimal sizing of them are important and challenging tasks in the designing of islanded micro-grids [5] because the coordination among distributed energy resources is very complicated. The problem can be formulated as a nonlinear integer optimization problem which can be solved by a suitable optimizing methodology. Our aim is to minimize the total costs of the system such that the demand is met. For standalone hybrid wind/PV power systems, a typical tangent method is used to fix the size of wind generator and optimize the size of PV panels and the capacity of batteries [5, 7]. Several research works have been done for selecting the parameters such as the size of wind generators, the size of PV panels and the capacity of batteries but the decision variables collectively taken without any optimizing methodologies [5- 12]. Recently, a genetic algorithm for the concerned problem has been proposed by Xu et al. [13] where genetic algorithm optimizes the size of wind generators, the size of PV panels and the capacity of batteries as decision variables. Although this method provides a better performance in comparison to the previous literature,

it is necessary to find a flexible generalized methodology for any kind of micro-grid designing with higher computational efficiency.

In this paper, the optimal sizing of a wind-PV-fuel cell-battery bank in micro-grid is considered. The optimization is carried out via Particle Swarm Optimization (PSO) algorithm. Generation of hydrogen by the reformer causes a higher reliability for the system.

First, we consider the micro-grid. And then the cost of the system presented by an objective function. Finally some simulation results are presented. This study is performed for Ganje site in northwest of Iran. It is located in a village with a population of 800.

## 2. Description of the micro-grid components

### 2.1. Wind turbine

The power of the wind turbine is described in terms of the wind speed by Ref [16]:

$$\begin{cases} 0 & V < V_{cut-in}, V > V_{cut-off} \\ P_{rated} \times ((V - V_{cut-in}) / (V_{rated} - V_{cut-in}))^3 & V_{cut-in} \leq V < V_{rated} \\ P_{rated} & V_{rated} \leq V \leq V_{cut-off} \end{cases} \quad (1)$$

In which  $V_{cut-in}$ ,  $V_{cut-off}$ ,  $V$ ,  $V_{rated}$  and  $P_{rated}$  are cut-in wind speed [m/s], cut-out wind speed [m/s], wind speed [m/s], nominal wind speed [m/s] and the rated power of wind turbine [kW] respectively. In this analysis, each wind turbine has a rated capacity of 1 kW. Cost of one unit is considered 2500\$, while replacement and maintenance cost are taken as 1500\$ and \$75/year. Lifetime of a turbine is taken to be 20 years [14].

### 2.2. PV

The output power of the PV generator  $P_{PV}$ , can be calculated according to the following equation:

$$P_{PV} = \eta_g * N * A_m * G_t \quad (2)$$

Where  $\eta_g$  is the instantaneous PV generator efficiency,  $A_m$  is the area of a single module used in a system ( $m^2$ ),  $G_t$  is the global irradiance incident on the titled plane ( $W/m^2$ ) and N is the number of modules. In this analysis, each PV generator has a rated power of 1 kW. Cost of one unit considered is 6000\$ while replacement and maintenance cost are taken as 5000\$ and 0\$/year respectively. Lifetime of a PV generator is taken to be 20 years [14].

### 2.3. Fuel cell

Proton exchange membrane (PEM) fuel cell is an environmentally clean power generator which combines hydrogen fuel with oxygen from air to produce electricity.

The capital cost, replacement cost and operational cost are taken as 3\$k, 2.5\$k and 175\$/year for a 1-kw system, respectively. Fuel cell's lifetime is considered to be 5 years [14].

### 2.4. Battery storage

At any hour the state of battery is related to the previous state of charge and to the energy production and consumption situation of the system during the time from t-1 to t.

In all cases the storage battery capacity is subject to the following constraints:

$$E_{bat\ min} < E_{bat}(t) < E_{bat\ max} \quad (3)$$

Where  $E_{bat\ max}$  and  $E_{bat\ min}$  are the maximum and minimum allowable storage capacities.

$E_{bat\ min}$  is determined by the maximum allowable depth of battery discharge (DOD) as follows:

$$E_{bat\ min} = (1 - DOD) * E_{bat\ max} \quad (4)$$

In this analysis, each battery bank capacity is 552Ah. Cost of each battery is considered 264\$ while replacement and maintenance costs are taken as 260\$ and 2.64\$/year. Lifetime of a battery is taken to be 3 years [14].

### 3. System modeling

The micro-grid consists of some wind turbines, PV arrays, fuel cells, reformers and battery banks (Fig. 1). Natural gas is used to produce fuel cells' required hydrogen.

It is desirable that the system meets the demand, the costs are minimized and the components have optimal sizes.

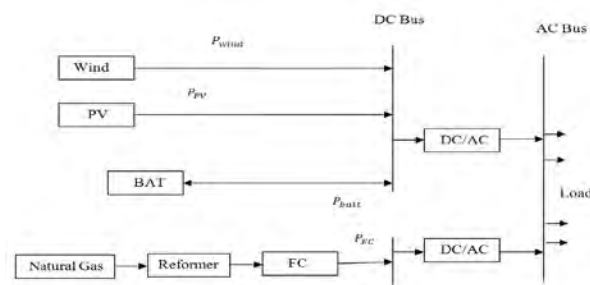


Fig.1. Schematic diagram of micro-grid

#### 3.1. Strategy

We consider three situations for the system: A. generation power produced by renewable energy (wind + PV) meets demand, B. over generation and C. over demand.

##### 3.1.1. Power generation produced by wind and PV meets demand

In this situation the power generated by the wind turbine plus the power produced by the PV array is equal to the demand ( $P_{wind}(t) + P_{PV}(t) = (P_{Load}(t) / \eta_{conv})$ ), hence:

$$E_{bat}(t) = E_{bat}(t-1), P_{FC}(t) = 0 \quad (5)$$

It is notable that the time steps  $\Delta t$  are taken to be 1 hour in this study.

##### 3.1.2. Over generation

The produced power of the wind turbine plus power produced by the PV array are more than the demand ( $P_{wind}(t) + P_{PV}(t) > (P_{Load}(t) / \eta_{conv})$ ).

The excess power is utilized for charging the batteries:

$$E_{bat}(t) = E_{bat}(t-1) + (P_{wind}(t) + P_{PV}(t) - P_{Load}(t) / \eta_{conv}) * \Delta t * \eta_{cha}, P_{FC}(t) = 0 \quad (6)$$

### 3.1.3. Over demand

The demand is more than the power generated by the wind turbines and power produced by the PV array ( $P_{wind}(t) + P_{PV}(t) < (P_{Load}(t)/\eta_{conv})$ ).

In this situation we have two cases:

a. Available battery banks' energy and power generation of wind turbine plus PV array can meet demand ( $P_{wind}(t) + P_{PV}(t) + (E_{bat}(t) - E_{bat\ min}) * \eta_{dech} / \Delta t > (P_{Load}(t)/\eta_{conv})$ ).

$$E_{bat}(t) = E_{bat}(t-1) + (P_{wind}(t) + P_{PV}(t) - P_{Load}(t)/\eta_{conv}) * \Delta t / \eta_{dech}, P_{FC}(t) = 0 \quad (7)$$

b. Available battery banks' energy and power generation of wind turbine plus PV array can not meet demand:

In this situation the battery banks are completely discharged and the energy in the battery banks is equal to  $E_{bat\ min}$ . In this state, load requirements are supplied from the fuel cell:

$$E_{bat}(t) = E_{bat\ min}, P_{FC}(t) = (P_{Load}(t)/\eta_{conv}) - P_{PV}(t) - P_{wind}(t) - (E_{bat}(t) - E_{bat\ min}) * \eta_{dech} / \Delta t \quad (8)$$

## 3.2. System's cost

In this paper we consider the capital and replacement costs, the operation and maintenance costs of each component of micro-grid.

We choose Net Present Cost (NPC) for calculation of system's cost.

### 3.2.1. Net Present Cost

The Net Present Cost (NPC) of each component is defined as [15]:

$$NPC = N * (capital\_cost + replacement\_cost * K + operation \& maintenance\_cost) * \frac{1}{CRF(ir, R)} \quad (9)$$

$$CRF(ir, R) = \frac{ir * (1 + ir)^R}{(1 + ir)^R - 1}, K = \sum_{n=1}^y \frac{1}{(1 + ir)^{L*n}} \quad (10)$$

L is the lifetime and N is the optimal number of each component.

### 3.2.2. The objective function

The objective function is the sum of all net present costs [16]:

$$NPC = NPC_{wind} + NPC_{PV} + NPC_{battery} + NPC_{FC} + NPC_{ref} + NPC_{conv} \quad (11)$$

The objective function must be minimized, such as minimization is done by PSO algorithm in this paper.

## 4. Simulation results

Lifetime of the project is 20 years. In this article, the optimum combination of the micro-grid considered shown in Fig.1 is calculated. The system data consists of the annual wind data and

solar radiation which belong to a region in northwest of Iran. The load curve which is actually an IEEE standard curve with 500 kW peak, the yearly wind speed and solar radiation are showed in fig.2. For the sake of simplicity, we have considered the weekly mean in input data in our simulation. The data is the wind velocity and the demand in every one hour in a day. So, an average of the input data in each hour is calculated during a week. The power of the wind turbine and PV array could be derived by Eq. (1.2) from the wind speed and solar radiation data. The optimal size of wind turbine, PV array, battery bank and Fuel cell are shown in table.1. Fig.3. shows the output power of wind turbine, PV array, fuel cell and Energy of battery storages. We see that at the time 940, fuel cell injects power to the micro-grid. Where the available battery storage energy is equal to minimum allowable storage capacity and output power of PV array is equal to zero. Also output power of wind turbine does not satisfy the micro-grid's demand, so fuel cell injects power to the micro-grid in order to compensate load requirements. Fig.4. Shows the system costs in terms of the iterations.

Table 1. Optimal size of each component.

Number Wind turbine	Number PV array	Number Battery bank	Number Fuel cell	Total cost \$
351	1758	4217	187	17.838M

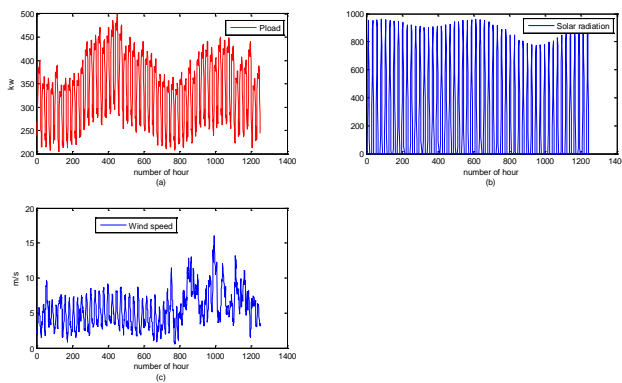


Fig. 2. (a). Load information. (b) Solar radiation information. (c) Wind speed information.

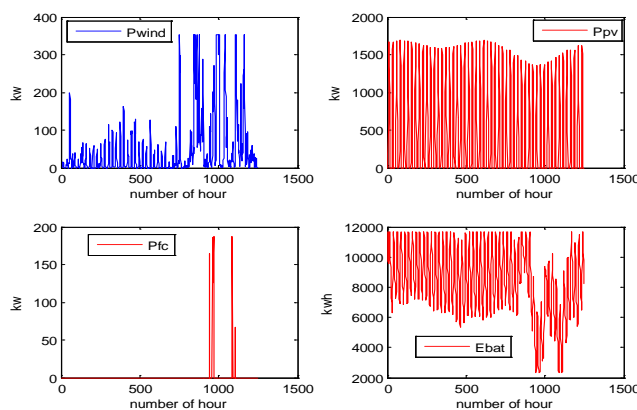


Fig. 3 (a) Output power of wind turbine. (b) Output power of PV array. (c) Output power of fuel cell. (d) Energy fluctuate of battery banks.

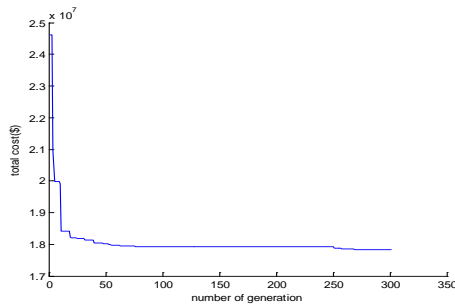


Fig. 4. The optimal cost of micro-grid in terms of the iterations

#### 4.1. Effect of the capital cost of PV arrays on simulation results

In this section, the effect of capital cost of PV arrays, on the optimal size of each component and total cost of micro-grid is regarded. Table.2 shows that increasing the capital cost of the PV array causes the micro-grid costs to increase and the optimal size of PV array to reduce.

Table 2. Effect of capital cost of PV array.

Capital cost of PV unit	Wind turbine	PV array	Battery bank	Fuel cell	Total cost \$
5000	337	1787	4154	193	16.149M
6000	351	1758	4217	187	17.838M
7000	383	1748	4263	172	19.558M
8000	523	1603	4732	106	20.646M

## 5. Reliability

Some notions of reliability are commonly used for systems with hourly demand and supply data. Loss of Load Expectation (LOLE), Loss of Energy Expectation (LOEE), Loss of Power Supply Probability (LPSP) and Equivalent Loss Factor (ELF) are some of them considered in this paper. ELF is described by:

$$ELF = \frac{1}{N} \sum_{t=1}^N \frac{Q(t)}{D(t)} \quad (12)$$

Where  $D(t)$  is the total energy demand,  $Q(t)$  is the loss-of-load and  $N$  is the number of hours. The  $ELF$  contains information about both the number of outages and their magnitude. In this paper we regard that  $ELF$  should be lower than 0.01 [17].

### 5.1. Simulation Result considering reliability parameters

In this micro-grid when the power of fuel cell to support the demand is greater than the optimal size,  $Q(t)$  is described by:

$$Q(t) = P_{FC}(t) - N_{FC} * P_{Fuel-Cell} \quad (13)$$

Where  $N_{FC}$  is the optimum size and  $P_{Fuel-Cell}$  is the rated power of fuel cell. The cost of electricity interruptions has been estimated. The value we use in our model is 5.6 \$/kWh. Fig.5. depicts the flowchart of the algorithm simulating the micro-grid considering reliability. The optimal size of wind turbine, PV array, battery bank, fuel cell and the total cost of micro-grid are shown in table. 3.

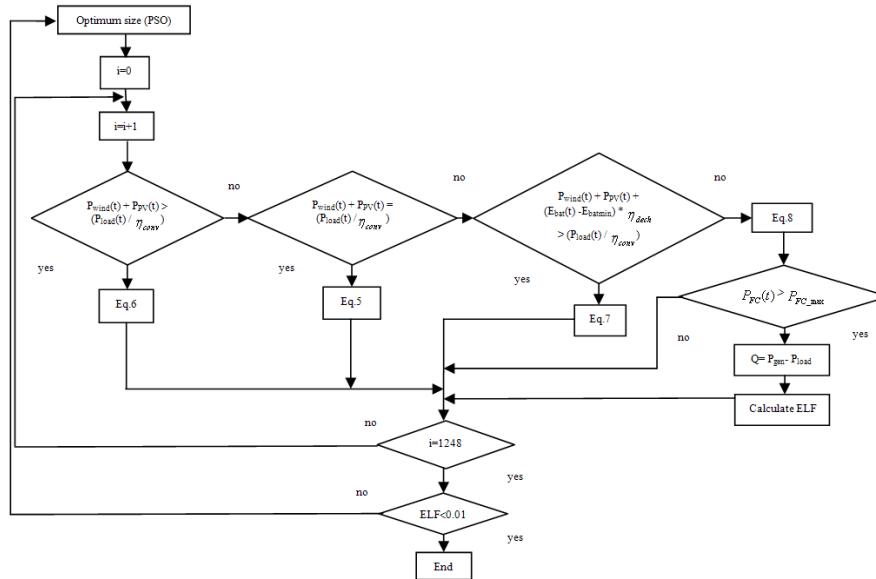


Fig.5. The flowchart of the algorithm simulating the micro-grid considering reliability.

Table.3. Optimal size of each component considering reliability parameters.

Wind turbine	PV array	Battery bank	Fuel cell	Total cost \$
515	1660	3150	14	15.33M

Table.3 shows that considering reliability parameters such as ELF for micro-grid (some of loads in some hours are not satisfied) reduces the total cost of micro-grid. Figure 6 shows the loss of energy in each hour.

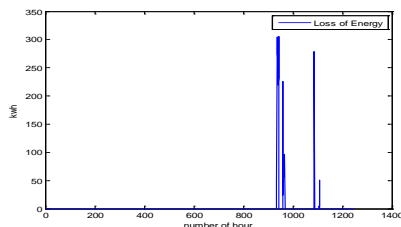


Fig. 6. Loss of energy in each hour.

We see that maximum loss of energy appears at the time between 900-1000. Where the available battery storage energy and output power of PV array to inject to the micro-grid is equal to zero. The value of some notions of reliability is shown in table. 4. Table 4 shows that ELF is in the acceptable confine.

Table 4. The amount of some notions of reliability

LOLE (hr/yr)	LPSP	LOEE (MWh/yr)	ELF	Penalty
24	$9.1098 \times 10^{-3}$	3.8623	$9.999 \times 10^{-3}$	0.21235M

## 6. Conclusion

In this paper the optimal sizing and operation strategy of micro-grid are considered. The system consists of wind turbines, PV arrays, fuel cells, battery banks, reformers and DC/AC converters. The micro-grid used in this study has high reliability because fuel cells are as a backup for wind turbines and PV arrays. The main problem of renewable energy source is that they are dependent on environmental conditions. So they could not cover the demand

perfectly. Entering storage component solves this problem significantly. In this study battery bank is used to cover the demand desirably. We assumed that in each hour micro-grid can interrupt loads subject to reliability constraint such as ELF. In this situation total cost of micro-grid reduces.

## References

- [1] R. Lasseter, A. Akhil, C. Marnay, J. Stephens, J. Dagle, R. Guttromson, A. Meliopoulos, R. yinger and J. Eto, "White paper on Integration of consortium Energy Resources. The CERTS MicroGrid Concept." CERTS, CA, Rep.LBNL-50829, Apr.2002.
- [2] MICROGRIDS: Large Scale integration of Micro-Generation to low Voltage Grids" EU contact ENK5-CT-2002-00610, Technical Annex, May 2002.
- [3] Lasseter RH. MicroGrids. IEEE Power Eng Soc Transm Distrib Conf 2002(1):305–8.
- [4] Marnay Chris, Venkataramanan Giri. Microgrids in the evolving electricity generation and delivery infrastructure. IEEE Power Eng Soc Gen Meet 2006:18–22.
- [5] H. L. Willis and W. G. Scott, Distributed Power Generation: Planning and Evaluation, Marcel Dekker, New York, 2000.
- [6] California Distributed Energy Resources Guide, Available at: <http://www.energy.ca.gov/distgen/>
- [7] B. S. Borowy and Z. M. Salameh, "Methodology for Optimally Sizing the Combination of a Battery Bank and PV Array in a Wind/PV Hybrid System," IEEE Trans. On Energy Conversion, pp.367-375, 1996.
- [8] M. A. Habib, S. A. M. Said, M. A. El-Hadidy and A. I. Zaharna," Optimization Procedure of Hybrid Photovoltaic Wind Energy System Energy," pp.919-929, 1999.
- [9] J. K. Kaldellis, "Parametric Investigation Concerning Dimensions of a Stand-alone Wind-Power System," Applied Energy, pp.35-50, 2004.
- [10] B. Ai, H. Yang, H. She and X. Liao, "Computer-aided Design of PV/wind Hybrid System," Renewable Energy, pp.1491-1512, 2003.
- [11] M. A. Elhadidy and S. M. Shaahid, "Optimal Sizing of Battery Storage for Hybrid (wind+diesel) Power Systems," Renewable Energy, pp.77-86,1999.
- [12] A. M. Al-Ashwal and I. S. Moghram, "Proportion Assessment of Combined PV-Wind Generating Systems," Renewable Energy. pp.43-51, 1997.
- [13] D. Xu, L. Kang and B. Cao, "Optimal Sizing of Standalone Hybrid Wind/PV Power Systems Using Genetic Algorithms," Proc. of IEEE Canadian Conference on Electrical and Computer Engineering, Canada, pp. 1705-1708, 2005.
- [14] M.J. Khan, M.T. Iqbal, "Pre-feasibility study of stand-alone hybridenergy systems for applications in Newfoundland", Renewable Energy 30 (2005) 835–854.
- [15] <[www.mahler-ags.com](http://www.mahler-ags.com)>
- [16] Hakimi SM, Moghaddas-Tafreshi SM. "Unit sizing of a stand-alone hybrid power system using particle swarm optimization (PSO)". IEEE ICAL Aug 2007; 18–21:3107–12.
- [17] Raquel S. Garcia, Daniel Weisser, "A wind–diesel system with hydrogen storage: Joint optimization of design and dispatch", Renewable Energy 31 (2006) 2296–2320.

---

## Evaluation of the Solar Hybrid System for Rural Schools in Sabah, Malaysia

Abdul Muhaimin Mahmud

Public Works Department of Malaysia, Kuala Lumpur, Malaysia.  
Tel: +603 92354399, E-mail: [muhaimin@jkr.gov.my](mailto:muhaimin@jkr.gov.my)

---

**Abstract:** The impact of the implementation of solar hybrid system which was installed at Penontomon Primary School in Sabah, Malaysia has been analyzed in this paper. The project was initiated by the Malaysia's Ministry of Education with the target to electrify rural schools that do not have grid connected electricity in Sabah with alternative power supply; ie, the renewable energy. The paper looked into the users' experiences, technical and the economical aspects of the system and found that alternative resources from renewable energy offers better electricity in providing power supply to the rural schools than the old and conventional diesel generator system. The technology gives benefit and impact to the pupils and teachers by creating more comfortable lifestyle and conducive learning environment.

**Keywords:** *Solar hybrid, Rural schools, SCADA, Battery, Inverter*

---

### 1. Introduction

Malaysia, although moving rapidly towards being a developed nation, has a considerable number of under-developed rural areas. Most of these are tiny pockets of inhibited villages, sprawling over large areas of Sabah and Sarawak (the Borneo Island part of Malaysia). In general, basic infrastructures are inadequate and grid connected electricity supply is the major one. Out of more than 10,000 schools in Malaysia, 809 in Sabah and Sarawak still lacked 24-hour electricity supply and have to rely on decentralized diesel generator as the main source. The main reasons can be attributed to (1) the remote locations of these villages and (2) the community size is very small. These factors caused the investment cost for grid supply prohibitively expensive and un-economic. The cost of electricity using this method is very high – primarily due to the fuel transportation to the sites. Furthermore, consistent electricity cannot be guaranteed because of the climatic and geographical conditions that may hamper the fuel supply route. To ensure that these areas are not lagging behind in the country's modernization strategy, the Ministry of Education (MOE) has initiated a large electrification program for rural schools in Sabah. It is recognized that stable and reliable electricity supply is the key element for conducive learning environment and enables the use of computers, communication system, lighting and etc [2]. The government has allocated over RM1.15 billion (USD365 Million) to improve the basic infrastructure [1]. Fittingly, electricity supply is given top priority.

Despite the fact that the program has been going on for two years, there is no documented literature describing the design methodology, performance analysis, economics evaluation and the social impact of the installed systems. It is envisaged that the lessons learned from these experiences can provide valuable guidelines for future rural electrification programs using SHS. Hence this work is carried out. The study can be divided into two parts (1) to analyze the technical and the economical aspects of the system design and daily operation based on real data (2) to study and analyze the impact of the SHS on their lifestyle and the learning environment.

## **2. Methodology**

This study used quantitative and qualitative methods in determining the impact of the Solar Hybrid System to the end users and to evaluate the system performance.

### **2.1 Impact On The Solar Hybrid System**

Structured questionnaires were distributed to the 40 selected respondents, which consists of the teachers and pupils. The questionnaire was developed to ensure that the impact of the system can be analyzed base on;

- a) Comparison of the users' experience before and after the system installed and how the system does affects their life and the learning environment.
- b) Comparison of the users' knowledge of renewable energy especially the Solar Hybrid System before and after the installation.
- c) Load management strategies which are being exercised by the users.
- d) Users' opinions on how the system can benefit the entire community should the same system implemented for their village as well.

### **2.2 Implementation and Operation of the Solar hybrid System**

The second part of the methodologies determines the Solar Hybrid System performance technically and economically. The design and actual load analysis compares the design load profile and the actual load profile (average) and the system operation analysis answers the sustainability and reliability issues of the system. The measurement data, recorded by the online monitoring system; ie, JKR Supervisory Control and Data Acquisition System (JSCADA) are used to analyze the system performance. The economic analysis includes both costs and benefits of the system. Parameters like investment cost, operating cost and cost of energy are used to measure the beneficial of the system as compared to the conventional diesel generator [4].

## **3. Solar Hybrid System**

The solar hybrid system integrates two power sources. The system is designed to supply electricity for every building in the school like class rooms, computer lab, guard house and teachers' quarters. For the purpose of the analysis, Penontomon Primary School which is located in Keningau District in Sabah (N 4°52.73' E 116°15.9') has been identified to be the sample site for evaluation and analysis processes.

### **3.1 Description of Loads & Load Profile**

The total installed rated load power for SK Penontomon is 15.23 kW [6]. The load usage has been distributed over 24 hours load profile which used to identify the maximum peak load during the day. The daily energy consumption for SK Penontomon was calculated from the load profile. During daytime, the energy demand is at 35,964 Wh which is 69.53% of the total daily energy demand. While at night it requires 30.47% of the daily energy demand (15,722 Wh). Daytime is considered from 06.00 hours to 18.00 hours which is the normal sun rise and sunset for the location.

### **3.2 System Configuration**

As shown in Figure 1 below, the 20 kW<sub>p</sub> PV array is used to supply power to the load and to charge the battery during day. Priority will be given to satisfy the day time load. A 3,500 Ah tubular vented deep cycle lead acid battery bank is used for storage and supply power to the loads mostly during night. The bidirectional inverter converts the DC-AC voltage and vice

versa. If there were insufficient power from the PV to charge the battery, the 27 kVA diesel generator will turn on automatically. Moreover, excess electricity from the generator will be used to electrify the loads. The generator is configured to be automatically turned on for one hour every week to warm up and also once a month for several hours for battery equalization.

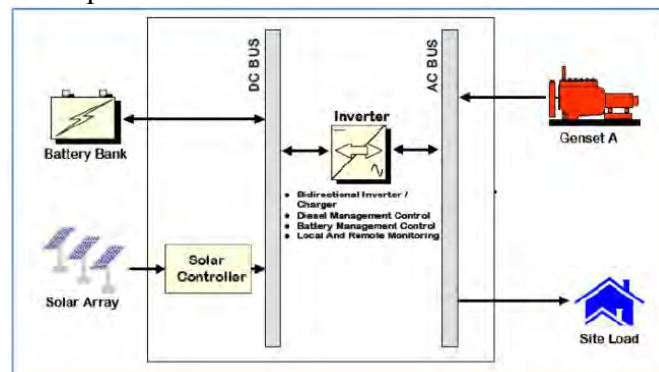


Figure 1 : The solar hybrid system configuration diagram [6].

## 4. Results and Analysis

### 4.1 User Experiences

#### 4.1.1 Knowledge

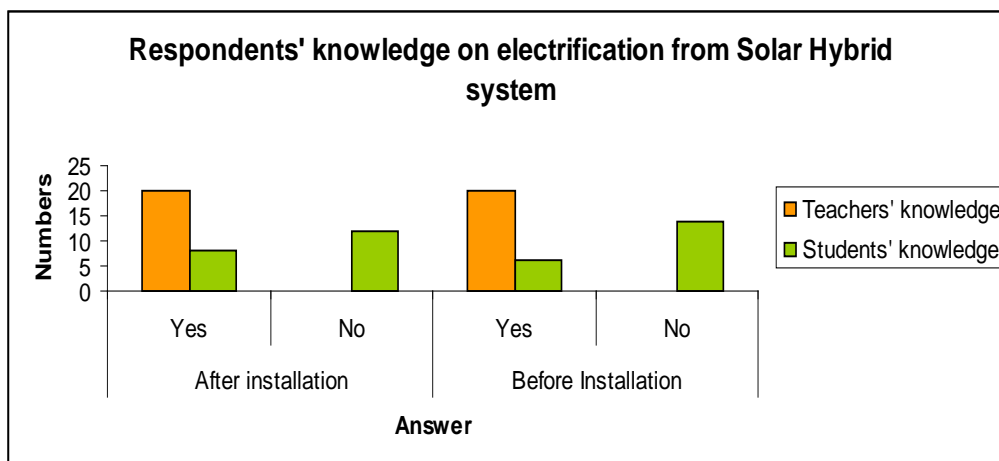


Figure 2 : Respondents' knowledge on electrification from solar hybrid technology system.

All of the teachers and only six pupils have some knowledge of the Solar Hybrid System before the installation of the system. The numbers of the pupils that gain information of the system after it is in operation increasing by 10%.

Books, magazines and newspapers are the popular sources of information of the system. 40% of the respondents have read about the technology. For the pupils, most of them knew about renewable energy by reading from the school library. Alternative information is from the internet as 20% of the respondents get the information from the World Wide Web (www.). The internet can be access from the school's computer lab or at other places/towns nearby.

35% of the respondents have seen the technology before at other places/villages. The technology was installed for village communities in several rural electrification programs like

Solar Home System (SHS) by Ministry of Rural and Region Development and Solar PV System for Rural ICT Centre by Ministry of Energy, Water and Communication.

The education system also provides some basic information on renewable energy system in standard six's Science subjects. 16% of the respondents learn/teach the subject and they are mostly the Science teachers and standard six pupils.

Four respondents replied that they get the information from other sources. Three of them by informal conversation and the other one have a standalone PV system installed at his house nearby.

#### *4.1.2 User Training*

At least a teacher from each school is required to attend training on solar hybrid technology. The teacher will be responsible to give the information on the technology to the other users. It is found out that only informal explanation was given to the users. As shown in figure 3 below, only 24 respondents were given informal information and eighteen respondents understand well about the technology, while another six respondents requested for more explanation and formal training.

The main barrier in implementing PV system in any rural electrification program is the operation period. PV system and its implementation are frequently looked upon in a very simplistic manner by a number of people which has resulted in a large number of failures [4]. Proper transfer of technology training program is required for the end users because the awareness and knowledge on the system technology are equally as important as the adequate financing and institutional framework.

#### *4.1.3 Load Management Strategies*

All of the respondents replied that they practiced load management when using the electricity. However, they do not have a schedule management or do not strategies their usage. All loads would only be turned on when required. For example, if during the class there was enough sunlight to light the room, lamps will not be used. All the loads in the school building would be turned off when there is no occupant in the room, except for the equipments that need 24 hours operation like refrigerator.

#### *4.1.4 Users' Opinions*

All of the respondents voted that technology gives benefit and impact to their lifestyle and the learning environment. Nowadays, the teaching and learning process is more comfortable as teachers can use interactive teaching methods using computers and projector at anytime during the school period. Besides, the teachers and pupils can get access to the internet from the already installed satellite communication system (Very Small Aperture Terminal – VSAT). There is no case of damage electronic equipments after the installation and for teachers who live in the teachers' quarters; they can access the latest news and entertainment from the television and radio, store food in the refrigerator, and stay awake for more time during the night. As for the pupils, they can have extra classes during the night especially for pupils who will sit for the national primary school examination.

The respondents believe that the nearby village should be connected by renewable energy technology especially the solar hybrid system. They believe that, electricity is an important element for developing a community and nation and therefore can bridge the development gap between the urban and rural areas in economy, education, lifestyle, communication and etc.

#### 4.2 Design and Actual Load Analysis

Figures 3 and 4 below show the comparison of the load profile for both schools.

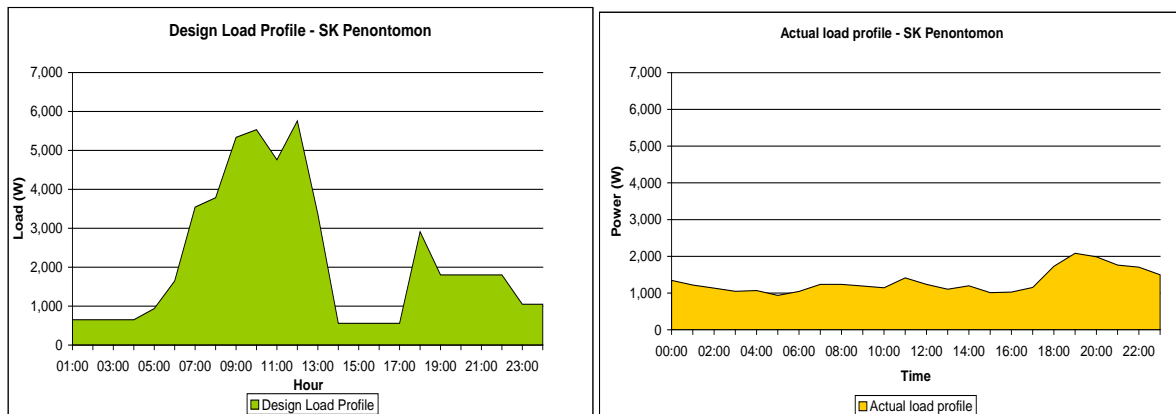


Figure 3 and 4 : The design load profile [6] (left) and the actual load profile (right) for SK Penontomon. The actual load profile was calculated based on the load consumption in September 2009 recorded from the JSCADA system.

The actual base load (minimum load) for the school is double the value of the design base load. The maximum actual load is half the value of the design load. The maximum actual load for SK Penontomon occurred at night instead of day as assumed in the design profile.

The total daily energy consumption was less 30% than the design values. The actual energy consumption at SK Penontomon was higher at night. The reason is the teachers' quarters in SK Penontomon contribute 41% of the total load sharing.

#### 4.2 System Operation Analysis.

Parameter that can determine the reliability of the PV system to supply electricity to the load is *Loss of Load (LL)*. Moreover, another two useful parameters are the *Generator Capacity,  $C_A$*  and the *Accumulator Capacity,  $C_S$* . " $C_A$ , is defined as the ratio of the daily energy output of the PV generator divided by the daily energy consumption of the load" [3]. " $C_S$  is the maximum energy that can be extracted from the accumulator divided by the daily energy consumption of the load" [3]. Hence the equations will be;

$$C_A = \frac{E_{PV}}{L} \quad (1)$$

$$C_S = \frac{C_U}{L} \quad (2)$$

Where  $E_{PV}$  is the daily energy output of the PV generator,  $L$  is the daily energy consumption of the load and  $C_U$  is the maximum energy that can be extracted from the battery. For rural electrification purposes as mentioned in [3], the values of both  $C_A$  and  $C_S$  are commonly used as  $C_A \approx 1.1$  and  $3 \leq C_S \leq 5$ . But  $C_A$  is also depending on the local solar climate condition.

*Solar fraction*, also known as renewable energy fraction, is the amount of energy provided by the solar technology system divided by the total energy required [5]. This shows the system dependency on the diesel generator as compared to the solar PV.

The *battery energy efficiency*,  $\eta_{wh}$  is the ratio of the energy discharged from the battery to the energy charged to the battery within a certain period of time [3]. In this study, one month energy efficiency is calculated.

Table 1 : Summary of the system energy parameters for both systems.

Parameter	Symbol	SK Penontomon
Loss of load	LL	0 %
PV Generator capacity	$C_A$	1.57
Accumulator capacity	$C_S$	5.76
Solar Fraction	SF	92%
Battery Energy Efficiency	$\eta_{wh}$	94%

The system satisfies the entire load required. Loss of load value of zero shows that the system which consists of PV, storage and generator is reliable and can produce sufficient and sustainable energy to satisfy the electricity demand by users.

The combination of the PV and the generator shows that the system is not very dependent on the usage of the generator and allows a significant lower quantity of diesel used during the measurement. The data also showed that the system can work without any major problems.

#### 4.4 Economic Analysis

Generally, for either systems (diesel generator only or solar hybrid system), the Cost of Energy (COE) is depending on the size of the system. A bigger system capacity reduces the COE. But, it will also increase the investment cost.

The operating cost of both systems shows that the client will be burdened by the higher cost for operating the diesel generator system compared to the solar hybrid system. For solar hybrid system, the service and maintenance routine should be done at least twice a year excluding the corrective maintenance. The generator has less services every year since the operation hours is minimum.

Table 2: Result from Homer simulation on the economic aspect [4].

Parameters	SK Penontomon	
	Diesel generator	Solar Hybrid System
Investment cost	€134,371.00	€568,131.00
Cost of Energy	€3.83/kWh	€5.86/kWh
Operating cost	€59,787.00/yr	€49,415.00/yr
Diesel Generator energy produced	29.36 MWh/yr	2.06 MWh/yr
Diesel consumption	12,514.00 L/yr	778.00 L/yr
Cost of Diesel <sup>1</sup>	€18,771.00/yr	€1,167.00/yr

Figure 5 below is the total cost of the project in twenty five years of its lifetime. It is based on the components cost including their replacement cost, civil works of building the power house, electrical works especially for mini grid installation, fuel cost and the operation and maintenance costs. Replacement of batteries is considered in every 6 years, diesel generator in 8 years and inverter and charge controller in 15 years [3]. It is clearly shows that the batteries are the most important component of the system as it contributes 45% of the lifetime project cost.

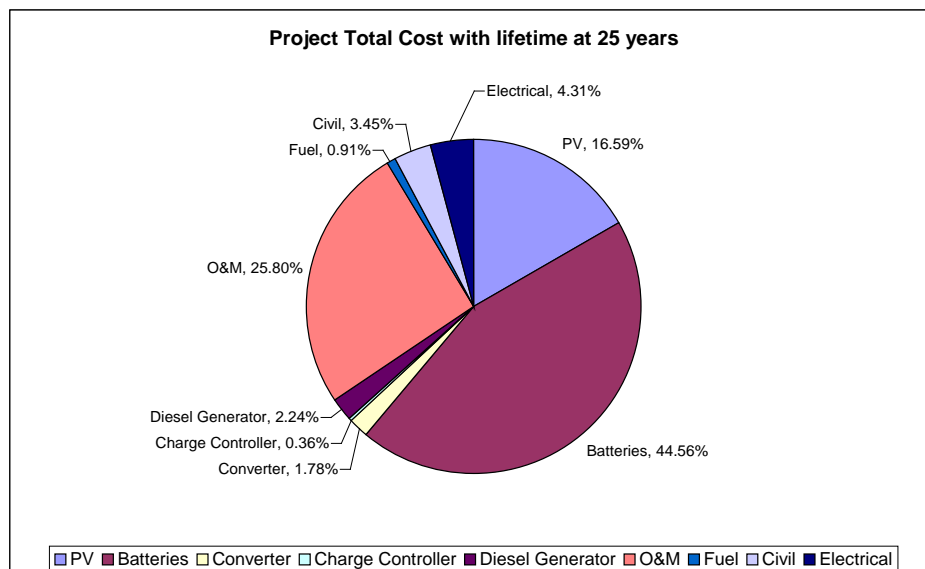


Figure 5 : Project total cost of the solar hybrid system. The project lifetime is at 25 years.

<sup>1</sup> Diesel price is assumed at €1.50 per litre of diesel at the sites. The diesel selling price in Malaysia is at € 0.34/litre due to subsidized by the government. The higher price as compared to the normal selling price is due to logistic cost to supply the diesel to the remote areas.

## 5. Conclusion

In general the solar hybrid system offers better electricity in providing power supply to the rural schools than the old and conventional diesel generator system. The technology gives benefit and impact to the pupils and teachers by creating more comfortable lifestyle and conducive learning environment.

The measurements and simulation of the system shows that the solar hybrid system can produce reliable power supply to meet the electricity need of rural schools. The system was designed and configured correctly but predicting the load pattern to be as accurate as the actual load consumption has always been the challenging part.

The combination of the PV-batteries-generator reduces the dependency of the fuel consumption and fully utilizes the clean energy from the sun. Even though a diesel generator system costs less than a solar hybrid system, but the fact that its operating costs in providing a proper service and maintenance makes the system less favorable compared to the solar hybrid system. The study shows that the heart of the system lies on the batteries as it contributes almost half of the total lifetime cost and almost half of the daily load consumption is served by the batteries. Improper conducts on the system may directly affect the batteries performance which may lead to the failure of the system.

## 6. Acknowledgement

My deepest gratitude to my supervisor; Mr. Hans Gerhard Holtorf of University of Oldenburg, Germany, my family, officers/friends at Electrical Engineering Branch, Public Works Department of Malaysia, and Public Service Department of Malaysia for sponsoring my study. Also thanks to my entire PPRE and EUREC classmates.

## References

- [1] *National Green Energy Technology Policy*, (2009), Ministry of Energy, Green Technology and Water, Malaysia.
- [2] United Nation Development Programme – Malaysia, *MDG7 – Achieve Universal Primary Education*, <http://www.undp.org.my/>
- [3] Luque, L., Hegedus, S., (2003), *Handbook of Photovoltaic Science and Engineering*, Wiley.
- [4] National Renewable Energy Laboratory, *HOMER – The Micropower Optimization Model*, <http://www.nrel.gov/homer>
- [5] Wikipedia, *Solar Saving Fraction*, [http://en.wikipedia.org/wiki/Solar\\_fraction](http://en.wikipedia.org/wiki/Solar_fraction)
- [6] Public Works Department of Malaysia, (2008), *Cadangan Merekabentuk, Membina, Membekal, Menyiapkan dan Menyelenggara Sistem Solar Hibrid Bagi Sekolah Luar Bandar Negeri Sabah Pakej 1 (Design, Build, Supply, Commission and Maintain of the Solar Hybrid System for Rural Schools in Sabah Package 1)*, Contract Document.

## Analysis of dust losses in photovoltaic modules

J. Zorrilla-Casanova<sup>\*1</sup>, M. Piliouguine<sup>1</sup>, J. Carretero<sup>1</sup>, P. Bernaola<sup>1</sup>, P. Carpena<sup>1</sup>,  
L. Mora-López<sup>2</sup>, M. Sidrach-de-Cardona<sup>1</sup>

<sup>1</sup> Dpto. de Física Aplicada II, Universidad de Málaga, 29071 Málaga, Spain

<sup>2</sup> Dpto. de Lenguajes y Ciencias de la Computación, Universidad of Málaga, 29071 Málaga, Spain

\* Tel: 34- 95-213-2772 , Fax: 34-95-213-1355, Email: ppz@ctima.uma.es

---

**Abstract:** The accumulation of dust on the surface of a photovoltaic module decreases the radiation reaching the solar cell and produces losses in the generated power. Dust not only reduces the radiation on the solar cell, but also changes the dependence on the angle of incidence of such radiation. This work presents the results of a study carried out at the University of Malaga to quantify losses caused by the accumulation of dust on the surface of photovoltaic modules. Our results show that the mean of the daily energy loss along a year caused by dust deposited on the surface of the PV module is around 4.4%. In long periods without rain, daily energy losses can be higher than 20%. In addition, the irradiance losses are not constant throughout the day and are strongly dependent on the sunlight incident angle and the ratio between diffuse and direct radiations. When studied as a function of solar time, the irradiance losses are symmetric with respect noon, where they reach the minimum value. We also propose a simple theoretical model that, taking into account the percentage of dirty surface and the diffuse/direct radiation ratio, accounts for the qualitative behavior of the irradiance losses during the day.

**Keywords:** optical losses, dust effects, energy losses

---

### 1. Introduction

The accumulation of dust on the surface of the photovoltaic modules decreases the incoming irradiance to the cell and produces power losses (see [1] and references therein). Previous studies [2] show that in dry areas, these losses could reach 15%. In these cases the only solution is to clean the modules with water. In large-scale photovoltaic plants this task is often expensive, especially in those areas with water shortage.

Some approaches to analyze and quantify the effect of dust on photovoltaic modules have been proposed in the literature. The early studies about the relationship between dust and transmittance date back to a few decades ago, all of them in the context of solar thermal collectors. For example, in [3], the effect of dust on the irradiance received by various inclined surfaces of flat-plate collectors have been studied. The performances of one photovoltaic and two thermal panels during several months of outdoor exposure in Saudi Arabia have been measured in [4]. For the photovoltaic panel, the average degradation rate of the efficiency was 7% per month. The authors of [5] made an experimental study of the effect of accumulation of dust on the surface of photovoltaic cells. Several kinds of dust having different physical properties were used. Experiments were performed using a solar simulator. They concluded that the results depend on many factors like the principal dust material, the size of dust particles and dust deposition density. We can see in [6] a computerized microscope system that has been developed for studying the physics of dust particles, which adhere to the surface of solar collectors and photovoltaic modules. The device enables investigators to calculate the particle size distribution of dust and the fraction of surface area covered by dust. Some examples are given for the use of such a measuring system for the study of photovoltaic and solar-thermal collector surfaces. Wind tunnel experiments were described in [7] to study the effect of wind velocity and air dust concentration on the drop of photovoltaic cell performance caused by dust accumulation on such cells. I-V characteristics were determined for various intensities of cell pollution. The evolutions of the  $I_{sc}$ ,  $V_{oc}$ ,  $P_{max}$ , and  $FF$  were examined.

This work presents measurements of radiation losses produced by the accumulation of dust. The experiment has been carried out at the roof of the Photovoltaic Laboratory of the University of Málaga (latitude 36.7 °N, longitude 4.5 °W, altitude 50 m) in the south of Spain. The campus is located between a residential and an industrial area surrounded by open fields with shrubs, weeds and some olive trees. Several roads with heavy traffic flow are very close to the building. At the time of the measurements, some excavations have been conducted in the vicinity of the building, which has increased the amount of inorganic dust particles present in atmospheric air.

## 2. Methodology

The objective of this work is to quantify losses caused by the accumulation of dust on the surface of photovoltaic modules. With this aim, irradiance values measured by two mSi cells have been recorded every ten minutes during a year. These cells have been previously calibrated against a reference pyranometer Kipp and Zonen CMP21. One of the reference cells has been cleaned daily, while the other has not been cleaned throughout the experiment (one year). Other parameters, such as rainfall and wind speed have been also measured.

Each reference cell has a low value shunt resistor between its terminals, and then the voltage drop across the shunt must be proportional to the short-circuit current and so it is further proportional to solar irradiance on the cell. The determination of the calibration constant for each cell is based on a comparison with a reference pyranometer under natural sun along a clear-sky day (only values of irradiance greater than 200 Wm<sup>-2</sup> have been taken into account). Both sensors (the reference cells and the pyranometer) are connected to an A/D module (cFP-AI-112) installed in Compact FieldPoint cFP-2120 data acquisition system that have been programmed to store a measure of all sensors at one-minute intervals. The manufacturer of the pyranometer provides a sensitivity constant that must be used to determine the actual irradiance value from the voltage its voltage output. Finally, a linear regression (setting offset to zero) between voltage values across each shunt and irradiance value have been performed to determine each constant.

Once the calibration procedure has been performed both cells remained installed and connected to the acquisition data system and measures of both of them have been recorded every three minutes along one year. The output value of each cell has been multiplied by the constant obtained by the calibration procedure in order to get the irradiance. Whereas one of them has been cleaned manually every day, the other cell has only been cleaned by rain. As well as registering irradiance values, the irradiation value along each day has been computed using trapezoidal integration too.

By comparing recorded irradiance values sensed by the two reference cells, dust influence on the received radiation can be quantified, and as consequence its effects on the solar energy received in the cell. Daily irradiation losses caused by dust are calculated comparing irradiation values sensed by the clean and the dirty cells. The two calibrated cells and the pyranometer are placed on a plane whose tilt angle is 30° (see Fig. 1). The period of measurements comprises from 12/15/08 to 12/14/09. Along that period, summer was dry without any rain, and winter and spring had rainfall more frequent than usual for this period. An autumn with low rainfall completes the meteorological period. The availability of data for the studied period has been 96.4%.

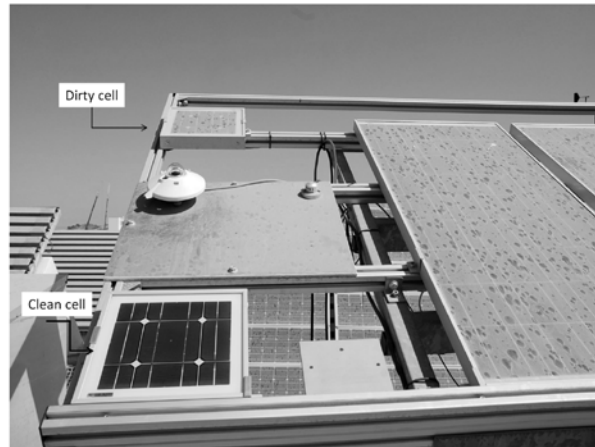


Fig. 1. The experimental setup used in the measurements.

### 3. Results

#### 3.1. Irradiation daily losses

The evolution of the irradiation daily losses along the year of measurements is shown in Fig. 2. These losses ( $HL$ ) represent the fraction of daily energy that a PV module will not receive as consequence of dust deposited on their surface, and are calculated as

$$HL(\%) = 100 \times \left( \frac{H_{CC} - H_{DC}}{H_{CC}} \right) \quad (1)$$

where  $H_{CC}$  is the daily irradiation measured by the clean reference solar cell ( $W\ h\ m^{-2}$ ) and  $H_{DC}$  is the daily irradiation measured by the dirty cell ( $W\ h\ m^{-2}$ ). As can be seen in Fig. 2, the losses produced by the presence of dust are strongly dependent on the rainfall. In rainfall periods, a good cleaning of the dirty cell is produced and it recovers its initial performance; even a light rain, below 1 mm, is enough to clean the cover glass, reducing daily losses  $HL$  below 5%. However, in long periods without rain, like summer, the accumulation of dust can cause daily losses exceeding 20%.

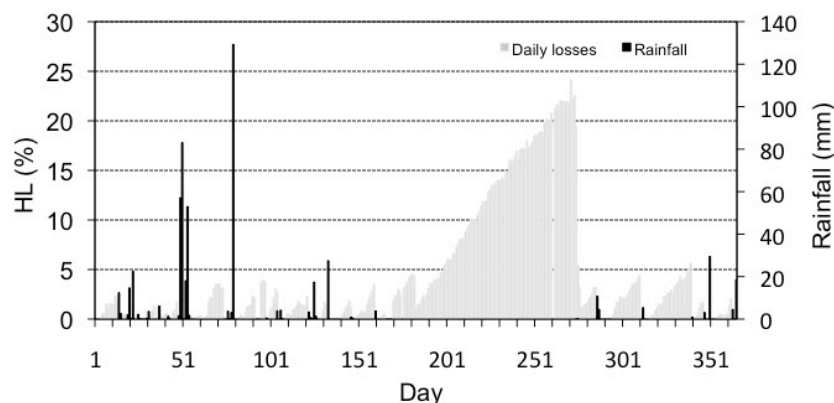


Fig. 2.  $HL$  values for all days of measurements along a whole year (left axis). We also plot daily values of rainfall (right axis).

The mean of the daily energy losses along a year caused by dust is 4.4%. Monthly averages of daily energy losses are lower than 2% except in summer months, when the lack of rain favors the accumulation of dust and causes the increase of losses above 15%. Note that the energy

production reaches its maximum in these summer months, and therefore the possible adverse effect of dust is very relevant.

### 3.2 Evolution of the dust losses along the day

As seen in the last section, accumulations of dust on the surface of a photovoltaic module reduce strongly the energy received. We have not observed any influence of the wind speed or direction on the losses, probably because the high relative humidity contributes to the adherence of the dust particles on the module surface. As shown in previous studies [7-10], these losses should not be constant during the day, but have to be dependent on the incidence angle of beam radiation. In order to study this dependency, irradiation values sensed by the clean and the dirty cells throughout the day are compared. In this case, relative irradiance losses are calculated as:

$$GL (\%) = 100 \times \left( \frac{G_{CC} - G_{DC}}{G_{CC}} \right) \quad (2)$$

where  $G_{CC}$  is the irradiance value measured by the clean reference solar cell ( $\text{W m}^{-2}$ ) and  $G_{DC}$  is the irradiance value measured by the dirty reference solar cell ( $\text{W m}^{-2}$ ). It should be pointed out that losses caused by the dependence of the transmission coefficient of the glass cover on the angle of incidence does not affect in the calculation of  $GL$  since it is identical in both cells. However, the presence of dust modifies the angular dependence of the irradiance, which is different for the clean and the dirty cell, and precisely this effect is measured with  $GL$ .

These losses represent the fraction of irradiance that the cell will not receive, and in the case of PV modules, power losses. When cells are clean, losses are approximately constant during the day. As dirt is deposited on the dirty cell, the behavior of the losses is not constant throughout the day in clear sky days, becoming dependent on the angle of incidence. Daily evolution of dust losses on the 08/06/09 is shown in Fig. 3. This is a clear sky summer day, almost two months after the last rains; as consequence, dust level deposited on the dirty cell surface is high, causing daily losses of 14.8%.

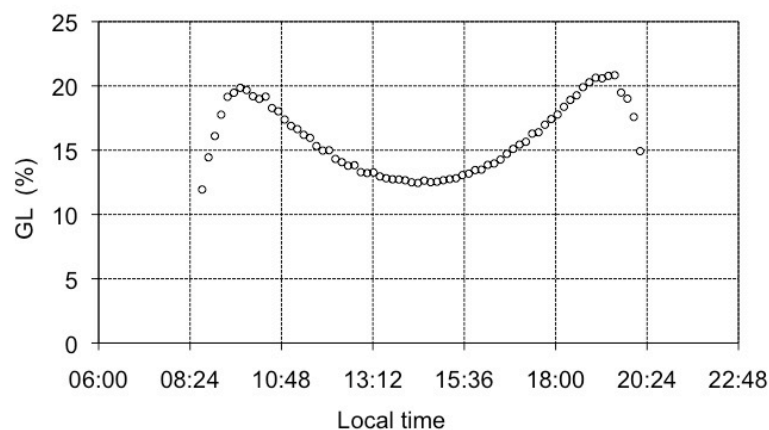


Fig. 3. Relative irradiance losses ( $GL$ ) along a day.

The typical behavior of  $GL$  as a function of the incident angle ( $\theta$ ) is shown in Fig. 4. In this figure, we plot  $GL$  curves obtained in several days with different  $HL$  values (i.e. with different amounts of dust). As expected, losses are strongly dependent of the incident angle of radiation. Minimum transmittance losses occur at noon (12.4%) when the incident angle is

minimum. As incidence angle increases, losses increases slowly, but the growth rate increases as the angle. Nevertheless, from an angle of about 60°, losses remain almost constant for a window of about 10° and then, after a maximum of about 21%, they decrease. This occurs at first and last hours of the day, when incidence angle is between 60-80° and irradiance value is about 200 Wm<sup>-2</sup>. (Note that morning maximum is slightly lower than afternoon maximum; the cause is that calibrated cells are no exactly in the same plane an there are a little bench between them). Dependence of dust losses with the angle is shown in Fig. 4.

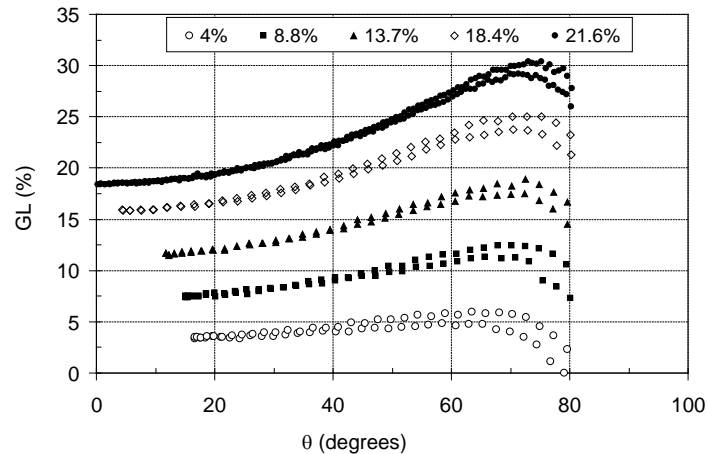


Fig. 4. Dependence of *GL* with the angle of incidence ( $\theta$ ) for several days with different *HL* values.

This behavior is related with the proportion of diffuse irradiance on global irradiance in the early morning and evening, when its value increases. In section 4, a theoretical model justifies this behavior. On cloudy days, when the global irradiance is mainly diffuse irradiance, losses remain almost constant throughout the day. Diffuse irradiance has not specific direction and hence losses are not dependent on the incidence angle.

Table I summarizes *HL*,  $\theta$  and *GL* at solar noon and the maximum value of *GL* for each day shown in Fig. 4. Values of *HL* are between 4.0% for the first day and 21.6% for the last day. It can be noticed that all the shape of the curves is generic and it is not dependent on the *HL* value.

Table I. Measured parameters of Fig. 4

Date	<i>HL</i> (%)	$\theta$ at solar noon (degrees)	<i>GL</i> at solar noon (%)	<i>GL</i> maximum (%)
27/06/2009	4.0	17.0	3.5	5.9
13/07/2009	8.8	15.1	7.5	12.5
30/07/2009	13.7	11.7	11.7	18.9
23/08/2009	18.4	4.4	16.0	25.0
04/09/2009	21.6	0.2	18.4	30.4

#### 4. Modeling the losses produced by the dirt

We have developed a simple model to justify the shape of the typical behaviour of the relative transmittance losses due to the presence of dust in the solar cell (see Fig. 3). The model is based on the following assumptions:

- a) Dust grains are modelled as spheres homogeneously distributed on the surface of the panel.
- b) Each sphere has a reflection coefficient  $R$ , which accounts for both specular and diffused reflection.
- c) Total incoming radiation from the Sun ( $I_T$ ) is composed of direct radiation ( $I_0$ ) and diffuse radiation ( $I_D$ ). We consider that this latter radiation comes homogeneously from any direction and it is kept constant along the day. Note that the total irradiance received by a clean solar cell is given by:

$$G_{CC} = I_0 \cos\theta + I_D \quad (3)$$

where  $\theta$  is the angle of incidence of direct radiation on the panel. The albedo radiation has been neglected.

- d) In the dirty solar cell, any sphere of dust shadows the panel thus reducing the light reaching it. However not all radiation reaching the spheres is lost because part of it is reflected (a factor  $R$ ) and can be partially recovered by the panel. Both effects, the shadowing and the recovery of light, depend on the angle of incidence of the direct radiation and thus vary along the day. On the other hand, there is no such dependence in the diffuse radiation since we assume that  $I_D$  is constant along the day.

To quantify the irradiance losses  $GL$  due to the presence of dust in the solar cell we use Eq. (2). In order to understand the effect of the dust on the losses we have to analyse separately the direct and diffuse radiations.

#### 4.1. Direct radiation

For the direct radiation the shadowing increases with the angle of incidence, reaching the maximum for  $\theta = 90^\circ$ . At the same time, the fraction of the light specularly reflected reaching the panel increases with  $\theta$  up to a maximum value and finally decreases for very large  $\theta$ . On the other hand, the fraction of light diffusely reflected reaching the panel is constant because the direction of the reflected rays is independent of the angle of incidence. The sum of all these contributions is not evident and therefore we simulate the phenomenon using a ray tracer [11]: For each angle of incidence  $\theta$  we trace  $10^6$  rays reaching a square cell of unit area with a single sphere on its center. We impose periodic boundary conditions. The reflection coefficient of the spheres is set to  $R = 65\%$  (19.5% specular and 45.5% diffuse), and the radius of the sphere is set to  $r = 0.315$  units, which is equivalent to a coverage of 31.17% of the surface of the cell. In Fig. 5 we show  $GL$  as a function of the angle of incidence for this simulation (dashed line). The values of the parameters are physically acceptable and have been chosen in order to fit the experimental results (also shown in Fig. 5) for small angles of incidence. As can be observed, the model does not reproduce at all the behaviour of  $GL$  for large angles of incidence. In particular it gives a monotonously increasing  $GL$  while the experimental one reaches a maximum and decreases for very large angles of incidence.

#### 4.2. Diffuse radiation

As we see, the contribution of direct radiation alone does not suffice to explain the experimental results. Therefore we incorporate the diffuse radiation to the model. Again we generate and trace  $10^6$  rays with directions uniformly distributed. The total amount of energy carried by these rays is equivalent to 23% of the total radiation that would reach the cell under normal incidence. When these rays are included in the simulation (solid line in Fig. 5)

the result obtained for  $GL$  agrees fairly well with the experimental results and in particular, it reproduces the reduction of the losses observed at large angles of incidence.

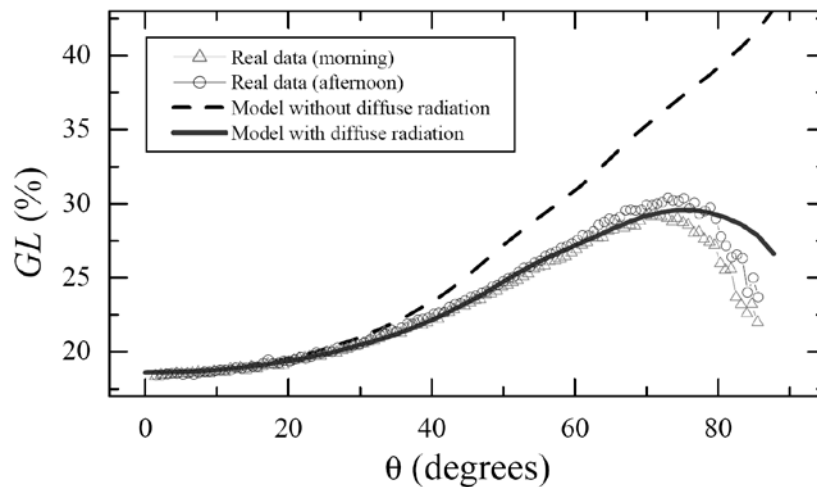


Fig.5. Relative irradiance losses of a dirty solar cell as a function of the angle of incidence of solar direct radiation. Hollow triangles (circles) correspond to real data measured in morning (afternoon) hours on the 4<sup>th</sup> of September, 2009 (Malaga, Spain). Dashed line corresponds to the results obtained with a simulation (see text for details) in which diffuse radiation is not considered whereas the solid one has been obtained by taking into account this radiation.

#### 4. Conclusions

In this work we have studied in general the energy losses due to accumulated dust on the surface of photovoltaic modules. First, we present results about daily irradiation losses and we show that the mean value of this quantity along a whole year is about 4.4%. In rainfall periods, the rain water cleans the dirty cell and it recovers its normal performance: even a light rain, below 1 mm, is enough to clean the cover glass, reducing daily losses  $HL$  clearly below the average value of 4.4%. However, in long periods without rain, like summer, the accumulation of dust can cause daily losses exceeding 20%.

Second, we present results of the dust-caused irradiance losses  $GL$  and its dependence on the angle of incidence  $\theta$ . The curve that describes the dependence of these losses on the angle of incidence has a very specific shape:  $GL$  has a minimum at solar noon, then increases with  $\theta$  up to a maximum value found when  $\theta \approx 75^\circ$ , and then decreases for larger values of  $\theta$ . This behavior can be explained by the influence of the diffuse radiation.

In addition, we have presented a simple model, simulated with the ray-tracing technique, to explain the behavior of losses in solar modules due to the presence of dust. With this model we have shown the relevance of diffuse radiation in order to understand the full behavior of losses as a function of the angle of incidence. Indeed, when only direct radiation is considered the model does not provide results comparable to experimental measures. On the other hand, when diffuse radiation is also taken into account, the model reproduces quite well the shape of the experimental data for reasonable values of the input parameters.

We conclude that the estimation of energy losses produced by the presence of dust have to be calculated in a different way for photovoltaic systems with fixed modules or with solar-tracking. In addition, the proportion of the diffuse component in the global radiation must be taken into account when estimating the energy losses produced by the dust on the system energy performance.

Finally, it is very important to quantify energy losses produced by dust in dry areas where such losses could reach large values and so producing a substantial decrease in the efficiency of photovoltaic systems. In these cases a regular cleaning of the modules would be necessary thus increasing maintenance costs.

### Acknowledgements

We acknowledge the Spanish “Ministerio de Ciencia e Innovación” (grant No. ENE07-67248) and “Junta de Andalucía” (grant No. P07-RNM-02504) for financial support.

### References

- [1] M. Mani, R. Pillai. Impact of dust on solar photovoltaic (PV) performance: Research status, challenges and recommendations, *Renewable and Sustainable Energy Reviews* 14, 2010, pp. 3124-3131.
- [2] M. Piliouge, J. Carretero, M. Sidrach-de-Cardona, D. Montiel, P. Sánchez-Friera. Comparative analysis of the dust losses in photovoltaic modules with different cover glasses. *Proceedings of 23rd European Solar Energy Conference*, 2008, pp. 2698-2700.
- [3] H.P. Garg, Effect of dirt on transparent covers in flat-plate solar energy collectors, *Solar Energy* 15 (4), 1974, pp. 299-302.
- [4] S.A.M. Said, Effects of dust accumulation on performances of thermal and photovoltaic flat-plate collectors, *Applied Energy* 37 (1), 1990, pp. 73-84.
- [5] M.S. El-Shobokshy, F.M. Hussein, Effect of dust with different physical properties on the performance of photovoltaic cells, *Solar Energy* 51 (6), 1993, pp. 505-511.
- [6] S. Biryukov, D. Faiman, A. Goldfeld, An optical system for the quantitative study of particulate contamination on solar collector surfaces, *Solar Energy* 66 (5), 1999, pp. 371-378.
- [7] D. Goossens, E. Van Kerschaever, Aeolian dust deposition on photovoltaic solar cells: the effects of wind velocity and airborne dust concentration on cell performance, *Solar Energy* 66 (4), 1999, pp. 277-289.
- [8] N. Martin, J.M. Ruiz, Calculation of the PV modules angular losses under field conditions by means of an analytical model, *Solar Energy Materials & Solar Cells* 70, 2001, pp. 25-38.
- [9] M. García, L. Marroyo, E. Lorenzo, M. Pérez, Soiling and other optical losses in solar-tracking PV plants in Navarra, *Progress in Photovoltaics: Research and Applications*, DOI: 10.1002/pip.1004.
- [10] N. Martin, J.M. Ruiz, Annual angular reflection losses in PV modules. *Progress in Photovoltaics: Research and Applications* 13, 2005, pp. 75-84.
- [11] A.S. Glassner (Ed), *An introduction to ray tracing*, Academic Press, 1993.

## An experimental study of combining a photovoltaic system with a heating system

R. Hosseini<sup>1,\*</sup>, N. Hosseini<sup>2</sup>, H. Khorasanizadeh<sup>2</sup>

<sup>1</sup> Amirkabir University of Technology (Tehran PolyTechnic), Tehran, Iran

<sup>2</sup> University of Kashan, Kashan, Iran

\* Corresponding author. Tel: +98 (21)64543433, E-mail:hoseinir@aut.ac.ir

---

**Abstract:** Solar photovoltaic and thermal systems are potential solutions for current energy needs. One of the most important difficulties in using photovoltaic systems is the low energy conversion efficiency of PV cells and, furthermore, this efficiency decreases further during the operational period by increasing the cells temperature above a certain limit. In addition, reflection of the sun's irradiance from the panel typically reduces the electrical yield of PV modules by 8-15%. To increase the efficiency of PV systems one way is cooling them during operation period. In this experimental study combination of a PV system cooled by a thin film of water with an additional system to use the heat transferred to the water has been considered. Experimental measurements for both combined system and conventional panel indicate that the temperature of the photovoltaic panel for combined system is lower compared to the conventional panel. The results show that the power and the electrical efficiency of the combined system are higher than the traditional one. Also since the heat removed from the PV panel by water film is not wasted, the overall efficiency of the combined system is higher than the conventional system.

**Keywords:** Cooling PV systems, Electrical efficiency, Combined system, Overall efficiency

---

### 1. Introduction

Environmental problems due to extensive use of fossil fuels for electricity production and combustion engines have become increasingly serious on a world scale in recent years. To solve these problems, renewable energy sources have been considered as new sources of clean energy. Solar energy is one of the most important sources among the renewable energies. Generally, solar energy conversion systems can be classified into two categories: thermal systems which convert solar energy into heat and photovoltaic systems which convert solar energy to electricity.

Intensive efforts are being made to reduce the cost of photovoltaic cell production and improve efficiency and narrow the gap between photovoltaic and conventional power generation methods such as steam and gas turbine power generators. In order to decrease the cost of PV array production, improve the efficiency of the system and collecting more energy for unit surface area different efforts have been made.

The performance of the PV system is affected by several parameters including temperature. The part of absorbed solar radiation that is not converted into the electricity converts into thermal energy and causes a decrease in electrical efficiency. This undesirable effect which leads to an increase in the PV cell's working temperature and consequently causing a drop of conversion efficiency can be partially avoided by a proper method of heat extraction. PV/T solar systems consisting of photovoltaic modules and thermal collectors are applied to cool photovoltaic panel and use the heat generated by the panel and increase total energy output of the system. By proper circulation of a fluid with low inlet temperature, heat is extracted from the PV modules keeping the electrical efficiency at satisfactory values. The extracted thermal energy can be used in several ways, increasing total energy output of the system. Many researchers have investigated and proposed different methods for design and optimization of the PV/T systems to improve the

system efficiency by cooling PV module and collecting more energy. The main concepts of hybrid PV/T systems have been presented by several researchers since 1978 [1-5]. Tripanagnostopoulos [6] studied hybrid PV/T solar systems experimentally and used water and air to extract heat from the PV module rear surface. He used a hybrid system with air duct under the PV module for heat extraction with air circulation and another hybrid system with thermal unit of water circulation through a heat exchanger. In the system he tested, water was circulated in pipes with the flat surface of a copper sheet placed at the rear surface of the PV module and in thermal contact with it. Kalogirou and Tripanagnostopoulos [7] proved analytically the potential benefits of PV/T systems compared to typical PV modules and presented justification of energy and cost results regarding system application. Their method could be considered as an estimation of the cost effectiveness of new solar energy systems in practice.

One method for cooling photovoltaic module is to flow a film of water over the PV module to decrease its temperature. By using this method reflection would also be reduced and therefore the electrical efficiency will improve. Krauter [8] studied the effects of cooling photovoltaic array surface with film of water on the power generated by the array. Abdolzadeh and Ameri [9] improved the operation of a photovoltaic water pumping system by spraying water over the front of the photovoltaic cells. Kordzadeh [10] studied the effects of nominal power array of 90 and 135 W on 16 m head of water pumping system on panel efficiency as well as the panel efficiency for 135W nominal power output on different heads of pumping system. A thin continuous film of water was running on the top of the PV panel without water being recirculated. The advantage of the later system (thin water running on top of the photovoltaic array) is obtaining better electrical efficiency because of decreasing the reflection loss, in addition to decreasing temperature of the array. The disadvantage of this system is that the heat gained by the water running on top of the photovoltaic array is wasted.

The aim of the present experimental research is to consider the combination of a PV system equipped with cooling system consisting of a thin film of water running on the top surface of the panel with an additional system to use the hot (or warm) water produced by the system.

## **2. Experimental procedure**

The experimental setup is composed of two similar but separate PV solar photovoltaic panels each with area of  $0.44 \text{ m}^2$ . The maximum output voltage and current are respectively 23V, 2.61A and with maximum power output of 60W. One of the panels is used in a combined system with a film of water running over its top surface without front glass and an additional fabricated system to use the heat generated by the panel. The other panel is a conventional PV as a reference panel. To produce a film of water over the photovoltaic panel, a tube with a slit along it has been installed on the top end of the photovoltaic panel (see Fig. 1). Water pumped to the feeding tube, leaves the slit and flows over the panel as a thin film. Power of the pump for circulation of water is 0.25 hp. The water collected at the lower end of the panel passes through a finned tube used as a heat exchanger and consumer of heat gained by the water. Another role of this finned tube is to dissipate heat to the environment and produce a constant low water temperature. Therefore when the water is pumped back to the feeding tube it would be at a desired temperature level to flow on the panel surface. The flow rate is 1 lit/min. Pumping system and the heat exchanger which are used in the combined system are shown in Fig. 2.



*Fig. 1. Front view of solar photovoltaic panel equipped with water film producer.*



*Fig. 2. Pumping system and the heat exchanger of experimental combined Photovoltaic/Thermal (PV/T) system.*

Maximum power output was obtained by utilizing an optimized ohmic load ( $8.7 \Omega$ ). Current and voltage were measured by Omega type multimeter with accuracy of 1 miliampere and 1 milivolt respectively. Both panels were facing south with an angle of inclination of  $29^\circ$ . Irradiance was measured by a Kimo SL100 solar meter installed on the corner of one of the panels with the same angle of inclination. Ambient temperature was measured in the shade at specified intervals. Patch type thermocouples (k type) were installed on the back surface of the two panels. Temperature of the top surface of the reference panel was occasionally measured by a surface probe and was almost  $1.5^\circ\text{C}$  above the temperature of the back surface of the same panel. Therefore, the temperature difference between top and back surfaces of both panels was considered to be about  $1.5^\circ\text{C}$ . Standard thermocouples (k type) were used for measuring the temperature of the water before running over the panel and at the lower end of the panel. Temperature of the water coming out of the heat exchanger was also measured by installing a standard thermocouple (k type) at the end of the finned tube. Measurements have been performed simultaneously over 14 days during September, 2010 in Tehran (latitude  $35^\circ 41'$  and longitude  $51^\circ 25'$ ) and recorded every 10 minutes.

### 3. Results

In this section results of measurements on the 18th of September, 2010 have been presented and analyzed. Variation of irradiance received by the surfaces of the panels during the test day is shown in Fig. 3.

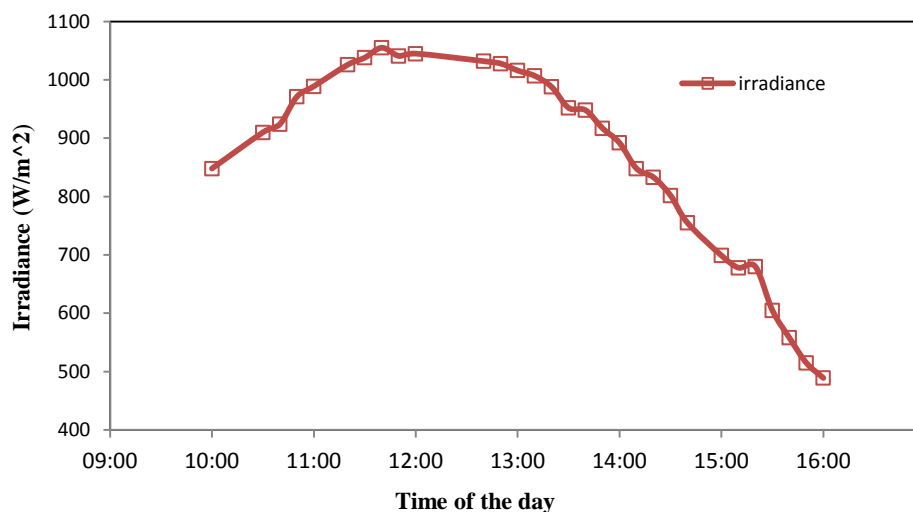


Fig. 3. Variation of irradiance during the test day.

Due to the water flow and additional cooling by water evaporation, the PV/T panel's operating temperature measured is much lower in comparison to the conventional reference panel. As could be seen in Fig. 4, maximum temperature difference of  $18.7^\circ\text{C}$  is observed. This temperature reduction has caused a noticeable improvement for electrical efficiency as shown in Fig. 5, such that for some hours the relative difference is more than 33%.

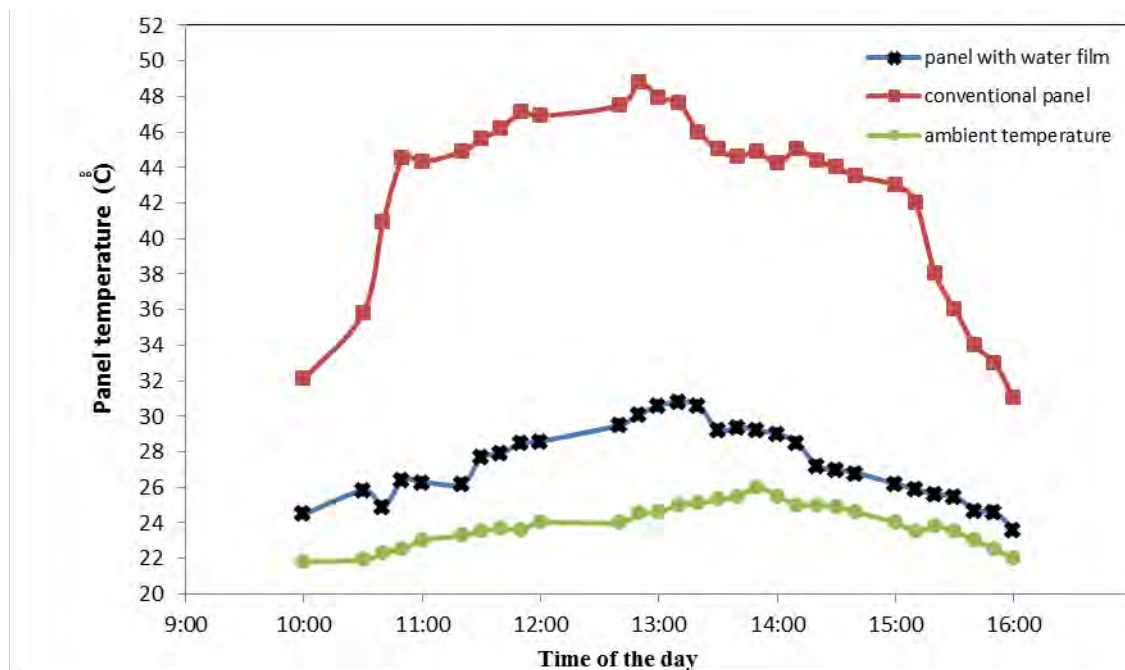


Fig. 4. Comparison of conventional photovoltaic panel temperature with the temperature of the panel in the combined system.

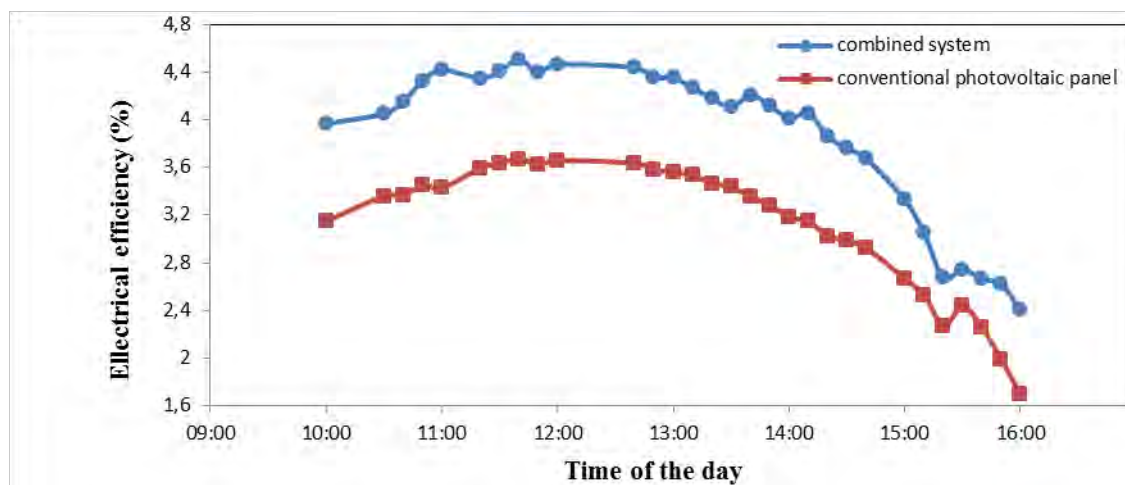


Fig. 5. Comparison of conventional photovoltaic panel electrical efficiency with the electrical efficiency of the combined system.

The experimental results showed that the continuous film of water on the surface of PV panel has two important effects on the operation of the system. First, it reduces the reflection of the solar irradiance. Second, it reduces the panel temperature by absorbing the heat generated by the panel. Temperature reduction is significant due to heat absorbed by the water. The heat removal from the PV panel by the water film increases the temperature of the water running over the panel surface and also causes evaporation. Calculations show that cooling is mainly by evaporation. In Fig. 6, temperature of the water before running down over the surface of the panel has been shown in comparison to temperature of the water collected at the lower end of the panel and temperature of the water coming out of the heat exchanger. As it is shown, the heat absorbed by

the water when running down the panel is removed when passing through the heat exchanger and the temperature reaches more or less to the water temperature at the top end of the panel.

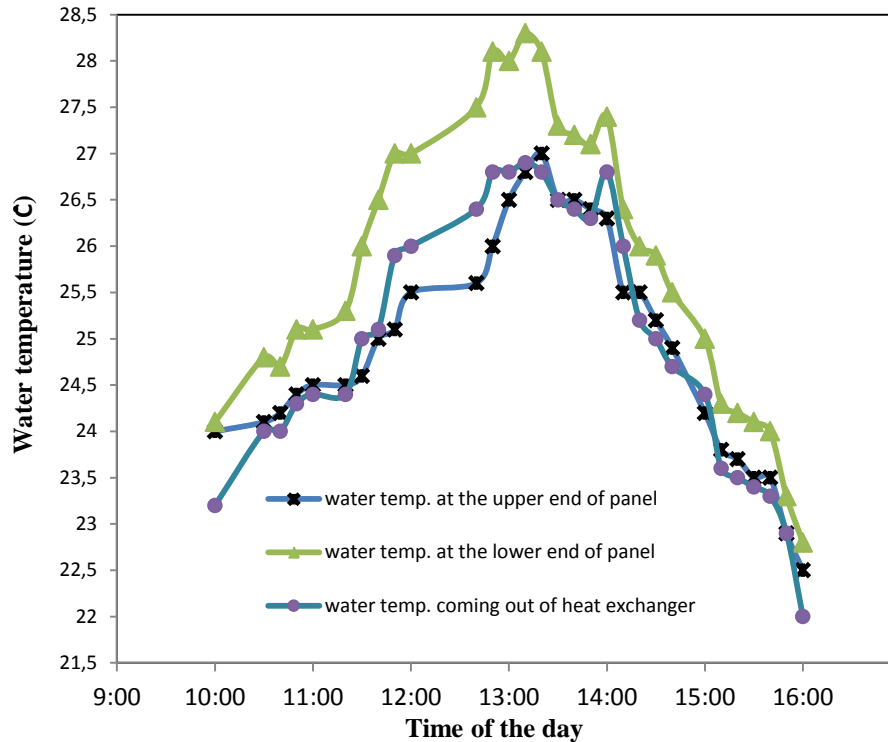


Fig. 6. Comparison of water temperature at the upper and lower ends of the panel and water coming out of the heat exchanger in the combined system.

Overall efficiency can be defined as the total energy output of the system compared to the radiant energy received by the system. For conventional system, total energy output of the system consists of electrical energy produced, but for the combined system it consists of both thermal and electrical energy produced. Thermal energy output is defined as the increase in the internal energy of the water running over the panel due to the increase in the temperature of the water ( $m \cdot c_p \cdot \Delta T$ ). Due to high specific heat of water the temperature increase is quite a bit. Also because of small surface area of the panel, the sensible heat added to water is a small amount. As could be seen in Fig. 7, there is a noticeable improvement in overall efficiency of the combined system in comparison to the conventional system.

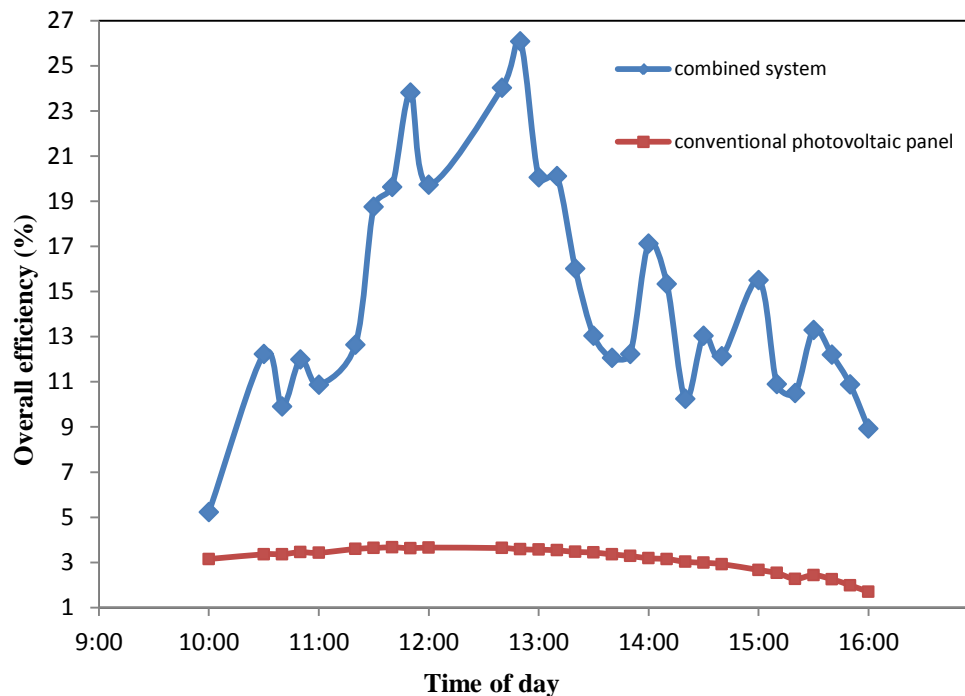


Fig. 7. Comparison of conventional photovoltaic panel overall efficiency with the overall efficiency of the combined system.

#### 4. Conclusion

The photovoltaic panel efficiency is sensitive to the panel temperature and decreases when the temperature of the panel increases. One of the ways for improving the system operation is covering the panel surface with a thin running film of water which decreases both reflection loss and temperature of the panel. Results of present work showed that while the temperature of the panel could be controlled at a desired temperature level, the water collected at the lower end of the panel can be used as a utility for heating purposes. Therefore when the water is pumped back to the upper end of the panel it would be at a desired temperature level to flow on the panel surface. In the combined system tested in this work, applying a film of water for cooling photovoltaic panel resulted in decreasing the temperature and reflection loss of the PV panel which increased electrical efficiency of the combined system. Also the heat removed by the water from the panel was used in a heat exchanger. Therefore, total energy output of the combined system (collected thermal and electrical energy for unite surface area) increased significantly compared to the electrical energy of the conventional photovoltaic panel. In this experimental study it has been shown that the overall efficiency of combined system at some hours is one order of magnitude more than the efficiency of conventional panel.

#### Acknowledgement

Special thanks to thermodynamic lab personals (technicians and instructors) in mechanical engineering department of Amirkabir University of Technology for their help and providing necessary facilities and measuring equipments. Also the financial support of Iranian Fuel Conservation Company is kindly acknowledged.

## **References**

- [1] E.C. Kern and M.C. Russel, Combined photovoltaic and thermal hybrid collector systems, Proceedings of the 13th IEEE Photovoltaic Specialists, 1978, pp. 1153–1157.
- [2] S.D. Hendrie, Evaluation of combined photovoltaic/thermal collectors, Proceedings of international ISES Conference, 1979, pp. 1865–1869.
- [3] L.W. Florschuetz, Extension of the Hottel-Whillier model to the analysis of combined photovoltaic/thermal flat plate collectors, Journal of Solar Energy 22, 1979, pp. 361–366.
- [4] P. Raghuraman, Analytical predictions of liquid and air photovoltaic/thermal, flat-plate collector performance, Journal of Solar Energy Engineering 103, 1981, pp. 291–298.
- [5] C. H. Cox and P. Raghuraman, Design considerations for flat-plate photovoltaic/thermal collectors, Journal of Solar Energy 35, 1985, pp. 227–241.
- [6] Y. Tripanagnostopoulos, Hybrid Photovoltaic/Thermal Systems, Journal of Solar Energy 72, 2002, pp. 217–234.
- [7] S.A. Kalogirou and Y. Tripanagnostopoulos, Industrial application of PV/T solar energy systems, Journal of Energy Conversion and Management 47, 2006, pp. 3368–3382.
- [8] S. Krauter, Increased electrical yield via water flow over the front of photovoltaic panels, Journal of Solar Energy Materials & Solar Cells 82, 2004, pp. 131–137.
- [9] M. Abdolzadeh and M. Ameri, Improving the effectiveness of a photovoltaic water pumping system by spraying water over the front of photovoltaic cells, Journal of Renewable Energy 34, 2009, pp. 91–96.
- [10] A. Kordzadeh, The effects of nominal power of array and system head on the operation of photovoltaic water pumping set with array surface covered by a film of water, Journal of Renewable Energy 35, 2010, pp. 1098–1102.